文部科学省 ハイテク・リサーチ・センター整備事業
(平成 17 年度～平成 21 年度)

工学院大学総合研究所

ナノ表面・界面研究センター

Nano Stuctured Surfaces and Interfaces Research Center

NASIC 中間報告会

平成 20 年 3 月

工学院大学総合研究所

目次

1. 生体分子のナノ表面

1．1 抗体および酵素を用いた微量生体成分の高感度分析法の確立

工学院大学工学部応用化学科　川喜田 正夫
工学院大学工学部応用化学科　今村 保忠
東京都臨床医学総合研究所がん治療プロジェクト　平松 恭子
都立駒込病院外科　高橋 慶一

Development of sensitive and accurate analytical systems for analysis of biomaterials utilizing the specificity of enzymes and antibodies

Masao Kawakita (Department of Applied Chemistry, Faculty of Engineering, Kogakuin University)
Yasutada Imamura (Department of Applied Chemistry, Faculty of Engineering, Kogakuin University)
Kyoko Hiramatsu (Tumor Therapy Project, Tokyo Metropolitan Institute of Medical Sciences)
Kei-ichi Takahashi (Department of Surgery, Tokyo Metropolitan Komagome Hospital)

N^1,N^{12}-Diacetylspermine (DiAcSpm), a minor component of urinary polyamines, was discovered through HPLC analysis using an enzymatic detection system, and was found to be elevated frequently in patients with various types of cancers. We developed an ELISA procedure using highly specific antibodies against DiAcSpm for more convenient measurement of DiAcSpm, and showed that it is much more sensitive in detecting early stage colorectal cancer than CEA and CA19-9. To establish urinary DiAcSpm test as an item for mass screening test we further attempted to develop a simpler analysis for urinary DiAcSpm utilizing aggregation of colloidal gold nanoparticles coated by anti-DiAcSpm antibody.

【研究の背景】

プトレッシン、カダベリン、スペルミジン、スペルミンなど複数のアミノ基をもつアルキルアミンをポリアミンと総称する。これらは活発に増殖する組織に多量に含まれ、またそのような組織で活発に代謝される [1]。ポリアミン合成欠損細胞はポリアミンを培地に加えてやらないと増殖することができず [2]、また、ポリアミン合成の律速酵素であるオルニチンデカルボキシラーゼ（ODC）を過剰発現させると細胞のトランスフォーメーションが起こることが知られている [3]。これらの事実はポリアミンが細胞増殖およびその制御に重要な役割を果たす物質の一つであることを示している。細胞の中で役割を果たしたポリアミンの一部はアセチル体として尿中に排泄される。したがって、がん組織のような活発に増殖する組織が体内にあると、ポリアミンの排泄量は増加することが期待される。事実、1971 年に Russell は、がん患者の尿中ポリアミン排泄量が増加することを報告し、尿中ポリアミンが腫瘍マーカーとして利用できる可能性があることを示唆した [4]。これを契機として多くの研究が行われる中で、1980 年代には酵素的定量法による尿中総ポリアミン測定キットが開発され、腫瘍マーカーへの期待をこめて一時は広く利用された。しかし、多数のデータが蓄積されるにつれて、「尿中総ポリアミン」は感度、がん特異度のいずれの面から見ても腫瘍マーカーとしては性能が不十分であるという評価が定着するようになり、1990 年代になると実用的な意味ではほとんどその地位を失ってしまった [5]。一方、我々は、尿中ポリア

ミン成分の HPLC による一斉分画と固定化酵素リアクターを用いたポリアミンの特異的定量法の組み合わせによる新たな測定法を開発し、新規の微量尿中ポリアミン成分 N^1,N^{12}-ジアセチルスペルミン（DiAcSpm）が存在することを見出した（Fig. 1）[6]。そして、その尿中レベルが、従来測定の対象であった各種の主要ポリアミン成分とは異なり、種々の悪性腫瘍において患者の病勢をよく反映した動きを示すことを明らかにして [7]、引き続き DiAcSpm を新規腫瘍マーカーとして臨床検査に利用するための研究を進めてきた。

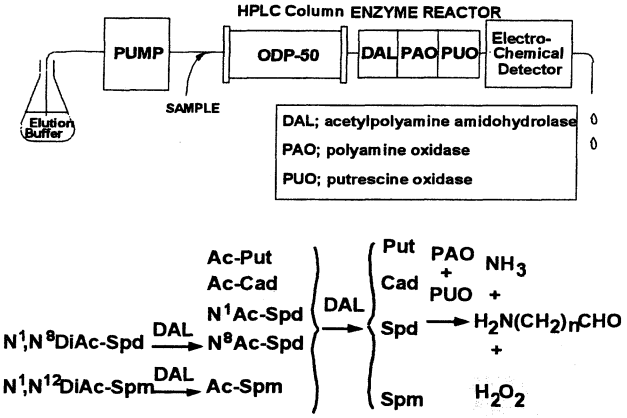

Fig. 1. A HPLC system for simultaneous determination of free and acetylated polyamines

HPLC による一斉分析は感度および正確さの点ではきわめて優れているが、検体の前処理も含めると１検体あたりの測定所要時間は数時間となり、多数の検体を短時間で処理することが求められる臨床検査の方法としては検体処理能力の点で大きな欠点をもつことが明らかであった。我々は、DiAcSpm 検査の実用化のためにはこの欠点を克服することができる、より簡便な測定法を開発することが不可欠であると考え、DiAcSpm 特異的抗体を用いた免疫学的測定系の開発に取り組み、DiAcSpm に高度に特異的な選択的結合性を示す抗体の作成に成功して酵素免疫測定法（ELISA 法）による DiAcSpm の高感度簡便測定系の開発に成功した（Fig. 2）[8]。

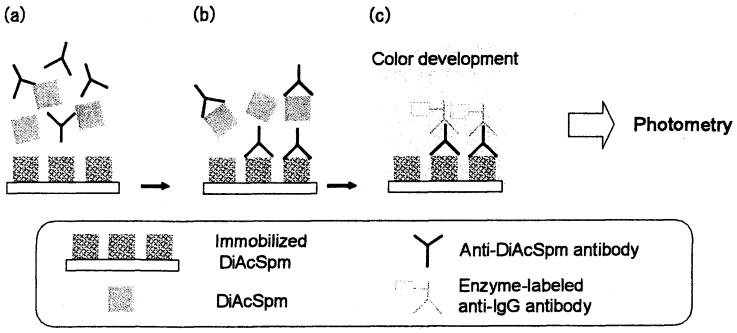

Fig. 2. An ELISA system for determination of DiAcSpm using antibodies highly specific for DiAcSpm

【研究の経過および成果】

ELISA 法による測定系の開発によって、多数のがん患者の尿中 DiAcSpm レベルの測定を進めることが可能になったため、我々は、診断指標、および経過観察中における病勢診断の指標としての観点から、DiAcSpm の腫瘍マーカーとしての特性を明らかにしようと考えて研究を進めた。以下に、これまでに得られた結果をまとめて述べる。

都立駒込病院で手術を受けた大腸がん患者 248 例について術前 DiAcSpm 値を測定し、術前血清 CEA 値との比較を行った。DiAcSpm および CEA のカットオフ値として 0.25μmol/g creatinine（健常者 53 名についての平均+2S.D.）および 5ng/ml をそれぞれ採用し、陽性率を比較したところ、DiAcSpm、CEA の陽性率はそれぞれ stage 0; 62%, 9.5%: stage I; 60%, 10%: stage II; 70%, 42%: stage III; 81%, 47%: stage IV; 88%, 63%となり、いずれの病期においても DiAcSpm は CEA よりも高い陽性率を示した。特に、stage 0 および stage I の比較的早期の癌に対しては DiAcSpm の陽性率は CEA の６倍であった（$p<0.0001$）[9]。現在、

臨床的には多くの腫瘍マーカーがすでに利用されているが、その多くはCEAなどと同様、早期がんにおいてはほとんど上昇しない。近年のがん治療法の進歩により、特に大腸がんに関してはstage 0およびstage Iの段階で発見された早期がんに対しては100%に近い５年生存率が得られるようになっている。したがって、早期がん発見のための手段を提供することは、がんを治癒可能な病気に変える上で大きな貢献をすることになる。ちなみに、ここで得られたDiAcSpmの陽性率は現在大腸がん検診に利用されている便潜血検査の感度とほぼ匹敵する値であり、便潜血検査との併用によって検診の精度を向上させ、癌の検出感度を向上させることが期待されている。

このようにDiAcSpmの早期がんマーカーとしての性能が明らかになり、がん検診も含めた検査項目としての実用化が期待されるようになるにつれて、従来のELISA法と比較してさらに迅速、高精度の測定系の開発が求められるようになった。このような高性能の測定系として、われわれは、金コロイド凝集法を用いたDiAcSpm測定系の開発を試みた。

金コロイドの表面に抗DiAcSpm抗体を吸着させ、ウシ血清アルブミン（BSA）に多数のDiAcSpm分子を化学修飾によって結合させたBSA-DiAcSpm複合体を加えると、金コロイド粒子が凝集し、色調がwine-redから灰色に変化する。この反応液中に検体を添加すると、もし検体中にDiAcSpmがあれば、それが抗体に結合し、BSA-DiAcSpm複合体の結合を妨害するために、結果的に金コロイド粒子の凝集は妨げられ、色調の変化が抑制される。凝集抑制は検体中のDiAcSpm濃度が高いほど強いので、この色調変化の大きさに基づいて、DiAcSpm濃度を判定することができる（Fig. 3）。

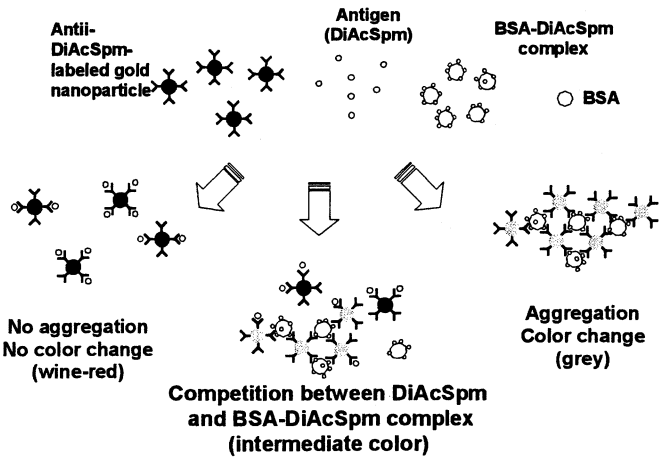

Fig. 3. Measurement of DiAcSpm utilizing aggregation of colloidal gold nanoparticles coated with anti-DiAcSpm antibody

この測定法を利用すると、臨床検査の場で実際に使用されている生化学自動分析機に搭載可能な試薬をキット化できる。現在開発中の試薬を用いる実際の測定の場合、検体と競合体（BSA-DiAcSpm複合体）を混合し、抗体標識金コロイドを添加した時点で吸光度を測り、凝集反応が進んだ５分後の吸光度との差を測定して、その差をDiAcSpm濃度に換算するまでを自動化し、１検体を１０分間で処理することができる。この試薬による測定の同時再現性（C.V.=1.1-2.5%）、日差再現性（C.V.=1.1-5.3%）、添加回収試験の成績（回収率94-115%）はいずれも満足すべき性能を示す数値であり、またDiAcSpmの検出感度5.4nMは、入院加療中に点滴の処置を受けている患者の希薄尿中のDiAcSpm測定にも十分に対応できる水準のものである。この測定法が開発された結果、従来よりもさらに大量の検体を迅速に処理し、正確な測定値を短時間で得ることが可能になった。

ポリアミン代謝の活性化が細胞増殖の活性化に伴うものであることを考慮すれば、DiAcSpmの上昇は癌の種類に大きく依存しない可能性があり、DiAcSpmは汎用の早期がん検出マーカーとして、がんの検診に広く適用できる可能性がある。このことは乳がんにおいてすでに一部明らかになり[8]、肺がんに関しても最近このことを示唆する結果が得られつつある。本研究において開発した高性能測定系は、汎

用腫瘍マーカーとしての観点から DiAcSpm の臨床的意義をさらに明らかにするうえで大きな寄与をすることが期待される。

このような早期がんマーカーとしての利用価値だけでなく、これまでの研究は DiAcSpm ががん患者の経過観察の過程における病勢判定の指標としても優れた特性をもつことを示唆している。さらに詳細な追跡調査を通じてこのことを実証し腫瘍マーカーとしての尿中ジアセチルスペルミン検査を確立すること、また、一般人が家庭で行うことができる簡便な検査法の開発に向けてさらに研究を進め、この検査の普及を図ることにより、がんによる死亡率の低下、がん患者の QOL（quality of life）の向上に寄与することが今後の課題である。

【参考文献】

1. Tabor CW, Tabor H. Polyamines. Ann Rev Biochem 1984; 53: 749-90.
2. Pohjanpelto P, Hölttä E, Jänne OA. Mutant strain of Chinese hamster ovary cells with no detectable ornithine decarboxylase activity. Mol Cell Biol 1985; 5: 1385-90.
3. Auvinen M, Paasinen A, Andersson LC, Hölttä E. Ornithine decarboxylase activity is critical for cell transformation. Nature 1992; 360: 355-8.
4. Russell DH. Increased polyamine concentrations in the urine of human cancer patients. Nature New Biol 1971; 233: 144-5.
5. Bachrach U. Polyamines as markers of malignancy. Prog Drug Res 1992;39: 9-33.
6. Hiramatsu K, Sugimoto M, Kamei S, Hoshino M, Kinoshita K, Iwasaki K et al. Determination of amounts of polyamines excreted in urine: demonstration of N^1,N^8-diacetylspermidine and N^1,N^{12}-diacetylspermine as components commonly occurring in normal human urine. J Biochem 1995; 117: 107-12.
7. Sugimoto M, Hiramatsu K, Kamei S, Kinoshita K, Hoshino M, Iwasaki K et al. Significance of urinary N^1,N^8-diacetylspermidine and N^1,N^{12}-diacetylspermine as indicators of neoplastic diseases. J Cancer Res Clin Oncol 1995; 121: 317-9.
8. Hiramatsu K, Miura H, Kamei S, Iwasaki K, Kawakita M. Development of a sensitive and accurate enzyme-linked immunosorbent assay (ELISA) system that can replace HPLC analysis for the determination of N^1,N^{12}-diacetylspermine in human urine. J Biochem 1998; 124: 231-6.
9. Hiramatsu, K., Takahashi, K., Yamaguchi, T. et al. (2005) N^1,N^{12}-Diacetylspermine as a sensitive and specific novel marker for early- and late-stage colorectal and breast cancers. Clin Cancer Res, 11, 2986-90.

【研究業績】

i) Hiramatsu K, Takahashi K, Yamaguchi T, Matsumoto H, Miyamoto H, Tanaka S, Tanaka C, Tamamori Y, Imajo M, Kawaguchi M, Toi M, Mori T and Kawakita M. (2005) N^1,N^{12}-Diacetylspermine as a Sensitive and Specific Novel Marker for Early- and Late-Stage Colorectal and Breast Cancers. Clin Cancer Res, 11, 2986-2990

ii) Miki T, Hiramatsu K and Kawakita M. (2005) Interaction of N^1,N^{12}-Diacetylspermine with polyamine transport systems of polarized porcine renal cell line LLC-PK_1. J Biochem, 138, 479-484

iii) Kawakita M and Hiramatsu K. (2006) Diacetylated Derivatives of Spermine and Spermidine as Novel Promising Tumor Markers. J Biochem, 139, 315-322

1．2 海洋性微細藻類による高度不飽和脂肪酸の生産

Poly unsaturated fatty acids production by marine microalgae

平野盛雄　（工学部応用化学科）

Morio Hirano　(Department of Applied Chemistry, Faculty of Engineering Kogakuin University)

The production of poly unsaturated fatty acids (PUFAs), such as γ-linolenic acid (γ-LA), eicosapentaenoic acid (EPA), and docosahexaenoic acid(DHA), from algae in marine water was investigated. Two kinds of marine microalgae (KUNK9201 and KUNK9431) which were collected in Iou island were used as algae of PUFAs production. It has become apparent that KUNK9201 was the alga containing γ-linolenic acid, and KUNK9431 was the precious alga containing both EPA and DHA. It has been established the culture conditions of KUNK9201 and KUNK9431.

1. はじめに

高度不飽和脂肪酸の生体内における生理学的意義が明らかにされるとともに、それらの化合物の医学、薬学、あるいは栄養学分野における利用、応用に関する研究が注目されている。たとえば、n-6 系高度不飽和脂肪酸の一つであるγ-リノレン酸（γ-LA）は、抗血栓作用、抗アレルギー作用、抗炎症作用等を示す。n-3 系高度不飽和脂肪酸であるエイコサペンタエン酸（EPA）は、抗血栓作用、抗動脈硬化作用等を、また、ドコサヘキサエン酸（DHA）は学習機能向上、コレステロール低減等の作用を示す。近年話題となっているメタボリック症候群（内臓脂肪型肥満）は血中脂質における中性脂肪、コレステロールの増加によって起こる。EPA や DHA は細胞の核内レセプターを刺激することによって、体内における過剰の中性脂肪やコレステロールを排出させるための指令を発し、それらの分解酵素を誘導する。さらに栄養化学的な研究によって、メタボリック症候群改善あるいは健康維持に、n-6 系高度不飽和脂肪酸と n-3 系高度不飽和脂肪酸の摂取量、あるいは摂取比率が明らかにされ、それらの値は、それぞれ約 7 g/ 日、約 2 g/ 日であり、摂取比率は 3:1～5：1 が良いとされている[1)]。

ところで、ヒトはこれらの高度不飽和脂肪酸の生合成に必要な酵素系が不十分であり、それらを食餌によって摂取しなければならない。そして現在、その食材としては、一部の藻類、あるいは魚類、特に青魚が挙げられる。しかし、特に日本においては、食生活の欧米化に伴い、魚類の摂取量が減少し、ここに、それらの高度不飽和脂肪酸を含む魚油の生産が必要となった。しかし、魚油由来の高度不飽和脂肪酸を関連商品へ利用、応用する上においては、その通年の安定供給が困難であり、また、複雑な精製過程を必要し、魚油臭も避けられない。さらに、重金属やダイオキシンといった環境汚染物質による品質低下も懸案事項として挙げられる。このような現状から、それらの問題点の解決策として、微細藻類による高度不飽和脂肪酸の生産が期待されている。魚類は、その生命活動において、植物性プランクトンである微細藻類を摂取し、そこに存在する高

度不飽和脂肪酸を体内に蓄積する。

そこで筆者らは、γ-LA、EPA、あるいはDHA等の高度不飽和脂肪酸を含有する微細藻類を、日本近海から採取した微細藻類のスクリーニングによって探索し、γ-LA高含有海洋性微細藻類、KUNK9201、およびEPA、DHAをともに含有する海洋性微細藻類、KUNK9431を見出した。そして、これらの微細藻類の人工培養条件の確立、含有高度不飽和脂肪酸の同定、定量を進めている。

2. 実験

本研究においては、鹿児島県硫黄島近海から採取したハプト藻KUNK9201およびプラシノ藻KUNK9431を用いた。それらの藻類の培養は、基本培地として栄養添加人工海水培地にSoil Extractを添加したEse培地を用い、培地のpHは0.1M HClおよび(あるいは)0.1M NaOHを用いて調製した。また、培養器には100mLの大型試験管を用いて、温度を25±2℃に維持しながら、通気培養を行った。光源には白色蛍光灯を用いた。培地中の藻体密度は分光光度計を用い、750nmの吸光度より算出した。藻体中の脂肪酸分析は、脂肪酸を5% HCl-MeOHによってメチルエステル化した後、ガスクロマトグラフィーによって定量分析した。内部標準物質としてヘプタデカン酸を用いた。

3. 結果および考察

3.1 海洋性微細藻類KUNK9201の増殖に及ぼす通気量の影響

KUNK9201の培養における炭素源は、空気中の二酸化炭素のみである。したがって、本藻類の増殖における重要な要素として、培地への通気量が挙げられる。そこで、培地に500～2000 mL(air)/min./Lの速度で通気したときのKUNK9201の増殖について検討した。その結果、通気速度1000 mL(air)/min./Lにおいて、藻体の増殖が最も高い値を示した。1000 mL(air)/min./L以下においては、藻体への二酸化炭素供給量不足、1000 mL(air)/min./L以上においては、過剰の二酸化炭素供給による培地のpHの低下が、それぞれ増殖に対するマイナス要因として考えられた。

3.2 海洋性微細藻類KUNK9201の増殖に及ぼす光強度の影響

光源に白色蛍光灯を用い、光強度140および200 μE/m²/sにおけるKUNK9201の増殖について比較検討した。その結果、いずれの光強度においても、増殖の過程に大きな差異は認められなかった。本実験の予備検討において、光強度が50～140 μE/m²/sの場合、光強度の上昇に伴う増殖量の増加が認められていた。したがって、現時点においては、本藻体の培養には140 μE/m²/s以上の光強度が必要であるといえる。

3.3 海洋性微細藻類KUNK9201が含有するγ-LAの定量

3.1、3.2に示すそれぞれの培養条件において得られたKUNK9201中のγ-LAの含有量をガスクロマトグラフィーによって定量した結果、培養条件の違いによるγ-LAの含有量にはほとんど差異が認められず、その値は約30 mg/g dry weight cellであった。この値は、γ-LA生産藻類と知られる*Spirulina*の約3倍の値であり[2)]、今後の増殖速度の向上研究によって、きわめて有

望なγ-LA 生産藻類として利用できるのではないかと期待される。

3.4　海洋性微細藻類 KUNK9431 の増殖に及ぼす培地中の窒素源およびリン源濃度の影響

海洋性微細藻類 KUNK9431 による EPA および DHA の同時生産に関するこれまでの研究において未解明となっていた、KUNK9431 の増殖に及ぼす培地中の窒素源およびリン源濃度の影響について検討した。すなわち、窒素源として KNO_3、リン源として K_2HPO_4 を用い、それらをそれぞれ 0.5 ～3.0 mM、および 0.125 ～ 0.750 mM の範囲で Ese 培地に添加した培地による KUNK9431 の増殖について比較検討した。その結果、KNO_3、K_2HPO_4 をそれぞれ 2.0、 0.50 mM 添加した培地において、最も優れた増殖を示し、培養８日目の藻体密度は、培養初日を 0.001 mg dry weight cell / L とした場合、0.33 mg dry weight cell / L に達した。

3.5　海洋性微細藻類 KUNK9431 が含有する EPA および DHA の定量

KNO_3、K_2HPO_4 をそれぞれ 2.0、0.500 mM 添加した培地において培養した KUNK9431 に含有する EPA および DHA の定量を行った結果、その値はそれぞれ 20 mg / g dry weight cell 、8 mg / g dry weight cell であった。この値は、EPA の場合、これまでに知られている EPA 生産株である *Monodus subterraneus* の約 30%、DHA については、*Isocrysis affgalbana* の約 50% に達し、これら EPA、DHA の両者をともに含有する微細藻類においてはきわめて高い含有量であり、今後の大量人工培養法の早期確立が期待される。

4.　終わりに

γ-LA などの n-6 系高度不飽和脂肪酸、および EPA、DHA などの n-3 系高度不飽和脂肪酸の積極的な摂取が提言されている今日、それらの高度不飽和脂肪酸の供給システムの構築は不可欠である。従来、それらの高度不飽和脂肪酸は一部の藻類や青魚の油から供給されてきた。しかし、魚油等による高度不飽和脂肪酸の生産においては、年間を通じての安定生産、流通過程における品質の安定化といった多くの問題をかかえている。そこで注目されるのが、それらの高度不飽和脂肪酸を含有する微細藻類の利用である。しかし、微細藻類を利用するためには、まず、有用な高度不飽和脂肪酸を含有する微細藻類を見つけ出すこと、それの人工大量培養系を確立することが最低限必要である。そうした観点から、本研究においては、高度不飽和脂肪酸の大量生産に用いることのできる微細藻類を、日本近海に生息する微細藻類に求め、その人工培養の可能性を明らかにした。

今後、バイオリアクターの有効利用により、海洋性微細藻類による高度不飽和脂肪酸の大量生産システムの早期構築を実現したいと考えている。

引用文献

1）Sutsmal, et al.,*Appl Microbiol Biotechnol.*, 64, 146-153 (2004)

2）Morio Hirano, et al., *Appl. Biochem. Biotechnol.*,**24/25**, 183-191 (1990)

研究業績

国際会議：

K. Abe, E. Takahashi, M. Hirano, Development of water purification system with biofilter of the aerial microalga, *Tretepohlia aurea*, 2005 環太平洋国際会議(ホノルル).

Morio Hirano, Takahiro Miyazaki, Docosahexaenoic acid and eicosapentaenoic acid production by marine microalga, International Symposium on Advanced Technology, (2006) 台湾

関連論文：

K. Abe, H. Hattori, M. Hirano 2007 Accumulation and antioxidant acivity of secondary carotenoids in the aerial microalga *Coelastrella striolata var. multistriata*, *Food Chemistry*, 100, 656-661.

K. Abe, E. Takahashi, M. Hirano, 2007, Development of laboratory-scale photobioreactor for water purification by use of a biofilter composed of the aerial microalga Tretepohlia aurea, *J. Appl. Phycol.*, in press (2007).

1．3 糖酸部位を含む新規高分子の設計とナノ表面での機能発現

マテリアル科学科　橋本 和彦、大川 春樹

Design of Novel Polymers Bearing Saccharic Moieties and Their Function on the Enzymatic Surface

Kazuhiko Hashimoto and Haruki Okawa
(Department of Materials Sciences & Technology, Faculty of Engineering, Kogakuin University)

Abstract: New styryl-type glycopolymers having D,L-xylaric and L-tartaric pendants were synthesized by the copolymerization of the glycomonomers, *N*-*p*-vinylbenzyl-D,L-xylaramic and *N*-*p*-vinylbenzyl-L-tartaramic acids respectively, with acrylamide. The resulting glycopolymers were found to inhibit the β-glucuronidase activity much more effectively than not only the corresponding saccharic acids but also the glycomonomers, especially at the lower concentration of saccharic unit. The inhibition mechanism of the glycopolymers was found to depend upon the structure of their saccharic units. In other hand, polystyrene-type microspheres with D-glucaric, D,L-xylaric, and L-tartaric units on the surface were also prepared and their inhibition to the enzyme activity was estimated by the hydrolysis .

1．はじめに

これまで大量に用いられてきた石油資源由来高分子材料に代わり、再生可能資源である植物資源からの高分子材料の開発が盛んになってきた。研究担当者らは、これまで高分子合成の出発原料(building block)としてほとんど用いられていなかったウロン酸や糖酸に注目した。これらのラクトンジオールとアミノ酸の一種であるリジン由来のジイソシアナートとから合成した新規ポリウレタンの加水分解速度が用いる糖誘導体の種類により制御できることを見出した[1]。

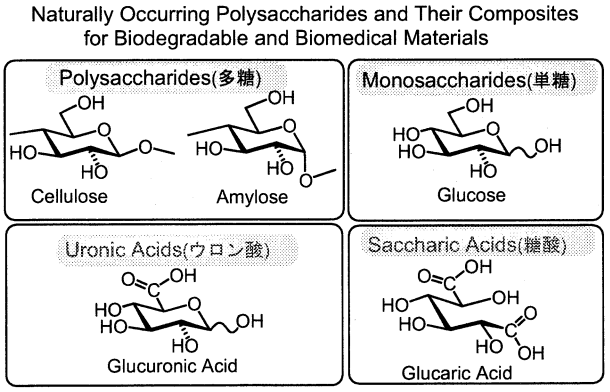

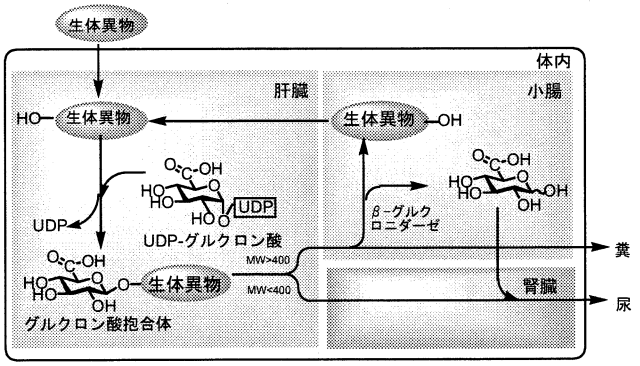

Fig.1 Metabolic Pathway & Enterohepatic Circulation of Xenobiotics

一方、D－グルカル酸のような糖酸およびそのラクトン類が、小腸に多量に存在するβ－グルクロニダーゼ活性を阻害することにも注目した。すなわち、生体異物（毒物）は肝臓でグルクロン酸抱合され、小腸を経て排出されるので、糖酸誘導体を効率よく小腸に送り込むことができれば、抱合体を分解するβ－グルクロニダーゼ活性を阻害し、生体異物の排出を促進できると考えられる。そこで、研究担当者らはD－グルカル酸部位を側鎖にもつ高分子（**1**）を設計合成したところ、得られた高分子が確かにβ－グルクロニダーゼ活性を阻害した[2]。本プロジェクト研究では、炭素数の異なる各種糖酸を側鎖にもつ高分子（**2**，**3**）を合成し、それらの酵素阻害機能を比較検討するとともに、糖酸部位を表面にもつポリスチレン型ミクロスフェアの調製も試みた。

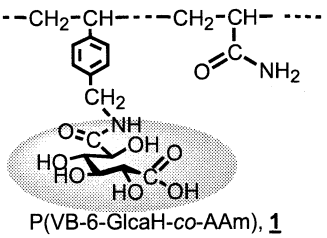

P(VB-6-GlcaH-*co*-AAm), **1**

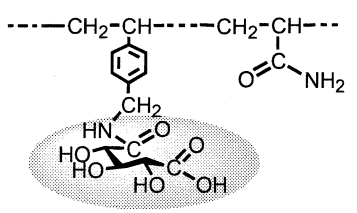

P(VB-D,L-XylaH-*co*-AAm), **2**

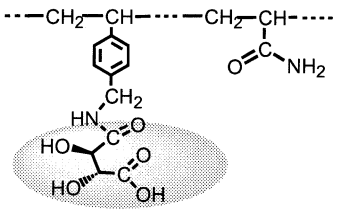

P(VB-L-TartaH-*co*-AAm), **3L**

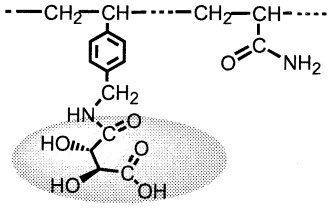

P(VB-D-TartaH-*co*-AAm), **3D**

２．糖酸部位を側鎖にもつ新規水溶性高分子の合成とその酵素阻害機能

まず、Ｄ－キシロース、Ｄ－およびＬ―酒石酸から、それぞれ２,３,４－トリ－*O*－アセチルキシラル酸無水物および２,３－ジ－*O*－アセチル酒石酸無水物を合成した。それらへの*p*-ビニルベンジルアミンの開環付加を経て、対応するスチレン誘導体を合成した。これらとアクリルアミドとのラジカル共重合をＤＭＦ中６０℃で行い、キシラル酸および酒石酸部位を側鎖にもつ高分子（**2**，**3**）を得た。基質に*p*-ニトロフェニル β－グルクロニドを用い、β－グルクロニダーゼによる加水分解を３７℃で行い、生成した*p*-ニトロフェノールの濃度の経時変比を分光学的に追跡し、分解速度を算出した。合成した高分子を添加した場合の分解速度の低下を、高分子無添加の場合の分解速度を基準として評価し、阻害率を算出した。

合成したキシラル酸および酒石酸のそれぞれを側鎖にもつ高分子（**2**，**3**）の構造解析および共重合体組成は主として^{1}H-NMR解析により行った。合成した高分子**2**，**3**は、*p*-ニトロフェニル β－グルクロニドのβ－グルクロニダーゼによる加水分解を、グルカル酸を側鎖にもつ高分子**1**と同様に、阻害することがわかった。しかし、糖酸部位の炭素数が減少するにつれて、その阻害率が低下した（図２）。高分子**1**の糖酸部位であるグルカル酸が、高分子**2**，**3**の糖酸部位であるキシラル酸、酒石酸よりも、基質であるＤ－グルクロン酸抱合体のＤ－グルクロン酸部位と似たコンフォメーションをとり得るためと思われる。

合成した高分子の阻害機構を考察するため、対応する糖酸部位を側鎖にもつスチレン型モノマー、および糖酸誘導体存在下での、β－グルクロニダーゼ活性に対する阻害率を調べ、図３および図４にまとめた。いずれの高分子阻害剤の場合も特に低濃度領域において、元の糖酸やモノマーよりも高い阻害能をもつことがわかった。酵素β－グルクロニダーゼが分子量約７５０００の４つのサブユニットからなることが知られていることを考慮すれば、この実験結果は糖酸部位が高分子鎖に沿って存在することによるクラスター効果が発現したものと推測する。

また、本質的にＤ－グルカル酸は阻害機能をもつ

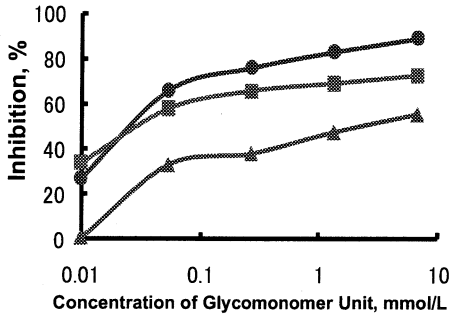

Fig. 2. Inhibition of β-glucuronidase activity by different glycopolymers at 37℃ .
● , P(VB-6-D-GlucaH-*co*-AAm) **1**, 27%,;
■ , P(VB-D,L-XylarH-*co*-AAm) **2**, 22%;
◆ , P(VB-L-TartaH-*co*-AAm) **3L**, 23%.

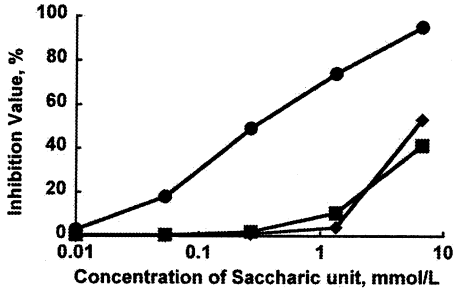

Fig. 3. Inhibition of β-glucuronidase activity by different glycomonomers at 37℃. .

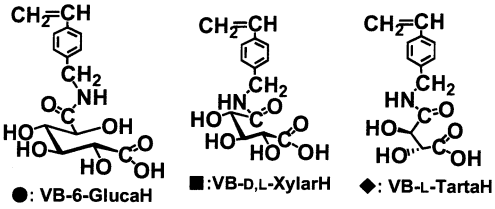

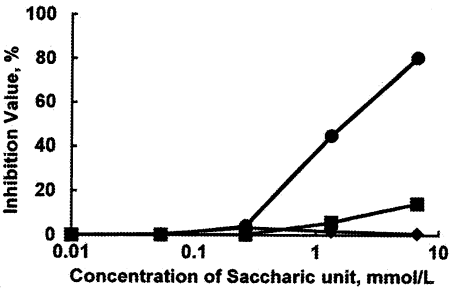

Fig. 4. Inhibition of β–glucuronidase activity by different saccharic derivatives at 37℃.

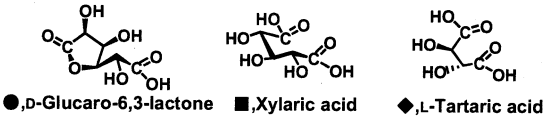

のに対しキシラル酸および酒石酸は阻害能が大変低いのは予想通りであったが、キシラル酸および酒石酸部位を側鎖にもつスチレン型モノマーが高濃度ではかなりの阻害能をもつこと、およびD－グルカル酸部位を側鎖にもつスチレン型モノマーも元のD－グルカル酸より阻害能が高いことは、疎水性の高いｐ－ビニルベンジル基も阻害能に何らかの寄与があることを示唆する。

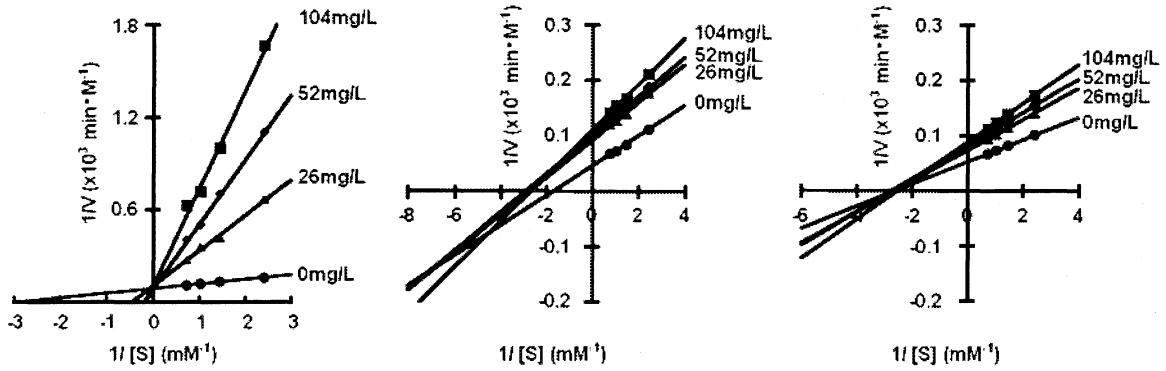

Fig. 5. Lineweaver-Burk plot for kinetic data on the hydrolysis of inhibition of *p*-nitrophenyl β-D-glucuronide by β-glucuronidase in the presence of different glycopolymers at 37℃.

図５に、高分子阻害剤量、酵素量を一定とし、基質濃度を変化させ、Lineweaver-Burkプロットも試みた結果を示す。高分子1は拮抗阻害型相互作用に近いことを示したが、高分子3では拮抗阻害よりもむしろ非拮抗阻害型作用であること示す結果を得た。糖酸を側鎖にもつ対応するスチレン型モノマーについてのLineweaver-Burkプロットでも同様な傾向であった。結局、酒石酸のような糖酸自身の、β－グルクロニダーゼ活性に対する阻害能は低く、また阻害機構も異なることがわかった。一方、酒石酸部位を含む高分子（3）は、D－グルカル酸を側鎖にもつ高分子（1）とはほどではないがかなりの阻害能を示すので、手に入りやすい酒石酸を用いて容易に合成できる特徴をもつ。

３．糖酸部位を表面に持つポリスチレン型ミクロスフェアの調製

前述の水溶性高分子阻害剤を、水不溶のミクロスフェア（微粒子）に変換することを試みた。ポリスチレンのミクロスフェア調整法を参考に、エタノールと２－メトキシエタノールとの混合溶媒中、ヒドロキシプロピルセルロースを加えて、各種糖酸を側鎖にもつスチレン誘導体とスチレンとの分散共重合を行った。

図６および表１に示したように、撹拌速度により得られるミクロスフェアの平均粒径が変化した。粒径分布を狭くするには、装置の改良が必要と思われる。

元素分析により算出した共重合体中の糖酸部位の含有量は、仕込みモノマー量より低かったが、その一部はミクロスフェアの表面に存在する

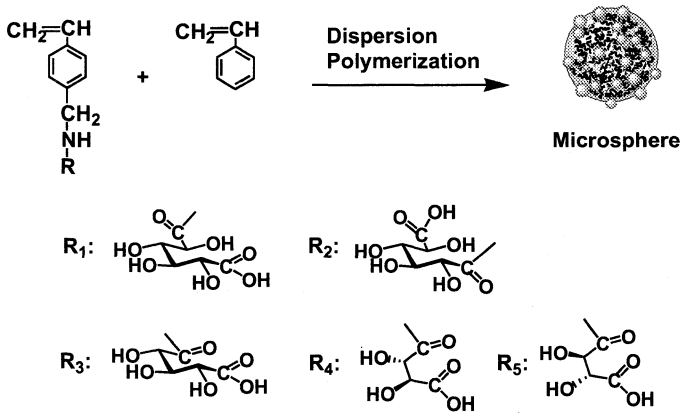

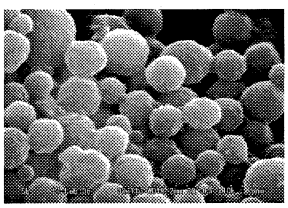

Fig. 6. SEM Image of Microsphere.
mole% of R_1 monomer unit, 7%. ϕ_m; 1.4 μm

と仮定し、調製したミクロスフェア存在下での、β－グルクロニダーゼによる加水分解試験を行った。

図7にその結果の一部を示したように、ミクロスフェアの平均粒径が小さい方が、阻害能が高かった。この結果は、β－グルクロニダーゼと相互作用するD－グルカル酸部位がミクロスフェアの表面に存在するが、その濃度が低いことを意味する。

同様にして、D－キシラル酸、および酒石酸部位を表面にポリスチレン型ミクロスフェアも調製したが、その阻害能は高くなかった。

Table 1 Preparation of Polystrene-type Microsphere Containing D-Glucaric Unit

Expt. No.	R_1 monomer g (mmol)	Styrene g (mmol)	mol % of R_1 in feed	rpm[b]	Polymer Yield g	Polymer Yield mol% of R_1[d]	ϕ[c] μm
1	0.32 (1.0)	0.94 (9.0)	10	200	0.26	7	2.4
2	0.32 (1.0)	0.94 (9.0)	10	300	0.43	7	1.9
3	0.32 (1.0)	0.94 (9.0)	10	500	0.37	8	1.3

[a] Temp., 75°C; Time, 24 h. [b] Rate of Stirring.
[c] Average Diameter of Microsphere. [d] Determined by Elemental Analysis.

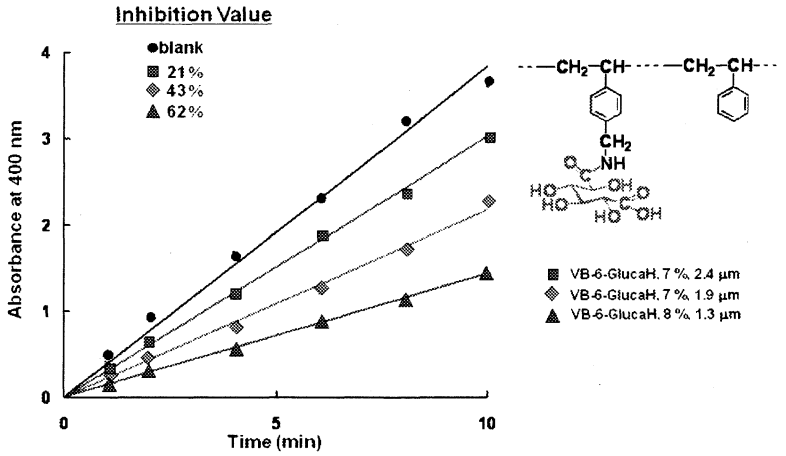

Fig. 7. Inhibition Test of β-Glucuronidase Activity by Microsphere Containing D-Glucaric Moiety (R_1).

4．総括

糖酸部位を側鎖にもつ高分子は、酵素β－グルクロニダーゼの阻害剤として有効に作用すること、水溶性の高分子のみならず、ミクロスフェアにしてその阻害活性を発現することがわかった。

セルロースや木質のような安全性の高い天然高分子への糖酸部位の導入も有効な方法と考え、現在検討中である。

文献 1．a) *J. Polym. Sci.: Part A: Polym. Chem.*: **33**, 1495 (1995). b) *Macro. Phys. Chem.*, 197(1), 135 (1996). c) *J. Polym. Sci.: Part A, Polym. Chem.*: **40**, 4158 (2002). d) *Polym. J.*, **37**, 384 (2005) 他。2．a) *J. Polym. Sci.: Part A: Polym. Chem.*: **37**, 303 (1999). b) *J. Polym. Sci.: Part A: Polym. Chem.*: **37**, 2773 (1999) .

研究業績 (雑誌論文)

1) Kazuhiko. Hashimoto, Kumiko Yanagida, Shin-ichi Nara, Haruki Okawa, "Synthesis of New Hydroxy-Bearing Polyurethanes. Polyaddition of D-Glucose-Derived Diols with Diisocyanates", *Polymer J.*, **37**(5), 384-390 (May, 2005).

2) K. Hashimoto, H. Satito, R. Ohsawa, "Glycopolymeric Inhibitors of β-Glucuronidase. III. Configurationnal Effects of Hydroxy Groups in Pendant Glyco-Units in Polymers upon Inhibition of β-Glucuronidase", *J. Polym. Sci.: Part A: Polym. Chem.*, **44** (16), 4895-4893 (Aug. 2006).

3) Asei Wiliam Kawaguchi, Takafumi Kaida, Haruki Okawa, Kazuhiko Hashimoto, "Glycopolymeric Inhibitors of β-Glucuronidase. IV. Synthesis of Glycopolymers Containing Pendant D,L-Xylaric and L-Tartaric Moieties", *J. Polym. Sci.: Part A: Polym. Chem., in preparation.*

研究業績 (国際学会発表および国内学会での発表) 省略

1.4 静電的相互作用を用いる分子積層型バイオ太陽電池の開発

Development of bio-solar fuel cell using layer-by-layer deposited multilayer films containing enzymes

工学部応用化学科　阿部　克也

Katsuya Abe, Department of Applied Chemistry, Faculty of Engineering

Abstract: Both dye-sensitized photoelectrochemical solar cells and biofuel cells are promising candidates for production of renewable energy. We have combined these two approaches into a single hybrid cell. The photoanode consists of an ITO electrode coated with a phthalocyanine sensitizer and enzymes. Key to the operation of the cell is the coupling of the oxidation of biological fuels such as alcohols by NADH/NAD^+ and $FADH_2/FAD^+$ carriers. In this study, films with alternating layers of the anion cupper phthalocyanine tetrasulfonate or enzymes and cationic poly(ethylenimine) were prepared by means of alternate electrostatic layer-by-layer assembly on the ITO electrode. The hybrid cell has several potential advantages over either the photoelectrochemical cell or the biofuel cell operating individually.

【1】研究背景

特有な性質や機能を有する分子を集積して配列よく組織化することは、その分子の性質を顕在化することでより高次の機能性を発現することが期待される。生体内においても巧みにタンパク質やリン脂質などが配列し、一つの分子集合体が形成された結果、優れた生物機能が発揮されている。生物がもつ優れた機能を利用してバイオテクノロジーへ展開させる場合、生体分子をどの様に基板上に順序よく配列させ、生体内と同じ反応機構を再現させ、さらに、必要最小限の要素を高密度に構築することが重要となってくる。生体分子などを基板上に薄膜として固定化する代表的な手法に、Langmuir-Blodgett 膜法、自己組織化単分子膜法、脂質二分子膜法、交互積層膜法がある。これらのうち交互積層膜法は、操作が非常に簡単であることが利点の一つとして挙げられる[1,2]。

さて、地球の環境問題や化石エネルギー資源枯渇問題等を解決するために、バイオデバイス、例えば、バイオ電池や太陽電池などの燃料電池を用いたエネルギー変換システムの研究開発が活発に行われている[3]。さらに、クリーンなエネルギー源として生物資源（バイオマス）を利用する試みが期待され、特に未利用バイオマスから燃料電池のエネルギー源（例えば、糖やアルコール類など）を生産する方法が注目されている。バイオ電池では、電極触媒として酵素や微生物を用いるため、電極不活性な糖やアルコール類などを燃料とすることができる。また、非常に穏和な条件下で作動でき、環境負荷が比較的少なく安全性が高いといった特徴をもっている。この様な特徴を有するバイオ電池は電極・電子メディエータ・酵素タンパク質からなるシンプルな構成であるが、これら物質間のスムーズな電子移動や酵素タンパク質の特徴が電池の性能に大きく反映する。このためには電極上に目的分子を上手にかつ穏やかに配列させることが重要であり、上述した交互積層法の利用はバイオデバイスの研究開発を行う上で有効な手段であると言える。この方法は、静電的相互作用を利用して分子（例えば、酵素タンパク質や色素）の層を薄く作ることが可能であり、得られた薄膜は分子同士が近くに配置されるためスムーズな電子移動が得られるものと考えられる。

そこで本研究では、生体分子の静電的相互作用を用いる新規バイオデバイスの開発の一環として、クリーンな太陽エネルギーとバイオマスからのエネルギー源を利用する分子積層型バイオ太陽電池の開発を目的とした。本電池は、太陽電池部分に化学的・物理的に安定な銅フタロシアニンの分子層を、バイオ電池部分に酵素タンパク質の分子層を組み合わせたものから構成された。Fig.1 に分子積層型バイオ太陽電池の模式図を示す。この電池の特徴として、①種々の酵素タンパク質からなる積層膜（補酵素の固定化も含む）の電子伝達サイクルによるアルコールの 2 段階酸化反応、②積層膜の電子サイクルを介したスムーズな電子移動、③化学的・物理的に安定な色素からなる分子積層膜の光励起反応が挙げられる。

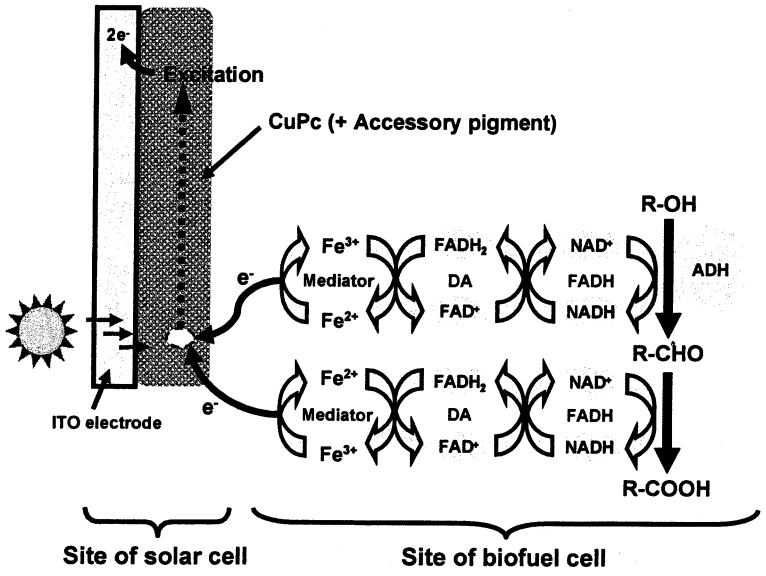

CuPc: CuPhthalocyanine.
DA: Diaphorase.
FADH: Formaldehyde dehydrogenase.
ADH: Alcohol dehydrogenase.
Mediator: Ferrocene-modified PEI (Fc-PEI).

Fig. 1 Schematic diagram of bio-solar fuel cell using layer-by-layer deposited multilayer films containing enzymes.

【2】研究経過

色素分子積層膜の作製および光電流測定：分子積層膜は、水溶液中で正電荷をもつポリエチレンイミン(PEI)と負電荷をもつ色素（銅フタロシアニン：CuPc）あるいは酵素タンパク質を用い、静電的相互作用によって水晶振動子の Au 電極あるいは ITO 電極（透明ガラス電極）上に作製した。これらの電極表面は、通常、負電荷をもった状態にある。

まず、太陽電池部分の CuPc 色素積層膜の作製結果について述べる。$(CuPc/PEI)_n$ 積層膜（n=積層回数）は pH 2.5 および pH 8.5 に調整した CuPc 水溶液において作製した。その膜形成過程を QCM 測定により監視した結果、Au 電極上への色素分子の吸着に基づく振動数減少量（$(CuPc/PEI)_5$、積層回数：5 回）は pH 2 の溶液を用いた方が pH 9 の溶液より約 2.5 倍大きいことが分かった (Fig.2)。また、水溶液の pH を 2～9 の間で調整した場合に、積層膜 5 層目の振動数変化量は Fig.3 のように酸性側の溶液において著しく大きくなることが認められた。一方、基板を ITO 電極に変えたときの$(CuPc/PEI)_5$ 積層膜の吸収スペクトルの測定結果を Fig.4 に示す。この場合

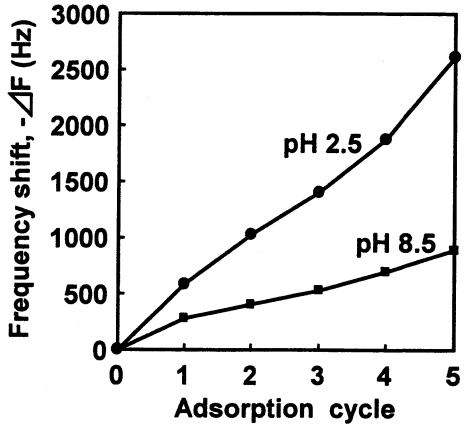

Fig. 2 Frequency shift in alternate adsorption of (CuPc/PEI)n (n = number of bilayer) on Au electrode at pH 2.5 and pH 8.5.

もCuPcの最大吸収波長（610 nm付近）における吸光度は溶液pHが酸性領域において増加する現象が見られた。1層当たりの色素吸着量に依存してエネルギー変換効率が高くなるものと考えられるため、以後のCuPc積層膜の作製はpH 2.5に調整した水溶液において行うことにした。したがって、溶液のpHがCuPc分子の基板表面への吸着に対して影響を及ぼしているものと考えられるが、現在のところ、その原因はよく分かっていない。今後、その吸着過程について詳細に検討する予定である。

次に、太陽光を充分に利用する目的でCuPcに他の色素を加えた広範囲な吸収波長を持つ分子積層膜の作製について検討した。今回、CuPc色素と組み合わせる補助色素の選定を行うために4種類の色素（コンゴーレッド、アシッドレッド27、アシッドレッド112、およびインジゴカーミン）を用いた。これらの色素はITO電極上に積層することが確認されたが、分光学的測定の結果、CuPcとコンゴーレッド(CR)を組み合わせた色素分子積層膜は広範囲な吸収波長を持つ薄膜であることが分かった。その積層膜〔$(CuPc/PEI)_4/(CR/PEI)_2$/ITO電極〕の表面は紫色を呈し、広範囲な吸収スペクトルを示した（Fig.5）。また、その膜厚（総積層回数：6層）はQCM測定結果に基づいて算出したところ[2]、約40 nmであった。この積層膜は非常に薄いものであったが、$(CuPc/PEI)_5$積層膜と比べ多少凹凸のある表面であることがAFM表面分析によって分かった(Fig.6)。

本研究では、静電的相互作用で作製した銅フタロシアニンとコンゴーレッドからなる積層膜〔$(CuPc/PEI)_x/(CR/PEI)_y$/ITO 電極：太陽電池部分〕に関する光電流発生の検討を行った。測定は3電極方式を用い、ウォータージャケット付き電気化学セル内で行った。光源にはハロゲンランプ(150 W)を用いた。発生する光電流値は色素分子の積層回数に依存したが、ある回数以上では減少する傾向が見られた。また、色素組成によっても光電流値は異なると考えられ、適切な条件を今後検討する必要はある。Fig.7に代表的な色素分子積層膜の光電流測定結果を示す。$(CuPc/PEI)_x/(CR/PEI)_y$/ITO電極（x：4層、y：2層）に対して光照射したとき、そのON-OFFに伴う光電流の発生が明確に観察された。したがって、色素分子積層膜が太陽電

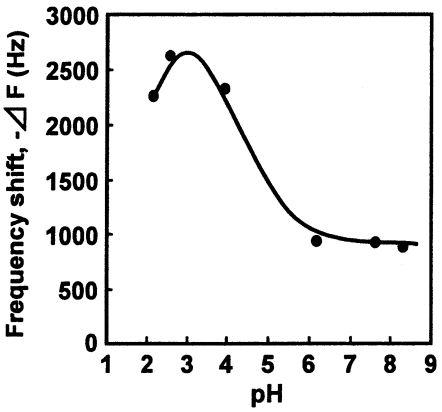

Fig. 3 Effect of pH on frequency shift in alternate adsorption of (CuPc/PEI)5 on Au electrode.

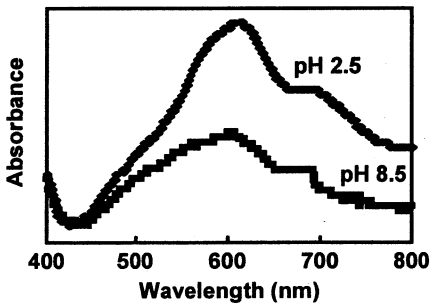

Fig. 4 Absorption spectra for (CuPc/PEI)5 films deposited on ITO electrodes at pH 2.5 and 8.5.

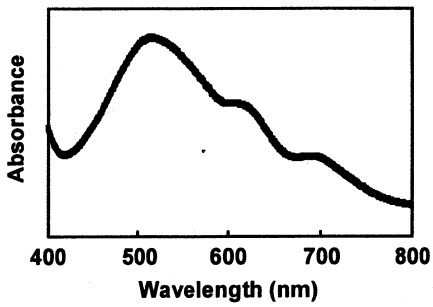

Fig. 5 Absorption spectrum for (CuPC/PEI)4/(CR/PEI)2 /ITO electrode.

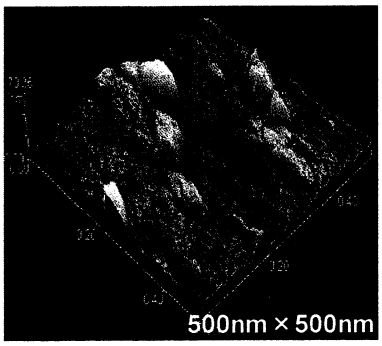

Fig. 6 AFM image of surface of (CuPc/PEI)4/(CR/PEI)2/ITO electrode.

池としての機能を持っていることが示唆された。

分子積層型バイオ太陽電池の作製：まず、Fig.1 に示した様に作製した色素分子積層膜上への酵素タンパク質（DA、FADH、および ADH）の積層膜の作製について検討した。複合タンパク質からなる積層膜の形成過程は QCM 測定により監視することで行った。この結果、各タンパク質は電子メディエータ分子(Fc-PEI)やポリイオン(PEI)と静電的に交互吸着することが分かった。今回は、ITO 電極上に $(CuPc/PEI)_4(CR/PEI)_2(DA/Fc\text{-}PEI)_2(FADH/Fc\text{-}PEI)_2(ADH/PEI)_2$ の積層膜を作製し、この分子積層型電極をバイオ太陽電池とした。

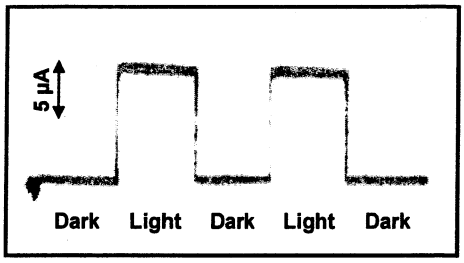

Fig. 7 Current responses to illumination of (CuPc/PEI)4/(CR/PEI)2/ITO electrode.

本研究では、作製した分子積層型電極に対して光照射したときに、積層膜内の電子伝達サイクルの駆動(Fig.1)によるメタノールからギ酸までの 2 段階酸化反応を定性的に検討した。第 1 段階目の反応は ADH と FADH の補酵素を利用するホルムアルデヒドまでの酸化反応であり、第 2 段階目は FADH によるギ酸までの酸化反応である。この結果、5 分間の光照射においてギ酸の生成が HPLC 分析により認められた。測定系に DA、FADH、および ADH を溶解させて同様な実験を行った場合にはギ酸の生成は見られなかった。おそらく、電極上に種々の酵素タンパク質分子が上手く配置されたことで電子移動が容易に行える環境が生まれ、その結果、電子伝達サイクルが駆動したものと考えられる。今後、太陽電池部分とバイオ電池部分との融合に向けて詳細な検討を行うことにより、バイオマスを燃料とする新規バイオデバイスの開発が期待される。

引用文献

1) Yuri M. Lvov, Geoffrey N. Kamau, De-Ling Zhou, James F. Rusling 2000 Assembly of Electroactive ordered multilayer films of cobalt phthalocyanine teterasulfonate and polycations. *J. Colloid Interface Sci.* **212**, 570-575.

2) Katsuya Abe, Atsushi Ishii, Morio Hirano, James F. Rusling 2005 Photoactivity characteristics of a biodevice using primary photosynthetic reaction centers. *Electroanalysis* **17**, 2266-2272.

3) Eugenii Katz, Itamar Willner 2003 A biofuel cell with electrochemically switchable and tunable power output. *J. Am. Chem. Soc.* **125**, 6803-6813.

研究業績

口頭発表：

1. 阿部克也、石井敦史、平野盛雄 J. Rusling、日本生物工学会大会(2005).
2. K. Abe, A. Ishii, M. Kaminaga, M. Hirano, 2005 環太平洋国際会議(ホノルル).
3. 阿部克也、石井敦史、神永雅弘、平野盛雄、第 85 回日本化学会春季年会(2006).
4. 阿部克也、神永雅弘、布施真紀子、平野盛雄、J. Rusling、日本生物工学会大会(2006).
5. 阿部克也、第 7 回 NASIC 研究発表会(2007).

論文発表（査読付）：

1. Katsuya Abe, Atsushi Ishii, Morio Hirano, James F. Rusling 2005 Photoactivity characteristics of a biodevice using primary photosynthetic reaction centers. *Electroanalysis* **17**, 2266-2272.

1.5 機能タンパク質および糖質の構造改変と有用物質生産への適用

菅原康里　坂口政吉
（工学部　応用化学科）

Structural Modification of Functional Protein and Sugar, and its Application to Production of Useful Materials

Yasusato Sugahara and Masayoshi Sakaguchi
Department of Applied Chemistry, Kogakuin University

Chitin was hydrolyzed with concentrated hydrochloric acid at 40℃ for 40 min. The degraded chitin was precipitated with acetone and filtered to obtain the residue. The residue was extracted by water and acetone mixture with changing their ratio. The filtrates were analyzed with high performance liquid chromatography (HPLC). The solubility of oligosaccharides was extremely affected by the acetone concentration. In the region of high acetone concentration, low molecular oligosaccharides were extracted, and in the region of low acetone concentration, high molecular oligosaccharides were extracted. By fractional dissolution, pure hexamer was obtained with high yield.

緒言

近年、キチンオリゴ糖が生理活性を持つことが見出され、これらオリゴ糖の簡便な調製法に関心がもたれている。一般に、これらオリゴ糖を得るには酸および酵素による加水分解が考えられる。酸加水分解はキチン分子のグルコシド結合をランダムに切断するためサイズの異なるキチンオリゴマーが混在して回収される。オリゴマー混合物としての利用も可能であるが、サイズの異なるキチンオリゴマーが混在したものよりも、単一のサイズで精製されたキチンオリゴマーの方が付加価値は高い。単一サイズのキチンオリゴマーが高価な原因の一つに、サイズごとに精製することが困難なことがあげられる。

本研究では、キチンオリゴマーを大容量かつ簡便にサイズごとに分画する方法として、分別溶解法を用いて、特に生理活性の高いと言われる、キチン6量体の分画について検討した。

2. 実験

キチン試料:東京化成工業製キチンをウイリーミルで 60mesh に粉砕した後、使用した。使用したキチンの分子量は 320000、脱アセチル化度は 3.2%であった。

加水分解反応:キチン 0.2 g に濃塩酸 8m L を加え、40℃ で所定時間加水分解を行った。反応後、加水分解物はアセトン 200m L 中に投入して、4℃ で 24 時間静置した。沈殿物は吸着した酸を除去するために、ろ過、アセトン洗浄を繰り返した。

分別溶解:　アセトン沈殿物にアセトン-H_2O 溶液 5ml を試料に加えて分別溶解を行った。マグネチックスターラーで攪拌しながら 20℃ で 1 日放置した後、遠心分離によって上清と沈殿に分けた。上清は HPLC によって分析し、オリゴマーを定量した。沈殿はアセトン-H_2O の割合を変化させ、分別溶解を繰り返した。

3. 結果と考察

3.1 抽出溶媒の検討

極性の差を利用した分別溶解を行うにあたり、用いる溶媒について検討した。試料には*N*-アセチルグルコースアミン(GlcNAc)を用い、溶媒にはH_2Oと親和性の高いアセトン、メタノール、エタノール、プロパノールを使用した。4種の有機溶媒とH_2Oを所定の割合で混合した溶液を調製し、その混合溶液にGlcNAcを過飽和になるまで溶解し、20℃で24時間静置した。GlcNAc過飽和溶液の上澄みを10ml分取し、溶液を蒸発、絶乾し析出したGlcNAcの重量を測定した。この結果、アセトンが最も溶解度の変化が大きいことから分別溶解操作にはアセトンを選択した。

3.2 アセトン-水系での分別溶解

90%アセトン-H_2O溶液5mlを試料に加えて分別溶解を行った。以後、沈殿にH_2Oの割合を10%ずつ増やした溶液を加え、6回繰り返し分別溶解を行った。

Fig.1のクロマトグラムから明らかなようにキチンオリゴマーのサイズごとに溶解性が異なることが分かる。1回目の90%アセトン抽出では(GlcNAc)1~3のピークしか確認できず、4量体以上のピークは確認されない。3回目の70%アセトン抽出から(GlcNAc)4のピークが現れる。60%アセトンでの抽出から(GlcNAc)5の大きなピークと、(GlcNAc)6出始めピークが確認できる。最後の水(0%アセトン)での抽出では(GlcNAc)6が現れる。

各段階の抽出液オリゴマーを定量した結果をFig.2に示す。収率は分解前のキチン0.2gを100%として計算した。totalは全てのオリゴマーの収率の合計である。この結果からアセトン-H_2O系での分別溶解の可能性が示唆された。以後、分別溶解の操作回数を減らすことについて検討した。

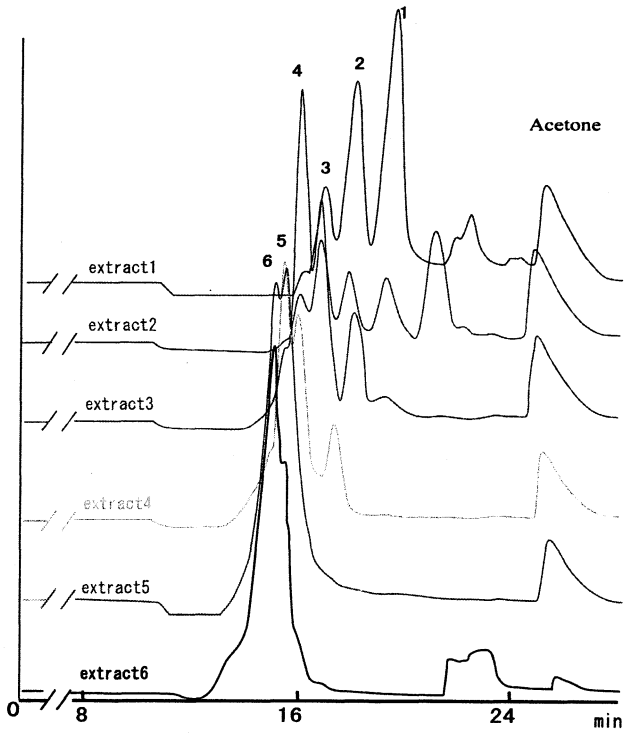

Fig.1 GPC analysis of oligosaccharides in extract by Acetone and H_2O.
Column: GS-220, 60°C; Eluent: H_2O; Flow: 0.5ml/min; Detector:UV210nm
extract1: 90%Acetone extract2: 80%Acetone extract3: 70%Acetone
extract4: 60%Acetone extract5: 50%Acetone **extract6: 0%Acetone(H_2O)**

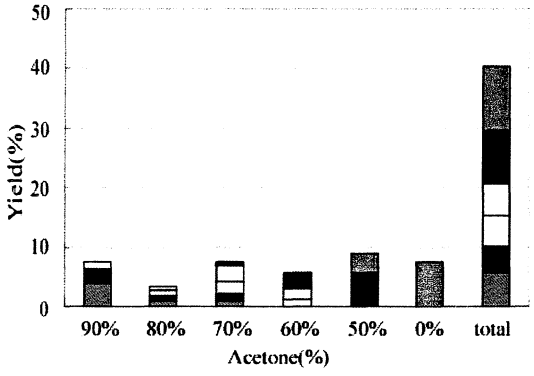

Fig.2 Effect of acetone concentration on yield of oligosaccharide.

3.3. 抽出回数の検討

抽出回数を減らすために、アセトンの比率を工夫した。 まず、(GlcNAc)1~2、(GlcNAc)3~4、(GlcNAc)5~6 の 3 組に大きく分けることを検討した。1 回目の抽出を 90%アセトン(以後 70、50%)、80%アセトン(以後 70%、50%)、70%アセトン(以後 60%、60%、0%)、60%アセトン(以後 50%、0%)で行った。(90%-70%-50%)と(80%-70%-50%)を用いた場合、(GlcNAc)1~2、(GlcNAc)3~4、(GlcNAc)5~6 の 3 組に分離でき、特に後者は前者よりもきれいに分別できた。(70%-60%-60-0%)と(60%-50%-0%)の組み合わせの場合は、最後の分別溶解によって(GlcNAc)6 の分別ができた。そこで、(GlcNAc)6 を分別溶解 3 回以内で、収量良く得ることを目的に、1 回目の抽出を 70%アセトンおよび 60%アセトンで行う分別溶解について検討した。

3.4 70%アセトンを用いた分別溶解

始めに 70%アセトンを用いた抽出を行い、以後、抽出溶液の比率を変え検討を行った。70%アセトンで 3 回抽出した後、水で抽出した結果(70%-70%-70%-0%)、70%アセトン溶液への(GlcNAc)6 の溶解性は無いことが分かった。また、(GlcNAc)5 は 70%アセトンに対して溶解性があるものの、この操作では全てを溶解することが出来なかった。(70%-30%-0%)を用いた場合、純度良く(GlcNAc)6 が得られたが、30%アセトンで抽出したところでかなりの量の(GlcNAc)6 が抽出され、収量は少なかった(Fig. 3)。

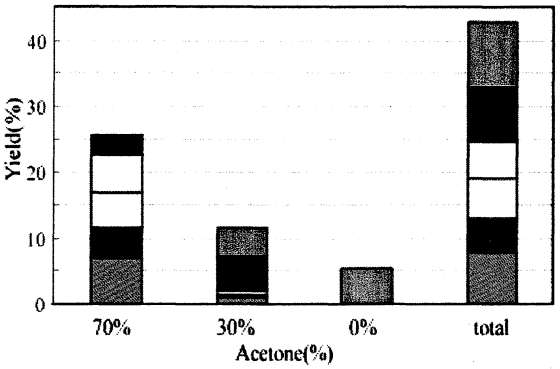

Fig.3 Effect of acetone concentration on yield of oligosaccharaides

■(GlcNAc) ■(GlcNAc)2 □(GlcNAc)3
□(GlcNAc)4 ■(GlcNAc)5 ■(GlcNAc)6

3.5 60%アセトンを用いた分別溶解

(GlcNAc)6 の分別溶解を目的に、抽出液量を 14mL に増やし、60%アセトンで 2 回抽出した後、水で抽出した(60%-60%-0%)。Fig.4 はその結果を示したものである。Fig.4 から明らかなように、60%アセトンで 2 回抽出を行うことにより、(GlcNAc)1~5 のほとんどが分別できた。

次に、60%アセトンで 2 回分別溶解する操作を、1 回に省略できないかについて検討した。60%アセトン 30ml で分別溶解した後、水で残りのオリゴマーの抽出を行った。 Fig.5 と Fig.6 から、60%アセトン 1 回の分別溶解の操作でも(GlcNAc)1~5 を十分に抽出できている事が分る。しかし、1 回の分別溶解の操作の場合、収率は高いものの、2 回分別操作を行った場合のクロマトグラムと比較すると、やや他の成分が含まれているようである。分別溶解に用いる溶液量を増やすより、少量の溶液で抽出回数を増やしたほうが純度の高い(GlcNAc)6 が得られることが分かった。

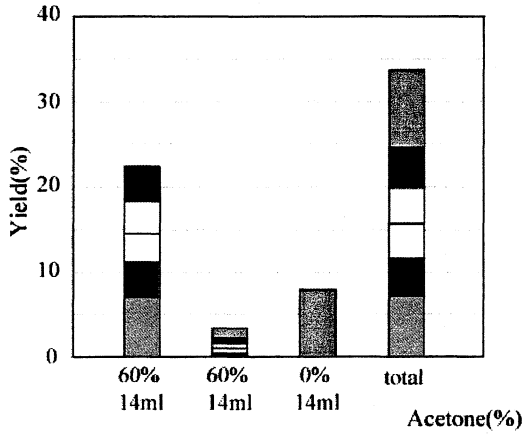

Fig. 4 Effect of acetone concentration on yield of oligosaccharide

■(GlcNAc) ■(GlcNAc)2 □(GlcNAc)3
□(GlcNAc)4 ■(GlcNAc)5 ■(GlcNAc)6

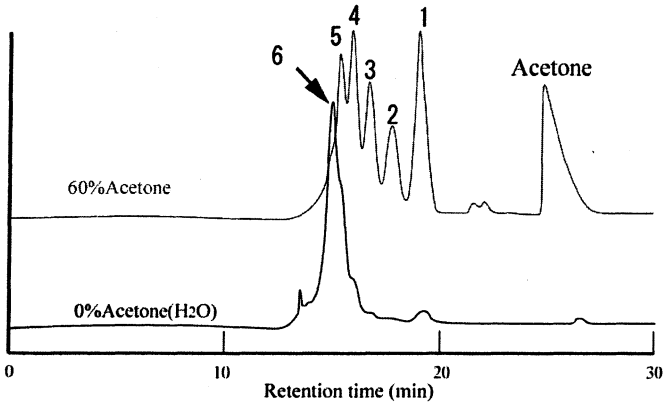

Fig.5 GPC analysis of oligosaccharaides in extract by Acetone and H2O

Column: GS-220, 60℃; Eluent: H2O; Flow: 0.5ml/min; Detector :UV210nm

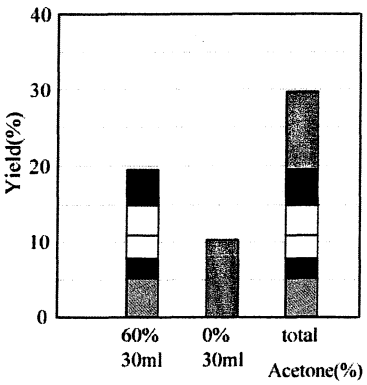

Fig.6 Effect of Acetone concentration on yield of oligosaccharaide

(GlcNAc) (GlcNAc)2 (GlcNAc)3
(GlcNAc)4 (GlcNAc)5 (GlcNAc)6

3.5 結論

抽出溶液(アセトン－水)の割合を変化させることにより、極性をコントロールし、キチンオリゴマーをサイズごとに分別溶解を行うことができた。特に、(GlcNAc)6 は免疫増強作用や腫瘍成長抑制作用等の報告が一番多く、(GlcNAc)1~6 の中でも一番高価な物質である。一連の操作はアセトンと水しか用いないため安価であり、操作も単純である。また、セルロースオリゴマー、デンプンオリゴマーなど、他のオリゴマー分画への応用にも有効な方法と考えられる。

1) 風見直、菅原康里、坂口政吉、川喜田正夫　「二段階加水分解によるキチンオリゴ糖の調製」、キチンキトサン学会、千葉工業大学、2005 年 8 月 5 日

2) 阿部高光、菅原康里、坂口政吉、川喜田正夫　「キトサンの塩酸加水分解挙動」、キチンキトサン学会、千葉工業大学、2005 年 8 月 4 日

3) 阿部高光、白石一徳、菅原康里、坂口政吉、川喜田正夫　「酸加水分解によるキチンオリゴマーの調製」、キチンキトサン学会、福井工業大学、2006 年 8 月 10 日

4) 宮川聡，清野淳一，南雲利之，坂口政吉，菅原康里，川喜田正夫　「細菌 *Caulobacter crescentus* CB15 の Glucoamylase 様遺伝子の発現とその解析」、日本応用糖質科学会、大阪府立大学　2006 年 9 月 27 日

2. ナノ薄膜

2. 1 超臨界流体を用いた有機薄膜作成技術の開発と発光素子への応用のための膜質制御と評価に関する研究

Organic Thin-Film Deposition Method using Supercritical Fluids and Its Application to Light Emitting Electronic Devices

工学院大学 工学部 電気システム工学科　坂本 哲夫
東京大学 環境安全研究センター、生産技術研究所　尾張 真則
Dept of Electrical Eng., Faculty of Eng., Kogakuin University　Tetsuo Sakamoto
Env. Sci. Center and Institute of Industrial Sci., the University of Tokyo Masanori Owari

Abstract

This study aims at the development of new methods for organic thin film deposition utilizing supercritical fluids. Supercritical fluids have unique properties such as high solvating power like a liquid and high diffusion coefficient like a gas. Two kinds of thin film deposition using supercritical fluid have been devised; supercritical fluid deposition (SFD) and rapid expansion of supercritical fluid solutions (RESS). Instruments for each technique have been made and fundamental properties of thin film deposition were investigated.

1．はじめに

有機薄膜は、発光素子・トランジスタ・太陽電池など今後著しい発展が期待される分野の基礎材料である。有機薄膜の作製においては蒸着法と塗布法(溶液法)が利用されているが、それぞれ、適用できる有機材料に大幅な制限がある。例えば高分子材料は蒸着法には適さない。また、塗布法では溶剤に可溶な物質しか使用できない。パターニングに関しては蒸着法ではマスクによるパターニングが可能であるが、塗布法では溶液のため一般に困難である。このように、有機材料の電子素子への応用は材料開発もさることながら、膜作製方法の問題が多く残されている。本研究では蒸着でも塗布法でもない新しい成膜方法を開発し、低分子型・高分子型両方に適用可能で、かつパターニングも可能な方法の実現を目指す。本研究では溶媒として超臨界流体を用いる点が特徴的である。超臨界流体は図１に示すように高圧の流体であり、気体と液体の両方の性質を併せもつ。つまり、気体のように拡散する一方、液体のように物質を溶かす性質がある。超臨界流体(CO_2)を用い、材料（有機および有機金属）を一度溶解させ、減圧または急速膨張により析出させることで有機膜を形成する。

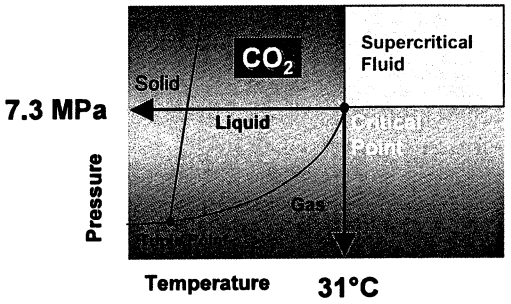

Fig.1: Phase diagram of CO_2.

2．研究計画

H17 年度：　有機物を超臨界流体へ溶解させる実験を行う。とくに、溶解状態を解析するための飛行時間型質量分析計(TOF-MS)を立ち上げる。超臨界流体導入部を専用に製作する。

H18 年度：　成膜について検討する。超臨界流体を僅かに減圧し、溶解度を下げて析出させる方法および極細ノズルから高圧噴射させ、基板上に吹き付ける急速膨張法を検討する。

H19 年度：　膜質の評価を行う。表面の平坦性、下地との密着性などを電子顕微鏡、二次イオン質量分析法を用いる。

以降：　多層膜を形成させる。成膜プロセスでは順次材料を切り替えて堆積させることで対応する。また、有機金属を材料とした成膜を試み、有機物・無機物(金属)が混在した実在デバイスに対応できる方法へと発展させる。

3．有機材料の溶解およびその場分析

有機材料の超臨界 CO_2 に対する溶解度はもっとも基礎的知見となるが、現状では溶解度は一部の物質についてのみ知られている程度である[1]。そこで、本研究では有機物を溶解した超臨界 CO_2 を直接、質量分析装置に導入し、リアルタイムに溶解状態を把握するため、プロジェクト設備として TOF-MS 装置を導入した。

全体としては Fig.2 に示すように超臨界流体生成部と TOF-MS 装置を結んだシステムである。通常、TOF-MS は大気圧～数気圧程度のガス導入しか前提としていないため、73 気圧以上の超臨界 CO_2 を直接導入することはできない。そこで、高圧と真空を結ぶインターフェイスを独自に開発した。流体噴出部に内径 20 μm の溶融シリカキャピラリーを用い、かつ、その先端のみを Fig.3 に示すような手順で内径数μm の開口部としたインターフェイスを作製した。これにより流量を制限しつつ超臨界 CO_2 と真空の圧力差を保持する。

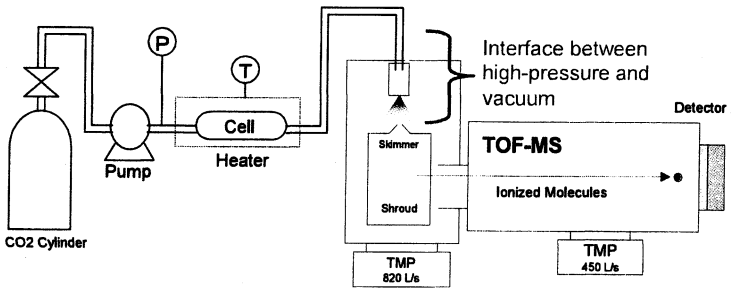

Fig.2: Illustration of an apparatus for direct analysis of supercritical fluid composition.

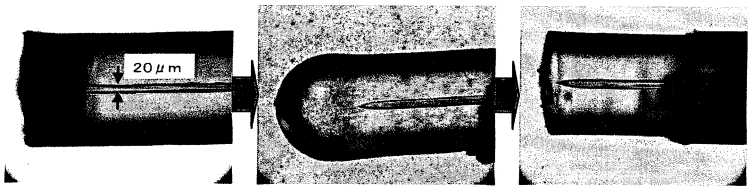

Fig.3: Optical micrographs depicting the preparation procedure of capillary interface.

Fig.4 に測定結果の一つを示す。試薬は有機金属化合物のフェロセンであり、流体条件は 30 MPa, 50℃であった。1 分間の信号積算により超臨界流体に溶解したフェロセン分子を検出することができた。なお、CO_2 分子に対してフェロセン分子のカウント比は 10^{-3} 程度であり、一般に有機溶媒よりは溶解力が弱いとされる超臨界流体としては妥当な値といえる。

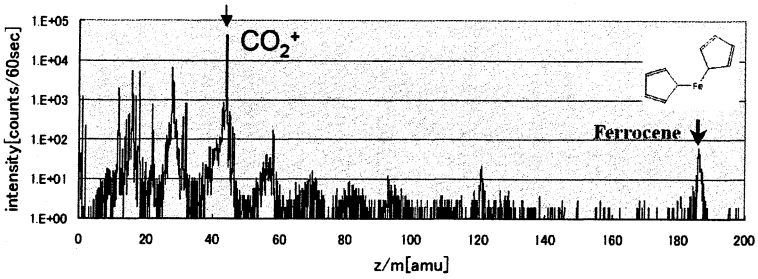

Fig.4: TOF-MS spectrum of ferrocene in supercritical CO_2.

4．成膜装置開発 I （超臨界流体析出法）

成膜方法については２種類の方法を試行している。流体の圧力または温度を僅かに下げ、溶解度を意図的に下げる析出方法では、過飽和度や析出速度の制御が可能である。装置は Fig.5 に示すように CO_2 を液化するための冷却部、加圧送液するポンプ、昇温させるヒーターおよび圧力制御のための背圧弁から成る。基板はヒーター外に設置した Cell2 内に入れておき、材料は Cell1 に導入する。Cell1 から溶出した材料が Cell2 に流入する際に温度低下により溶解度が変化する仕組みである。これまでに、種々の条件で実験を試みたが析出条件と析出物のモフォロジーのはっきりとした関係は判っていない。しかしながら、圧力操作ではなく温度を自然冷却によってきわめて緩やかに下げていった場合、結晶性の析出物(Fig.6a)が得られ、比較的低温(30℃)一定としながら流体条件を変えず、流通を続けた場合は膜状の析出物(Fig.6b)が得られる傾向を把握している。

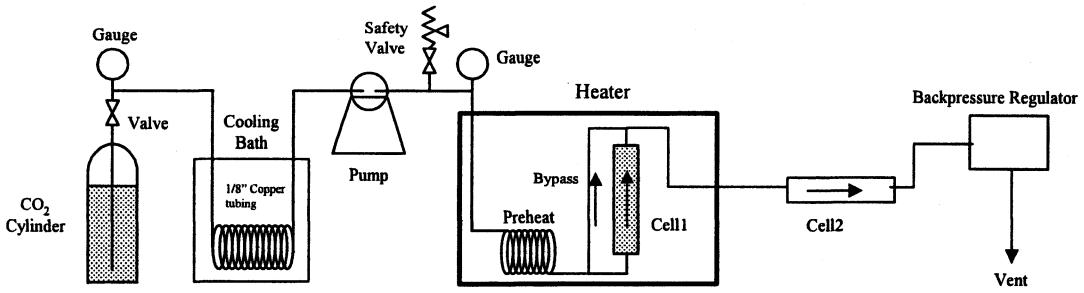

Fig.5: Schematic diagram of a supercritical fluid deposition apparatus.

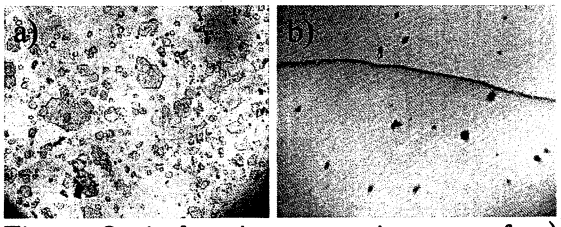

Fig.6: Optical microscope images of a) anthracene crystals and b) thin films deposited on ITO glass plate in supercritical CO_2.

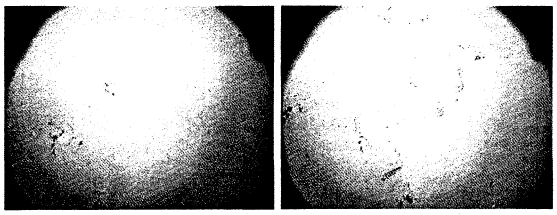

Fig.7: Optical micrograph images of Alq3 thin film on ITO glass plate. (left: as-received, right: scratch)

膜状析出物は低分子系有機EL材料であるAlq3においても見られた(Fig.7)。一方、超臨界状態から急速に圧力を下げた場合は数μm以下の微粒子が得られることも判った。この場合の析出は第2の方法である急速膨張法と同様の原理により微粒子の析出が起こっていると考えられる。

5．装置開発Ⅱ（超臨界急速膨張法）

超臨界流体を急激に容器外(大気圧)に放出することにより、溶解度は急激に低下し、溶媒であるCO_2は瞬時に気化する。その過程で溶質は微粒子化すると考えられる。この方法は急速膨張(Rapid Expansion of Supercritical Solution; RESS)法と呼ばれる。RESS法はスプレー法の一種でありながら有機溶媒を使用しない完全な乾式法による成膜方法である。単層薄膜ならばスピンコート法やインクジェット法などが容易であるが多層構造化となるとこれらの作成方法は一転して不向きな手法となる。その点で完全な乾式法で有機薄膜を作成する事が出来れば画期的でありこれらの問題を解決した新たな薄膜作成方法として特長付けることができる。装置はFig.8に示すように、超臨界析出装置と同様であるが、セル出口に極細キャピラリーノズルを接続し、連続的に流体が大気圧に開放されるようにしてある。ノ

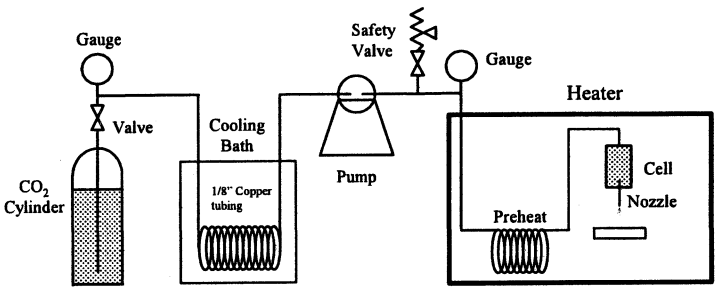

Fig.8: Schematic diagram of the rapid expansion of supercritical fluid solution (RESS) apparatus

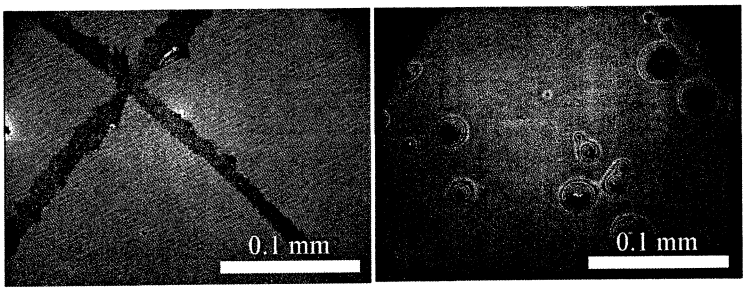

Fig.9: Optical microscope images of MEH-PPV films made with spin-coating (left) and RESS (right).

ズルから基板までは数mm～数cmとしてある。本装置では主として高分子系材料であるMEH-PPV を材料として用いている。MEH-PPV の成膜はスピンコート法に代表される溶液法が用いられることが多い。比較のため、スピンコート法にて成膜したMEH-PPV 膜の光学顕微鏡像を Fig.9(左)に示す。一方、RESS 法では同図右に示すように何らかの膜が形成され、島状の模様が見られた。MEH-PPV は目視では赤色であるが、RESS 法による膜は無色に近く、スピンコート膜とは材質的に異なる可能性があった。そのため、本研究室で別途開発しているImaging-TOF-SIMS 装置を用い、表面スペクトルを取得した(Fig.10)。スピンコート膜と RESS 膜を比較すると主だった質量ピークは一致しており、RESS 法においてもMEH-PPV が堆積しているものと思われたが、本測定では低マス成分しか検出していないため、各々においての分子量分布は把握できていない。今後の検討事項であるが、仮に分子量分布がスピンコートと RESS 法で異なる場合、超臨界流体に対する高分子成分の溶解度不足が原因として想定されるため、分子量分布の確認と溶解度向上のための工夫が必要である。しかしながら、完全なドライプロセスで高分子膜が作製できたことの意味は大きく、高分子材料の多層化やパターニングに向けて予定通りの結果が得られたといえる。

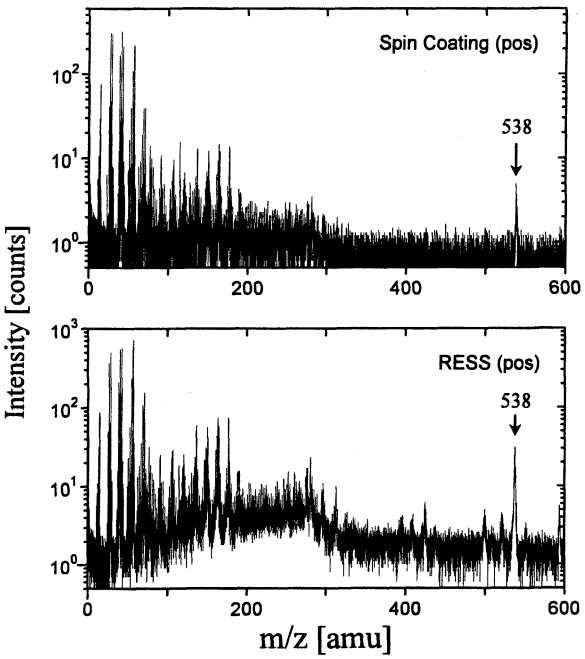

Fig.10: TOF-SIMS spectra of MEH-PPV surfaces deposited on ITO glass substrates.

6．今後の予定

パターニングとの整合性から今後はRESS 法を中心に開発を進める。多層化やパターニングは従来の方法ではきわめて限られた条件でのみ実現されていたが、本方法では通常の操作で可能となる。低分子系・高分子系を問わず利用できる点もメリットである。そのため、これまでに未解決である高分子系材料の溶解特性について、TOF-MS による直接測定を行いながら流体条件の最適化を行う予定である。

参考文献

[1] T. Furuya and A.S. Teja, J. Supercritical Fluids, 29 (2004) 231.

研究業績

[1] 池田一洋、池田大成、宮田亘、坂本哲夫、超臨界流体組成のリアルタイム分析装置の開発、第67回応用物理学会学術講演会、31p-G-15、2006年8月.

[2] 池田大成、池田一洋、宮田亘、坂本哲夫、超臨界流体を用いた有機微粒子・薄膜作製方法の開発、第67回応用物理学会学術講演会、29p-M-3、2006年8月.

[3] 池田一洋、池田大成、宮田亘、坂本哲夫、超臨界流体組成のリアルタイム分析装置の開発、第54回応用物理学関係連合講演会、28p-SK-9、2007年3月.

[4] 池田大成、池田一洋、宮田亘、坂本哲夫、超臨界流体を用いた微粒子・薄膜作製方法の開発(2)、第54回応用物理学関係連合講演会、30a-N-10、2007年3月.

2．2 各種生分解性樹脂へのイオンビームミキシング法等による薄膜付与による機能化

矢ケ﨑　隆義

工学院大学　マテリアル科学科

Multi-Functionalization on Biodegradable Polymeric Resins Through Forming Thin Films by Ion Beam

by

Takayoshi YAGASAKI,

Department of Materials Science and Technology, Kogakuin University

Abstract: We tried to modification and functionarization of biodegradable plastics by giving amorphous carbon thin films to biodegradability resin with ion beam because of coverage expansion of the biodegradable plastics. When this system achieve, because end processing is easy, it is expected to apply as environment low load and electrical /electronic materials. In this study, we try to given amorphous carbon thin film by ion beam assist method and surface carbonization by ion beam modification (ion implantation) method, besides perform establishment of an amorphous carbon thin film. After through forming, carried out structure analysis and evaluated function of thin film.

1　緒　　言

近年、廃棄物処理に関わる問題が多く挙げられる中、既存のプラスチック材料の代替として、環境に配慮した植物由来の生分解性プラスチックスが注目されている。しかしながら，生分解性プラスチックスは耐熱性が低く、構造部材料として考えた場合、汎用のプラスチックと比較して機械物性が低いという理由等から、その適用範囲が制限されている現状にある。このような背景から、報告者らは、生分解性プラスチックの更なる適用範囲の拡大を図るために、イオンビームミキシング法を用いた薄膜形成による生分解性プラスチックの機能化を試みてきた。現在までの研究において、イオンビームを用いた製膜法により、生分解性プラスチックをはじめとする各種高分子材料表面への安定な金属薄膜の付与条件等を明らかにしてきた[1)~4)]。さらに、これらの結果を基に、薄膜部を含む環境負荷軽減材料システムの実現を目的として、金属薄膜の代替となるアモルファス炭素を薄膜とした新しい薄膜付与材料の創成を試みてきた。因みに、アモルファス炭素はその構造により、導電性やトライボロジー特性など様々な機能を発現し得ることから、多様な機能化を図ることが出来るものと考えられる。また，アモルファス炭素の構造は炭素と水素から成ることから、薄膜成分の完全分解が可能である場合，生体材料等への適応をも含む広範囲な領域での適用が期待される。

本研究では、被薄膜付与基板材料として生分解性プラスチックスを、また基板の耐熱性すなわち微細構造が製膜時に及ぼす影響等を比較するための材料としてエンジニアリングプラスチックを選定、これらの基板材料に対し、アモルファス炭素のイオンビームアシスト法による堆積薄膜の形成とイオンビーム表面改質（イオン注入）法による炭化改質層の形成とを試み、アモルファス炭素の堆積薄膜や表面改質層の形成条件等の確立を目指すとともに，得られた薄膜や改質層の構造と機能との関係を精査することを通し、環境低負荷型電気・電子材料や医療・福祉支援材料等としての可能性を評価することにした。本報では、これらの結果の一部を示し報告する.

2.　供試材料および実験・評価方法

2.1　供試材料

堆積薄膜や表面改質層（以後、堆積薄膜と表面改質層とを総じて示す場合には薄膜と称す）を付与する材料（基板）には、既存のプラスチック材料と同等の機械的物性を有し、且つ植物由来の硬質系生分解性樹脂であり今後汎用の可能性が高いとされている化学合成法により製造されるポリ乳酸樹脂（PLA）の内からLACEA（三井化学㈱製）を主として用いた。また、比較材料には、軟質系生分解性プラスチックであるポリブチレンサクシネートBIONOLLE（昭和高分子㈱製）を用いた。尚、基板の耐熱性すなわち表面近傍部の微細構造が製膜時に及ぼす影響等を比較検討するために、各種エンジニアリングプラスチックを比較対象基板材料に選定した。薄膜形成方法の

違いに加え、これら数種類の樹脂の有する微細構造や結晶性の違いが、表面に形成した硬質アモルファス薄膜の構造・機能にどの様な影響を及ぼすのか等を精査した。

2.2 実験・評価方法

プラスチック基板の表面上に、大電流イオン注入装置（日立製作所：HIIB-200-B）を用いて、アモルファス炭素薄膜の形成を試みた。薄膜の形成には、イオンビームアシスト法とイオンビーム表面改質法との2種の方法を用いた。前者はトルエンガス導入下にて He^+イオンビームを照射し分解生成したアモルファス炭素を基板上に堆積させ薄膜を得る方法であり、後者はイオンビーム照射効果（He^+イオン注入）を用い基板の表面自体を炭化させることにより表面改質層を形成する方法である。堆積薄膜および表面改質層の形成プロセスの概念を Figure 1 に、両法による薄膜の形成条件を Table 1 に示す。

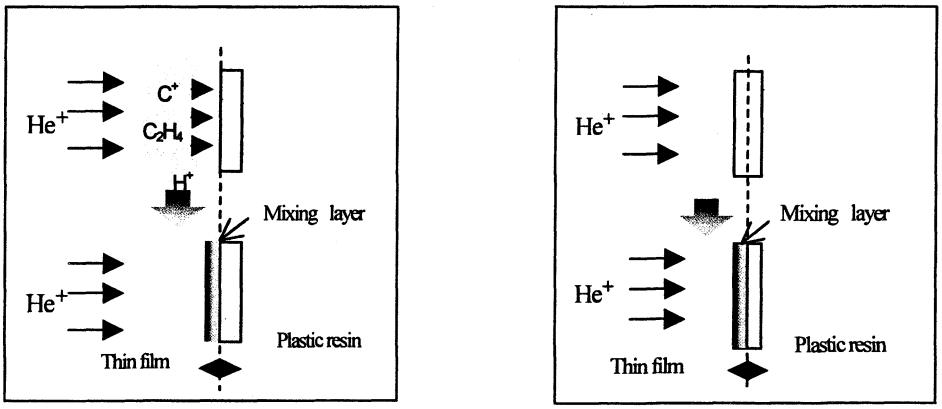

（a）Ion beam assist method　　（b）Ion beam modification method

Figure 1　Thin film forming methods.

Table 1　Thin film formation conditions

	Ion beam assist	Ion beam modification
Ion species	He^+	He^+
Pressure (Torr)	6.0×10^{-5}	6.0×10^{-45}
Toluene gas pressure (Torr)	2.0×10^{-4}	—
Accelerating voltage (kV)	1	1
Current density ($\mu A/cm^2$)	20 or 40	20 or 40
Irradiation time (s)	0 ～ 7200	0 ～ 7200

尚、付与した堆積薄膜および表面改質層の表面形態の観察・分析には、主としてレーザー顕微鏡と電子顕微鏡とを用いた。また、堆積薄膜および表面改質層の表面近傍部の微細構造を把握解析するために、ラマン分光分析と赤外吸収分析とを実施した。さらに、堆積薄膜および表面改質層の機能については、表面・体積電気抵抗率測定法、透過吸収測定法等を用い、それぞれ、形成方法及び基板材料の違いによる機能性の相違等を精査した。

3.　結果および考察

3.1　ラマン分光分析による堆積薄膜および表面改質層の微細構造の確認

生分解性プラスチックの表面上に、イオンビームアシスト法あるいはイオンビーム表面改質法により炭素薄膜の形成を試みた後、表面に形成された薄膜の微細構造を把握するために、ラマン分光分析を実施した。その結果を Fig. 2 および Fig. 3 に示す。Fig. 2 の結果より、イオンビームアシスト法により形成した堆積薄膜について、薄膜付与前には確認されなかったアモルファス炭素に特有の二つのピーク、すなわちグラファイト結晶構造の存在を示す1580cm^{-1}付近のGピークと歪んだsp^2構造を示す1360cm^{-1}付近のDピークの存在が確認されたことから、堆積薄膜の主体はアモルファス炭素であると判断した。さらにその存在は、照射時間の経過に伴い明確になるこ

とが確認された。一方、Fig. 3 の結果より、イオンビーム表面改質法により得られた表面改質層についてもブロード状のG ピークの存在が認められたことから、同法を用いた基板樹脂表面部の炭化によるアモルファス炭素層の形成に可能性のあることが確認された。尚、形成方法の異なるこれらのスペクトルを比較した結果、それぞれのピーク高さ比（G／D）やピーク位置などに相違が存在することから、製膜方法により微細構造が微妙に異なるアモルファス炭素薄膜が得られることが示唆される。

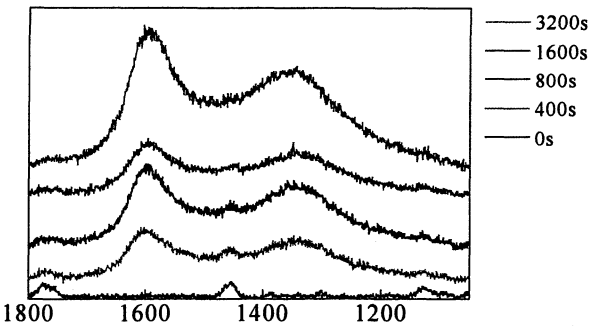

Figure 2 Raman spectroscopy results of film formed by ion beam assist method.

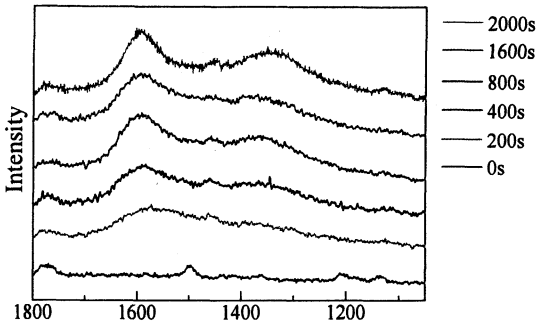

Figure 3 Raman spectroscopy results of reforming layer formed by ion beam modification method.

3. 2 種類の異なる形成法により形成した堆積薄膜および表面改質層の表面電気抵抗率の確認

イオンビームアシスト法あるいはイオンビーム表面改質法を用い、加速電圧 1kV、電流密度 20 μA/cm^2 とし、製膜に関わる照射時間が比較的短い条件で形成した薄膜の電気的機能性を評価するために、それぞれの表面電気抵抗率を測定した。その結果をFig. 4 に示す。同結果より、イオンビームアシスト法により形成した堆積薄膜の表面電気抵抗率値は、製膜時間が 800 秒を越えた時点でほぼ一定値をとることが明らかとなった。因みに、堆積薄膜形成に用いる電流密度を変化させた場合、すなわちイオン注入量を変化させた場合であっても同様の結果が得られることから、イオン注入量は堆積薄膜の表面電気抵抗率の変化に寄与していないことが確認された。他方、イオンビーム表面改質法により形成した表面改質層の表面電気抵抗率は、イオンビームアシスト法のそれとは異なり、照射時間すなわちイオン注入量の増加に伴いさらに低下して一定値を示すことが確認された。いずれの薄膜についても、最終的には半良導体領域(10^4～$10^{12}\Omega$)に相当する表面電気抵抗率値を有することが確認された。今後，イオンビームアシスト法あるいはイオンビーム表面改質法により、比較的短時間で形成した薄膜の微細構造の解析をさらに進めると共に、薄膜の構造と表面電気抵抗値との関係について精査を進めていく必要がある。

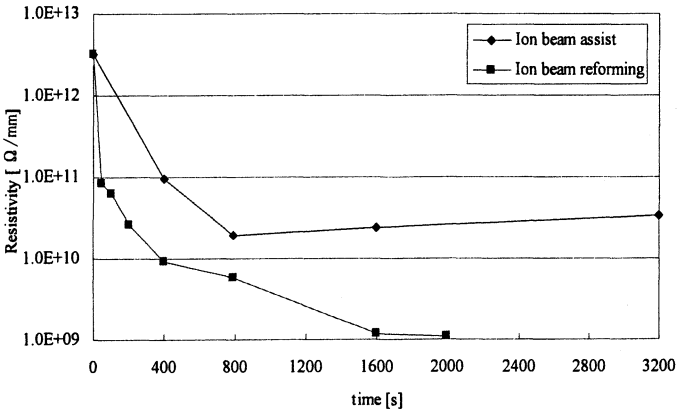

Figure 4 Results of measured surface resistivity of thin films (20μA/cm^2)

3. 3 種類の異なる生分解性プラスチック基板に形成した堆積薄膜および表面改質層の表面電気抵抗率の確認

種類の異なる生分解性プラスチック基板上に、加速電圧 1kV、電流密度 40 μA/cm^2、イオン照射時間を比較的長

い7200秒に設定して形成した堆積薄膜および表面改質層の表面電気抵抗率をFig. 5に示す。同結果より、薄膜を付与した場合、いずれについても表面電気抵抗率が低下することが確認された。また、堆積薄膜については基板の種類によらず表面電気抵抗率がほぼ一定値となることが明らかとなった。他方、表面改質層の表面電気抵抗値については、基板の種類により異なる値を示すことが認められた。表面改質層の形成の場合、基板自体を炭化改質することから、基板とする材料の抵抗値や表面構造に大きく影響を受け、さらに表面粗度にも影響が及ぶものと考えられる．尚、グラファイトの結晶構造を示す顕著なGピークが確認された堆積薄膜の表面電気抵抗率は，Gピークが明瞭に確認されなかった改質層の表面抵抗率と比べると低い値になっている。今後，イオンビームアシスト法およびイオンビーム表面改質法により、比較的長時間で形成した薄膜の表面粗度や微細構造の解析をさらに進めると共に、薄膜の構造と表面電気抵抗値との関係について精査を進めていく必要がある。

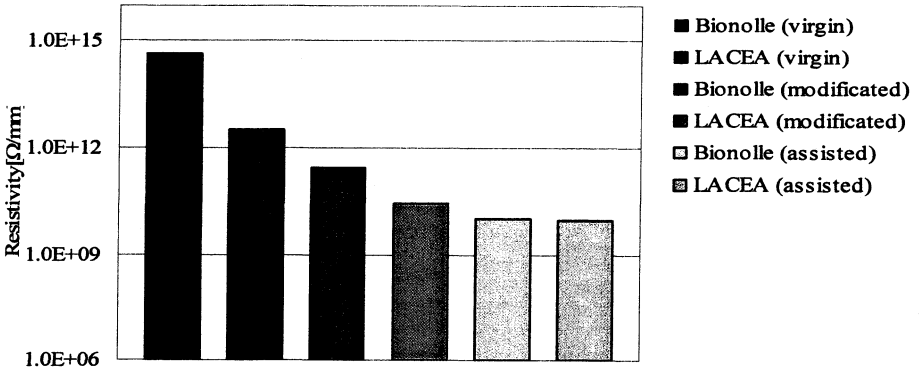

Figure 5　Results of measured surface resistivity of the film formed on various biodegradable plastic substrate.

4. 結言

生分解性プラスチックス基板の表面部に、イオンビームアシスト法によりアモルファス炭素の堆積膜あるいはイオンビーム表面改質法によりアモルファス炭化改質層の形成を試み，それら薄膜の付与及び形成条件等の確立を目指すとともに、得られた薄膜の構造と機能との関係を精査することを通し、環境低負荷型電気・電子材料や医療・福祉支援材料としての可能性を評価した。

その結果、イオンビームアシスト法およびイオンビーム表面改質法により得られるアモルファス炭素薄膜および表面改質層の構造比は、イオンビームの照射時間やエネルギー等の製膜条件には依存せずほぼ一定であることが明らかとなった。他方、イオンビームアシスト法により得られた堆積薄膜の表面電気抵抗率がイオン注入量に依存せず一定の値を示すのに対し、イオンビーム表面改質法により形成した表面改質層の表面電気抵抗率はイオン注入量により変化することが確認された。

本研究は、主として平成17年度の文部科学省“ハイテク・リサーチ・センター整備事業”に採択された研究開発プロジェクト「ナノ表面・界面の創製と応用」（平成17年度～21年度）の研究施設および研究費を用いて遂行中である。また、研究の一部は、工学院大学総合研究所プロジェクト研究費補助を受け実施された。尚、本研究を遂行するにあたり、三井化学株式会社および長野技研株式会社には、それぞれ供試材料のご提供を頂いた。さらに、工学院大学の学生であった大島和巳氏および本学大学院修士課程に在学中の金子睦氏に実験の協力を得た。以上、記して謝意を表す。

参考文献

1) 矢ケ崎隆義、木村雄二、材料、47、84（1998）.
2) 山田香織、矢ケ崎隆義、木村雄二、鷹野一朗、材料、54、79-84（2005）.
3) 大島和巳、矢ケ崎隆義、木村雄二、鷹野一朗、材料の科学と工学、43、4、180-186（2006）.

研究業績

1) 矢ケ崎隆義、Material Stage、6、8、18-23（2006）.
2) 矢ケ崎隆義、新材料工学研究会・第22回研究発表講演会論文集・特別講演別冊、4、1-10（2006）.
3) 金子睦、矢ケ崎隆義、鷹野一朗、木村雄二、下田高志、日本材料学会・第56期学術講演会講演論文集、269-270（2007）.
4) 金子睦、矢ケ崎隆義、鷹野一朗、木村雄二、下田高志、日本材料科学会・第19年度学術講演大会講演予稿集、2007、7-8（2007）.
5) 金子睦、矢ケ崎隆義、鷹野一朗、木村雄二、下田高志、日本機械学会・創立110周年記念・年次大会講演論文集、6、283-284（2007）.
6) 金子睦、矢ケ崎隆義、鷹野一朗、木村雄二、下田高志、新材料工学研究会・第23回研究発表講演会論文集、39-40（2007）.

〔研究成果報告会では、本研究より派生した「スクリーン印刷法を用いて形成した炭素粒含有膜」についても言及する予定である。〕

2．3 イオンビーム照射によるナノレベルでの表面モルフォロジー制御

Formation of Surface Nano-morphology Controlled by Ion Beam Irradiation

鷹野一朗 （工学院大学 電気システム工学科）
Ichiro TAKANO (Depertment of Electrical Engineering, Kogakuin University)
佐々木道子 （理化学研究所）
Michiko SASAKI (RIKEN)

Abstract

The surface properties can be changed by controlling with nano-level even the surface on the material consisting of the same element. For example the leaves of some kinds have the roughness of nano-level. The roughness plays the role of repelling water. It's possible to produce the excellent properties such as the water repellant to the materials surface. In this study, the PTFE surface was irradiated by ion beams of He, N_2, Ar gas. The morphology of PTFE was changed by the effects of sputtering and heating of ion beam. The surface morphology changed by the ion beams produced the high water repellency to the PTFE surface.

1．はじめに

イオンビームを材料に照射するとスパッタリング現象により表面モルフォロジー（形態）が原子レベルで変化する。表面モルフォロジーは照射イオン種とエネルギー，電流密度，さらに材料の種類（金属，化合物，高分子等）によって変化が異なる。表面モルフォロジーをナノレベルで制御することが，親水性や撥水性，表面コーティング膜（特に電子部品を対象としためっき膜等）の密着性や表面反応（光触媒効果等）の向上に大きな影響を及ぼすと考えられている。特に高分子材料では，表面モルフォロジーによって特性が大きく変化することが知られている。

高分子材料に対する表面処理については多くの研究がなされ，その手法も紫外線，レーザー，プラズマの利用など多岐にわたる。高分子材料の場合，分子の結合エネルギーが弱いため，様々な方法で比較的容易に表面に変化を与えることができ，形態の変化だけではなく発生した官能基などが表面特性に影響を与えることになる。特に，エネルギー粒子を用いたプラズマ法では，Ar などの不活性ガスプラズマ中で高分子材料を処理することで接着性を向上させ，さらにフリーラジカルを誘引することで－OH などを含んだ表面を形成するなど，ぬれ性の改善に用いられている。また，不活性ガス以外の NH_2, O_2, N_2 などのプラズマによっても，様々な官能基が作られることが知られている[1)]。

一方，プラズマを用いた場合そのエネルギー分布は一様ではないため，高分子表面に与えるエネルギーの詳細な調査をする場合には問題が残る。そこで，イオンビームなどの一様なエネルギーをもつ粒子を使用すれば，高分子表面に与えるエネルギーと電流密度制御を精密に行うことができる。イオン照射は周知のように半導体製造においてなくてはならない技術として発展してきている。イオン照射の特長は，多種の元素の中から任意のイオンを選択して材料に照射でき，またイオンの加速エネルギーや照射量を任意に設定できることから制御性に優れている点である[2)]。

本研究では，イオンのエネルギーにばらつきのあるプラズマを用いるのではなく，一様のエネルギーを持つイオンビームを利用することで，精密に表面形態の制御を行う。本報では特に高分子材料として PTFE（ポリテトラフルオロエチレン）を用い，表面形態の変化と PTFE において重要な特性とされている摩擦係数及び水の接触角について評価した。PTFE を対象としたイオン照射の研究は井上ら[3)]が報告しているように，様々なエネルギーや照射電流で Ar^+イオンを照射した場合，その表面形態は大きく変化し撥水性に強く影響するがそのメカニズムは明らかになっていない。さらに，鈴木らは生体への使用が認可された ePTFE（expanded polytetra-fluoroethylene，ゴアテックス社：人工硬膜 DM-03100）に対して細胞接着性を試みる研究を行っている[4)5)]。He^+やNe^+イオンを様々な条件で照射した結果，エネルギー150keV の Ne^+イオンを電流 0.2μA/cm^2 以下で照射すると細胞の付着性を付与できることを明らかにしており，実用化のための研究が期待されている。

2．実験装置

イオン照射装置はイオン源，加速器，イオンビーム質量分離器などから構成されている。イオン源はイオン

化方式の違いで高周波放電や低電圧アーク放電など幾つかの方式に区分けされ，それらを基にフリーマン形やホローカソード形など多種多様のイオン源が開発されている[6]。イオン源自体には通常 50kV 程度までの引き出し電極が含まれ，この電圧より高いエネルギーを得るためには，加速器をビームラインに設置する必要がある。イオンビーム質量分離器は，磁界分離方式が多く用いられており，磁界の中にイオンを通過させローレンツ力により30～90度の角度で曲げることで目的のイオン種のみを分離する。この際には一部中性粒子も排除されることになり，ターゲットに打ち込まれるイオンは非常に高純度で，エネルギーも精密に制御される。以上のようなタイプに対し，質量分離器を用いないものを直進型(ビームを曲げるのに対して)として区別することがある。直進型の場合はイオンの質量分離をしないためイオンの純度は劣るが，装置はコンパクトになり，マルチアパーチャー(多孔)電極を備えたイオン源等を用いることで大口径のイオンビームが発生でき大面積処理が行える。従って，質量分離型は研究開発や金属イオンを用いる場合に，直進型は生産性を重視しかつイオンがアルゴンや窒素のような場合に用いられることが多い。

本研究では，直進型のマルチアパチャータイプの電極を持つ大電流イオン照射装置と質量分離器を備えたマルチプロセスコーティング装置を用いる。大電流イオン照射装置ではイオンエネルギー1keVから20keVまで，電流密度は最大 300μA/cm^2 が照射可能である。マルチプロセスコーティング装置ではイオンエネルギー500eVから30keVまで，電流密度は最大 80μA/cm^2 が照射可能である。

3. 実験方法

試料として用いる PTFE(ニチアス㈱)の物性は，溶解温度 357℃，密度 2.1g/cm^3，比熱 1.05kJ/(kg･K)，熱伝導率 25.1W/(m･K)である。PTFE へのイオンビーム照射は直進型イオン源を持つ大電流イオン注入装置(日立製作所㈱)を用いて行った。サンプルホルダーに試料を装着後，照射チャンバー内を 6×10^{-4}Pa まで排気し，He, N_2 または Ar ガスを導入して 1×10^{-2}Pa とした。イオンエネルギーは 10keV，照射量電流密度は 40μA/cm^2 とし，照射時間を変化した場合とイオンエネルギーと照射電流密度の関係から，表面形態の変化を観察した。摩擦試験は表面性試験機(新東科学㈱)を用いて固定荷重 20gf とし，摺動幅 5mm の往復摩擦試験により相手材 SUJ2 球に対する摩擦係数を測定した。

水接触角試験は接触角計(協和界面科学㈱)を用いて，蒸留水 1μℓを滴下して水滴の接触角を測定した。接触角は，液滴の左右端点と頂点を結ぶ直線の固体表面に対する角度から $\theta/2$ 法で求めた。

4. 実験結果

Fig.1 には各イオンを照射した PTFE の SUJ2 球に対する摩擦係数を示す。摩擦係数は，700s 間摺動測定を行いその平均値とした。He$^+$イオン照射後の PTFE の摩擦係数は急激に上昇し，照射時間300sにおいて最大となり，その後 600s 以降では初期値と同じ値で一定となった。Ar$^+$と N_2^+イオン照射では大きな違いは無く，照射後 N$^+$イオンでは少し摩擦係数が高くなるが Ar$^+$イオンでは摩擦係数はほぼ一定を保つ。600s 以降徐々に摩擦係数は上昇し始め約0.3で飽和した。He$^+$と Ar$^+$および N$^+$イオンでこのような傾向が現れたのは，質量の違いによるものと考えられる。He の質量数は 2，N_2 は 28，Ar は 40 であり，N と Ar でも違いはあるが He に比べると質量

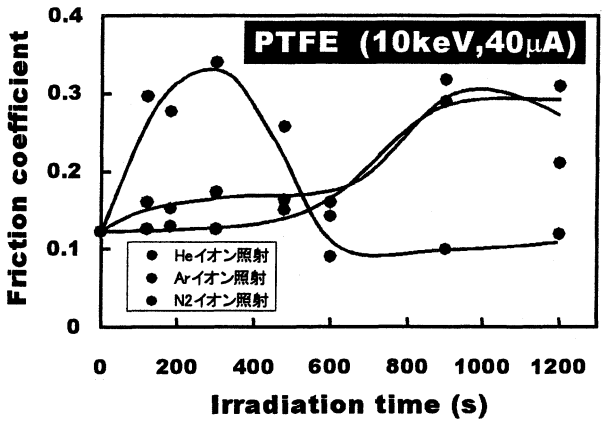

Fig.1 Friction coefficient of PTFE irradiated by He^+, N_2^+ or Ar^+ ion beam

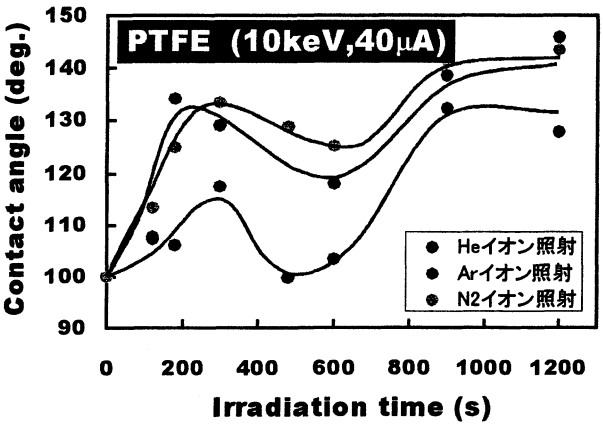

Fig.2 Contact angle of PTFE irradiated by He^+, N_2^+ or Ar^+ ion beam

数はかなり大きい。一般にイオン注入の場合，固体に与えるイオンの物理現象の大きなものとして侵入深さが挙げられる。軽いイオンは固体内部への侵入距離が長く，重いイオンは侵入距離が短くなるり，これらの違いが摩擦係数に影響を与えていると考えられる。

Fig.2 には摩擦係数と同様の条件で作製した試料に対する水の接触角変化を示す。PTFE は良く知られているように元々撥水性の高い材料である。一般に物体の表面では，物体の分子がもつ力によって近接する水の分子を引き寄せようとする性質があるが，その度合はその表面の物理的・化学的構造によって異なる。双方の関係は水の凝集力と基材表面引力との関係で決まる。接触角 θ が 90° 以上の場合を撥水性，110° から 150° の場合が高撥水性，150° 以上の場合は超撥水性となる。ここでは，イオン照射した PTFE の撥水性がどのように変化するか測定した。Fig.2 の水接触角測定において，未照射 PTFE の接触角初期値は 100° で，この値から出発してイオン照射とともに接触角は照射時間約 300s まで上昇する。N^+と Ar^+イオンは，摩擦係数の場合と同様に似たような特性を示すが，He^+イオンでは，変化が小さいものの，一度上昇し再び下降，再度上昇する傾向は各イオンに共通の特性であった。各イオンとも照射時間 900s で接触角 130° 周辺に収束した。Fig.1と Fig.2 を比べると，両者に共通していることは，He^+イオン照射 300s，各イオン照射共通で 600s と 900s の試料付近で変化が生じているようである。詳細については今後さらなる調査を必要とするが，現時点では表面形態の変化が影響を及ぼしていることが電子顕微鏡による表面観察から推測される。Fig.3 には未照射 PTFE と He^+イオン照射 900s での表面形態の変化を示す。未照射 PTFE は細かい傷は存在するもの大きな凹凸は存在しない。一方，900s の He^+イオン照射の表面形態においては，針状の突起が多数成長していることがわかる。この針状の突起により PTFE

Fig.3 Surface morphologies of PTFE un-irradiated and irradiated by He^+ ion beam

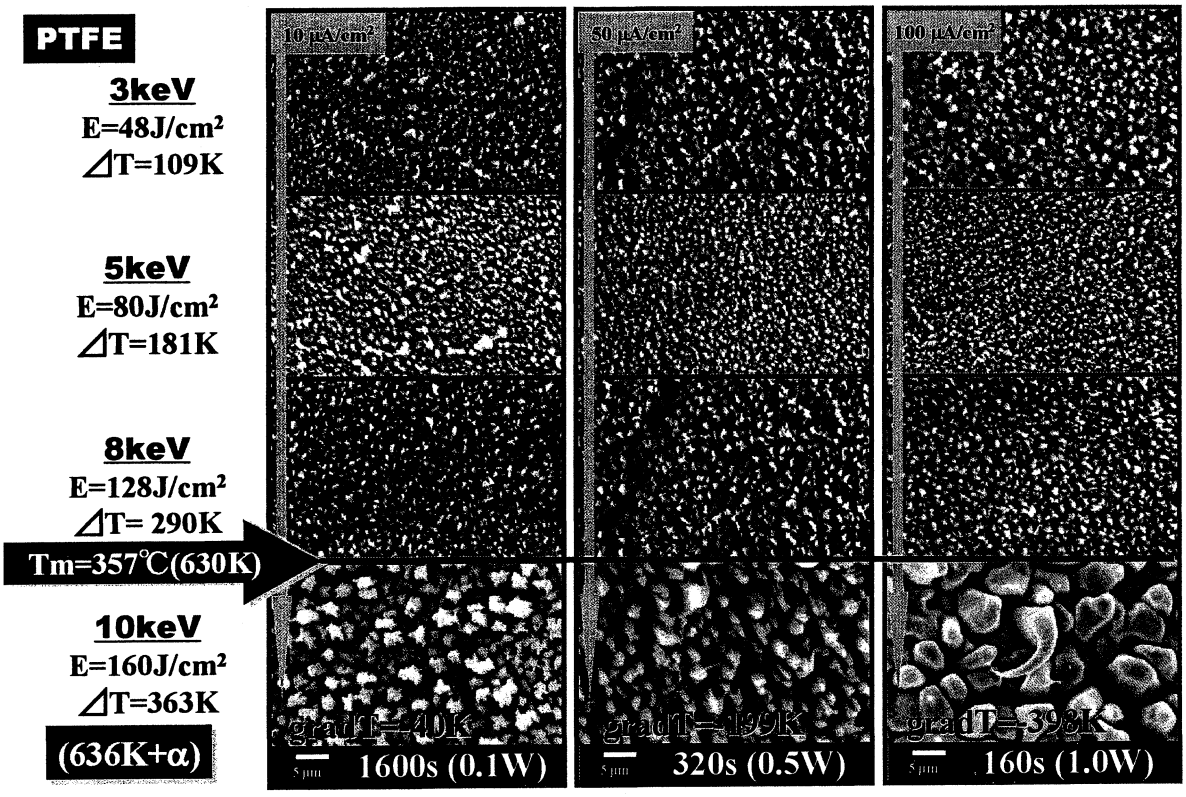

Fig.4 The surface morphology of PTFE irradiated by Ar^+ ion beam ($1x10^{17}$ ions/cm²)

ン照射の表面形態においては，針状の突起が多数成長していることがわかる。この針状の突起により PTFE

側の水に対する引力が減少し，撥水性が高まったものと考えられる。

そこで，照射条件との関連性を検討するため Ar^+イオン照射されたPTFE表面形態を電子顕微鏡により観察した結果をFig.4に示す。マトリックス状に並べられた写真において，縦方向のイオンエネルギーは3, 5, 8, 10keV の順の変化を示している。横方向の並び順は照射電流密度を示しているが，照射のイオン数は $1x10^{17}$ions/cm^2 で一定としているため，照射時間は 10μA/cm^2 で 1600s, 50μA/cm^2 で 320s, 100μA/cm^2 で 160s となる。すなわち，照射イオン数は一定なので試料に投入される総エネルギーは一定である。一方，縦方向の並び順においてはイオンエネルギーがそのまま PTFE への投入エネルギーの違いとなる。図中の E の値は単位面積当たりのエネルギーとなり，⊿T は PTFE の比熱から計算した温度上昇を示している。写真からわかるように，イオンエネルギー3keV～8keV において，また照射電流密度 10μA/cm^2, 50μA/cm, 100μA/cm^2 で大きな変化はなく，スパッタリングにより表面に細かい突起が形成されている。ところが 10keV になると表面形態は一変し，8keV 以下とは異なる状況を示す。さらに，総エネルギーが同じである電流密度 10μA/cm^2, 50μA/cm^2, 100μA/cm^{2}の場合においても，異なった形態を示すようになりスパッタリング以外の要因が関連していることを予想させる。筆者らはこれがイオン照射による温度上昇によるものと考え，PTFE表面の温度を計算によって求めた。イオンエネルギー10keV では，⊿T=363K となりこの温度は PTFE の溶解温度以上となっていることがわかる。すなわち，10keV ではイオン照射による熱的な効果により PTFE は溶融状態となり，そこにイオンが照射されていると考えられる。また，照射電流密度を変化した場合については，本来であれば温度による影響は考えにくいが，その表面形態は激しく変化している。ここでも、温度による影響が考えられるため，図中に示すように単位時間当たりのエネルギー、すなわち電力 0.1W, 0.5W, 1.0W/cm^2 の影響を考えた。試料は水冷するサンプルホルダーに密着しており，イオン照射中の PTFE の表面と裏面での温度差は非常に高いことが予想される。ここでは、単純に試料の厚さに依存する表面と裏面の温度勾配を求めて比較した。照射電流密度 10μA/cm^2 ではgradT=-40K, 50μA/cm^2 ではgradT=-199K , 100μA/cm^2 ではgradT=-398K となり，照射イオン個数が同じでも単位時間当たりにおけるエネルギーから見ると，表面の温度上昇は激しいものとなり、この違いが表面形態に影響していると考えられる。以上より，PTFE表面の突起形成メカニズムを推測すると，PTFEの溶解温度以下ではイオン照射によるスパッタリング効果で微細な突起が形成されるが，それ以上突起の形態に変化は生じない。PTFEの溶解温度以上に表面温度が上昇したとき，表面形態はスパッタリングと照射加熱の影響により，微小突起が合体し大きな突起となり針状部分が成長する。さらにエネルギーが増すと針状部分が合体し，大きな柱状の形態となることが推測される。

5. おわりに

PTFE に対するイオン照射により，表面形態に大きな変化が得られたため今後の展開が期待できる。今回基板温度などを計算により求めたが，表面形態との関連性が良い一致を示しており，温度を実測して詳細なメカニズムを検討する予定である。さらに，イオン種については安全性や扱い易さなどから不活性ガスや窒素，炭素などのイオンが使われることが多く，特に生体への応用を考えた場合，窒素などのガスイオンを用いることは生体への影響を小さく抑えることができ，安全性の面からは不活性ガスを使うことが良いと言えよう。イオン種については現在のものの他に C^+イオンを追加して実験を進めたいと考えている。

参考文献

1)筏義人編"高分子表面の基礎と応用"化学同人(1986)

2)鷹野一朗，表面技術，**52**, 12 (2001) 9

3)井上陽一，吉村保廣，池田由紀子，河野顕臣，表面技術，**51** (2000) 512

4)鈴木嘉昭，村上 泰，中尾愛子，岩木正哉，貝原 真，神尾正巳，IONICS, **25** (1999) 47

5)鈴木嘉昭，岩木正哉，貝原 真，谷 論，大橋元一郎，神尾正巳，IONICS, **27** (1999) 3

6)石川順三"イオン源工学"アイオニクス(1987)p 397

研究業績

1)鷹野一朗，他;"高分子材料へのイオンビーム照射による表面機能評価"日本真空協会・真空に関する連合講演会(2007.11)

2)佐々木道子，他;"低エネルギーAr^+イオン照射によるPTFEの表面改質"表面技術協会・第116回講演大会(2007.9)

3)Ichiro Takano, et al." Surface modification of biodegradable plastic by ion beams "Vacuum, **80**(2006)788-792

2. 4 ポーラス構造を持つ薄膜材料を用いた新規ナノデバイスの開発
Fabrication of novel nano-devices based on thin solid films with porous structure

水酸アパタイトの析出に及ぼす軽金属表面に付与されたナノ構造の効果
Effect of Nanostructured Surfaces of Light Metals on Hydroxyapatite Coating

小野幸子，阿相英孝，安川雪子
Sachiko ONO and Hidetaka ASOH

工学部応用化学科，総合研究所
Faculty of Engineering, Dept. of App. Chem., Res. Inst. Sci. Tchnol.

Abstract: Hydroxyapatite coating by alternative dipping method on light metals such as Al, Mg and Ti having porous surface was studied with focusing on the morphology and composition of the surface layer. HAp coating is significantly enhanced by porous substrates having a pore size of 10 nm ~ 30 nm, i.e., mesoporous range. Incorporated electrolyte species into the substrates assist the precipitation of HAp in the following order: sulfuric acid ≧ sodium hydroxide > oxalic acid > phosphoric acid. Thus, it was clarified that the meso-porous size as well as incorporated anions of porous substrate strongly affected to the HAp coating.

1. INTRODUCTION

Hydroxyapatite (HAp) coating on various metals has attracted considerable attention due to the expectation to allow their use as artificial bones even under load-bearing conditions. The basic requirements of the artificial bones and dental implants are biocompatibility, mechanical integrity, and osteoconductivity. To provide effectively such properties on the metal substrates, dense hydroxyapatite coating is essential. In particular, improvement of the bonding between substrate and HAp, which is strongly dependent on the surface micro/nano-structure of the substrate, would be an urgent requirement [1].

Recently, other than titanium, the biomedical usage of magnesium such as a stent has widely generated attention because of its lightness, harmlessness and expected biodegradability in the human body after bone generation [2, 3]. In the present study, therefore, we studied the micro/nano size effect of the substrate surface on HAp coating with the use of porous anodic alumina film, in which the pore size and interval can be controlled easily by changing the applied voltage [4, 5]. In this study, HAp coating was conducted using the alternative immersion method by dipping specimens alternatively in a saturated calcium hydroxide and subsequently in ammonium hydrogen phosphate.

2. EXPERIMENTAL

High purity (99.99 %) aluminum sheets were electropolished in an ethanol / perchloric acid solution before anodization to obtain a flat and glossy surface. Anodization was carried out at constant voltage in different electrolytes, i.e., 1.5 mol dm^{-3} sulfuric acid at 20 °C, 0.3 mol dm^{-3} oxalic acid at 30 °C, 0.25 mol dm^{-3} phosphoric acid at 25 °C, 0.3 mol dm^{-3} chromic acid at 40 °C and 0.04 mol dm^{-3} sodium hydroxide, following each conventional anodizing condition. The thickness of the anodic films was fixed to approximately 1 μm by changing electrolysis time. HAp coating was conducted using the alternative

immersion method by dipping specimens alternatively five cycles in a saturated $Ca(OH)_2$ and subsequently in 0.02 mol dm^{-3} $(NH_4)_2$ HPO_4 at 20 °C for 1 min each. Finally, specimen were dipped in a saturated $Ca(OH)_2$ again. Each bath was agitated at 350 rpm.

3. RESULTS AND DISCUSSION

Figure 1 indicates the cross sections of anodic porous alumina films formed in various electrolytes after HAp coating. Apparently, HAp growth was strongly dependent on the type of electrolyte used for anodization. Platelet-like and granular deposits were found on the films formed in sulfuric acid, oxalic acid and sodium hydroxide solutions. The platelet-like deposit seemed to be grown densely attached to the porous film surface. On the film formed in chromic acid solution, only granular type deposit was found. However, no deposition was detected in the case of phosphoric acid solution. As shown in Fig. 2, thin film X-ray diffraction analysis of deposits after heating at 1300 °C indicated that the deposit was HAp.

To clarify the cause of difference in HAp growth on the porous anodic films, the effect of pore diameter was first examined. The relation between anodization voltage and pore diameter formed in different electrolytes are shown in Fig. 3 (after ref. 5). The pore size is substantially proportional to the anodization voltage; however, the pore size of the film formed in phosphoric acid is almost two times larger than that of sulfuric acid. Figure 4 indicates the effect of formation voltage, namely, the effect of pore diameter on HAp deposition in the case of porous alumina films formed in sulfuric acid. HAp deposition decreased with decreasing formation voltage from 20 V, 10V and 5 V, i.e., decreasing pore diameter from 16 nm, 11 nm and 9 nm according to the data of Fig. 3. Appearance of specimens, which changed from deep white to pale white, is coincident with the SEM observation. In addition, platelet-like deposits appear to form isolated bundles in the size of approximately 20 μm suggesting the nucleation process of deposits.

When anodic films were formed in oxalic acid, growth ratio of deposits on the films was relatively low than those of sulfuric acid. As shown in Fig. 5, platelet-like deposits slightly increased when formation voltage decreased from 40 V to 10 V, i.e., pore size decreased from 35 nm to 13 nm. However, HAp did not found when formation voltage lowered to 10 V, which corresponds to the pore diameter of 11 nm. Thus, HAp growth on porous anodic film seems to have optimum range of pore diameter. In addition, HAp growth on the film formed in sulfuric acid is more preferable than that associated with oxalic acid.

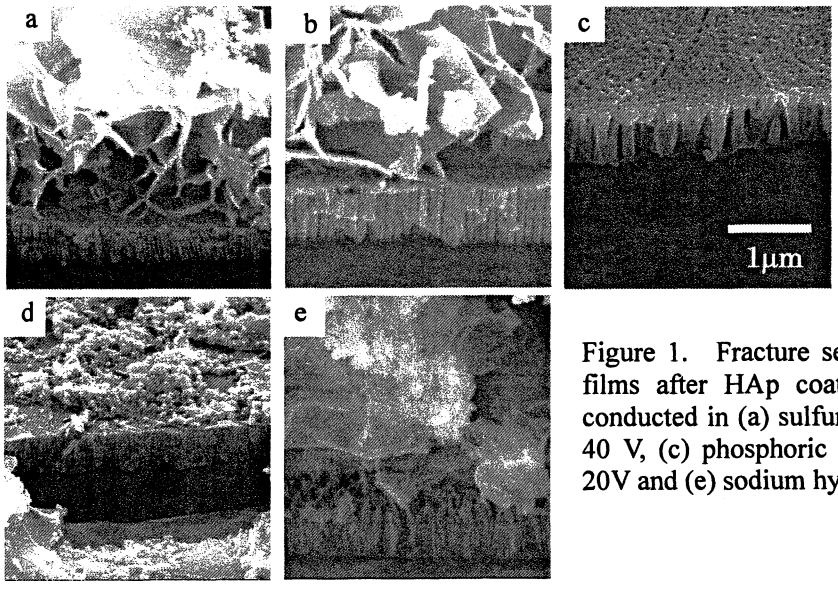

Figure 1. Fracture sections of porous anodic alumina films after HAp coating treatment. Anodization was conducted in (a) sulfuric acid at 20 V, (b) oxalic acid at 40 V, (c) phosphoric acid at 80V, (d) chromic acid at 20V and (e) sodium hydroxide at 40 V.

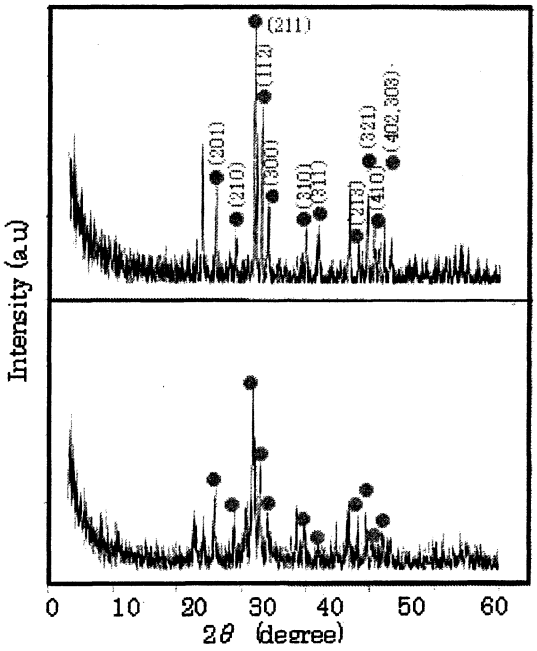

Figure 2. TF-XRD analysis of deposits after HAp coating treatment of anodic films formed in (a) sulfuric acid at 20V and (b) sodium hydroxide at 40V.

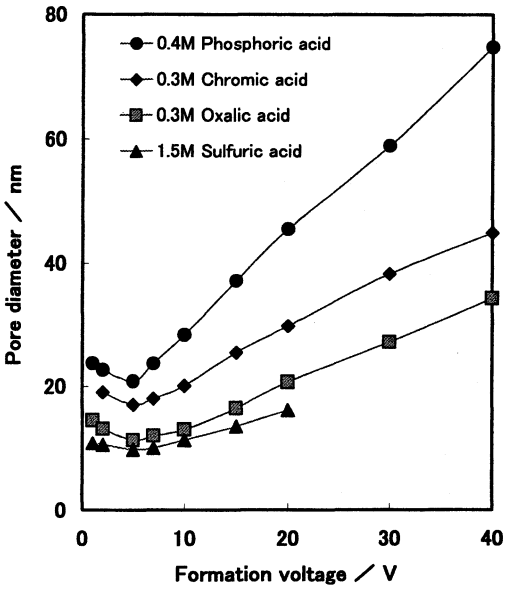

Figure 3. Change in pore diameter with formation voltage and anodizing electrolytes. After ref. 5.

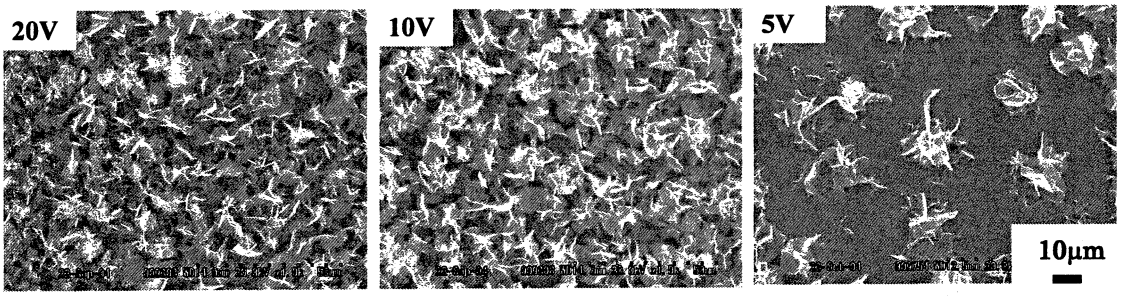

Figure 4. SEM images of the surfaces after HAp coating treatment of anodic films formed on aluminum. Anodization was performed at 20 V, 10 V and 5 V in 1.5 mol·dm^{-3} sulfuric acid. The size of pore decreases with decreasing voltage from 16 nm to 9 nm according to the relation shown in Fig. 3.

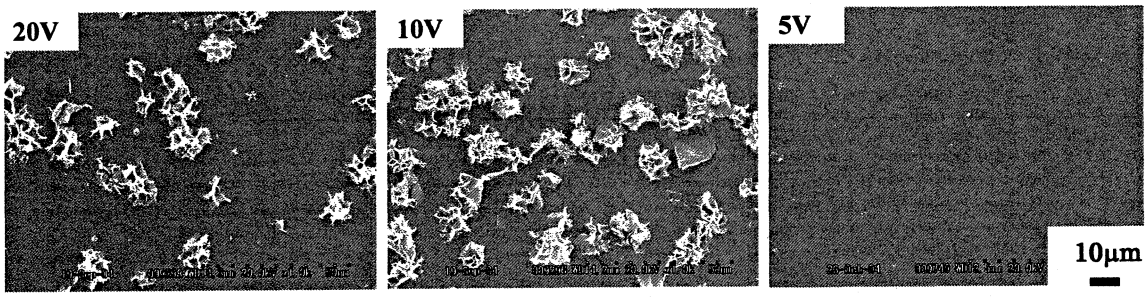

Figure 5. SEM images of the surfaces after HAp coating treatment of anodic films formed on aluminum. Anodization was performed at 20 V, 10 V and 5 V in 0.3 mol·dm^{-3} oxalic acid. The size of pore decreases with decreasing voltage from 16 nm to 9 nm according to the relation shown in Fig. 3.

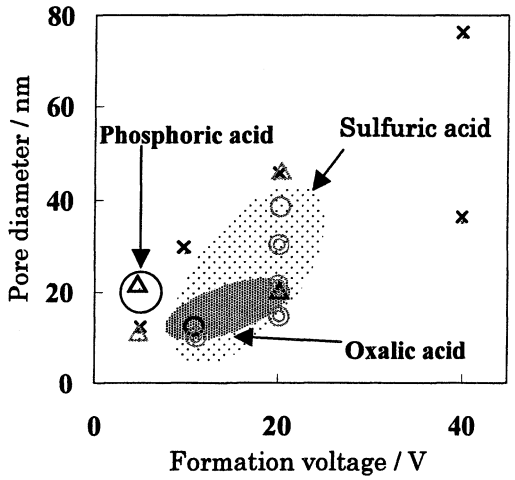

Figure 6. Relationship between formation voltage, pore diameter and coefficient of HAp deposition.

◎excellent, ○good, △fair, ×bad

HAp growth was strongly dependent on pore size and electrolyte species as summarized in Fig. 6. Especially, the HAp growth was predominant at the pore size of 10 to 30 nm and the films formed in sulfuric acid. The growth rate and quantity of the HAp deposition decreased in the following order; sulfuric acid ≧ sodium hydroxide > oxalic acid > phosphoric acid. At the same time, they increased with the increasing depth of pores. In particular, the pores with the size of meso-porous range significantly accelerated the growth of hydroxyapatite.

4. CONCLUSION

Hydroxyapatite coating by alternative dipping method on light metals such as Al having porous substrate surface was studied with focusing on the morphology and composition of the surface layer. As a result, following conclusions have been obtained. (1) HAp coating is significantly enhanced by porous materials having a pore size of 10 nm ~ 30 nm, i.e., mesoporous range. (2) Incorporated electrolyte species assist the precipitation of HAp. Thus, it was clarified that the meso-porous size as well as incorporated anions strongly affected to the HAp coating.

REFERENCES

1. B. Otsuki, M. Takemoto, S. Fujibayashi, M. Neo, T. Kokubo and T. Nakamura, *Biomaterials* **27**, 5892 (2006).
2. F. Witte, V. Kaese, H. Haferkamp, E. Switzer, A. Meyer-Lindenberg, C.J. Wirth and H. Windhagen, *Biomaterials* **26**, 3557 (2005).
3. R. Erbel, C. Di Mario, J. Bartunek, J. Bonnier, B. de Bruyne, F. R Eberli, P. Erne, M. Haude, B. Heublein, M. Horrigan, C. Ilsley, D. Böse, J. Koolen, T. F Lüscher, N. Weissman and R. Waksman, *Lancet* **369**, 1869 (2007).
4. J. P. O'Sullivan and G. C. Wood, *Proc. Roy. Soc. Lond. A.* **317**, 511 (1970).
5. S. Ono and N. Masuko, *Surf. Coat. Technol.*, **169-170**, 139 (2003).

【研究業績（2005年4月－2008年2月）】：研究論文16報，著書2報，国際会議17件，国内会議72件

1. Y. Yasukawa, H. Asoh and S. Ono, *Electrochemistry Communications*（印刷中）
2. S. Ono, A. Kiyotake and H. Asoh, *ECS Transactions*（印刷中）
3. 奥平浩平，阿相英孝，小野幸子, *Electrochemistry*, **75** (11), 873-878 (2007)
4. H. Asoh, K. Nakamura and S. Ono, *Electrochimica Acta*, **53** (1), 83-86 (2007)
5. 小野幸子，阿相英孝，*工業材料*, **55** (8), 62-65 (2007)［解説］
6. 小野幸子，阿相英孝，*機能材料*, **27** (7), 13-20 (2007)［解説］
7. 小野幸子，*表面技術* (J. Surf. Finish. Soc. Jpn.), **58** (6), 342-346 (2007)［解説］
8. S. Ono, M. Saito and H. Asoh, *Electrochimica Acta*, **51** (5), 827-833, (2005)
9. H. Asoh and S. Ono, *Applied Physics Letters*, **87** (10), 103102/1-103102/3, (2005)
10. S. Ono, C. Wada and H. Asoh, *Electrochimica Acta*, **50** (25-26), 5103-5110, (2005) 他

2.5 超音速フリージェットPVDによるナノ組織・ナノコンポジット膜の形成

工学院大学	機械システム工学科	丹羽 直毅，廣木 富士男，湯本敦史
工学院大学	マテリアル科学科	塩田 一路，桑折仁
東京大学大学院	新領域創成科学研究科	山本 剛久
NASIC客員研究員		鈴木 敏之
サレジオ高専		大杉 功
サレジオ高専		加藤 雅彦

Development of Nano structure and Nano Composite Coatings with Supersonic Free-Jet PVD

N. Niwa, F. Hiroki, A. Yumoto: Dept. of Mecanical Systems Eng., Kogakuin University

I. Shiota, H. Kohri: Dept. of Materials Science and technology, Kogakuin University

T. Yamamoto: Dept. of Advanced Materials Science, University of Tokyo

T. Suzuki: Nasic

I. Ohsugi, M. Kato: Salesian Polytecnic

ABSTRACT: The aim of our present work is to produce ceramic films on a metal substrate with Supersonic Free-Jet PVD (SFJ-PVD) and to investigate the relationships between the microstructure and the tensile properties of it. With SFJ-PVD, We produce a film that has smooth, compact and defect-free microstructure both in the film and at the interface between the substrate and the film and excellent adhesive strength to the substrate.

1. 緒 言

セラミックスコーティングは，構造材料の特性向上を目的とした皮膜素材として代表的な素材である．とりわけ，侵入型窒化物であるTiNは，B2（NaCl型）構造となり高い導電性，大きい熱伝導率と高硬度など優れた諸特性を有するため，耐摩耗性材料として，また半導体材料の分野ではその低抵抗率と熱的安定性から電極金属と半導体との間の拡散障壁として用いられようとしている．さらにTiNは美麗な金色を呈することから，時計やメガネフレームの装飾用コーティングとしての利用も進められてきているなど，様々な分野で幅広く活用されている．TiNの形成技術として窒化・熱処理などによる基材（主にTi合金）の表面改質と共に各種PVD，CVDによるTiN皮膜として基材表面に形成の試みが注目されている．しかし，高い成膜速度のプロセスにより緻密なTiN皮膜を得た研究報告は少ない．

これまで，高い成膜速度が得られる一般的な溶射法では，炭化物あるいは窒化物などの分解・昇華性材料の成膜は困難であるため，溶射原料を窒素と反応させ，その反応生成物である窒化物を堆積させる，いわゆる反応性溶射法の適用などが検討されてきた．福本らは，高周波熱プラズマを用いた反応性溶射により窒化物Ti皮膜，Ti基材から連続的に組成を変化させることにより界面強度の確保を目的とした傾斜組成窒化Ti皮膜の形成を試みている．しかし，同法においても皮膜中に多くの欠陥が存在し，緻密な皮膜の形成には至っていない．

著者らは，次世代コーティング技術に必要とされるこれらの性能を持つ新しいコーティング技術として，超音速フリージェットPVD（Supersonic Free-Jet PVD; SFJ-PVD）の開発，研究を行っている．本法は，ナノ粒子の積層により成膜させる技術であり，メゾスコピック領域において発現する特異な現象も成膜に期待でき，本法の発展によっては既存技術の限界を打破する可能性がある．本研究では，高硬度皮膜として

多くの分野で期待されながら，緻密で厚膜の形成の成功例が少ない TiN 皮膜を超音速フリージェット PVD にセラミックス粒子生成技術である「活性プラズマ-金属」反応を組み込むことにより形成を試みる．さらに，実用化を念頭に，金属基材とセラミックス皮膜の異種界面での強度を確保するため Ti 基板から連続的に窒素組成を変化させた傾斜組成 TiN 皮膜の形成も試みた．傾斜組成皮膜とすることにより耐摩耗性皮膜などとして使用する場合の熱応力の緩和が期待できる．

2. 超音速フリージェット PVD

2.1「活性プラズマ-金属」反応

プラズマアークにより活性化した H_2, N_2, O_2 などの 2 原子分子ガス雰囲気下で金属を溶解すると，多量の金属ナノ粒子が生成，また，雰囲気ガスにより反応生成させた化合物ナノ粒子が形成するなどの現象がみられる．これを利用して宇田らは新しいナノ粒子生成技術を開発し，これを「活性水素-金属」反応法，「活性プラズマ-金属」反応法と名付けている．以下に宇田の考察および宇田ら報告を基に本反応法に対する明石の考察を纏める．

金属中に H_2, N_2, O_2 などの 2 原子分子ガスが溶解するときは，金属表面で解離し原子状となって進入するため，金属中へのガス溶解量は一定温度においてガス分圧の平方根に比例する（Sieverts の法則）．プラズマアークの高温下ではこれら 2 原子分子ガスは容易に解離して原子状になることは，水素および窒素の解離度と温度の関係（H_2=2H, N_2=2N の高温平衡）からも推測できる．原子状の気体が金属との反応性に富むことは言うまでもない．窒素との親和力の大きい金属（Zr, Ti, Al, Si）を窒素，アルゴン混合ガス下で窒素分圧を種々に変えて（$P_{N2}+P_{Ar}$=0.1MPa）アーク溶解および非アーク溶解したときの金属中の窒素溶解量を比較すると，アークによって解離した窒素原子を含む前者の方が，分子状窒素下の溶解時の約 20 倍の窒素溶解量を示す．アーク溶解時に溶解金属は一般にアーク気相と非アーク気相とに接触しているので，アーク直下で活性化ガスが多量に溶解金属中に溶け，対流によって移動し，非アーク気相に放出されるためであると考えられる．事実，溶解した金属中の窒素溶解量が分子状窒素における窒素溶解度を超えて窒素が放出されるときに，微小粒子を生じさせる現象が観察されている．

窒化物ナノ粒子生成の一例として「活性プラズマ-金属」反応による TiN ナノ粒子を形成させた報告した宇田と大野の報告によると，TiN ナノ粒子は粒径が小さくなっても立方体晶癖を有し（金属の場合，粒径が小さくなると球形を呈する），NaCl 型構造で，粒径範囲は 10ー150nm（平均 45nm）である．TiN ナノ粒子の XRD 分析では格子定数 a=0.4243nm と化学量論的 TiN 組成の形成が確認されている．

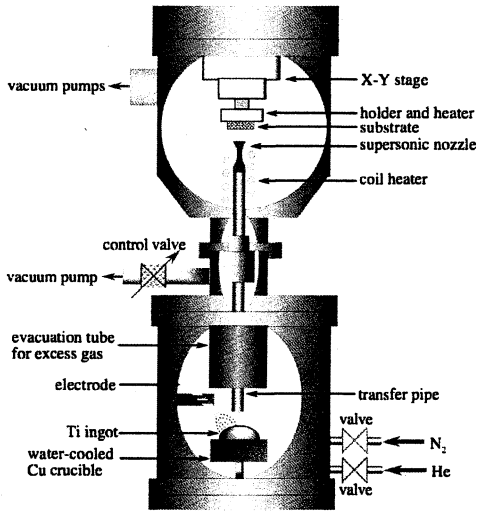

Fig. 1 Schematic diagram of Supersonic Free-Jet PVD apparatus.

2.2 実験方法

蒸発素材として高純度 Ti（≧99.999mass%）を用い，基板は純 Ti（JIS1 種材）とオーステナイトステンレス鋼 SUS304 の 2 種類を用意した．基板サイズは Ti 板，SUS304 共に 20 mm×20 mm，板厚 1 mmの圧延材をアセトン中で 10 分間超音波洗浄したものを使用した．皮膜は，基板を保持するホルダを X-Y ステージを駆

動させることにより，基板上の5 mm×5 mmの面積に形成させた．「活性プラズマ-金属」反応を組み込んだ超音速フリージェットPVD装置をFig. 1に示す．本実験では組成の制御すなわち傾斜組成の可否を検討すること共に皮膜の構成相の制御の可否も検討する．従ってXRD分析によって皮膜素材TiおよびTiとN化合物と異なるピークを有するSUS304基板により基板からのピークを排除し，TiN単相の皮膜の形成が可能であるか検討するため，TiおよびSUS304の2種類の基板を用意した．

皮膜の表面および断面の性状は，OMおよびSEMにより観察し，皮膜断面の組成はEPMAにより分析した．皮膜の結晶構造の同定はXRDにより測定した．

3. 結果および考察

Fig. 2は，本法により形成させたTiN皮膜表面写真である．成膜させた皮膜はTiN特有の金色を呈しており，皮膜表面にクラックなどの欠陥は確認されず緻密な皮膜が形成されている．

Ti基板に形成させた傾斜組成TiN皮膜，SUS304基板に形成させたTiN単相層皮膜，それぞれのXRD結果をFig. 3に示す．また，皮膜を形成させていないTi基板，SUS304基板そのもののXRD結果についても同時に示す．Fig. 3の結果から，傾斜組成TiN皮膜からは，Ti，Ti_2N，TiNの回折ピークが，TiN単相皮膜からはTiNとSUS304基板からのピークのみが確認された．以上の結果は，本法の成膜条件を制御することにより皮膜の構成相を制御することが可能であることを示している．

傾斜組成TiN皮膜の断面EPMA線分析結果をFig. 4に示す．Ti基板から連続的に窒素組成が増加していることが確認された．したがって，「活性プラズマ-金属」反応を組み込んだ本法において，ナノ粒子生成室の窒素ガス流量を制御することにより，皮膜組成の制御可能であることが明らかとなった．

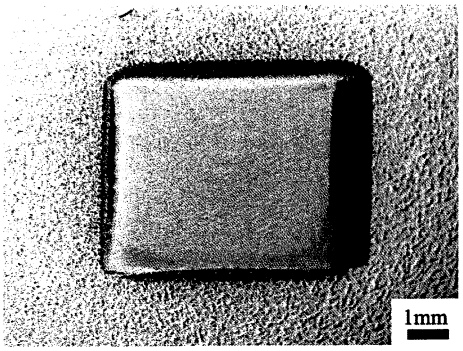

Fig. 2 Photograph of a graded TiN film surface.

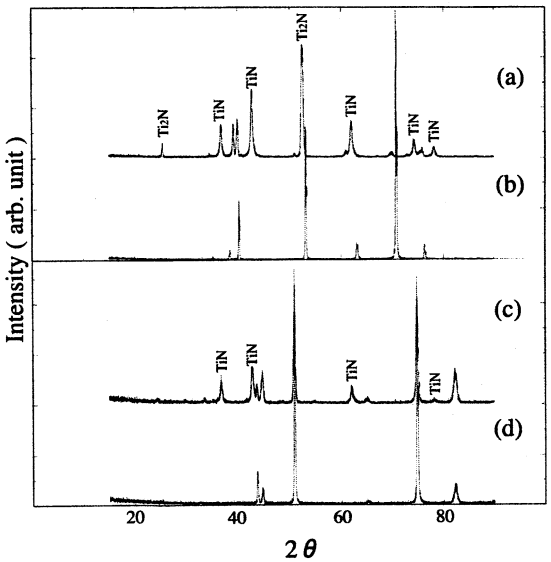

Fig. 3 X-ray diffraction profiles of (a) Graded TiN, (b) uncoated Ti substrate, (c) TiN coating on SUS304 and (d) uncoated SUS304 substrate.

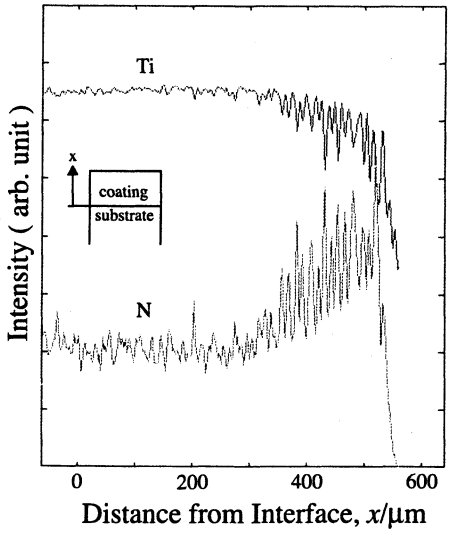

Fig. 4 EPMA line analysis of the cross-section of a graded TiN film.

4. 結 言

本研究では，超音速フリージェット PVD に「活性プラズマ-金属」反応を組み込み，TiN ナノ粒子の積層させることにより，低温での TiN 皮膜の形成を試みた．さらに窒素ガス流量の制御により Ti 基板からの窒素組成を傾斜化させた傾斜組成 TiN 皮膜の形成を試みた．その結果，以下の知見が得られた．

(1) 窒素ガス流量および He ガスと窒素ガス分圧を制御することにより，単相の TiN 皮膜および傾斜組成 TiN 皮膜を形成させることに成功した．すわなち，「活性プラズマ-金属」反応を組み込んだ超音速フリージェット PVD の成膜条件を制御することにより組成，皮膜の構成相の制御が可能であることが明らかとなった．

(2) 形成させた TiN 皮膜は，XRD および TEM 観察から，B2 構造（NaCl）であることが明らかとなった．

(3) 傾斜組成 TiN 皮膜，TiN 単相皮膜共にクラック，ボイド，ポアなどの欠陥の存在は確認されず，緻密な皮膜が形成されていることが明らかとなった．

研究業績

1. 湯本敦史，廣木富士男，塩田一路，丹羽直毅：超音速フリージェット PVD による金属膜の形成と密着性評価，溶射技術第 26 巻 2 号（2007），pp.44-50.
2. A. Yumoto, T. Yamamoto, F. Hiroki, I. Shiota and N. Niwa: Fabrication of Nanostructure Composites in Functionally Graded Coatings with Supersonic Free-Jet PVD, Materials Science Forum, vol.492-493(2005), pp.341-346.
3. 湯本敦史，山本剛久，廣木富士男，塩田一路，丹羽直毅：超音速フリージェット PVD による傾斜組成皮膜の形成,傾斜機能材料論文集 2005（2005），pp.115-120.
4. H. Takahashi, F. Hiroki, A. Yumoto and K. Yamamoto: Mixing chamber utilizing oscillation phenomena of coaxial impinging jets, 8th International Symposium on Fluid Control, Measurement and Visualization (8FLUCOM), Chengdu(Chaina), August. 22-25 2005. CD-ROM proceedings. (6-1)
5. T. Tanaka, F. Hiroki, A. Yumoto and K. Yamamoto: Development of Micro Fluidic Devices, 8th International Symposium on Fluid Control, Measurement and Visualization (8FLUCOM), Chengdu(Chaina), August. 22-25 2005. CD-ROM proceedings. (11-1)

2.6 紫外光増感可視光応答型アナターゼ薄膜の形成
－チタン錯体を含有するプレカーサー溶液の応用－
Enhanced UV-sensitivity of VIS-responsive anatase thin films fabricated by using precursor solutions involving Ti complexes

永井裕己[a]・望月千尋・原広樹・鷹野一郎・佐藤光史
Hiroki Nagai[a], Chihiro Mochizuki[b], Hiroki Hara[b], Ichiro Takano[c], Mitsunobu Sato[b]
[a]化学応用学専攻、[b]共通課程、[c]電気工学科
[a] Department of Applied Chemistry, Graduate School, Kogakuin University,
[b] Department of General Education, Faculty of Engineering, Kogakuin University,
[c] Department of Electrical Engineering, Faculty of Engineering, Kogakuin University

Abstract

Fabrication of VIS-responsive anatase thin films with enhanced UV-sensitivity was attained on an ITO pre-coated glass substrate by applying two precursor solutions involving Ti complexes of oxalic acid and EDTA. The transparent and crack-free thin films were characterized by XRD, XPS, UV-VIS and FE-SEM observation. The highest sensitivity to UV light of the VIS-responsive film, whose photocatalytic activity was measured by the decomposition rate of methylene blue, was 4 times as compared with that formed by a sol-gel method under the same conditions. The VIS-responsive films showed a characteristic absorption band at around 480 nm.

1. 序論

アナターゼは、天然に産出する二酸化チタンの結晶形態の一つで、無害な光触媒材料としてさまざまな応用が期待されている．光触媒作用は、紫外光照射によって誘起された電子とホールが粒子表面で酸素や水と化学反応できることに基づく[1]．このように紫外光励起によってｎ型半導体として作用する原理を、可視光によって実現できれば、太陽光の有効利用に役立つ．

このため、アナターゼの Ti^{4+}サイトに遷移金属イオンを物理的にドープして可視光化する研究が最近行われた[2,3]．この光触媒は、可視光に応答するものの UV 光への応答が低下することが知られている[4]．また、Asahi らによる窒素のドーピングによる物理的乾式法による可視光化に引き続き[5]、硫黄や炭素のドープによる可視光化も実現されて注目されている[6-11]．また、ゾル-ゲル法による膜のアンモニア修飾による窒素ドープも実現された[12]．しかし、これら従来の可視光応答膜は、いずれもより高エネルギーの紫外光に対する応答性が低下するため、光エネルギー有効利用の観点から、ほとんど価値がない．本研究の目的である、可視光応答型透明薄膜太陽電池においても、作成電極の紫外光応答が維持または増感させるためには、可視光応答アナターゼ薄膜の紫外光応答メカニズム解明が必須である．

先にアナターゼなどの酸化物薄膜やリン酸カルシウム化合物薄膜の形成を分子プレカーサー法によって達成した[13-19]．欠陥のない成膜法であるこの方法を利用して、紫外光に増感し、かつ可視光化を達成する成膜について検討した結果、目的を達成したので報告する．単層膜および多層膜を ITO 基板上に成膜し[20]、光触媒活性によって光増感能を確認した．

2. 実験

1) コーティング溶液の合成

2種類の分子プレカーサー溶液を合成した．シュウ酸を配位子とするTi錯体を含む新規な S_{OX} と、既報[14]を改良してEDTAを配位子とするTi錯体を含む S_{ED} を合成した．参照として、ゾルゲル法によるコーティング溶液 S_{SG} を常法に従って合成した[21,22]．アセトアルデヒドまたは酢酸を添加したゾルゲル法による溶液 $S_{SG\text{-}AL}$ と $S_{SG\text{-}AC}$ も合成した．いずれもスピンコートによって100 nmまたは50 nmになるように濃度を調整した．

2) 薄膜の形成と分析

各溶液をITO基板上にスピンコートし、乾燥後にAr気流（0.1 L min^{-1}）中で加熱処理した．S_{OX} と S_{SG} によるプレカーサー膜は475°Cで、S_{ED} では500°C で30 min加熱した．形成した単層膜を順に **OX**、**SG** および **ED** とした．空気中で、対応する OX_{air}、SG_{air} と ED_{air} も成膜した．

また、各コーティング溶液で、合計200 nmの膜厚で2層および3層膜を形成した．多層膜の命名法は、単層膜をハイフンで下層を左側から示した．膜厚は触針計で測定した．膜のXRDによって結晶構造を、XPSで元素分析し、深さ方向分析も実施した．表面形態はFE-SEMで観察した．

3) 薄膜の光学的バンド端と光触媒活性

薄膜の吸収スペクトルから、Tauc式[23]を用いて、アナターゼの光学的バンド端を決定した．

光触媒活性は、メチレンブルー水溶液の退色試験の標準化された方法によって評価した [24, 25].

3. 結果と考察

1) 薄膜の結晶構造と表面形態

各単層膜のXRDパターンをFig. 1に示した．Ar気流中での熱処理膜は、空気中の形成膜より結晶性は低かったが、いずれもアナターゼと ITO 基板に帰属できるピークを示した．外部からの酸素供給が無くともアナターゼに結晶化できることが分かった．多層膜もほとんど同じパターンを示した．分子プレカーサーを利用した膜の表面形態は、ゾルゲル法による膜に見られる波打ち構造も無く、平滑で亀裂やピンホールなどの欠陥は全く観察されなかった．

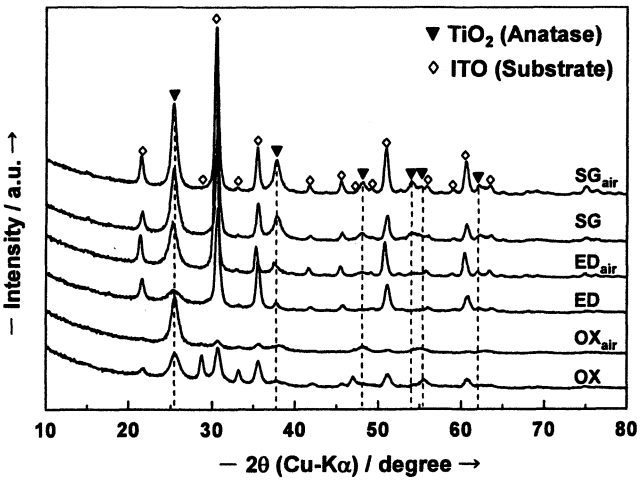

Fig. 1 XRD patterns of the single-layer films whose thickness is 100 nm.

2) 薄膜の化学組成

薄膜 **ED** のXPSから、Ti–OとTi–Nの結合エネルギーは459と455 eVで、典型的な値であった．N 1sの結合エネルギーは396 eVで、存在する窒素が酸素置換型であることが分かった[26]．アナターゼ薄膜中への置換型窒素の形成が、1回の成膜によって直接実現できた最初の例であることが分かった．Ar気流中処理によって、錯体中のTi-N結合をアナターゼ中に残存させる方法を実証できた．

Fig. 3に、膜厚200 nmの **OX-ED-OX** 膜のXPSによる深さ方向元素分析を示した．EDを2層目にもち、錯体中のTi-N結合に由来する窒素が、炭素と共に有効に局在化していることが分かる．

重要なことは、このような窒素の局在化は、**ED** 膜の上層部に還元剤をもつプレカーサー溶液

を用いて再度アナターゼを形成したときに現れることである．このことは、Ar気流中で **ED** 膜を形成した際に残存した窒素や炭素の化合物が還元されて、それが膜中に安定に取り込まれたことを示している．後述のように、還元反応によって生じた生成物は未だ特定されていないが、可視光への応答性と直接関わっていることが本研究によって明らかとなった．

3) 薄膜の光触媒活性と光学的バンド端のシフト

Table 1 に、紫外光および可視光応答性の指標として、光触媒活性をまとめた．単層膜の活性はこれらより低く、また暗所における参照値は約 4 である．したがって、可視光に応答する膜の特徴が上述のとおり分かる．注目すべきは、これら可視光応答膜の紫外光活性が対応する参照膜に比較してかなり高い値を示すことである．これら可視光応答膜の吸収スペクトルには、480 nm 付近に特徴的な吸収が現れた．さらに、紫外光活性の高い膜ほど光学的バンド端は高エネルギー側にシフトした．

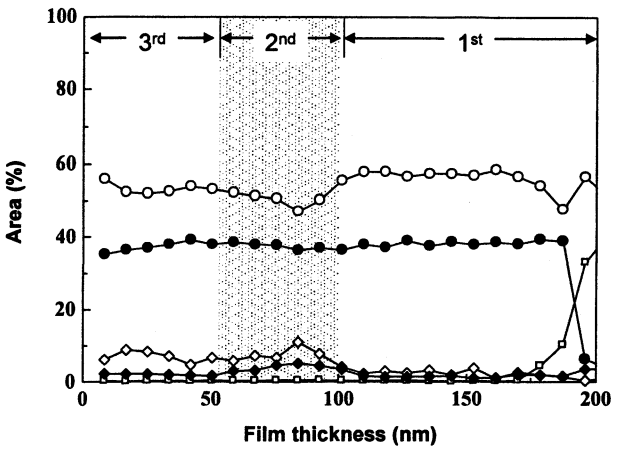

Fig. 2 Depth profile of the amount of components in the 3-layer thin film **OX-ED-OX**. Notations indicate the energy levels of five atoms in parentheses, —●— (Ti 2p), —○— (O 1s), —♦— (N 1s), —◇— (C 1s), —□— (In 3d).

Table 1 Index of photocatalytic activity (IPCA) for multilayer films of 200 nm thickness. IPCA values were obtained from the pseudo-first order kinetic constants of the decomposition reaction of MB in aqueous solution both under UV irradiation and under VIS irradiation, which were estimated by the decrease of absorption value at 664 nm.

Multilayer film	IPCA[1)]	
	under UV irradiation	under VIS irradiation
OX-OX	11.9(3)	3.5(3)
OX-ED	4.9(5)	3.2(3)
ED-OX	9.0(10)	5.4(6)
OX-OX-OX	19.4(11)	3.1(4)
OX-ED-OX	23.9(12)	9.4(6)
OX-ED-SG	14.3(10)	3.7(3)
OX-ED-SG$_{AL}$	15.8(11)	11.4(5)
OX-ED-SG$_{AC}$	14.3(10)	3.6(5)

1) Estimated standard deviations are presented in parentheses.

従来の可視光応答膜は、バンド端を低エネルギー側にシフトさせる不純物を添加する方法によって実現され、その結果、増感メカニズムの解明はこれからであるが、現在までの検討結果は、新たな増感方法の存在を示唆している．考慮すべきこととして、遷移金属イオンの注入を深くすると可視光に応答しやすいことがある[27]．また、WO_3 との積層膜も可視光に応答することが分かっている[28]．しかし、いずれも紫外光活性が増感することはない．これらを総合すると、可視光応答、紫外光増感メカニズムは、色素増感アナターゼ薄膜に相当すると考えられる[29]．膜と基板との歪による増感や[30]、電子トラップ機構による増感[31]のみでも説明は不可能である．むしろ、太陽エネルギー有効利用の観点から、紫外光増感を重要視すべきことが、本研究によって明確となった．

4. 結言

2 種類のアナターゼプレカーサー溶液を交互に積層して、欠陥のない可視光応答型透明薄膜の形成を達成した．この薄膜は、従来の紫外光応答性が低下することなく、むしろ著しく増感できた．この特徴は、形成した 3 種類の薄膜 **ED-OX**, **OX-ED-OX** と **OX-ED-SG$_{AL}$** で達成され、**ED**

膜の上層に還元剤が存在する時に実現することを明らかにした．XPS による薄膜の化学分析は、Ti-EDTA 錯体から引き継がれた Ti-N 結合が、可視光応答物質の形成と紫外光増感の両方に有効に作用したことを示唆した．形成した薄膜は安定で、p 型半導体との組み合わせによる太陽電池の形成に有効なだけでなく、光燃料電池の電極材としても有効と期待される．

文献

[1] K. Honda, A. Fujishima, Nature 238 (1972) 37. [2] M. Anpo, S. Kishiguchi, Y. Ichihashi, M. Takeuchi, H. Yamashita, K.Ikeue, B. Morin, A. Davidson, M. Che, Res. Chem. Intermed. 27 (2001) 459. [3] M. Anpo, Bull. Chem. Soc. Jpn. 77 (2004) 1427. [4] E. Borgarello, J. Kiwi, M. Gratzel, E. Pelizzetti, M. Visca, J. Am Chem. Soc. 104 (1982) 2996. [5] R. Asahi, T. Morikawa, T. Ohwaki, K. Aoki, Y. Taga, Science 293 (2001) 269. [6] H. Irie, Y. Watanabe, K. Hashimoto, Chem. Lett. 32 (2003) 772. [7] S. Sakthivel, H. Kisch, Angew. Chem. Int. Ed. 42 (2003) 4908. [8] T. Ohno, T. Tsubota, M. Toyofuku, R. Inaba, Catal. Lett. 98 (2004) 255. [9] T. Ohno, T. Mitsui, M. Matsumura, Chem. Lett. 32 (2003) 364. [10] T. Umebayashi, T. Yamaki, H. Itoh, K. Asai, Appl. Phys. Lett. 81 (2002) 454. [11] T. Umebayashi, T. Yamaki, S. Tanaka, K. Asai, Chem. Lett. 32 (2003) 330. [12] M. Miyauchi, A. Ikezawa, H. Tobimatsu, H. Irie, K. Hashimoto, Phys. Chem. Chem. Phys. 6 (2004) 865. [13] M. Sato, H. Hara, H. Kuritani, T. Nishide, Sol. Energ. Mater. Sol. Cells 45 (1997) 43. [14] M. Sato, H. Hara, T. Nishide, H. Kuritani, Y. Sawada, J. Mater. Chem. 6 (1996) 1767. [15] M. Sato, T. Tanji, H. Hara, T. Nishide, Y. Sakashita, J. Mater. Chem. 6 (1999) 1539. [16] T. Hayakawa, K. Takahashi, M. Yoshinari, H. Okada, H. Yamamoto, M. Sato, K. Nemoto, Int. J. Oral Maxillofac. Implants 21 (2006) 851. [17] T. Hayakawa, K. Takahashi, M. Yoshinari, H. Hara, M. Sato, K. Nemoto, J. Oral Tissue Eng. 3 (2006) 139. [18] T. Hayakawa, K. Takahashi, M. Yoshinari, H. Hara, K. Nemoto, M. Sato, J. Oral Tissue Eng. 3 (2005) 17. [19] K. Takahashi, T. Hayakawa, M. Yoshinari, H. Hara, C. Mochizuki, M Sato, K. Nemoto, Thin Solid Films 484 (2005) 1. [20] J. W. Yoon, T. Sasaki, N. Koshizaki, Thin Solid Films 483 (2005) 276. [21] C. J. Brinker, G. W. Scherer, Sol-gel Science Academic Press, California, 1990, Ch. 3. [22] D. W. Bruce, D. O'Hare, Inoganic Materials, Wiley, Chichester, 1992, pp. 519-525. [23] S. Tanemura, L. Miao, P. Jin, K. Kaneko, A. Terai, N. Nabatova-Gabain, Appl. Surf. Sci. 212-213 (2003) 654. [24] C. H. Kwon, H. Shin, J. H. Kim, W. S. Choi, K. H. Yoon, Mater. Chem. Phys. 86 (2004) 78. [25] T. Ohno, T. Tsubota., Chem. Lett. 33 (2004) 750. [26] N. C. Saha, H. G. Tompkins, J. Appl. Phys. 72 (1992) 3072. [27] M. Anpo, M. Takeuchi, J. Catal. 216 (2003) 505. [28] M. Miyauchi, A. Nakajima, T. Watanabe, K. Hashimoto, Chem. Mater. 14 (2002) 2812. [29] B. O'regan, M. Graetzel, Nature, 353 (1991) 737. [30] L. Miao, P. Jin, K. Kaneko, A. Terai, N. Nabatova-Gabain, S. Tanemura, Appl. Sur. Sci. 212–213 (2003) 255. [31] B. Xin, Z. Ren, P. Wang, J. Liu, L. Jing, H. Fu, Appl. Surf. Sci. 253 (2007) 4390.

研究業績

(1) Hiroki Nagai, Chihiro Mochizuki, Ichiro Takano and Mitsunobu Sato、日本化学会第 85 春季年会, 神奈川大学, 2005 年 3 月. (2) Hiroki Nagai, Chihiro S. Mochizuki, Ichiro Takano and Mitsunobu Sato、SPACC 12th, 天津理工大学, 2005 年 7 月. (3) Hiroki Nagai, Chihiro S. Mochizuki, Ichiro Takano and Mitsunobu Sato、ISNST 9th, 南台科技大学, 2005 年 11 月. (4) Hiroki Nagai, Chihiro S. Mochizuki, Ichiro Takano and Mitsunobu Sato、Pacifichem 2005, ハワイ, 2005 年 12 月. (5) Hiroki Nagai, Chihiro S.Mochizuki, Ichiro Takano and Mitsunobu Sato、SPACC 13th, 北海道大学, 2006 年 8 月. (6) Hiroki Nagai, Kazuhisa Fujita, I-Ling Huang, Chien-Hsin Yang, Chihiro S.Mochizuki and Mitsunobu Sato、ISAT 5th , 南台科技大学, 2006 年 11 月. (7) Hiroki Nagai, Chihiro S.Mochizuki, Ichiro Takano and Mitsunobu Sato、無機マテリアル学会 第 115 回 学術講演会, 岩手大学, 2007 年 10 月. (8) Hiroki Nagai, Chihiro Mochizuki, Hiroki Hara, Ichiro Takano, Mitsunobu Sato、ISAT 6th, 工学院大学, 2007 年 11 月. (9) Hiroki Nagai, Chihiro S.Mochizuki, Ichiro Takano and Mitsunobu Sato、SPACC 14th, 国立台湾大学, 2007 年 12 月. (10) Hiroki Nagai, Moyu Hasegawa, Chihiro Mochizuki, Ichiro Takano, Mitsunobu Sato、SPACC 14th, 国立台湾大学, 2007 年 12 月. (11) Hiroki Nagai, Chihiro Mochizuki, Ichiro Takano and Mitsunobu Sato、Sol. Energ. Mater. Sol. Cells 投稿中.

3. ナノ界面・粒子

3.1.1　1．ナノ機能表面を有する生物規範型ロボットの開発研究

撥水性微細加工表面を有する水面移動ロボットの研究

鈴木健司，高信英明，三浦宏文（機械システム工学科）

Abstract

This paper describes biomimetic water strider robots with microfabricated hydrophobic legs. Various kinds of supporting legs with hydrophobic microstructures on their surfaces were developed using MEMS (microelectromechanical systems) techniques. Lift force of the legs were investigated both theoretically and experimentally. The experimental results are in good agreement with the calculations. Furthermore, two different mechanisms for autonomous water strider robots have been developed. The robot with twelve microfabricated legs driven by a vibration motor successfully moved on water surface and also made left/right turns utilizing difference of resonant frequencies of the legs. The other robot with six microstructured legs also successfully moved on water by creating elliptical motions of the middle legs, which is similar to the motions of water strider's legs.

1．はじめに

本研究は，撥水性の支持脚を用いて表面張力により水面に浮くアメンボ型水面移動ロボットを開発することを目的とする．表面張力を利用した水面移動ロボットは，Hu ら[(1)]の弾性体を駆動源とするロボット，Song ら[(2)(3)]の脚の振動を利用したロボットなどが開発されているが，本研究は，MEMS 技術により表面に微細加工を施し，撥水性を高めた支持脚を用いることを特徴とする．開発した脚の支持力を測定し，理論との比較を行った．また，製作した脚を用いて 2 種類の自立型水面移動ロボットを開発した．アメンボロボットは浅瀬や狭い水面上での移動が可能であり，環境モニタリングなどへの応用が期待できる．

2．水面上の脚の支持力

アメンボの脚は多数の毛に覆われており，足先からはロウのような物質を分泌している[(4)]．分泌物質の撥水性が，表面の毛の凹凸構造で強められ，水面を破らずに表面張力で浮くことができる．Fig.1 は支持脚の断面に働く力を示している．脚を無限に長い円柱と考えると，単位長さあたりに働く支持力 F は，円柱が水から受ける浮力 F_b と，円柱・水・空気の境界線に働く表面張力 γ の垂直成分 F_s の和になる．

$$F = F_B + F_S,\ F_B = \rho g S_1\ ,\ F_S = 2\gamma \sin\theta_0 \qquad (1)$$

ここで，S_1 は円柱の断面積とその上部の排除された水の断面積の和である．表面張力 F_s の最大値は $\theta_0 = 0°$ のときに 2γ となり，この値は脚の材料が撥水性であれば直径や接触角に

よらず一定である．一方，浮力は直径の減少とともに小さくなるため，アメンボのような細い支持脚では，浮力に比べて表面張力が支配的になる．

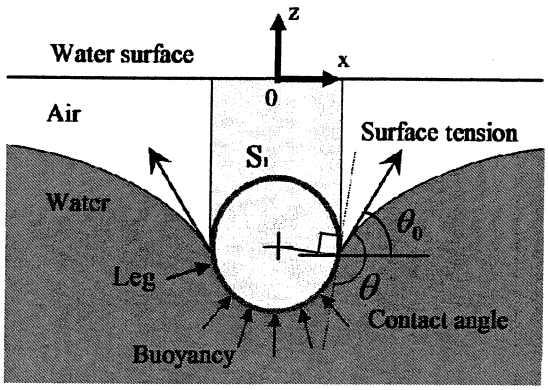

Fig.1 Two-dimensional model of a supporting leg

3. 表面に凹凸構造を持つ支持脚の製作

撥水性は，表面の化学的な性質と表面の形状によって決定され，表面に凹凸加工を施すことにより撥水性が強化される．本研究，MEMS 技術を用いて表面に凹凸構造を持つ３種類の支持脚を製作した．

① 櫛形フィルムの巻きつけによる細毛構造の加工 (Fig.2)

シリコンウエハ上に厚膜フォトレジストの SU-8 で鋳型を作製し(Fig.2 a)，シリコーンゴムの一種である PDMS(Polydimethylsiloxane) を流し込み櫛形のフィルムを製作する(Fig.2 b)．これを ϕ0.5mm の黄銅線に巻き付け，撥水剤 FS-1010 を塗布することで，アメンボの毛のような構造を製作した(Fig.2 c).

② SU-8 を使用した円筒面への凹凸加工 (Fig. 3)

厚膜フォトレジストである SU-8 を浸漬により ϕ1.0mm の黄銅線に塗布し，円筒面を 5

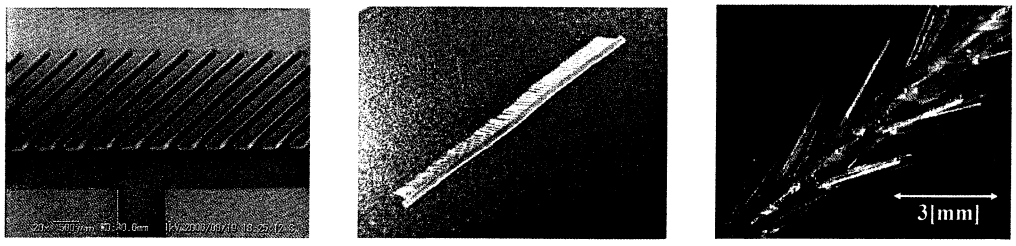

(a) SU8 mold (b) PDMS comb-shaped structure (c) Wrapping on a wire

Fig. 2 PDMS hair-like structure

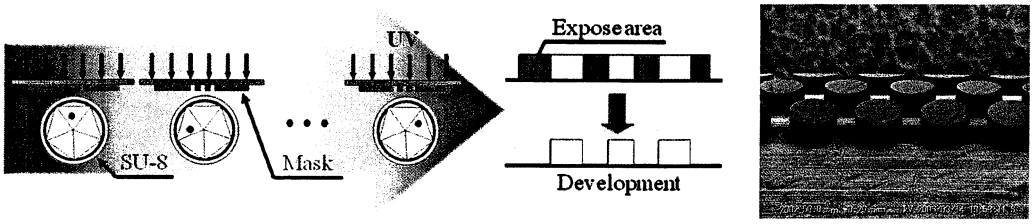

Fig. 3 SU-8 structures fabricated with UV lithography

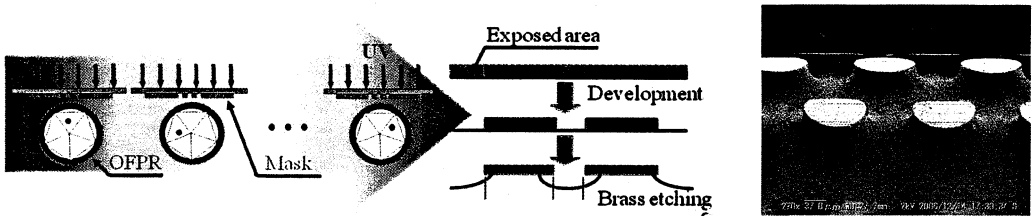

Fig. 4 Wet-etched structures on the surface of a brass wire.

回に分けて露光し現像することでSU-8の凹凸面の製作する．パターンの形状は直径100 μm，間隔 50 μmである．

③ 金属ワイヤのエッチングによる凹凸加工 (Fig. 4)

紫外線フォトレジストのOFPRを浸漬によりφ1.0mm金属ワイヤに塗布し，円筒面を5回に分けて露光，現像する．その後，レジストをマスクとして金属ワイヤのウットエッチングを行い凹凸面を製作する．金属材料は，アルミと真鍮を用いた．パターンの形状は直径100 μm，間隔 80 μmである．

4. 支持力の測定

前節で製作した支持脚を水面に押し付けたときの支持力を測定した．支持脚は長さ30mm，脚端にR加工を施したものを用いた．Z軸ステージ上に水槽を設置し，平行平板ばねの先端に支持脚を水面と平行になるように固定する．水面と支持脚が接触する瞬間をゼロ点として，支持脚が完全に水没するまで水面を上昇させる．平行平板ばねの変位をレーザー変位計で測定し，ばね定数を乗じることにより支持力を求めた．

押し込み深さと支持力の測定結果をFig. 5 に示す．支持力はある深さで最大値を取り，sその後わずかに減少して水没した． Fig.6 に最大支持力の理論値と測定値の比較を示す．両者はよく一致していることから，表面張力は支持脚によらず最大値2γとなり，支持力に差が生じるのは脚の直径の違いによる浮力の差に起因していると考えられる．脚の自重に対して支持力を増加させるためには，毛などの構造により見かけの直径を大きくして比重を小さくし，細長くして表面張力を大きくすることが有効である．

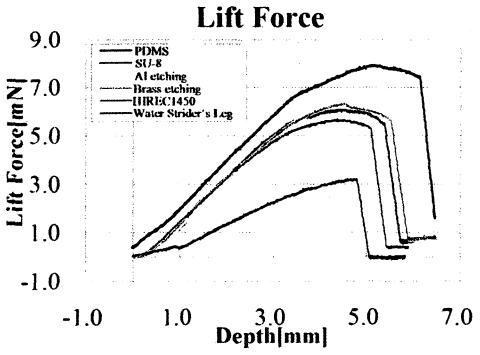

Fig. 5 Lift force

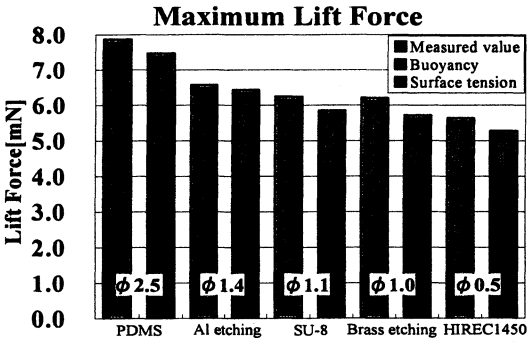

Fig. 6 Maximum Lift Force

5. 水面移動ロボット

表面に凹凸を加工した脚を用いて，２種類の水面移動ロボットを製作した．１つは12本の脚を持ち，脚の振動により移動するロボットである（Fig.7）．支持脚には，振動による表面構造の破損を防ぐためφ0.5mmの真鍮線をエッチングしたものを用いた．アクチュエータには偏心質量を持つ振動モータを用い，回転数をPWM制御 (Pulse Width Modulation) して振動数を制御した．振動モータに支持脚が共振すると脚は大きく振動し，水面を蹴るこ

とでロボットが移動する．また，それぞれの脚の長さを変えることで，振動数によって共振する脚が変化し，109Hz で直進，115Hz で左旋回，132Hz で右旋回の移動が可能である．リチウムポリマー電池とモータ，制御回路を搭載し，自立的に振動数を変化させ，水面上で直進，右旋回，左旋回を順次行わせることに成功した．ロボットの質量は 7.85g，移動速度は 70mm/s であった．

もう一種類のロボットは　6 本の脚を持ち，実際のアメンボと同様に中脚が楕円軌道を描くことにより水面を掻いて移動する (Fig.9)．楕円軌道を描かせる機構としてピストンクランク機構を用い，リチウムポリマー電池と DC モータを搭載して自立化した．前脚と後脚の表面には PDMS の細毛構造を加工し (Fig.2)，支持力を高めた．動作実験の結果，平均速度 40mm/s で自立的に移動させることに成功した．

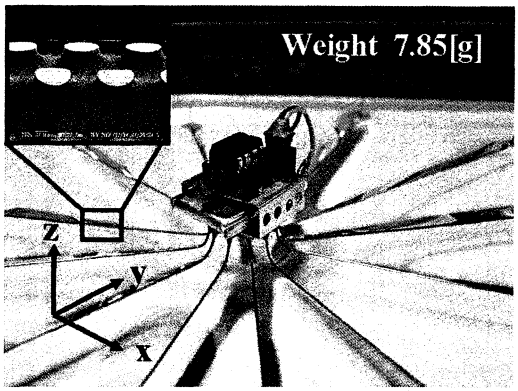

Fig.8 Water strider robot driven by a vibration motor

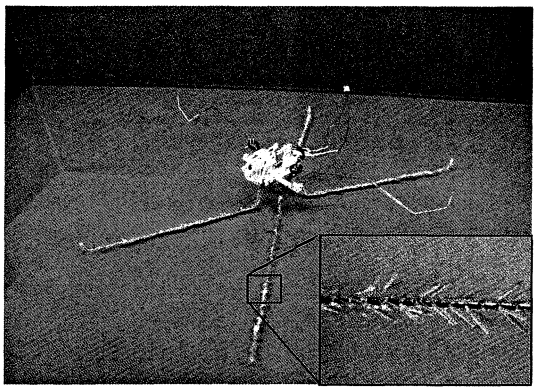
Fig. 9 Hexapod water strider robot

6. 結言

1) MEMS 技術により円筒面に凹凸加工を施した 3 種類の撥水性支持脚を開発した．
2) 開発した脚の支持力を測定し，大きな支持力が得られることを確認した．実験結果は理論とよく一致した．
3) 表面に凹凸を持つ支持脚を搭載した 2 種類の水面移動ロボットを開発し，自立的な水面移動を実現した．

参考文献

(1) Davld L. Hu, Brlan Chan, and John W. M. Bush, "The hydrodynamics Water Strider locomotion" Nature, Vol.424, 2003, pp. 663 – 666.

(2) Y.S.Song, S. Suhr, and M. Sitti, "Modeling of the Supporting Legs for Designing Biomimetic Water Strider Robots," Proc. of the IEEE Robotics and Automation Conference, 2006, pp. 2303 - 2310.

(3) Yun Seong Song and Metin Sitti, "Surface-Tension-Driven Biologically Inspired Water Strider Robots: Theory and Experiments," IEEE Transactions of Robotcis, Vol. 23, No. 3, June 2007, pp.578-589.

(4) Xuefeng Gao and Lei Jiang, "Water-repellent legs of water strider," Nature, Vol. 432, 4 November 2004, p.36.

3.1.2 作動温度低温化を目指した固体酸化物形燃料電池の電極・電解質材料開発と界面構造の制御

工学院大学工学部環境化学工学科　長本 英俊
東京大学大学院新領域創成科学研究科　大友　順一郎

Development of SOFCs Working at Lower Temperatures by Controlling Interface Nano-Structure

Hidetoshi Nagamoto
Department of Environmental Chemical Engineering
Junichiro Otomo
Graduate School of Frontier Sciences, The University of Tokyo

The stabilization of superprotonic phase CsH_2PO_4/SiO_2 composites as well as the anomalous phase transformation with a large hysteresis was investigated. In CsH_2PO_4/SiO_2 composites, a large asymmetric thermal hysteresis in the conductivity appeared, i.e. significant supercooling in the superprotonic phase was induced in silica matrices. A differential thermal analysis revealed that the temperature of a reverse transition from the cubic phase (superprotonic phase) to the monoclinic phase decreased in the composites. The stabilization of superprotonic phase (cubic phase) in the composites will be induced by shear elastic forces at the interface between CsH_2PO_4 and silica particles.

１．緒言　　固体酸化物形燃料電池は、作動温度が９００℃以上の高温であるが故に高いエネルギー変換効率を有し、水素のみならず一酸化炭素、炭化水素など多くの燃料を用いることが可能である。他方、高温であるが故に、電池および電池スタックの構成材料に制限を受け、高価な材料を用いざるを得ない欠点を持っている。その点、自動車にも搭載され始めた固体高分子形燃料電池は作動温度が８０℃程度と低いが故に高始動性を持ち、使い易いものになっている。しかしながら、高価な電極触媒であるPtを十分に活用するためには、燃料である水素中に混じってくる一酸化炭素の濃度を10ppm以下に低下させなければならず、安価な炭化水素の改質により水素を得ようとする場合には、一酸化炭素を低減させる装置を余計に付けねばならない。

固体酸化物形燃料電池を活用する観点から見た場合、７００℃程度の低い温度（中温域）で用いることの出来る固体電解質の燃料電池を開発すること、および２５０℃程度（低温域）で高いイオン導電性を示す固体電解質の燃料電池への応用が考えられ、本研究では、中温域（600-800℃）におけるセリア系酸化物（$(CeO_2)_{1-x-y}(ZrO_2)_x(Y_2O_3)_y$）、および低温域（250-300℃）における酸素酸塩（CsH_2PO_4（CDP））を用いた電解質材料の合成をナノ界面を制御して行うことを目的としている。

前者では、サブミクロンの酸化物粉体を混合して固相反応する方法、共沈法と酸化物ゾルを用いる方法を適用して、作製された固体電解質板の物理的性質や電気的な性質を測定して、作製法との関連を検討した。後者では、CDPとメソ多孔質シリカとの複合化がCDPのプロトン導電率

に顕著な影響を与える現象に着目した。これまでの我々の研究において、CsH_2PO_4は適切な加湿制御により、230℃付近で構造相転移（単斜晶→立方晶）に伴って高いプロトン導電率を示すことを報告している [1]。また、同じく酸素酸塩の一種である硫酸水素セシウム（$CsHSO_4$）については、メソ多孔質シリカとの複合化によってそのプロトン導電率が著しく上昇することが報告されている [2-5]。本研究では、メソ多孔質シリカとの複合化がCsH_2PO_4のプロトン導電率に顕著な影響を与える現象に着目した。すなわち、CsH_2PO_4の系では、メソ多孔質シリカの添加により昇・降温に対する導電率の温度変化が著しいヒステリシス現象を示す [6]。CsH_2PO_4 /SiO_2 複合体のSiO_2 体積分率に対する導電率の依存性を詳細に観測し、併せて熱分析測定を行うことでCsH_2PO_4/SiO_2複合体中のCsH_2PO_4の構造相転移とプロトン導電率の相関について検討した。

2．実験方法

セリア系の固体電解質の調製法として、1)酸化物ナノ粒子の固相反応、2)共沈法、3)複合ゾル法の 3 種の方法を用いた。1)ではそれぞれの酸化物の特級試薬、2)ではそれぞれの金属イオンの酢酸塩（特級）を用い、3)については日産化学工業㈱から提供されたモル比 CeO_2:ZrO_2:Y_2O_3＝81.0:8.8:10.2 ものを用いた。調製された複合ゾル組成と異なる組成にする場合には、共沈法を組み合わせた。粉体の混合には湿式ボールミルを用い、混合と熱処理を組み合わせて段階的に熱処理温度を上げていった。固相反応が終わった粉体はＸＲＤで結晶構造を確認した。また 3t/cm^2 の圧力で 3 分間加圧成型し、5.0×3.0×10.0［mm］ブロックにし、最終の焼結温度を 1300℃および 1450℃として導電率の比較を行った。

導電率として、イオン導電率を大気中で測定し、電子導電率を水素と水蒸気で調整した雰囲気で酸素分圧の関数として、交流四端子法で測定した。測定は、600℃から 100℃刻みで、900℃までの 4 温度で行った。

所定のモル比のCsH_2PO_4粉末とSiO_2粉末（平均粒径 5.1 μm、比表面積 297 m^{2}g^{-1}、細孔容積 1.3 cm^{3}g^{-1} 、平均細孔径 16 nm）を減圧下で水に懸濁させ、攪拌しながら蒸発乾固させることにより CsH_2PO_4/SiO_2 混合粉末を得た。乾燥後、圧縮成型により導電率測定用のペレット試料を作製した。雰囲気（湿度）を制御した条件において、交流インピーダンス測定により、150-250 ℃の温度域における導電率を算定した。作製した CsH_2PO_4/SiO_2 混合粉末は TG-DTA による熱分析測定を行った。200 ℃以上ではCsH_2PO_4の脱水反応が進行するため、スチール製のカプセルに粉末サンプルを封入し、脱水反応を抑制した状態で構造相転移の挙動を観測した。

3．実験結果および考察

Fig. 1 に用いた CeO_2-ZrO_2-Y_2O_3 ゾルの SEM 画像を示す。一次粒子が数 nm、二次粒子が数十 nm と十分小さいサイズであることが分かる。前述の３つの方法で固相反応させて XRD パターンをとったところ、1)の酸化物ナノ粒子の固相反応が 1450℃とするまで均一な組成とならなかったが、共沈法および複合ゾル法では 1050℃でも十分固溶していることが分かった。また、ブロック焼結体の相対密度に関しては、酸化物固相反応法では、焼結温度を 1450℃に上げても 90%に満たないのに対して、共沈法では 95%以上、複合ゾル法では 1150℃で 95%以上の値となった。更に、生成した CeO_2-ZrO_2-Y_2O_3 固溶体の平均粒子径を BET 法を用いて測定したところ、Table 1 のような結果となり、複合ゾル法が最も粒子径が小さいものとなった。しかしながら、BET 法による測定では、個数の多い粒子の性質に引きずられるため、体積分率の大きい粒子、即ち SEM で観察される結果と必ずしも一致しない。

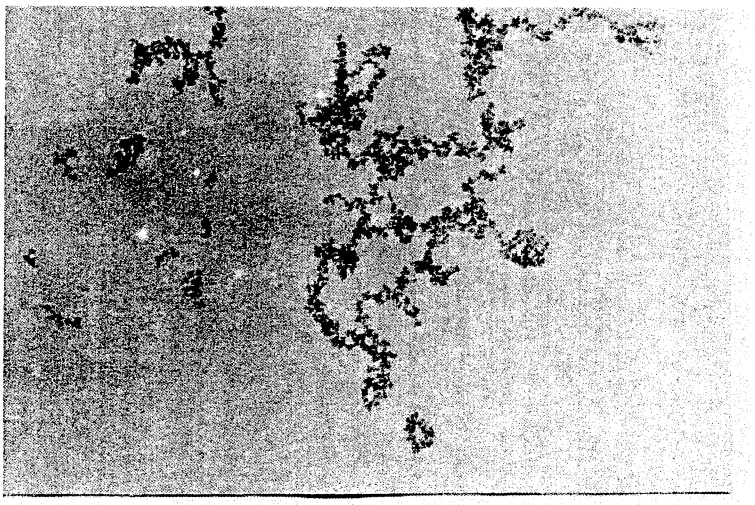

Fig. 1 SEM image of CeO_2-ZrO_2-Y_2O_3 sol

Table 1 BET surface area and mean particle size of ceria-based powders prepared

	Solid-state reaction	Co-precipitation	Complex sol
BET surface area [m^2/g]	2.6	3.4	9.8
Mean particle diameter [nm]	350	260	90

導電率の測定結果の一例を Fig. 2 に示す。Lee らの結果[7]とは異なり、低酸素分圧で電子伝導性が現れず、また 700℃のイオン導電率が目標である 10^{-2} S/cm 以上を辛うじて満足している。

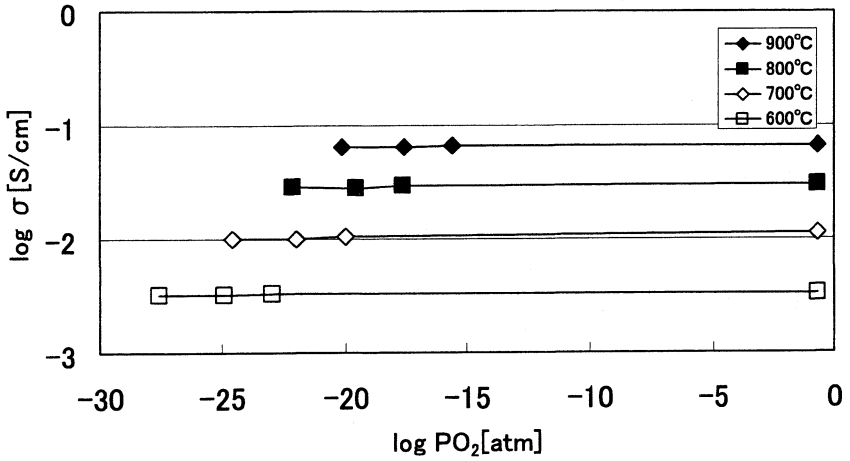

Fig. 2 Electrical conductivity of $(CeO_2)_{0.81}(ZrO_2)_{0.09}(Y_2O_3)_{0.10}$ sintered at 1300℃

Fig. 3 に CsH_2PO_4 単体および CsH_2PO_4/SiO_2 複合体の降温時における導電率測定結果を示す。CsH_2PO_4 単体は、220 ℃付近で高伝導相から低伝導相へ転移する。この相転移は立方晶から単斜晶への構造相転移に対応する。一方、CsH_2PO_4 /SiO_2 複合体の導電率は、220 ℃以下の温度域においても高伝導相が保持される。すなわち、SiO_2 との複合化により、高伝導相である CsH_2PO_4 の立方晶が転移温度以下まで保持される過冷却現象が生じていると推測される。ただし、各温度における導電率の値は SiO_2 の体積分率の増加により減少する。Fig. 4 に、CsH_2PO_4 単体および

CsH_2PO_4/SiO_2 複合体の降温時における DTA 曲線を示す。CsH_2PO_4 単体の場合は、立方晶から単斜晶への構造相転移に伴う発熱ピークが観測された(peak A)。一方、CsH_2PO_4/SiO_2 複合体の場合は、ブロードな２つの発熱ピーク(peak B, C)が観測され、いずれのピークも CsH_2PO_4 単体のそれと比較して、より低温側へシフトする現象が観測された。この現象は、CsH_2PO_4/SiO_2 界面での界面応力によって、構造相転移の際に高いエネルギー障壁がもたらされたために生じたと推定される。従って、CsH_2PO_4/SiO_2 複合体は $CsH_2PO_4-SiO_2$ 間の界面応力によってそのプロトン伝導特性が支配されるユニークな系であると考えられる。

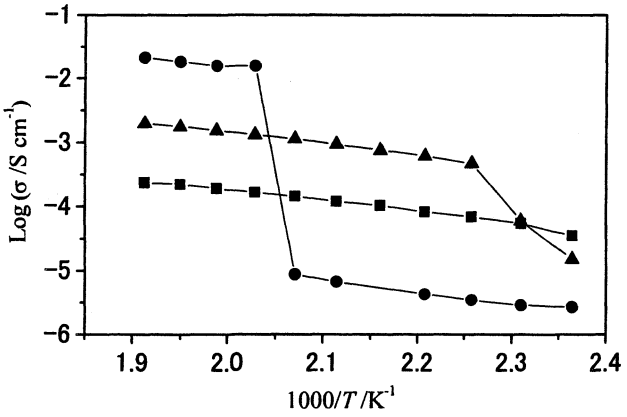

Fig. 3 Temperature dependence of electrical conductivity of neat CsH_2PO_4 and CsH_2PO_4/SiO_2 composites.
●: neat CsH_2PO_4 ; ▲: composite 1 (volumetric fraction of SiO_2 = 0.45) ; ■: composite 2 (volumetric fraction of SiO_2 = 0.6)

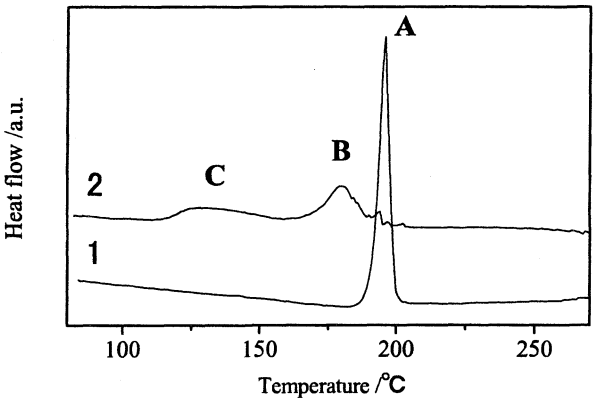

Fig. 4 DTA of neat CsH_2PO_4 and CsH_2PO_4/SiO_2 composite at cooling rate of 5K/min.
Curve 1: neat CsH_2PO_4 ; Curve 2 : composite 3 (volumetric fraction of SiO_2 = 0.37).

4．まとめ

一次平均粒子径が数 nm の CeO_2-ZrO_2-Y_2O_3 複合ゾルを用いて酸化物固溶体電解質を作製したところ、平均粒子径の最も小さい粉体を得ることができた。また、$(CeO_2)_{0.81}(ZrO_2)_{0.09}(Y_2O_3)_{0.10}$ という組成の電解質では、700℃で酸素分圧が 10^{-25} atm で電子導電性を抑えられることが分った。

CsH_2PO_4/SiO_2 複合体の導電率と構造相転移挙動を観測した。SiO_2 の添加により、降温過程において CsH_2PO_4 の高伝導相（立方晶）が臨界温度より低い温度まで保持されることが分かった。メソ多孔質シリカと CsH_2PO_4 の間における界面応力によって CsH_2PO_4 の構造相転移の過冷却現象が生じたためと結論づけた。

［引用文献］

[1] J. Otomo, N. Minagawa, C. Wen, K. Eguchi, H. Takahashi, *Solid State Ionics* **156**, 357 (2003).

[2] V.G. Ponomareva, N.F Uvarov, G.V. Lavrova, E.F. Hairetdinov, *Solid State Ionics* **90**, 161 (1996).

[3] H. Shigeoka , J. Otomo, C.-j. Wen, M. Ogura, H. Takahashi, *J. Electrochem. Soc.* **151**, J76 (2004).

[4] S. Wang, J. Otomo, M. Ogura, C.-j. Wen, H. Nagamoto, H. Takahashi, *Solid State Ionics* **176**, 755 (2005).

[5] J. Otomo, H. Shigeoka , H. Nagamoto, H. Takahashi, *J. Phys. Chem. Solids* **66**, 21 (2005).

[6] 大友順一郎, 高橋宏, 長本英俊, 電気化学および工業物理化学 **73**, 841 (2005).

[7] J. -H. Lee, J. Kim, S. -W. Kim, H. -W. Lee and H. S. Song, *Solid State Ionics* **166**, 45-52(2004).

[研究業績]

・J. Otomo, H. Nagamoto et al., "Kinetic process of phase separation in Co-SiO2 thin films and preparation of mesoporous SiO2 thin films with mesopore channels aligned perpendicularly to substrate surfaces," *Vacuum* **81**, 1003-1011 (2007).

3. 1. 3 ポリ乳酸(PLA)の動的結晶化挙動及び機械的物性に及ぼす充填材の影響

Influence of Filler on the Mechanical Properties and Kinetic Crystallization Behavior of Polylactic Acid (PLA)

佐藤貞雄、西谷要介、満田　諒

Sadao Sato, Yosuke Nishitani and Ryo Mitsuta

工学部　機械工学科

Dept. of Mech. Eng., Faculty of Engineering

Abstract

The kinetic crystallization behavior of PLA (polylactic acid) and PLA/MMT nanocomposites containing 3 wt% montmorillonite (MMT) was examined in order to develop a new technique for obtaining the relative crystallization degree of a material from the spherulite occupation area based on images obtained using a charge-coupled device (CCD) camera. In addition, the relative crystallization degree is discussed in terms of the Ozawa theory. The effect of MMT filler on the mechanical properties of PLA/MMT nanocomposites, the number of spherulites generated in the nanocomposites, and the linear growth rate of these spherulites were also examined experimentally. The relative crystallization curves obtained by CCD and by DSC measurement were found to be approximately the same. Moreover, it was found that the Ozawa theory could be applied not only to PLA but also to PLA/MMT nanocomposites. In these nanocomposites, the number of spherulites decreased and the linear growth rate slightly increased; moreover, the rate of crystallization also increased. The tensile and flexural modulus of the PLA/MMT nanocomposites containing 3 wt% MMT were 5.2-14.3% greater than those of PLA, and annealing resulted in a further increase of about 4.0-20.7%. However, the Izod impact value decreased due to the increase in rigidity caused by annealing and the addition of filler.

Key words: PLA/PLA/MMT nanocomposites/CCD camera/Relative crystallization degree/Ozawa theory

1．緒　　言

プラスチック材料は自然界の環境下では分解され難くその廃棄物が環境汚染となって問題となっている．また，プラスチックの原料についても石油資源の枯渇問題が現実に迫っており，今日では原料を石油に頼らない天然資源由来の原料に求めようとしている[1]．例えば，ジャガイモやトウモロコシなどのでんぷんから生成されるポリ乳酸 (Polylactic acid：PLA) 系高分子は結晶性で，溶融成形加工の際の結晶化挙動がその物性に大きく影響することが知られている．

Okamoto[2]らはポリ乳酸 (PLA) /モンモリロナイト (MMT) ナノ複合材料の等温結晶化挙動について検討し，MMT 充填により球晶数が増加し，球晶径は減少することを明らかにしている．また，汎用プラスチックのポリプロピレン (PP) に MMT を充填することにより結晶化速度が増し微細結晶が発生して物性が増大するという報告もされている[3)~6)]．すなわち，結晶化度が高く，結晶サイズ微細化によって剛性が増し，諸物性が向上することを述べている．このことから結晶性高分子の結晶化度，結晶サイズ及び結晶数のコントロールは結晶性高分子の各種物性の支配因子となっていることが推測できる．例えば，結晶核数が多く，結晶サイズが微細で結晶化度が高いと剛性や靭性を向上させ，伸び率，耐衝撃性に優れた高分子になる．Fujiyama[7]は核生成剤として γ-キナクリドン (γ-quinacridone) 0.01 g 添加によって結晶化度，耐衝撃性及び耐熱性が向上することを報告している．また，Fillon[8]らはアイソタックチックポリプロピレン (iPP) に 4-ビフェニルカルボン酸 (4-biphenyl Carboxylic acid) 2 wt%添加す

*1 工学院大学大学院
東京都八王子市中野町 2665-1 (〒192-0015)
Kogakuin University graduate school
2665-1, Nakanocho, Hachiojishi, Tokyo, 192-0015, Japan
*2 工学院大学機械工学科
Mechanical Engineering, Kogakuin Univ.
2007. 5. 2 受理

ると結晶化温度128.8℃，結晶化度66%まで上がることを報告している．結晶化挙動に関する理論的な検討の面で古くは，等温下ではAvrami[9]，非等温下ではOzawa[10]とNakamura[11]らによるものがあり，何れもDSCによる結晶化曲線を基に解析している．Eder[12]らはPPとHDPEについて検討した結果，HDPEは小澤理論が成り立たないことを報告している．またLim[13]とNagarajan[14]らは結晶核剤としてアジピン酸及び安息香酸などの有機質添加剤を，Ma[15]らはMMTなどの無機質充填材を用いることにより球晶のサイズをコントロールできることを報告している．

本研究は，ポリ乳酸（PLA）にナノコンポジット充填材として多用されるMMTを3 wt%充填したPLA/MMTナノコンポジットの結晶化挙動について，従来のDSCによらないCCD（Charge-coupled device）カメラを用いた結晶化曲線からその化挙動をリアルタイムで観察し，これら画像上の球晶の占有面積から相対結晶化度を求める新しい手法を提案するとともに小澤理論を用いて結晶化挙動に及ぼす充填材の影響及びPLA/MMTナノコンポジットの結晶状態と機械的物性の相関について実験的に検討した．

2．実　　験

2.1 試　料

実験に供した試料は，母材にPLA（三井化学㈱製LACEA H-100）を，充填材として結晶表面に4級アンモニウムカチオンを変性したモンモリロナイト（MMT）(㈱ホージュン製　S-BEN NX）を用いた．

まず試料の作製はPLAとMMTを3時間100℃で乾燥させた後，MMT 3 wt%を充填してコンパウンディング用二軸押出機を用いて溶融混練し，ストランド状に押し出されたPLA/MMT複合材はペレタイザー（東洋精機㈱）によりペレットにした．結晶化挙動観察のための試料は複合化したペレットを加熱圧延ローラーにより溶融圧延し厚さ40～60 μmのフィルムを作製し，直径7 mmのポンチで打ち抜いて使用した．

2.2 結晶化挙動の観察

フィルム試料の加熱・冷却装置は図1に示すように，試料温度コントロールユニット（ジャパンハイテック㈱製，LK-600 PH，L-600 A）を光学偏光顕微鏡のステージ上に設置し，先の試料ユニットセル内部に実験フィルムを直径12 mmの耐熱性プレパラートでサンドイッチにして配置した．光源からの光は偏光板を通った後，試料フィルム，検光板，対物レンズを経て上部に設置したCCDに入り，結晶画像が観察できる仕組みになっている．CCDカメラの映像は全てパソコンに取り込み保存した．なお，同装置は水道水，液体窒素による冷却により±0.5℃の精度で温度コントロールすることが可能である．また，溶融試料は窒素ガスを封入してシールした．

2.3 相対結晶化度

結晶化挙動の観察は，まず試料を190℃まで加熱した後，5分間保持し0.3，0.5，0.7，1.0，1.5℃/minの各冷却速度で冷却させ，CCDカメラにより結晶発生から完了までの変化をリアルタイムで記録し，パソコンに保存した．保存した画像をベースに結晶開始点を目視により決めた．この結晶開始から画面全体に結晶が成長し完了するまで，

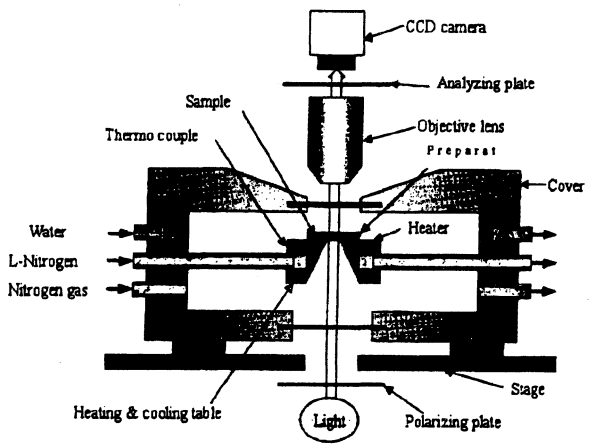

Fig. 1 Spherulite observational system by CCD camera and cooling and heating cell for sample

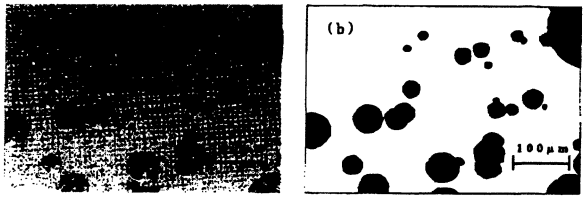

Fig. 2 The left side(a) is a spherulites image of PLA obtained by using a CCD camera and optical polarizing microscope together, and the right side(b) is spherulite image painted out to obtain the relative crystallization degree from occupation area of crystal part

1℃毎の画像をピックアップした．（冷却速度0.5℃/minの場合は2分毎，1.0℃/minの場合は1分毎にした）．得られた画像を図2の左側に示す．この図から，画面全体の面積X_∞に対してある温度Tにおける結晶部の占有面積X_T（図2右側の塗りつぶした部分の面積の総計）を求めて，相対結晶化度$R_c = X_T/X_\infty$とした．結晶部占有面積の測定は画像解析ソフト（Win ROOF）により求めた．

2.4 結晶化挙動の解析

非等温冷却過程における動的な結晶化挙動の解析は小澤理論を用いて解析した．小澤の式は，相対結晶化度と冷却速度の関係について示したもので，次の式(1)に示すようなものである．

$$\ln\left(1-\frac{X_T}{X_\infty}\right) = -\frac{\kappa(T)}{\phi^n} \qquad (1)$$

ここで，X_Tは結晶過程の温度Tにおける結晶部の占有面積，X_∞は画像全体の面積，nは小澤指数（アブラミ指数に相当），ϕは冷却速度，$\kappa(T)$は結晶化速度である．式(1)を対数表示すると次の式(2)のように表わせる．

$$\log\left[-\ln\left(1-\frac{X_T}{X_\infty}\right)\right] = n\log\left(\frac{1}{\phi}\right) + \log\kappa(T) \qquad (2)$$

式(2)の相対結晶化度（X_T/X_∞）は冷却速度ϕの関数で，右辺の第二項は結晶化速度$\log\kappa(T)$を示し，温度の関数

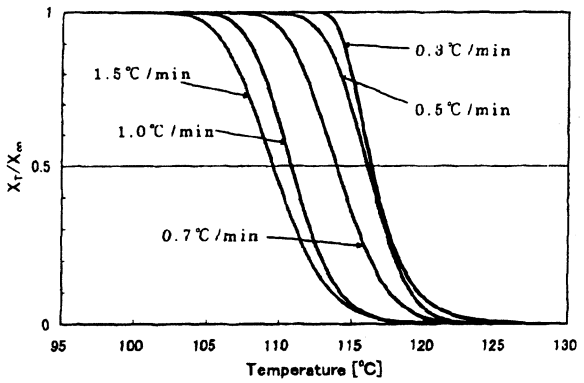

Fig. 3 Relative crystallization curves for PLA at various cooling rates

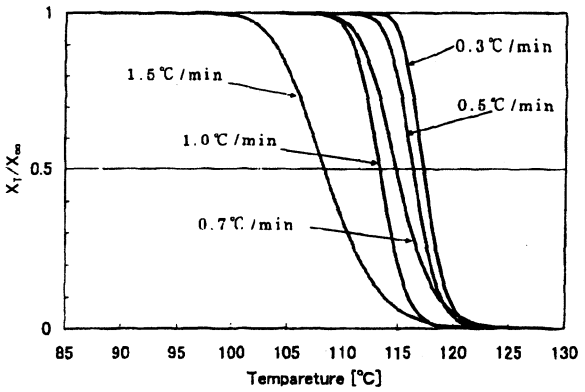

Fig. 4 Relative crystallization curves for PLA/MMT nanocomposites at various cooling rates

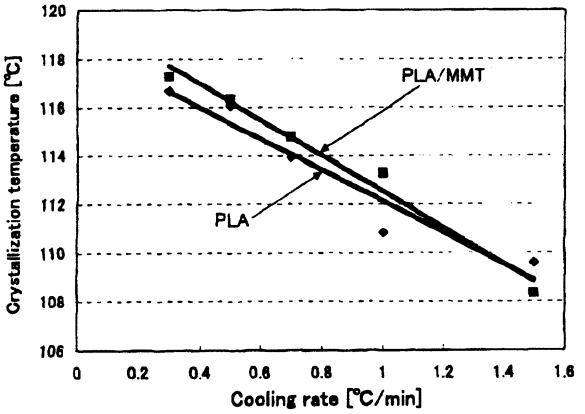

Fig. 5 Cooling rate dependence of crystallization temperature for PLA and PLA/MMT nanocomposites

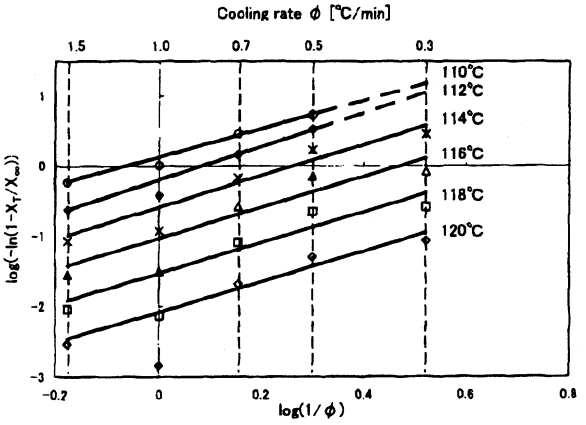

Fig. 6 Relationship between relative crystallization degree and cooling rate for PLA

で，各種冷却速度下における相対結晶化度を求め，結晶化挙動解析を行った．

2.5 線成長速度と球晶数

充填材の有無や冷却速度の影響を検討するため，球晶数と球晶の線成長速度の計測を行った．球晶の線成長速度は1℃毎に撮影した画像をWin ROOFにより計測した球晶径から，球晶数も同様に静止画中に発生した球晶数をカウントして求めた．

2.6 成形加工とアニーリング

成形加工に供した試料は先に溶融混練して作製したペレットを80℃，3時間乾燥後，樹脂温度230℃，室温に放置した金型を用い，簡易射出成形機により引張，曲げ及び衝撃の各試験片を成形した．また，加工した試験片は結晶化を促進させるために60℃，80℃，100℃で3時間アニーリングを行い引張，曲げ及びアイゾット衝撃に及ぼすアニーリングの影響を検討した．

3．結果と考察

3.1 結晶化挙動解析

PLAおよびPLA/MMT複合材について結晶化開始から終了までの各温度における相対結晶化度曲線を冷却速度毎に示したものが図3，4である．同図において相対結晶化度$X_T/X_\infty=0.5$はDSCによる結晶化温度（放熱ピーク温度）に相当し，同図から明らかなように相対結晶化度曲線は，冷却速度が速くなるにつれて低温側にシフトする．このような結晶化挙動は，DSC法による結晶化曲線から相対結晶化度を求めた結果にほぼ一致することを確認している[*1),2)]．また，先述のように$X_T/X_\infty=0.5$は結晶化温度を示し，PLA，PLA/MMTの結晶化温度を比較したものが図5である．これより，PLA/MMT複合材の結晶化温度はPLAに比べ少しPLA/MMTが高い．これはMMTの充填により母材との相対接触面積の増大，充填材間距離が短くなることによる熱流の流れ易さに因り熱伝導率が高くなるためで，試料自体の冷却速度が速くなることに起因していると思われる．

求められた相対結晶化度を式(2)に代入すると図6，7のようになる．各温度におけるX_T/X_∞と$1/\phi$の関係はほぼ一次式の直線で示されることからPLAとPLA/MMTの両者は小澤理論が成り立つことを証明している．しかしなが

脚注＊1) 井上遼平：結晶性高分子複合材の動的結晶化挙動に及ぼす充填材の影響と機械的物性，工学院大学大学院工学研究科機械工学専攻修士論文（2007-3）

＊2) 原　良輔：結晶性高分子のDSCとCCDカメラによる結晶化挙動の相関性に関する研究，工学院大学機械工学科卒業論文(2007-3)

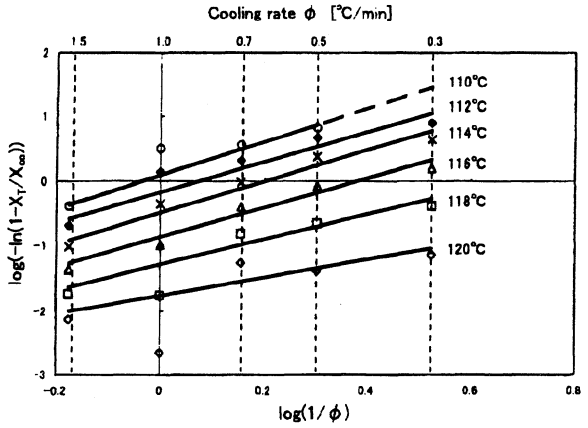

Fig. 7 Relationship between relative crystallization degree and cooling rate for PLA/MMT nanocomposites

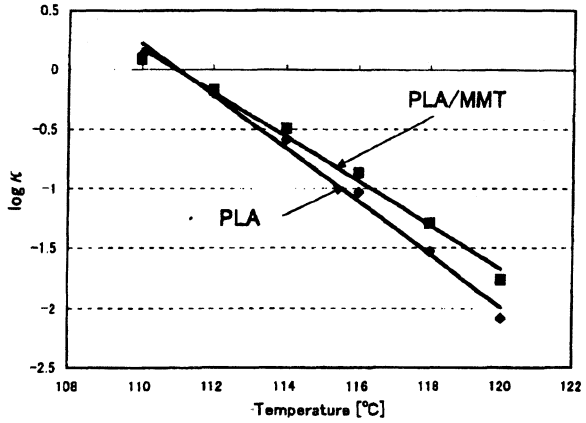

Fig. 8 Temperature dependence of crystallization rate logκ for PLA and PLA/MMT nanocomposites

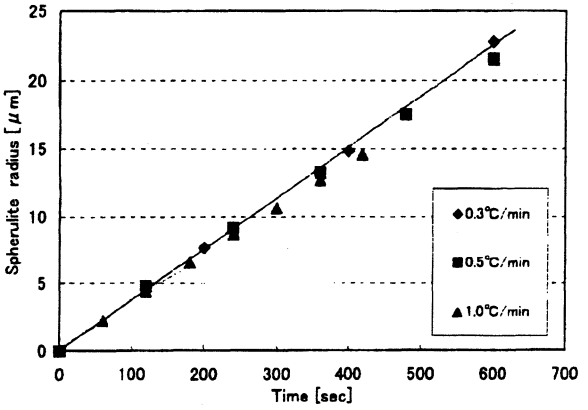

Fig. 9 Relationship between spherulite radius and time for PLA at various cooling rates

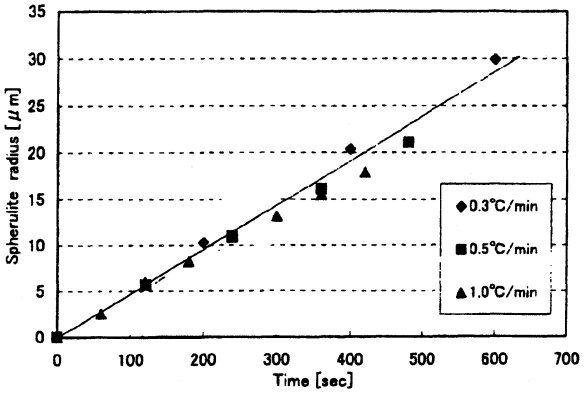

Fig. 10 Relationship between spherulite radius and time for PLA/MMT nanocomposites at various cooling rates

ら，計測上のバラツキが log(1/φ)=0 軸上に見られる．ここで，結晶化速度 logκ は図 6，7 における log(1/φ)=0 軸と温度をパラメータにした直線との交点読み取ることで求めることができる．これらの関係を示したのが図 8 である．同図より PLA/MMT 複合材の結晶化速度は PLA に比べて速く，特に高温域側において速い．このことは，先に述べたように MMT の充填により熱伝導率が高くなることに因る冷却速度依存性によるものと推定される．

3.2 線成長速度と球晶数

冷却過程における球晶径変化の計測結果は図 9，10 に示したように時間の経過とともに増大する．しかし，PLA，PLA/MMT それぞれは，冷却速度による影響はあまり見られない．これに対して線成長速度は図 11 のように PLA/MMT 複合材の方が PLA よりも約 25% 程度速い．このことから充填した MMT は結晶の成長を促進させる働きをしているものと考えられる．一方，球晶数は図 12 に示すように冷却速度に依存して発生数は時間とともに多くなるが，PLA/MMT 複合材の球晶数は PLA に比べ冷却速度 0.3 及び 1.0℃/min の場合の結晶化前半（前者は約 35 分，後者は 8 分）においては多い．しかし，結晶化後半になると逆転し少なくなる．このことから，非等温下における結晶過程では，MMT は結晶核材としての働きは一般に

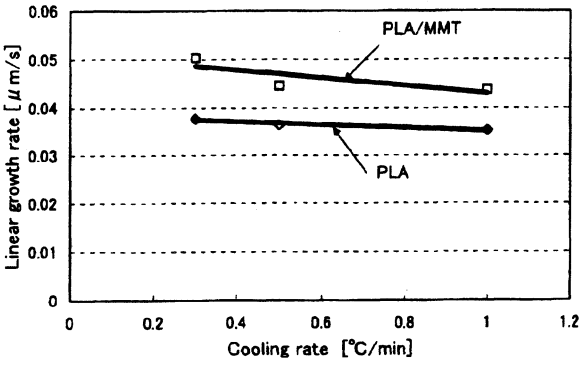

Fig. 11 Cooling rate dependence of linear growth rate for PLA and PLA/MMT nanocomposites

認められているものの，その働きは幾つかの要因に支配されることから，ここでは顕著な核材として認めるまでには至らなかった．そこで，予測される要因としては，MMT 充填が核誘起材として作用するためには層間剥離による適正な繊維間距離とナノオーダーの分散が必須になることから，有機処理が施されているとは言え，核材として働くための条件が不十分であったように思われる．今後，TEM

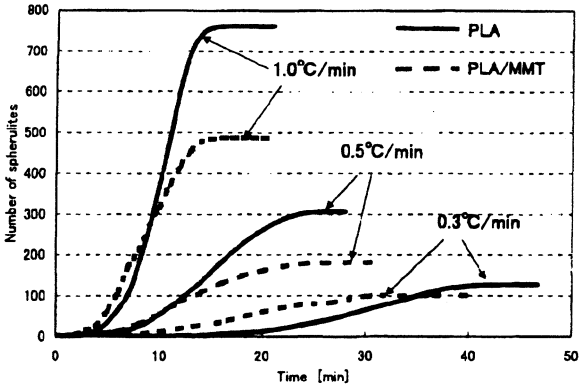

Fig. 12 Relationship between number of spherulites and crystallization time for PLA and PLA MMT nanocomposites under various cooling rates

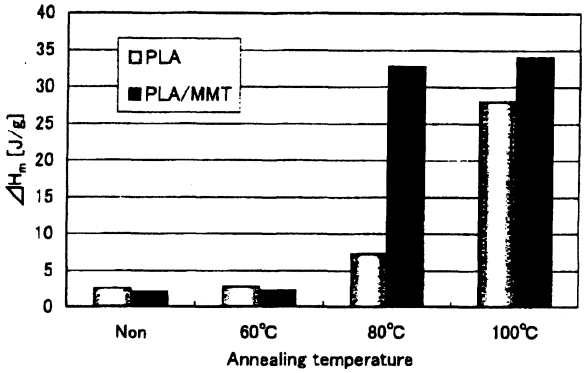

Fig. 13 Effect of annealing temperature on heat of transitions ΔH_m in PLA and PLA/MMT nanocomposites

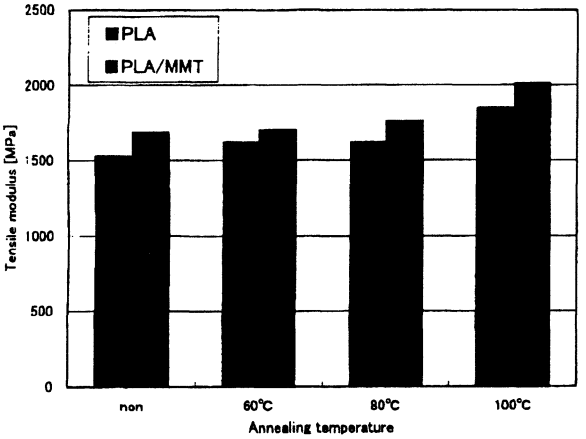

Fig. 14 Effect of annealing temperature on tensile modulus in PLA and PLA/MMT nanocomposites

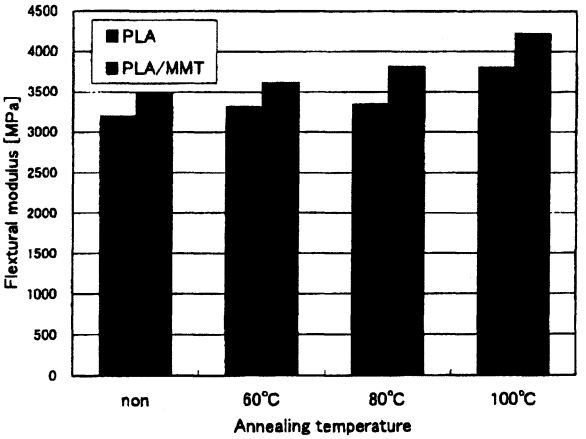

Fig. 15 Effect of annealing temperature on flexural modulus of PLA and PLA/MMT nanocomposites

などによる分散状態の評価と合わせて検討していく．

3.3 アニーリングによる結晶化

各種温度でアニーリングした試験片について結晶化の程度を検討するための一手法として，DSCにより試験片の転移熱量 ΔH_m[J/g]を測定した．転移熱量は試料の昇温過程における吸熱量と放熱量との差で示され，この値が大きいほど結晶化が進行していることを示している．すなわち，結晶化度に準じるものである．図13から明らかなようにアニーリング温度60℃では無しのものとあまり変わらない．したがって，結晶化の促進はほとんど生じていない事を示している．また，アニーリング温度80℃においてはMMTを充填したことにより結晶化が低い温度でも促進されていることがわかる．また100℃ではPLA，PLA/MMT複合材ともに同程度結晶化が促進されることが分った．

3.4 機械的物性

PLA及びPLA/MMT複合材の引張弾性率および曲げ弾性率は図14，15に示すように，MMTの充填およびアニーリングによりそれぞれ5.2～14.3%，4.0～20.7%程度増加した．このことから，アニーリングとMMT充填の効果は，顕著に見られ，結晶化度と剛性が高くなったことによるものと考えられる．しかしながら，弾性率が向上する一方で，図16，17に示すように，アニーリング，MMTとの複合化によって伸び率と引張強さは減少した．これは，剛性率の向上による脆性的性質が現れたこと，図18に示したアイゾット衝撃値が減少していることから明らかである．これらのことはMMTの充填による剛性の向上およびアニーリング由来の球晶径成長による脆性的性質の出現に起因するものである．

4．結　　論

CCDカメラによってリアルタイムで撮影された画像から求めた相対結晶化度は従来のDSCによるものにほぼ一致し，結晶性高分子の相対結晶化度を評価することが可能である．PLAおよびPLA/MMT複合材の結晶化挙動解析における相対結晶化度と冷却速度との関係は，温度をパラメータに取って示すと何れの場合もほぼ直線性を示すことから小澤理論が適用できることがわかった．また，PLAにMMTを3 wt%充填することにより，結晶化温度は0.3～2.4℃高温側にシフトする．PLA/MMT複合材の結晶化速度 $\log\kappa$ はPLAに比べて15%程度上昇した．球晶の

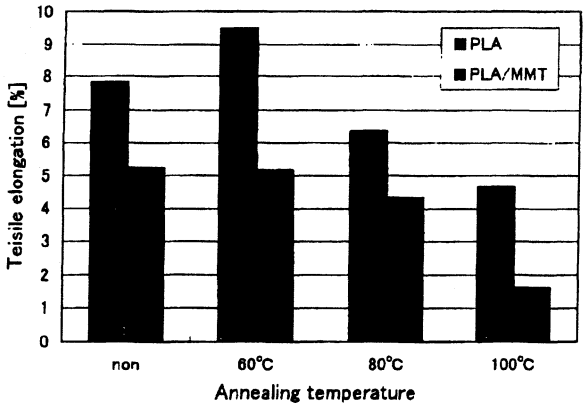

Fig. 16 Effect of annealing temperature on tensile elongation of PLA and PLA/MMT nanocomposites

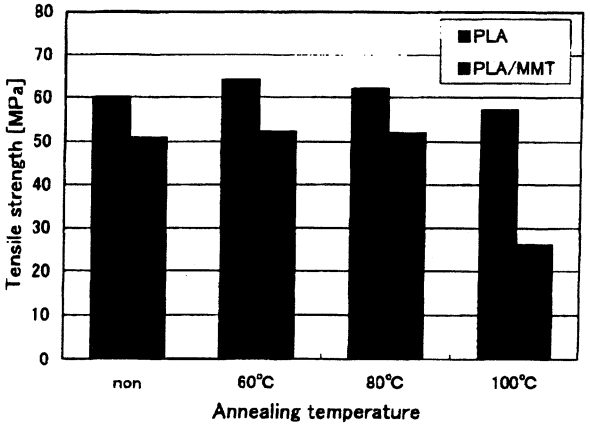

Fig. 17 Effect of annealing temperature on tensile strength for PLA and PLA/MMT nanocomposites

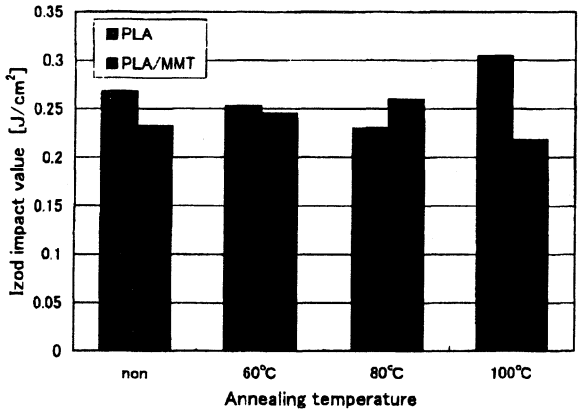

Fig. 18 Effect of annealing temperature on Izod impact value for PLA and PLA/MMT nanocomposites

線成長速度と球晶数は，MMT の充填により線成長速度は 25% 程度増大し，結晶数は 30% 程度減少した．引張および曲げ弾性率は MMT の充填により 10% 程度，アニーリングによって 20% 程度それぞれ増大した．しかし，伸びと引張強さは減少し，脆性的性質が見られた．

追記：本研究は文部科学省「ハイテク・リサーチ・センター整備事業」研究開発プロジェクト「ナノ表面・界面の創製と応用」」の中の一課題として遂行されたものである．

参 考 文 献

1) 川島信之，松尾充記，杉正浩：高分子論文集，**62**(6)，233 (2005)
2) Nam, J. Y., Ray, S. S. and Okamoto M：*Macromolecules*, **36**(19), 7126(2003)
3) ZHOU, C., LI, J. and GANG, W.：*Polymer Testing*, **22**(2), 217(2003)
4) XU, W., HE, P. and GE, M.：*J. Polym. Sci. Part B*, **40**(5), 408(2002)
5) XU, W., LIANG, G., WANG, W., TANG, S., HE, P. and PAN, W. P.：*J. Appl. Polym. Sci.*, **88**(14), 3093(2003)
6) LIU, X. and WU, Q.：*Polymer*, **42**(25), 10013(2001)
7) Fujiyama, M.：*Intern. Polym. Processing*, **10**(3), 251 (1995)
8) Fillon, B., Thierry, A., Lotz, B. and Wittman, J. C.：*J. Thermal Analysis*, **42**(4), 721(1994)
9) Avrami, M.：*J. Chem. Phys.*, **7**, 1103(1939)
10) Ozawa, T.：*Polymer*, **12**, 150(1971)
11) K. Nakamura, K. Katayama and T. Amano：*J. Appl. Polym. Sci.*, **17**, 1031(1973)
12) Eder, M. and Wtochowiez, A.：*Polymer*, **24**, 1593 (1983)
13) Gordon, B. A. Lim and D. R. L. Loyd：*Polym. Eng. and Sci.*, **33**, 529(1993)
14) Nagarajan, K., Levon K. and Myerson, A. S.：*J. Therm. Anal. Calorimetry*, **59**, 497(2000)
15) Ma, J., Zhang, S., Qi, Z., Li G. and Y. Hu：*J. Appl. Polym. Sci.*, **83**(9), 1978(2002)

3. 1. 4 コポリマーブラシを用いたナノ相分離構造薄膜の創製

Creation of thin films with nano-structure by intermolecular phase-separation of copolymer brush.

川井忠智、寺町信哉、伊藤雄三
Tadatomo KAWAI, Shinya TERAMACHI, Yuzo ITOH
マテリアル科学科
Department of Materials Science and Technology

Abstract: Hetero-arm cylindrical copolymer brushes were synthesized by free radical copolymerization of two kinds of macromonomers. Utilized macromonomers were polydimethylsiloxane, polystyrene, poly(methyl methacrylate) and poly(ethylene oxide) macromonomer. These macromonomers were copolymerized in the benzene solution. In the much combination system, there was the phase separation. The copolymer brushes were analyzed by dual detection size-exclusion chromatography, eluent gradient HPLC and FT-IR.

1. はじめに

ポリマクロモノマーは、末端に反応性基を持つ高分子(マクロモノマー)を重合することにより得られるブラシ状高分子で、側鎖間の排除体積効果により棒状分子としてふるまい液晶性を示すことが知られている。この棒の太さは、マクロモノマーの分子量により nm～数 10nm オーダーに調整できる。一方で、ブロックコポリマーやグラフトコポリマーは、それぞれの同じブロック鎖が集合し、ミクロ相分離構造を作ることがよく知られている。これらの性質を利用すれば、異種マクロモノマーの共重合により生成したブラシ状のコポリマクロモノマー、すなわちコポリマーブラシは、分子内相分離により自己組織化能を発揮し、配向したナノスケールの幅を調節できる縞状構造の表面を有する、ナノ相分離構造薄膜を創製することが期待できる。両ポリマクロモノマーの種類、主鎖および枝の分子量、などを調節することにより、こうした異種高分子によるナノスケールの縞状構造の実現は可能と考えられる。

本研究では、種々のマクロモノマーの組合せによる共重合を行いコポリマーブラシを合成し、その分子構造の解析を行う。それらのコポリマーブラシから薄膜を調製し、ナノ相分離構造薄膜の、分子構造と機能性の関係を明らかにすることを目的としている。

現在までに、ポリジメチルシロキサン(PDMS)、ポリスチレン(PS)、ポリメタクリル酸メチル(PMMA)、ポリエチレンオキシド(PEO)のマクロモノマー間の各組み合わせについて共重合を行い、共重合性について検討してきたが大部分の組み合わせは、異種ポリマー、共通溶媒系に特有の液-液相分離を示し、各々の相中で共重合が起こることが明らかとなった。本報告では、その主要な点を述べることとする。

2. 実験

2.1 試料

本研究では、ポリジメチルシロキサン-マクロモノマー(PDMS-m, MW 5,000, チッソ社提供)、ポリスチレン-マクロモノマー(PS-m, MW 6,000, 東亞合成社提供)、ポリメタクリル酸メチル-マクロモノマー(PMMA-m, MW 5,000, 東亞合成社提供)、ポリエチレンオキシド-マクロモノマー(PEO-m, MW 2,080,シグマアルドリッチ社製)を使用した。末端反応基は、いずれもメタクリル基である。なお示した分子量はカタログ値である。

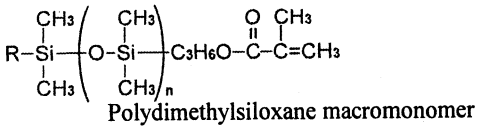

Polydimethylsiloxane macromonomer

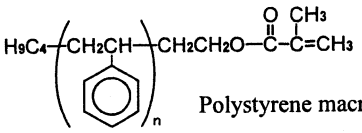

Polystyrene macromonomer

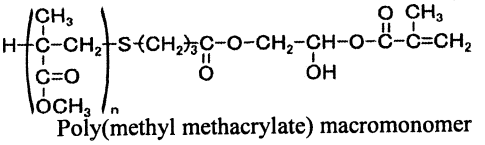

Poly(methyl methacrylate) macromonomer

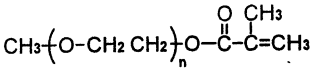

Poly(ethylene oxide) macromonomer

Fig.-1. Sample of macromonomers

2.2 共重合系での相状態の確認

マクロモノマーの共重合に先立ち、溶媒にベンゼンを用いた系の相状態を、反応温度と同じ 60℃で確認した。

2.3 共重合

種々のマクロモノマーの仕込み組成において、溶媒にベンゼン、開始剤に AIBN を用い、60℃にてラジカル共重合を行った。共重合後、巨視的に2相分離状態が認められた系は、それぞれの相を分取しポリマー成分を回収した。

2.3 分子構造解析

コポリマーの生成確認には、サイズ排除クロマトグラフィー(SEC)を用いた。平均組成は、^{1}H NMR により求めた。また、溶離液グラジエント高性能液体クロマトグラフィー(グラジエン

トHPLC)により組成分布の解析を、FT-IR により高次構造の解析を、それぞれ試みた。

3. 結果と考察

3.1 Macromonomer 1／Macromonomer 2／Benzene 系の相状態

相状態の確認は、Fig.-1 に示したマクロモノマーを組み合わせ行った。特徴的な組み合わせの擬三成分系相図を Fig.-2 に示す。

Fig.-2(a)には、PDMS-m／PS-m／Benzene 系の相図を示した。溶媒約 80%付近に相分離曲線が認められ、広い組成範囲で相分離することがわかった。さらに仕込み組成にかかわらず巨視的に相分離を起こし、相分離したそれぞれの相の組成が非常に偏り、上相は下相に比べ著しくスチレン含率が低かった。同様の結果は、PDMS-m／PMMA-m／Benzene 系、PDMS-m／PEO-m／Benzene 系、でも得られた。

Fig.-2(b)には、PS-m／PMMA-m／Benzene 系の相図を示した。溶媒約 50%付近に相分離曲線が認められ、若干曖昧さがあるものの巨視的に相分離を起こした。また、PS-m／PEO-m／Benzene 系においても溶媒約 50%付近に相分離曲線が認められたが、この系では、巨視的な相分離は起きず系全体が白濁した相分離状態であった。

Fig.-2(c) には、PEO-m／PMMA-m／Benzene 系の相図を示した。この系では、60℃において広い組成範囲で均一相となることが見出された。

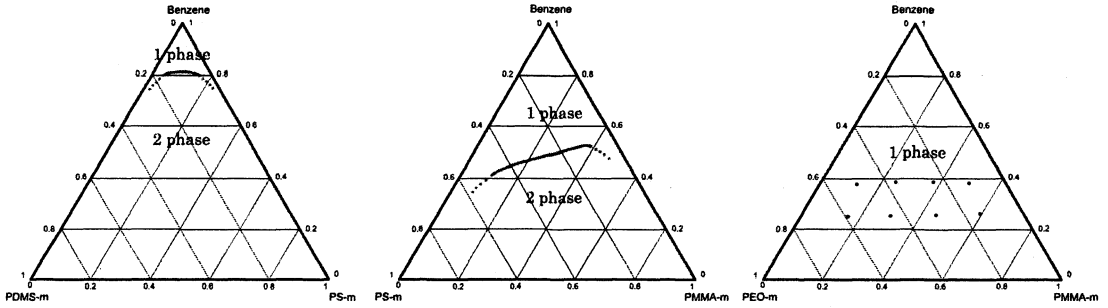

(a) PDMS-m／PS-m／Benzene (b) PS-m／PMMA-m／Benzene (c) PEO-m／PMMA-m／Benzene

Fig.-2 Cloud points curves of Macromonomer 1／Macromonomer 2／Benzene at 60℃

3.2 コポリマーブラシの合成と解析

コポリマーブラシの合成は、Fig.-1 に示したマクロモノマーの組み合わせで行った。そのうち PDMS-m／PS-m、PS-m／PMMA-m、PS-m／PEO-m について示す。

3.2.1 PDMS-m／PS-m／Benzene 系

PS-m／PDMS-m／Benzene 系は、均一系ではマクロモノマー濃度が低いため、相分離系でラジカル共重合を行った。

まず共重合に先立ち、溶媒 75%での未反応の両相を分取しその組成を決定した。相分離したそれぞれの相の組成は非常に偏り、上相は下相に比べ著しくスチレン含率が低かった。

共重合は、種々のマクロモノマー仕込組成で、溶媒 75%、開始剤に AIBN を用い 60℃で 48 時間行った。共重合後も巨視的に 2 相分離状態が維持されていたので、それぞれの相を分取し、ポリマー成分を回収した。それぞれの相から得られたコポリマー組成は、上相はスチレン含率が低く、下相はスチレン含率が高く、概ね未反応系のそれぞれの相の組成に対応していることが明らかとなった。

この系では、未反応マクロモノマーとコポリマーが SEC により分離可能であったため、コポリマーを分別

Table 1. Preparation of Poly(PS-*co*-PDMS)by radical copolymerization in benzene at 60℃for 48h.

Sample Code	Feed (g)				Styrene Content (wt.%) [1]		
	PS-m	PDMS-m	Benzene	AIBN	phase	Composition in the respective phase	Fractionated Copolymer [2]
PSPDMSS28	0.6876	2.6730	8.6881	0.0504	Upper	3.33	3.20
					Lower	75.67	79.03
PSPDMSS46	1.3316	2.0195	5.6994	0.0494	Upper	8.06	3.82
					Lower	92.07	88.13
PSPDMSS64	2.0191	1.4158	8.7458	0.0508	Upper	8.44	5.24
					Lower	82.78	88.70
PSPDMSS82	2.7406	0.7020	8.9234	0.0511	Upper	5.36	16.19
					Lower	88.72	90.20

1) Determined by ^{1}H NMR; JEOL EX270, $CDCl_3$

2) Fractionated by SEC

し、紫外吸収検出器(UV)－示差屈折検出器(RI)二重検出 SEC により見かけの分子量に対する組成を調べた。二重検出 SEC は、RI 検出器によりコポリマーの、UV 検出器によりスチレンユニットのそれぞれの濃度を見積もる方法で、鎖状ホモポリマーにおいては溶液中での分子サイズから分子量を見積もることが可能で、二重検出 SEC により分子量に対するスチレンユニットの組成を求めることができる。コポリマーブラシでは、分子サイズがそのまま分子量へ変換できないが、コポリマーと未反応マクロモノマーの区別には有効である。二重検出 SEC の結果もコポリマー部分のスチレン含率が未反応の各相に対応していた。この系においては、それぞれの相で共重合が起こり、大きく組成の異なるコポリマーが生成することが、明らかとなった。

また粗共重合体を用いグラジエント HPLC による組成分布の解析を試みた。グラジエント HPLC は、極性の異なる 2 種の溶離液の組成を漸次変化させることにより組成の異なるポリマー分子を分離する方法で、統計コポリマーやグラフトコポリマーの組成分布の決定に適用されてきた。本法をコポリマーブラシの組成分布の解析に適用し解析を試みた。しかし、多岐にわたる分離条件の検討にもかかわらず、未反応マクロモノマーとコポリマーの明瞭な分離が得られず、また、組成に応じた溶出位置とは異なる溶出順のクロマトグラムとなり組成分布を明らかにすることはできなかった。本法での解析が困難なのは、コポリマーブラシという特徴的な分子構造に由来することが示唆された。

以上より、PS-m／PDMS-m／Benzene 系では、均一系の組成範囲が狭く任意の組成のコポリマーブラシを合成することが困難であること、これらコポリマーブラシの分子特性解析に至るまでに多くの困難さが明らかとなった。

3.2.2 PS-m／PMMA-m／Benzene 系

PS-m／PMMA-m／Benzene 系では、均一系と相分離系で共重合を行った。

まず共重合に先立ち、溶媒50%での未反応の両相を分取しその組成を決定した。各相の組成は偏りがあり、上相は下相に比べスチレン含率が高かった。

共重合は、種々のマクロモノマー仕込組成で、溶媒 65%の均一系と溶媒 50%の相分離系とで、開始剤に AIBN を用い 60℃で 48 時間行った。均一系では重合終了まで均一 1 相で進行し、粗共重合体の回収率はほぼ 100%であった。一方、相分離系では、重合の進行に伴い溶液の粘性が上昇した。重合後は、曖昧さはあるものの巨視的な 2 相分離状態であったため、それぞれの相を分取しポリマー成分を回収した。しかし粘性が高く回収に困難を伴ったため、回収率は 85%から 95%であった。回収した各試料の組成は、上相はスチレン含率が高く下相はスチレン含率が低く、概ね未反応系のそれぞれの相の組成に対応していることが明らかとなった。

SEC において、未反応マクロモノマーより高分子量側にコポリマーと考えられるピークが認められたため、SEC によりコポリマーを分別し UV－RI 二重検出 SEC により見かけの分子量に対する組成を調べた。結果は、コポリマー部分のスチレン含率が未反応の各相に対応していた。相分離系では、それぞれの相で共重合が起こり、仕込み組成とは異なる組成のコポリマーが生成することが明らかとなった。

SEC 分取したコポリマーを用い、グラジエント HPLC による組成分布の解析を試みた。しかし、いくつかの分離条件で検討したが、組成に応じた溶出位置とは異なる溶出のクロマトグラムが得られ、また、カラムへの試料残留が起こり、定量的な組成分布を明らかにすることはできなかった。コポリマーのカラムへの強い残留は、コポリマーブラシという特徴的な分子構造に由来することが示唆された。

これらコポリマーブラシについて高次構造の解析を、FT-IR にて試みた。粗共重合体の場合、仕込み組

Table 2. Preparation of Poly(PS-*co*-PMMA)by radical copolymerization in benzene at 60℃for 48h.

Sample Code	Feed (g)				Styrene Content (wt.%) [1]			
	PS-m	PMMA-m	Benzene	AIBN	phase	Crude Copolymer	Composition in the respective phase	Fractionated Copolymer [2]
PSPMMA731	1.0507	0.4520	2.8198	0.0067		69.5		57.0
PSPMMA551	0.7750	0.7506	2.8100	0.0066		50.4		41.3
PSPMMA371	0.4497	1.0501	2.8306	0.0066		28.8		21.7
PSPMMA732	1.0575	0.4610	1.5252	0.0045	Upper	73.4	70.2	65.8
					Lower	55.2	44.9	44.0
PSPMMA552	0.7540	0.7590	1.5179	0.0045	Upper	59.6	55.6	45.9
					Lower	35.8	31.8	21.6
PSPMMA372	0.4532	1.0640	1.5096	0.0047	Upper	32.8	55.6	28.9
					Lower	23.1	23.7	21.6

1) Determined by ^{1}H NMR; JEOL EX270, $CDCl_3$

2) Fractionated by SEC

成に応じベンゼン環由来のシグナルのシフトと強度比変化が認められた。ただし、PMMA 由来のシグナルには変化が認められなかった。一方、SEC 分取したコポリマーブラシにおいては、約 30%より低スチレン含率においてベンゼン環由来のシグナルのシフトと強度比変化が認められたがそれ以外の組成では粗共重合体の場合と異なり変化は認められなかった。また、粗共重合体においては変化が認められなかった PMMA 由来のエステルのシグナルは、スチレン組成の低いものほど低波数側にシフトする変化が認められた。これらの変化が、どのような高次構造を示しているのかは、今後さらなる解析が必要であるが、組成に応じ凝集構造が変化していることは示唆された。

以上より、PS-m／PMMA-m／Benzene 系では、任意の組成のコポリマーブラシを合成するには、やはり均一系の組成範囲が若干狭く制限があること、これらコポリマーブラシの分子特性解析には多くの困難があることが明らかとなった。

3.2.3 PS-m／PEO-m／Benzene 系

PS-m／PEO-m／Benzene 系では、均一系で共重合を行った。PS-m と PEO-m のマクロモノマー仕込組成は、3:7、5:5、7:3 とし、溶媒 65%の系と溶媒 55%の重合の進行に伴い相分離する可能性のある系とで、開始剤に AIBN を用い 60℃で 24 時間行った。共重合開始直後は、均一相であったが重合の進行に伴い溶液の粘性が上昇し、すべての試料で弱い白濁が認められた。なお、溶媒 55%の PS-m:PEO-m＝3:7、5:5、のはゲル成分を生じた。しかし、それぞれの相を分取回収することが困難であったため、分取せず全体を一つとして回収した。

この系では、未反応マクロモノマーとコポリマーは、SEC 的に分離が不可能であったため、透析により未反応 PEO-m を溶媒抽出法により未反応 PS-m の除去を試みた。未反応マクロモノマーの除去確認は、SECと、統計コポリマーの組成分別に有効であるグラジエントHPLCにて行った。結果は、未反応マクロモノマーの除去が不十分であり、^{1}H NMR による組成解析からも未反応マクロモノマーが残存している可能性が示唆された。

これらコポリマーブラシについて高次構造の解析を、FT-IR にて試みた。粗共重合体の場合、仕込み組成に応じベンゼン環由来のシグナルのシフトと強度比変化が認められた。ただし、PMMA 由来のシグナルには変化が認められなかった。一方、SEC 分取したコポリマーブラシにおいては、約 30%より低スチレン含率においてベンゼン環由来のシグナルのシフトと強度比変化が認められたがそれ以外の組成では粗共重合体の場合と異なり変化は認められなかった。また、粗共重合体においては変化が認められなかった PMMA 由来のエステルのシグナルは、スチレン組成の低いものほど低波数側にシフトする変化が認められた。これらの変化が、どのような高次構造を示しているのかは、今後さらなる解析が必要であるが、組成に応じ凝集構造が変化していることは示唆された。

以上より、PS-m／PEO-m／Benzene 系では、低い溶媒濃度の系でゲルの生成が認められ 2 官能性マクロモノマーの混在が疑われること、任意の組成のコポリマーブラシの合成に制限があること、さらに、これらコポリマーブラシの分子特性解析に至るまでに多くの困難さが明らかとなった。

3.2.4 その他の系

PDMS-m／PEO-m／Benzene 系とPDMS-m／PMMA-m／Benzene 系は、均一系ではマクロモノマー濃度が低いため、相分離系でラジカル共重合を行った。SEC による解析では、未反応マクロモノマーとコポリマー分離ができず、共重合反応にける溶媒濃度と開始剤濃度のさらなる検討必要であることが示唆された。PMMA-m／PEO-m／Benzene 系は、広い組成範囲で均一相となったため、種々のマクロモノマー濃度における共重合を検討した。結果、高 PEO-m 組成においてゲル化が起こり多官能性 PEO-m の混在も疑われた。この系でも、未反応マクロモノマーとコポリマーは、SEC 的に分離が不可能であったため、透析により未反応 PEO-m を溶媒抽出法により未反応 PMMA-m の除去を試みた。未反応マクロモノマーの除去確認は、SEC による分子量的、グラジエント HPLC にて組成分別的に行った。結果は、未反応マクロモノマーの除去が不十分であり、また、^{1}H NMR による組成解析からも未反応マクロモノマーが残存している可能性が示唆された。

4. まとめ

以上より、低マクロモノマー濃度領域では共重合が起こりにくく、さらに相分離した系ではコポリマーブラシの組成を任意に調節することが困難であること、さらに、重合条件の検索と共に解析方法の確立も重要であることがわかった。

【研究業績】

学会発表　「マクロモノマー間共重合と反応系の相分離」 川井忠智、高分子討論会(H18.9.22)

3. 2. 1 溶液からの核発生および結晶粒径分布の制御
Control of Nucleation and Size Distribution of Crystals from Solution

環境化学工学科　加藤　尚武
環境化学工学科　後藤　雄一
早稲田大学　平沢　泉
Department of Environmental Chemical Engineering　Naotake Katoh
Department of Environmental Chemical Engineering　Yuuichi Goto
Waseda University Izumi Hirasawa

(Abstract) In order to generate nano-size crystals, we attempted to irradiate ultrasonic wave into a batch cooling crystallizer. In case of usual batch cooling operation, nucleation did not occurred at saturation concentration and occurred at supersaturation condition. Conversely, in case of batch cooling operation with ultrasonic wave, nucleation occurred at undersaturation concentration. Experimental results showed that KNO_3 crystal size of order 1 micrometer was obtained at undersaturation concentration by use of ultrasonic wave.

1.緒言

最近注目されている技術にナノレベルでの超微粒子の製造がある。超微粒子は通常の結晶では見られない、量子サイズ効果、面積効果、化学結合効果、体積効果などの多くの性質を有しており、その用途は医薬品や機能化学品、食品や触媒など多岐にわたって期待されている。

本研究では、まず、晶析操作の中で最も基本的な冷却回分晶析をとり上げ、これまでの種晶添加操作に加え超音波照射という新たな操作、さらにそれらをオンライン粒度分布測定装置(FBRM)によって観察した。そこから超音波照射を伴う晶析現象の理解、さらに操作条件の影響を把握し、最終的に超微粒子結晶の生成を目指すことを目的とした。

実験は硝酸カリウム（KNO_3）の冷却回分晶析を用いた。

次に、反応晶析に対して、超音波放射がどのような影響を与えるか、とくに反応物と生成物への超音波の影響そして核発生や結晶粒径およびその分布への影響を検討する予定である。

実験は、塩化カルシウム($CaCl_2$)と炭酸ナトリウム(Na_2CO_3)から炭酸カルシウム($CaCO_3$)の結晶を生成する反応晶析を予定している。

2.理論

結晶成長が起こるためには溶液中に存在する溶質分子が脱水和を起こし、結晶の界面に拡散・吸着する必要がある[1]。すなわち、界面に存在する溶媒分子を押しのけて、溶質分子が吸着しなければならない。

Fig.1 は超音波を照射することにより、溶質分子が結晶の界面に吸着する様子を示している[2]。　また、平沢らは、超音波照射により生成する気泡が壊れるときに周辺が非常に高圧になり、この圧力差を推進力として一次核化が起こり、そして結晶が生成するとしている[3]。

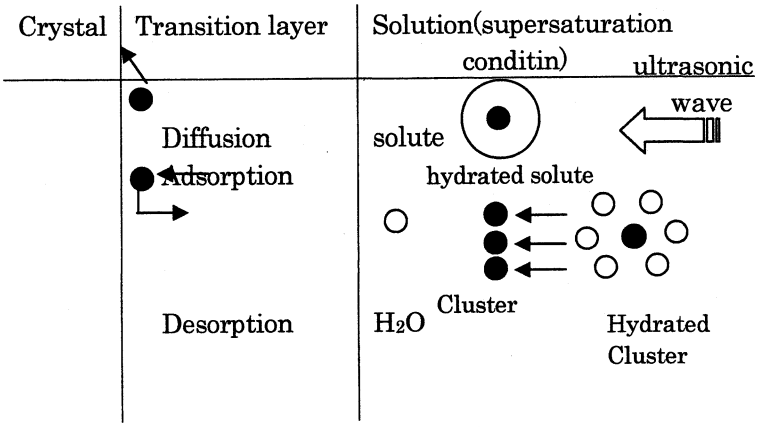

Fig.1　Effect of ultrasonic wave on crystal growth

このように、核発生、結晶成長への超音波の影響について諸説があるが、実験的に十分検討されているわけではない。

3.実験装置および方法

3.1 実験装置

実験装置の概略を Fig.2 に示す。

本実験の特長は、①のオンライン粒度分布測定装置（米国レーゼンテック社製）を用いて晶析槽内の結晶生成の刻々の変化を観察できることである。この装置の原理は、レーザービームが粒子を横切る時間と粒子径とが比例するということにもとづく。

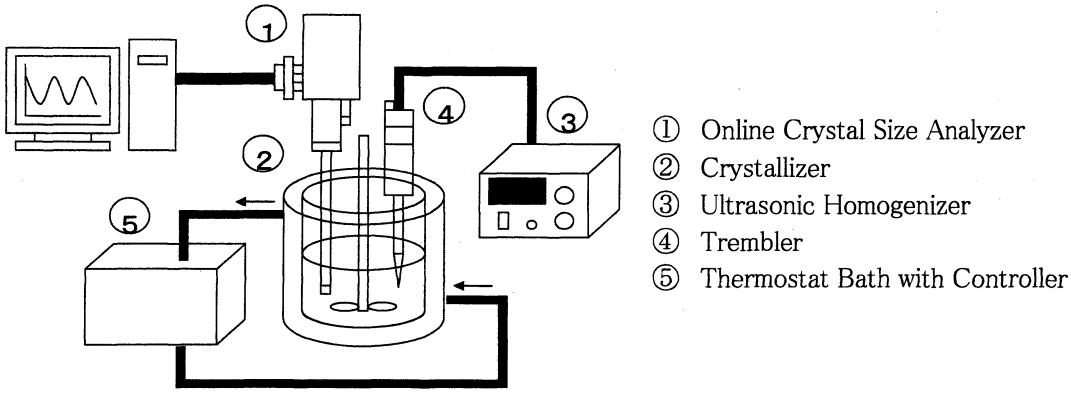

Fig.2 Schematic diagram of experimental apparatus

3.2 実験方法

実験手順の概略を Fig.3 に示す。純水 200 [mL]を容量 500 [mL]のジャケット付晶析槽②に入れ、冷却水をジャケットに流し、純水を 35 [℃]程度にする。次に硝酸カリウム(KNO_3)を 75.68[g]純水に投入し、完全に溶かす。この 75.68 [g]は、純水 25 [℃]、200 [mL]での硝酸カリウムの溶解度に対応する。温度を測定開始温度 28 [℃]まで下げ、FBRM①による核発生および結晶成長の測定を開始し、プログラムバス⑤(東京理科器械社PCC-7000)によって 40 [min]かけて 20[℃]まで冷却した。超音波発生装置③(エスエムテー UH-50)は周波数 20 [kHz]、出力 50 [W]で測定開始とともに照射し、測定終了まで照射し続けた。前述したように本実験の特長は、回分冷却晶析における結晶成長の様子が FBRM①により、オンラインで測定できること、したがって、超音波の核発生、結晶成長への影響を刻々知ることができることである。また、FBRM は 0.5 μmから 1000μmまでの粒径を測定することができる。

超音波により晶析槽内に気泡が発生することは十分考えられる。そこで、結晶の有無、粒径は光学顕微鏡（オリンパス製、BX51）によっても測定した。このとき、サンプルの温度と室温がほぼ同じになるようにしてサンプル中の結晶の生成や溶解を防ぐために、温度範囲を 20℃から 28℃とした。

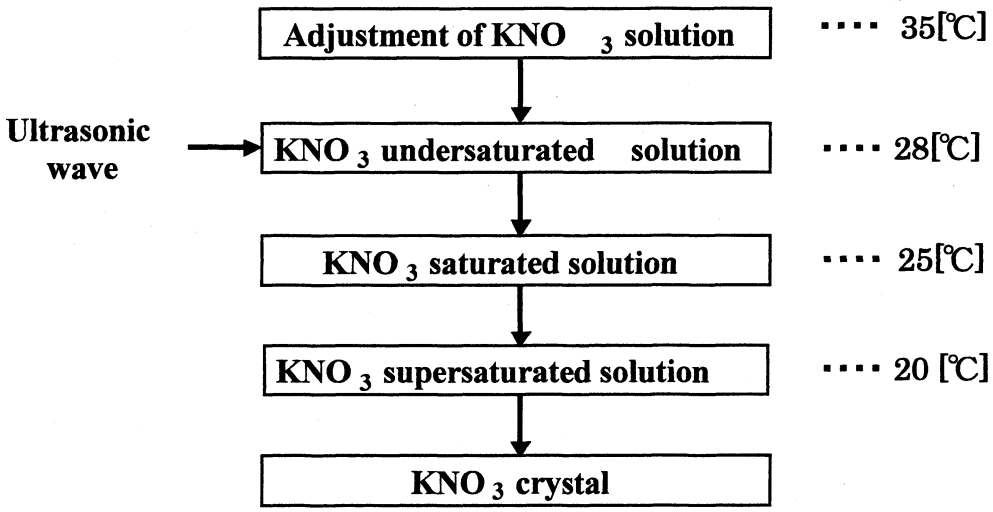

Fig.3 Experimental scheme

4.結果及び考察

超音波照射の核化、結晶成長および晶析槽内温度への影響を検討した。

超音波無照射の場合の実験結果を Fig.4 に示す。縦軸のカウント数はレーザー光線が粒子に当たり、その反射光を計数したもので、結晶個数に対応する。Fig.4 の通常の回分冷却晶析では、槽内温度が飽和温度 25℃に下がっても、結晶は観測されず、10 分ほど遅れて、約 23.3℃で結晶の生成が認められる。そして晶析熱により 2 分ほど温度が低下せず一定になっていることが認められる。実験開始から約 27 分までは FBRM のカウント数はゼロであり、光学顕微鏡による観察でも結晶は認められなかった。実験終了時,t=40 分における結晶粒径分布（CSD）を光学顕微鏡で観察した結果も Fig.4 に示す。このと FBRM によるカウント数の結果を比較すると両者の測定結果は大体一致している。

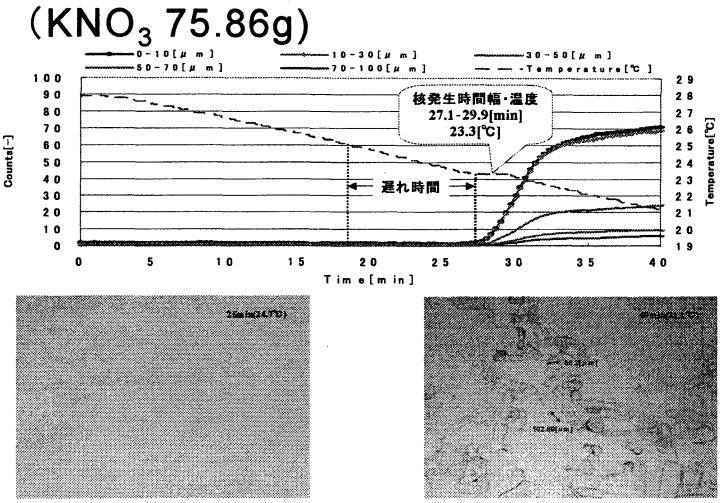

Fig.4 CSD and Temperature transients(without ultrasonic

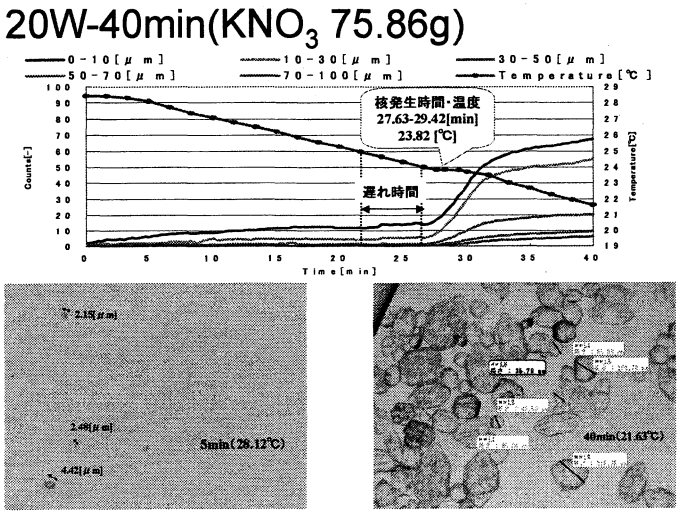

Fig.5 CSD and temperature transients(with ultrasonic wave)

Fig.5 は、槽内温度が 28℃になったときに超音波を照射したときの結果である。超音波のないときに比べて冷却による核発生の温度が 23.8℃と,Fig.4 の場合よりやや高い温度になっているがそれほどの差はない。興味深いのは、実験開始から冷却による急激な核発生にいたるまで、粒径 0～10μm および 10～30μm の微細結晶のカウント数がすこしずつ増加していることである。このカウント数は超音波による気泡の発生の影響を受けている可能性もあるので、晶析槽内の溶液を約 0.1mL サンプリングし、すばやく光学顕微鏡で観察した。その結果も Fig.5 に示す。 t =5min の場合は飽和温度 25℃以上の未飽和領域であり、それでも 1～5μm の範囲の結晶が生成している点が注目される。 超音波により、局所的に過飽和領域が実現されたものと推測される。

Fig.6 には、Fig.4 の超音波を照射しない場合、Fig.5 の超音波を照射した場合、そして溶質 KNO_3 なしで溶媒のみに超音波を照射した場合の３つのケースについて槽内温度を比較したものを示す。

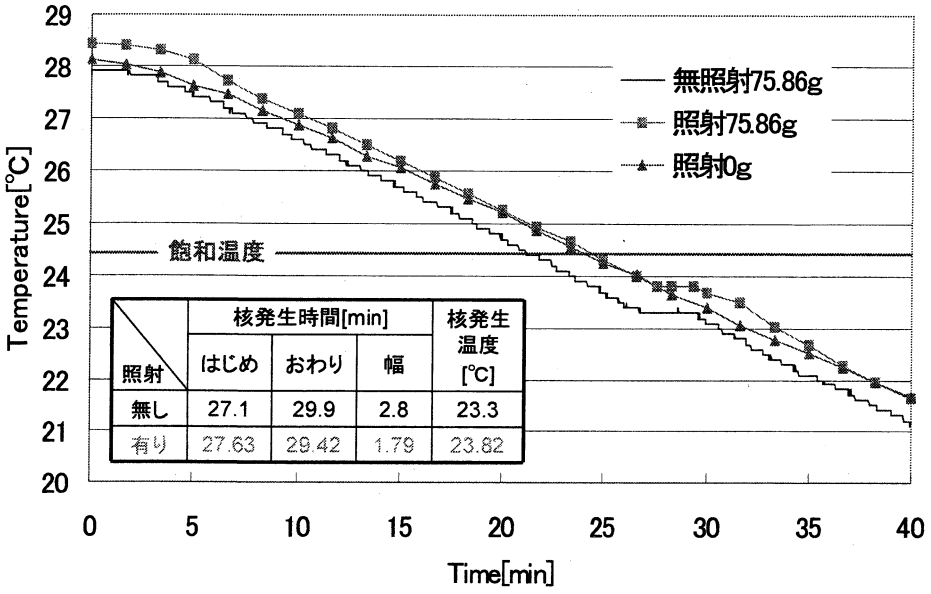

照射	核発生時間[min] はじめ	おわり	幅	核発生温度[℃]
無し	27.1	29.9	2.8	23.3
有り	27.63	29.42	1.79	23.82

Fig.6 Comparison between three temperature transients

①の超音波を照射しない場合は、実験開始から25分のところで冷却による晶析熱が発生している以外には、低温恒温水槽による温度が実現されている。③の溶質0gに超音波を照射した場合は、超音波による温度上昇のみが起こっており、その分①を上回る温度を示している。②の場合は3つのケースで一番高い温度を示しているが、これは、超音波による核発生が実験開始からつねに起こっているため、常に③を上回る温度を示していると推測される。

結言

KNO_3を用いた回分冷却晶析操作に超音波を照射する実験を行い次の知見が得られた。

（1） FBRMを用いて、超音波を照射しないときは未飽和領域でカウント数はゼロであったが、超音波を照射すると、0から10μmくらいまでの微細結晶のカウント数が時間とともに増加することを観察した。

（2） 超音波により水溶液中に気泡が発生することが十分考えられるので、水溶液の温度を２５℃前後で実験し、室温と差のないように注意し、光学顕微鏡で観察したところ、FBRMによるカウント数と１～4μmの微細結晶とが対応していることを確認した。確かに未飽和領域で微細結晶が生成していることがわかった。

（3） 未飽和領域で微細結晶が生成していることを裏付けるために、晶析槽内温度変化に注目した。溶質のある場合とない場合、超音波のある場合とない場合でそれぞれ晶析熱により温度が異なり、槽内温度変化の比較からも未飽和領域で微細結晶が生成していることを示唆した。

（4） 冷却による一次核化発生の起こる温度と結晶成長速度は超音波を照射する場合としない場合で大差なかった。すなわち、本実験条件では、超音波は冷却による結晶成長にはほとんど影響しないことがわかった。

引用文献

1） Randolph,A.D. and M.A.Larson : Theory of Particulate Processes,p177,Academic Press(1988)
2)佐藤　清隆他：溶液からの結晶成長、p95、共立出版（2002）
3）小寺、黒谷、平沢：化学工学会第39回秋季大会(2007)

研究業績

1．長谷部　拓、加藤　尚武、平沢　泉：化学工学会第72回年会、福岡（2007）
2．後藤　雄一、加藤　尚武、平沢　泉：化学工学会第40回秋季大会、札幌(2007)
3．長谷部　拓：工学院大学修士論文（２００７）
4．後藤　雄一：工学院大学修士論文（２００８）

3. 2. 2 ナノ表面制御による白金族触媒の白金族使用量の低減または代替

Reduction in platinum use or substitution of platinum by nano surface control for platinum-based catalyst

五十嵐 哲、飯田 肇
Akira IGARASHI, Hajime IIDA
工学院大学工学部 環境化学工学科
Department of Environmental Chemical Engineering,
Faculty of Engineering, Kogakuin University

Abstract

In order to reduce in the use of Pt for Pt/TiO_2 (R: Rutile) catalyst that has a high catalytic activity for low-temperature water gas shift reaction, the effects of the Re addition and the kind of Pt precursor on the Pt dispersion and the catalytic activity were examined. As the results, the Re addition brought about the increase in the Pt dispersion and the catalytic activity. In addition, the $Pt\text{-}Re/TiO_2$(R) catalyst prepared with $Pt(C_5H_7O_2)_2$ exhibited the highest catalytic activity among the examined catalysts. From above facts, it is clarified that the Re addition and the use of $Pt(C_5H_7O_2)_2$ are effective for the reduction in the use of Pt.

1. 緒言

白金族触媒は、石油化学工業における重質ナフサの改質やオレフィンの水素化を始めとして、自動車の排ガス浄化や揮発性有機化合物(VOC)の分解など、さまざまな触媒反応に使用されている。通常、白金族触媒は、担体とよばれる高表面積をもつ活性炭および無機酸化物などの表面上に金属を分散させた担持金属触媒として使用される。白金族は資源量の制約があり高価であるにもかかわらず、最近では環境保全触媒としての利用が急増しており、これらの触媒の白金族使用量の低減あるいは白金族代替触媒の開発が切望されている。

さて、固体高分子形燃料電池(PEFC)のための炭化水素の水蒸気改質による水素製造プロセスでは、PEFC の燃料極を被毒する CO の低減のために、改質工程に続いて低温水性ガスシフト(LT-WGS)反応が行なわれる。通常、LT-WGS 反応に用いられる Cu-Zn 系触媒は低温ですぐれた活性を示すものの、酸化雰囲気下での耐久性に問題があることから、白金族触媒を適用する試みがある。しかし、白金族触媒は Cu-Zn 系触媒と比べて低温活性が低いことから、触媒反応器の小型化および白金族使用量の低減のために、すぐれた触媒活性を示す担持白金族触媒の開発が必要とされている。

そこで本研究は、白金族のなかでもLT-WGS反応にすぐれた触媒活性を示す担持Pt触媒の活性向上および Pt 使用量の低減のために、担体上への Pt ナノ粒子の高分散担持による高機能化を目的とした。これまでに、担体の種類が Pt 分散度と触媒活性に与える影響について検討を加えたところ、ルチル型 TiO_2 担体の使用が Pt 使用量の低減に有効であることを明らかにしている[1)]。今年度は、一層の触媒活性向上のために、Pt/TiO_2 (R: ルチル型)触媒への Re の添加や Pt 出発原料の種類が触媒活性に与える影響ついて検討を加えた。

2. 実験

すべての触媒は、含浸法によって調製した。担体である TiO_2 (R)は、触媒学会参照触媒である

JRC-TIO-3 に焼成処理(500 ℃, 1 h 昇温, 同温度, 1 h 保持、空気気流中)を施して得た。Pt の出発原料には Fig. 2 に示した 5 種類を、Re のそれには過レニウム酸アンモニウムを使用した。そして、担持順序を変えて 3 種類の触媒を調製した。予め Re を担持してから Pt を担持した触媒(Re→Pt)、逆に Pt を担持してから Re を担持した触媒(Pt→Re)、そして Pt と Re を同時に含浸して調製した触媒(Pt･Re)である。なお、比較触媒として市販の Cu-ZnO 触媒(C18-7; ズードケミー触媒)を使用した。

性能試験には、常圧固定床流通式反応装置を使用した。まず、触媒 0.5ml をパイレックスガラス製の反応管に充填し、触媒に還元処理(500 ℃, 1 h 昇温, 同温度, 1 h 保持, H_2 気流中)を施した。つぎに、N_2 雰囲気下で 175 ℃まで降温した後、H_2O、原料ガスの順で供給を開始した。原料ガスには CO(99.95 %)あるいは擬似改質ガス(CO: 10 %, CO_2: 15 %, H_2: 75 %)を使用した。反応温度は 175 ℃から 275 ℃、空間速度は 9,500 h^{-1}(CO 基準)または 40,000 h^{-1}(total)である。

反応後触媒の TEM 観察には JEM-2010F(JEOL)を使用した。CO 化学吸着量の測定には、定容型自動吸着装置(ASAP2010C; Micromeritics)を用いた。その際、触媒には予め脱気処理(200 ℃, 8 h, 真空排気)と加熱処理(300 ℃, 0.5 h, He 気流中)を施し、35 ℃ で吸着等温線を得た。なお、Pt 分散度は、CO がすべて Pt 上に Pt / CO = 1 の量論比で吸着したと仮定して、CO 化学吸着量から算出した。また、ターンオーバー頻度(TOF)、すなわち活性サイトである Pt 露出表面積当たりの活性は、以下のように定義した。

$$TOF = F_{CO} \times X_{CO} / (V_{CO} \times M / 0.0224) \quad (1)$$

ここで、F_{CO} は供給した CO モル流量 (mol s^{-1})、X_{CO} は 250℃における CO 転化率 (-)、V_{CO} は CO 化学吸着量 ($m^3_{\text{-STP}}/g_{\text{-cat}}$)、そして M は触媒量 (g)である。

3. 結果と考察

3.1 Re 添加効果

担持金属触媒に第二金属を添加した二元金属触媒の代表的な触媒として、ナフサ改質用レニフォーミング触媒がある。Pt/Al_2O_3 触媒への Re 添加が Pt 粒子の微細化をもたらし、結果としてパラフィンの水素化分解を抑制して、芳香族炭化水素を主成分とする高オクタン価ガソリンの収率の向上をもたらすことが報告されている [2]。そこで、Pt/TiO_2 (R)に対する Re 添加が触媒活性に与える効果について調べた。Fig. 1 は、Pt と Re の担持比率と担持順序を変えて調製した触媒の触媒活性である。図から, Pt 担持量が 3.0 wt%、Re 担持量が 2.0 wt%のときに、もっとも触媒活性が高いことがわかる。一方、担持順序を変えて調製した触媒の触媒活性を比較すると、触媒活性に与える影響は Pt と Re の担持比率ほど大きくないが、もっとも高い触媒活性を示したのは、Pt と Re を同時に担持した触媒であり、市販の Cu-ZnO 触媒を超える

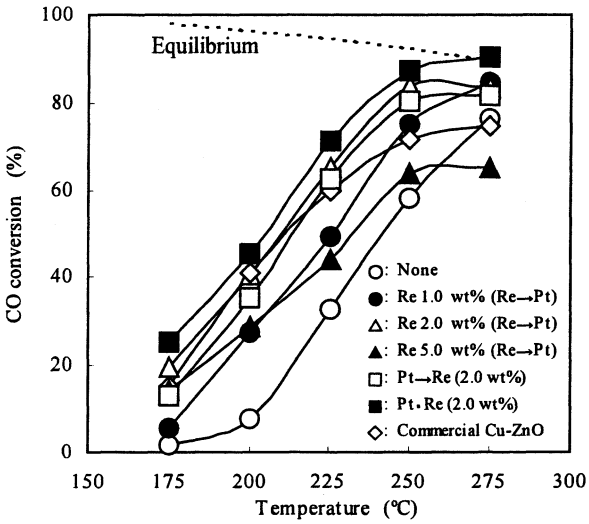

Fig. 1 Effect of Re addition to Pt/TiO_2 (R) on catalytic activity. Pt content : 3.0 wt%, Pt precursor : $H_2PtCl_6 \cdot 6H_2O$, Feed gas: CO (10 %) - CO_2 (15 %) - H_2 (75 %), S.V.: 40,000 h^{-1}, H_2O / CO = 5.0.

触媒活性を示すことがわかる。なお、どの触媒も 250 ℃ 以上で微量のメタンの副生が認められたが、CO_2 選択率は 99 %以上であった。Table 1 は Pt/TiO_2 (R)と $Pt\text{-}Re/TiO_2$ (R)の TEM 像から得られた Pt 粒子の平均径(メジアン径)と CO 転化率、それらから算出した TOF、Pt 1g あたりの触媒活性を示した。表から、

Table 1 Catalytic activities and properties of Pt and Pt-Re catalysts

	Pt particle size (nm)	CO Conv.[1)] (%)	TOF[1),2)]×10^2 (s^{-1})	Catalytic activity per unit mass of Pt ($mol_{\text{-}CO}/(h\ g_{\text{-}Pt})$)
Pt/TiO_2 (R)	3.2	33.0	16.9	1.11
$Pt\text{-}Re/TiO_2$ (R)	2.1	65.0	21.6	2.18

1) Reaction temperature: 225 ℃
2) TOF was calculated from the Pt particle size on TEM micrograph.

Pt/TiO_2 (R)への Re 添加が Pt 粒子の微細化をもたらし、それが触媒活性の向上に寄与していることがわかる。また、Pt 1g 当たりの触媒活性は、Re の添加によって約 2 倍に増加し、Re の添加が Pt 使用量の低減をもたらすことが示唆された。

3.2 Pt 出発原料の影響

活性金属の分散状態は、担体の表面積や活性金属の担持方法、そして金属の出発原料に大きく依存する。このことは、活性金属種の触媒担体に対する吸着特性や分解温度、あるいはそれらに由来する不純物の残留などの様々な要因が活性金属の分散状態に影響を与えるためである。そこで、種々の Pt 出発原料を用いて $Pt\text{-}Re/TiO_2$ (R)触媒を調製し、触媒活性に与える影響について検討を加えた。Fig. 2 はそれらの触媒の触媒活性である。なお、Pt 担持量は 1.0 wt%、Re 担持量は 0.67 wt%である。触媒活性の序列は、$Pt(C_5H_7O_2)_2$ > $H_2PtCl_6 \cdot 6H_2O$ > $[Pt(NH_3)_4]Cl_2$ > $[Pt(NH_3)_4](NO_3)_2$ > cis-$[Pt(NO_2)_2(NH_3)_2]$であった。

Table 2 に、種々の Pt 出発原料から調製した $Pt\text{-}Re/TiO_2$ (R)触媒の触媒活性と物性をまとめた。表から、ビスアセチルアセトナト白金から調製した触媒の Pt 分散度がもっとも高いことがわかる。したがって、同触媒のすぐれた触媒活性は、ビスアセチルアセトナト白金の使用による Pt の高分散化に起因すると考えられる。また、Pt 1g 当たりの触媒活性は、従来の塩化白金酸六水和物から調製した触媒のそれの約 1.3 倍である。さらに、同触媒の触媒活性は、反応温度 250 ℃ で市販の Cu-ZnO 触媒を超えていることから、ビスアセチルアセトナト白金の使用によって Pt 使用量を 1.0 wt%以下に低減できることが示唆された。

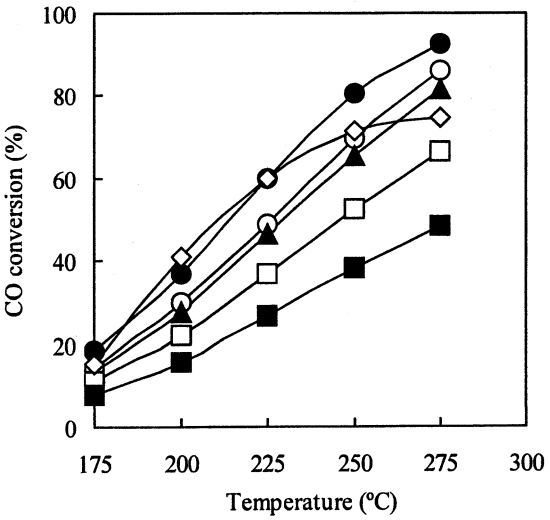

○: $H_2PtCl_6 \cdot 6H_2O$, ●: $Pt(C_5H_7O_2)_2$, ▲: $[Pt(NH_3)_4]Cl_2$, □: $[Pt(NH_3)_4](NO_3)_2$, ■: cis-$[Pt(NO_2)_2(NH_3)_2]$, ◊: Commercial Cu-ZnO

Fig. 2 Catalytic activities and properties of $Pt\text{-}Re/TiO_2$ (R) catalysts prepared from various Pt precursors.
Pt content: 1.0 wt%, Impregnation procedure: Pt•Re, Feed gas : CO(99.95 %), S.V. =9,500 h^{-1}, H_2O / CO = 1.5.

Table 2 Catalytic activities and properties of Pt-Re/TiO_2 (R) catalysts prepared from various Pt precursors

Precursor	CO conversion[1] (%)	Pt dispersion[2] (%)	TOF (s^{-1})	Catalytic activity per unit mass of Pt ($mol_{CO}/(h\ g_{Pt})$)
$Pt(C_5H_7O_2)_2$	59.7	52.5	2.2	21.4
$H_2PtCl_6 \cdot 6H_2O$	48.6	38.5	2.3	16.6
$[Pt(NH_3)_4]Cl_2$	46.4	27.6	3.2	16.3
$[Pt(NH_3)_4](NO_3)_2$	36.8	24.5	2.9	13.0
cis-$[Pt(NO_2)_2(NH_3)_2]$	26.9	11.0	4.8	9.7

1) Reaction temperature: 225 °C, 2) After reaction

4. 総括

低温水性ガスシフト反応のための高い触媒活性をもつ Pt/TiO_2 (R)の Pt 使用量の低減のために、Re の添加や Pt 出発原料の種類が Pt 分散度と触媒活性に与える影響について調べたところ、以下のことが明らかとなった。

Pt/TiO_2 (R)への Re 添加は Pt 粒子の微細化をもたらし、それが触媒活性の向上に寄与していることが示された。また、Pt 1g 当たりの触媒活性は、Re の添加によって約 2 倍に増加し、Re の添加が Pt 使用量の低減に有効であることが明らかとなった。また、種々の Pt 出発原料から調製した触媒のなかで、ビスアセチルアセトナト白金から調製した Pt/TiO_2 (R)触媒がもっとも高い触媒活性を示した。また、同触媒は，反応温度 250 °C において市販の Cu/Zn 触媒を超える触媒活性を示したことから、ビスアセチルアセトナト白金の使用によって Pt 使用量を 1.0 wt%以下に低減できることが示唆された。

引用文献

1) H. Iida and A. Igarashi, *Appl. Catal. A: Gen.*, **298**, 152 (2006).
2) 斉藤 泰和ら, 日本化学会編, "*化学総説 No.34, 触媒設計*", 学会出版センター, 55 (1982).

研究業績

《審査付論文》

1) "Structure Characterization of Pt-Re/TiO_2 (Rutile) and Pt-Re/ZrO_2 catalysts for Water Gas Shift Reaction at Low-temperature", H. Iida and A. Igarashi, *Appl. Catal. A: Gen.*, **303**, 192 (2006).
2) "Difference in the Reaction Behavior between Pt-Re/TiO_2 (Rutile) and Pt-Re/ZrO_2 Catalysts for Low-temperature Water Gas Shift Reactions", H. Iida and A. Igarashi, *Appl. Catal. A: Gen.*, **303**,48 (2006).
3) "Effect of Pt Precursors on Catalytic Activity of Pt/TiO_2 (Rutile) for Water Gas Shift Reaction at Low-temperature", H. Iida, K. Kondo, and A. Igarashi, *Catal. Commun.*, **7**, 240 (2006).
4) "Catalytic Activities and Properties of Pt-Re/TiO_2 Catalysts Prepared from Various Pt precursors for Low-temperature Water Gas Shift Reaction", H. Iida, M. Someya, K. Kondo, and A. Igarashi, *Stud. Surf. Sci. Catal.*, **172**, 265 (2007).

《学会発表》

1) "Catalytic Activities and Properties of Pt-Re/TiO_2 Catalysts Prepared from Various Pt precursors for Low-temperature Water Gas Shift Reaction", H. Iida, M. Someya, K. Kondo, and A. Igarashi, *5 th Tokyo Conference on Advanced Catalytic Science and Technology(TOCAT5)*, B05 (2006), Tokyo.
2) 飯田肇, 五十嵐哲, "低温水性ガスシフト反応のための Pt-Re/TiO_2 および Pt-Re/ZrO_2 触媒の活性発現機構",*石油学会第 36 回石油・石油化学討論会*, 2B07(2006), 鹿児島.
3) "Reaction mechanism for low-temperature water gas shift reaction over Pt-Re catalysts", H. Iida and A. Igarashi, *The 11th Korea-Japan Symposium on Catalysis*, (2007), Seoul.

3．2．3 触媒活性を有する遷移金属ナノクラスターの合成と応用

Synthesis of Novel Transition-Metal Nano-Clusters and Their Application to Organic Synthesis

河野博之†，南雲紳史‡

Hiroyuki KAWANO† and Shinji NAGUMO‡

†工学院大学　工学部　共通課程，‡工学院大学　工学部　応用化学科

†General Education, Faculty of Engineering, Kogakuin University
‡Department of Applied Chemistry, Faculty of Engineering, Kogakuin University

Abstract: A dihydridoruthenium complex $RuH_2(CO)(PPh_3)_3$ is a good starting compound for generating the zerovalent ruthenium atom. The zerovalent ruthenium atom combines with each other to form a novel ruthenium-metal particle with diameters less than 1000 nm. On the other hand, the active zerovalent ruthenium atom reacts with another metal complex to form a ruthenium-containing compound. The ruthenium-containing compound also forms nano-sized particles. The zerovalent ruthenium atom is the key species in both chemical processes for the novel ruthenium-containing nano-particles.

Index Terms: Inorganic and Organometallic Chemistry, Ruthenium Complexes, Nano-Sized Metal-Containing Particles, Chemical Process for Nano-Particles.

緒言

1．金属ナノ粒子の化学的合成法

金属ナノ粒子とは、その直径がナノメートル(nm, 10^{-6}-10^{-9} m)サイズの金属微粒子であり、数十から千個程度の金属原子から構成されている。この程度の大きさの金属微粒子には非常に高い比表面積の効果や量子サイズ効果が期待されること、生体細胞の細胞膜を傷つけずに通過できることなどから、近年ナノサイエンスあるいはナノテクノロジーの分野における重要な素材として注目されている。

これまで、金属ナノ粒子はバルクの金属を粉砕して粒子を細かくする「物理的」な方法で、主に調製されてきた(Scheme 1)。この物理的調製法には、大きさの揃った金属ナノ粒子を大量に得ることが

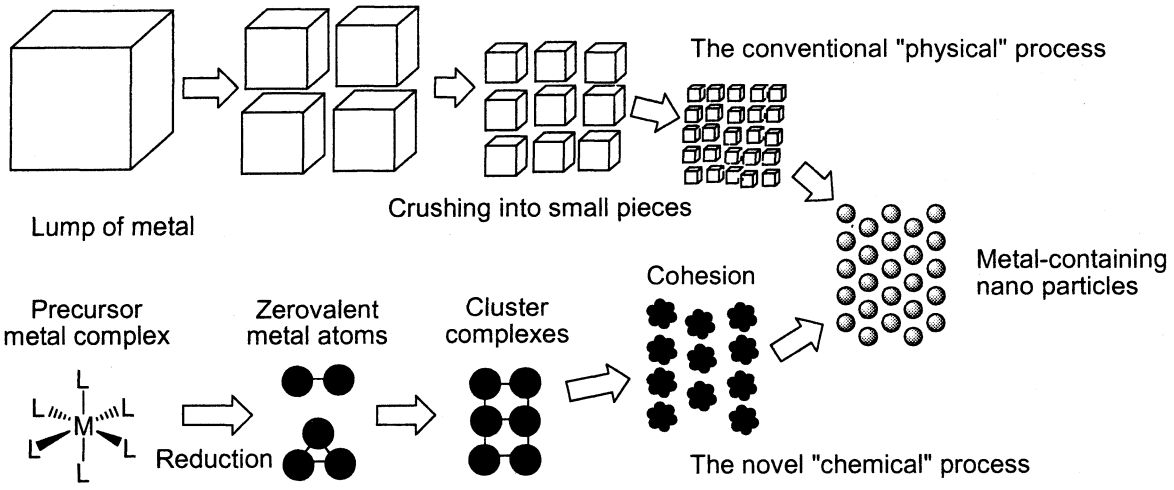

Scheme 1. The "physical" process vs. the "chemical" process for the metal-containing nano particles.

困難であるという欠点がある。その欠点を克服するため、最近「化学的」な金属ナノ粒子合成法が精力的に研究されている。化学的金属ナノ粒子合成法では、制御された条件下で、まず金属イオンを「化学的」に還元して電荷をもたない単独の金属原子を発生させる。発生した金属原子は直ちに互いに凝集してサイズの大きい金属粒子となるが、凝集の際の条件をコントロールすることで、大きさをナノメートルサイズに留めた金属微粒子を大量に得ることができる。

化学的金属ナノ粒子合成法の出発物質としては金属錯体がよく利用される。金属錯体とは、金属原子または金属イオンの周囲に、配位子と呼ばれる種々の陰イオンや中性分子が結合した分子である。一般に裸の金属原子や金属イオンは不安定で、多くの場合はただちに酸化されたり凝集したりして単独では存在できないが、配位子で周囲を取り囲むことで安定化されて一個の金属中心を持つ分子として存在しうる。一方、金属ナノ粒子もそのままでは安定に存在できず、互いに凝集してよりサイズの大きい固体となってしまう。金属ナノ粒子同士を接触させて凝集させず、安定に分散させておくために、通常は保護剤とよばれる分子でナノ粒子の周囲を囲み凝集を防いでいる。したがって、金属錯体分子にとっての配位子と金属ナノ粒子にとっての保護剤の作用は共通であり、このことから金属錯体の配位子を一部取り除き、制御した条件下で凝集させれば金属ナノ粒子が生成すると予想できる。この考えが本研究課題の動機である。

2．遷移金属錯体とナノマテリアルの関係

遷移元素を中心金属とする遷移金属錯体の特徴は、複数の配位子が、遷移金属原子の周囲に多面体型の構造をかたちづくるように結合していることと、それら配位子の種類と配列が制御されることで中心金属の反応性が多様に変化することである。遷移金属錯体が有するこれらの特徴は、金属錯体を利用するナノマテリアルへの応用と密接に関連している(Scheme 2)。遷移金属錯体を用いて金属原子を意図的に凝集させる手法で、遷移金属錯体を金属あるいは金属酸化物の薄膜やナノサイズ微粒子の合成前駆体として利用することができる。また、遷移金属錯体の持つ多面体構造を基本構造単位として、それらを一定の秩序で配列させた超分子もナノマテリアルの一種と考えることができ、金属錯体を直線状(一次元)に配列した分子電線や、立体的に配列した三次元超分子のホストーゲスト化合物などに関する研究が数多く行なわれている。

本研究課題の対象の中心となるルテニウム錯体の場合、ルテニウムの酸化状態は-2 から+8 までのあらゆる状態を取ることができ、それに結合している配位子数も 4 から 7 までとバラエティに富んでいるので、様々な構造のルテニウム錯体が形成される。また、ルテニウム原子間で結合し、ルテニウム中心を複数有する多核錯体をしばしば形成することも特徴の一つであり、このことはルテニウム原子が凝集したルテニウム含有ナノ粒子が容易に生成する可能性を示している。

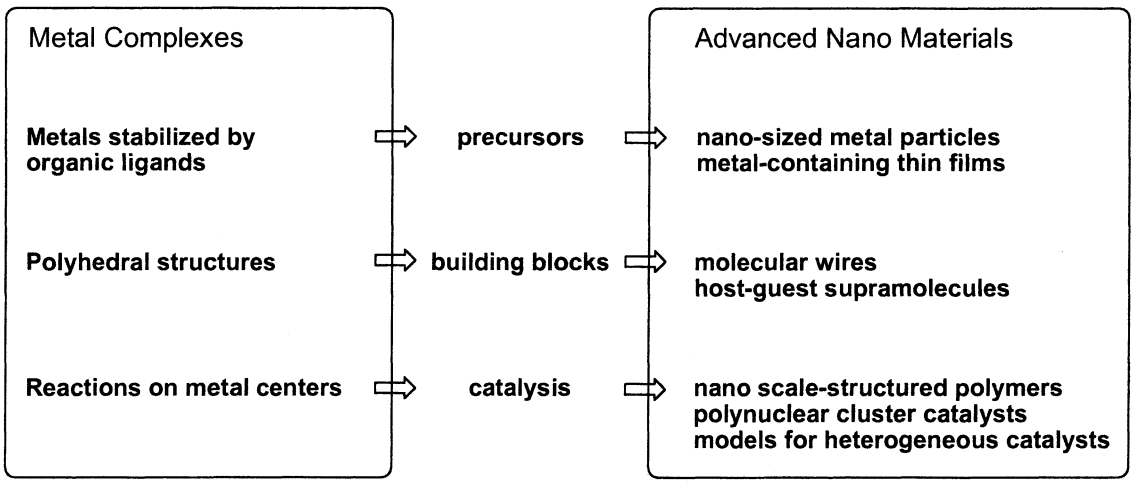

Scheme 2. Metal complexes and advanced nano materials.

研究成果

1．ルテニウム錯体触媒からルテニウム金属ナノ粒子への展開

低原子価のルテニウム錯体は、有機合成反応の均一系触媒(分子触媒)としての応用例が数多く報告されており、実用化に至った高活性で高選択的な反応も知られている。それらのうちでも、村井らによるルテニウム(0)錯体を触媒に用いての芳香環 C-H 結合のオレフィンへの付加反応[1, 2]は大きな成功を収めた例であり、多くの類似の反応が開発される契機となった。この触媒反応は、通常活性化されにくい有機化合物の C-H 結合や C-C 結合をルテニウム(0)錯体で直接活性化・切断することを鍵反応としており、低原子価ルテニウム錯体が不活性な結合を効果的に活性化できることを証明した。

この分野において、我々はジヒドリドルテニウム(II)錯体、$[RuH_2(CO)(PPh_3)_3]$とオレフィンとの反応で反応溶液中に発生する活性ルテニウム(0)錯体種(現時点で組成は$[Ru(CO)(PPh_3)_n]$ (n = 2 or 3)と推定されている)が、芳香環上の C-H 結合やメチル基の C-H 結合を活性化できることを明らかにしてきた。また、ルテニウム(0)錯体種が生成した後、直ちに反応する有機化合物が周囲に存在しない場合には、自分自身に結合した PPh_3 配位子の C-H 結合まで切断してしまうことが明らかとなった[3]。

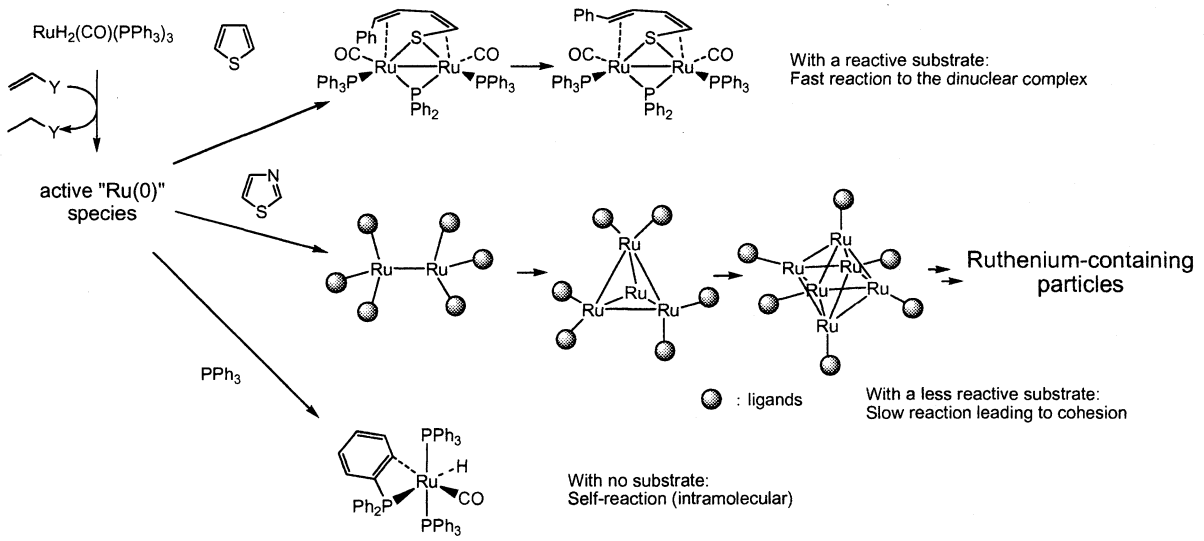

Scheme 3. A possible route to the nano-sized ruthenium-containing particles.

このことは、芳香環 C-H 結合を有する化合物よりも活性ルテニウム(0)錯体との反応が遅い化合物を利用すれば、分子内での PPh_3 配位子 C-H 結合切断を抑えつつ、ルテニウム錯体分子間の凝集を制御できる可能性を示している(Scheme 3)。実際、チオフェンを活性ルテニウム(0)錯体と反応させた場合には、チオフェン 1 分子に対しルテニウム錯体が 2 分子反応した二核錯体が得られた[4]。さらに、活性ルテニウム(0)錯体とチアゾールとの反応では、単核あるいは二核のルテニウム錯体種の生成は確認できず、ルテニウム(0)錯体、すなわち配位子をまとったルテニウム原子の凝集が進み、多核クラスターを経て 1000 ナノメートル未満の粒径のものを含むルテニウム金属微粒子が生成した。同様の微粒子は、ルテニウム(0)錯体とベンゾフランとの反応でも生成した。これらの微粒子の粒径はさらなる配位子 PPh_3 の添加で制御可能であり、配位子 PPh_3 が微粒子表面のルテニウム原子に配位して凝集による粒径の増大を抑えていることがわかった。

2．ルテニウム含有混合金属微粒子の合成

ルテニウム(0)錯体の凝集を制御することでルテニウム金属微粒子を合成できることが明らかになったので、さらに混合金属微粒子の合成にこの手法を応用することを検討した。ルテニウム(0)錯体が凝集する際別の遷移金属錯体が反応系に共存していれば、ルテニウムのみが凝集するのでなくその金属をも取り込んで混合金属微粒子となることが予想できる。そこで、ルテニウム(0)錯体に、酸化状態の異なるルテニウム(II)錯体およびロジウム(I)錯体を共存させての微粒子合成を試みた。

ルテニウム(0)錯体に等しい物質量のルテニウム(II)錯体、$[RuCl_2(1,5\text{-cyclooctadiene})]_n$, $[RuCl_2(PPh_3)_3]$

およびロジウム(I)錯体[$RhCl(PPh_3)_3$]を反応させたところ、いずれの場合にもルテニウム(0)原子とルテニウム(II)イオンあるいはロジウム(I)イオンが 1：1 で反応した組成の生成物が再現性良く得られた。生成物を溶媒に再分散させて粒径を測定したところ、数 10 ないし数 100 ナノメートルの粒径をもつルテニウム含有微粒子であることが判った。すなわち、生成物はルテニウム(0)とルテニウム(II)の混合原子価微粒子あるいはルテニウムとロジウムの混合金属微粒子であることが明らかになった。再分散させたこれらの微粒子の凝集挙動は出発物質に用いた遷移金属錯体の種類により異なっていたが、一般に凝集しやすく配位子 PPh_3 を添加しても微粒子の凝集を完全に制御することはできなかった。

ここで用いたルテニウム(II)錯体とロジウム(I)錯体のいずれにも塩化物イオン(Cl^-)が配位子として含まれている。生成した微粒子にも塩化物イオンが含まれていることが確かめられており、これらの微粒子は単純な金属微粒子ではなく金属塩化物からなる化合物微粒子であるともいえる(Scheme 4)。

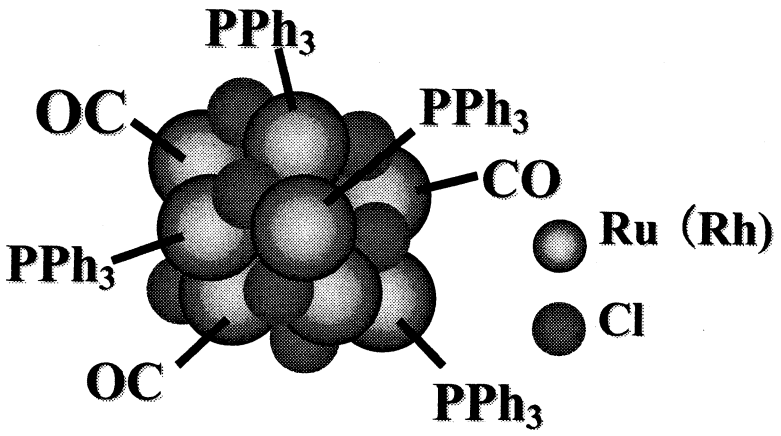

Scheme 4. A schematic view of the Ru, Rh mixed-metal chloride particle.

結論

以上に述べたように、ルテニウム(0)錯体種をルテニウム原子の供給源とする化学的金属ナノ粒子合成法で、ルテニウム金属ナノ粒子および混合金属化合物微粒子を合成できることが明らかとなった。この方法はさらにさまざまな遷移金属錯体への応用が可能であり、単なるナノ粒子の合成のみにとどまらず、触媒機能などの付加価値を有するナノ粒子の設計と合成を可能にするものであるといえる。

引用文献

[1] The first report on the synthetic use of the active ruthenium species: S. Murai, F. Kakiuchi, S. Sekine, Y. Tanaka, A. Kamatani, M. Sonoda, and N. Chatani, *Nature*, **366**, 529 (1993).

[2] F. Kakiuchi, S. Sekine, Y. Tanaka, A. Kamatani, M. Sonoda, N. Chatani, and S. Murai, *Bull. Chem. Soc. Jpn.*, **68**, 62 (1995).

[3] K. Hiraki, S. Kira, and H. Kawano, *Bull. Chem. Soc. Jpn.*, **70**, 1583 (1997).

[4] H. Kawano, H. Narimatsu, D. Yamamoto, K. Tanaka, K. Hiraki, and M. Onishi, *Organometallics*, **21**, 5526 (2002),

研究業績

[1] 年会特別企画「化学的金属ナノ粒子合成法の進歩」，日本化学会第 87 春季年会（関西大学）2007 年 3 月；
上記シンポジウムの企画・開催・趣旨説明.

3. 2. 4 高分散性セラミックナノ粒子・ナノポア構造体の創製とキャラクタリゼーション

Development and Characterization of
Nano-porous Ceramics and High-dispersive Ceramic Nano-particles
— リン酸塩ガラスによる模擬高レベル放射性廃棄物の固定化 —
Immobilization of Simulated High Level Nuclear Wastes with Phosphate Glasses

（工学院大学工学部マテリアル科学科）門間英毅・大倉利典
Hideki Monma and Toshinori Okura
Department of Materials Science and Technology, Faculty of Engineering,
Kogakuin University

The leaching behavior and structure of magnesium phosphate glasses containing 45-55 mol% MgO incorporated with simulated high-level nuclear waste (HLW) were studied. The gross leach rate of the glass waste form containing 50 mol% MgO and 45 mass% simulated HLW is of the order of 10^{-6} g/cm^2·day at 90°C, which is small enough as compared with the corresponding release from a currently used borosilicate glass waste form. The isolated ions such as dimeric $(P_2O_7)^{4-}$ and monomeric $(PO_4)^{3-}$ increase as increasing the incorporating amount of the simulated HLW. The changes in properties can be attributed to the structure changes owing to the incorporation of the simulated HLW.

1. 緒言

原子力発電所から発生する使用済核燃料には、再び燃料として使用できるウランやプルトニウムが含まれている。これらを再利用するための再処理工程で、高レベル放射性廃液が分離される。この高レベル放射性廃液は、ガラスと混ぜて溶かし、「キャニスター」と呼ばれるステンレス製の容器に注入したあと、冷やして固める（ガラス固化体）。このガラス固化体は崩壊熱を出すため、冷却期間として30～50年間一時貯蔵し、最終的に地下300メートルより深い安定な深地層中に処分される。現在、固化ガラスにはホウケイ酸塩ガラスが使用されており、放射性廃棄物の含有量は最大で25mass%となっている。しかし、このガラスはP_2O_5の濃度が増加すると分相してしまうことが報告されている。また、もともとシリカ成分（SiO_2）とホウ酸成分（B_2O_3）とは十分に溶け合わない分相傾向をもっており、分相傾向が一層増大するような元素も廃棄物成分の中に存在する（たとえばモリブデン）。そこで、高レベル放射性廃棄物固化ガラスのベースガラスとして、融点が低く、より多く様々な種類の元素を取り込める特性を持つリン酸塩ガラスに着目した[1, 2]。なかでも、リン酸マグネシウムガラスは、メタ組成（モル比で$MgO/P_2O_5=1$）付近で組成 - 物性間にリン酸異常現象と呼ばれる非線形性を示し、anomalousタイプに分類されている。多くのリン酸塩ガラスは鎖状構造を有することが知られているが、リン酸マグネシウムガラスは組成により二つのタイプの構造を含むと考えられ、一つは $MgO/P_2O_5<1$ のときでテトラメタリン酸構造を含むもの、もう一つは$MgO/P_2O_5>1$のときでピロリン酸構造を含むものである。テトラメタリン酸タイプとピロリン酸タイプの

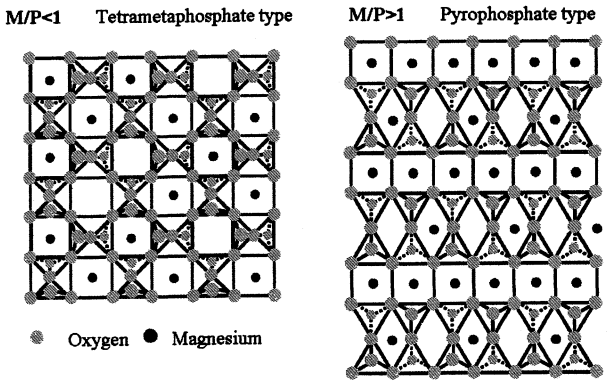

Fig. 1 The two type structure models of M-P glasses.[3]

構造モデルをFig. 1に示す。この構造変化が異常現象を引き起こしていると考えられる[1]。本研究では、リン酸マグネシウムガラスを用いて、模擬放射性廃棄物を固化させたガラス固化体について、熱的安定性や耐水性の評価、振動スペクトルを用いた構造変化の検討を行い、さらにγ線を照射させたときの影響についても検討した。また、normalタイプのリン酸カルシウムガラスを用いた固化体についても同様の検討を行った。

Table 1 Composition of simulated nuclear wastes.[4]

廃棄物元素	原料	mass%
Na	$NaNO_3$	64.8
Sr	SrO	2.9
La	La_2O_3	16.1
Mo	MoO_3	7.5
Mn	MnO_2	1.2
Fe	Fe_2O_3	6.6
Te	TeO_2	0.9

2. 実験方法

2.1 ガラス固化体の作製

母体となる$MgO-P_2O_5$系ガラス（M-Pガラス）および$CaO-P_2O_5$系ガラス（C-Pガラス）は、リン酸と酸化マグネシウム（あるいは酸化カルシウム）をモル比で$MgO:P_2O_5$＝40:60, 47:53, 50:50, 55:45および$CaO:P_2O_5$＝40:60, 50:50, 55:45になるように秤量・混合し、600℃で3時間加熱後、さらに1250℃で1時間加熱溶融し、急冷してガラス化させたものを用いた。模擬放射性廃棄物固化ガラスは、作製したM-Pガラス（C-Pガラス）を粉砕し、Table 1に示した模擬廃棄物を固化ガラス中の含有率が25および45 mass%になるようにそれぞれ混合し、1250℃で2時間溶融後、急冷して得た。

2.2 密度測定、DTA・XRD・FT-IR・Laser Ramanによる評価

得られたガラス固化体の密度は、比重ビン法を用いて測定した。DTA測定よりガラス転移点（Tg）と結晶化開始温度（Tc）を求め、Tg-Tcよりガラス（固化体）の安定性を求めた。XRD測定はガラス固化体と、それらを500℃で2時間加熱処理した試料についてそれぞれ行い、結晶質か非晶質かを判断した。さらにFT-IR測定とLaser Raman測定を行い、廃棄物含有量の増加によるガラス（固化体）の構造変化を調べた。

2.3 浸出試験

粉砕した試料約1 gをテフロンビーカーに入れ、純水50 mlに浸し、90℃で20日間保持した後、ろ過した試料を乾燥させ、試料全体の重量減少より浸出率を求めた（MCC-2法[5]）。

2.4 γ線照射

放射性物質を閉じ込めることにより、ガラス固化体自体が放射線を常に照射されている状態になる。放射線のなかでもα線はガラス固化体に最も影響を与えると考えられるが、α線を照射すると試料が放射化して危険なため、本実験では透過率が高いγ線（Co-60）をM-PおよびC-Pガラスそれぞれの固化体において浸出率が低かったものに照射し（全線量で10 μR）、その影響を調べた。照射後の試料に対して、浸出試験、FT-IR測定、Laser Raman測定を行った。

3. 結果と考察

得られたガラス固化体に対する各実験の結果をTable 2に示す。M-Pガラスでは廃棄物含有量が増加しても均一なガラス状態の試料を作製することができたのに対し、C-Pガラスでは廃棄物を含有させるとすべての組成において結晶化した。

TgおよびTcは廃棄物含有量が増加すると低下する傾向にあった。ガラスの安定性は廃棄物含有量が増加すると低下したが、$MgO:P_2O_5$＝40:60以外のM-Pガラスと$CaO:P_2O_5$＝50:50のC-Pガラスは、廃棄物含有量にあまり影響を受けないことがわかった。M-Pガラスにおいては、ピロリン酸構造を多く含む組成のほうが安定性は高くなるのではないかと考えられる。

水に対する浸出試験の結果から、M-PおよびC-Pガラスのどちらの場合も、模擬廃棄物を含まな

い場合はそれほど値に変化はなく、耐水性も悪いが、模擬廃棄物含有量が増加するにつれ、耐水性は高くなった。全体的に比較して、M-P ガラスのほうが C-P ガラスよりも明らかに浸出率が低い結果になった。M-P ガラスにおいては、$MgO:P_2O_5$＝47:53 で模擬廃棄物含有量が 45mass%の固化ガラスの浸出率は $10^{-6}g/cm^2\cdot day$ オーダーとなり、現在使用されているホウケイ酸塩ガラス固化体（廃棄物含有量 25 mass%）の浸出率 $2.5\times10^{-5}g/cm^2\cdot day$ と比べてかなり低い値となった。この結果から、今回の実験においては、この組成が固化ガラスとして適していると考えられる。C-P ガラスにおいては、$CaO:P_2O_5$＝50:50 で模擬廃棄物含有量が 45mass%の固化ガラスの浸出率が比較的低い値を示したが、$6.85\times10^{-5}g/cm^2\cdot day$ とホウケイ酸塩ガラス固化体よりも高い値となった。

ガラス固化体の FT-IR スペクトルを Fig. 2 と Fig. 3 に、FT-IR 測定および Laser Raman 測定の結果を Table 3 と Table 4 にまとめて示す。Laser Raman 測定の結果から、M-P および C-P ガラスのどちらにおいても、環状や鎖状の構造が模擬廃棄物元素によって切断されるために、$P_2O_7^{4-}$やPO_4^{3-}などのピークの増加が観察された。しかし、FT-IR スペクトルにおいては、M-P ガラスでは PO_3^-やPO_4^{3-}の吸収ピークは減少していた。これは、模擬廃棄物含有量が増加すると環状構造や鎖状構造は切断され、PO_3^-やPO_4^{3-}の構造単位は増加するが、非対称の架橋酸素 M-O-P（M=廃棄物元素）の構造が増加したため、見かけ上吸収ピークは減少したものと考えられる。このような構造が増加するとガラスネットワーク中のクロス・リンケージの密度が増加したことになり、このことが固化ガラスの耐水性を向上させたものと考えられる。しかし、C-P ガラスにおいては、PO_3^-やPO_4^{3-}も増加していたため、ガラスネットワーク中のクロス・リンケージの密度が耐水性に大きく影響するのではないかと考えられる。

γ 線を照射することによって、浸出率は一桁近く悪くなったが、FT-IR、Laser Raman どちらのスペクトルにも照射前後に変化が見られず、大きな構造的変化は起きないことが分かった。

Table 2　Properties of obtained glass waste forms.

組成比 (mol 比)	廃棄物含有量 (mass%)	密度 (g/cm^3)	XRD 結果		ガラスの安定性 (Tg-Tc/℃)	浸出率 ($g/cm^2\cdot day$)
			加熱前	加熱後		
$MgO:P_2O_5$=40:60	0	2.454	○	○	235	4.69×10^{-4}
	25	2.670	○	○	166	2.06×10^{-4}
	45	2.913	○	○	119	1.11×10^{-5}
$MgO:P_2O_5$=47:53	0	2.247	○	○	244	5.90×10^{-4}
	25	2.725	○	×	129	1.44×10^{-4}
	45	2.890	○	×	132	6.85×10^{-6}
$MgO:P_2O_5$=50:50	0	2.465	○	○	151	6.26×10^{-4}
	25	2.734	○	×	110	2.18×10^{-4}
	45	2.946	○	×	108	3.81×10^{-5}
$MgO:P_2O_5$=55:45	0	2.507	○	○	136	4.08×10^{-4}
	25	2.750	×	×	109	2.01×10^{-4}
	45	3.017	○	×	106	3.24×10^{-5}
$CaO:P_2O_5$=40:60	0	2.671	○	×	170	1.42×10^{-3}
	25	2.856	○	×	170	9.18×10^{-4}
	45	2.992	×	×	91	2.99×10^{-4}
$CaO:P_2O_5$=50:50	0	2.755	○	×	83	1.23×10^{-3}
	25	2.936	×	×	106	4.07×10^{-4}
	45	3.044	×	×	98	6.85×10^{-5}
$CaO:P_2O_5$=55:45	0	2.911	○	×	77	1.01×10^{-3}
	25	2.963	×	×	140	5.00×10^{-4}
	45	3.141	×	×	105	2.73×10^{-4}

○：非晶質 ×：結晶質

Table 3 Results of FT-IR measurements.

波数 (cm^{-1})	帰属			廃棄物含有量の増加に対する影響 M-P ガラス	C-P ガラス
1300	$(P=O)$		(stretching)	減少	減少
1200	$(PO_2)_{asym}$	Q2	(stretching)	増加	増加
1100	$(P-O)^-$			増加	変化なし
1050	(PO_3)	Q1		減少	増加
980	$(PO_4)^{3-}$	Q0	(stretching)	減少	増加
920	$(P-O-P)_{asym}$		(stretching)	高波数側にシフト	変化なし
720-790	$(P-O-P)_{sym}$		(stretching)	減少	変化なし
480-570	$(PO_4)^{3-}$	Q0	(deformation)	高波数側にシフト	高波数側にシフト

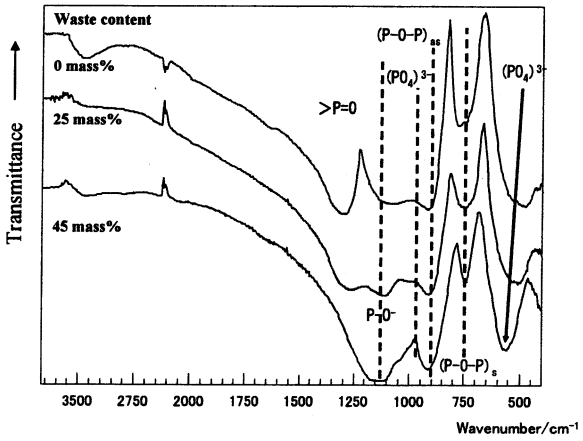

Fig. 2 FT-IR spectra of M-P glass waste forms.

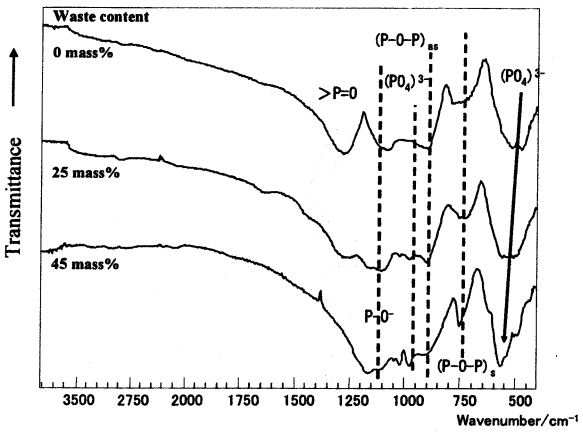

Fig. 3 FT-IR spectra of C-P glass waste forms.

Table 4 Results of Laser Raman measurements.

波数 (cm^{-1})	帰属			廃棄物含有量の増加に対する影響 M-P ガラス	C-P ガラス
1300	$(P=O)$	(stretching)		減少	減少
1200	$(PO_2)_{asym}$	(stretching)	$(P_2O_7)^{4-}$	減少	減少
1050	$(PO)_{sym}$	(stretching)	$(PO_4)^{3-}$	増加	増加
950	$(PO_4)^{3-}$			増加	増加
760	$(P-O-P)_{sym}$	(stretching)	$(PO_4)^{3-}$	増加	増加
700	$(P-O-P)_{sym}$	(stretching)	$(P_2O_7)^{4-}$	減少	減少

文献

1) T. Okura, T. Miyachi, H. Monma, *Trans. Mater. Res. Soc. Japan*, 29, 2175 (2004).

2) 大倉利典, 特開 2005-207885.

3) T. Okura, K. Yamashita, T. Kanazawa, *Phys. Chem. Glasses*, **29**, 13 (1988).

4) M. Ishida, T. Yanagi, R. Terai, *J. Nucl. Sci. Technol.*, **24**[5], 404 (1987).

5) D.M, Strachan, "Scientific Basis for Nuclear Waste Management", Vol.3, Ed. by J.D. Moor, Plenum Press, New York (1980) p.347.

研究業績

1) T. Okura, H. Monma, "Nuclear Waste Research Advances" [New magnesium phosphate glasses for high level nuclear waste immobilization], Nova Science Publishers, New York, in press.

2) 大倉利典, "エコマテリアルハンドブック"「放射性廃棄物処理のためのガラス固化体」, 丸善 (2006).

3) T. Okura, T. Miyachi, H. Monma, *J. Eur. Ceram. Soc.*, **26**[4-5], 831 (2006).

4) 大倉利典, "ガラスによる高レベル放射性廃棄物の固化処理", J. Soc. Inorg. Mater. Japan, **3**, 448 (2006).

4. デバイスへの応用

4．1 デバイスへの応用

1．電子デバイス微細接合部の熱サイクル信頼性評価

マイクロサイズ材料の疲労特性

後藤芳樹，立野昌義，小久保邦雄（機械工学科）

Abstract

The size of the components used in Micro-sized machine devices is considered to be in the order of microns, and the mechanical properties of such micro-sized materials are considered to be different from those of bulk (ordinary sized) materials. The evaluation of mechanical properties including static and fatigue behavior are essential issue for developing a reliable micro-sized machine in service operation. There has been an absence of the Standards for the test procedure in order to micro-sized materials. Therefore, the evaluation of mechanical properties including reliability and durability has not been performed. This is due to lack of suitable testing equipment for micro-sized materials.

In the present study, we have designed a simple fatigue tester for micro-size materials. Fatigue tests have been performed for Aluminum bonding wire specimen. The results obtained in this investigation are important information on the fatigue test method for micro-sized materials.

1．はじめに

近年，電子機器の進歩にともない，機器の小型化により，集積回路の微細化・高密度化が進んでいる。従来からICチップとパッケージの接続にはボンディングワイヤーが使用されているが，電子デバイスの信頼性の向上のためには，このような極細線の機械的性質を評価する必要がある。しかし，現状では，このようなマイクロサイズ材料を評価するための標準的な試験方法は確立されていない。したがって，マイクロサイズ材料の機械的性質の信頼性の高いデータを得るためには試験方法の標準化が不可欠である。マイクロサイズ材料の引張試験については，これまでに研究が行われ[1) 2)]，プラスチックタブに試験片を接着して引張試験を行なう方法について報告されており[3)～5)]，我々もこの方法を採用して引張試験を行い，その有効性を報告した[6)]。しかし，動的な疲労試験については，タブを用いることについての有効性については，ほとんど研究が行われていない。

そこで，本研究では，一定繰返し変位を負荷できる簡単な疲労試験機を製作し，直径25μmのアルミニウムボンディングワイヤーの繰返し荷重に対する疲労特性について検討した結果について報告する。

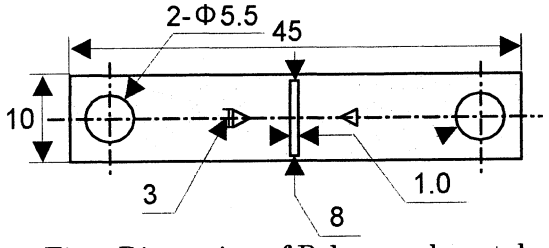

Fig.1 Dimension of Polypropylene tab

2. 試験方法

2. 1 供試材料および試験片

供試材料には Kulicke&Soffa Ltd 製，直径 25μm のワイヤーボンディング用アルミニウム線（Al：98.8－99.05%）を使用した。この Al 線を適当な長さに切断して試験片とし，Fig.1 のような形状のポリプロピレン製タブに瞬間接着剤で接着して取り付けた。なお，このままでは試験片に荷重が加わらないので，試験の直前にタブの両サイドを加熱したカッターで焼き切り，試験片にのみ荷重が加わる状態で試験に供した。

2. 2 疲労試験機

Fig.2 に示すような，簡単な疲労試験機を設計・製作した。アクチュエータは容量 9.8N の電磁式加振機（旭製作所製 WaveMaker01，周波数 1.0～2000Hz）を用いた。加振変位はレーザー変位センサー（KEYENCE 製）で計測し，荷重は容量 500mN（共和電業製）のロードセルで測定した。

疲労試験は加振機で一定変位の正弦波を加え，片振り引張りの繰返し荷重を加えた試験を行った。疲労試験システムを Fig.3 に示す。

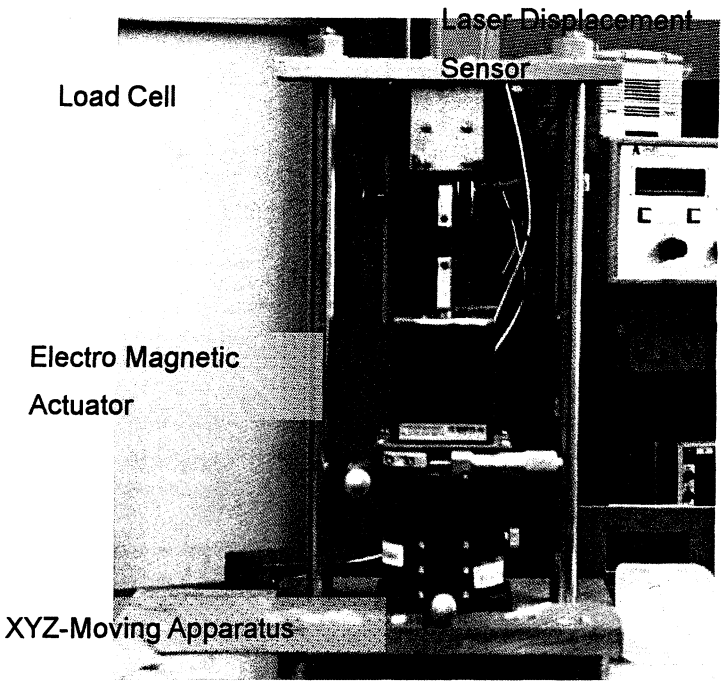

Fig.2 Fatigue tester

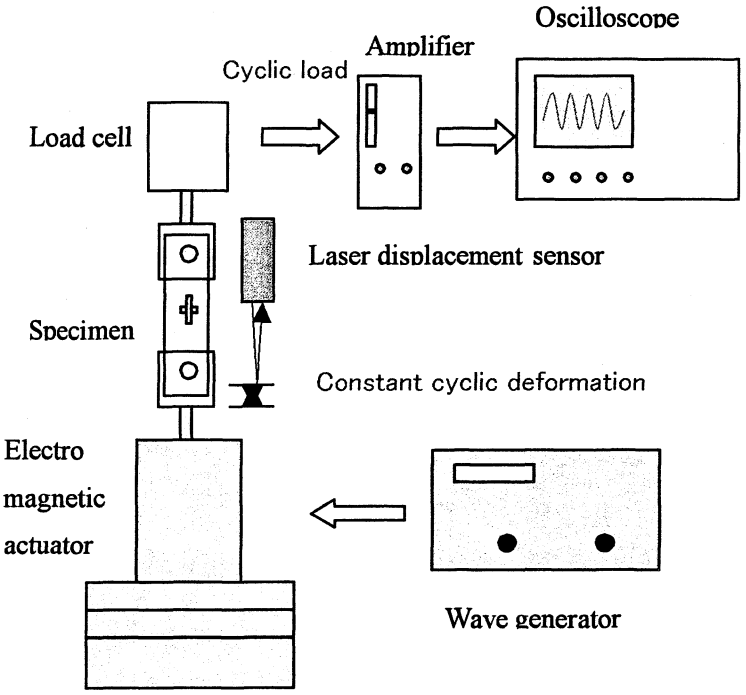

Fig.3 Block diagram of fatigue testing system.

3. 実験結果および考察

疲労試験の結果，縦軸に繰り返し最大応力，横軸に破断繰返し数をとり，S-N 曲線を表すと Fig.4 のようになる。試験データはバラツキが多い。これは，初期の試験データ（TEST A）に対し，加振機の出力を微調整可能に改良後のデータ（TEST B1，接着部で剥離の起こったものを TEST B2），接着剤を変更したものを TEST C と

して，全てのデータを示しているためである。この図から，直径 25μm のアルミニウムボンディングワイヤーの 10^7 回の疲労限度は最大応力で 170MPa 付近にあると推定できる。また，繰り返し最大応力 σmax＝176MPa，破断繰返し数 N=1.35×10^4 で破断した試験片の破断面を Fig.5 に示す。この破断面から，アルミニウムボンディングワイヤーは，破断部にくびれを生じており，右の略図に示すように，破面のA部は滑らかな破面を示しており，疲労き裂が進展した部分であり，B部は最終破断部分であることがわかる。つまり，この破面から，A部は第一段階のすべり面分離により，き裂が進展し，第二段階のき裂進展がほと

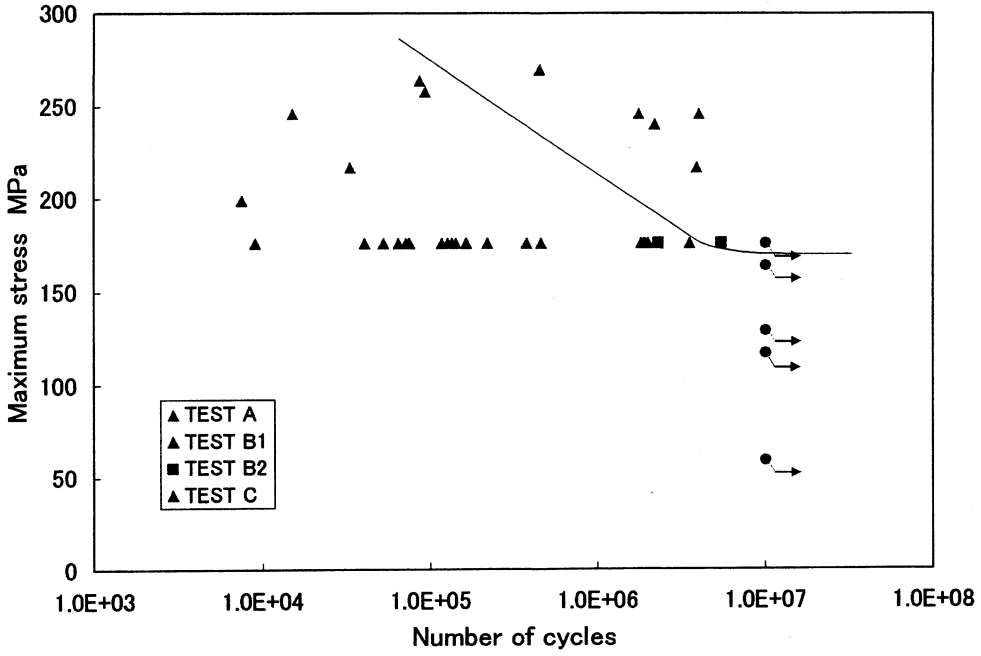

Fig.4　S-N curve of Aluminum binding wire.

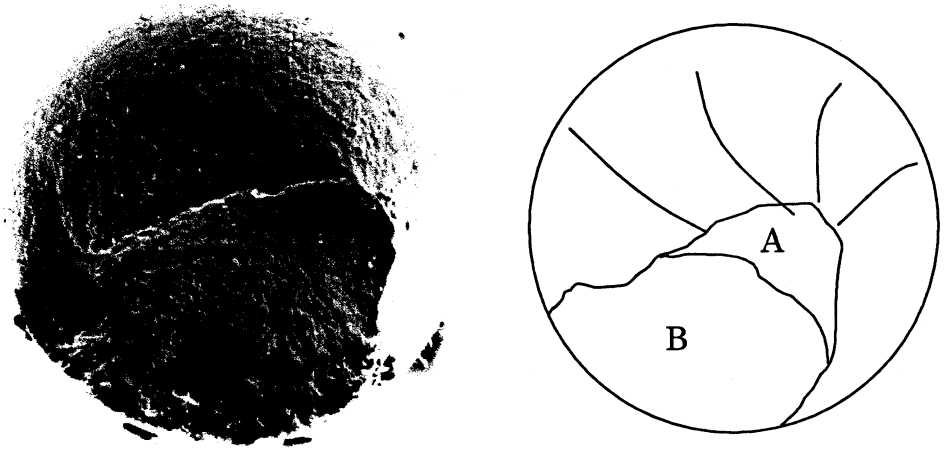

3.0 Fig.5　Failure surface of Aluminum bonding wire

んどないまま，不安定破壊に到ったことが推定される。これは，試験片寸法が小さいため，第二段階のき裂伝播距離がきわめて短いものと推定される。また，繰り返し最大応力σmax＝246MPa，破断繰返し数 N=1.77×10^6 で破断した試験片は，疲労破面はほとんど見られず，ネッキングを起こして破断していることが観察された。このような，ネッキングによる破断は微小寸法材料において生じやすい[6]といわれている。

4. まとめ

本疲労試験においては，温度の影響，試験片をタブに取り付ける際の接着の影響，試験片の伸びの補正の影響など，解決しなければならない問題が多くあるが，タブを用いることにより，マイクロサイズ材料の疲労試験が可能であることが分かった。

今後の課題

今後，より精度の高い疲労試験が行なえるように，タブの加工方法の改良をはじめとして，タブの材質，試験環境など，寿命のバラツキに影響を与える要因について，ひとつひとつ検討し，試験方法や疲労試験機の改良を行なって行きたい。

引用文献

1）小川，石川，北原：機械技術研究所所報，Vol.49,No.2，pp.57-62(1995)

2）H.Ogawa, K.Suzuki, S.Kaneko, Y.Nakano, Y.Ishikawa and T.Kitahara：Pro IEEE Micro Electro Mechanical Systems'97,pp430-435(1997)

3）箕島，田中，石田：日本材料学会　第269回疲労部門委員会　第27回マイクロマテリアル部門委員会研究討論資料，p. 44-45（2004-5）

4）K.Minosima, Y.Maekawa, K.Komai：日本材料学会 第269回疲労部門委員会 第27回マイクロマテリアル部門委員会研究討論資料，p. 35-43（2004-5）

5）砂田，松村，浅田，木之本，越智，政木：日本機械学会2005年度年次大会講演論文集（1），p. 315-316(2005-9)

6）後藤，新井，宮坂，立野，小林，小久保：材料試験技術，Vol. 53，No. 1，pp. 38-42（2008）

7）中井，橘本，竹谷：材料，Vol.54,No.3，pp.284-289(2005)

発表論文

1）後藤芳樹，新井裕介，宮坂勝利，立野昌義，小林光男，小久保邦雄：マイクロサイズ材料の引張試験と強度評価，材料試験技術，Vol. 53，No. 1，pp. 38-42（2008）

2）後藤芳樹，新井裕介，宮坂勝利，立野昌義，小林光男，小久保邦雄：マイクロサイズ材料の引張試験と強度評価，第234回材料試験技術シンポジュウム，(2008-1)

ハイテクリサーチセンタ第6回研究会資料
2008年3月25日開催

4.2 原子レベルで界面を制御したヘテロエピタキシャル半導体による新機能発光・電子デバイスの開発研究

-（副題）深紫外AlGaN多重量子井戸型半導体レーザー光の光学的異方特性-

(Optical Anisotropic Characteristics of Deep-UV AlGaN Multiple-Quantum-Well Lasers)

川西英雄
Hideo Kawanishi

工学院大学　工学部
Faculty of Engineering, Kohgakuin University
〒192-0015　東京都八王子市中野町　2665-1
Nakano-machi 2665-1, Hachioji-shi Tokyo 192-0015, Japan.

Abstract
End of October 1993, room temperature deep-UV lasing was demonstrated at around 240nm by AlGaN multiple-quantum-well laser under optical pumping, for the first time. The unique optical anisotropic polarization of laser output was discovered in the AlGaN MQW lasers lasing shorter than 280-290nm. The anisotropic polarization is the reflection of an anisotropic dipole moment, which directly related in laser gain, in the AlGaN active layer with high Al content.

1．はじめに

これまで実施してきた研究を基礎とし、半導体結晶界面を原子レベルで制御し成長したヘテロエピタキシャル半導体結晶を利用し、光デバイスを同時に製作した。今回は、本研究によって改良・改善してきた半導体結晶製作技術を実際のデバイスへと応用した。今回はその成果をまとめてみた。

この方法によって成長したAlGaN多重量子井戸型半導体レーザーで、深紫外波長域、240nm近傍での室温レーザー発振を初めて実現した。[1] その大きな理由の一つは、高品質なAlGaNのエピタキシャル法として、「交互供給法」と称せられる新技術が提案されたことであろう。[2] 現在、我々はその方法を、特に、「ASFE法（Alternate Source-Feeding Epitaxy）によるMO-VPE」と呼んでいる。

もう一つの理由は、これまでの常識にとらわれることなく研究を進めて来たからではないだろうか。すなわち、Al組成が大きく、発光波長が約280ー290nm以下で発光するAlGaNエピタキシャル層では、表面（c面）側からは、殆どその発光は観測されなかったにも拘わらず、その試料を励起し、レーザー発振の可能性を確かめたからではないだろうか。その結果、表面に平行な方向、言い換えれば、m面に垂直な方向（劈開端面方向）には、十分な発光過程とレーザー利得とがあり、発振閾値以上に強く励起することでレーザー発振が達成出来た。

この事は、AlGaN活性領域における発光過程が「等方的（これまでの常識ではこのように信じられてきた）」であれば、この実験結果は理解出来ない。発光過程が「非等方的」であるとすると、この実験結果は容易に理解出来る。すなわち、新しい「謎」が生まれたのである。

その「謎」を解明すべく、深紫外域でのAlGaN多重量子井戸型半導体レーザー

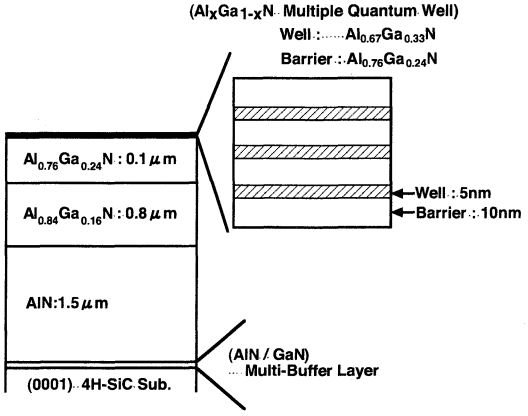

Fig.1: Scematic structure of AlGaN MQW deep-UV laser.

の光学的偏波特性など、最近筆者らが行った研究成果の一部をここで紹介したい。尚、ここでの研究成果は、深紫外域発光デバイスの高効率化にも直接関係する可能性があり、この分野の研究者の皆さんに興味を持って頂けると幸いである。

1. AlGaN 多重量子井戸型半導体レーザーの構造

深紫外域でレーザー発振が得られたAlGaN 多重量子井戸型半導体レーザーの断面構造を図.1 に示している。図.1 は、240nm でレーザー発振した試料の場合を示している。光学的特性に直接関連する点は、(0001) 面SiC 基板（すなわちc 面基板）を用いていることである。その他の詳しい内容は、別の報告を参照願いたい。[3)]

特に、発光過程に直接影響を与える可能性のある結晶の品質は、x 線回折によりc 軸のチルト角の変位及びc 軸を中心とした結晶のツイスト角の変位を、それぞれ、ω及びφに関するXRC（X 線ロッキングカーブ）半値幅で評価した。ωとφには高品質領域で強い相関があることも

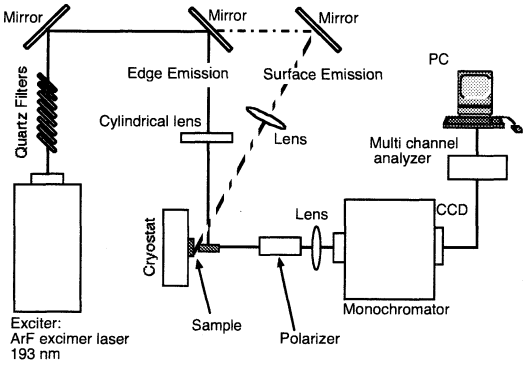

Fig.2: Optical Setup for Polarization and Emission Characteristics.

解り、ωスキャン特性を改善することで、φスキャン特性も改善した。現在、最も狭いものでΔω=78arcsec、及びΔφ=800arcsec となった。すなわち、今後更なる改善も必要であるが、半導体レーザーを構成するAlGaN エピタキシャル層は、c 軸に強く配向し、その品質は現時点で得られている最も高品質なAlGaN 結晶であろう。

2. 深紫外レーザー光の光学的偏波特性

AlGaN 多重量子井戸型半導体レーザーの、①表面発光及び、②端面発光の偏波特性は、図.2に示した光学系で測定した。試料は固定したまま、光学系を簡単に変更することによって、表面発光、及び端面発光が測定出来るよう工夫している。励起光源にはArF エキシマレーザーの193nm の発振線を用い、励起光強度は、直列に並べた石英板の枚数を変え、変化した。尚、偏波特性の測定では深紫外域を含む 190nm－400nm の波長域で有効なGlan-Taylor 型偏光器を利用し、その特性は、300nm 以上の波長域で有効な通常型の平板型偏光板と、355nm 域のレーザー発振光で精密に注意深く校正した。

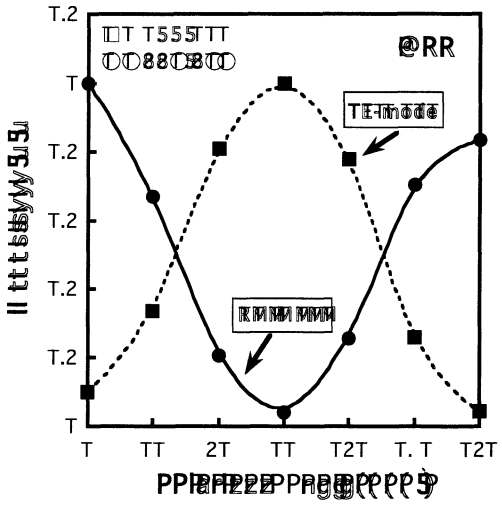

Fig.3: Optical Polarization Characteristics of UV and Deep-UV AlGaN MQW Lasers.

図.3 は組成の異なる二種類のAlGaN 多重量子井戸型半導体レーザーで得た紫外域レーザー光（発振波長：355.1nm）及び深紫外域レーザー光（発振波長：240.8nm）の偏波特性の測定結果をまとめたもので

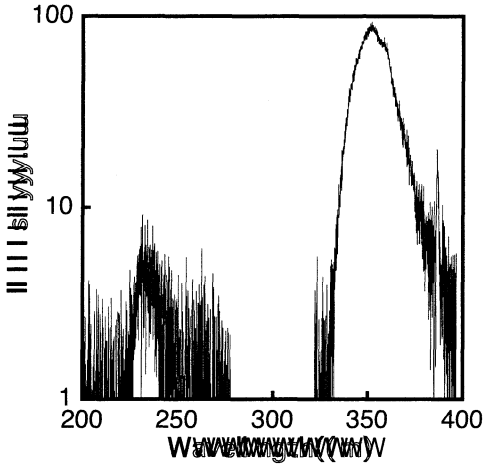

Fig.4: Surface Emission Intensity from c-plane AlGaN MQW Structure for different spectral region.

ある（いずれも室温）。測定結果は、紫外域レーザー光は、TE モードで発振しているのに対し、深紫外域レーザー光は、TM モードで発振している。TE モードでのレーザー発振は、GaAs 系、InP 系などの半導体レーザーでよく知られている通りである。すなわち、発光強度及びレーザー利得は等方的であり、TE モードに対する等価屈折率（伝搬定数を真空の波数で除したもので、屈折率の分散項は含まれていない）が、TM モードのそれに比べ僅かに大きいために、TE モードに対する端面の「モード反射率」が僅かに大きくなり、その結果、閾値利得が僅かに小さくなった。すなわち、閾値利得の面からレーザー発振モードの選択が起こっている。尚、この時の表面発光強度の異方性は殆ど観測出来なかった。

一方、深紫外域 AlGaN では発光特性及び利得は非等方的であり、TE モード方向の利得は無いか、有るにしても極めて小さく、TM モードに対するレーザー利得のみしか確保され無い。その結果、深紫外域 AlGaN では、レーザー利得の面から TM モードでのレーザー発振モードの選択が起こっている。

この事は、図.4 に示した測定結果のように、二種類の試料で、表面からの自然放出光強度が大きく違うことで明らかになる。[4] この図.4 は、AlGaN 多重量子井戸型半導体レーザーのそれぞれの試料を変えることなく、図.3 の測定の励起強度を下げ（レーザー発振をしない励起強度）測定した。但し、励起強度は、それぞれの試料での測定でほぼ同じとした。その結果、AlGaN の c 軸方向から検出した深紫外域の表面発光強度（波長、約 240.8nm）は、極端に微弱であり、端面発光強度（c 軸に垂直な方向から検出）に比べ約一桁程度以上強かった。　他方、紫外域の自然放出発光強度（波長、約 355.1nm）では、表面発光強度は端面発光強度に比べ、逆転し、約 1 桁強かった。[4]

この実験事実から以下のことが推定出来る。すなわち、Al 組成の大きな AlGaN 活性層内には、深紫外域の発光に関わる「電気双極子モーメント」が c 軸方向に偏っているため、c 軸方向への光の放出が観測出来ない、と古典的に考えるのが妥当である。

上に示した二つの実験事実を理解しやすくするために、図.5 に、紫外域及び深紫外域で発光する AlGaN に関する「電気双極子モーメント」の形成方位と発光強度との関係をまとめてみた。

紫外域発光の AlGaN 量子井戸型半導体レーザーでは、「電気双極子モーメント」は、c 面内に等方的に形成されるとともに、それと垂直な c 軸方向にも形成されている。その結果、TE モード及び TM モードいずれの場合にもレーザー利得が確保されている。一方、深紫外域発光の AlGaN 量子井戸型半導体レーザーでは、「電気双極子モーメント」は、c 軸方向に偏り形成されるために、TM モードに対するレーザー利得のみしか確保出来ない。

以上述べた実験結果に対する我々の主張は、別の測定結果からも確認出来ている。ページ数の関係で割愛するが、端面からの自然放出光の偏波面依存性を測定することで明らかになった。[4] このような現象が顕著に表れるのが、発光波長として 280-290nm 以下の波長域である。AlGaN の Al の組成にして約 40%の辺りからであった。

GaN 及び AlN のバンド構造が、第一原理

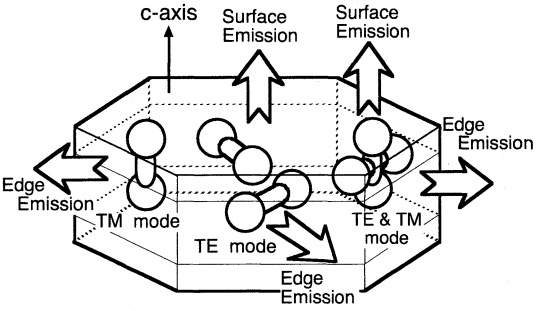

Fig.5: Possible Direction-Models for c-plane AlGaN with Different Al Content.

計算により既に求められている。バンド構造に関する詳しい議論は参考文献を参照願いたい。[5] 結論として、我々の実験結果は、この理論計算と、紫外域に発光波長を有するGaNにおいても、その光学的偏波特性とともに、それぞれのバンドのエネルギー差においても、いずれも一致しないようである。ここでは、問題点を指摘するだけに留めておく。より詳しい議論は、今後の皆さんの精密な測定と、実験・理論両面からの詳細な検討に任せるとする。

3. 深紫外AlGaN多重量子井戸半導体レーザーの今後に期待すること

深紫外域で動作する半導体レーザーの実現は、一つの技術的な夢である。このとき、常識に囚われることなく、この分野の研究を進めることが極めて重要ではないか、そんなことを、体験したように思う。発光強度が弱い半導体を、電流注入ではなく、光励起でレーザー発振を試みる、そんな実験・研究は決してしないだろう。それを、愚直に試みたことで、常識では理解出来ない、そんな実験結果が、突然、現れてきた。たくさんの「謎」が出現したことになる。

ここでの議論は、より詳細な追跡と、今後の詳細な考察が必要であろう。この分野の研究に興味を持つ研究者・技術者の人たちにそれを委ねたい。

本研究は、文部科学省・科学研究補助金。基盤研究(S)（課題番号：17106005）及び、特定領域研究（課題番号：）としても実施しているものである。研究を進める機会を与えて頂いたことに感謝する。また、日頃から貴重な議論を頂いている、本学・特別専任教授・長谷川文夫教授、また、結晶内の歪み解析と、AlN・AlGaN結晶の高品質化を手伝って頂いている本学・新倉栄一郎君及び村川浩一君に感謝する。

参考文献

1) T. Takano, Y. Narita, A. Horiuci and H.Kawanishi: “Room-temperature deep-ultraviolet lasing at 241.5 nm of AlGaN multiple-quantum-well laser” Appl. Phys. Lett, **84**(2004) 3567-3569.

2) T. Takano, Y. Ohtaki, Y. Narita and H. Kawanishi: “Improvement of Crystal Quality of AlGaN Multi Quantum Well Structure by Combination of Flow-Rae Modulation Epitaxy and AlN/GaN Multi-Buffer Layer and Resultant Lasing at Deep Ultra-Violet Region”, Japan. J. Appl. Phys, **43**(2004) L1258-L1260.

3) 川西英雄、高野隆好、瀬沼正憲、貫井猛晶：「光励起によるAlGaN多重量子井戸型深紫外レーザの発振特性」応用物理、**74**(2005)1458-1462.

4) H. Kawanishi, M. Senuma, T. Nukui: “ Anisotropic polarization characteristics of lasing and spontaneous surface and edge emissions from deep-UV AlGaN MQW lasers”, Appl. Phys. Lett., **89**(2006)041126*1-041126*3

5) M. Suzuki, T. Uenoyama and A. Yanase: ”First-principles calculations of effective-mass parameters of AlN and GaN” Phys. Rev. **B 52**(1995) 8132-8139.

4.3 単一方向ラビング処理による双安定アンカリング界面の形成
Formation of Bi-Stable Anchoring Surface for Nematic LCs by Unidirectional Rubbing

Kazunori SHIMOYAMA, Taiju TAKAHASHI and Susumu SAITO
下山　和則、高橋　泰樹、齊藤　進、

工学院大学・工学部・情報通信工学科
Department of Information and Communications Engineering, Faculty of Engineering, Kogakuin University

In this study, a novel method is proposed to adapt bi-stable anchoring properties on the substrate. A mixed solution of PVCi and PI in same weight was used as an alignment material. It has been confirmed that two types of domains coexist in the sample cell, and molecules of liquid crystal align with the angle of ±45degree with respect to the rubbing direction. When an electric field parallel to the electrode plane was applied using interdigital electrode, a homogeneous state of alignment changed to a twisted alignment. The twisted state was kept throughout over 50 h after the transition. Furthermore, the surface free energy density function was determined for the bistable anchoring substrate.

1. はじめに

双安定表示モードのLCDには,配向層表面に2つの方向に配向容易軸を形成し,その双方向アンカリング特性によって双安定な分子配向形態を発現させる方法と,配向層表面には一方向の配向容易軸しか付与されていなくても電極間で2つの双安定な分子配向形態を発現させる方法とがある。これまでに、双安定な配向層を形成する方式として基板表面にグレーティング状の溝を形成し、その表面に垂直配向処理を施す方法[1],特定の蒸着角でナノオーダ膜厚にSiO_2を斜方蒸着する方法[2], 互いに隣接する微少領域のラビング方向が直交するようにAFMの探針を用いてナノラビングする方法[3]が提案されている。しかし、いずれの方法も大面積化が困難な点が実用上問題視されている。そこで、本研究では、既に工業的に確立されている手法,例えばラビングのような一般的な処理によって双安定な配向層を形成することを目的とする。

2. 混合配向材の相分離によって生じるナノ組織化表面の形成による双方向アンカリング特性発現のモデル

本報告では、双方向のアンカリング特性を発現させるために、未架橋時にラビング方向に直交する方向に液晶分子を配向させるポリビニルシンナメート(PVCi)[4]とラビング方向に平行な方向に配向させるリイミド(PI)系配向材とを混合し,それを基板表面に塗布して形成した膜の表面にラビング処理を施す方法を提案する。

混合配向材溶液を基板表面にスピンコートすると溶媒が蒸発し、次第に濃度が増し、混合した2種類の原材料(ここではPVCiとPI)の内で溶媒への溶解度が低い方のPVCiが先に相分離し、微少領域を形成し、最終的に、PI薄膜の中にPVCiの微少領域が分散した構造が発現すると考えられる。その様な膜の表面をラビングした場合、PVCiに接する液晶分子がラビング方向に直交する方向に、PIに接する液晶分子はラビング方向と平行な方向に配向するが、その表面から離れるにつれて液晶分子は弾性歪みエネルギーが最少になるようにラビング方向からずれた方向に一様

に配向すると考えられる。そのとき、ラビング方向から正負方向にずれた配向の弾性歪みエネルギーが等しくなるので、巨視的にその二つの配向状態が混在する状態が観測されると考えられる。

3．単一方向ラビング処理による双安定アンカリング界面の形成

3-1 試料の作製

ラビング方向に液晶分子を配向させる PI 系配向材として PI-C(日産化学),ラビング方向に直交する方向に配向させる PVCi を用い,それらを 2:1 の重量比で溶媒に溶かしたものを配向材として用いた。スピンコート法によって基板表面に塗布し,250 ℃で 60 min. 焼成することによって成膜した。成膜後はその表面をラビングし,ラビング方向がアンチパラレルになるように上下基板を貼り合わせた。尚,ギャップ材は直径 6μm の真絲球(触媒化成工業)を使用した。液晶はネマティック液晶である 5CB(Merck)を用い,セルに液晶を注入後,偏光板を用いクロスニコル下での目視,及び偏光顕微鏡による配向状態の観測を行なった。

3-2 クロスニコル下での配向状態の観測

図 1 に混合配向材を用いて作製したセルのクロスニコル下での目視によって観測した配向状態の様子を示す。

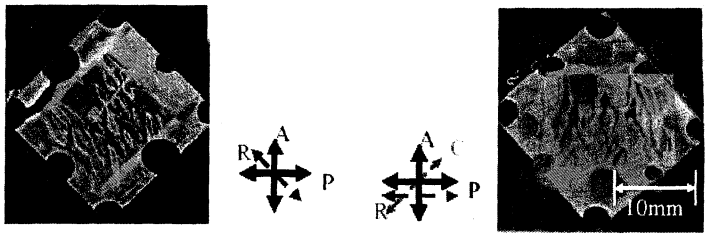

(a) (b)

Fig.1: Photographs of the cell under the cross Nicol condition

図 1 において,R はセルのラビング方向を P 及び A は偏光子及び検光子の透過軸方向を示す。偏光子の透過軸方向とセルのラビング方向をパラレルに配置した場合には消光位は観測されなかった。図 1(a)と図 1 (b)は, 偏光子の透過軸方向に対してセルのラビング方向を方位角方向にそれぞれ＋45 deg.と－45 deg. 傾けたときの観測結果である。これらの状態で消光位が現れているので、PI-C と PVCi の混合配向材を用いた場合、液晶分子はラビング方向に配向せず,ラビング方向から方位角方向に約±45 deg.ずれた方向に配向していることが確認された。

3-3 櫛歯電極を用いた In-plane 電界印加による配向状態間の遷移

ラビング方向に対して方位角方向に±45deg.ずれた 2 つの配向容易軸を形成することが出来たので櫛歯電極を用いて in-plane 電界を印加することによって 2 状態間の配向の遷移を試みた。電極間 35 μm,電極幅 25 μm の櫛歯電極を用いた。

図 2 に AC 電圧 100V を印加前後のセルの配向状態の変化を示す。実験結果から液晶分子配向が平行配向から他のツイスト状態へ遷移したことが確認できた。遷移後クロスニコル下でセルを回転させても消光位が観測されなかったことからツイスト配向への遷移であることがわかる。この遷移後のツイスト配向が 50 h 以上保持されていたので, 表示のメモリー性を有していると言える。また遷移後のツイスト配向のツイスト角はおおよそ 70 deg.であった。平行配向から 90 deg.

ツイスト配向へと遷移したが, 双方向の容易軸の方位角アンカリングエネルギーは90 deg.を保持できるだけの強さがなく,対向基板側に引っ張られる形でツイスト角が 70 deg.になったと予想される。

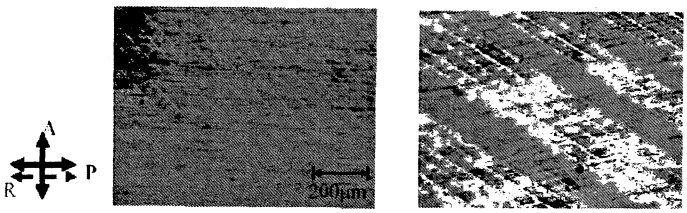

Fig.2 Photographs for transition of LC alignment by voltage application
(a) before voltage application, (b) after voltage application

3-4 表面エネルギー密度関数の実験式と双安定状態のエネルギーバリアの測定

表示にメモリー性を有する双安定型 LCD を議論する上で双方向容易軸間のエネルギーバリアの高さの算出は最も重要な事柄の 1 つであるといえる。双方向容易軸間のエネルギーバリアを算出するために片側の基板(基板 B)は双安定なアンカリング特性を有し,もう片方の基板(基板 A)は単安定で且つ強アンカリングな基板であり,それぞれの基板のラビング方向がアンチパレルになるように構成されたセルを仮定する。

セルのセル厚方向に Z 軸をとり基板 A,B はそれぞれ Z=0,Z=d にあるものとする。ここで双方向アンカリング特性を有する基板 B における表面自由エネルギーの関数 Fs として米谷等によって提案された次のような表現式[7]を採用する。

$$Fs = \frac{1}{2}A_2\left\{\sin^2\phi(d) + a_r\cos^2\phi(d)\right\} + \frac{1}{4}A_4\left\{\sin^4\phi(d) + a_r\cos^4\phi(d)\right\} \quad , \qquad (1)$$

ここで$\phi(d)$はラビング方向からの方位角方向の表面ダイレクターの角度でありA_2とA_4は次元がJ/m^2の定数を表している。双方向アンカリング特性を有する基板側の方位角方向の液晶分子配向方向がラビング方向に対して方位角方向にそれぞれ$\pm\Phi_d$の時, a_rは次式により与えられる。

$$a_r = \frac{1 + a_{42}\sin^2\Phi_d}{1 + a_{42}\cos^2\Phi_d} \quad \text{ただし、} \quad a_{42} = \frac{A_4}{A_2} \qquad (2)$$

液晶の連続体理論に変分原理を適用すると、A_2に関する以下の式を得ることができる。

$$A_2 = -\frac{2\phi(d)K_{22}}{d\sin 2\phi(d)\left[(1-a_r) + a_{42}(\sin^2\phi(d) - a_r\cos^2\phi(d)\right]} \qquad (3)$$

$\phi(d)$とΦ_dを実測し、a_{42}を0.2と仮定して式(3)に代入することによってA_2の値を得ることができる。$Fs(\phi(d))$はa_{42}に依存するがエネルギーバリア$Fs(0)-Fs(\Phi_d)$はa_{42}に依存しない。

以下に示す方法によって、$\phi(d)$とΦ_dを実測した。ラビング方向に対する方位角方向の配向容易軸方向を測定するために片側基板に双方向アンカリング特性を有する基板,もう片側に垂直配向材SE-1211(日産化学)を用いて垂直配向処理した基板と貼り合わせることでHAN(Hybrid Aligned Nematic)セルを作製した。ラビング方向からの方位角方向の角度$\pm\Phi_d$は偏光顕微鏡を用いてクロスニコル下でセルを回転させ消光位を観測することによって求めた。

一方片側に双方向アンカリング特性を有する基板を,もう片側にラビング処理を施した単安定

基板を用いてセルを作製しツイスト角φ(d)を測定した。尚,双方向アンカリング特性を有する基板BはHANセル作製時に使用したものと同様の基板を用いた。φ(d)の値に関しても偏光顕微鏡を用いて測定した。単安定側の基板Aのラビング方向と偏光子の透過軸を一致させ検光子を回し透過率が最大になる角度としてφ(d)が得られる。測定結果をA_2の計算結果と共に表1として示す。 式(1)にΦdとφ(d)を代入することで図3に示すような表面自由エネルギー関数が得られる。この結果からエネルギーバリアの高さは1.1×10^{-7} [J/m^2]と計算できる。

Table 1 Experimental results on Φ_d and ϕ (d)

d [μm]	Φ_d [deg.]	φ(d) [deg.]	A2 [J/m^2]
9.0	36	27	9.1×10^{-6}

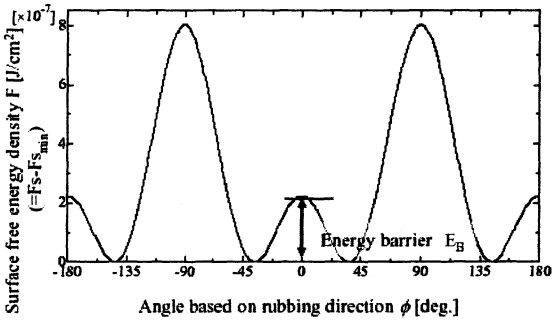

Fig.3 Surface free energy density curve

4．結論

PVCiとPIを同量混ぜた混合配向材を使用し、製膜後ラビング処理を施すことによって基板表面に双方向アンカリング特性を付与することに成功した。混合配向材を用いた基板同士をラビング方向がアンチパラレルになるように貼り合わせたセルにおいて,ラビング方向から方位角方向に±45deg.の角度を持った平行配向が得られ,櫛歯電極を用いてin-plane AC界を印加することによって、平行配向からツイスト配向へ遷移させることに成功した。遷移後のツイスト配向は50h以上の長期間配向を保持していた。

また双方向アンカリング特性を有する基板表面における表面自由エネルギー関数の実験式を求め双方向アンカリング間のエネルギーバリアとして10^{-7}[J/m^2]のオーダーの値を得た。[5),6)]

参考文献

1) G. P. Bryan-Brown, C. V. Brown, J. C. Johns, E. L. Wood, I. C. Sage, P. Brett and J. Rudin: SID '97 Digest, pp.37 (1997)

2) R. Barberi, M. Boix, and G. Durand: Appl. Phys. Lett., 55, pp.2506 (1989)

3) J. H. Kim, M. Yoneya, J. Yamamoto, and H. Yokoyama: Appl. Phys. Lett.,78, pp.3055 (2001)

4) Y. Iimura, S. Kobayashi, and K. Katoh: IEICE Trans. Elecron,. Vol. E79-C, No.8 August, pp.1040 (1996)

5) K. Shimoyama, T. Takahashi and S. Saito: EuroDisplay '07 Digest, pp.223-224 (2007)

6) 下山和則, 高橋泰樹, 齊藤進: 日本液晶学会討論会予稿集, pp.146 (2007)

7) M. Yoneya, J. H. Kim and H. Yokoyama: Appl. Phys. Lett., 80, pp.374 (2002)

研究業績

1. 生体分子のナノ表面

N^1,N^{12}-Diacetylspermine as a Sensitive and Specific Novel Marker for Early- and Late-Stage Colorectal and Breast Cancers

Kyoko Hiramatsu,[1] Keiichi Takahashi,[2] Taturo Yamaguchi,[2] Hiroshi Matsumoto,[2] Hidenori Miyamoto,[2] Souichi Tanaka,[5] Chikako Tanaka,[2] Yoshiko Tamamori,[3] Mari Imajo,[6] Masashi Kawaguchi,[6] Masakazu Toi,[2] Takeo Mori,[4] and Masao Kawakita[6]

Abstract

Purpose: N^1,N^{12}-diacetylspermine (DiAcSpm) in the urine of colorectal and breast cancer patients was examined to establish its usefulness as a novel diagnostic tool for detecting these cancers at clinically early stages.

Experimental Design: Urine samples from 248 colon cancer patients and 83 breast cancer patients as well as 51 patients with benign gastrointestinal diseases treated in Tokyo Metropolitan Komagome Hospital during the period of August 1999 to January 2004 were collected. DiAcSpm was analyzed by ELISA and its sensitivity for malignant conditions was compared with that of serum carcinoembryonic antigen (CEA), CA19-9, and CA15-3.

Results: The sensitivity of urinary DiAcSpm for colon cancer patients (n = 248) was 75.8% (mean ± 2 SD for 52 healthy controls as a cutoff value), which was markedly higher than the sensitivities of serum CEA (39.5%, $P < 0.0001$) and CA19-9 (14.1%, $P < 0.0001$). DiAcSpm was elevated in 60% of tumor-node-metastasis cancer stage 0 + I patients, whereas only 10% ($P < 0.0001$) and 5% ($P < 0.0001$) of these patients were CEA- and CA19-9–positive, respectively. The sensitivity of urinary DiAcSpm for 83 cases of breast cancer (60.2%) was higher than the sensitivities of CEA (37.3%, $P = 0.0032$) and CA15-3 (37.3%, $P = 0.0032$). DiAcSpm was elevated in 28% of tumor-node-metastasis stage I + II patients, whereas only 3% ($P = 0.0064$) and 0% ($P = 0.001$) of these patients were CEA- and CA15-3–positive, respectively.

Conclusion: The observations indicate that urinary DiAcSpm is a more sensitive marker than CEA, CA19-9, and CA15-3 and that it can efficiently detect colorectal and breast cancers at early stages.

We reported previously that N^1,N^{12}-diacetylspermine (DiAcSpm) is excreted in the urine of healthy persons, with small individual variations in the amount (1). We devised a high-performance liquid chromatography separation system connected to an in-line enzymatic detection system for DiAcSpm and carried out precise analyses of urinary DiAcSpm in healthy persons as well as patients with malignant diseases.

Our analysis revealed that DiAcSpm may be useful as a novel diagnostic and prognostic tumor marker in that its excretion in urine is elevated significantly and frequently in patients with urogenital malignancies and tends to recover to the normal level on remission (2, 3). At the same time, we noted that monoacetylpolyamines that constitute a major part of urinary polyamines, including N-acetylputrescine, N^1-acetylspermidine, and N^8-acetylspermidine, were much less sensitive as markers for these urogenital malignancies than DiAcSpm and could not be considered practical tumor markers. The part of our observations concerning conventional monoacetylpolyamines was very well in accord with the popular evaluation of urinary polyamines at that time (4), but our results on DiAcSpm analysis were radically different from those on other polyamine derivatives and looked highly promising (2, 3).

Although the biochemistry and clinical chemistry of DiAcSpm remain largely obscure at present because of the lack of intensive studies of its metabolism, it is quite reasonable that various cancers might excrete increased amounts of DiAcSpm, because polyamine metabolism is activated in association with various types of cell proliferation (5). In this study, we examined the excretion of DiAcSpm in the urine of colon and breast cancer patients and compared the urinary DiAcSpm level with serum levels of other established tumor markers, including carcinoembryonic antigen (CEA), CA19-9, and CA15-3. Our analysis revealed that DiAcSpm is a more sensitive marker than these established markers for colon and breast cancers and that it can efficiently detect cancers at early clinical stages.

Materials and Methods

Urine samples from 248 colon cancer patients and 83 breast cancer patients treated at the Tokyo Metropolitan Komagome Hospital during

Authors' Affiliations: [1]Medical Research and Development Center, Tokyo Metropolitan Institute of Medical Science, [2]Department of Surgery, [3]Clinical Laboratory, [4]Tokyo Metropolitan Komagome Hospital, [5]Department of Surgery, Tokyo Metropolitan Bokutou Hospital, and [6]Department of Applied Chemistry, Kogakuin University

Received 11/9/04; revised 12/16/04; accepted 1/6/05.

Grant support: Ministry of Education, Culture, Sports, Science and Technology of Japan grants-in-aid for scientific research and Suzuken Memorial Foundation.

The costs of publication of this article were defrayed in part by the payment of page charges. This article must therefore be hereby marked *advertisement* in accordance with 18 U.S.C. Section 1734 solely to indicate this fact.

Note: C. Tanaka is currently at the Department of Radiology, Tokyo Metropolitan Komagome Hospital, Tokyo, Japan.

Requests for reprints: Masao Kawakita, Department of Applied Chemistry, Kogakuin University, 1-24-2 Nishi-shinjuku, Shinjuku-ku, Tokyo 163-8677, Japan. Phone: 81-3-33402731; Fax: 81-3-33400147; E-mail: bt13004@ns.kogakuin.ac.jp.

the period of August 1999 to January 2004 were collected and analyzed for DiAcSpm. Serum CEA, CA19-9, and CA15-3 levels were determined for these patients at the Clinical Laboratory of the Tokyo Metropolitan Komagome Hospital. Urine samples were also collected from 51 patients with the following benign gastrointestinal diseases (with the number of cases in parentheses; also see Table 1): benign tumors, including adenoma (n = 15), carcinoid (n = 2), neurilemoma (n = 1), and lipoma (n = 1); inflammatory bowel diseases, including ulcerative colitis (n = 4), Crohn's disease (n = 2), and radiation enterocolitis (n = 1); acute inflammatory diseases, including cholecystitis (n = 1) and appendicitis (n = 1); other disorders, including hemorrhoids (n = 8), hernia (n = 3), uterine prolapse (n = 1), intestinal obstruction (n = 2), gastric ulcer (n = 1), intestinal ulcer (n = 1), gallstone disease (n = 2), and malabsorption syndrome (n = 1). Post-operative cancer cases that were in complete remission (n = 4) were also included. We obtained written informed consent from all patients, and the study was approved by the institutional ethics committees at the Tokyo Metropolitan Institute of Medical Science and Tokyo Metropolitan Komagome Hospital. The clinical stage of the disease was determined according to the tumor-node-metastasis classification. Urine samples from 52 healthy volunteers (27 males and 25 females, ages 22-52 years) were also obtained. All the urine samples were collected in the morning, immediately supplemented with 3 mmol/L NaN_3 and stored at −20°C until use. Under these conditions, polyamines are stable for at least 10 years, and analyses of the same sample on different occasions gave consistent results.

DiAcSpm in urine was measured by ELISA essentially as described previously (6). DiAcSpm-specific antibody was obtained from rabbit antiserum against N-acetylspermine coupled to mercaptosuccinylated bovine serum albumin via N-(4-maleimidobutyryloxy)succinimide through several steps of affinity purification to minimize the cross-reaction with N^1-acetylspermidine (N^1-AcSpd), which would otherwise severely interfere with the determination of DiAcSpm (6). Cross-reaction of this purified DiAcSpm-specific antibody with N^1-AcSpd was reduced to 0.03%, and the accuracy of the ELISA system using this antibody was verified by comparing the analytic results with those obtained with high-performance liquid chromatography (6) and mass spectroscopy measurements (7). We made the following slight modification of the ELISA system: AcSpm was conjugated to a peptide, WMQSWYYHWGGGTFPIC, via N-(8-maleimidocapryloxypropyl)succinimide to make a solid-phase antigen to obtain more stable attachment of the resulting AcSpm-conjugated (DiAcSpm mimicking) antigen peptide to the microtiter plate than that in the previous system. DiAcSpm was a kind gift from Drs. K. Samejima and A. Shirahata at the Josai University, Saitama, Japan. The creatinine concentration in the urine samples was determined enzymatically using Determiner L CRE (Kyowa Medex, Tokyo, Japan). Serum CEA, CA19-9, and CA15-3 values were determined at the Clinical Laboratory, Tokyo Metropolitan Komagome Hospital. The following values were used as cutoff values: DiAcSpm, 0.25 μmol/g creatinine (mean ± 2 SD for 52 healthy persons); CEA, 5 ng/mL; CA19-9, 37 units/mL; CA15-3, 23 units/mL. Using these cutoff values, 95% to 98% of healthy persons were negative with respect to a given marker.

Table 1. Summary of DiAcSpm levels in benign gastrointestinal disease cases and postoperative cancer cases in complete remission

	No. cases	DiAcSpm/cutoff value	
		<1	>1
Benign tumors			
Adenoma	15	13	2
Carcinoid	2	2	0
Neurilemoma	1	1	0
Lipoma	1	1	0
Inflammatory bowel diseases			
Ulcerative colitis	4	2	2*
Crohn's disease	2	0	2*
Radiation enterocolitis	1	0	1*
Acute inflammatory diseases			
Cholecystitis	1	0	1
Appendicitis	1	0	1
Others			
Hemorrhoids	8	7	1
Hernia	3	2	1
Uterine prolapse	1	1	0
Intestinal obstruction	2	2	0
Gastric ulcer	1	1	0
Intestinal ulcer	1	1	0
Gallstone disease	2	2	0
Malabsorption syndrome	1	0	1†
Postoperative cancer cases in CR	4	4	0

*Patients in the active phase of the disease.
†Patient with hepatitis C.

Results

DiAcSpm was found a sensitive marker for colon and breast cancers. The urinary DiAcSpm level (in μmol/g creatinine) before surgical operation or chemotherapy in colon and breast cancer patients was compared with the levels in patients with non-malignant diseases and in healthy persons, as shown in Fig. 1.

The sensitivity of DiAcSpm (100 × number of true positives / total patients) in the 248 colon cancer and 83 breast cancer patients examined was 75.8% and 60.2%, respectively, in reference to the cutoff value (mean ± 2 SD of healthy persons), whereas the specificity of DiAcSpm (100 × number of true negatives / total subjects in a control group) was 96% for the 52 apparently healthy controls and 77% for the 51 benign disease cases (Table 1). The raw median value for patients with benign diseases (with the range in parentheses) was 0.148 μmol/g creatinine (0.027-1.48). Patients with active inflammatory symptoms, including those with acute appendicitis (0.413 μmol/g creatinine) or acute cholecistitis (0.282 μmol/g creatinine) and those in the active phase of inflammatory bowel diseases tended to give DiAcSpm values above the cutoff level. Inflammatory bowel diseases were sometimes accompanied by unusually high levels of DiAcSpm (1.48, 1.19, and 0.74 in ulcerative colitis, Crohn's disease, and radiation enterocolitis, respectively). These cases are indicated by solid symbols in Fig. 1. Except for these cases with easily discernible active inflammation, patients with benign diseases had DiAcSpm values closely similar to those of healthy persons on average, with mean ± SD values of 0.16 ± 0.10 μmol/g creatinine compared with 0.15 ± 0.05 μmol/g creatinine for healthy persons, and their urinary DiAcSpm values did not usually exceed twice the cutoff values. It is worth noting here that only 2 of 15 adenoma cases were DiAcSpm-positive (0.34 and 0.41 μmol/g creatinine), and other cases of benign tumors, including two cases of carcinoid, one case of neurilemoma, and once case of lipoma, showed DiAcSpm values below the cutoff level. The specificity of DiAcSpm as a malignant tumor marker for these benign tumors (n = 19) was 90%.

Serum CEA and CA19-9 levels in colon cancer patients were measured and their sensitivity for the detection of colon cancer

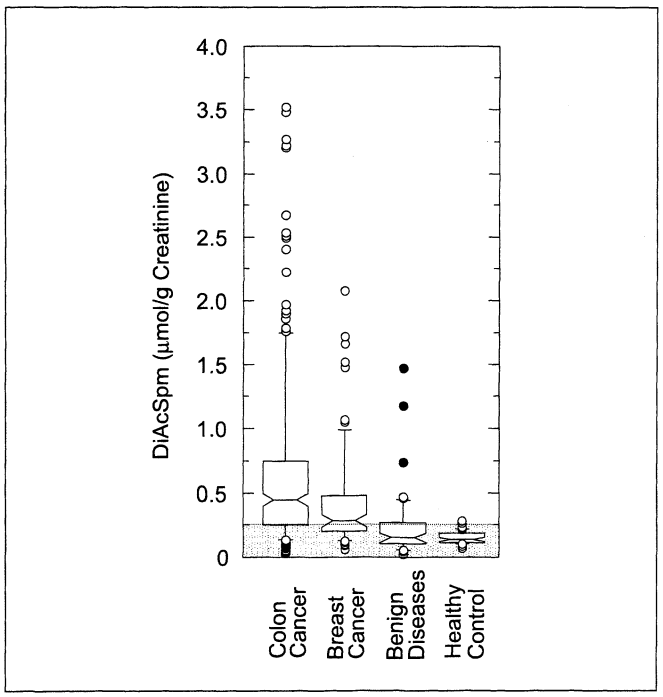

Fig. 1. Sensitivity of DiAcSpm for colon cancer and breast cancer. Urinary DiAcSpm levels (percentiles) in cancer patients, patients with benign diseases, and healthy controls. DiAcSpm values are expressed as μmol/g creatinine and are in box plot format. Values included in each box, middle 50% of values of the studied population. Middle bar, median value, with the 95% confidence interval (*notches*). Values included between the bottom and top bars, values of 90% of the population. Dots outside the bars, values of the remaining individuals. Points above 4.0 μmol/g creatinine (8 and 1 among colon and breast cancer patients, respectively) are omitted. Raw median values (with ranges in parentheses) of DiAcSpm for 248 colon cancer patients, 83 breast cancer patients, and 52 healthy controls were 0.457 μmol/g creatinine (0.035-24.6), 0.283 μmol/g creatinine (0.069-6.4), and 0.139 μmol/g creatinine (0.077-0.285), respectively. Solid symbols in the benign disease group are patients who were in the active phase of inflammatory bowel diseases (see text).

was compared with that of urinary DiAcSpm (Fig. 2). The sensitivity of DiAcSpm was much higher than that of these tumor markers currently in clinical use. The analytic data were normalized by the cutoff value of each marker and plotted as in Fig. 1. The sensitivity of DiAcSpm for colon cancer (75.8%) was significantly higher than the sensitivities of CEA (39.5%, $P < 0.0001$) and CA19-9 (14.1%, $P < 0.0001$). For these colon cancer cases, the raw median values (with ranges in parentheses) were 0.457 μmol/g creatinine (0.035-24.6) for DiAcSpm, 3.14 ng/mL (0-5.5 × 10^2) for CEA, and 10.9 units/mL (0-1.3 × 10^3) for CA19-9. The sensitivity was increased to 84.2% when a patient positive with respect to either DiAcSpm, CEA, or CA19-9 was defined as positive ($P = 0.018$ compared with DiAcSpm alone by 2 × 2 χ^2 test).

Serum CEA and CA15-3 levels in breast cancer patients were measured, and their sensitivity for the detection of breast cancer was compared with that of DiAcSpm in urine (Fig. 3). The analytic data were normalized by the cutoff value of each marker. The sensitivity of urinary DiAcSpm for breast cancer (60.2%) was also significantly higher than the sensitivities of serum CEA (37.3%, $P = 0.0032$) and CA15-3 (37.3%, $P = 0.0032$). For breast cancer cases, the raw median values (with ranges in parentheses) for DiAcSpm, CEA, and CA15-3 were 0.283 μmol/g creatinine (0.069-6.4), 3.6 ng/mL (0-4 × 10^5), and 14.2 units/mL (4.6-7.6 × 10^2), respectively.

One of the most potentially useful features of DiAcSpm is that it can detect early-stage colon and breast cancers in patients. The sensitivity of DiAcSpm and other markers was compared among colon cancer patients grouped according to tumor stage (Table 2). The proportion of positives with respect to each marker increased with the progression of the cancer, but the sensitivity of DiAcSpm was higher than the sensitivities of CEA and CA19-9 at every clinical stage. Notably, DiAcSpm values were above the cutoff level in 60% of stage 0 and I colon cancer patients, whereas only 10% and 5% of early-stage colon cancer patients were CEA- or CA19-9–positive, respectively. The difference in the sensitivity between DiAcSpm and CEA, and that between DiAcSpm and CA19-9, was significant for both stage 0 ($P = 0.002$ and 0.0004, respectively; $n = 20$) and stage I ($P < 0.0001$ and $P < 0.0001$, respectively; $n = 40$) patients. Combination of DiAcSpm with CEA and CA19-9 did not significantly improve the sensitivity of early-stage cancer detection compared with DiAcSpm alone. It is important that adenoma, carcinoid, and other benign tumor cases were mostly DiAcSpm negative, as described above. This indicates that urinary DiAcSpm may efficiently discriminate between benign and malignant tumors.

The proportion of positives with respect to each marker also increased with the progression of breast cancer, and the sensitivity of DiAcSpm was again higher than the sensitivities of CEA and CA15-3 at every clinical stage (Table 3). The sensitivity of DiAcSpm for earlier stage breast cancer (stages I and II; 28.1%) was not as high as that for early-stage colon cancers but was significantly higher than those of CEA (3.1%, $P = 0.018$) and CA15-3 (0%, $P = 0.0010$). It should be noted

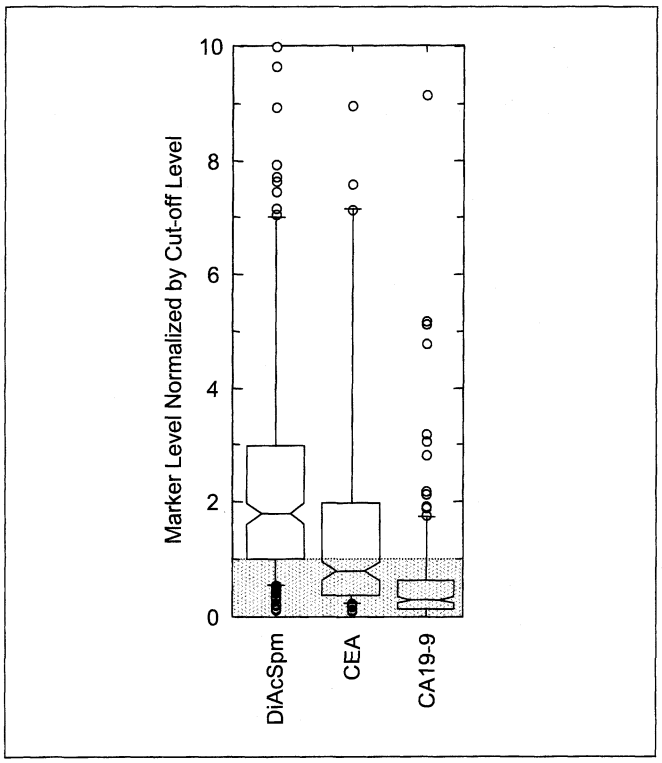

Fig. 2. Sensitivity of DiAcSpm, CEA, and CA19-9 for colon cancer. Urinary DiAcSpm level (percentiles), serum CEA level (percentiles), and serum CA19- 9 level (percentiles) in colon cancer patients are in box plot format as in Fig. 1. Shaded area, range below the cutoff values of the respective markers (0.25 μmol/g creatinine, 5 ng/mL, and 37 units/mL for DiAcSpm, CEA, and CA19-9, respectively).

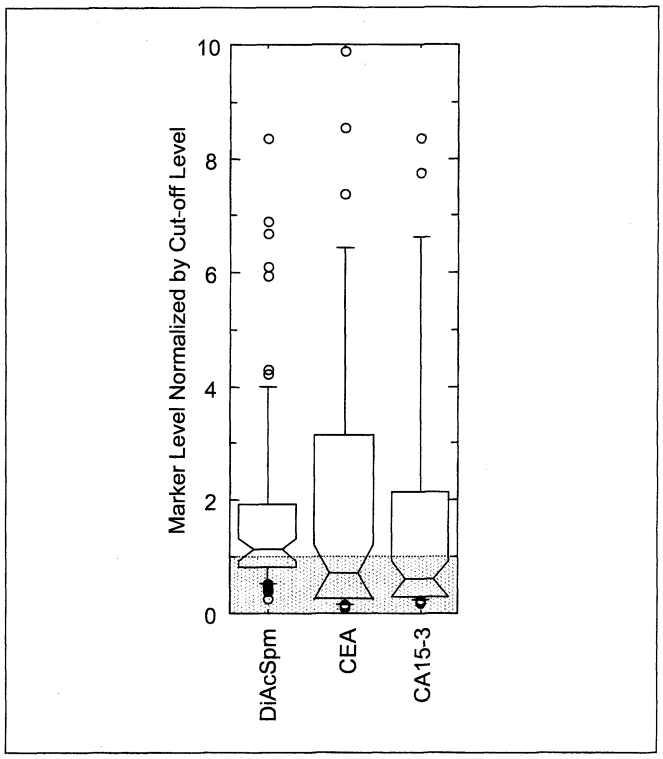

Fig. 3. Sensitivity of DiAcSpm, CEA, and CA15-3 for breast cancer. Urinary DiAcSpm level (percentiles), serum CEA level (percentiles), and serum CA15-3 level (percentiles) in breast cancer patients are in box plot format as in Fig. 1. Shaded area, range below the cutoff values of the respective markers (0.25 μmol/g creatinine, 5 ng/mL, and 23 units/mL for DiAcSpm, CEA, and CA15-3, respectively).

that the sensitivity of these currently available markers for the detection of breast cancer at earlier stages was negligibly low.

Discussion

Serum CEA and CA19-9 have been widely used as tumor markers for colon cancers. The present study showed that the urinary DiAcSpm level is much more sensitive than these established tumor markers for detecting colon cancers. Patients with active inflammatory symptoms also tended to have high DiAcSpm values, but these patients could be easily identified by their characteristic symptoms. Besides these easily discernible patients, those who were being treated for benign diseases generally excreted similar amounts of DiAcSpm as healthy persons. Urinary DiAcSpm may thus be considered a novel high-performance tumor marker for colon cancers that can be favorably compared with the markers CEA and CA19-9. The urinary DiAcSpm level was also frequently elevated in breast cancer cases. Its sensitivity was significantly higher than that of established markers such as CEA and CA15-3. Our previous analysis using high-performance liquid chromatography procedure indicated that DiAcSpm was elevated frequently and markedly in urogenital malignancies, including prostate cancer, testicular cancer, renal cancer, and renal pelvic cancer, with a very low false-negative incidence (2). Further examination revealed that urinary diacetylpolyamines tended to decrease when cancer patients entered partial remission. The prognosis of patients was generally good when the diacetylpolyamine level was normal or nearly normal, whereas the prognosis was poor when the diacetylpolyamine level remained far above the normal limit after apparently effective treatment (3). DiAcSpm in urine was also reported to be increased in patients with leukemia (8, 9). The present results together with these previous observations strongly suggest that DiAcSpm may be useful to detect a wide variety of neoplastic diseases and that more extensive and detailed analyses of the usefulness of DiAcSpm as a diagnostic and prognostic marker for these as well as other types of cancer are warranted.

It is particularly important that DiAcSpm was frequently increased in urine from stages 0 and I colon cancer patients. Serum CEA and CA19-9 are virtually unable to detect these early-stage colon cancers. Moreover, DiAcSpm was not usually increased in cases of adenoma, thus allowing us to discriminate between malignant and nonmalignant tumors. The sensitivity of DiAcSpm for detecting early-stage colon cancer was comparable with that of the fecal occult blood test, which is widely used in screening for colon cancer. DiAcSpm was also able to detect the occurrence of early-stage breast cancer that could not be detected by either CEA or CA15-3. Early diagnosis is of great importance in cancer therapy, because cancers can often be cured if detected early enough, owing to the recent progress in cancer therapy. The availability of a tumor marker that would enable us to find cancers in patients at an earlier

Table 2. Colon cancer stage and tumor marker levels

		DiAcSpm			CEA			CA19-9		
Stage	*n*	Positive	Negative	Sensitivity (%)	Positive	Negative	Sensitivity (%)	Positive	Negative	Sensitivity (%)
0	20	12	8	60.0*	2	18	10.0	1	19	5.0
I	40	25	15	62.5†	4	36	10.0	2	38	5.0
II	60	43	17	71.7‡	25	35	41.7	3	57	5.0
III	107	89	18	83.2†	53	54	50.5	24	83	22.4
IV	21	19	2	90.5§	14	7	66.7	5	16	23.8
Total	248	188	60	75.8†	98	150	39.5	35	213	14.1

NOTE: *P* values were obtained by 2 × 2 χ^2 test, or where the 2 × 2 table contained numbers less than 4 in the data, by Fisher's test.
*$P = 0.002$ compared with CEA and $P = 0.0004$ compared with CA19-9.
†$P < 0.0001$ compared with CEA and CA19-9.
‡$P = 0.0009$ compared with CEA and $P < 0.0001$ compared with CA19-9.
§$P < 0.0001$ compared with CA19-9.

Table 3. Breast cancer stage and tumor marker levels

		DiAcSpm			CEA			CA15-3		
Stage	*n*	Positive	Negative	Sensitivity (%)	Positive	Negative	Sensitivity (%)	Positive	Negative	Sensitivity (%)
I + II	32	10	22	31.3*	1	31	3.1	0	32	0
III + IV	51	41	10	80.3†	30	21	58.8	31	20	60.8
Total	83	51	32	61.4‡	31	52	37.3	31	52	37.3

NOTE: *P* values were obtained by $2 \times 2\ \chi^2$ test, or where the 2×2 table contained numbers less than 4 in the data, by Fisher's test.
*$P = 0.0029$ compared with CEA and $P = 0.0004$ compared with CA15-3.
†$P = 0.018$ compared with CEA and $P = 0.030$ compared with CA15-3.
‡$P = 0.0019$ compared with both CEA and CA15-3.

stage than is possible using currently available methods would contribute much to reducing fatal cases of cancer. DiAcSpm seems a promising candidate for such a marker. Urine samples are easily obtained noninvasively from individuals and are thus suitable test materials for analysis in health examinations. In addition, highly specific anti-DiAcSpm antibody was obtained and a simple procedure to determine urinary DiAcSpm was established and is available (6). For these reasons, we suggest that urinary DiAcSpm be used in health examinations as a sensitive marker for screening cancer patients at early stages.

Actively proliferating cells tend to excrete more polyamines as a result of the activation of intracellular polyamine metabolism and turnover. Vujcic et al. recently reported that MCF-7 breast cancer cells accumulate DiAcSpm together with N^1-acetylspermidine and N^1-acetylspermine on conditional overexpression of spermidine/spermine N^1-acetyltransferase, and that this overexpression leads to growth inhibition of the cells (10). Chen et al. also observed an increase in DiAcSpm level associated with the induction of spermidine/spermine N^1-acetyltransferase in melanoma cell lines treated with polyamine analogues (11). The induction of spermidine/spermine N^1-acetyltransferase stimulates oxidative catabolism of polyamines on the one hand, and excretion of acetylated polyamines on the other, together leading to down-regulate the elevated cellular polyamine level and thus, suppress their uncontrolled growth (12). This may represent a homeostatic mechanism to lower intracellular polyamines under conditions of sustained high levels of ornithine decarboxylase in cancer cells. It is also possible that increased excretion of acetylpolyamines, including DiAcSpm, from cancer cells may be a consequence of a feedback response of rapidly growing cells in the tissues to down-regulate the elevated cellular polyamine level to suppress their uncontrolled growth.

Polyamines excreted into the circulation are once filtered through the glomerular basement membrane in the kidney, but a significant portion of them is soon reabsorbed from the glomerular filtrate into tubular cells and is reused in the body. Monoacetylpolyamines are recovered from the glomerular filtrate and converted by cellular polyamine oxidase to yield free polyamines to replenish the cellular polyamine pool (13). Measurement of polyamine uptake using polarized cultured cells derived from renal proximal tubular cells indicated that monoacetylpolyamines were actively transported into the cells from the apical surfaces, whereas DiAcSpm was not.[7] It is likely that DiAcSpm excreted from cells is recovered in the urine without significant loss, whereas the amount of urinary monoacetylpolyamines is diminished by an indeterminable proportion compared that originally excreted from the cells in the body due to renal reabsorption and reutilization. This may provide a partial explanation of why the urinary level of DiAcSpm reflected the presence of cancer in the body with high sensitivity and at early clinical stages, whereas the urinary levels of monoacetylpolyamines failed to do so.

Mechanisms underlying the increased excretion of DiAcSpm in the urine of cancer patients as well as further clinical significance of urinary DiAcSpm measurement are currently under investigation in our laboratory.

[7] T. Miki, et al., unpublished observation.

References

1. Hiramatsu K, Sugimoto L, Kamei S, et al. Determination of the amounts of polyamines excreted in urine: demonstration of N^1,N^8-diacetylspermidine and N^1,N^{12}-diacetylspermine as components commonly occurring in normal human urine. J Biochem 1994;117:107–12.
2. Sugimoto M, Hiramatsu K, Kamei S, et al. Significance of urinary N^1,N^8-diacetylspermidine and N^1,N^{12}-diacetylspermine as indicators of neoplastic diseases. J Cancer Res Clin Oncol 1995;121:317–9.
3. Hiramatsu K, Sugimoto M, Kamei S, et al. Diagnostic and prognostic usefulness of N^1,N^8-diacetylspermidine and N^1,N^{12}-diacetylspermine in urine as novel markers of malignancy. J Cancer Res Clin Oncol 1997;123:539–45.
4. Bachrach U. Polyamines as markers of malignancy. Prog Drug Res 1992;39:9–33.
5. Tabor CW, Tabor H. 1,4-diaminobutane (putrescine), spermidine, and spermine. Annu Rev Biochem 1976;45:285–306.
6. Hiramatsu K, Miura H, Kamei S, et al. Development of a sensitive and accurate enzyme-linked immunosorbent assay (ELISA) system that can substitute the HPLC analysis for the determination of N^1,N^{12}-diacetylspermine in human urine. J Biochem 1998;124:231–6.
7. Kobayashi M, Samejima K, Hiramatsu K, Kawakita M. Mass spectrometric separation and determination of N^1,N^{12}-diacetylspermine in the urine of cancer patients. Biol Pharm Bull 2002;25:372–4.
8. Berg GA van den, Muskiet FAJ, Kingma AW, Silk W van den, Halie MR. Simultaneous gas-chromatographic determination of free and acetyl-conjugated polyamines in urine. Clin Chem 1986;32:1930–7.
9. Lee SH, Suh JW, Chung BC, Kim SO. Polyamine profiles in the urine of patients with leukemia. Cancer Lett 1998;122:1–8.
10. Vujcic S, Halmekyto M, Diegelman P, et al. Effects of conditional overexpression of spermidine/spermine N^1-acetyltransferase on polyamine pool dynamics, cell growth, and sensitivity to polyamine analogs. J Biol Chem 2000;275:38319–28.
11. Chen Y, Kramer DL, Li F, Poter CW. Loss of inhibitor of apoptosis proteins as a determinant of polyamine analog-induced apoptoses in human melanoma cells. Oncogene 2003;22:4964–72.
12. Casero RA, Pegg AE. Spermidine/spermine N^1-acetyltransferase: the turning point in polyamene metabolism. FASEB J 1993;654:653–61.
13. Seiler N. Functions of polyamine acetylation. Can J Physiol Pharmacol 1987;65:2024–35.

J. Biochem. 138, 479–484 (2005)
doi:10.1093/jb/mvi141

Interaction of N^1,N^{12}-Diacetylspermine with Polyamine Transport Systems of Polarized Porcine Renal Cell Line LLC-PK$_1$

Toshiaki Miki[1], Kyoko Hiramatsu[2] and Masao Kawakita[3,*]

[1]Department of Molecular Physiology and [2]Medical Research and Development Center, The Tokyo Metropolitan Institute of Medical Science, Bunkyo-ku, Tokyo 113-8613; and [3]Department of Applied Chemistry, Kogakuin University, Shinjuku-ku, Tokyo 163-8677

Received May 31, 2005; accepted July 30, 2005

LLC-PK$_1$ cells grown on porous membrane filters were employed as a model system to explore the renal transport of polyamines. The polarity of LLC-PK$_1$ monolayers was confirmed by the exclusive appearance of a Na^+-dependent α-methylglucoside transport system on the apical surface. The uptake of free polyamines from the basolateral side of monolayers was consistent with the existence of a single class of transport system, while the existence of two kinetically distinct polyamine transport systems with higher and lower affinities on apical membranes was suggested. The results of competition studies indicated that each of these transporters was able to interact with putrescine, spermidine and spermine. LLC-PK$_1$ cells incorporated monoacetylspermine from the apical surface of monolayers at about half the rate of spermine uptake. Monoacetylspermine inhibited spermidine uptake, indicating that free polyamine transport systems also recognized the monoacetylated derivative. In contrast, N^1,N^{12}-diacetylspermine did not inhibit spermidine uptake, nor was it incorporated into the cells, indicating the absence of transport systems that recognize N^1,N^{12}-diacetylspermine on the apical membranes of LLC-PK$_1$ cells. These results may be relevant as to our previous observation that the content of diacetylpolyamines in urine is relatively constant, and may explain the excellence of N^1,N^{12}-diacetylspermine as a tumor marker.

Key words: diacetylspermine, polyamine, renal cell, transport, tumor marker.

Abbreviations: DiAcSpm, N^1,N^{12}-diacetylspermine; PBS, phosphate-buffered saline; PCMPS, *p*-chloromercuriphenyl sulfate.

Recently, we developed a highly sensitive analytical system for urinary polyamines based on fractionation by HPLC, and reported that N^1,N^8-diacetylspermidine and N^1,N^{12}-diacetylspermine (DiAcSpm) are found in urine samples from healthy persons as relatively minor but regular constituents (*1*, *2*). Subsequent analysis indicated that these diacetylpolyamines were frequently and markedly increased in the urine of urogenital cancer patients, implying that the urinary level of diacetylpolyamines, DiAcSpm in particular, is useful for the diagnosis of urogenital malignancies (*3*, *4*). More recently, we developed an ELISA system for DiAcSpm determination involving a highly DiAcSpm-specific antibody preparation (*5*, *6*), and further substantiated that DiAcSpm serves as a sensitive and specific novel marker for many cancers including early and late stage colorectal and breast cancers (*7*). Urinary polyamines were first proposed by Russell (*8*) to be potential tumor markers. This evoked a surge of intensive studies, but later studies revealed that the clinical use of the total polyamines or the major urinary polyamine components including acetylputrescine and N^1- and N^8-acetylspermine in the urine as tumor markers is not feasible, since there were too many false negative as well as false positive cases, as judged based on this parameter (*9*).

The sharp increase in the level of DiAcSpm in the urine of cancer patients is not surprising in view of the requirement of polyamines for cell proliferation and activation of polyamine metabolism in rapidly growing tissues (*10*, *11*). However, the reason why only diacetylpolyamines, *i.e.* not monoacetylpolyamines, are highly sensitive and tumor-specific for various types of malignant diseases remains obscure.

To establish the usefulness of DiAcSpm as a tumor marker, it is important to define factors that determine the DiAcSpm content in the urine. One such factor would be the reabsorption of low molecular weight substances at the renal brush border. As a model for the transport systems in the renal brush border we investigated polyamine uptake by polarized monolayers of pig kidney epithelia–derived LLC-PK$_1$ cells. Measurement of polyamine transport using this system revealed that high and low affinity transport systems for free polyamines are expressed on the apical surface of the polarized cells, and that these systems were able to transport monoacetylspermine as well. In contrast, there was no sign of uptake of DiAcSpm by LLC-PK$_1$ cell monolayers. This may partly explain the excellence of DiAcSpm as a tumor marker.

MATERIALS AND METHODS

Materials—[2,3-^{3}H]Putrescine dihydrochloride (1,493 GBq/mmol) and [1,8-^{3}H]spermidine trihydrochloride

*To whom correspondence should be addressed. Tel: +81-3-3340-2731; Fax: +81-3-3340-0147; E-mail: bt13004@ns.kogakuin.ac.jp

(781 GBq/mol) were obtained from DuPont NEN (Boston, MA, USA). Methyl(α-D-[*U*-^{14}C]gluco)pyranoside (10.8 GBq/mol) was purchased from Amersham International. [1,10-^{3}H]Spermine tetrahydrochloride (1,480 GBq/mol) was a product of American Radiolabeled Chemicals Inc. (St. Louis, MO, USA). [1,12-^{3}H]N^{1},N^{12}-diacetylspermine (2.0 GBq/mol) was a kind gift from Dr. A. Shirahata at Jyosai University. [^{3}H]Monoacetylspermine was prepared by partial deacetylation of [^{3}H]diacetylspermine with acylpolyamine amidohydrolase, and subsequently purified by HPLC on an ODP column using 0.1 M phosphate buffer (pH 7.0) (*1*) . Other chemicals used were of the highest grade commercially available.

Cell Culture—LLC-PK$_1$ cells were obtained from the American Type Culture Collection (ATCC CRL-1392) and grown in Dulbecco's modified Eagle's medium supplemented with 10% fetal calf serum supplied by JRH Bioscience (Lenexa, KS, USA), 0.1 mg of streptomycin/ml, and 100 units of penicillin/ml. For uptake studies, the cells were seeded on collagen-coated membrane filters (3 μm pores, 4.71-cm^{2} growth area) placed in a Transwell cell culture chamber (Coster, Cambridge, MA, USA) at a cell density of 1–2 × 10^{6} cells/filter. The cell monolayers were fed with fresh medium every 2 days, and usually used on the 6th or 7th day for the uptake studies. At this stage, the cell monolayers showed transepithelial electrical resistance ranging from 230 to 320 Ω/cm^{2}, as measured by Millicell-EPR (Millipore, Bedford, MA, USA).

Uptake Assay—For measurement of polyamine uptake in LLC-PK$_1$ cells grown on filters, both sides of a monolayer were washed twice with phosphate-buffered saline (PBS; 140 mM NaCl, 2.7 mM KCl, 8.1 mM Na_2HPO_4, 1.5 mM KH_2PO_4, 1 mM $CaCl_2$, and 0.5 mM $MgCl_2$), and then the cells were preincubated in PBS for 10 min at 37°C prior to uptake assays. Uptake was started by adding a ^{3}H-labelled polyamine substrate in PBS (2 ml) to either the apical or basolateral side of the monolayer. The monolayer was incubated at 37°C for the indicated time under a normal atmosphere. The medium was then removed, and the cells were washed twice with ice-cold PBS containing 0.1 mM of the unlabelled substrate polyamine. After the filter with the monolayer had been removed from the chamber, the cells were solubilized in 0.4 ml of 1 N NaOH at 70°C for 30 min. Following the addition of 0.1 ml of 4 N HCl, radioactivity was measured with a liquid scintillation counter. Protein was quantitated by the method of Bradford (*12*). In the case of Na^{+}-dependent α-methylglucoside uptake, 50 μM methyl(α-D-[*U*-^{14}C]gluco)pyranoside in PBS was added to either the apical or basolateral side. In Na^{+}-free medium, NaCl and Na_2HPO_4 in PBS were replaced with the same concentrations of choline chloride and K_2HPO_4.

For determination of the kinetic parameters of polyamine uptake, the polyamine concentration was varied by adding increasing concentrations of a non-radioactive substrate polyamine to a fixed amount of the tritium-labelled substrate polyamine. The Michaelis constant (K_m) and maximum velocity were determined by Eadie-Hofstee analysis. Competition for polyamine uptake was measured by adding increasing concentrations of competing polyamines in the presence of a fixed amount of [^{3}H]putrescine or [^{3}H]spermidine.

RESULTS

Polarity of LLC-PK$_1$ Cells as Assessed by the Na^{+}-Dependent Glucose Transporting Activity—A confluent LLC-PK$_1$ monolayer grown on a microporous membrane filter should exhibit polarity with the apical surface facing the upper compartment and the basolateral surface facing the lower compartment (*13*). To establish the validity of our experimental system as a model for renal epithelia, we measured the activity of Na^{+}-dependent glucose transporter on both sides of a monolayer (Fig. 1). This transporter serves as an appropriate marker for the apical surface judging from previous results obtained with this cell line (*14*). When 50 μM α-methyl-D-glucoside was placed on the apical side, LLC-PK$_1$ cells took up the glucose analogue at a rate of 20.7 nmol/mg protein/hr in the presence of Na^{+}, but not at all in its absence (0.43 nmol/mg protein/h). The uptake of the glucose analogue from the basolateral side in the presence and absence of Na^{+} was 0.29 and 0.19 nmol/mg protein/h, respectively. These results indicate that a LLC-PK$_1$ monolayer exhibits the expected polarity with the preferential localization of Na^{+}-dependent glucose transporter on the apical surface. The maximal rate of the Na^{+}-dependent uptake of α-methyl-D-glucoside from the apical side was attained on the 4th day after seeding and was still maintained on the 10th day (data not shown).

Time Course of Polyamine Uptake by a LLC-PK$_1$ Monolayer—Figure 2 shows the characteristics of putrescine and spermidine uptake by polarized LLC-PK$_1$ cells. The cells took up both substrates from both the apical and basolateral sides at 37°C in a time-dependent manner. Lowering of the temperature to 6°C greatly redued the uptake of polyamines.

Kinetics of Polyamine Uptake by Polarized LLC-PK$_1$ Cells—To define kinetic parameters for putrescine and spermidine uptake by LLC-PK$_1$ monolayers, cells were incubated with increasing concentrations of these polyamines. As shown in Fig. 3A, Eadie-Hofstee analysis of putrescine uptake from the basolateral side gave a straight

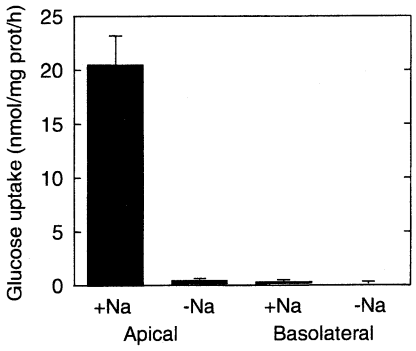

Fig. 1. **Uptake of α-methyl-D-glucose by LLC-PK$_1$ monolayers.** LLC-PK$_1$ cells were grown to confluence on collagen-coated filters. On the 6th day after seeding the cells were preincubated in PBS or Na^{+}-free medium at 37°C for 10 min, and then 50 μM α-methyl-D-[^{14}C]glucoside was added to either the apical or basolateral side in the presence and absence of Na^{+}. The uptake of α-methyl-D-[^{14}C]glucoside was measured as described under "MATERIALS AND METHODS" after incubation at 37°C for 1 h. Each column represents the mean ± SE for 4 independent measurements.

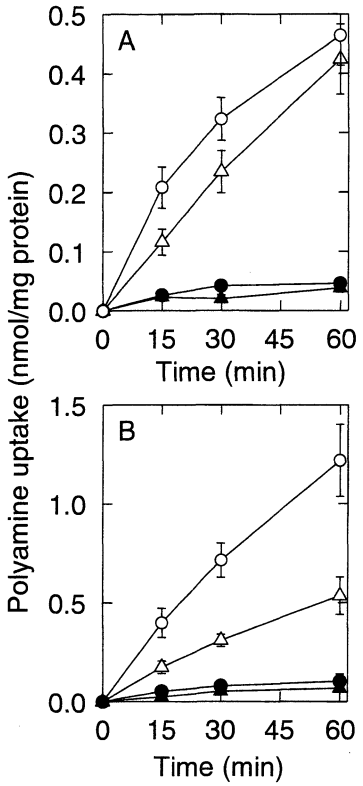

Fig. 2. **Time- and temperature-dependent uptake of spermidine and putrescine by polarized LLC-PK$_1$ cells.** LLC-PK$_1$ monolayers were incubated with 5 μM [^{3}H]putrescine (A) or 5 μM [^{3}H]spermidine (B) in PBS added to either the apical (open circles, solid circles) or basolateral side (open triangles, solid triangles) at 37°C (open circles, open triangles) or 6°C (solid circles, solid triangles). Cellular polyamine uptake was determined at the times indicated as described under "MATERIALS AND METHODS." Each point represents the mean ± SE for 3 experiments.

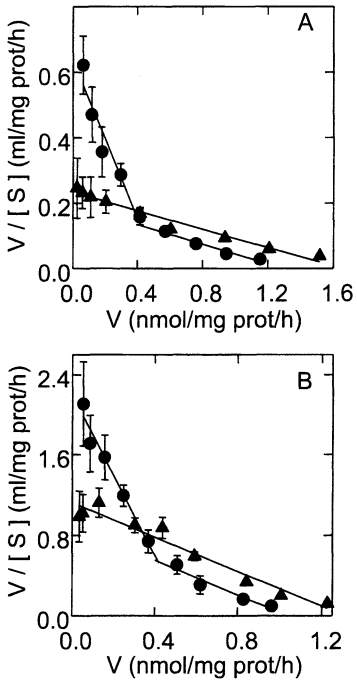

Fig. 3. **Eadie-Hofstee analysis of putrescine and spermidine uptake by polarized LLC-PK$_1$ cells.** LLC-PK$_1$ monolayers were incubated at 37°C for 30 min with various concentrations of [^{3}H]putrescine (A) or [^{3}H]spermidine (B) added to either the apical (solid circles) or basolateral side (solid triangles) of the monolayers Other conditions were as in Fig. 2. Each point represents the mean ± SE for 3 experiments.

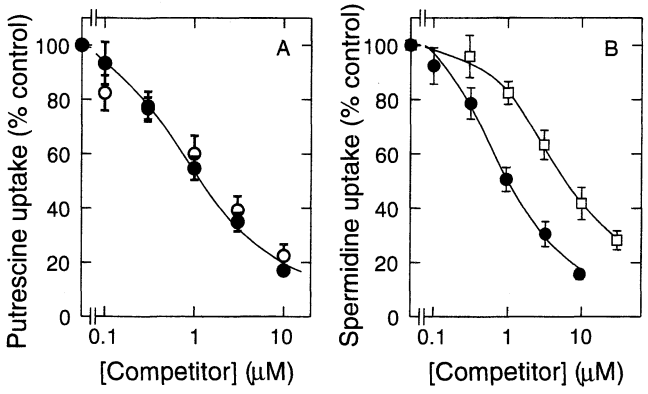

Fig. 4. **Specificity of putrescine and spermidine uptake by polarized LLC-PK$_1$ cells.** The uptake of 0.1 μM [^{3}H]putrescine (A) or 0.1 μM [^{3}H]spermidine (B) from the apical side of monolayers was measured in the presence of increasing concentrations of putrescine (open squares), spermidine (open circles), or spermine (solid circels). Other conditions were as in Fig. 3. Each point represents the mean ± SE for 3 independent experiments.

line characterized by single K_m and V_{max} values of 14 μM and 3.3 nmol/mg protein/h, respectively, which is consistent with the existence of a single class of transporter. In contrast, uptake of putrescine from the apical side was biphasic, suggesting the interaction of putrescine with two sites. The K_m and V_{max} values for the high and low affinity sites were estimated to be 2.3 μM and 1.1 nmol/mg protein/h, and 13 μM and 2.6 nmol/mg protein/h, respectively. Spermidine was also accumulated in the cells, the kinetic features being similar to as for putrescine (Fig. 3B), but the K_m values for spermidine were much lower than those for putrescine. K_m and V_{max} for basolateral uptake of spermidine were 2.3 μM and 2.6 nmol/mg protein/h, respectively. As to apical uptake, K_m and V_{max} were determined to be 0.52 μM and 1.1 nmol/mg protein/h for the high affinity site, and 2.3 μM and 2.1 nmol/mg protein/h for the low affinity site, respectively. The kinetic characteristics of spermine uptake by LLC-PK$_1$ monolayers were very similar to those for spermidine (data not shown), for which K_m = 2.5 μM and V_{max} = 2.9 nmol/mg protein/h for basolateral uptake, and K_m = 0.60 μM and V_{max} = 1.2 nmol/g protein/h for the high affinity site and K_m = 2.0 μM and V_{max} = 2.4 nmol/mg protein/h for the low affinity site for the apical uptake system.

Specificity of Polyamine Uptake by Polarized LLC-PK$_1$ Cells—The substrate specificity of the putrescine and spermidine uptake systems was assessed by analysis of the competition by other polyamine species (Fig. 4). When putrescine uptake was measured in the presence of increasing concentrations of spermidine or spermine, the uptake of putrescine from the apical side of the monolayers was inhibited by these polyamines (Fig. 4A). Spermidine uptake

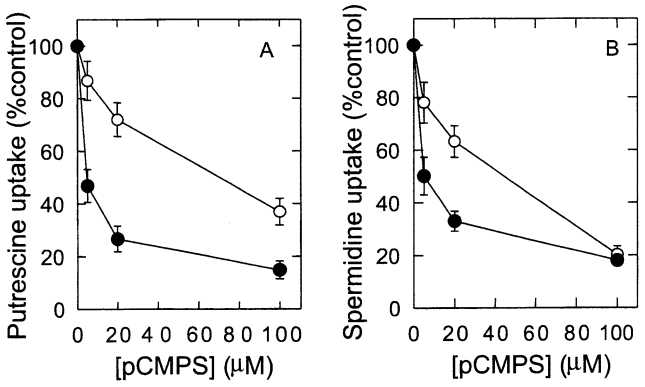

Fig. 5. **Inhibition of putrescine and spermidine uptake by PCMPS in polarized LLC-PK$_1$ cells.** LLC-PK$_1$ cells were preincubated with the indicated concentrations of PCMPS dissolved in PBS at 37°C for 10 min prior to the uptake assay. After washing the cells with PBS, 0.1 μM [^{3}H]putrescine (A) or 0.1 μM [^{3}H]spermidine (B) was added to either the apical (open circles) or basolateral (solid circles) side of the monolayers. Polyamine uptake was determined after incubation at 37°C for 30 min as described under "MATERIALS AND METHODS." Each point represents the mean ± SE for 3 experiments.

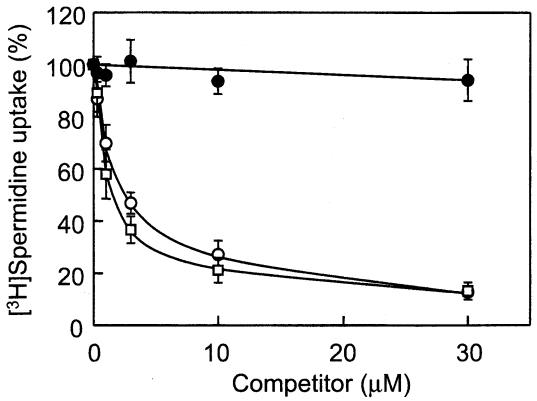

Fig. 6. **Effects of spermine and its acetylated derivatives on spermidine uptake by polarized LLC-PK$_1$ cells.** The uptake of 0.1 μM [^{3}H]spermidine from apical membranes was assayed in the presence of increasing concentrations of spermine (open squares), monoacetylspermine (open circles), or diacetylspermine (solid circles). Other conditions were as in Fig. 4. Each point represents the mean ± SE for 3 experiments.

from the apical surface also decreased in the presence of putrescine or spermine (Fig. 4B). The uptake of putrescine and spermidine from the basolateral surface was similarly affected mutually and also by spermine to that from the apical surface (data not shown). These results indicate that a common transport system(s) is present for the uptake of putrescine, spermidine, and spermine in the apical and basolateral membranes of LLC-PK$_1$ cells. Putrescine and spermidine uptake were inhibited by other polyamines in lower concentration ranges on the apical side than on the basolateral side, indicating the presence of a transport system with higher affinity for polyamines on the apical side. This is consistent with the data obtained in the kinetic study on polyamine transport shown above and in Fig. 3.

Effect of PCMPS on the Polyamine Uptake by Polarized LLC-PK$_1$ Cells—Figure 5 shows the effect of *p*-chloromercuriphenyl sulfate (PCMPS) on polyamine uptake by polarized LLC-PK$_1$ cells. The basolateral uptake of polyamines was inhibited by 50% with about 5 μM PCMPS, while the polyamine transport system on the apical side was much less sensitive to PCMPS. These results indicate that a polyamine transport system with lower sensitivity to PCMPS is present in the apical membranes of LLC-PK$_1$ cells. The transport system with lower PCMPS sensitivity likely represents the high affinity transport system, because polyamine uptake *via* the low affinity system constitutes only 20–30% of total polyamine uptake from the apical surface under the experimental conditions used in Fig. 5. The partial but significant inhibition of apical spermidine transport noted at a PCMPS concentration as low as 5 μM may represent the contribution by the low affinity transport system.

Uptake of Acetylated Derivatives of Spermine by LLC-PK$_1$ Cells—Figure 6 shows the effects of acetylated derivatives of spermine on the uptake of spermidine across the apical membranes of polarized LLC-PK$_1$ cells. Acetylspermine and spermine inhibited the uptake of spermidine from the apical side, suggesting their interaction with the spermidine transport systems in the apical membranes.

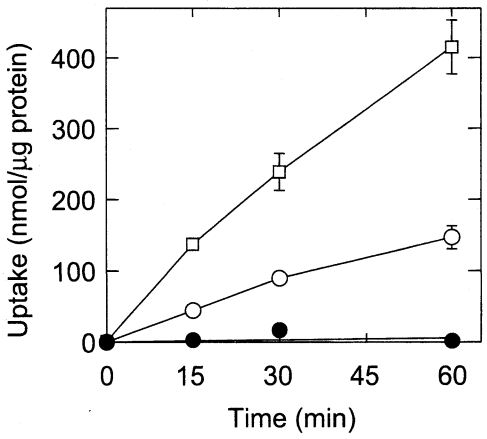

Fig. 7. **Time course of uptake of spermine and its acetylated derivatives by polarized LLC-PK$_1$ monolayers.** The uptake of 1.0 μM [^{3}H]spermine (open squares), [^{3}H]monoacetylspermine (open circles), and [^{3}H]diacetylspermine (solid circles) from apical membranes was assayed as described in Fig. 2. Each point represents the mean ± SE for 2 experiments.

We estimated K_i values for acetylspermine, assuming two competition sites in the apical transport system. They were 0.49 μM and 3.6 μM for the apical uptake systems, which were comparable to the K_m values of the apical transport systems for spermine. In contrast, DiAcSpm did not affect the spermidine uptake at all, indicating a lack of its interaction with these spermidine transport systems.

Figure 7 shows the time course of the uptake of mono- and diacetylspermine into polarized LLC-PK$_1$ cells from the apical membranes. Monoacetylspermine was taken up from the apical side of LLC-PK$_1$ monolayers, although the rate of uptake was about half that of spermine. Its uptake was temperature-sensitive, being more than 10 times lower at 6°C than at 37°C (data not shown). These results together with those in Fig. 6 indicate that monoacetylspermine is incorporated into LLC-PK$_1$ cells through transport systems that are common to free polyamines. In contrast, the uptake of DiAcSpm was not observed at

all, indicating the absence of a transport system that can carry DiAcSpm into the cytoplasm of LLC-PK$_1$ cells.

DISCUSSION

Polarized monolayers of LLC-PK$_1$ cells cultured on membrane filters were utilized as a model for the polyamine transport systems in renal epithelia. Using radiolabeled putrescine and spermidine as substrates, we were able to show the existence of one and two kinetically distinguishable transport systems on the basolateral and apical surfaces of the monolayers, respectively. Each of these transport systems was shown to interact with putrescine, spermidine and spermine as mutually competing transport substrates, judging from the results of competition experiments. The low affinity transport systems in the apical and basolateral membranes seem to be identical or closely similar judging from their K_m and V_{max} values for these three polyamine species.

Polyamine transport in mammalian cells has long been a matter of considerable interest (*15*), but attempts to identify the polyamine transporter genes in mammals have not yet been successful. Previous studies involving polarized cultures of LLC-PK$_1$ cells indicated the existence of Na^+-dependent and Na^+-independent polyamine transport systems in these cells (*16–18*). The former was inhibited by a low concentration of PCMPS, while the latter was relatively insensitive to PCMPS. In view of these reports it is tempting to assume that the uptake of polyamines from the basolateral surface is mainly carried out by a PCMPS-sensitive Na^+-dependent transporter, while the apical polyamine transport is due to both types of transporters. However, previous studies indicated that the Na^+-dependent polyamine transport system exhibits higher affinity for polyamines than the Na^+-independent system. We carried out the present polyamine transport study in the presence of 140 mM NaCl so that all polyamine transport systems present in the membranes were operating while we were examining the capacity of cellular polyamine transport systems to recognize polyamine conjugates including DiAcSpm. The identity of the PCMPS-sensitive basolateral polyamine transporter with lower affinity with the Na^+-sensitive polyamine transporter reported in the literature thus remains to be seen.

The most important finding in this study is that DiAcSpm did not inhibit any polyamine transport system expressed in the apical membranes of LLC-PK$_1$ cell monolayers, nor was it incorporated into the cells. In contrast, monoacetylspermine was able to interact with cellular polyamine transporters with an affinity almost as high as that of spermine, and was transported into the cells. This implies that renal brush border membranes may incorporate relatively low concentrations of unconjugated and monoacetylated polyamine species through their high affinity transport system, but are unable to transport DiAcSpm.

Polyamines excreted from various organs and tissues into the circulation are filtered through the glomerular basement membrane in the kidney, but a significant portion of monoacetylpolyamines as well as unconjugated polyamines is soon reabsorbed from the glomerular filtrate into tubular cells through polyamine transport systems as described above, and converted to free polyamines by cellular polyamine oxidase to be reutilized in the body (*19*). The present results indicate that this reabsorption route is not available for DiAcSpm. It is therefore likely that DiAcSpm excreted from cells in the body is recovered in the urine without significant loss, while the amount of urinary monoacetylpolyamines decreases by an unknown amount compared to that originally excreted from the cells due to renal reabsorption and reutilization. This may partially explain why the urinary level of DiAcSpm reflects the presence of cancer in the body with high sensitivity and at early clinical stages (*7*), while the urinary levels of monoacetylpolyamines do not (*3*, *4*).

REFERENCES

1. Hiramatsu, K., Kamei, S., Sugimoto, M., Kinoshita, K., Iwasaki, K., and Kawakita, M. (1994) An improved method of determining free and acetylated polyamines by HPLC involving an enzyme reactor and an electrochemical detector. *J. Biochem.* **115**, 584–589
2. Hiramatsu, K., Sugimoto, M., Kamei, S., Hoshino, M., Kinoshita, K., Iwasaki, K., and Kawakita, M. (1995) Determination of amounts of polyamines excreted in urine: demonstration of N^1,N^8-diacetylspermidine and N^1,N^{12}-diacetylspermine as components commonly occurring in normal human urine. *J. Biochem.* **117**, 107–112
3. Sugimoto, M., Hiramatsu, K., Kamei, S., Kinoshita, K., Hoshino, M., Iwasaki, K., and Kawakita, M. (1995) Significance of urinary N^1,N^8-diacetylspermidine and N^1,N^{12}-diacetylspermine as indicators of neoplastic diseases. *J. Cancer Res. Clin. Oncol.* **121**, 317–319
4. Hiramatsu, K., Sugimoto, M., Kamei, S., Hoshino, M., Kinoshita, K., Iwasaki, K., and Kawakita, M. (1997) Diagnostic and prognostic usefulness of N^1,N^8-diacetylspermidine and N^1,N^{12}-diacetylspermine in urine as novel markers of malignancy. *J. Cancer Res. Clin. Oncol.* **123**, 539–545
5. Hiramatsu, K., Miura, H., Sugimoto, K., Kamei, S., Iwasaki, K., and Kawakita, M. (1997) Preparation of antibodies specific to N^1,N^8-diacetylspermidine and development of an enzyme-linked immunosorbent assay (ELISA) system for its sensitive detection. *J. Biochem.* **121**, 1134–1138
6. Hiramatsu, K., Miura, H., Kamei, S., Iwasaki, K., and Kawakita, M. (1998) Development of a sensitive and accurate enzyme-linked immunosorbent assay (ELISA) system that can replace HPLC analysis for the determination of N^1,N^{12}-diacetylspermine in human urine. *J. Biochem.* **124**, 231–236
7. Hiramatsu, K., Takahashi, K., Yamaguchi, T., Matsumoto, H., Miyamoto, H., Tanaka, S., Tanaka, C., Tamamori, Y., Imajo, M., Kawaguchi, M., Toi, M., Mori, T., and Kawakita, M. (2005) N^1,N^{12}-diacetylspermine as a sensitive and specific novel marker for early and late stage colorectal and breast cancers. *Clin. Cancer Res.* **11**, 2986–2990
8. Russell, D.H. (1971) Increased polyamine concentrations in the urine of human cancer patients. *Nature New Biol.* **233**, 144–145
9. Bachrach, U. (1992) Polyamines as markers of malignancy. *Prog. Drug Res.* **39**, 9–33
10. Pohjanpelto, P., Hölttä, E., and Jänne, O.A. (1985) Mutant strain of Chinese hamster ovary cells with no detectable ornithine decarboxylase activity. *Mol. Cell. Biol.* **5**, 1385–1390
11. Tabor, C.W. and Tabor, H. (1984) Polyamines. *Annu. Rev. Biochem.* **53**, 749–790
12. Bradford, M.M. (1976) A rapid and sensitive method for the quantitation of microgram quantitites of protein utilizing the principle of protein-dye binding. *Anal. Biochem.* **72**, 248–254
13. Saito, H., Yamamoto, M., Inui, K., and Hori, R. (1992) Transcellular transport of organic cation across monolayers of kidney epithelial cell line LLC-PK$_1$. *Am. J. Physiol.* **262**, C59–66

14. Mullin, J. M., Weibel, J., Diamond, L., and Kleinzeller, A. (1980) Sugar transport in the LLC-PK_1 renal epithelial cell line: similarity to mammalian kidney and the influence of cell density. *J. Cell. Physiol.* **104**, 375–389
15. Seiler, N., Delcros, J.G., and Molinoux, J.P. (1996) Polyamine transport in mammalian cells. An update. *Int. J. Biochem. Cell Biol.* **28**, 843–861
16. Hauser, M.R. and Cook, J.S. (1990) Uptake and metabolism of putrescine in confluent LLC-PK_1 cells. *Am. J. Physiol.* **259**, C84–91
17. De Smedt, H., Van den Bosch, L., Geuns, J., and Borghgraef, R. (1989) Polyamine transport systems in the LLC-PK1 renal epithelial established cell line. *Biochim. Biophys. Acta* **1012**, 171–177
18. Van Den Bosch, L., De Smedt, H., Missiaen, L., Parys, J.B., and Borghgraef, R. (1990) Transport systems for polyamines in the established renal cell line LLC-PK_1. *Biochem. J.* **265**, 609–612
19. Seiler, N. (1987) Functions of polyamine acetylation. *Can. J. Physiol. Pharmacol.* **65**, 2024–2035

JB Minireview—Polyamines

J. Biochem. **139**, 315–322 (2006)
doi:10.1093/jb/mvj068

Diacetylated Derivatives of Spermine and Spermidine as Novel Promising Tumor Markers

Masao Kawakita[1,*] and Kyoko Hiramatsu[2]

[1]Department of Applied Chemistry, Kogakuin University, 1-24-2 Nishi-shinjuku, Shinjuku-ku, Tokyo 163-8677; and [2]Tumor Therapy Project, Tokyo Metropolitan Institute of Medical Science, 3-18-22 Hon-komagome, Bunkyo-ku, Tokyo 113-8613

Received January 20, 2006; accepted February 6, 2006

N^1,N^{12}-diacetylspermine (DiAcSpm) and N^1,N^8-diacetylspermidine (DiAcSpd) are minor components of human urinary polyamine to which little attention has been paid until recently. HPLC analysis of urinary polyamines has revealed that the excretion of these diacetylpolyamines, in particular, into urine was frequently and markedly increased in association with every type of cancer so far examined. Remission was usually accompanied by recovery of urinary diacetylpolyamines to the normal level. DiAcSpm was more sensitive than CEA for detecting colorectal cancer patients, while DiAcSpd was highly specific for malignant conditions in that the excretion of the latter was scarcely elevated in cases of benign urogenital diseases. An ELISA procedure for rapid determination of DiAcSpm was developed to promote the clinical application of these new tumor markers, and subsequent studies indicated that DiAcSpm was elevated in 60% of colorectal cancer patients at early stages (stage 0 + I), whereas only 10% of these patients were CEA-positive. DiAcSpm may also be useful as a follow-up marker that is efficient for detecting recurrence and sensitive to changes in the clinical condition of patients. The evidence accumulated so far indicates that DiAcSpm and DiAcSpd are promising novel tumor markers. They deserve more intensive studies, including studies of their biochemistry and metabolism.

Key words: cancer diagnosis, diacetylspermidine, diacetylspermine, tumor marker, urine.

Diacetylpolyamines, what are they?

N^1,N^{12}-Diacetylspermine (DiAcSpm) and N^1,N^8-diacetylspermidine (DiAcSpd) are the least studied among the polyamine species that occur in human urine. They have a number of attractive features as diagnostic and prognostic indicators of malignant states, but unfortunately were discovered too late (*1*, *2*), only after the big tide of research on polyamines as tumor markers had almost ebbed away by the end of 1980's. For this reason they have failed so far to gain due interest even among clinical chemists involved in tumor marker study. This article aims to summarize the current status of diacetylpolyamine study, so that a wide audience can properly recognize the potential usefulness of this tumor marker.

Polyamines are alkylamines with multiple amino groups and are ubiquitous among both eukaryotic and prokaryotic cells. Putrescine, cadaverine, spermidine, spermine, and their acetylated derivatives are among most abundant organic polycations in the human body and are thought to fulfill multiple functions in biological processes (for review, see Refs. *3* and *4*). *Di*acetylated polyamine derivatives, N^1,N^8-diacetylspermidine (DiAcSpd) and N^1,N^{12}-diacetylspermine (DiAcSpm), which are featured in this article, are derivatives of spermidine and spermine, respectively, in which both of the primary amino groups are acetylated. In the past, these diacetylated derivatives did not receive much research attention since they were not detected by conventional methods, as explained later in this article.

Polyamines and their metabolism are supposed to be intimately involved in the process of cell multiplication and its regulation, although the details of their functions have not been fully elucidated in spite of extensive studies (*5*, *6*). Thus, exogenously added polyamines are indispensable for mutant cells defective in polyamine synthesis to grow in culture, and overexpression of ornithine decarboxylase, the key enzyme in polyamine biosynthesis, led to transformation of NIH 3T3 cells (*7*). Rapidly growing tissues usually have active polyamine synthesizing systems and contain large amounts of polyamines. Polyamine excretion in the urine may rise when such tissues are present in the body, as a result of either increased secretion from the proliferating cells themselves, or of release from dead cells that increase in number as a consequence of the active replacement of cells in growing tissues. In fact, Russell (*8*) reported in 1971 that the amount of polyamines excreted in urine was higher in patients with cancer than in healthy persons. This evoked a surge of studies on polyamine analysis that were intended to answer the question of whether the level of polyamines in urine could serve as indicators of malignant diseases.

There seemed to be sound reasons for expecting an increased excretion of polyamines in urine as a consequence of uncontrolled proliferation of cancer cells,

*To whom correspondence should be addressed. Phone: +81-3-3340-2731, Fax: 81-3-3340-0147, E-mail: bt13004@ns.kogakuin.ac.jp

because of the close relationship between cell growth and polyamine metabolism as described above, but the results obtained were, on the whole, rather disappointing. It was once claimed that the amount of N^1-acetylspermidine (N^1-AcSpd) and the ratio of N^1-AcSpd to N^8-acetylspermidine (N^8-AcSpd) were increased in cases of malignant diseases and that these polyamines might serve as tumor markers (*9*, *10*). However, the performance of these indicators was too poor for practical application because there were too many false negative as well as false positive cases due to large individual variations in polyamine excretion, and also because benign disorders were often found to be associated with considerable increases in urinary polyamine levels. The accumulated evidence, therefore, seemed to indicate that *free* and *mono*acetylated polyamines in urine were of little practical use as tumor markers, even though their average urinary levels are certainly higher in patients with cancer than in healthy persons (*11*). The tide of polyamine research as tumor markers was thus waning when we encountered the *di*acetylated derivatives of spermidine and spermine, namely, DiAcSpd and DiAcSpm (*1*).

At this point, a brief introductory description of diacetylpolyamines would be pertinent to convince the reader that they do have attractive features as tumor markers that are distinct from those of monoacetylpolyamines. The latter had been extensively studied so far, but were finally shown not to have practical value as tumor markers. Polyamines are excreted in human urine mainly as monoacetylpolyamines. Acetylputrescine (AcPut) is the most abundant urinary polyamine, constituting 43% of total polyamines, followed by acetylcadaverine, N^1-AcSpd and N^8-AcSpd in decreasing order. Diacetylpolyamines represent minor polyamine species in human urine. The average amounts of DiAcSpd and DiAcSpm are only approximately 1.4 and 0.46%, respectively, of total polyamines, but their CV values are very small, taking their low content into account (*1*). This indicates that variation of these diacetylpolyamines in urine is very small from one individual to another, and may imply that they are secreted in a highly controlled manner.

The amounts of individual polyamine components in urine were compared among healthy persons and patients with benign or malignant urogenital diseases (Fig. 1). The amounts of total polyamines, acetylputrescine and N^8-AcSpd were not significantly increased in a number of cancer patients as compared to those in healthy controls, while N^1-AcSpd was often elevated substantially even in cases of benign diseases. This is consistent with the orthodox judgement about urinary polyamines that they cannot be useful as practical tumor markers (*12*, *11*). In contrast, DiAcSpm was sensitive for detecting cancer patients in that it increased markedly in about 80% of patients with cancer, reaching as high as 150 times the normal limits, while DiAcSpd was highly specific for cancer in that it was elevated only marginally in cases of benign diseases (*2*). This strongly suggested that *di*acetylpolyamines but *not* monoacetylpolyamines would serve as novel tumor markers, and these early observations prompted us to perform further studies of diacetylpolyamines.

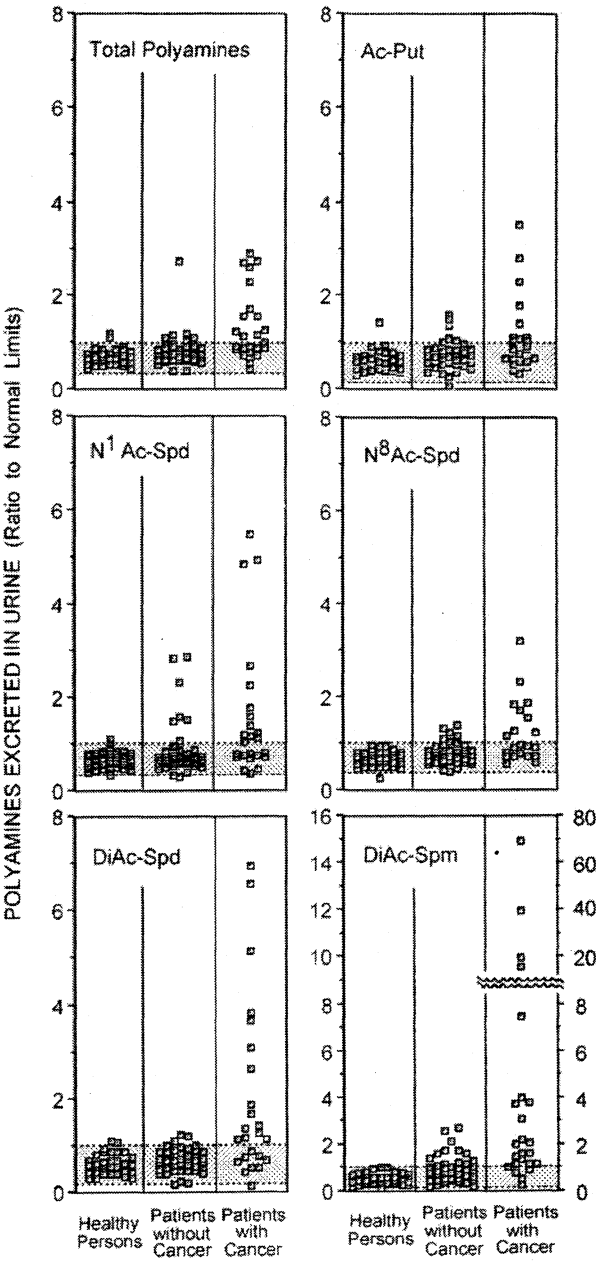

Fig. 1. **Polyamines excreted in urine of healthy persons and patients with benign or malignant urogenital diseases.** Shaded areas represent the mean ± 2 SD for healthy persons. Mean (SD) values (μmol/g creatinine) for healthy persons are as follows: total polyamines 22.2 (6.1), acetylputrescine (Ac-Put) 9.6 (3.5), N^1-acetylspermidine (N^1Ac-Spd) 2.7 (0.8), N^8-acetylspermidine (N^8Ac-Spd) 2.4 (0.6), diacetylspermidine (DiAc-Spd) 0.30 (0.11), diacetylspermine (DiAc-Spm) 0.10 (0.047). (With permission, Sugimoto *et al.*, *J. Cancer Res. Clin. Oncol.*, **121**, 317, Copyright 1995: Springer Verlag)

Simultaneous detection and determination of polyamine components including diacetylpolyamines

Several methods were reported so far in the literature to determine the amounts of diacetylpolyamines in biological fluids and tissues. It should be noted that conventional

polyamine detection systems utilizing primary amino groups for post-column derivatization of polyamine components (*13*) are unsuitable for detection of diacetylpolyamines which lack primary amino groups.

Gas chromatography with nitrogen phosphorus detection was used by van den Berg *et al.* to detect DiAcSpm in five arbitrarily selected patients with stage III and IV non-Hodgkin's lymphoma (*14*). This was the first report that described the occurrence of DiAcSpm in human body fluid, but the correlation between DiAcSpm and cancer was not pursued further by the Dutch group. Their analysis failed to detect DiAcSpm in the urine of healthy persons and they did not describe the occurrence of DiAcSpd either.

Diacetylpolyamines can also be determined by fractionation with HPLC connected to an enzymatic detection system (*1*). In this system, urine samples pretreated with a cation exchange resin to remove interfering substances were applied to a polymer-based C18-column and polyamine components were eluted with phosphate buffer. Polyamines separated by HPLC were introduced into an enzyme reactor composed of three successive small columns of immobilized enzymes, namely acylpolyamine deacylase (DAL), polyamine oxidase (PAO) and putrescine oxidase (PUO). In this enzyme reactor, acetylated polyamines were first deacetylated and then oxidized to generate H_2O_2 that was then quantitated by an electrochemical detector. In this way, all the polyamine components naturally occurring in human urine may be determined precisely and simultaneously (*15*). This procedure was sensitive enough to detect DiAcSpm and DiAcSpd in the urine of healthy persons, and further led us to the finding that these diacetylated polyamine species, but not monoacetylated polyamines, are frequently and sometimes markedly increased in cancer patients, as described in the preceding section. Unfortunately, however, these enzymes are now unavailable commercially, for companies that used to distribute these enzymes have ceased their production. More recently, a procedure was developed that fractionates dansylated polyamines by HPLC using a C18 column (*16*, *17*). This procedure allowed the fractionation and detection of diacetylated polyamines. Polyamine components including DiAcSpm may also be determined by ionspray ionization-mass spectrometry (IS-MS) after heptafluorobutyryl derivatization (*18*).

Development of diacetylpolyamine-specific antibodies and immunochemical determination of diacetylpolyamines

Simultaneous determination of urinary polyamines clearly indicated that only diacetylpolyamines (DiAcSpm and DiAcSpm), but not monoacetylpolyamines, had very attractive features that deserved further examination regarding whether they were useful as novel tumor markers. To open pathways leading to clinical applications of diacetylpolyamines, it was necessary to devise a reliable procedure for the determination of DiAcSpm and DiAcSpd that is simpler and more convenient than HPLC analysis, since the latter is too time-consuming to be useful in clinical practice.

An enzyme-linked immunosorbent assay (ELISA) procedure involving specific antibodies was thus developed. Antibodies used in the immunochemical determination of DiAcSpm needed to be highly specific for this component. Human urine usually contains N^1-AcSpd in amounts that are in approximately 30-fold molar excess of DiAcSpm (*1*). This implies that the cross-reactivity of N^1-AcSpd with DiAcSpm should be less than 0.1% in order to keep the overestimation of urinary DiAcSpm due to contaminating N^1-AcSpd less than 10%. Polyclonal antibodies were raised in rabbits by immunization with a carefully designed hapten-BSA conjugate. In this conjugate monoacetylspermine (AcSpm) was coupled to the protein carrier *via* a cross-linker, γ-maleimidobutyryloxysuccinimide, to form an acylamide linkage between the primary amino group of AcSpm and the butyryl group of the cross-linker (*19*). This gave a hapten structure that closely mimics the structure of DiAcSpm. The rabbit antiserum obtained through immunization with this antigen showed much better preference for DiAcSpm as compared to antipolyamine antibodies reported in the literature, with cross-reactivity with N^1-AcSpd of about 5–6%, but still failed to meet the requirement for the specificity of an antibody to be used in the determination of urinary DiAcSpm. Antibodies highly specific for DiAcSpm, with cross-reactivity with N^1-AcSpd as low as 0.03%, were eventually obtained from this antiserum through several steps of affinity purification (*19*). In the final step of this purification, DiAcSpm-specific antibodies were adsorbed on an affinity resin containing DiAcSpm-mimicking ligands, and the fraction of the adsorbed antibodies that remained bound to the affinity resin after elution with N^1-AcSpd was recovered as the final preparation of DiAcSpm-specific antibody.

A competitive ELISA system for DiAcSpm was developed using this antibody preparation. The system was sensitive enough to allow accurate determination of DiAcSpm at concentrations that are usually excreted in healthy human urine. DiAcSpm concentrations in urine determined by this procedure correlated very well with those obtained by HPLC analysis (*19*). The development of more convenient procedures for determining DiAcSpm using specific antibodies which are adapted for automatic analytical apparatus is currently being attempted.

Monoclonal antibodies specific for diacetylpolyamines were also reported, but their specificity did not seem to be sufficient for use in the determination of urinary DiAcSpm and DiAcSpd (*20*, *21*). Very recently, success in the production of a monoclonal anti-DiAcSpm antibody that was highly specific for DiAcSpm was announced by a company.

DiAcSpd-specific polyclonal antibodies were also prepared (*22*), but procedures for determining the urinary DiAcSpd level using these antibodies have not been established yet.

Sensitivity of DiAcSpm as a marker for various cancers

Diurnal variation of DiAcSpm excretion into the urine tends to parallel that of creatinine (Fujie, N. and Kawakita, M., unpublished observation). The daily excretion of DiAcSpm in the urine of individuals may thus be compared in terms of the amount of DiAcSpm excreted per g creatinine, using arbitrarily collected spot urine samples. The amount of DiAcSpm excreted in the urine of healthy

persons was small as compared with that of monoacetylated polyamine derivatives, and was distributed in a very narrow range, with a mean ± SD value of 0.15 ± 0.05 μmol/g creatinine for 52 apparently healthy volunteers (*1*), but was frequently increased in patients with neoplastic diseases.

Thus, the sensitivity of DiAcSpm (100 × number of true positives/total patients) in the 248 colon cancer patients examined was 75.8% in reference to 0.25 μmol/g creatinine (mean + 2 SD of healthy persons) as a cutoff value, whereas the specificity of DiAcSpm (100 × number of true negatives/total subjects in a control group) was 96% for the 52 apparently healthy controls and 77% for the 51 patients with benign gastrointestinal diseases (*23*). Patients with active inflammatory symptoms, including those with acute appendicitis and acute cholecystitis and those in the active phase of inflammatory bowel diseases tended to give DiAcSpm values above the cutoff level (*23*), but these patients could be easily identified by their characteristic symptoms. Besides these easily discernible patients, those who were being treated for benign diseases including adenomas excreted similar amounts of DiAcSpm as healthy persons.

The sensitivity of DiAcSpm for colon cancer (75.8%) was much higher than that of tumor markers which are currently in clinical use, such as serum CEA (39.5% with 5 ng/ml as a cutoff value, $P < 0.0001$) and CA19-9 (14.1% with 37 units/ml as a cutoff value, $P < 0.0001$) (*23*). Urinary DiAcSpm may thus be considered a novel high-performance tumor marker for colon cancers that can be favorably compared with these tumor markers.

Urinary DiAcSpm levels were examined for patients with various cancers. Earlier analysis using an HPLC procedure indicated that DiAcSpm was elevated frequently and markedly in urogenital malignancies, including prostate cancer, testicular cancer, renal cancer and renal pelvic cancer, with a very low false-negative incidence (*2*). DiAcSpm was also reported to be increased in patients with leukemia (*14*, *24*). More recently, DiAcSpm levels in pancreatobiliary adenocarcinoma were shown to be increased significantly ($P < 0.001$) as compared to those in a control group consisting mainly of patients with benign inflammatory diseases and adenomas. The sensitivity of urinary DiAcSpm for malignant conditions was 75%, which was higher than that of CEA (44%, $P = 0.044$) and the same as that of CA19-9 (75%) (*25*). Analysis of urine samples from 83 breast cancer patients further indicated that DiAcSpm was above the cutoff value in 60.2% of the patients. The sensitivity of DiAcSpm for breast cancer was significantly higher than the sensitivities of serum CEA (37.3%, $P = 0.0032$) and CA15-3 (37.3%, $P = 0.0032$) (*23*). Patients with hepatocellular carcinoma also show a high incidence of elevated urinary DiAcSpm (*26*). Thus, urinary DiAcSpm was increased more frequently than most tumor markers currently in clinical use in patients with various types of cancers. Our preliminary studies suggested that DiAcSpm in the urine was also increased in cases of brain tumors and lung cancers.

These results strongly suggest that DiAcSpm may be useful to detect a wide variety of neoplastic diseases. It is quite reasonable that various cancers are associated with increased DiAcSpm excretion in the urine, because polyamine metabolism is activated in association with various types of cell proliferation.

Sensitivity of DiAcSpm for early-stage cancers

One of the most prominent features of DiAcSpm is that it can detect early-stage colon, breast and other cancers in patients (*23*). The proportion of positives with respect to known tumor markers is usually very low for early-stage cancers. For instance, when the proportion of positives with respect to a given marker was compared among colon cancer patients grouped according to tumor stage, the serum CEA values were above the cutoff value in only 10% of stage 0 ($n = 20$) and stage I ($n = 40$) patients. On the other hand, urinary DiAcSpm was positive in 60% of these early stage colon cancer patients. The difference in the sensitivity between DiAcSpm and CEA was significant for both stages ($P = 0.002$ for stage 0 and $P < 0.0001$ for stage I) (Table 1). The sensitivity of DiAcSpm for detecting early-stage colon cancer was comparable to that of the fecal occult blood test, which is widely used in screening for colon cancer.

Similarly, the sensitivity of DiAcSpm for early-stage breast cancer (stages I and II; 28.1%) was significantly higher than those of CEA (3.1%; $P = 0.018$) and CA15–3 (0%; $P = 0.001$) (*23*). Although the sensitivity of DiAcSpm for early-stage breast cancer was not as high as that for early-stage colon cancer, it would certainly be useful in the early diagnosis of breast cancer, since the sensitivity of currently available markers such as CEA and CA15-3 is negligibly low for breast cancer at earlier stages.

DiAcSpm and CA19-9 showed comparable sensitivity for stage IIb pancreatobiliary carcinoma cases, being positive in 3 and 4 out of 6 cases, respectively, whereas CEA was positive in none of these cases (*25*). It seems likely that the

Table 1. Colon cancer stage and tumor marker levels.

Stage	*n*	DiAcSpm			CEA			CA19-9		
		Positive	Negative	Sensitivity (%)	Positive	Negative	Sensitivity (%)	Positive	Negative	Sensitivity (%)
0	20	12	8	60.0[1]	2	18	10.0	1	19	5.0
I	40	25	15	62.5[2]	4	36	10.0	2	38	5.0
II	60	43	17	71.7[3]	25	35	41.7	3	57	5.0
III	107	89	18	83.2[2]	53	54	50.5	24	83	22.4
IV	21	19	2	90.5[4]	14	7	66.7	5	16	23.8
Total	248	188	60	75.8[2]	98	150	39.5	35	213	14.1

[1] $p = 0.002$ compared to CEA and $p = 0.0004$ compared to CA19-9. [2] $p < 0.0001$ compared to CEA and CA19-9. [3] $p = 0.0009$ compared to CEA and $p < 0.0001$ compared to CA19-9. [4] $p < 0.0001$ compared to CA19-9. (With permission, Hiramatsu *et al.*, *Clin. Cancer Res.*, **11**, 2986, Copyright 2005: Am. Assoc. Cancer Res.)

urinary DiAcSpm level would also be sensitive for malignant conditions at earlier stages which have not been examined so far.

It should be noted that DiAcSpm was not usually increased in cases of adenoma, thus allowing us to discriminate between malignant and nonmalignant tumors (*23*, *25*). The molecular basis for this distinction between malignant and nonmalignant tumors remains to be elucidated. Early diagnosis of malignant conditions is of great importance in cancer therapy, because cancers can often be cured if detected early enough, owing to the recent progress in cancer therapy. The availability of a tumor marker that would enable us to find cancers in patients at an earlier stage than is possible using currently available methods would contribute much to reducing fatal cases of cancer. DiAcSpm seems a promising candidate for such a marker.

DiAcSpm as an indicator of effectiveness of treatments and of recurrence

The urinary level of DiAcSpm and DiAcSpd in patients with prostate cancer and testicular cancer tended to be lowered in response to treatment, when effective, and the diacetylpolyamine level after treatment was correlated with the prognosis of a patient (*27*). Patients fell into 3 groups in terms of the change in urinary DiAcSpm and DiAcSpd level in response to treatment. In the first group, a precipitous decrease of both DiAcSpm and DiAcSpd to the normal level was noted. The physical conditions of the patients in this group were markedly improved as a result of the treatment, and they were usually free from recurrence of cancer for 3 years. In the second group of patients, in contrast, DiAcSpm and DiAcSpd remained much higher than the normal level even when the patients were clinically judged to be in a state of partial remission. These patients suffered from recurrence within 6 months with a concomitant elevation of urinary diacetylpolyamine level, and eventually died from prostate cancer. In some patients (the third group of patients) the response of the urinary diacetylpolyamine level to treatment for cancer was not clear-cut, with the DiAcSpm level remaining for some time in a range slightly higher than normal. Further studies indicated that patients in this group were not threatened by an immediate risk of recurrence, and that they usually tended to achieve complete remission in 3 years with concomitant recovery of a normal DiAcSpm level (*27*).

The sensitivity of urinary DiAcSpm for the detection of recurrence of pancreatobiliary carcinoma was slightly higher than that of serum CEA and CA19-9, while its specificity was slightly lower than that of these serum markers (*25*).

These results indicate that DiAcSpm and DiAcSpd in the urine may be useful in assessing the effectiveness of treatment, and the diacetylpolyamine level during the follow-up period of patients in remission may serve as a sensitive indicator of the recurrence of cancer. It is also important that the level of these diacetylpolyamines after treatment may be informative of the prognosis of patients with prostate cancer and testicular cancer. However, the number of cases as well as types of cancers so far analyzed in these respects has been quite limited. It is necessary to accumulate enough information to verify the above-noted characteristics of DiAcSpm and DiAcSpd. Preliminary examination of colorectal cancer and brain tumor cases seems to support the usefulness of urinary DiAcSpm as a follow-up marker and prognostic indicator (Hiramatsu *et al.*, unpublished observation).

Possible metabolic events leading to increase in excretion of diacetylpolyamines in the urine

The metabolism of DiAcSpm and DiAcSpd is not fully understood yet. Spermidine/spermine N^1-acetyltransferase (SSAT) catalyzes the acetylation of the N^1-amino groups of spermidine, spemine and N^1-acetylspermine, but not of N^8-acetylspemidine *in vitro* (*28*, *29*). At the cellular level, conditional overexpression of SSAT in MCF-7 human breast cancer cells led to an accumulation of high levels N^1-AcSpd, N-AcSpm and DiAcSpm. Concomitantly, intracellular putrescine and spermidine pools were lowered, and cell growth was inhibited (*17*). Chen et al. also observed an increase in DiAcSpm level associated with the induction of SSAT in SK-MEL-28 human melanoma cell line treated with diethylnorspermine (DENSPM) (*30*).

A gradual increase in the SSAT activity was noted during the tumor growth of Yoshida AH-130 ascites hepatoma cells (*31*) and an increase in N^1-AcSpd concentration was observed in many kinds of cancers (*32*). Production of DiAcSpm would also be increased under such situations, although an elevated level of intracellular DiAcSpm has not been demonstrated so far. The induction of SSAT may stimulate oxidative catabolism of polyamines *via* polyamine oxidase on the one hand, and excretion of acetylated polyamines on the other, together leading to lowering the intracellular polyamine pools (*17*). This may represent a homeostatic mechanism to lower intracellular polyamines under conditions of sustained high levels of ornithine decarboxylase in cancer cells. It is possible that increased excretion of acetylated polyamines, including DiAcSpm, from cancer cells may be a consequence of a feedback response of rapidly growing cells in the tissues to down-regulate the elevated cellular polyamine levels to suppress their uncontrolled growth. On the other hand, enhanced polyamine catabolism seemed positively correlated with carcinogenesis in some cases (*33*).

We do not fully understand yet how an elevated urinary polyamine level may actually be attained in patients with cancer. In spite of the fact that the SSAT activity tends to be increased in cancer cells, it is still unclear whether the increase in the DiAcSpm level in the urine of patients with cancer could be explained directly by an increase in the amount of DiAcSpm excreted as such from cancer cells or tissues themselves. It is also possible that active polyamine metabolism in rapidly growing tissues including cancer tissues leads to an elevation of the whole polyamine level in the circulation and that the acetylation of circulating polyamines takes place in other tissues or organs which remain to be identified, leading to an elevated level of acetylated polyamine derivatives, including DiAcSpm. It is worth mentioning here that the erythrocyte spermidine and spermine levels, which would reflect the activity of whole-body polyamine metabolism, were reported to be correlated well with the tumor stage of prosthetic carcinoma patients and tended to

increase in metastatic and hormonal escape patients (*34*, *35*).

In considering the polyamine level in the urine we should not ignore the reabsorption of polyamines at the renal brush border. Polyamines excreted from various organs and tissues into the circulation are filtered through the glomerular basement membrane in the kidney, but a significant portion of monoacetylpolyamines as well as unconjugated polyamines are soon reabsorbed from the glomerular filtrate into tubular cells through polyamine transport systems, and converted to free polyamines by cellular polyamine oxidase to be reutilized in the body. Although polyamine transporter genes in mammals have not yet been identified, the properties of polyamine transport systems in renal epithelia can be examined by using polarized monolayers of cells derived from renal proximal tubules such as porcine LLC-PK_1 cells (*36*, *37*). Measurement of polyamine uptake using this model system indicated that monoacetylpolyamines were actively transported into the cells from the apical surfaces. DiAcSpm did not inhibit any polyamine transport system expressed in the apical membranes of the cell monolayers, nor was it incorporated into the cells (*38*). This implies that the renal reabasorption route is available for monoacetylpolyamines, but not for DiAcSpm. It is therefore likely that DiAcSpm excreted from cells in the body is recovered in the urine without significant loss, while the amount of urinary monoacetylpolyamies decreases by an unknown amount compared to that originally excreted from the cells due to renal reabsorption and reutilization. This may at least partially explain why the urinary level of DiAcSpm reflects the presence of cancer in the body with high sensitivity and at early clinical stages, while the urinary levels of monoacetylpolyamines do not (*38*).

As described in a previous section, DiAcSpd behaved differently from DiAcSpm. It was not as sensitive as DiAcSpm for detection of urogenital malignancies, but was highly specific for malignant conditions in that the DiAcSpd level in patients with benign urogenital diseases was very similar to that in healthy persons (see Fig. 1) (*2*). It is worth noting that the excretion of DiAcSpm was tremendously increased in the urine of pregnant women (*39*), while that of DiAcSpd was not (Hiramatsu et al., unpublished observation). This implies that the induction of the enzyme activity responsible for the synthesis of DiAcSpd may be closely related to malignant conditions. Unfortunately, however, the molecular identity of the acetyltransferase responsible for the synthesis of DiAcSpd is not yet known. The identification, characterization and regulation of this enzyme would be of great interest. It will also be important to examine the behavior of urinary DiAcSpd in various malignant conditions other than urogenital malignancies. A precise and convenient procedure for determination of DiAcSpd should be developed for this purpose. The studies on DiAcSpd as a tumor marker have lagged behind those on DiAcSpm for various reasons, but it certainly deserves more attention than so far paid to it.

Future perspectives

The activation of polyamine metabolism is closely related to active cell proliferation. The increased excretion of DiAcSpm and DiAcSpd in cancer patients so far examined is clearly related to this phenomenon. It is therefore highly likely that urinary diacetylpolyamine levels are increased in various types of cancers and that they could serve as novel tumor markers applicable to a wide variety of cancers, since active and uncontrolled cell proliferation is a common characteristic of cancer cells. Intensive examination of urinary diacetylpolyamine levels in cancers which have not been fully examined yet would be worthwhile.

Early detection of patients with cancer would greatly improve the efficacy of treatment and help in reducing the fatal cases of cancers. One of the prominent features of DiAcSpm may be that it is highly sensitive for early-stage cancers, including colorectal cancer, breast cancer and pancreatobiliary cancer (*23*, *25*). On the other hand, its sensitivity for hepatocellular carcinoma at earlier stages may not be higher than that of other markers such as AFP or PIVKA II, although the number of cases analyzed has been rather limited so far (*26*). The usefulness of DiAcSpm as a sensitive indicator of cancers at earlier stages should be carefully examined. Urine samples are easily obtained noninvasively from individuals and are thus suitable test materials in health examinations. The use of urinary DiAcSpm as an item in public health examination for screening of potential cancer-bearing patients, perhaps in combination with other markers such as the fecal occult blood test, may considerably improve the efficiency of early colorectal cancer detection. In this context, whether the results of the fecal occult blood test and the urinary DiAcSpm value are correlated is a very intriguing question.

The increase of DiAcSpm in the urine does not specify the location of a cancer tissue in the body. It should be noted, however, that specificity to a particular type of cancer is unnecessary when a tumor marker is considered as an item for screening of unspecified cancer patients, as a follow-up marker, and as a prognostic indicator. Such specificity may rather restrict the applicability of the marker to a narrow range of diseases. Results accumulated so far indicate that DiAcSpm may be useful as a tumor marker in various respects, as noted above. The characteristic of DiAcSpm that it is not tumor type specific would then be considered as one of its attractive features. A follow-up marker that is efficient in detecting recurrence and correlates well with the prognosis of a patient would be invaluable in improving the QOL of the patient. DiAcSpm may be a candidate for such an attractive follow-up marker.

REFERENCES

1. Hiramatsu, K., Sugimoto, M., Kamei, S., Hoshino, M., Kinoshita, K., Iwasaki, K., and Kawakita, M. (1995) Determination of the amounts of polyamines excreted in urine: Demonstration of N^1,N^8-diacetylspermidine and N^1,N^{12}-diacetylspermine as components commonly occurring in normal human urine. *J. Biochem.* **117**, 107–112
2. Sugimoto, M., Hiramatsu, K., Kamei, S., Kinoshita, K., Hoshino, M., Iwasaki, K., and Kawakita, M. (1995) Significance of urinary N^1,N^8-diacetylspermidine and N^1,N^{12}-diacetylspermine as indicators of neoplastic diseases. *J. Cancer Res. Clin. Oncol.* **121**, 317–319
3. Tabor, C.W. and Tabor, H. (1976) 1,4-diaminobutane (putrescine), spermidine, and spermine. *Annu. Rev. Biochem.* **45**, 285–306

4. Tabor, C.W. and Tabor, H. (1984) Polyamines. *Ann. Rev. Biochem.* **53**, 749–790
5. Pegg, A. (1986) Recent advances in the biochemistry of polyamines in eukaryotes. *Biochem. J.* **234**, 249–262
6. Wallace, H.M., Fraser, A.V., and Hughes, A. (2003) A perspective of polyamine metabolism. *Biochem. J.* **376**, 1–14
7. Auvinen, M.P.A., Andersson, L.C., and Hölttä, E. (1992) Ornithine decarboxylase activity is critical for cell transformation. *Nature* **360**, 355–358
8. Russell, D.H. (1971) Increased polyamine concentrations in the urine of human cancer patients. *Nature New Biol.* **233**, 144–145
9. Abdel-Monem, M.M., and Ohno, K. (1978) Polyamine metabolism III: Urinary acetylpolyamine in human cancer. *J. Pharm. Sci.* **67**, 1671–1673
10. Abdel-Monem, M.M., Merdink, J.L., and Theologides, A. (1982) Urinary excretion of monoacetyl polyamines in patients with non-Hodgkin's lymphoma. *Cancer Res.* **42**, 2097–2098
11. Bachrach, U. (1992) Polyamines as markers of malignancy. *Prog. Drug Res.* **39**, 9–33
12. Löser, C., Fölsch, U.R., Paprotny, C., and Creutzfeldt, W. (1990) Polyamines in colorectal cancer, evaluateion of polyamine concentrations in colon tissue, serum and urine of 50 patients with colorectal cancer. *Cancer* **65**, 958–966
13. Seiler, N. and Knödgen, B. (1985) Determination of polyamines and related compounds by reversed-phase high-performance liquid chromatography: improved separation systems. *J. Chromatogr.* **339**, 45–57
14. van den Berg, G.A., Muskiet, F.A.J., Kingma, A.W., van den Slik, W.,and Halie, M.R. (1986) Simultaneous gas-chromatographic determination of free and aceyl-conjugated polyamines in urine. *Clin. Chem.* **32**, 1930–1937
15. Hiramatsu, K., Kamei, S., Sugimoto, M., Kinoshita, K., Iwasaki, K., and Kawakita, M. (1994) An improved method of determining free and acetylated polyamines by HPLC involving an enzyme reactor and an electrochemical detector. *J. Biochem.* **115**, 584–589
16. Kabra, P.M., Lee, H.K., Lubich, W.P., and Marton, L.J. (1986) Solid-phase extraction and determination of dansyl derivatives of unconjugated and acetylated polyamines by reversed-phase liquid chromatography: improved separation systems for polyamines in cerebrospinal fluid, urine and tissue. *J. Chromatogr.* **380**, 19–32
17. Vujcic S, Halmekyto, M., Diegelman P, Gan, G., Kramer, D.L., Janne, P., and Porter, C.W. (2000) Effects of conditional overexpression of spermidine/spermine N^1-acetyltransferase on polyamine pool dynamics, cell growth, and sensitivity to polyamine analogs. *J. Biol. Chem.* **275**, 38319–38328
18. Kobayashi, M., Samejima, K., Hiramatsu, K., and Kawakita, M. (2002) Mass spectrometric separation and determination of N^1,N^{12}-diacetylspermine in the urine of cancer patients. *Biol. Pharm. Bull.* **25**, 372–374
19. Hiramatsu, K., Miura, H., Kamei, S., Iwasaki, K., and Kawakita, M. (1998) Development of a sensitive and accurate enzyme-linked immunosorbent assay (ELISA) system that can substitute the HPLC analysis for the determination of N^1, N^{12}-diacetylspermine in human urine. *J. Biochem.* **124**, 231–236
20. Fujiwara, K., Kaminishi, Y., Kitagawa, T., Tsuru, D., Yabuuchi, M., Kanetake, H., and Nomata, K. (1998) Preparation of monoclonal antibodies against N-(γ-maleimidobutyryloxy)succinimide (GMBS)-conjugated acetylspermine, and development of an enzyme-linked immunosorbent assay (ELISA) for N^1,N^{12}-diacetylspermine. *J. Biochem.* **124**, 244–249
21. Hamaoki, M., Hiramatsu, K., Suzuki, S., Nagata, A., and Kawakita, M. (2002) Two enzyme-linked immunosorbent assay (ELISA) systems for N^1,N^8-diacetylspermidine and N^1,N^{12}-diacetylspermine using monoclonal antibodies. *J. Biochem.* **132**, 783–788
22. Hiramatsu, K., Miura, H. , Sugimoto, K. , Kamei, S., Iwasaki, K., and Kawakita, M. (1997) Preparation of antibodies highly specific to N^1,N^8-diacetylspermidine, and development of an enzyme-linked immunosorbent assay (ELISA) system for its sensitive and specific detection. *J. Biochem.* **121**, 1134–1138
23. Hiramatsu, K., Takahashi, K., Yamaguchi, T., Matsumoto, H., Miyamoto, H., Tanaka, S., Tanaka, C., Tamamori, Y., Imajo, M., Kawaguchi, M., Toi, M., Mori, T., and Kawakita, M. (2005) N^1,N^{12}-Diacetylspermine as a sensitive and specific novel marker for early- and late-stage colorectal and breast cancers. *Clin. Cancer Res.* **11**, 2986–2990
24. Lee, S.H., Suh, J.W., Chung, B.C., and Kim, S.O. (1998) Polyamine profiles in the urine of patients with leukemia. *Cancer Lett.* **122**, 1–8
25. Yamaguchi, K., Nakamura, M., Shirahane, K., Konomi, H., Torata, N., Hamasaki, N., Kawakita, M., and Tanaka, M. (2005) Urine diacetylspermine as a novel tumor marker for pancreatobiliary caracinomas. *Digest. Liver Dis.* **37**, 190–194
26. Enjoji, M., Nakamuta, M., Arimura, E., Morizono, M., Kuniyoshi, M., Fukushima, M., Kotoh, K., and Nawata, H. (2004) Clinical significance of urinary N^1,N^{12}-diacetylspermine levels in patients with hapatocellular carcinoma. *Int. J. Biol. Markers* **19**, 322–327
27. Hiramatsu, K., Sugimoto, M. , Kamei, S. , Hoshino, M., Kinoshita, K., Iwasaki, K., and Kawakita, M. (1997) Diagnostic and prognostic usefulness of N^1,N^8-diacetylspermidine and N^1,N^{12}-diacetylspermine in urine as novel markers of malignancy. *J. Cancer Res. Clin. Oncol.* **123**, 539–545
28. Della Ragione, F. and Pegg, A.E. (1983) Studies of the specificity and kinetics of rat liver spermidine/spermine N^1-acetyltransferase. *Biochem. J.* **213**, 701–706
29. Seiler, N. (1987) Functions of polyamine acetylation. *Can. J. Physiol. Pharmacol.* **65**, 2024–2035
30. Chen, Y., Kramer, D.L., Li, F., and Porter, C.W. (2003) Loss of inhibitor of apoptosis proteins as a determinant of polyamine analog-induced apoptoses in human melanoma cells. *Oncogene* **22**, 4964–4972
31. Desiderio, M.A. and Bardella, L. (1994) Expression of Spermidine/spermine N^1-acetyltransferase in growing Yoshida AH130 hepatoma cells. *Hepatology* **19**, 728–734
32. Takenoshita, S., Matsuzaki, S., Nakano, G., Kimura, H., Hoshi, H., Shoda, H., and Nakamura, T. (1984) Selective elevation of the N^1-acetylspermidine level in human colorectal adenocarcinomas. *Cancer Res.* **44**, 845–847
33. Halline, A.G., Dudeja, P.K., Jacoby, R.F., Llor, X., Teng, B.B., Chowdhury, L.N., Davidson, N.O., and Brasitus, T.A. (1990) Effect of polyamine oxidase inhibition on the colonic malignant transformation process induced by 1,2-dimethylhydrazine. Carcinogenesis, **11**, 2127–2132
34. Cipolla, B., Moulinoux, J.-Ph., Quemener, V., Havouis, R., Martin, L.-A., Guille, F., and Lobel, B. (1990) Erythrocyte polyamine levels in human prostatic carcinoma. *J. Urol.* **144**, 1164–1166
35. Cipolla, B., Guille, F., Moulinoux, J.-Ph., Bansard, J.-Y., Roth, S., Staerman, F., Corbel, L., Quemener, V., and Lobel, B. (1994) Erythrocyte polyamines and prognosis in stage D2 prostatic carcinoma patients. *J. Urol.* **151**, 629–633
36. Seiler, N., Delcros, J.G., and Moulinoux, J.P. (1996) Polyamine transport in mammalian cells. An update. *Int. J. Biochem. Cell Biol.* **28**, 843–861

37. van den Bosh, L., de Smedt, H., Missiaen, L., Parys, J.B., and Borghgraef, R. (1990) Transport system for polyamines in the established renal cell line LLC-PK_1. *Biochem. J.* **265**, 609–612
38. Miki, T., Hiramatsu K. ,and Kawakita, M. (2005) Interaction of N^1,N^{12}-diacetylspermine with polyamine transport systems of polarized porcine renal cell line LLC-PK_1. *J. Biochem.* **138**, 479–484
39. van den Berg, G.A., Kingma, A.W., Visser, G.H.A., and Muskiet, F.A.J. (1988) Gestational-age-dependent concentrations of polyamines, their conjugates and metabolites in urine and amniotic fluid. *Brit. J. Obst. Gynaecol.* **95**, 669–675

Polymer Journal, Vol. 37, No. 5, pp. 384–390 (2005)

SHORT COMMUNICATIONS

Synthesis of New Hydroxy-bearing Polyurethanes: Polyaddition of D-Glucose-derived Diols with Diisocyanates

Kazuhiko HASHIMOTO,† Kumiko YAGINUMA, Shin-ichi NARA, and Haruki OKAWA

Department of Materials Science and Technology, Faculty of Engineering, Kogakuin University, Nakano-cho, Hachioji 192-0015, Japan

(Received September 22, 2004; Accepted February 17, 2005; Published May 15, 2005)

KEY WORDS Polyurethanes / D-Glucose / Renewable Resources / Degradation / Hydroxy Group / Carbon Circulation /
[DOI 10.1295/polymj.37.384]

In the past 20th century many kinds of polymeric materials had been produced for our life, from fossil resources such as coal and petroleum, which were important storage carbon resources on the earth. In the 21st century the development of the macromolecular synthesis from the renewable carbon resources and their circulation system is essential for modern human life.[1]

Thus naturally occurring polymers and their repeating units, such as saccharides, amino acids and so on, have been frequently adopted as renewable starting blocks for biodegradable and/or biomedical polymeric materials.[2–25] In our previous articles, we had already reported the macromolecular syntheses from D-glucose(**1**)-derived diols such as D-glucaro-1,4:6,3-dilactone (**2**), methyl D-glucofuranosidurono-6,3-lactone, and 1,4:3,6-dianhydro-D-glucitol (**3**) (as shown in Scheme 1), and from another aldose derivative, for example D-mannaro-1,4:6,3-dilactone, and found that the polyurethanes containing the dilactone or lactone rings could be hydrolyzed in a neutral phosphate buffer solution to the corresponding saccharide derivatives, diamines, and carbon dioxide at 27 °C more quickly than polyurethanes containing no lactone ring.[20–22]

In the present work, another D-glucose-derived diols such as methyl 4,6-*O*-benzylidene-α-D-glucopyranoside (**4**) and 1,2:5,6-di-*O*-isopropylidene-D-glucitol (**5**) were prepared through the selective protection of hydroxy groups in D-glucose derivatives with benzylidene or isopropylidene groups, respectively, whereas the D-glucose-derived diols **2** and **3** were prepared by the intramolecular cyclization of D-glucaric acid and D-glucitol, respectively. Then these D-glucose-derived diols **4** and **5** were applied to the macromolecular syntheses of novel polyurethanes (**7** and **8**) by their polyaddition with hexamethylene diisocyanate (**6a**) and methyl (*S*)-2,6-diisocyanatohexanoate (lysine diisocyanate, **6b**) as shown in Scheme 2. In addition, novel hydroxy-bearing polyurethanes (**9** and **10**) were synthesized by the subsequent deprotection in trifluoroacetic acid aqueous solution.

EXPERIMENTAL

Reagents

Hexamethylene diisocyanate (**6a**) was purchased from Tokyo Kasei Co. (Japan) and methyl (*S*)-2,6-diisocyanatohexanoate (**6b**) prepared from L-lysine was provided from Kyowa Hakko Kogyo Co. Ltd. (Japan). They were purified by the distillation under reduced pressure just before use. *N*,*N*-Dimethylformamide (DMF) and dimethyl sulfoxide (Me_2SO) were dried over calcium hydride and distilled under reduced pressure. D-Glucose (**1**), D-glucitol, dibutyltin dilaurate and other reagents were used without purification.

Methyl 4,6-O-Benzylidene-α-D-glucopyranoside (4)

In a 300-mL round-bottomed flask, a mixture of **1** (50.5 g) and 2.5% hydrochloric acid methanol solution (134 mL) was refluxed for 5.5 h, until **1** was completely consumed, which was confirmed by the TLC analysis. Then the solution was cooled down, and the resulting crude crystals of methyl α-D-glucopyranoside were collected and purified by the recrystallization from methanol: yield, 16.5 g (30%); mp, 166 °C (lit, 166 °C).[26]

According to the method described by M.E. Evans,[27] methyl α-D-glucopyranoside (10.0 g), benzaldehyde dimethyl acetal (7.8 g), and *p*-toluenesulfonic acid monohydrate (25 mg) were dissolved in 40 mL of DMF in a 300-mL flask equipped with an evaporator. The mixture was refluxed at 60 °C under reduced pressure for 1 h during the stirring of the flask, and

†To whom correspondence should be addressed (E-mail: hashimot@cc.kogakuin.ac.jp).

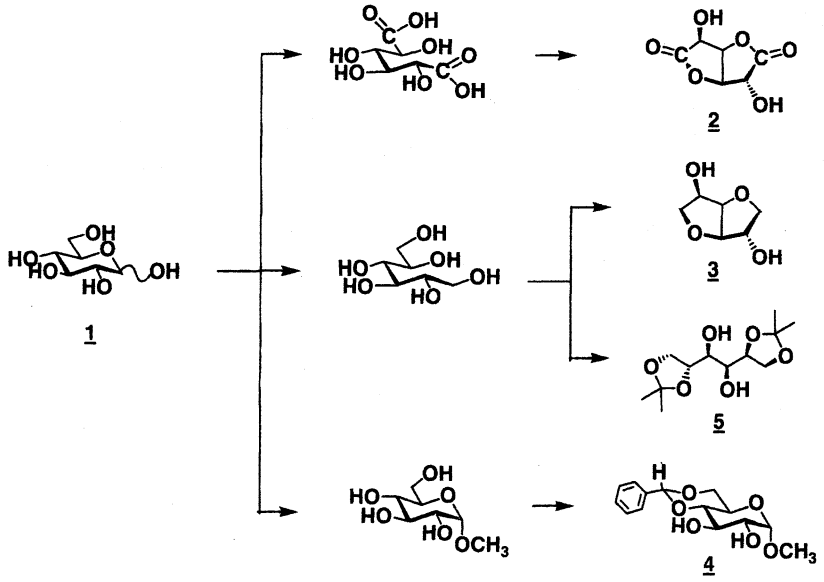

Scheme 1.

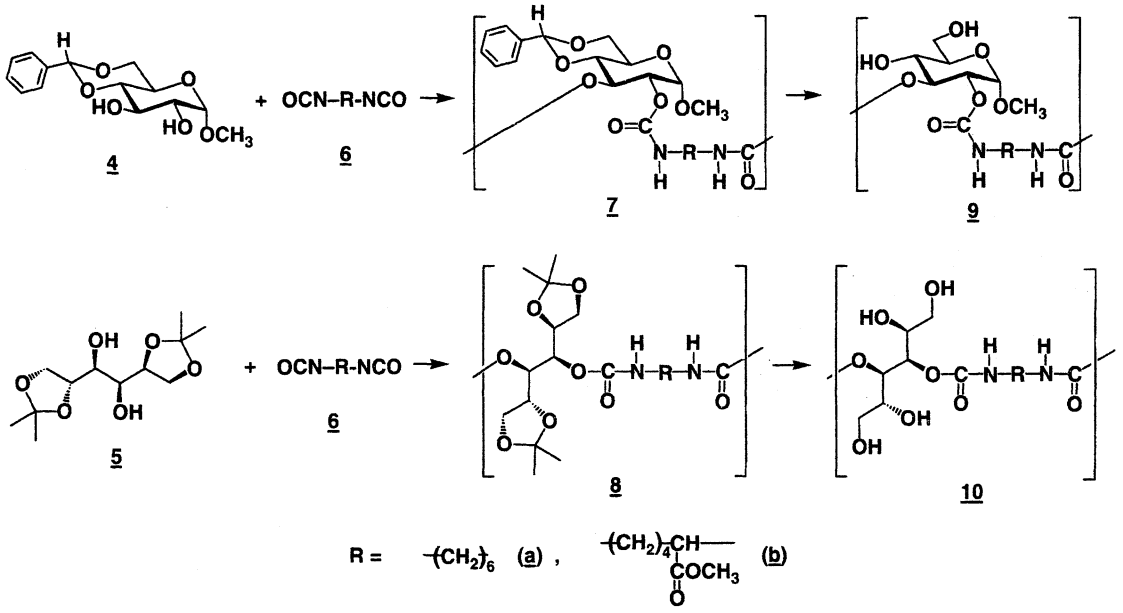

Scheme 2.

then DMF was distilled out at 100 °C to give a colorless residue. Sodium hydrogen carbonate (1.0 g) in 50 mL of deionized water was added to the flask, and the mixture was heated at 100 °C in order to disperse the residual solid in the solution. After cooling at room temperature, the insoluble part was collected, washed with deionized water, and dried *in vacuo*, which was recrystallized from 1-propanol to isolate **4** as colorless powder.

Yield, 11.4 g (79%); mp, 171 °C (lit, 167.5–168.5 °C).[27] ^{1}H NMR [Me_2SO-d_6, δ, ppm]: 7.43 and 7.34 (m, 3H + 2H, aromatic protons), 5.56 (s, 1H, –O–C*H*–O– in a benzylidene group), 5.2 and 4.9 (broad singlet, 1H + 1H, –O*H*), 4.63 (d, ^{1}C*H* in a pyranose ring), 4.15 (dd, 1H, ^{5}C*H* in a pyranose ring), 3.70, 3.58, 3.35 (m, 1H + 2H + 2H, ^{2}C*H* + ^{3}C*H* + ^{4}C*H* + ^{6}CH_2 in a pyranose ring), 3.32 (s, 3H, –OCH_3).

1,2:5,6-Di-O-isopropylidene-D-glucitol (5)

By reference to the method described by Chittenden,[28,29] D-glucitol (25 g) was suspended with vigorous stirring in 1,2-dimethoxyethane (60 mL) containing tin(II) dichloride (25 mg). Then 2,2-dimethoxypropane (40 mL) was added to the suspension, and it was refluxed with continuous stirring for 1 h, until an almost clear solution was obtained. The solution was cooled, treated with a few drops of pyridine, and concentrated under reduced pressure. The residue

was found to contain at least six components by the TLC analysis (Rf, 0.73, 0.46, 0.22, 0.19, 0.13, 0.10, 0.00). Therefore the residue was chromatographed on silica gel by using ethyl acetate–*n*-hexane mixture (1:1 v/v) as an eluent. The eluate containing the third component (Rf, 0.22) was collected and concentrated under pressure. The resulting crude crystals were purified by the recrystallization from di-*n*-butyl ether to give colorless needle crystals of **5**.

Yield, 3.6 g (10%); mp, 94–96 °C (lit. 95–95.5 °C).[30] ^{1}H NMR [Me_2SO-d_6, δ, ppm]: 4,74 and 4.68 (d, 1H × 2, –O*H*), 4.09 and 4.03 (t, 1H × 2, –C*H*– in five-membered rings), 3.94, 3.83, and 3.54 (1H+2H+1H, –CH_2– in five-membered rings), 3.47 and 3.20 (t, –C*H*–OH), 1.32, 1.30, 1.27, and 1.25 (s, 3H × 4, –CH_3). ^{13}C NMR [Me_2SO-d_6, δ, ppm]: 108.1 and 108.0 (quaternary carbon in isopropylidene groups), 77.5 and 75.2 (methine carbons in five-membered rings), 71.5 and 71.0 (–*C*H–OH), 66.1 and 65.4 (methylene carbons in five-membered rings), 26.8, 26.7, 25.6, 25.4 (–*C*H_3).

*Polyaddition of D-Glucose-derived Diol (**5**) with Hexamethylene Diisocyanate (**6a**)*

In a dry box filled with dry nitrogen, equimolar amounts of **5** (2.62 g, 9.93 mmol) and **6a** (1.67 g, 9.93 mmol) were strictly weighed and dissolved in 6.2 mL of DMF in a glass ampoule, and di-*n*-butyltin dilaurate (91 mg) was added to the solution drop by drop with stirring at room temperature. Then the ampoule was kept in a bath controlled at 50 °C for 24 h. After quenching with a small amount of methanol for 24 h, the reaction mixture was poured into 100–200 mL of diethyl ether. The resulting polymer was collected, washed with deionized water repeatedly, and dried *in vacuo*. Yield of **8a**, 3.73 g (87%).

Deprotection of Polyurethanes

Polyurethane (**7a**, 513 mg) prepared from **4** and **6a** was added into a mixture of trifluoroacetic acid (50 mL) with deionized water (25 mL), and the mixture was stirred vigorously at 15 °C for 5 h. Then the solvent was distilled out under reduced pressure, and the residue was powdered in deionized water and dried *in vacuo*. Yield of **9a**, 367 mg (89%).

Measurements

Polymeric structures were examined by ^{1}H NMR, ^{13}C NMR, and their two-dimensional analysis with a JEOL EX-270 Fourier transform high-resolution nuclear magnetic resonance spectrometer. Deuteriodimethyl sulfoxide and tetramethylsilane (TMS) were used as a solvent and an internal standard, respectively. The average molecular weight of the polyurethanes was determined by a TOSOH Model HLC-8120 high-performance liquid chromatograph (column, TOSOH TSK-gel GMHXL, ϕ7.8 × 600 mm or Super HM-M, ϕ6.0 × 300 mm; solvent, Me_2SO; rate, 0.15 mL/min). The fractionated pullulans with different molecular weight were provided as standards. Thermal stability was examined with a Rigaku Model TG8120 thermagravimetric analyzer from 30 to 500 °C at a heating rate of 10 °C/min under dry nitrogen atmosphere. The degradation point was defined as a temperature at which 10 wt % of the polymer was reduced. The differential scanning calorimetry (DSC) was carried out on a Rigaku Model DSC8230L instrument under dry nitrogen atmosphere at a heating rate of 10 °C/min, after keeping at near decomposition temperature for 15 min and cooling down to room temperature at a rate of 10 °C/min.

RESULTS AND DISCUSSION

Monomer Synthesis

The selective protection of hydroxy groups at the 4th and 6th positions in methyl α-D-glucopyranoside proceeded in high yield according to the literature:[27] yield of methyl 4,6-*O*-benzylidene-α-D-glucopyranoside (**4**), 79%. However, the synthesis of 1,2:5,6-di-*O*-isopropylidene-D-glucitol (**5**) from D-glucitol was more troublesome, because the reaction of D-glucitol with excess of 2,2-dimethoxypropane proceeded step by step to give the corresponding mono-, di-, and triisopropylidene derivatives. After reflux for 1 h, **5** was isolated by the preparative chromatography of silica gel from the reaction mixture containing more than six components. Therefore the yield of **5** was relatively low (10%). After the purification, the monomers were dried *in vacuo* in the presence of phosphorous pentoxide before use.

*Polyaddition of D-Glucose-derived Diols (**4** and **5**) with Diisocyanates (**6**)*

As described in the experimental section, equimolar amounts of D-glucose-derived diols (**4** or **5**) with hexamethylene diisocyanate (**6a**) or methyl (*S*)-2,6-diisocyanatohexanoate (**6b**) were allowed to react by using di-*n*-butyltin dilaurate as a catalyst at 25 or 50 °C. The polyaddition proceeded smoothly and the reaction mixture became viscous.

The yield of the resulting colorless polymers was almost quantitative except in the case of the polyaddition of **5** and **6b** accompanied with mechanical loss, as shown in Table I.

The average molecular weights of the polymers obtained from **5** and **6** were estimated by the gel permeation chromatography (GPC) in dimethyl sulfoxide to be higher than those obtained from **4** and **6**. The higher temperature (50 °C) is thought to be preferential for

Table I. Polyaddition of D-glucose-derived diols (**4** and **5**) with diisocyanates[a]

Diol		Diisocyanate		DMF	Temp.	Time	Polymer yield		$M_n \times 10^{-3}$[b]
	g (mmol)		g (mmol)	(mL)	(°C)	(h)		%	
4	0.92 (3.26)	**6a**	0.55 (3.26)	2.5	25	24	**7a**	90	4.8
4	0.94 (3.33)	**6a**	0.56 (3.33)	2.5	25	72	**7a**	91	9.0
4	1.02 (3.62)	**6b**	0.76 (3.60)	2.5	25	24	**7b**	100	3.1
4	0.95 (3.36)	**6b**	0.71 (3.36)	2.5	25	72	**7b**	99	5.2
5	2.60 (9.93)	**6a**	1.67 (9.93)	6.2	50	24	**8a**	87	13.2
5	1.58 (6.00)	**6b**	1.27 (6.00)	6.2	50	24	**8b**	32[c]	12.2

[a]Mole ratio of diol to diisocyanate, 1.00; catalyst, di-*n*-butyltin dilaurate, 1 mol %/monomer. [b]By GPC in Me_2SO (standard, fractionated pullulan). [c]A portion of polyurethane was lost mechanically.

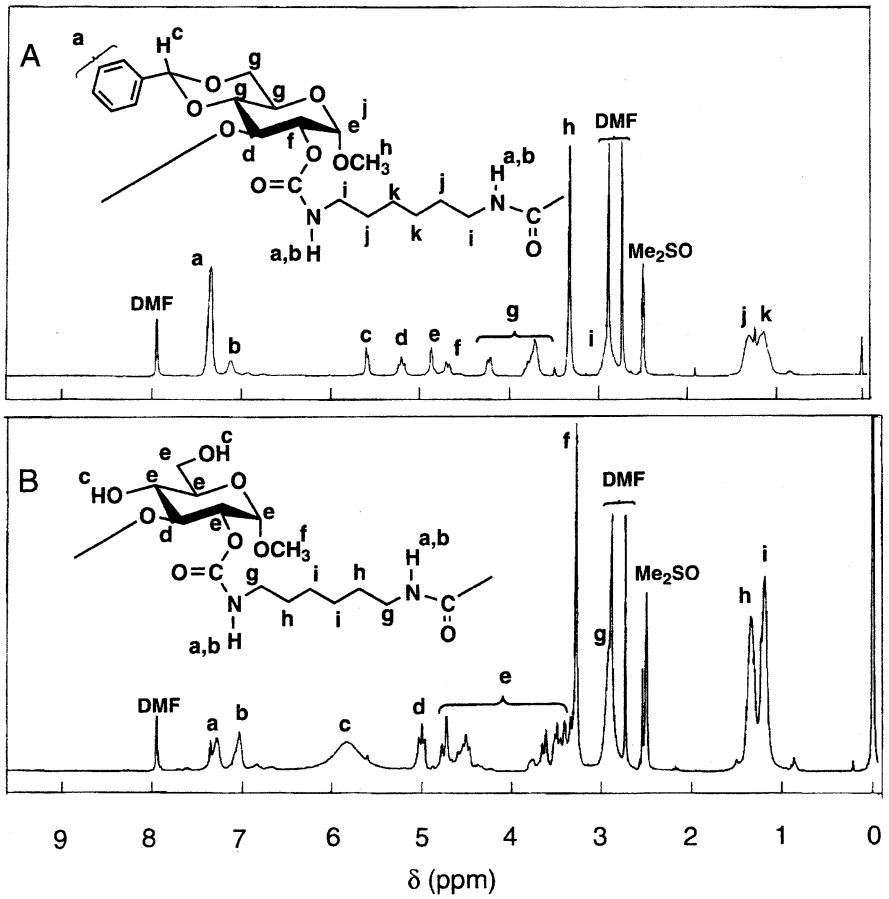

Figure 1. ^1H NMR spectra of polyurethanes prepared from methyl 4,6-*O*-benzylidene-D-glucopyranoside (**4**) and hexamethylene diisocyanate (**6a**): (a) before deprotection (**7a**); (b) after deprotection (**8a**) (5% Me_2SO-d_6 solution, TMS, room temperature, 270 MHz).

the present polyaddition. A similar behavior has been observed in the polyaddition of another saccharide-derived diols, 1,2:5,6-di-*O*-isopropylidene-D-mannitol, and 1,2-*O*-isopropylidene-D,L-erythritol with diisocyanates in our unpublished data.[31]

Another reason may be caused by the difference of the steric hindrance in the D-glucose-derived diols. The hydroxy groups in both diols **4** and **5** are surrounded by bulky groups, which may slow down the polyaddition rate. In addition, the hydroxy groups in **4** are located in the rigid pyranose ring, of which the conformational transition may be disturbed by the benzylidene group. Therefore the hydroxy groups in **5** may rotate more freely than **4**.

The main signals in the ^1H NMR spectrum of the polymer obtained from **4** and **6a** are assigned to the protons in the expected polyurethane structure (**7a**) as shown in Figure 1(A), although it is contaminated with DMF.

Deprotection of Polyurethanes

The resulting polyurethanes (**7a**, **7b**, **8a**, and **8b**) prepared from diols (**4** and **5**) and diisocyanates (**6a** and **6b**) respectively were stirred in a mixture of

Table II. Deprotection of polyurethanes (**7** and **8**) prepared from D-glucose-derived diols (**4** and **5**) and diisocyanates (**6**)[a]

Polyurethane			Temp.	Recovered polymer yield		$M_n \times 10^{-3}$[b]
	$M_n \times 10^{-3}$	mg	(°C)		%	
7a	9.0	513	15	**9a**	89	7.1
7b	4.6	597	15	**9b**	90	14.4
8a	13.2	500	20	**10a**	86	3.2
8b	12.2	250	20	**10b**	68	6.8

[a]A mixture of trifluoroacetic acid with water (volume ratio 2:1), 75 mL; time, 5 h. [b]By GPC in Me_2SO (standard, fractionated pullulan).

trifluoroacetic acid and deionized water (2:1 v/v) at 15 °C or 20 °C. During the stirring for 5 h, the suspension solution became more transparent to give a homogeneous solution. After the removal of the solvents, the residual syrup from **7** and **8** was powdered in deionized water or ethyl acetate, respectively, and dried *in vacuo* (see Table II).

The ^1H NMR spectrum in Figure 1(B) indicated that the benzylidene groups in the original polyurethane (**7a**) completely disappeared and that new polyurethanes (**9a**) bearing two hydroxy groups in the pyranose ring was obtained quantitatively. The isopropylidene groups in the polyurethanes (**8**) were also removed in a similar condition to give different types of polyurethanes (**10**) having four hydroxy groups in each repeating unit.

Solubility and Thermal Property of the Polyurethanes

The solubility of the polyurethanes synthesized from diols **4** and **5** (**7** and **8**) in different organic solvents was examined and summarized in Tables III and IV, respectively. Both polyurethanes were soluble in aprotic polar solvents such as DMF, *N,N*-dimethylacetamide, and dimethyl sulfoxide, but insoluble in water, diethyl ether, and *n*-hexane. The solubility of the polyurethanes prepared from methyl (*S*)-2,6-diisocyanatohexanoate (**7b** and **8b**) was found to be higher than that of the polyurethanes prepared from hexamethylene diisocyanate (**7a** and **8a**), respectively.

On the other hand, the solubility of the polyurethanes having hydroxy groups in each repeating unit (**9** and **10**) was lower than that of the original polyurethanes (**7** and **8**), respectively, mainly in non-polar solvents. Another noteworthy point is that the polyurethanes (**10**) with four hydroxy groups in each repeating units were dissolved even in water, but the polyurethanes (**9**) with two hydroxy groups in the corresponding units were not.

All of the polyurethanes obtained in the present work were heated at a constant rate and the weight loss was monitored as shown in Figures 2 and 3.

The degradation temperature was defined as a temperature at which 10 wt % of the samples were reduced, and summarized in Tables III and IV. The degradation temperature of the protected polyurethanes (**7** and **8**) was relatively high (about 280 °C), regardless of diisocyanates provided for the polyaddition, whereas the deprotected polyurethanes (**9** and **10**) began to degrade at lower temperature than in the cases of the protected ones. Such a thermal degradation of

Table III. Properties of polyurethanes prepared from methyl 4,6-*O*-benzylidene-α-D-glucopyranoside (**4**)

	Polyurethanes			
	7a	**7b**	**9a**	**9b**
Solubility[a]				
Water	I	I	I	I
Me_2SO	S	S	S	S
DMF	S	S	S	S
Methanol	I	s	S	S
Ethanol	I	I	s	s
Acetone	S	S	I	I
Tetrahydrofuran	S	S	S	S
Ethyl acetate	S	S	I	I
Chloroform	S	S	I	I
Diethyl ether	I	I	I	I
n-Hexane	I	I	I	I
Thermal property				
Degradation temperature,[b] °C	280	282	202	195

[a]1 g/100 mL; S, soluble at room temperature; s, soluble at 40 °C; I, insoluble. [b]Defined as the temperature at which 10 wt % of the polyurethane was lost.

Table IV. Properties of polyurethanes prepared from 1,2:5,6-di-*O*-isopropylidene-D-glucitol (**5**)

	Polyurethanes			
	8a	**8b**	**10a**	**10b**
Solubility[a]				
Water	I	I	S	S
Me_2SO	S	S	S	S
DMF	S	S	S	S
Methanol	S	S	S	S
Ethanol	I	I	S	I
Acetone	I	S	I	I
Tetrahydrofuran	S	S	I	i
Ethyl acetate	I	S	I	I
Chloroform	S	S	I	I
Diethyl ether	I	I	I	I
n-Hexane	I	I	I	I
Thermal property				
Degradation temperature,[b] °C	258	257	216	211

[a]1 g/100 mL; S, soluble at room temperature; s, soluble at 40 °C; I, insoluble. [b]Defined as the temperature at which 10 wt % of polymer was lost.

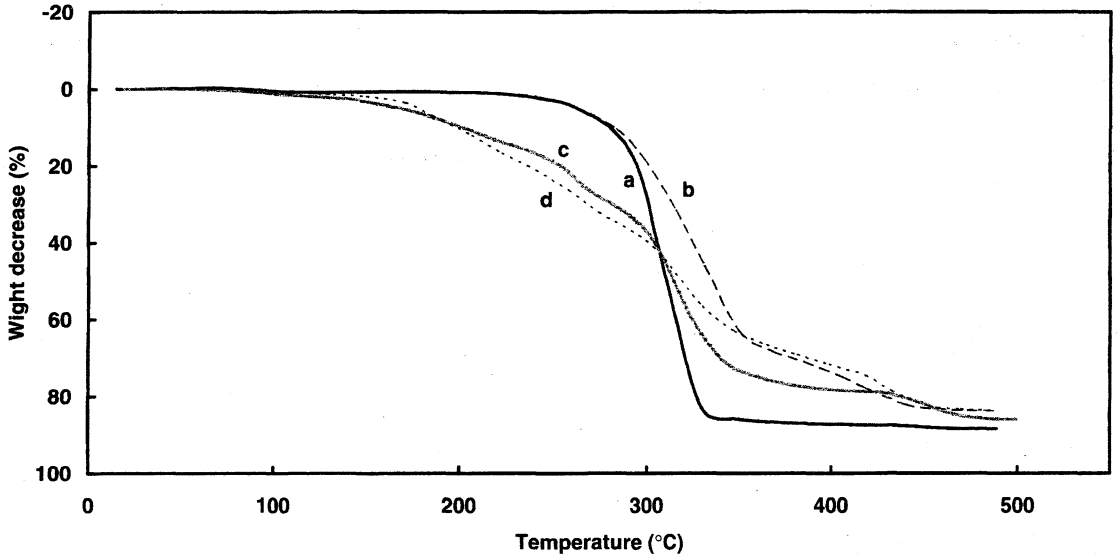

Figure 2. Thermogravimetric curves for several polyurethanes prepared from methyl 4,6-*O*-benzylidene-α-D-gluco-pyranoside (**4**) and diisocyanates (heating rate, 10 °C/min). (a) Polyurethane **7a** (prepared from **4** and hexamethylene diisocyanate (**6a**)); (b) polyurethane **7b** (prepared from **4** and methyl (*S*)-2,6-diisocyanatohexanoate (**6b**)); (c) polyurethane **9a** (isopropylidene group of **7a** was deprotected); (d) **9b** (isopropylidene group of **7b** was deprotected).

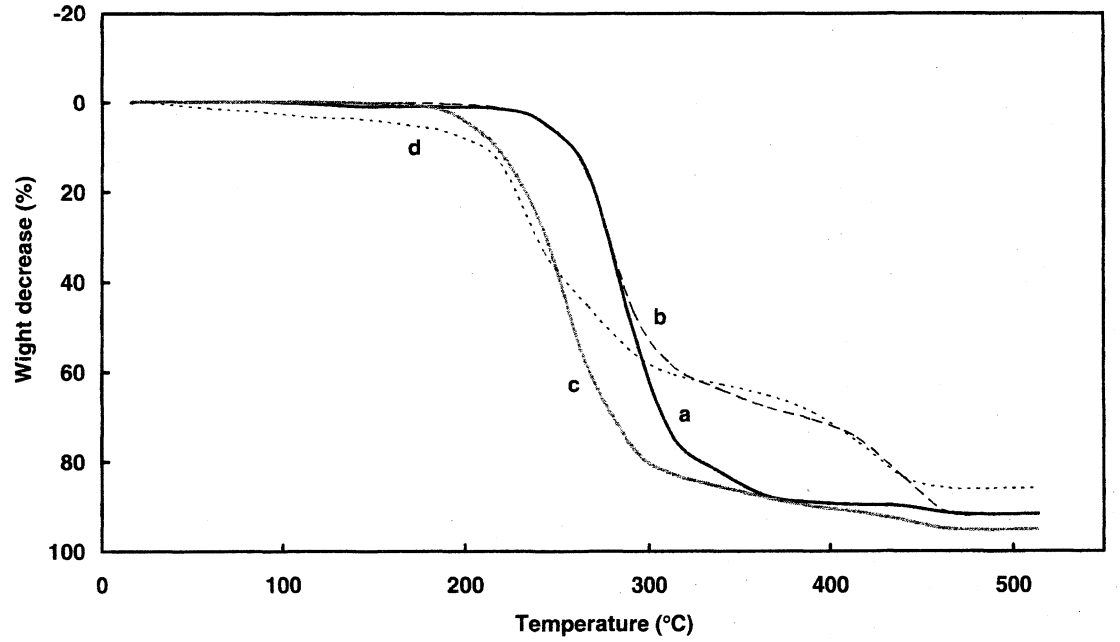

Figure 3. Thermogravimetric curves for several polyurethanes prepared from 1,2:5,6-di-*O*-isopropyliden-D-glucitol (**5**) and diisocyanates (heating rate, 10 °C/min): (a) Polyurethane **8a**; (b) polyurethane **8b**; (c) polyurethane **10a**; (d) polyurethane **10b**.

the hydroxy-bearing polyurethanes at relatively low temperature may be attributed to the degradation associated with the sugar moieties, and the degradation at about 280 °C is due to the degradation of the urethane bonds in the main chains.

On the differential scanning calorimetric analysis of all the resulting polyurethanes, no clear endothermic peak due to their melt or recrystallization was found below the degradation temperature on the repeated heating or cooling process. This fact indicates that the polyurethanes prepared in the represent work are almost amorphous. The influence of hydroxy groups on the hydrolyzability of the polyurethanes will be investigated and reported near future.

In summary, new polyurethanes (**9** and **10**) bearing two and four hydroxy groups in the repeating units were obtained almost quantitatively by the polyaddition of the D-glucose-derived diols, methyl 4,6-*O*-benzylidene-α-D-glucopyranoside (**4**) and 1,2:5,6-di-*O*-isopropylidene-D-glucitol (**5**), with diisocyanates (**6a**

and **6b**) and the following deprotection. The thermal stability of polyurethanes bearing hydroxy groups (**9** and **10**) was found to be much lower than that of the corresponding protected polyurethanes (**7** and **8**).

Acknowledgment. The authors are grateful to Mr. Hikaru Fujimoto, Mr. Takehiko Kamaya, Mr. Naoya Hashimoto, and Mr. Junya Yoshioka for their help in a part of the work. This work was partly supported by Grant-in-Aid for establishing the High Technology Research Center in Private Universities and Research Project for the Ministry of Education, Culture, Sports, Science and Technology, Japan.

REFERENCES

1. A. Gandin, in "Comprehensive Polymer Science: First Supplement," G. Allen and J. C. Bevington, Ed., Pergamon Press, Elmsford, N.Y., 1992, chapt. 19, p 527.
2. S. J. Huang, in "Comprehensive Polymer Science," Vol. 6, G. Allen and J. C. Bevington, Ed., Pergamon Press, Elmsford, N.Y., 1989, chapt. 21, p 597.
3. A.-C. Albertsson and S. Karlsson; in "Comprehensive Polymer Science: First Supplement," G. Allen and J. C. Bevington, Ed., Pergamon Press, Elmsford, N.Y., 1992, chapt. 13, p 285.
4. Y. Teramoto and Y. Nishio, *Biomacromolecules*, **5**, 397 (2004).
5. T. Takamoto, H. Uyama, and S. Kobayashi, *Macromol. Biosci.*, **1**, 215 (2001).
6. S. Matsumura, H. Ebata, and K. Toshima, *Macromol. Rapid Commun.*, **21**, 860 (2000).
7. K. Kurita, N. Hirakawa, and Y. Iwakura, *Makromol. Chem.*, **180**, 855 (1979).
8. K. Kurita, N. Hirakawa, H. Morinaga, and Y. Iwakura, *Makromol. Chem.*, **180**, 2769 (1979).
9. K. Kurita, N. Hirakawa, and Y. Iwakura, *Makromol. Chem.*, **181**, 1861 (1980).
10. T. E. Lipatova, G. A. Pkhakadze, A. I. Snegirev, V. V. Vorona, and V. V. Shilov, *J. Biomed. Mater. Res.*, **18**, 129 (1984).
11. F. Bachmann and J. Thiem, *J. Polym. Sci., Part A: Polym. Chem.*, **30**, 2059 (1992).
12. F. Bachman, J. Reimer, M. Ruppenstein, and J. Thiem, *Makromol. Chem. Rapid Commun.*, **19**, 21 (1998).
13. F. Bachman, J. Reimer, M. Ruppenstein, and J. Thiem, *Macromol. Chem. Phys.*, **200**, 3410 (2001).
14. F. Bachman, M. Ruppenstein, and J. Thiem, *J. Polym. Sci., Part A: Polym. Chem.*, **39**, 2332 (2001).
15. S.-I. Lee, S.-C. Yu, and Y.-S. Lee, *Polym. Degrad. Stab.*, **72**, 81 (2001).
16. T. Hanada, Y.-J. Li, and T. Nakaya, *Macromol. Chem. Phys.*, **202**, 97 (2001).
17. K. Hashimoto, M. Okada, and N. Honjoh, *Makromol. Chem. Rapid Commun.*, **11**, 393 (1990).
18. K. Hashimoto, K. Mori, and M. Okada, *Macromolecules*, **25**, 2592 (1992).
19. K. Hashimoto, S. Wibullucksanakul, and M. Okada, *J. Polym. Sci., Part A: Polym. Chem.*, **31**, 3141 (1993).
20. K. Hashimoto, S. Wibullucksanakul, and M. Okada, *Makromol. Chem. Rapid Commun.*, **14**, 591 (1994).
21. K. Hashimoto, S. Wibullucksanakul, and M. Okada, *J. Polym. Sci., Part A: Polym. Chem.*, **33**, 1495 (1995).
22. S. Wibullucksanakul, K. Hashimoto, and M. Okada, *Macromol. Chem. Phys.*, **197**, 135 (1996).
23. S. Wibullucksanakul, K. Hashimoto, and M. Okada, *Macromol. Chem. Phys.*, **197**, 1865 (1996).
24. S. Wibullucksanakul, K. Hashimoto, and M. Okada, *Macromol. Chem. Phys.*, **198**, 305 (1997).
25. C. Yamanaka and K. Hashimoto, *J. Polym. Sci., Part A: Polym. Chem.*, **40**, 4158 (2002).
26. B. Helferich and W. Schafer, *Org. Synth.*, **1**, 364 (1941).
27. M. E. Evans, *Carbohydr. Res.*, **21**, 473 (1972).
28. G. J. F. Chittenden, *Carbohydr. Res.*, **84**, 350 (1980).
29. G. J. F. Chittenden, *Carbohydr. Res.*, **108**, 81 (1982).
30. B. C. Pressman, L. Anderson, and H. A. Lardy, *J. Am. Chem. Soc.*, **72**, 1404 (1950).
31. K. Hashimoto, T. Kamaya, N. Hashimoto, and H. Okawa, unpublished data.

Glycopolymeric Inhibitors of β-Glucuronidase. III. Configurational Effects of Hydroxy Groups in Pendant Glyco-Units in Polymers upon Inhibition of β-Glucuronidase

KAZUHIKO HASHIMOTO, HIROSHI SAITO, RYO OHSAWA

Department of Materials Science and Technology, Faculty of Engineering, Kogakuin University, Nakano-Cho, Hachioji, Tokyo 192-0015, Japan

Received 12 November 2005; accepted 26 May 2006
DOI: 10.1002/pola.21584
Published online 17 July 2006 in Wiley InterScience (www.interscience.wiley.com).

ABSTRACT: Two kinds of new glycopolymers, (P(VB-1-GlcaH-*co*-AAm), **9**) and (P(VB-1-Glco-*co*-AAm), **10**), were synthesized through the radical copolymerization of styrene derivatives bearing pendant D-glucaric and D-gluconic moieties, *N*-(*p*-vinylbenzyl)-1-D-glucaramide (VB-1-GlcaH, **7**), and *N*-(*p*-vinylbenzyl)-D-gluconamide (VB-1-Glco, **8**), with acrylamide (AAm). Glycopolymer **9** bearing the pendant glucaric moiety at the first position inhibited the hydrolysis of a model compound for xenobiotics-β-glucuronide conjugates, *p*-nitrophenyl β-D-glucuronide, uncompetitively, in contrast to the competitive inhibition in the presence of the corresponding isomeric glycopolymer bearing the pendant D-glucaric unit at the sixth position (P(VB-6-GlcaH-*co*-AAm), **3**) reported in our previous article. On the other hand, another copolymer **10** bearing the gluconic moiety was found not to inhibit the hydrolysis as well as the corresponding copolymer bearing pendant gulonic unit (P(VB-6-Glco-*co*-AAm), **4**). These results indicate that the hydrolysis is influenced not only by existence of pendant carboxyl units but also by the direction on the linkage of the glyco-units to the polymer frame. Therefore the configurational position of hydroxy groups in pendant glyco-units in macromolecular inhibitors may be essential for the interaction with β-glucuronidase.
 J Polym Sci Part A: Polym Chem 44: 4895–4903, 2006
Keywords: β-glucuronidase; D-glucaric acid; D-gluconic acid; glycopolymer; inhibitor; xenobiotics

INTRODUCTION

The development of macromolecular syntheses from renewable carbon resources and the circulation system of the macromolecules are essential for human life.[1] Thus acidic saccharide derivatives such as aldaric, aldonic, and alduronic acids have also been in use as starting blocks, for biomedical and/or biodegradable polymeric materials.[2–24]

In addition, several potentially bioactive saccharides have been introduced into the pendants of several artificial polymers, and such glycopolymers have also been applied to new biomedical fields.[25–27]

Xenobiotics are molecules that are foreign to a living organism, and during the process of detoxification, they are conjugated with UDP-D-glucuronic acid in the liver. The resulting β-D-glucuronide are excreted through the small intestine and kidney.[28] However, β-glucuronidase in the small

Correspondence to: K. Hashimoto (E-mail: hashimot@cc.kogakuin.ac.jp)

intestine is known to hydrolyze the conjugates, and the freed xenobiotics are absorbed through the wall of small intestine and returned to the liver.[28] In the case of toxic xenobiotics, the discharge should be enhanced by the inhibition of the activity of β-glucuronidase. Since, a kind of aldaric acid, D-glucaric acid, and its derivatives behave as inhibitors on the hydrolysis of the β-D-glucuronide conjugates by β-glucuronidase in the small intestine, the exclusive transport of inhibitors into the small intestine may be useful for clinical research on its activity in a human body.[29–33]

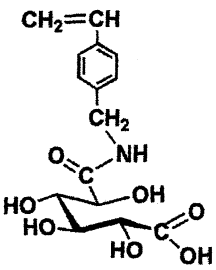

VB-6-GlcaH, 1

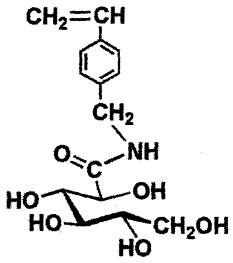

VB-6-Glco, 2

In our previous work,[32,33] novel styryl-type monomers bearing D-glucaric and L-gulonic moieties, *N*-*p*-vinylbenzyl-6-D-glucaramide (VB-6-GlcaH, **1**) and *N*-*p*-vinylbenzyl-L-gulonamide (VB-6-Glco, **2**), were synthesized through ring-opening addition of D-glucaro-6,3-lactone and L-gulono-1,4-lactone with *p*-vinylbenzylamine, in which the saccharide moieties were linked to the styrene frame at the sixth position of the corresponding glucose unit. The glycopolymers prepared through the radical copolymerization of **1** with acrylamide (P(VB-6-GlcaH-*co*-AAm), **3**) and of **2** with acrylic acid (P(VB-6-Glco-*co*-AAK), **5**), respectively, were found to suppress the hydrolysis of a model compound for xenobiotics-β-D-glucuronide conjugates, *p*-nitrophenyl β-D-glucuronide (**6**), but the copolymer prepared from **2** and acrylamide (P(VB-6-Glco-*co*-AAm), **4**) to inhibit the hydrolysis scarcely (Scheme 1).[32,33] Therefore, the existence of the carboxy group in the glycopolymeric unit is inferred to be essential for the inhibition. In addition, the kinetic analysis of the hydrolysis using the Lineweaver-Burk plot suggested that the inhibition mechanism in the presence of glycopolymer **3** was different from that of glycopolymer **5**, that is, the former competitive and the latter uncompetitive, respectively.[32,33]

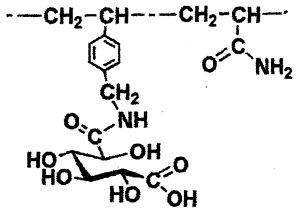

P(VB-6-GlcaH-*co*-AAm), 3

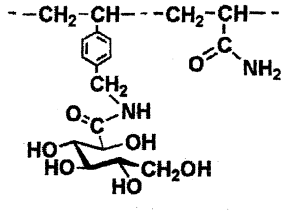

P(VB-6-Glco-*co*-AAm), 4

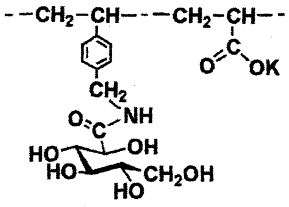

P(VB-6-Glco-*co*-AAK), 5

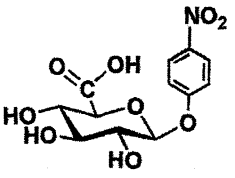

6

In the present work, another new glycopolymers bearing pendant D-glucaric and D-gluconic moieties at the anomeric position (the 1st position) were synthesized and the effects of the direction on the linkage of the glyco-units to the polymeric chain upon the activity of β-glucuronidase were investigated kinetically. Thus two kinds of styrene monomers, *N*-(*p*-vinylbenzyl)-1-D-glucaramide (VB-1-GlcaH, **7**) and *N*-(*p*-vinylbenzyl)-D-gluconamide (VB-1-Glco, **8**) were synthesized and copolymerized with acrylamide (AAm) and acrylic acid (AA) by using azobisisobutyronitrile as an initiator. The hydrolysis of *p*-nitrophenyl β-D-glucuronide (**6**) with β-D-glucuronidase in the presence of the glycopolymers prepared from **7** and AAm (P(VB-1-GlcaH-*co*-AAm), **9**), from **8** and AAm (P(VB-1-Glco-*co*-AAm), **10**), and from **8** and acrylic acid (P(VB-1-Glco-*co*-AAK), **11**) was kinetically determined and discussed in detail.

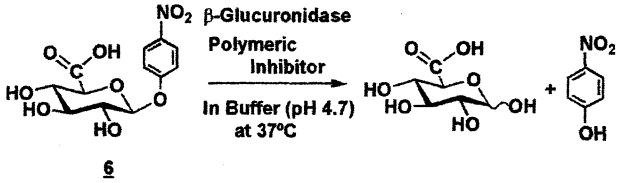

6

Scheme 1

DOI 10.1002/pola

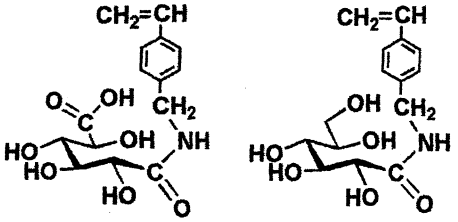

VB-1-GlcaH, 7 VB-1-Glco, 8

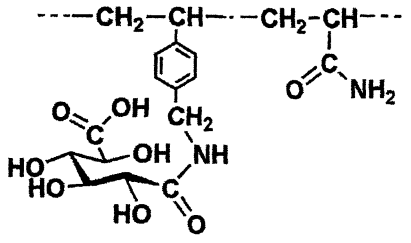

P(VB-1-GlcaH-*co*-AAm), 9

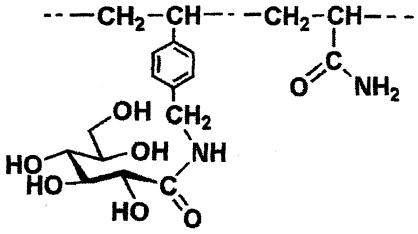

P(VB-1-Glco-*co*-AAm), 10

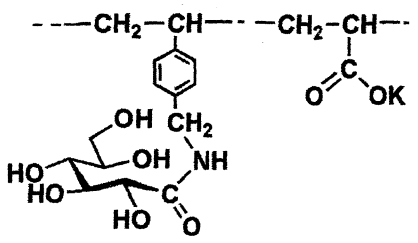

P(VB-1-Glco-*co*-AAK), 11

RESULTS AND DISCUSSION

Monomer Synthesis

A novel styrene monomer, *N*-(*p*-vinylbenzyl)-1-D-glucaramide (VB-1-GlcaH, **7**) was synthesized by the addition of two equivalents of *p*-vinylbenzylamine to D-glucaro-1,4-lactone in methanol and the subsequent stirring at 50 °C for 2 h with no catalyst, as described in the preparation of *N*-(*p*-vinylbenzyl)-6-D-glucaramide (VB-6-GlcaH, **3**) in our previous article.[32] After the treatment of the reaction mixture with acetic anhydride, the chloroform-insoluble portion was recrystallized from ethanol to give **7** as colorless powder in 76% yield (Scheme 2).

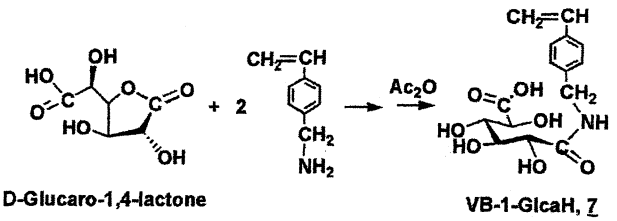

D-Glucaro-1,4-lactone VB-1-GlcaH, 7

Scheme 2

Another styrene monomer bearing a pendant D-gluconic moiety, *N*-(*p*-vinylbenzyl)-D-gluconamide (VB-1-Glco, **8**) was prepared from an equimolar amount of D-glucono-1,5-lactone and *p*-vinylbenzylamine in methanol at 50 °C according to the literature.[34] Yield, 98% (Scheme 3).

Monomers **7** and **8** are soluble in aprotic polar solvents such as dimethyl sulfoxide (DMSO) and *N*,*N*-dimethylformamide at room temperature. They are also soluble in protic polar solvents such as water, methanol, and ethanol at 50 °C, but not in diethyl ether, chloroform, benzene, ethyl acetate, and acetonitrile.

Radical Copolymerization of Glycomonomers (7 and 8) with Vinyl Monomers

The radical copolymerization of glycomonomers (**7** and **8**) with acrylamide (AAm) and acrylic acid (AA), in which the mole fraction of the glycomonomers in feed was 0.20, was carried out in DMSO by using azobisisobutyronitrile as an initiator at 60 °C for 24 h, and the resulting copolymers were precipitated in chloroform (Table 1).

Copolymer **9**, P(VB-1-GlcaH-*co*-AAm), prepared from **7** and AAm was purified by the reprecipitation in the methanol–chloroform system. Copolymer **10**, P(VB-1-Glco-*co*-AAm), from **8** and AAm was dissolved in deionized water, dialyzed, and then lyophilized. On the other hand, the copolymer obtained from **8** and AA was dissolved in potassium hydroxide aqueous solution, dialyzed in aqueous solution, and isolated as white powder by freeze-drying. Therefore the copolymer was

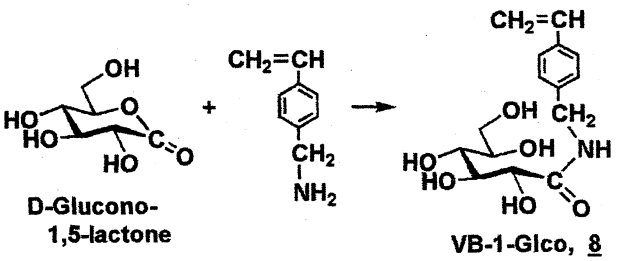

D-Glucono-1,5-lactone VB-1-Glco, 8

Scheme 3

Table 1. Radical Copolymerization of Glycomonomers (**7** and **8**) with Acrylamide and Acrylic Acid[a]

Glycomonomer		Comonomer		Mole Fraction	Me_2SO		Yield	Mole Fraction of M_1	
(M_1)	mg (mmol)	(M_2)	mmol	of M_1 in Feed	(mL)	Polymer	(mg; %)	in Polymer[b]	$M_n \times 10^4$ [c]
7	325 (1.00)	AAm	4.00	0.20	5.0	**9**	173 (28)	0.31	0.59
8	154 (0.50)	AAm	2.00	0.20	2.5	**10**	146 (49)	0.35	1.69
8	308 (1.00)	AA	4.00	0.20	5.0	**11**	411 (69)	0.22	1.69

[a] Initiator, azobisisobutyronitrile, 1 mol % to monomer; temperature, 60 °C; time, 24 h.
[b] By ^1H NMR spectroscopy in deuterated oxide.
[c] By GPC in 0.5*M* acetic buffer solution (pH 4) (standard, fractionated pullulan).

isolated as the copolymer containing potassium carboxylate group (P(VB-1-Glco-*co*-AAK), **11**).

The copolymer yield and the molecular weight of glycopolymer **7** containing the pendant carboxy groups seem to be lower than those of glycopolymer **8** containing no carboxy group, respectively. Similar behavior has been observed in the cases of glycopolymers **3** and **4** in our previous work.[33]

In addition, glycopolymer **3** has been inferred to be random copolymer of glycomonomer **1** with AAm but not alternating one, because the copolymer composition was dependent upon the mole fraction of glycomonomer **1** in feed on the radical copolymerization. Therefore, glycopolymer **9** obtained in the present work is also speculated to be random copolymer.

Copolymers **9** and **10** were soluble in water, methanol, and DMSO, and the solubility of **9** in these solvents was much higher than that of **3**. On the other hand, copolymer **11** was soluble only in water as well as copolymer **5**. Therefore, the glycopolymers obtained in the present work can be applied to the following inhibition test.

Hydrolysis of *p*-Nitrophenyl β-D-Glucuronide (6) with β-Glucuronidase in the Presence of Different Polymers

A model compound for the β-D-glucuronide conjugates of xenobiotics, *p*-nitrophenyl β-D-glucuronide (**6**), was hydrolyzed with β-glucuronidase in the absence or presence of polymers (**9**, **10**, and **11**) using 14 IU/L of the hydrolase, 7 mmol of **6**, and 0.002–6.67 mmol/L of the glycomonomer unit in the copolymer in an acetic buffer solution controlled at pH 4.7 at 37 °C. The hydrolysis was kinetically analyzed by the determination of the absorbance of the *p*-nitrophenol freed from the glucuronide at 400 nm. The inhibition value (%) was calculated from the hydrolytic rates in the absence and presence of the copolymer (v_0 and v, respectively) as shown in eq. 1.

$$\text{Inhibition value } (\%) = \{(v_o - v)/v_o\}100 \quad (1)$$

As shown in Figure 1, the inhibition value of copolymer **9** (P(VB-1-GlcaH-*co*-AAm)) prepared from VB-1-GlcaH (**7**) and AAm, increased up to more than 80% with the concentration of the corresponding glycomonomer unit in the copolymer, as well as in the case of the corresponding isomeric glycopolymer (P(VB-6-GlcaH-*co*-AAm), **3**) in our previous work.[33]

The most noteworthy point is in the fact that the inhibition value for glycopolymer **9** is higher than that for glycopolymer **3** in all concentration of the glycomonomer unit, although both copolymers have lots of D-glucaric group in the pend-

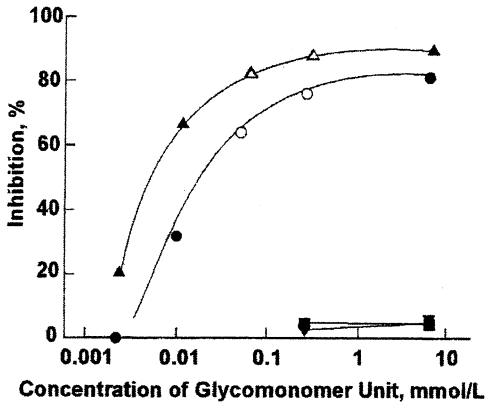

Figure 1. Inhibition of β-glucuronidase activity by different glycopolymers at 37 °C (*p*-nitrophenyl β-D-glucuronide, 7 mM; β-glucuronidase, 14 IU/L; pH, 4.7). ●: P(VB-6-GlcaH-*co*-AAm) **3**, 30% 3.27 g/L, $M_n = 1.04 \times 10^4$; ▲: P(VB-1-GlcaH-*co*-AAm) **9**, 31% 3.80 g/L, $M_n = 0.59 \times 10^4$; ■: P(VB-6-Glco-*co*-AAm) **4**, 39% 2.82 g/L, $M_n = 1.74 \times 10^4$; ▼: P(VB-1-Glco-*co*-AAm) **10**, 35% 2.95 g/L, $M_n = 1.69 \times 10^4$. (Note: ▲●◆, Transparency; △○◇, turbidity.)

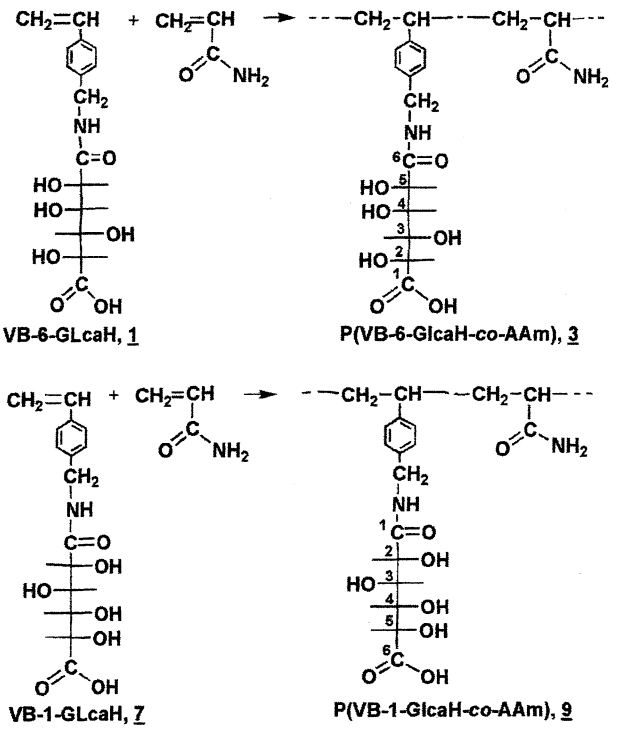

Scheme 4

ants. The structural difference between the copolymers is in the direction of the linkage of the glucaric unit to the polymer chain. The former copolymer (**9**) has an amide bond between the carboxy group at the first position in D-glucaric moiety and the amine group in the benzyl unit, while the carboxy group at the sixth position in the corresponding glyco-moiety in the latter copolymer (**3**) is coupled with the amine group. In other words, the steric structure is different from each other as shown in Scheme 4.

Therefore, such a configurational difference of hydroxy groups in the pendant glyco-units between the copolymers was found to have significant effects on the inhibition on the hydrolysis of *p*-nitrophenyl β-glucuronide (**6**) with β-glucuronidase.

On the other hand, copolymer **10** (P(VB-1-Glco-*co*-AAm)) prepared from VB-1-Glco (**8**) and AAm did not inhibit the activity of the hydrolase significantly, as well as in the case of the corresponding isomeric glycopolymer (P(VB-6-Glco-*co*-AAm), **4**) reported in our previous work.[33] Since the copolymers **10** and **4** have amide groups derived from the amine group in the benzyl unit and the carboxy groups in D-gluconic and L-gulonic moieties, respectively, each carboxy group corresponds to the first and sixth carbon atom in D-glucose unit, respectively. Therefore, the steric structure difference between **10** and **4** is similar to that between **9** and **3**, as shown in Scheme 5.

Consequently the existence of carboxy group in the glycomonomer units was proved to be a more essential factor for the inhibition than the configurational difference of hydroxy groups in the pendant glyco-units.

Figure 2 shows that copolymer **11** (P(VB-1-Glco-*co*-AAK)) inhibited strongly the hydrolysis of glucuronide **6** with β-glucuronidase as well as copolymer **9**. In our previous work, a similar behavior had been observed in the case of glycopolymer **5** containing glycomonomer unit **2**.[33]

Although both **11** and **5** have no carboxy group in the glycomonomer units, the carboxylate group in the comonomer (AAK) in **11** and **5** are inferred to enhance the inhibition. However, the inhibition mechanism is not clear now.

As reported in our article,[33] a mixture of PVB-6-Glco and poly(potassium acrylate) (PAAK) also inhibited the activity of β-glucuronidase, but the inhibition value was lower than that of copolymer **5**. Therefore the carboxy group in the glyco-unit is speculated to inhibit the enzyme more effectively than that in the comonomer unit.

To discuss the inhibition mechanism, the hydrolytic rate (v) in different concentrations of

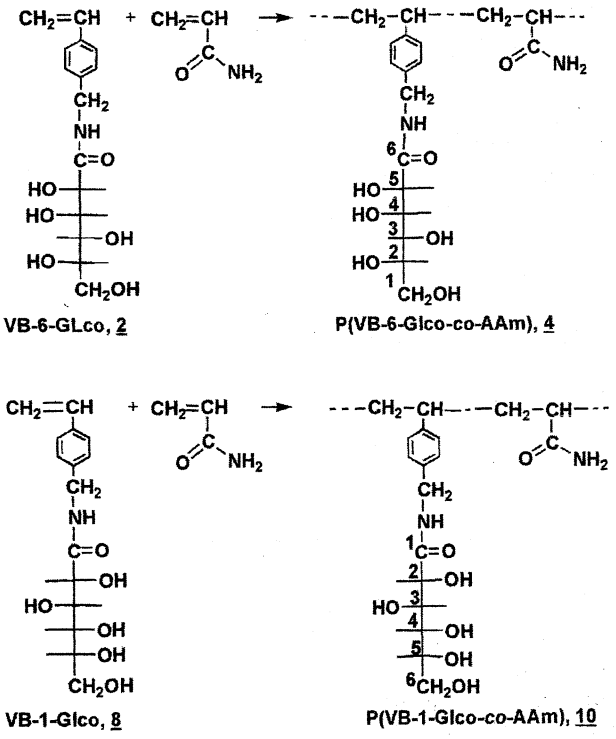

Scheme 5

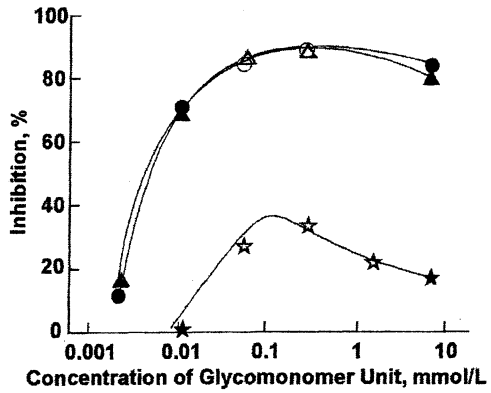

Figure 2. Inhibition of β-glucuronidase activity by different glycopolymers at 37 °C (*p*-nitrophenyl β-D-glucuronide, 7 m*M*; β-glucuronidase, 14 IU/L; pH, 4.7). ●: P(VB-6-Glco-*co*-AAK) **5**, 23%, M_n = 1.31 × 10^4; ▲: P(VB-1-Glco-*co*-AAK) **11**, 22%, M_n = 1.69 × 10^4; ★: PVB-6-Glco (M_n = 1.50 × 10^4) + PAAK (2.84 × 10^4). (Note: ●▲★, transparency; ○△☆, turbidity.)

β-D-glucuronide **6** with β-glucuronidase was determined in the presence of copolymers **9** and **11**. Their kinetic data were applied to a Lineweaver-Burk plot (eq 2),[35,36] as shown in Figures 3 and 4, respectively, and Table 2.

$$1/v = (1 + [I]/K_i)\{K_m/V_{max}\}(1/[S]) + (1 + [I]/K'_i)/V_{max} \quad (2)$$

where S, I, K_m, K_i, K'_i, and V_{max} are the substrate, inhibitor, equilibrium coefficient for the enzyme–substrate complex, coefficient for the enzyme–inhibitor complex (inactive), coefficient for the enzyme–substrate–inhibitor complex (inactive), and maximum value of v, respectively.

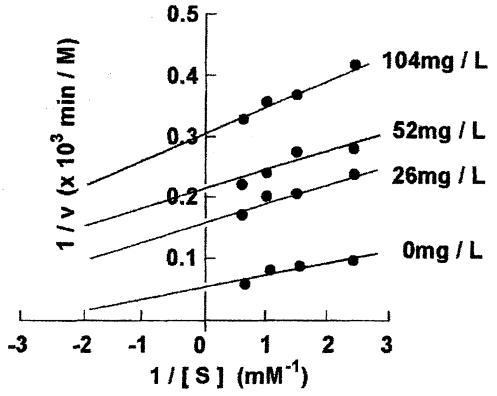

Figure 3. Lineweaver-Burk plot for kinetic data on the hydrolysis of Inhibition of *p*-nitrophenyl β-D-glucuronide by β-glucuronidase in the presence of copolymer **9** (PVB-1-GlcaH-*co*-AAm). Glycopolymer unit, 31%; M_n = 0.59 × 10^4.

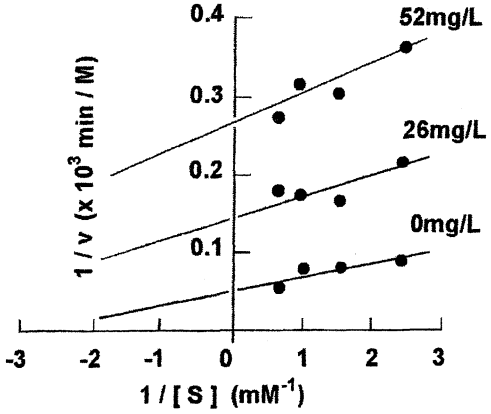

Figure 4. Lineweaver-Burk plot for kinetic data on the hydrolysis of Inhibition of *p*-nitrophenyl β-D-glucuronide by β-glucuronidase in the presence of copolymer **11** (PVB-1-Glco-*co*-AAK). Glycopolymer unit, 22%; M_n = 1.69 × 10^4.

In both cases of the hydrolytic tests using copolymers **9** and **11** as macromolecular inhibitors, the intercept of the *y*-axis increased with the amount of the copolymers, and the gradient was almost constant and independent of the concentration of the glycomonomer units as shown in Figures 3 and 4. Therefore, both copolymers are supposed to inhibit the activity of the enzyme uncompetitively. In other words, the copolymers may interact exclusively with the enzyme–substrate complex but not with the enzyme apparently. These results are in striking contrast to the competitive inhibition in the case of the isomeric macromolecular inhibitor (**3**), in which the D-glucaric moieties are linked at its sixth carbon position.[33] These results may reflect the differ-

Table 2. Kinetic Data on the Hydrolysis of *p*-Nitrophenyl β-Glucuronide with β-Glucuronidase in the Presence of Macromolecular Inhibitors at 37 °C

Macromolecular Inhibitor (mg/L)	$V_{max} \times 10^{-3}$ (M/min)	K_m (mM)	(K_m/V_{max}) $\times 10^{-1}$ (min)
9			
0	23.4	0.4	0.2
26	6.0	0.2	0.4
52	4.6	0.2	0.4
104	3.3	0.2	0.5
11			
26	6.7	0.2	0.4
52	4.0	0.2	0.5

[a] Shown in Figure 3.
[b] Shown in Figure 4.

ence in interaction of the inhibitors (glycopolymers) with the active sites in the hydrolase for the recognition and/or hydrolysis. Therefore the steric structure of β-glucuronidase itself will also be taken into account to discuss the inhibition mechanism in detail.

In summary, both glycopolymers **3** and **9** bearing the D-glucaric moieties in the opposite direction were found to inhibit the activity of β-glucuronidase but the inhibition mechanism seem to be different from each other. In addition, the inhibition was proved to be influenced not only by existence of carboxy groups but also by the configuration of hydroxy groups in the glyco-units.

EXPERIMENTAL

Reagents

D-Glucaro-1,4-lactone and D-glucono-1,5-lactone were purchased from Aldrich and Wako Junyaku(Tokyo, Japan), respectively. β-Glucuronidase isolated from calf liver and *p*-nitrophenyl β-D-glucuronide were obtained from Sigma. *p*-Vinylbenzylamine was prepared from *p*-vinylbenzyl chloride through Gabriel synthesis.[34,37] DMSO was dried over calcium hydride and distilled under reduced pressure before use.

N-(*p*-Vinylbenzyl)-1-D-glucaramide (VB-1-GlcaH, 7)

D-Glucaro-1,4-lactone (0.97 g, 5 mmol) was dissolved in methanol (15 mL) in a 50 mL flask and then *p*-vinylbenzylamine (1.36 g, 10 mmol) was added to the solution under dry nitrogen atmosphere. The mixture was stirred at 50 °C for 2 h, until white powder was precipitated. After addition of acetic anhydride (6 mL), the mixture was stirred at room temperature for 0.5 h, and subsequently condensed with an evaporator under reduced pressure. The residue was washed with chloroform (50 mL) and then recrystallized from ethanol: yield of **7**, 1.18 g (76%); Mp, 155–156 °C. Elem. Anal. Calcd for $C_{15}H_{19}NO_7$: C, 55.38%; H, 5.89%; N, 4.31%. Found: C, 55.37%; H, 5.85%, N, 4.29%.

IR (KBr disk) cm^{-1}; 3365 (ν_{O-H} and ν_{N-H}), 1701 ($\nu_{C=O}$, carboxy), 1616 ($\nu_{C=O}$, amide), 1546 (δ_{N-H}), 1432, 1003, 925 ($\delta_{CH2=CH-}$). ^1H NMR (7.5%, DMSO-d_6, 25 °C) δ, ppm; 8.18 (t, 1H, amide N*H*), 7.39 (d, 2H, 3,5-position of phenyl C*H*), 7.26 (d, 2H, 2,6-position of phenyl C*H*), 6.71 (dd, 1H, C*H*=CH_2), 5.79 (d, 1H, CH=CH_2 (cis)), 5.22 (d, 1H, CH=CH_2 (trans)), 4.31 (d, 2H, benzyl CH_2), 4.09 (d, 1H, ^{2}C*H*), 3.97 (m, 2H, ^{3}C*H*, ^{5}C*H*), 3.77 (m, 1H, ^{4}C*H*). ^{13}C NMR (7.5%, DMSO-d_6, 25 °C) δ, ppm; 174.4 (NH—*C*O (^{6}*C*)), 172.5 (*C*OOH (^{1}*C*)), 139.4 (NH—CH_2—*C* (phenyl)), 136.5 (CH_2=CH), 135.6 (CH_2=CH—*C* (phenyl)), 127.4 (3,5-position of phenyl *C*), 126.0 (2,6-position of phenyl *C*), 113.7 (*C*H_2=CH), 73.2 (^{2}*C*, ^{4}*C*), 71.6 (^{5}*C*), 70.2 (^{3}*C*), 41.6 (benzyl *C*H_2).

N-(*p*-Vinylbenzyl)-D-gluconamide (VB-1-Glco, 8)

According to the literature,[34] D-glucono-1,5-lactone (1.78 g, 10 mmol) was dissolved in methanol (70 mL) in a 300 mL flask and subsequently *p*-vinylbenzylamine (1.34 g, 10 mmol) was added to the solution under dry nitrogen. The mixture was stirred at 55 °C for 2 h, and then the solvent was removed under reduced pressure. The residual colorless crystalline was recrystallized from methanol; yield of **8**, 3.04 g (98%); Mp, 179 °C (dec.) (lit.,[34] 184 °C).

IR (KBr disk): 3300 cm^{-1} (ν_{O-H}, ν_{N-H}), 1646 ($\nu_{C=O}$, amide), 1544 (δ_{N-H}), 1421, 991, 904 ($\delta_{CH2=CH-}$). ^1H NMR (7.5%, DMSO-d_6, 25 °C) δ ppm; 8.16 (t, 1H, amide N*H*), 7.40 (d, 2H, 3,5-position of phenyl C*H*), 7.26 (d, 2H, 2,6-position of phenyl C*H*), 6.71 (dd, 1H, C*H*=CH_2), 5.79 (d, 1H, CH=CH_2 (cis)), 5.45 (d, 1H, ^{2}CO*H*), 5.22 (d, 1H, CH=CH_2 (trans)), 4.58 (d, 1H, ^{4}CO*H*), 4.53 (d, 1H, ^{3}CO*H*), 4.45 (d, 1H, ^{5}CO*H*), 4.36 (t, 1H, ^{6}CO*H*), 4.30 (t, 2H, benzyl CH_2), 4.07 (t, 1H, ^{2}C*H*), 3.98 (m, 2H, ^{3}C*H*), 3.58 (m, 1H, ^{5}C*H*), 3.50 (m, 1H, ^{4}C*H*), 3.36 (m, 1H, $^6CH_2$). ^{13}C NMR (7.5%, DMSO-d_6, 25 °C) δ, ppm; 172.6 ppm (NH—*C*O (^{1}*C*)), 139.4 (NH—CH_2—*C* (phenyl)), 136.5 (CH_2=CH), 135.6 (CH_2=CH—*C* (phenyl)), 127.4 (3,5-position of phenyl *C*), 126.0 (2,6-position of phenyl *C*), 113.7 (*C*H_2=CH), 73.8 (^{2}*C*), 72.5 (^{5}*C*), 71.6 (^{4}*C*), 70.2 (^{3}*C*),, 63.4 (^{6}*C*), 41.6 (benzyl *C*H_2).

Radical Copolymerization of Glycomonomers with Acrylic monomers

N-(*p*-Vinylbenzyl)-1-D-glucaramide (VB-1-GlcaH, **7**) (325 mg, 1.0 mmol) and acrylamide (AAm) (282 mg, 4.0 mmol), and azobisisobutyronitrile (AIBN) (0.05 mmol) were dissolved in DMSO (5 mL) in a testing tube. After an exhausting cock was attached to the tube, the solution was frozen and degassed in a dry ice-methanol bath. The testing tube was sealed after being degassed for three times, and stored in a bath controlled at

60 °C for 24 h. After cooling the tube in ice for quenching, the reaction mixture was poured in a large amount of chloroform. The resulting copolymer (P(VB-1-GlcaH-*co*-AAm), **9**) (173 mg) was collected as a colorless powder, and purified by the reprecipitation in a methanol–chloroform system.

The copolymerization of another glycomonomer, *N*-(*p*-vinylbenzyl)-D-gluconamide (VB-1-Glco, **8**) with AAm was also carried out in a similar method. Copolymer **10** (P(VB-1-Glco-*co*-AAm) was purified by dialysis in deionized water and the following lyophilization.

In the case of the radical copolymerization of **8** and acrylic acid (AA), the polymerization solution was diluted by 0.1N potassium hydroxide aqueous solution and dialyzed in a cellulose tube (cut off 3500) for 3 days. The residual aqueous solution was lyophilized to give copolymer **11** (P(VB-1-Glco-*co*-AAK) as a colorless powder.

Inhibition Test of Different Glycopolymers for the Activity of β-Glucuronidase

As described in our previous article,[32,33] hydrolytic rate of a model compound, *p*-nitrophenyl β-glucuronide, by β-glucuronidase was determined from the time dependence of the absorbance of *p*-nitrophenol freed from the glucuronide at 400 nm under the following conditions: 14 IU/L of hydrolase, 7 mM of substrate in an acetic buffer solution (pH, 4.7), 37 °C. The inhibition value of the glycopolymer (%) was calculated from the hydrolytic rates in the absence and presence of the glycopolymer by using eq 1.

The Lineweaver-Burk plot was tried by using the data determined in 0.4–1.4 mM of *p*-nitrophenol β-glucuronide in the presence of different amount of the glycopolymers.

Measurements

^{1}H- and ^{13}C NMR spectra were taken with a JEOL JNM-EX-270 Fourier transform high-resolution NMR spectrometer. Tetramethylsilane (TMS) was used as an internal standard in DMSO-d_6. Infrared spectra were recorded on a JEOL JIR-WINSPEC-50 Fourier transform infrared spectrometer. GPC chromatograms were measured with a Tosoh HLC-8120 high performance liquid chromatogram apparatus (Tosoh TSK-gel α-M column, ϕ7.8 × 600 mm; solvent, acetic buffer solution; rate, 0.8 mL/min). Molecular devices SPECTRSA$_{MAX}$™ 250 microplate spectrophotometer was used for the determination of *p*-nitrophenol resulting during the hydrolytic test.

This work was partly supported by Grant-in-Aid for "High Technology Research Center" from the Japanese Ministry of Education, Culture, Sports, Science, and Technology. The authors thank Mr. Asei William Kawaguchi for help in a part of the work and important discussion.

REFERENCES AND NOTES

1. Gandin, A. In Comprehensive Polymer Science, First Supplement; Allen, G.; Bevington, J. C., Eds.; Pergamon Press: Elmsfor, New York, 1992; Ch. 19, p 527.
2. Liu, Y.; Reineke, M. J Am Chem Soc 2005, 127, 3004.
3. Hashimoto, K.; Yaginuma, K.; Nara, S.; Okawa, H. Polym J 2005, 37, 384.
4. Liy, Y.; Wenning, L.; Lynch, M.; Reineke, T. M. J Am Chem Soc 2004, 126, 7422.
5. Henkensmeier, D.; Abele, B. C.; Candussio, A.; Thiem, J. Polymer 2004, 45, 7053.
6. Styron, S. D.; Kiely, D. E.; Ponder, G. J Carbohydr Chem 2003, 22, 123.
7. Yamanaka, C.; Hashimoto, K. J Polym Sci Part A: Polym Chem 2002, 40, 4158.
8. Bachman, F.; J Reimer, J.; Ruppenstein, M.; Thiem, J. Macromol Chem Phys 2001, 200, 3410.
9. Bachman, F.; Ruppenstein, M.; Thiem, J. J Polym Sci Part A: Polym Chem 2001, 39, 2332.
10. Lee, S.-I.; Yu, S.-C.; Lee, Y.-C. Polym Degrad Stab 2001, 72, 81.
11. Hanada, T.; Li, Y.-J.; Nakaya, T. Macromol Chem Phys 2001, 202, 97.
12. Kiely, D. E.; Chen, L.; Lin, T. H. J Polym Sci Part A: Polym Chem 2000, 38, 594.
13. Morton, D. W.; Kiely, D. E. J Polym Sci Part A: Polym Chem 2000, 38, 604.
14. Morton, D. W.; Kiely, D. E. J Appl Polym Sci 2000, 77, 3085.
15. Bachman, F.; Reimer, J.; Ruppenstein, M.; Thiem, J. Makromol Chem Rapid Commun 1998, 19, 21.
16. Wibullucksanakul, S.; Hashimoto, K.; Okada, M. Macromol Chem Phys 1997, 198, 305.
17. Wibullucksanakul, S.; Hashimoto, K.; Okada, M. Macromol Chem Phys 1996, 197, 1865.
18. Wibullucksanakul, S.; Hashimoto, K.; Okada, M. Macromol Chem Phys 1996, 197, 135.
19. Hashimoto, K.; Wibullucksanakul, S.; Okada, M. J Polym Sci Part A: Polym Chem 1995, 33, 1495.
20. Hashimoto, K.; Wibullucksanakul, S.; Okada, M. Makromol Chem Rapid Commun 1994, 14, 591.
21. Hashimoto, K.; Wibullucksanakul, S.; Okada, M. J Polym Sci Part A: Polym Chem 1993, 31, 3141.
22. Bachmann, F.; Thiem, J. J Polym Sci Part A: Polym Chem 1992, 30, 2059.

23. Hashimoto, K.; Mori, K.; Okada, M. Macromolecules 1992, 25, 2592.
24. Hashimoto, K.; Okada, M.; Honjoh, N. Makromol Chem Rapid Commun 1990, 11, 393.
25. Kobayashi, K.; Usui, T.; Akaike, T. In Advanced Biomaterials in Biomedical Engineering and Drug Delivery Systems; Springer: 1996; p 215.
26. Kobayashi, K.; Tsuchida, A. Macromolecules 1997, 30, 2016.
27. Miura, Y.; Ikeda, T.; Kobayashi, K. Biomacromolecules 2003, 4, 410.
28. Glazko, A. J.; Dill, W. A.; Wolf, L. M. J Pharmacol Exp Therapeut 1952, 104, 452.
29. Sacco, C.; Calabrese, E. J. J Environ Sci Health Toxicol 1992, A27, 1249.
30. Sacco, C.; McEwen, W. E.; Calabrese, E. J. Hum Exp Toxicol 1993, 12, 181.
31. Sacco, C.; Calabrese, E. J. Hum Exp Toxicol 1994, 13, 759.
32. Hashimoto, K.; Ohsawa, R.; Imai, N.; Okada, M. J Polym Sci Part A: Polym Chem 1999, 37, 303.
33. Hashimoto, K.; Ohsawa, R.; Saito, H. J Polym Sci Part A: Polym Chem 1999, 37, 2773.
34. Kobayashi, K.; Sumitomo, H.; Ina, Y. Polym J 1983, 15, 667.
35. Stryer, L. In Biochemistry, 3rd ed.; Freeman: New York, 1993; p 189.
36. Lineweaver, H.; Burk, D. J Am Chem Soc 1934, 56, 658.
37. Kondo, S.; Ohtsuka, T.; Ogura, K.; Tsuda, K. J Macromol Sci Chem 1979, 13, 767.

DOI 10.1002/pola

Proceeding of International Symposium on advances Technology (ISAT-6th), p.87-90 (Nov. 4-6, 2007). Kogakuin University,

Synthesis of New Polymers Having Xylaric and Tartaric Pendants and Their Inhibition for β-Glucuronidase Activity

[a] Asei William Kawaguchi, Haruki Okawa, and [b]Kazuhiko Hashimoto
Department of Materials Science and Technology, Faculty of Engineering, Kogakuin University
Address: 2665-1 Nakanocho, Hachioji, Tokyo 192-0015, Japan
E-mail: [a] bd06001@ns.kogakuin.ac.jp, [b] hashimot@cc.kogakuin.ac.jp

Keywords: β-Glucuronidase / Inhibition / Xylaric Acid / Tartaric Acid

Abstract

New styrene derivatives having *D*-xylaric and *L*-tartaric moieties, *N*-*p*-vinylbenzyl-*meso*-xylaramic and *N*-*p*-vinylbenzyl-*L*-tartaramic acids (VB-*meso*-XylarH and VB-*L*-TartaH) were synthesized by the ring-opening addition of 2,3,4-tri-*O*-acetyl-*D*-xylaric anhydride and 2,3-di-*O*-acetyl-*L*-tartaric anhydride respectively, and their subsequent hydrolysis under basic condition. The glycomonomers were copolymerized with acrylamide to give novel polymers having xylaric and tartaric moieties in the pendants (P(VB-*meso*-XylarH-*co*-AAm) and P(VB-*L*-TartaH-*co*-AAm)) respectively. The glycopolymers were found to inhibit the β-glucuronidase activity much stronger than not only the corresponding saccharic acids but also the glycomonomers, respectively by spectrophotometry.

Introduction

In a human body, β-glucuronidase in the small intestine is known to hydrolyze β-glucuronide conjugates which are produced from UDP-D-glucuronic acid and xenobiotics (medicine and toxic substance) in the liver. The free xenobiotics are absorbed through the wall of the small intestine and returned to the liver via the portal vein. If the xenobiotics are toxic, they should be exhausted to outside of the body promptly by the inhibition of the activity of β-glucuronidase.

D-Glucaric acid and its lactone derivatives are well-known to inhibit the β-glucuronidase activity. Therefore, in our previous work[1,2], novel styryl-type glycopolymers bearing D-glucaric pendants were synthesized and found to suppress the enzymatic hydrolysis of a model compound for xenobiotics-β-glucuronidase conjugate.

In this presentation, we will investigate the inhibition ability of four- or five-carbon saccharic acids such as xylaric and tartaric acids, their glycomonomers, and also the glycopolymers to β-glucuronidase, and compare them with those of the glucaric analogs.

Experimental

Syntheses of the Glycomonomers

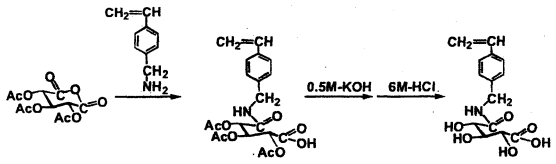

The xylaric type monomer (VB-*meso*-XylarH) was prepared as followed: *p*-Vinylbenzyl amine and 2,3,4-tri-*O*-acetylxylaric anhydride, which was prepared from D-xylaric acid and acetic anhydride, were stirred in ethyl acetate at room temperature for 1 night. Then, precipitated white crystal (*N*-*p*-vinylbenzyl 2,3,4-tri-*O*-acetyl-xylaramic acid) was collected, hydrolyzed with 0.5M-KOH and then neutralized with 6M-HCl to produce the xylaric monomer. The tartaric type monomer (VB-*L*-TartaH) was also prepared in a similar method.

Preparation of the Glycopolymers

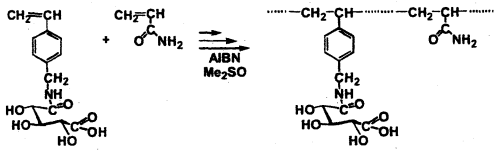

VB-*meso*-XylarH or VB-*L*-TartaH, acrylamide (AAm) and azobisisobutyro-nitrile were dissolved in dimethyl sulfoxide in a testing tube. After degassing three times in a cooling bath, the tube was sealed and heated in a bath controlled at 60°C for 24 hours. Then, the tube was cooled down at –20°C for quenching. After the seal was broken, the solution was poured to a large amount of chloroform and the resulting polymer was collect on a glassfilter. The polymer was purified by the reprecipitation from its methanol solution into chloroform three times and dried under reduced pressure. The copolymer composition was estimated from the intensity ratio of the signals in the ^{1}H-NMR.

Inhibition Test of the Glycopolymer for β-Glucuronidase Activity

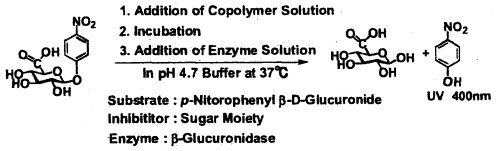

A model compound for the β-D-glucuronide conjugates of xenobiotics, *p*-nitrophenyl β-D-glucuronide, was hydrolyzed with β-glucuronidase in the absence or presence of the resulting glycopolymer. The amount of *p*-nitrophenol liberated from the glucuronide was determined by spectroscopy. The inhibition value (%) was calculated from the hydrolytic rates of the substrate in the absence and presence of the copolymers. The inhibition values of xylaric and tartaric acid and the corresponding monomers were also determined in a similar method. The Lineweaver-Burk plot was tried by

Table 1 Radical Copolymerization of Glycomonomers (1 and 2) with Acrylamide [a]

Monomers			$[M]_0$	AIBN	Time	Polymers		M_n[c]	M_w/M_n[c]
M_1[b]	mg (mmol)	AAm mmol	mol/L	mol%	h	Yield mg	mol% of 1 or 2[b]	x10^{-4}	
1	170(0.6)	2.4	1.5	1.00	24	210	27	0.84	1.53
2	474(1.8)	4.2	1.5	0.13	12	408	23	0.88	1.51

[a] Solvent, DMSO; Temp., 60°C. [b] M_1=1, VB-*meso*-XylarH; 2, VB-*L*-TartaH.
[c] By ^{1}H-NMR in D_2O. [d] By GPC in Acetic Buffer (Standard, PEG).

using the data determined in 0.4-1.4mM of *p*-nitrophenyl β-glucuronide in the presence of different amount of the glycomonomers and glycopolymers.

Result and Discussion

Preparation of the Glycopolymers

The radical copolymerization of the glycomonomers (1 and 2) with acrylamide was carried out in DMSO solution, in which the mole ratio of the glycomonomer was 0.3 in feed. The number average molecular weight of the copolymer (P(VB-*meso*-XylarH-*co*-AAm) and P(VB-*L*-TartaH-*co*-AAm)) was also controlled to ~0.8x10^4 as in Table 1.

Inhibition Test of the Glycopolymers for β-Glucuronidase Activity

The inhibition value (%) of each glycopolymers, the corresponding glycomonomers and saccharic acid was determined at various concentrations of saccharic units as shown in Figure 1 ((A) : Xylaric type, (B) : Tartaric type).

The values of glycopolymers (P(VB-*meso*-XylarH-*co*-AAm), and P(VB-*L*-TartaH-*co*-AAm)) were higher than those of the corresponding glycomonomers (VB-*meso*-XylarH, VB-*L*-TartaH), and saccharic acid, respectively, increased with the concentration of saccharic units, and attained 70% and 51%, respectively at 6.67mmol/L. The glycomonomers also inhibited the β-glucuronidase activity, but their values were lower than those of the corresponding glycopolymers especially at lower concentration of saccharic units. On the other hand, both saccharic acids could not inhibit β-glucuronidase strongly. From the comparison of the values of saccharic acids with those of the corresponding glycomonomers, the existence of hydrophobic p-vinylbenzyl group seems to play an important part in the inhibition. Another noteworthy point is in the fact that the inhibition value of glycopolymers was much higher than the corresponding monomers especially in the lower concentration of saccharic units, which may be one of

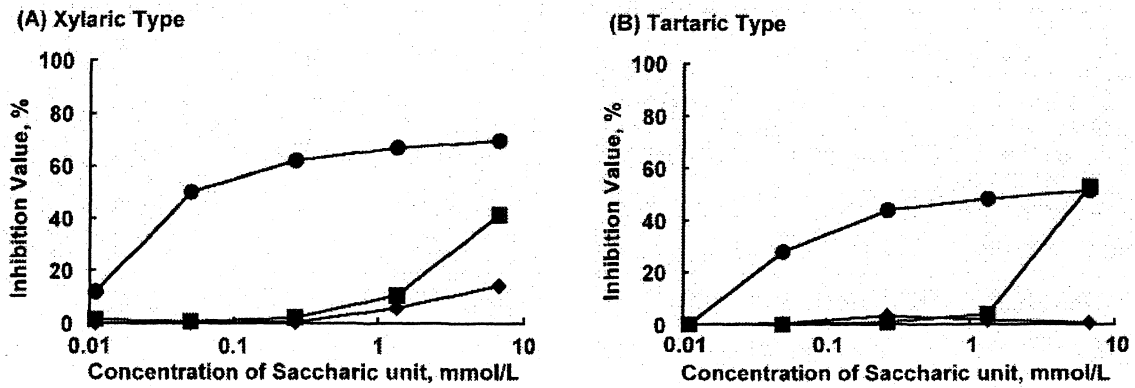

Fig. 1 Inhibition of β-Glucuronidase Activity by glycopolymers, corresponding glycomonomers and saccharic acids at 37°C (*p*-nitrophenyl β-D-Glucuronide, 7 mmol/L; β-glucuronidase, 14 IU/L).

(A), ●: P(VB-*meso*-XylarH-*co*-AAm), ■: VB-*meso*-XylarH, ◆: D-Xylaric acid.

(B), ●: P(VB-*L*-TartaH-*co*-AAm), ■: VB-*L*-TartaH, ◆: *L*-Tartaric acid.

positive cluster effects. In the glycopolymer, the saccharic units were linked along the polymer chain and might exist as a cluster. Hence, even in the lower concentration of saccharic unit, the units are supposed to become locally high concentration and to inhibit the enzyme activity cooperatively.

References

[1] K. Hashimoto *et al., J. Polym. Sci.: Part A: Polym. Chem.,* 37, 303 (1999) ; ibid, 37, 2773 (1999).

[2] K. Hashimoto *et al., J. Polym. Sci.: Part A: Polym. Chem.,* 44, 4895 (2006).

[3] A. W. Kawaguchi, T. Kaida, H. Okawa, K. Hashimoto, *Polym. Prep. Jpn.*, 54(2), 4893 (2005).

[4] A. W. Kawaguchi, T. Kaida, H. Okawa, K. Hashimoto, *Prep. of 8th Int. Polym. Conf. Fukuoka (IPC 2005),* 316 (2005).

[5] A. W. Kawaguchi, H. Okawa, K. Hashimoto, *Polym. Prep. Jpn.*, 56(2), 5076 (2007).

Full Paper

Photoactivity Characteristics of a Biodevice Using Primary Photosynthetic Reaction Centers

Katsuya Abe,[a] *Atsushi Ishii*,[a] *Morio Hirano*,[a]* *James F. Rusling*[b,c]

[a] Department of Applied Chemistry, Faculty of Engineering, Kogakuin University, 1-24-2 Nishi-Shinjuku, Shinjuku-ku, Tokyo 163-8677, Japan
[b] Department of Chemistry, University of Connecticut, Storrs, CT 06269-3060, USA
[c] Department of Pharmacology, University of Connecticut Health Center, Farmington, Connecticut 06032, USA
*e-mail: bt10807@ns.kogakuin.ac.jp

Received: June 8, 2005
Accepted: September 9, 2005

Abstract
Films with alternating layers of thylakoid membrane from the cyanobacterium *Spirulina platensis* and the positively charged polyion poly(ethylenimine) (PEI) were prepared by means of alternate electrostatic layer-by-layer assembly. The thylakoid membrane/PEI bilayers were functionally and structurally characterized by visible spectra, electrochemical methods and SEM techniques, respectively. The films deposited onto gold electrodes were molecularly smooth and consistent with thylakoid membrane/PEI bilayers as observed by SEM. The photoactivity of the thylakoid membrane/PEI assembly was dependent on thickness of the film that increased with the number of bilayers. There was an obvious difference in the current responses of 1- and 5-bilayer thylakoid membrane/PEI films under illumination. The photosynthetic electron transfer process in the thylakoid membrane/PEI single-bilayer film was demonstrated by an inhibition of the photoactivity by herbicide. Biodevices for the detection of phytotoxicity were constructed using the isolated thylakoid membrane from chloroplast as biosensing elements by means of electrostatic layer-by-layer assembly.

Keywords: Thylakoid membrane, Layer-by-layer films, Photoactivity, Biodevice, Herbicide

DOI: 10.1002/elan.200503370

1. Introduction

The high selectivity provided by biomolecules such as antibodies and enzymes, or higher order biological assemblies involving receptors, ion channels, organelles and whole cells can be utilized in biosensors that integrate the biological sensing element with an appropriate transducer [1]. The incorporation of biomolecules in well-ordered lipid membranes provides interesting models for biological membranes can be used for studying specific interactions, and is a convenient tool for designing artificial systems with biological functions. In particular, conventional or synthetic lipid membranes have been used to employ molecular mechanisms of biomembrane function such as ion sensing [2], antigen – antibody binding [3 – 5], energy conversion [6], and so on. On the other hand, composite modified electrodes with biomolecules or biomembranes in the cells were prepared for amperometric detection of compounds toxic to photosynthetic organisms. For example, biosensors for the detection of herbicides via phytotoxicity were constructed using isolated photosynthetic reaction center protein or thylakoid membrane from chloroplast as biosensing elements [7, 8]. A photosystem II-based multibiosensor offered a sensitive detection method for herbicides and prescreening analyses of natural waters [9, 10].

Recently, construction of multiprotein systems has attracted much attention as an important research target in modern protein engineering. Many approaches for multiprotein architecture use self-assembly to build up active enzyme monolayers at electrode surfaces. Examples include artificial molecular systems based on Langmuir – Blodgett films [11], biotin/avidin interactions [12, 13], and layer-by-layer alternate electrostatic adsorption. In these systems, layer-by-layer alternate adsorption has the great advantage of simplicity and versatility [14 – 25]. The alternate adsorption of monolayers of biomolecules and polyions is a more general method developed by Decher, Lvov and others [16, 26 – 29]. This technique has been used to make ultrathin films (with molecular-level thickness control) of a wide variety of proteins and oppositely charged polyions. Also, several different enzymes can be incorporated and spatially separated on the normal axis of the film in this way. The step-by-step electrostatic adsorption of oppositely charged molecules in solution onto charged surfaces, with surface charge reversal, allows design of protein film architecture to desired specification and thickness. Rusling et al. showed that this method provided good stability for enzymes on electrodes and catalyzed reactions with the resulting films [30, 31]. Many of these polyion – protein multilayer films were used as enzyme biosensors. Calvo et al. have reported the layer-by-layer alternate adsorption of glucose oxidase

(GOD) and polycationic redox polymer. The GOD catalysis for the oxidation of β-D-glucose was achieved with the multilayer polyion/GOD assembly [32, 33]. Simple biosensors fabricated through the layer-by-layer technique have been developed to detect compounds essential or hazardous to animal cells. Particularly, DNA in these films provided active elements for sensors for screening the toxicity of chemicals and detection of oxidative stress by monitoring DNA damage [34–36].

There is continued and growing concern about the pollution of aquatic systems by agricultural pollutants. Some herbicides are continuously discharged into lakes and rivers with rainwater, resulting in contaminated aquatic environments which are hazardous to organisms. Recently, much attention has been focused on determining the toxicity of these pollutants to living organisms in aquatic systems. We have previously demonstrated that degree of water pollution with inorganic compounds (such as nitrate, ammonium, etc.) could be expressed by the change in color of cells of microorganisms [37]. In general, photosynthetic organisms have a thylakoid membrane which cleverly organizes many kinds of proteins to convert solar energy into electrical/chemical energy in products of ATP and NADPH. The thylakoid membrane has sensitivity to temperature, light, and physical/chemical factors of its environment. In this study, we prepared a biodevice using thylakoid membrane from a photosynthetic microorganism by means of the layer-by-layer alternate adsorption with an accompanying polycation. . The aim of this study is to characterize the simple biodevice fabricated through the layer-by-layer technique for detection of herbicides. Layer-by-layer film growth on gold electrode was monitored using a quartz crystal microbalance (QCM) and characterized by its photoelectrochemical activity.

2. Experimental

2.1. Regents

All solvents and reagents were of analytical or laboratory grade. Deionized water was used throughout.

2.2. Isolation of Thylakoid Membranes

All the operations in the isolation of thylakoid membranes were carried out at 4 C and as rapidly as possible. Thylakoid membranes were isolated from the cyanobacterium *Spirulina platensis* (cells grown at 25 C) according to the procedure described by Melis et al. [38]. Cells were harvested by centrifugation at 1000 × g for 3 min. After discarding the supernatant, the cell pellets were frozen at −40 °C for subsequent analyses. Samples were thawed on ice and diluted with sonication buffer containing 100 mM Tricine – KOH, 100 mM sodium chloride, 5 mM magnesium chloride, 0.2% sodium ascorbate, 0.2% poly(vinylpyrrolidone), 1mM aminocaproic acid, and 1mM aminobenzamidine adjusted to pH 8.0. The amount of the buffer solution was about two-times the volume of sample. The cells in the buffer were disrupted by sonication for 5 min at 28 kHz. Unbroken cells were removed by centrifugation at 3000 × g for 4 min. Then, the supernatant was centrifuged at 75000 × g for 30 min (Optima TL Ultracentrifuge, BECKMAN Co., Ltd.) getting thylakoid membrane pellet. The amount of photosynthetic material was quantified by measuring chlorophyll concentration in the following way. Thylakoid membranes were suspended in 5 mL of methanol and the suspension was sonicated for 3 min, and centrifuged at 3000 rpm for 10 min. The total content of chlorophyll in the methanol layer was estimated from the specific absorption coefficients given by Mackinney [39]. In determination of protein content, the membranes were suspended in water, and the total protein content was measured by the Lowry method [40].

2.3. Thylakoid Membrane Immobilization

The thylakoid multilayer films were assembled on gold-coated resonator electrodes (cross-sectional area: 0.18 cm^2) of a quartz crystal microbalance (QCM, TamaDevice Co., Ltd., Japan) or a Au disk electrode (BAS, OD:6.0 mm, ID:3.0 mm) by repeating alternate adsorption of polycation {branched poly(ethylenimine):PEI, MW 70,000, Wako Co., Japan} and isolated thylakoid membrane. The polycation at a concentration of 1.5 mg mL^{-1} was dissolved in pure water. The chlorophyll concentration was adjusted to 60 μg mL^{-1}. Au electrodes were polished with emery paper and then alumina slurry to obtain a mirror finish. Gold electrode resonators or Au electrodes were washed according to the procedure described in reference [16]. A negatively charged surface was prepared by immersing the cleaned gold electrodes in 10mM ethanolic 2-mercaptoethanesulfonic acid (MESA, sodium salt, Aldrich Co.) for 12 h, then rinsed in pure ethanol and water. In a typical procedure, layers of thylakoid membrane were immobilized on the gold QCM resonator or the Au electrode by repeating alternate adsorption of thylakoid membrane and PEI {(thylakoid membrane/PEI)$_n$, n = number of bilayer} for the required number of times. The thylakoid membrane was first suspended in buffer containing 100 mM Tricine – KOH, 100 mM sodium chloride, 5 mM magnesium chloride, 0.2% sodium ascorbate, 0.2% poly(vinylpyrrolidone), 1mM aminocaproic acid, and 1 mM aminobenzamidine adjusted to pH 8.0.

2.4. Monitoring Film Growth

In this study, the assembly process was monitored by visible absorption spectroscopy (UV-2450, Shimadzu) and QCM measurements (Universal Counter 53131A, Agilent). QCM resonators were immersed in a sample solution for a given period of time, and then dried by nitrogen stream. The resonators were covered by evaporated gold electrodes on

both faces, and their resonance frequency was approximately 9 MHz (AT-cut). All experiments were carried out at ca. 25 °C. Micrographs of assembled films were obtained with a Hitachi S-4200 (Japan) scanning electron microscope (acceleration voltage of 5.0 kV).

2.5. Electrochemical Measurements

The three-electrode cell employed a Ag/AgCl reference electrode (BAS), a Pt wire counter electrode (BAS), and the Au disk electrode (BAS) working electrode. Electrochemical measurements were thermostated at 25 °C. The buffer was 10 mM sodium phosphate (Na_2HPO_4 –KH_2PO_4) adjusted at pH 7.0 containing 50 mM NaBr. The buffer was purged with purified nitrogen for at least 20 min to remove oxygen. The three-electrode system was connected to a potentiostat (HAB-151, HOKUTO DENKO Co. Ltd.). The current was monitored on a recorder (SEKONIC Co. Ltd.). The light beam from a 150W halogen lamp (CS-15, CABIN INDUSTRIAL Co., Ltd.) was directed onto the surface of the Au electrode.

2.6. Oxygen Evolution Measurement

A multienzyme film was prepared using anionic glucose oxidase (GOD) and peroxidase (POD) and polycation (PEI) on a gold-coated glass plate (5 × 15 mm) by alternate layer-by-layer adsorption. Then, oxygen evolved by the thylakoid membrane/PEI films in the electrochemical cell was assayed using the {$(POD/PEI)_2$ + $(PSS/PEI)_2$ + $(GOD/PEI)_2$/MESA} immobilized gold-coated glass at 25 °C. The buffer solution in the electrochemical cell was purged with purified nitrogen for at least 20 min to remove oxygen completely, in advance. The multienzyme film was immersed in the buffer solution (2.9 mL) with a small amount of solution (0.1 mL, 10 mM sodium phosphate, pH 7.0) containing D-glucose (56 mM) and an indicator {(10-carboxymethylaminocarbonyl)-3,7-bis(dimethylamino)-phenothiazine sodium salt, Wako Co., Japan} (10 mM) for 1 min. Finally, the POD in the multienzyme film can oxidize the indicator using hydrogen peroxide as oxidant in the solution, monitoring oxygen evolution. The reaction was followed by measuring the absorbance of oxidized indicator at 665 nm. The solution was stirred continuously as avoided to contaminate with air.

3. Results and Discussion

3.1. Thylakoid Membrane Immobilization Monitored by QCM

QCM frequency changes were measured on dry films to obtain the weight of each layer. The quartz resonator frequency was stable within ±5 Hz for several hours. Figure 1 shows frequency shifts upon alternate adsorption of thylakoid membrane and PEI on a QCM resonator. The first few steps resulted in smaller amounts of adsorption, but the subsequent steps provided larger logarithmic adsorption. These frequency shifts were similar to that of alternate adsorption of anionic glucose oxidase and PEI, as previously described by Lvov et al. [14], and probably reflect deposition of incomplete initial layers that eventually fill in to become smooth films upon deposition of the upper layers [16]. In later steps, the QCM frequency shifts for thylakoid membrane/PEI bilayer (3rd to 5th step cycle) were 4200 to 6800 Hz at a thylakoid concentration of 60 μg mL^{-1} and pH 8.0. It was reported that frequency shift upon glucose oxidase with PEI was about 2000 Hz per step. The larger frequency shift of thylakoid membrane is attributed to the formation of molecular assembly involving lipid membranes, proteins, photosynthetic pigments and other components.

In photosynthesis, light is adsorbed by pigments (chlorophylls, carotenoids, etc.) and converted into chemical energy in ATP and NADPH, which are used in the synthesis of organic compounds form carbon dioxide. For example, photosystem II in thylakoid membranes is a multiprotein complex with a function of photoassisted oxidation of water to donate electrons to the cytochrome B_6/f protein complexes in vivo. Therefore, layer of negatively-charged thylakoid membranes including multiprotein complexes as described above was successfully assembled with oppositely-charged polyions (PEI). Previously, isolated thylakoid membranes, photosystem I or II particles and bacterial reaction centers were applied in various types of electrochemical cells. Rusling and co-workers have previously demonstrated that photosynthetic reaction centers from *Rhodobacter sphaeroides* and from Spinach could be reconstituted in lipid film on pyrolytic graphite electrodes [41, 42]. It is particularly interesting that a direct fast

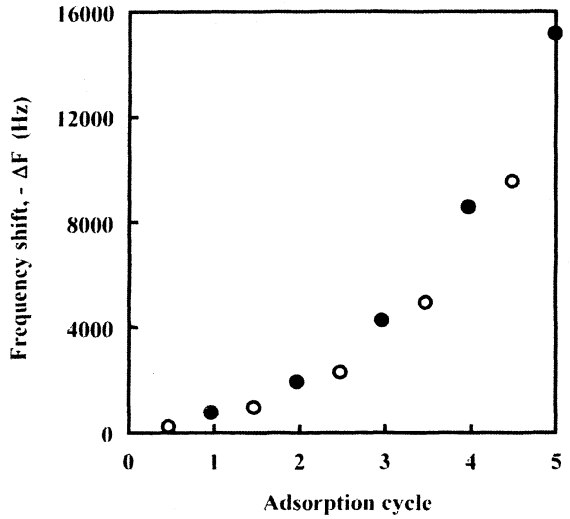

Fig. 1. Frequency shift ($-\Delta F$) in the alternate adsorption of thylakoid membrane/PEI at pH 8.0 and 25 °C. (●) Thylakoid membrane adsorption steps and (○) PEI adsorption steps. The amount of thylakoid membrane was quantified by measuring chlorophyll concentration and the concentration was adjusted to 60 μg mL^{-1}.

reversible electron transfers were observed for the cofactors in the reaction centers photosynthetic protein.

In the present study, the QCM frequency shift for thylakoid membrane/PEI bilayer was monitored at different pH conditions. Buffer solutions containing thylakoid membrane were as follows: 100 mM sodium phosphate at pH 6.0 and pH 8.0, 100 mM Tricine-KOH at pH 8.0 and pH 9.0. The thylakoid membrane was suspended in buffer containing 100 mM Tricine-KOH with 100 mM sodium chloride, 5 mM magnesium chloride, 0.2% sodium ascorbate, 0.2% poly(vinylpyrrolidone), 1mM aminocaproic acid, and 1 mM aminobenzamidine. As a result, larger amounts of adsorption of thylakoid membrane and PEI was obtained using the Tricine buffer solution at pH 8.0, although the QCM frequency shift could be monitored in all of the buffer solutions at the first step of the adsorption cycle. Additionally, it was observed that adsorption of anionic thylakoid membrane and cationic PEI reached saturation in ca. 15 min. In this study, the solid substrates were alternately immersed for 20 min.

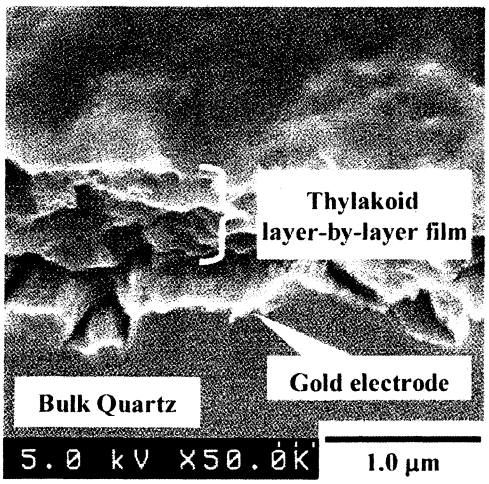

Fig. 2. Scanning electron micrograph image of (thylakoid membrane/PEI)$_{10}$ film deposited onto gold-coated resonator electrode showing a top/edge view.

3.2. Surface Characterization of Immobilized Thylakoid Membrane Films

Figure 2 shows a SEM of (thylakoid membrane/PEI)$_{10}$ film deposited onto a gold-coated resonator electrode. The deposited film is clearly seen and molecularly smooth. In the SEM observation, the deposited film was found to be composed of the thylakoid membrane/PEI bilayers and the thickness of (thylakoid membrane/PEI)$_{10}$ film was presumed to be 650 nm. The QCM frequency shift of the 10-bilayer film was ca. 35000 Hz. Thickness (d) and QCM frequency shift (ΔF) are related [14] by d (Å) $\approx A \times -\Delta F$ (Hz) where A is the cross-sectional area of quartz covered by QCM electrodes: $A = 0.18$ cm^2. Thus, the QCM frequency change of 35000 was converted to a thickness value of 630 nm with the above equation. This value was in good agreement with the SEM observation. In Figure 1, the frequency changes (650 and 15200 Hz) of the 1st and 5th step cycle were calculated to be 11 and 274 nm in the thickness of the bilayers film, respectively. It was previously reported that mass and thickness of individual layers were estimated on dry films of photosynthetic reaction center protein (from *Rhodobacter*)/polycation by QCM measurement [43]. The reaction center and polycation (PEI) in the bilayers film was ca. 6.4 and 0.5 nm in thickness, respectively. The thickness (ca. 10.5 nm) of thylakoid membrane on the gold electrode is thicker than that of the reaction center protein, because the membrane consists of lipid bilayers, other proteins and as organelles.

Figure 3 shows absorption spectrum for a thylakoid membrane/PEI film deposited on quartz slides. The bilayers film was peeled off from the surface of quartz slide in the buffer solution by sonication, and then monitored by visible absorption spectroscopy. As a result, the adsorption spectrum of the film was quite similar to that of suspension of thylakoid membrane as isolated from cells of cyanobacterium, *Spirulina platensis*. In the assembly process, the

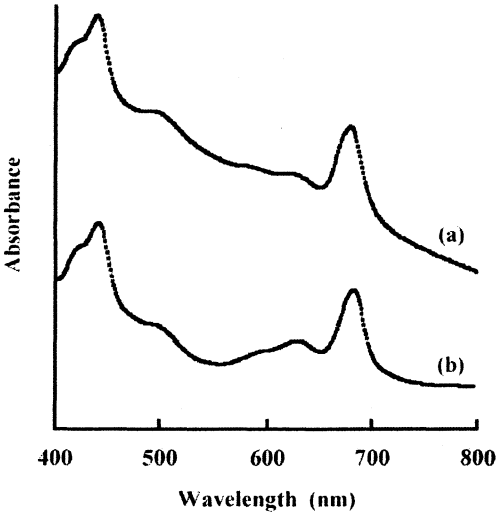

Fig. 3. Absorption spectra for thylakoid membrane/PE assembly and thylakoid membrane suspension. (a) Thylakoid membrane/PEI bilayer film and (b) thylakoid membrane suspension.

amounts of chlorophyll a and protein in thylakoid membrane deposited on Au electrodes increased with the number of adsorption cycles (Fig. 4a and b) and were proportional to the frequency shift per step (Fig. 1). The same result was also obtained using thylakoid membrane/PEI film deposited on Au electrode. Accordingly, it was showed that isolated thylakoid membrane was assembled alternately with polycation (PEI) on gold electrodes by means of electrostatic layer-by-layer adsorption.

3.3. Photoactivity of Immobilized Thylakoid Membrane

The thylakoid membrane/PEI films on Au disk electrodes (OD: 6.0 mm, ID: 3.0 mm) were prepared using electrostatic

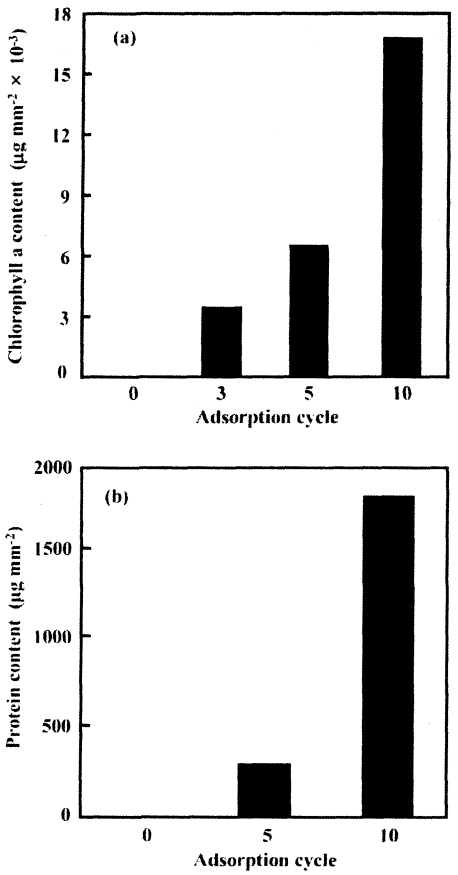

Fig. 4. Contents of chlorophyll a (a) and protein (b) in thylakoid membrane/PEI bilayer film with the number of adsorption cycles.

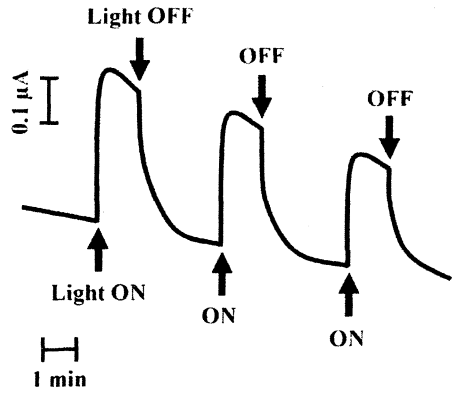

Fig. 5. Current response to illumination of (thylakoid membrane/PEI)$_5$ film deposited onto Au electrode.

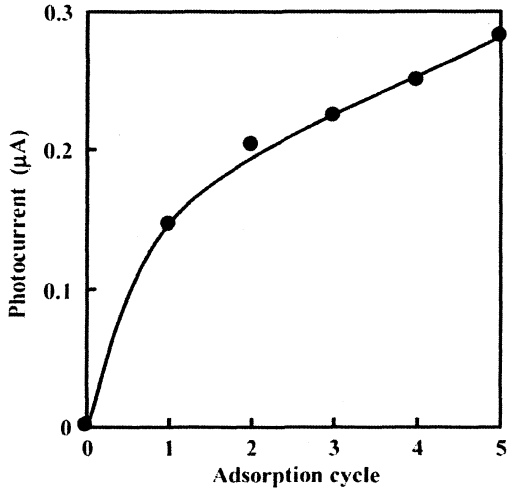

Fig. 6. Dependence of photocurrent produced from thylakoid membrane/PEI bilayer film on the number of the bilayer.

layer-by-layer adsorption as described above. The Au electrodes were polarized at 0.75 V to the reference Ag/AgCl electrode. Typical photocurrent measurement of (thylakoid membrane/PEI)$_5$ film deposited on Au electrode is shown in Figure 5. From Figure 1, a 5-bilayer film was found to be 274 nm in thickness, containing chlorophyll a at 0.6 μg/cm^2. It is worth noting that the maximum photocurrent (83 μA/10 μg Chlorophyll/cm^2) produced from the nano-order thin film was 10-fold higher than the photocurrent obtained from thylakoids immobilized in a cross-linked albumin-glutaraldehyde matrix [7], even in the absence of electron acceptors such as potassium ferricyanide or benzoquinone derivatives for the photosystem II reaction in this study. This result implies that the layer-by-layer method provides possibility of higher concentrations of electroactive species in the films.

Figure 6 shows the dependence of photocurrent produced from the thylakoid membrane/PEI bilayer film with the umber of the bilayer. The large photocurrent was observed at the 1st step cycle, then begins to bend off after the 2nd step cycle. These values were indicated as current produced when the light was turned on at the imposed potential of 0.75 V. This result suggests that the photocurrent generation based on charge transport in the bilayer films may be limited by electron diffusion into and out of the films. The current responses of 1- and 5-bilayer thylakoid membrane/PEI films to the illumination are shown in Figure 7. When the 1-bilayer film was illuminated, the photocurrent started to appear and attained a steady state in 3 min, resulting in the maximum current (Fig. 7a). On the other hand, it was found that the 5-bilayer film could generate the maximum photocurrent immediately following light on (Fig. 7b). There is an obvious difference in the induction of the photocurrent generation by the layer films. In this study, oxygen evolved by the thylakoid membrane/PEI films in the electrochemical cell was assayed using the {(POD/PEI)$_2$ + (PSS/PEI)$_2$ + (GOD/PEI)$_2$/MESA} immobilized gold-coated glass at 25 C. It was observed that, when the 1- and 5-bilayer thylakoid membrane/PEI films immobilized Au electrodes were illuminated, the 1-bilayer film electrode only produced the anodic current to result in oxygen evolution at ca. 0.5 μmol min^{-1}. Additionally, the magnitude of the steady-state photocurrent produced by the 1-bilayer film was strongly sensitive to the temperature in the electrochemical cell. The 1-bilayer thylakoid membrane/PEI film showed a different

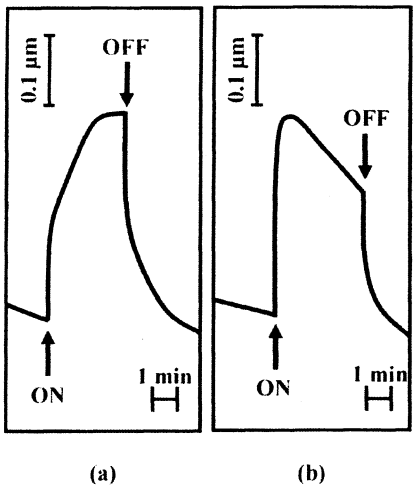

Fig. 7. Deference of current response of 1- (a) and 5- (b) bilayer thylakoid membrane/PEI films on the number of the bilayer.

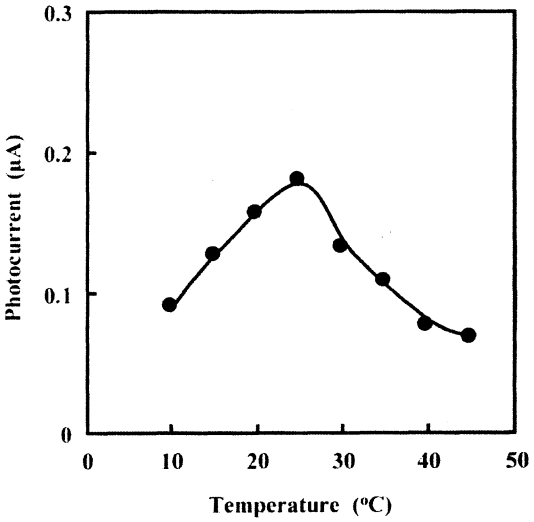

Fig. 8. Temperature dependence of steady-state photocurrent measured with thylakoid membrane/PEI 1-bilayer film. The current response was measured using thylakoid membrane isolated from *Spirulina platensis* grown at 25 °C.

photocurrent-temperature dependency (Fig. 8). A maximum current was obtained at 25 °C, and the current decreased both above and below 25 °C. Using thylakoid membrane isolated from *Spirulina platensis* grown at 15 °C (the low temperature culture), a 1-bilayer thylakoid membrane/PEI film was prepared on the Au disk electrode to investigate the dependence of temperature on the photocurrent. As a result, the photoactivity of the film was well-maintained below 25 °C, compared with that of thylakoid membrane isolated from the cells cultured at 25 °C.

In Figure 9, we show the effect of herbicide {*N*'-(3,4-dichlorophenyl)-*N*,*N*-dimethylurea: DCMU, Tokyo Kasei Co., Ltd.} on the steady-state photocurrent of the 1-bilayer thylakoid membrane/PEI film. DCMU binds irreversibly to

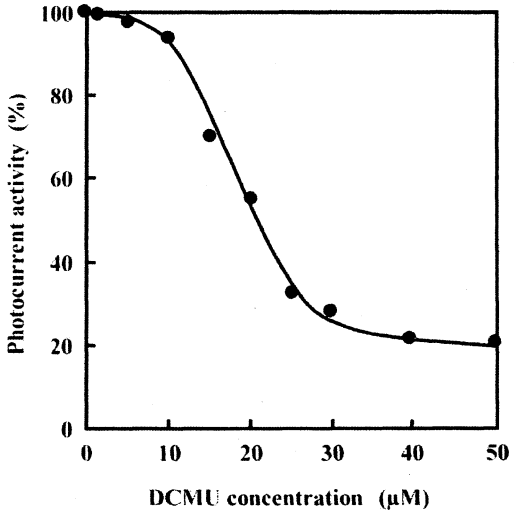

Fig. 9. Effect of DCMU on steady-state photocurrent of 1-bilayer thylakoid membrane/PEI film. The current response was measured using thylakoid membrane isolated from *Spirulina platensis* grown at 25 °C.

the Q_B site of photosystem II (PS II) proteins in thylakoid membrane and causes a loss of activity of the PS II reaction. The photocurrent activity became very small when measured in the solution containing 25 μM DCMU. Above 40 μM DCMU, 20% of the activity was still generated by the bilayer film. Such remained activity probably indicates that charge separation may occur only in the reaction center of photosystem I, due to the inhibition of the PS II reaction. On the other hand, no loss of the photoactivity was observed in the 5-bilayer thylakoid membrane/PEI film. The above results suggest that the photoactivity is dependent on thickness of the thylakoid membrane/PEI bilayer film which increases with the number of bilayers, leading to optimized oxygen evolution in the ultrathin film.

4. Conclusions

This films of thylakoid membrane, which cleverly organizes so many kinds of proteins to convert solar energy into electrical/chemical energy in products of ATP and NADPH in chloroplast, could be prepared by means of electrostatic layer-by-layer adsorption alternating with polycations. The films deposited onto gold electrodes were confirmed to be composed of the thylakoid membrane/PEI bilayers by SEM observation. It is worth noting that the maximum photocurrent produced from the nano-scale thin film was much higher than films made by other techniques, even in the absence of electron acceptors for PS II. The photoactivity of the thylakoid membrane/PEI film depended on thickness, allowing optimized oxygen evolution and photocurrent at optimum thickness. The photosynthetic electron transfer origin of the1-bilayer thylakoid membrane/PEI film was demonstrated by an inhibition of the photoactivity after addition of herbicide. This study provides proof of concept

that biodevices for the detection of phytotoxicity can be constructed using isolated thylakoid membrane from chloroplast as biosensing elements by means of electrostatic layer-by-layer adsorption.

5. Acknowledgement

Participation of JR in this work was supported by the US Department of Agriculture (USDA) through Grant No. 2002-35318-12484.

6. References

[1] A. F. P. Turner, *Fundamentals and Applications, Biosensors* (Eds: A. F. P. Turner, I. Karube, G. S. Wilson), Oxford University Press, Oxford **1987**, pp. V–VIII.
[2] A. Ottova, V. Tvarozak, J. Racek, J. Sabo, W. Ziegler, T. Hianik, H. T. Tien, *Supramolecular Sci.* **1997**, *4*, 101.
[3] K. Abe, R. E. Schmukler, J. F. Rusling, *Electroanalysis* **1998**, *10*, 948.
[4] A. A. Karyakin, M. Y. Vagin, M. A. Choba, N. L. Klyachko, *Electroanalysis* **1999**, *11*, 1094.
[5] S. Dai, M. Meyerhoff, *Electroanalysis* **2001**, *13*, 276.
[6] H. T. Tien, A. L. Ottova, *J. Membr. Sci.* **2001**, *189*, 83.
[7] S. Lemieux, R. Carpentier, *Photochem. Photobiol.* **1988**, *48*, 115.
[8] M. Koblížek, J. Malý, J. Masoiídek, J. Komenda, T. Kučera, M. T. Giardi, A. K. Mattoo, R. Pilloton, *Biotechnol. Bioeng.* **2002**, *78*, 110.
[9] K. Amako, H. Yanai, T. Ikeda, T. Shiraishi, M. Takahashi, K. Asada, *J. Electroanal. Chem.* **1993**, *362*, 71.
[10] E. Touloupakis, L. Giannoudi, S. A. Piletsky, L. Guzzella, F. Pozzoni, M. T. Giardi, *Biosens. Bioelectron.* **2005**, *20*, 1984.
[11] J.-W. Choi, Y.-S. Nam, B.-K. Oh, W. H.Lee, M. Fujihira, *Synth. Metals* **2001**, *117*, 241.
[12] T. Hoshi, J. Anzai, T. Osa, *Anal. Chem.* **1995**, *67*, 770.
[13] X. Cui, R. Pei, Z. Wang, F. Yang, Y. Ma, S. Dong, X. Yang, *Biosens. Bioelectron.* **2003**, *18*, 59.
[14] Y. Lvov, K. Ariga, Izumi Ichinose, T. Kunitake, *J. Am. Chem. Soc.* **1995**, *117*, 6117.
[15] M. Onda, K. Ariga, T. Kunitake, *J. Biosci. Bioeng.* **1999**, *87*, 69.
[16] a) Y. Lvov, *Protein Architecture: Interfacing Molecular Assemblies and Immobilization Biotechnology* (Eds: Y. Lvov, H. Möhwald), Marcel Dekker, New York **2000**, pp. 125–167; b) Y. Lvov, *Handbook Of Surfaces And Interfaces Of Materials*, Vol. 3, *Nanostructured Materials, Micelles and Colloids* (Ed: W. R. Nalwa), Academic Press, San Diego **2001**, pp. 170–189.
[17] M. K. Ram, M. Adami, S. Paddeu, C. Nicolini, *Nanotechnology* **2000**, *11*, 112.
[18] K. V. Gobi, F. Mizutani, *Sen. Actuators B* **2001**, *80*, 272.
[19] E. Baldini, V. C. Dall'Orto, C. Danilowicz, I. Rezzano, E. J. Calvo, *Electroanalysis* **2002**, *14*, 1157.
[20] S. Berchmans, R. Sathyajith, V. Yegnaraman, *Mater. Chem. Phys.* **2002**, *77*, 390.
[21] Z. S. Chickneyan, A. L. Briseno, X. Shi, S. Han, J. Huang, F. Zhou, *J. Nanosci. Nanotech.* **2003**, *4*, 1.
[22] E. J. Calvo, C. Danilowicz, C. M. Lagier, J. Manrique, M. Otero, *Biosci. Bioeng.* **2004**, *19*, 1219.
[23] L.-P. Lu, S.-Q. Wang, X.-Q. Lin, *Anal. Chimi. Acta* **2004**, *519*, 161.
[24] S. Zhang, W. Yang, Y. Niu, C. Sun, *Anal. Chimi. Acta* **2004**, *523*, 209.
[25] M. Wang, L. Wang, H. Yuan, X. Ji, C. Sun, L. Ma, Y. Bai, T. Li, J. Li, *Electroanalysis* **2004**, *16*, 757.
[26] G. Decher, J.-D. Hong, *Ber. Bunsen-Ges. Phys. Chem.* **1991**, *95*, 1430.
[27] G. Decher, J.-D. Hong, J. Schmett, *Thin Solid Films* **1992**, *210/211*, 831.
[28] Y. Lvov, G. Decher, H. Möhwald, *Langmuir* **1993**, *9*, 481.
[29] Y. Lvov, G. Decher, G. Sukhorukov, *Macromolecules* **1993**, *26*, 5396.
[30] J. F. Rusling, Z. Zhang, *Biomolecular Films* (Ed: J. F. Rusling), Marcel Dekker, New York **2003**, pp. 1–64.
[31] J. F. Rusling, Z. Zhang, *Handbook Of Surfaces And Interfaces Of Materials, Vol. 5. Biomolecules, Biointerfaces, and Applications* (Ed: R. W. Nalwa), Academic Press, New York **2001**, pp. 33.
[32] J. Hodak, R. Etchenique, E. J. Calvo, K. Singhal, P. N. Bartlett, *Langmuir* **1997**, *13*, 2708.
[33] E. J. Calvo, R. Etchenique, L. Pietrasanta, A. Wolosiuk, *Anal. Chem.* **2001**, *73*, 1161.
[34] A. Mugweru, J. Yang, J. F. Rusling, *Electroanalysis* **2004**, *16*, 1132.
[35] L. Dennany, R. J. Foster, B. White, M. Smyth, J. F. Rusling, *J. Am. Chem. Soc.* **2004**, *126*, 8835.
[36] J. F. Rusling, *Biosens. Bioelectron.* **2004**, *20*, 1022
[37] K. Abe, H. Takizawa, S. Kimura, M. Hirano, *J. Biosci. Bioeng.* **2004**, *98*, 34.
[38] J. H. Kim, J. A. Nemson, A. Meils, *Plant Physiol.* **1993**, *103*, 181.
[39] G. Mackinney, *J. Biol. Chem.* **1941**, *140*, 315.
[40] O. H. Lowry, N. J. Rosebrough, A. L. Farr, R. J. Randall, *J. Biol. Chem.* **1951**, *193*, 265.
[41] Bernard Munge, Zeus Pendon, Harry A. Frank, J. F. Rusling, *Bioelectrochemistry* **2001**, *54*, 145.
[42] B. Munge, S. K. Das, R. Ilagan, Z. Pendon, J. Yang, H. A. Frank, J. F. Rusling, *J. Am. Chem. Soc.* **2003**, *125*, 12457.
[43] J. Kong, Z. Lu, Y. M. Lvov, R. Z. B. Desamero, H. A. Frank, J. F. Rusling, *J. Am. Chem. Soc.* **1998**, *120*, 7371.

研究業績

2.　ナノ薄膜

[1] 第 67 回応用物理学会学術講演会、31p-G-15、2006 年 8 月.

31p-G-15 超臨界流体組成のリアルタイム分析装置の開発

Development of a real time analyzer of super critical fluid composition

工学院大院工, ○池田 一洋, 池田 大成, 宮田 亘, 坂本 哲夫
Kogakuin Univ. , Kazuhiro Ikeda, Hironari Ikeda, Wataru Miyata, Tetsuo Sakamoto
cm06005@ns.kogakuin.ac.jp

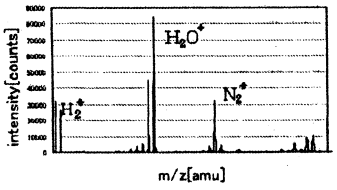

流体の圧力・温度を臨界点以上にすると超臨界状態になることは知られている。また、超臨界状態で温度・圧力を変化させることで溶解度・拡散性が大きく変わるという性質がある。超臨界流体のユニークな特性は抽出・洗浄といった形で応用されつつあるが、有機物をはじめ各物質の溶解度データを多く集める必要がある。これらのデータをリアルタイムで測定することができれば、温度・圧力をパラメータとしたときの過渡的な特性変化をより詳細に知ることができ、また測定系の制御方法次第でデータ収集を短時間で行うことが可能になる。本研究ではリアルタイム計測に適した手法として、電子衝撃イオン化と飛行時間型質量分析計を組み合わせた装置を試作し、超臨界流体に溶解した有機物を測定するシステムの構築を目指す。

高圧力の超臨界流体を真空の質量分析計に入れるために、今回は先端を細く加工したキャピラリーカラムを用いた。また、キャピラリーカラムからイオン化空間への導入口付近へスキマーを用意し、TOF-MS の検出部と直結するシュラウド内で質量分析を行うことで、超臨界流体がチャンバー内に入った状態でも高真空を維持し、TOF-MS が正常動作するよう工夫した。図は TOF-MS 装置側と接続したキャピラリーカラムのもう片方の先端を大気開放したときの質量スペクトルである。大気圧程度の導入圧力においては真空度の低下は少なく、TOF-MS が正常動作することが確認できた。

[2] 第 67 回応用物理学会学術講演会、29p-M-3、2006 年 8 月.

29p-M-3 超臨界流体を用いた有機微粒子・薄膜作製方法の開発

Development of a method to make organic-particles and thin films in super critical fluids

工学院大工 ○池田大成、池田一洋、宮田 亘、坂本哲夫
Kogakuin University, Hironari Ikeda, Kazuhiro Ikeda, Wataru Miyata, Tetsuo Sakamoto
c202004@ns.kogakuin.ac.jp

【はじめに】近年、超臨界流体 CO_2(臨界温度 31.3℃、臨界圧力 7.3MPa)はユニークな特性を活かして抽出、洗浄、乾燥技術などの分野に応用されている。我々は、超臨界流体が有機物を溶解する能力があり、且つ、溶解度が温度と圧力により大幅に可変であることを利用し、有機物の微粒子および薄膜の作製に応用できると考えた。この技術が確立されれば、低温で有機溶媒を使わない製造プロセスが実現できる。本発表では超臨界流体装置の開発並びに有機化合物の析出の基本特性について報告する。

【実　験】CO_2 冷却槽、液体 CO_2 送液ポンプ、超臨界耐圧容器、恒温槽、および保圧弁からなる超臨界流体装置を製作した。粒子や薄膜の材料となる有機化合物は上流に位置する一つめの耐圧容器（材料セル）に入れ、超臨界 CO_2 に溶解した有機物は流路を通り、第２の耐圧容器（析出セル）に送られる。析出セル側の温度を材料セル側よりも低くすることにより、有機物が析出するようにした。

【結　果】有機物材料として anthracene($C_{14}H_{10}$)を用い、材料セルを 17MPa、40℃、析出セルを室温(25℃)とした場合の析出物の顕微鏡写真を右図に示す。粒子状の結晶が時間とともに大きく成長している様子が見られ、超臨界流体溶解していた anthracene が析出したことが判った。

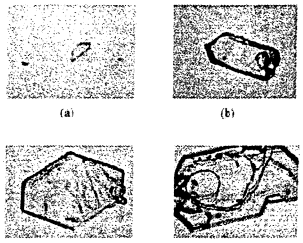

図: 析出した anthracene の顕微鏡写真 (a)10 分後 (b)20 分後、(c)30 分後、(d)40 分後

[3] 第 54 回応用物理学関係連合講演会、28p-SK-9、2007 年 3 月.

28p-SK-9 超臨界流体組成のリアルタイム分析装置の開発

Development of an apparatus for real-time analysis of supercritical fluid composition

工学院大院工, ○池田 一洋, 池田 大成, 宮田 亘, 坂本 哲夫
Kogakuin University, Kazuhiro Ikeda, Hironari Ikeda, Wataru Miyata, Tetsuo Sakamoto
cm06005@ns.kogakuin.ac.jp

種々の流体の圧力と温度が臨界点を超えると超臨界流体になることが知られている。超臨界流体は圧力や温度を変化させることにより、溶解力・拡散性が大きく変化するという特性がある。我々はこのユニークな特性を有機トランジスタ・有機ＥＬといったデバイスの作成に応用するべく検討を進めているが、超臨界流体中における材料有機物の溶解度およびその圧力・温度依存性は重要なパラメーターとなっている。そこで、本研究は超臨界流体中の溶質をそのまま質量分析計で測定する分析法・装置の開発を目的としている。

開発している装置(右図)では、数 MPa という高圧力の超臨界 CO_2 を高真空の飛行時間型質量分析計へ入れるため、特殊なインターフェイスが必要となった。今回は、内径数 μm のキャピラリーカラムの先端をテーパー状に加工し、圧力降下を真空への噴出し直前に集中させる構造とした。その結果、溶出の析出による噴出しの不安定性が解消され、安定した測定が可能となった。溶質としてアントラセンを用いた測定結果について報告する。

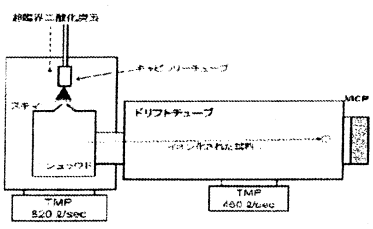

図:　装置の主な構成

[4] 第 54 回応用物理学関係連合講演会、30a-N-10、2007 年 3 月.

30a-N-10 超臨界流体を用いた微粒子・薄膜作製法の開発(2)

Development of a method to make organic-particles and thin films in super critical fluids, part 2

工学院大工. ○池田 大成, 池田 一洋, 宮田 亘, 坂本 哲夫
Kogakuin University, Hironari Ikeda, Kazuhiro Ikeda, Wataru Miyata, Tetsuo Sakamoto
c202004@ns.kogakuin.ac.jp

【緒 言】半導体デバイスの微細化が益々進む中で、現行の薄膜作製技術は大量のエネルギーを消費し、装置の大型化や有害廃棄物の問題も抱えている。本研究では、超臨界 CO_2 を用いて有機薄膜を形成する技術を開発している。超臨界 CO_2 は、高密度の流体であり、低温(室温～100℃前後)で有機物を溶解することができる。また、溶解度は流体の圧力や温度に大きく依存するため、溶解度を制御することにより溶質を析出し、薄膜化・微粒子化できるものと考えた。また、流体の特性を活かし、複雑な基板形状にも追従できるものと考えている。

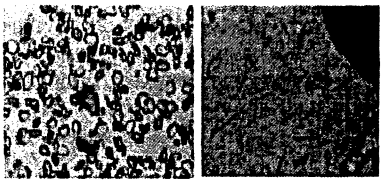

図: 析出したアントラセンの光学顕微鏡画像
(視野 : 125×75 μm^2)

【実 験】超臨界 CO_2 装置は各々汎用の装置・部品を組み合わせて作製した。材料セルに有機材料を充填し、析出セルに ITO 基板を設置する。ITO 基板設置部分にはヒーターが組み込まれており基板の加熱が可能になっている。有機物は材料セルから材料セルへと流入し、ITO 基板を通過するときに溶解度の低下により薄膜を生成させることを試みた。

【結 果】今回は有機材料としてアントラセン($C_{14}H_{10}$)を用いた。材料セル、析出セルそれぞれの圧力、温度が 11MPa, 40℃,70℃、および 17 MPa,50℃,100℃のときに析出したアントラセンの顕微鏡写真を図に示す。結晶化した微粒子及び、また、一部ではあるが薄膜の生成も行うことができることがわかった。基板温度を低く設定した場合には粒子状、高く設定した場合には薄膜状になる傾向がある。

ポリ乳酸の薄膜付与による多機能化の試み

矢ケ﨑隆義　工学院大学　工学部　マテリアル科学科　教授

(株)技術情報協会

月刊 MATERIAL STAGE Vol. 6, No.8 2006　抜刷

ポリ乳酸の薄膜付与による多機能化の試み

Trials for Multi-Functionalization on Polyactic Biodegradable Resins Through Forming Thin Films

矢ケ崎隆義　工学院大学　工学部　マテリアル科学科　教授

〒163-8677　東京都新宿区西新宿 1-24-2, Tel 03-3340-2671 (DI), E-mail：yagasaki@cc.kogakuin.ac.jp

1 はじめに

新しい機能を有する材料システムの実現を求めて，金属あるいはセラミックス系材料に各種薄膜を付与しようとの試みが数多くなされてきた[1]。近年，比較的耐熱性の高いプラスチックス系材料についても，気相凝縮制御法などによる薄膜付与の試みが紹介されている[2,3]。他方，プラスチックス系廃棄物量の急増という事実がある。現在，同系廃棄物のほとんどが，埋立てあるいは焼却処分されているのが現状であり，埋め立て処分については埋立て処分地の確保が，焼却処分については有害物質の発生等が，大きな社会問題となっている[4]。その解決法の一つとして，環境保全および資源保護の立場から，既存のプラスチック系材料に替えて環境低負荷型である生分解性樹脂材料の適用が考えられている[5-8]。当然，生分解性樹脂が実用材料として適用され得るためには，その多機能化は必要不可欠である。

このような観点から，報告者らは，電気・電子部材料および医療・福祉支援材料等への適用を目的とした環境低負荷型機能性材料の実現のために，生分解性樹脂材料の表面への各種薄膜の付与に関わる研究を遂行してきた。その第 1 段階として，既に，生分解性樹脂表面にイオンビームミキシング法による薄膜付与を試みた結果，耐熱性の低い生分解性樹脂であっても，その表面に安定且つ各種機能を有する Ti，Cu 薄膜を付与することが出来ること，およびそれらの製膜条件等の詳細を明らかにしてきた[9,10]。現在，これらの結果を受け各種高分子材料への各種化合物薄膜付与に取り組んでいる。さらに，薄膜部分の環境負荷低減を実現するために，DLC (Diamond Like Carbon) 薄膜[11]付与材料の創製に着手，DLC 薄膜の製膜条件の精査および得られた DLC 薄膜付与材料の評価等を試みている。本報では，これらの結果の内，生分解性樹脂の耐熱性に係わる部分について報告する。

2 薄膜の付与方法

多くの薄膜付与方法の中に，イオンの照射効果を応用した製膜法がある[2]。同法は，物質のイオン化によりその移動を電界にて容易に制御出来ることを応用する薄膜製造技術である。イオンの照射効果に注目してこれを大別した場合，1) プラズマ中にてイオンを直接利用するプラズマ法と，2) 高真空領域へイオンを引き出して利用するイオンビーム法[2,12,13]とになる。両者には真空チャンバー内の動作真空度に大きな差があり，前者の真空度がほぼ 10^{-3} から 10^{-5} (Torr) であるのに比して後者のそれは 10^{-5} から 10^{-10} (Torr) と高い。耐熱性と電気伝導性とが低いプラスチックス材料への薄膜付与には，印加電圧を変えるだけでイオンビームの照射エネルギーが調整でき，その程度によって堆積膜形成，スパッタ，イオン注入，イオン注入改質等の操作[13]を実行出来得るイオンビーム法が有利と考えられる。そこで報告者らは，薄膜付与に図 1 に示す大電流イオン注入装置を用いた。

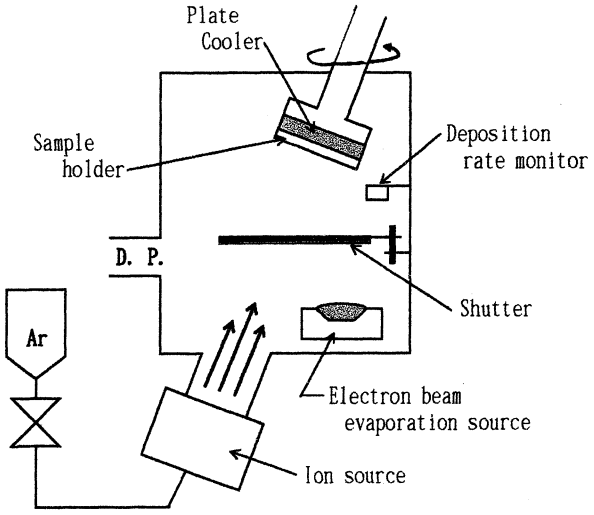

図1 Ion implantation equipment
(large electric current type)

3 供試材料

金属薄膜あるいはDLC薄膜を付与する供試(基板)材料には，環境中で加水分解と微生物とによる分解が励起され炭酸ガスおよび水になる生分解性樹脂を用いた。同樹脂は，主として微生物生産法，化学合成法，天然物加工法，等により製造されている。本報での薄膜付与には，汎用の可能性が最も高いとされている化学合成法による樹脂であり，ガラス転移点が室温より高い硬質樹脂であるポリ乳酸(PLA)樹脂『レイシア』[14](三井化学(株))を選択した。また，樹脂の耐熱性が薄膜付与にどのような影響を及ぼすのかを把握するために，比較材料として化学合成法の中でも若干耐熱性の高い『ビオノーレ』(昭和高分子(株))を用いた。さらに，耐熱性の高いエンジニアリングプラスチックスとして実績のあるポリエーテルイミド(PEI)樹脂である『ウルテム』[15-18](GEプラスチック(株))を比較材料とした。

4 金属薄膜の付与

4.1 金属薄膜製膜方法

大電流イオン注入装置を用い，イオンビームミキシング法[19]によりPLA樹脂の表面[20]にTi薄膜およびCu薄膜の付与を試みた。真空蒸着法[19]のみにより形成される薄膜に比して，この方法による薄膜はAr^+イオン注入と電子ビーム蒸着やスパッタなどによる製膜とを同時に行うことから，薄膜形成の初期に基板と薄膜との間に界面ミキシングと同様の効果を有する混合層が形成されるために界面の無い密着性に優れた薄膜が得られる可能性がある。また，イオンビームミキシング法は非熱平衡プロセスであるため，表層に形成される薄膜の組成を広範囲で制御することが出来，さらに注入イオンと蒸着材料の組み合わせにより単金属薄膜およびセラミック薄膜を含む各種化合物薄膜の形成が可能となる利点をも有している。真空蒸着法およびイオンビームミキシング法による製膜プロセスの概要を図2に示す。

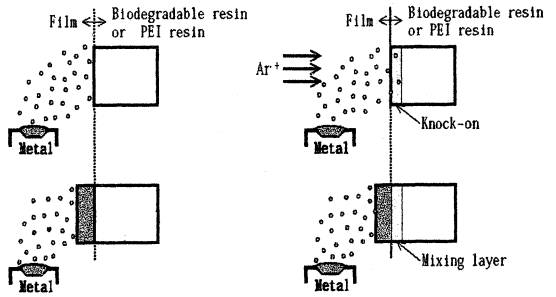

図2 General idea of process of forming
the deposited films

従来，イオンビームミキシング法は耐熱性の高い金属およびセラミックスに対して適用され，耐熱性の低い高分子系材料には不向きであるとされてきた。そこで報告者らは，熱的損傷を回避する手法として1)加速電圧を下げる方法，2)試料ホルダーを水冷する方法，による製膜を試み，両者を比較することにした。また，それらの結果を基に，イオンビーム照射により形成した薄膜の上に真空蒸着を堆積させる組み合わせ製膜をも試みた[10]。尚，基板は，大電流イオン注入装置内の真空チャ

ンバー上部に設けたサンプルホルダーに固定，膜付けの均一化のためにこのホルダーを回転させた。

4.2 金属薄膜の製膜結果および考察

4.2.1 最適製膜条件の決定

表1 Formed conditions of thin films

	(a)	(b)	(c)	(d)	
Method	IBM	IBM	IBM	IBM	VD
Film material	Ti	Ti	Ti	Ti, Cu	
Base pressure [Pa]	4×10^{-4}	4×10^{-4}	5×10^{-4}	$<6\times10^{-4}$	
Ar pressure [Pa]	2×10^{-2}	2×10^{-2}	2×10^{-2}	2×10^{-2}	-
Acceleration V [kV]	5	1	1	1	-
Sample current [μA/cm^2]	20	20	20	20	
Deposition rate [Å/s]	1.5	1.5	1.5	1.5	
Film thickness [nm]	100	100	100	15	20
					85
Water-cooling	×	×	○	○	

表1に示した4つの製膜条件に基づきPLA樹脂『レイシア』基板表面にTi薄膜を形成，その表面および断面とを電子顕微鏡にて観察，比較した。その結果，製膜条件(b)によるものに比べ，条件(a)のそれには大きなき裂が高い密度で存在することが確認された。次に，ホルダーの冷却を実施した条件(c)による薄膜の表面に存在するき裂寸法は条件(b)によるそれに比して小さくなりその数も激減していることが明らかとなった。さらに，イオンビームの照射による熱損傷を極力少なくするために，イオンビームミキシング法により15nmと真空蒸着法により85nmの薄膜を堆積させる条件(d)での製膜を実施した。その結果，条件(a)～(c)による製膜結果に比してき裂などがまったく認められない良好な薄膜の得られることが確認された。

また，FT-IRによる分析結果より，薄膜形成条件(c)と(d)による薄膜付与材料の薄膜/樹脂界面部には側鎖のC-CH_3の分解を示すC-Hピークが1400cm^{-1}付近にいずれも確認されたのに対して，イオンビームミキシング法と真空蒸着法とを組み合わせた条件(d)で形成された薄膜付与材の薄膜/樹脂界面部については1400cm^{-1}のC-Hピーク高が条件(c)と比較して低く，この結果からも薄膜形成条件として(d)が優れていることが示唆される。製膜条件(a)および(d)にて製膜した薄膜の表面形態を図3に，FT-IR分析結果を図4に示す。

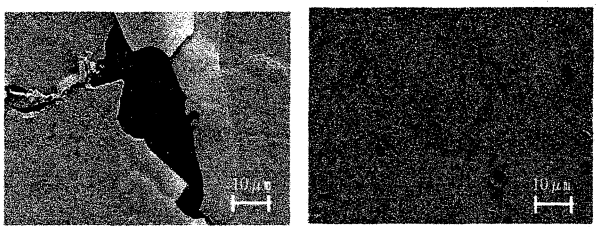

Condition (a) Condition (d)

図3 SEM morphologies of Ti film surface

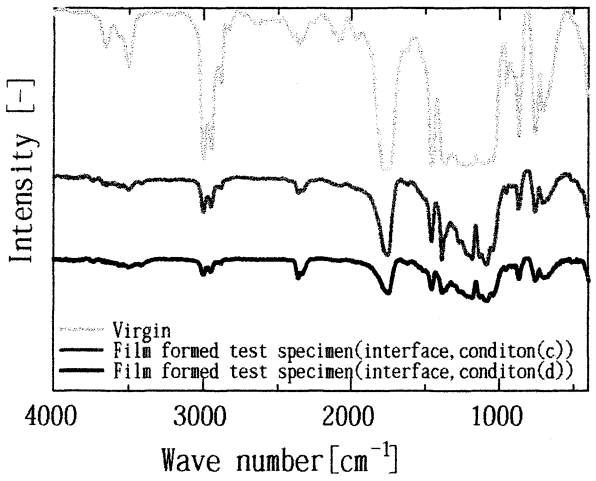

図4 Results of FT-IR analysis

4.2.2 金属薄膜/樹脂界面と混合層の確認，薄膜の密着性の評価

製膜条件(d)にて形成した薄膜の表面部深さ方向のTi元素，C元素，O元素のそれぞれの濃度分布をXPS分析装置により測定した。その結果を図5に示す。この結果より，Ti濃度が100%である表面から深さ方向へその濃度が徐々に低下して最終的に0%になっている濃度傾斜部の存在が確認された。また，Tiの傾斜領域内で，樹脂成分に由来する炭素元素Cの増加を示す領域とが合致する部分が薄膜成分であるTiと樹脂の分子とが混合して形成されたミキシング層に相当するものと考え得

る。

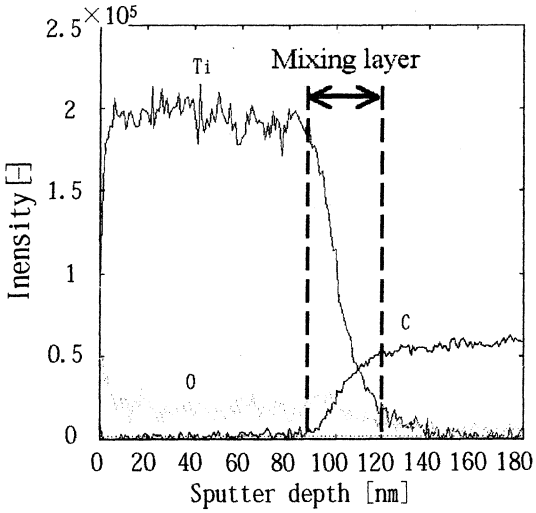

図5 XPS pattern of Ti thin film (condition(d))

次に，共に熱影響を考慮した製膜条件 (c) と (d) により形成された薄膜の密着性を確認するために，スクラッチ試験[10]を実施した。その結果，条件 (c) による薄膜では臨界剥離荷重 Lc 値が 67.7g であるのに対し，条件 (d) では 61.4g であることが確認された。これらより，わずかなイオンビームミキシング法による薄膜付与操作であっても，高い密着性が得られることが明らかとなった。更に，製膜条件 (d) によるビオノーレへの Ti 薄膜付与材料に対するスクラッチ試験を実施した結果を図 6 に示す。レイシア基板では Lc 値が 61.4g であるのに対しビオノーレ基板でのそれは 89.1g と高くなっており高い密着性が得られることが確認された。この差は，ビオノーレ基板の方が比較的耐熱性が高いことから照射による熱変性の影響が少ないためもたらされたものと考えられる。次に，ビオノーレ基板に対し，イオンビームミキシング膜厚 15nm に加え，真空蒸着膜の厚さ (85nm) を基準としてその 1/2 倍 (42.5nm)，2 倍 (170nm)，5 倍 (425nm) の薄膜を付与した基板に対し，スクラッチ試験を実施した。これらより，膜厚による有意差はなくむしろ膜厚を厚くすることにより薄膜にクラック等が生じてしまい膜の状態が悪くなることが確認される等，膜厚が厚いものに比して薄いものの方が良好な結果をもたらすことが明確となった。

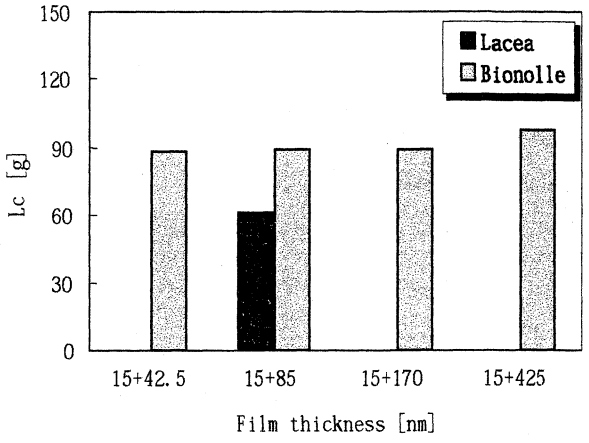

図6 Results of scratch tests

4.2.3 金属薄膜の電気特性の評価

イオンビームミキシング法と真空蒸着法とを組み合わせた条件下でのビオノーレ薄膜付与材料について，表面抵抗率および体積抵抗率とを測定して評価した。その結果，表面抵抗率については薄膜未付与材料の 10^{15} Ω に対しいずれの薄膜付与材料についても 10^{4} Ω と下がること，体積抵抗率については未付与材料とほぼ同等の抵抗値を示すこと等が確認された。スクラッチ試験の結果と同様に電気特性についても膜厚の差による有意差がないことが認められ，密着性およびコストの面からも膜厚が薄い方が良いということが確認された。また，膜厚が薄くても密着性に有意差等がないことから，イオンビームミキシング法と真空蒸着法とを組み合わせた条件で薄膜をさらに薄くすると共に，基板の種類を変化させて表面抵抗率を測定・評価した。その結果を図 7 に示す。結果より，生分解性樹脂（レイシア，ビオノーレ共に）自体およびポリエーテルイミド自体が有する表面抵抗率は 10^{15} Ω程度であるのに対し，製膜結果が最良であった組み合わせによる条件では，レイシア，ビオノーレ，ポリエーテルイミドすべてにおいて表面抵抗率が 10^{3} Ω と下がったことが確認された。次に，薄膜の種類を電気・電子部材料への適用を想定して Ti から Cu に変えて薄膜を付与し，表面抵抗率および体積抵抗率を測定した。また，イオンビームミキシング法で 15nm 製膜した後に真空蒸着法で 85nm 製膜したもので評価を行った。その結果，Ti 薄膜に比して Cu 薄膜では，表面

抵抗率 267 Ω以下という良好な導電性を示した。また，体積抵抗率は Ti 薄膜，Cu 薄膜共に未付与材料とほぼ同等の値を示したことから，Cu 薄膜付与材料は電気・電子部材料として適していることが明らかとなった。

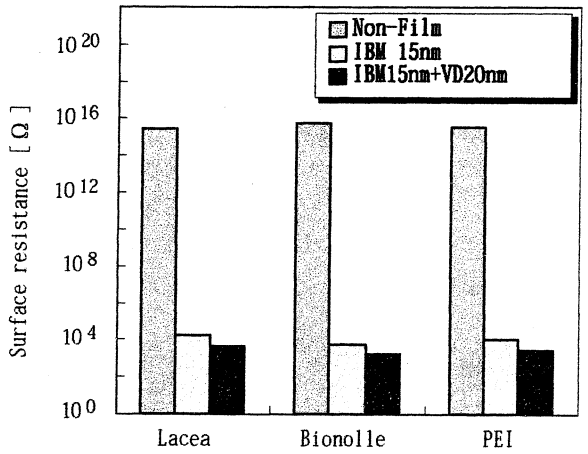

図7 Results of surface resistance measurement

5 DLC 薄膜付与による機能化の可能性

DLC とは Diamond-Like-Carbon の略称であり，通常，その薄膜を構成する化学結合の 90％以上が sp^3 混成軌道で構成されることから，ダイヤモンド構造に対応する sp^3 結合を主体とするアモルファスな硬質炭素型薄膜となる。すなわち，この DLC 薄膜は長距離秩序を有さず非晶質ではあるが三次元的な結合を含有していることに起因して，高硬度による優れた耐摩耗性と低い摩擦係数を特徴とするダイヤモンドと似た性質を有することになる。CR ゴムや PE などの高分子系材料についても DLC 薄膜付与が表面潤滑性をもたらし，さらには薄膜の膜厚と硬度とを調整することにより良好なガスバリア性をも得ることが出来たこと，等が報告され実用化が進められている[18]。一方，この DLC 薄膜を生分解性樹脂に施した場合，生分解性樹脂の多機能化に加えて環境低負荷型材料システムとしての可能性も考えられるが，その方面での研究は少ない。報告者らは，DLC 薄膜の付与にイオン注入装置を用いた（1）イオンビーム照射下で炭化水素ガスを導入することにより炭素成分を堆積させるイオンビームアシスト法，および（2）イオンビーム照射効果により基板表面部の樹脂自体を炭化するイオンビーム改質法（イオン注入改質）の 2 通りの方法を考えた。前者は，生分解性樹脂等の基板上に DLC 薄膜を形成し且つ不活性ガス元素をイオン注入することから，薄膜の結晶性や基板との付着性を制御出来る方法であり，樹脂基板の構成元素と注入イオンとが相互に侵入・拡散しあったミキシング層が形成されるために，生分解性樹脂/DLC 薄膜の界面がなく互いに濃度傾斜化することから薄膜と基板との接着性が向上することが期待される。このミキシング層の形成後は，蒸着速度，イオンエネルギーおよび照射量等を制御することにより目的とする DLC 薄膜をミキシング層の上に堆積することが出来ることになる。後者は，イオンビームの照射効果を用いて基板とする生分解性樹脂等の表面部を照射エネルギーにより直接炭化する方法である。いずれも，生分解性樹脂上に DLC 薄膜を形成させるためには，最適なイオン照射エネルギーを決定せねばならない。

尚，DLC 薄膜の物性は，ダイヤモンド構造に対応する sp^3 結合に対してグラファイト構造に対応する sp^2 結合の存在割合を増加させるなどの調整することにより，制御することが可能となるはずである。さらに製膜手法により，水素を殆ど含まない無定形炭素薄膜（a-C）から水素化された無定形炭素薄膜（a-C：H）とが生成出来ることとも併せ，薄膜の物性を連続的且つ多様に変化させ得ることが可能になるものとも考えられる。それらの概念を，図 8 に示す。現在，報告者らは，DLC 薄膜に占めるダイヤモンド構造 / グラファイト構造の割合および水素含有量とを積極的に変化させることを通して，薄膜が有する性質を変化させることにより新しい物性等を有する薄膜付与材料の実現に可能性のあることを確認しつつある。

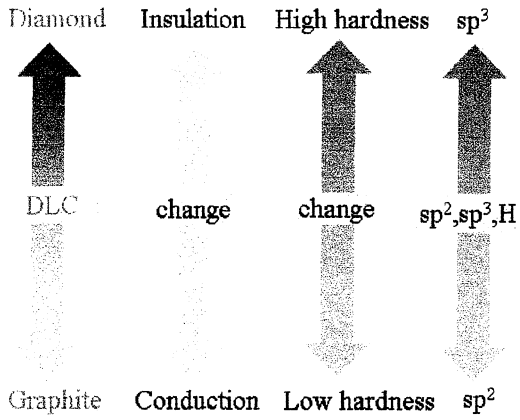

図8 General idea that chemical combination state and density of hydrogen give to change of properties of the DLC film

6 まとめ

環境低負荷型材料である生分解性樹脂の表面に，機能化を目的としてイオンビームミキシング法により薄膜の形成を試みた。その結果，耐熱性の低い生分解性樹脂であっても，冷却下におけるイオンビームミキシング法による薄膜形成とその後の真空蒸着による薄膜の堆積とを組み合わせることにより，き裂などが確認されない薄膜を形成出来得る事，薄膜/樹脂界面にミキシング効果による濃度勾配を有するミキシング層が形成されることから薄膜接着強度効果が得られること，わずかなイオンビームミキシング操作による薄膜の付与であっても高い接着強度が得られること，基板となる樹脂の耐熱性の違いによって薄膜の密着性が左右されること，等が明らかとなった。また，イオンビームミキシング法による薄膜形成は，電気的機能をもたらすこと，Cu薄膜は電気・電子部材料として適する導電性をもたらすこと，膜厚による薄膜自体の特性には有意差はなく，薄膜の表面状態および製膜の際にかかるコストの面から，膜厚は薄い方が良好であること，等が明確となった。さらに，薄膜部分の環境負荷軽減を意図したDLC薄膜の付与についても可能性のあることが明らかとなった。

参考文献

1) 権田俊一，多賀康訓，塚田俊久，平尾孝，他 “薄膜作成応用ハンドブック”（1995）エヌ・ティー・エス
2) 権田俊一，小川正毅，多賀康訓，八瀬清志，他 “21世紀版 薄膜作成応用ハンドブック”（2003）エヌ・ティー・エス
3) 産業技術会議， 2000年版 資源・環境・リサイクル－循環型産業経済システムの確立－，283（2000）
4) 環境省・総合環境政策局環境計画課，平成15年版・環境白書（2003）環境省
5) 筏 義人，“生分解性高分子”（1999）アイピーシー
6) 郷田秀清，化学装置，別冊，220（1999）
7) 古河電気工業，古河電工時報，102，119（1998）
8) DEFOSSE M, Mod Plast. Int., 29-1, 31（1999）
9) 矢ケ崎隆義，木村雄二，鷹野一朗，伊藤紀子，“高分子材料のイオンビームミキシング法による薄膜付与と多機能化” 平成7年度～9年度科学研究費補助金（基礎研究（C）（2））研究成果報告書（1998）
10) 山田香織，矢ケ崎隆義，木村雄二，鷹野一朗，材料，54-1，79（2006）
11) 斉藤秀俊，大竹尚登，中東孝浩，“DLC膜ハンドブック”（2006）エヌ・ティー・エス
12) 鷹野一朗，笹瀬雅人，磯部昭二，真空，35-3，110（1992）
13) 鷹野一朗，表面技術，52-12，805（2001）
14) 井門修平，プラスチックエージ，122（1999）
15) 矢ケ崎隆義，木村雄二，材料，47-1，84（1998）
16) T. YAGASAKI,（社）未踏技術協会傾斜機能材料研究会・会報，10-31，21（1996）
17) 矢ケ崎隆義，木村雄二，材料，45-3，328（1996）
18) T. YAGASAKI, Y. KIMURA, Proceedings of 7th. Int. Conference of Mechanical Behavior of Material, 5, 707 （1995）
19) CAPPS N, CARTER D, ROCHE G, Semicond. Int., 23-8, 251（2000）
20) 大島和巳，矢ケ崎隆義，木村雄二，鷹野一朗，材料の化学と工学，43-4，180（2006）

日本材料科学会

材料の科学と工学　巻　号（　年　月）

研究論文

生分解性プラスチック(ポリ乳酸)へのイオンビームミキシング法を用いた金属薄膜付与条件の評価

大島和巳*，矢ケ崎隆義**，木村雄二**，鷹野一朗***

Evaluation of Metallic Thin Film Giving Condition to Biodegradable Plastic (Poly Lactic Acid) by Ion Beam Mixing Method

by

Kazumi Oshima, Takayoshi Yagasaki, Yuji Kimura and Ichiro Takano

(Received on Dec. 16, 2005)

Abstract

In recent years, the plastics product has been complicated by making to the compound to request of making of plastics product function and the complication by coating as a plastic usage expands. Therefore, the plastic made a compound waste has become a social problem. As a solution, the biodegradable plastics are attracting attention as an alternative material of plastic that is the base and in addition, it is requested to add new functionality on it. From this viewpoint, we formed a copper thin film on the biodegradable plastic surface and the basic data of the performance was obtained. To understand the effect of the plastic surface smoothness on the thin film adhesion, we pretreated the plastic surface by buff polishing and beam irradiation. The thin film coating was applied under various conditions and the functionality of the thin films was evaluated. The following conclusions were revealed: 1) A thin film formed by ion beam irradiation over a short time had excellent adhesion and electroconductivity; 2) A combination of ion beam mixing and vacuum deposition is an effective method for coating a thin film on biodegradable plastics.

Keywords: Biodegradable plastics, Ion beam mixing method, Vacuum deposition method, Pretreatment, Beam irradiation, Thin film

1. 緒論

日本は，戦後から高度経済成長により材料の大量生産・大量消費の社会になっている．しかし，近年になって使用後の材料の廃棄物処理が問題視されている．中でも高分子材料，特にプラスチックは石油由来の材料であり，資源の枯渇化が懸念される現在は，これに変わる代替材料の検討が必要とされている．また，プラスチックは基本的に良好な絶縁体であり，電気・電子部材での分野で広く使われているが，分離・再資源化が困難なため，物質循環に組み込めず，環境負荷の高い材料として位置付けられているのが現状である．更に，そのような分野ではプラスチック単体として使われるのではなく，複合化されており，廃棄後の分別回収が難しく，そのためリサイクルが更に困難となっている．また，プラスチックの中でも広く汎用されている材料であり，耐薬品性に優れたPVCについても塩素を含む

平成17年12月16日受付

* 旭硝子エンジニアリング株式会社：千葉県千葉市美浜区中瀬2-6 WBGマリブウエスト19階
Asahi Glass Engineering Co., LTD.: WBG MARIVE WEST 19F, 2-6 Nakase Mihama-ku, Chiba-shi, Chiba 261-7119, Japan

** 工学院大学工学部マテリアル科学科：東京都新宿区西新宿1-24-1
Department of Materials Science and Technologies, Kogakuin Univ.: 1-24-1 Nishishinjuku, Shinjuku-ku, Tokyo 163-8677, Japan

*** 工学院大学工学部電気工学科：東京都新宿区西新宿1-24-1
Department of Electric Engineering, Kogakuin Univ.: 1-24-1 Nishishinjuku, Shinjuku-ku, Tokyo 163-8677, Japan

ため，廃棄後の焼却処理では環境に悪影響を及ぼすと考えられ，材料の大量廃棄につながる[1),2)]．そこで最近微生物によって分解され，循環サイクルに還元できる生分解性プラスチックが，環境低負荷材料として注目されている．このような生分解性プラスチックに，更なる高機能を付与することで，生分解性プラスチックの適用分野の拡大が考えられる．材料の機能化については，近年，金属薄膜を付与することにより導電性・耐磨耗性などの特殊機能を付与する表面改質技術が求められている．しかしながら，生分解性プラスチックへの薄膜付与に関わる系統的な研究例は少ない．

このような観点から本研究では，イオンビームミキシング(Ion Beam Mixing：IBM，以下 IBM と略す)法を用いて，電気・電子部材に多く用いられている Cu を選択し，生分解性プラスチックへの Cu 薄膜付与を試みた．尚，イオンビームミキシング法は，薄膜付与技術である PVD の中でも，Ar 等の不活性ガスイオンを電子ビーム蒸着，またはスパッタ法による製膜と同時に照射することにより，薄膜と基板との界面が消失し，混合層を形成するため，従来の製膜法にはない高い付着力を得ることが期待できる．更に，本法が非熱平衡プロセスであるために，構成される薄膜組成を広範囲に制御することができる．また，製膜時に反応性ガスを導入することで，単金属のみならず，化合物薄膜の形成をも可能とし，多種多様な薄膜形成が実現できる方法でもある[3)~10)]．実験では主として，生分解性プラスチックへの金属薄膜付与による前処理を含む最適な条件を確立し，薄膜付与の基礎的データを収集した．更には，この薄膜付与材の電気・電子部材への適用を想定し各種分析・評価を実施した．

2. 供試材料および実験方法

2.1 供試材料

供試材料として用いた生分解性プラスチックには，化学合成系，微生物合成系，天然合成系の 3 種類が挙げられるが，原料が大量にあり，生産コストが低く抑えられるという点で，化学合成系のプラスチックを選択した．また，化学合成系の中でも，加水分解により分解が容易なポリ乳酸系の生分解性プラスチックである LACEA(製造：三井化学㈱，成型・提供：長野技研㈱)を選択した[11),12)]．尚，供試材料である LACEA(板状，300mm×300mm×3mm)より試験片を切り出す際，その寸法を 10mm×20mm×3mm とした．また，導電性の評価を実施する時のみこの寸法を 20mm×20mm×3mm に変更した．因みに本研究の範囲において，製膜性に及ぼす試験片寸法の違いは予め無視できることを確認している．試験片はそれぞれ 7 個用意し，実験に供した．有効製膜面積については，用いた試料ホルダーの構造上，175mm^2 を標準とした．

2.2 実験方法および評価方法

イオンビームミキシングによる製膜装置(㈱日立製作所製 HIIB-200-B)の概念図を Fig. 1 に示す．本実験では，基板にある傷や凹凸が製膜結果に多大な影響及ぼすことが懸念されるため，前処理として，基板表面の平滑化を期待し，バフ研磨とビーム照射を行った．尚，バフ研磨ではバフ布に水を滴下して供試材表面のみを研磨した．ビーム照射条件は加速電圧 1kV，電流密度 20μA/cm^2 の下 60 秒間照射した．製膜条件を Table 1 に示す．

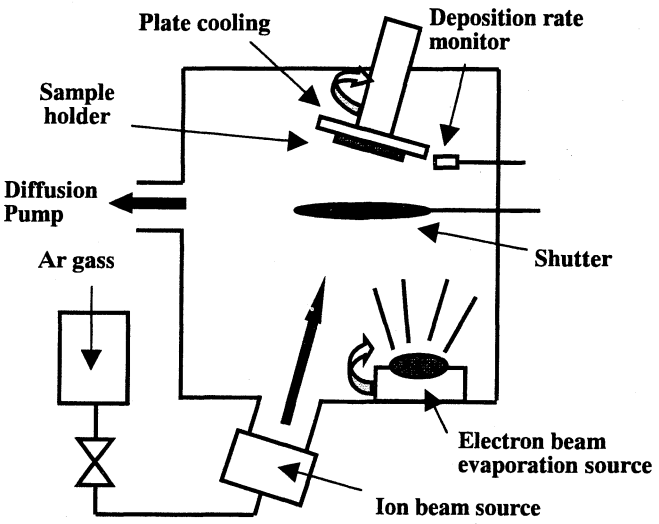

Fig. 1 Ion beam mixing equipment.

Table 1 Conditions of thin film formation.

Condition	(a)		(b)		(c)		(d)	
Ar pressure [Pa]	6×10^{-4}		6×10^{-4}		6×10^{-4}		6×10^{-4}	
Acceleration voltage [kV]	1		1		1		1	
Sample current [μA/cm^2]	20		20		20		20	
Base pressure [Pa]	6×10^{-6}		6×10^{-6}		6×10^{-6}		6×10^{-6}	
Deposition rate [Å/sec]	1.5		1.5		1.5		1.5	
Water cooling	○		○		○		○	
Buff polish	○	×	○	×	○	×	○	×
Beam irradiation	○		○		○		○	
Method	IBM		IBM	VD	IBM	VD	IBM	VD
Film thickness [nm]	100		70	30	40	60	15	85

因みに，条件(a)では製膜方法を IBM 法のみで作製した．以下，安定した膜付与を実現するために，IBM 法と VD(Vapor Deposition：VD，以下 VD と略す)法との比率を変え，試験片を作製した．また，製膜操作では，膜厚の目標値を 100nm として膜を形成した．

尚，薄膜表面観察には電界放射型走査電子顕微鏡(FE-SEM，㈱日立製作所製 S-4200)，非接触型原子間力顕微鏡(NC-AFM，セイコーインスツルメンツ㈱製 SPA-300)，製膜時における基板への熱影響評価に赤外分光分析(FT-IR，日本分光㈱製 FT-IR-420)，薄膜の構造解析に薄膜 X 線回折分析(XD，㈱リガク製 RINT2500VHF)，薄膜構成元素の深さ方向への組成分布の把握には X 線光電子分光分析(XPS，Φ PHYSICAL ELECTRONICS 製 Quantum2000 SCANNING ESCA MICROPROBE)により分析・評価した．また，薄膜と基板との密着性評価にスクラッチ試験装置(新東科学㈱製 HEIDON-22)を用いて，臨界はく離荷重 Lc[13]を求め評価し，Cu 薄膜の機能評価として，電気抵抗測定装置(東亜 DKK㈱製 SM-8001，SM8210)を用いて評価した．X 線回折分析の測定条件は 2θ ＝20～100°，X 線入射角度 α=1.0, 2.0 とし，スクラッチ試験については Table 2 にスクラッチ条件を，Fig. 2 にスクラッチ試験による破壊模式図を示し，Fig. 3 にはサファイア圧子による実際の薄膜部の破壊形態を示した．また，スクラッチ試験による破壊様相を次の 3 段階に分類した．[MODE 1]：き裂(ヘアークラック)，[MODE 2]：局所的なはく離，[MODE 3]：全面はく離．破壊は MODE1 から 2, 3 の順序で進行すると考えられ，これら薄膜付与材の様々な用途を考慮した場合，[MODE2]での破壊形態が最も重要と考え，局所的なはく離を生じた際の荷重を破壊開始荷重 Lc 値と定義し評価した．

Table2 The conditions of scratch test.

Indenter	Radius of curvature	100 μm
	Material	Sapphire
Scratch speed		0.19mm/sec
Load $_{max}$		150gf

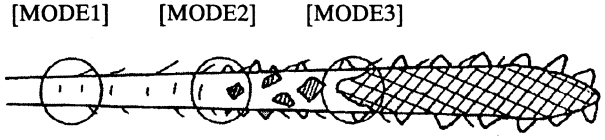

Fig. 2 Schematic diagram of destruction of thin film by scratch test.

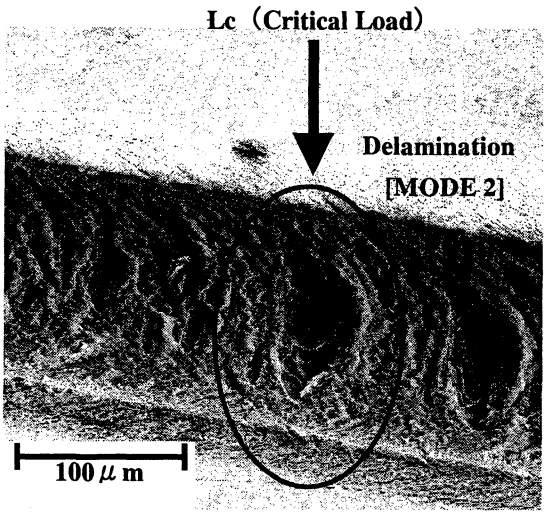

Fig. 3 MODE 2 delamination of Cu thin film by scratch test. The film was formed in the condition of (d) shown in Table 1.

3. 実験結果および考察

3.1 薄膜表面の形態の把握

3.1.1 FE-SEM による表面形態観察

基板表面の前処理として，バフ研磨とビーム照射とを施し，その後，各製膜条件下で Cu 薄膜付与を試みた．それらの膜表面を，電界放射型走査電子顕微鏡を用いて観察した．観察結果を Fig. 4 に示す．製膜条件(a)，(b)，(c)，(d)下でバフ研磨を施し，膜付与を行った薄膜すべてに Fig. 4 に示すようなき裂やはく離が生じていた．これは，基板の最表面である分子量の高い部分を除去することで，基板内部でのビーム照射によりガスが発生し，その影響で薄膜にき裂やはく離をもたらしたものと考えられる．

次に，これらを確認するために，バフ研磨を施さずビーム照射のみを施した後，各条件下で製膜を試み Cu 薄膜表面を観察した．観察結果を Fig. 5 に示す．条件(a)及び(b)では，製膜結果共にき裂やはく離を生じた．これは，製膜時の基板に対する熱影響のためだとも考えられる．他方，ビーム照射時間の比較的少なく熱損傷の生じない条件(c)及び(d)での製膜結果については，薄膜にき裂やはく離等の欠陥は全く確認されず，外観上は良好な薄膜の形成に至った．

3.1.2 NC-AFM による 3 次元表面形態観察

バフ研磨の影響を確認するために，バフ研磨とビーム照射とを施した後 Cu 薄膜を形成させた製膜条件(c)及び(d)での薄膜表面を非接触型原子間力顕微鏡を用いて観察した．観察結果を Fig. 6 に示す．両者の薄膜には多くの深さ 60～80nm 程度の寸法を有する穴が確認された．これは，製膜時に基板内部からの揮発性ガスの脱泡によるものだと考えら

れる．先述の FE-SEM の表面観察結果と併せ考えると，揮発性ガスの脱泡が生じ，膜強度が低下することから薄膜にき裂やはく離を生じたものと考えられる．

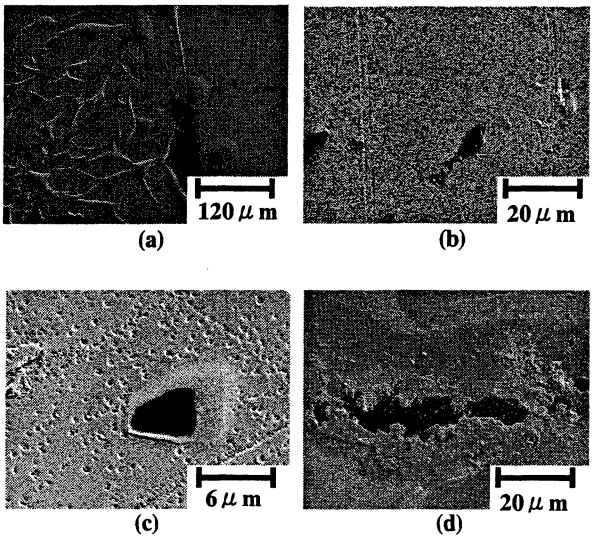

Fig. 4 FE-SEM observations of Cu thin films on LACEA pretreated by buff polish and beam irradiation. (a), (b), (c) and (d) correspond to the conditions of film formation shown in Table 1.

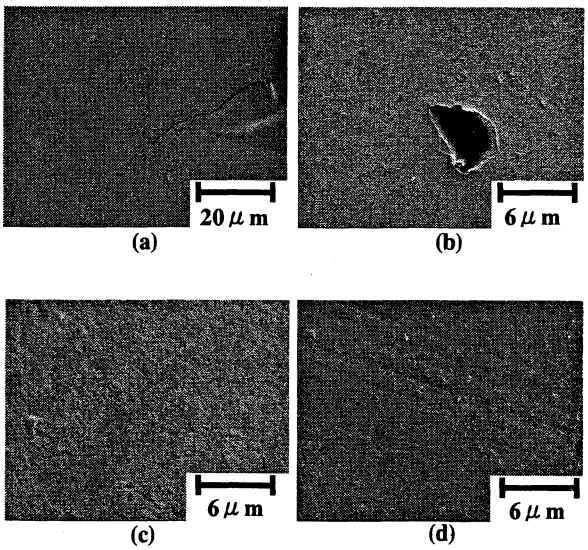

Fig. 5 FE-SEM observations of Cu thin films on LACEA pretreated by beam irradiation. (a), (b), (c) and (d) correspond to the conditions of film formation shown in Table 1.

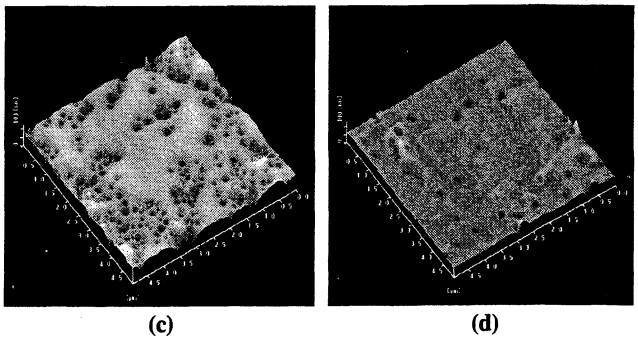

Fig. 6 NC-AFM observations of Cu thin films on LACEA pretreated by buff polish and beam irradiation. (c) and (d) correspond to the conditions of film formation shown in Table 1. (X, Yscale=5 μ m).

次に，前処理として，バフ研磨を施さずビーム照射のみを施し，その後，製膜条件(c)及び(d)で Cu 薄膜を形成し，その表面を観察した．観察結果を Fig. 7 に示す．前処理として，バフ研磨とビーム照射とを施した薄膜と比較して，揮発性ガスの脱泡の跡と考えられる穴の数は明らかに減少したことが確認された．これは，製膜以前に表面をバフ研磨した際に基板内部の揮発性ガスが抜け出たためだと考えられる．これらの事柄から，バフ研磨が製膜に悪影響を及ぼしていることが明らかとなった．

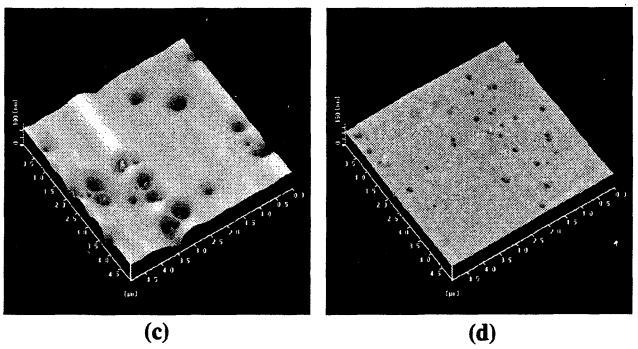

Fig. 7 NC-AFM observations of Cu thin films on LACEA pretreated by beam irradiation. (c) and (d) correspond to the conditions of film formation shown in Table 1. (X, Yscale=5 μ m).

3.2 ビーム照射が基板に及ぼす熱損傷の FT-IR を用いた評価

薄膜の形態にビーム照射による熱損傷の影響を及ぼすことが明らかとなったことから，製膜による基板への熱影響評価を行うために，薄膜直下の樹脂部を出来るだけ均等に削り取り，これに対し赤外分光分析を行った．分析には KBr 法(錠剤法)を用い，積算回数 100 で，薄膜と基板との界面の

評価を行った．結果を Fig. 8 に示す．

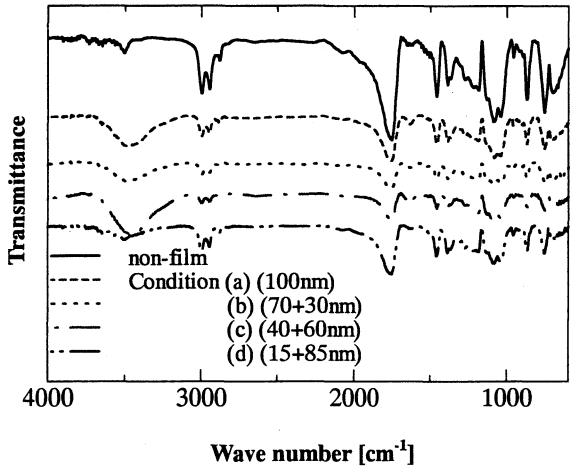

Fig. 8 FT-IR spectra of beam-irradiated and non-irradiated specimens.

前処理としてビーム照射を施し，その後製膜条件(a)での製膜を試みた薄膜付与材と，製膜をしていない薄膜未付与材とを比較して，分子構造に明らかな変化のあることが確認された．まず，3400cm^{-1} 付近に水酸基のピークの存在が認められ，且つ，1700cm^{-1}，1200cm^{-1} 付近にあるエステルのピーク高が相対的に低くなっていることから，エステル結合の開裂による水酸基の増加が考えられる．すなわち，製膜時のビーム照射による基板の熱劣化が生じたものとも考えられることから，イオンビームによる熱損傷が示唆される．尚，水分吸収に伴う劣化挙動とも考え得ることから今後の精査が必要である．他方，ビーム照射時間の比較的短い製膜条件である(d)による薄膜付与材については，3400cm^{-1} 付近に水酸基の明確なピークは認められないことから，イオンビームによる基板への熱損傷が生じていないことが明確になった．このことより，条件(d)での製膜条件が最も優れていることが示唆されるに至った．

3.3 スクラッチ試験による薄膜と基板との接着強度評価

薄膜の密着性を評価するために，スクラッチ試験を行った．その試験結果を Fig. 9 に示す．

前処理としてバフ研磨を施した薄膜付与材については，すべての条件において密着性の程度に大きな差異は認められず，更に，製膜条件の違いによる明確な差異も確認されなかった．他方，前処理としてビーム照射のみを施した薄膜付与材については，製膜条件(a)から(d)へと，ビーム照射時間が短くなるにつれ密着性の向上が確認された．因みに，バフ研磨を施した薄膜付与材における接着強度はビーム照射を施したそれに比して，すべてについて低下した．これはバフ研磨により，基板最表面を除去することから，薄膜の接着強度に寄与する凹凸がなくなり，その結果，薄膜の接着強度の低下が生じたものと考えられる．

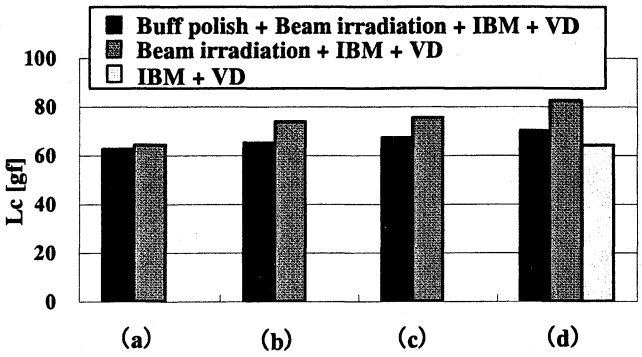

Fig. 9 The results of scratch test.

3.4 XD による薄膜の結晶構造解析

薄膜の結晶構造の評価のために，薄膜 X 線回折分析を行った．分析には，最も優れていると考えられる条件(d)下で製膜を行った薄膜付与材を用いた．測定結果を Fig. 10 に示す．結果より，微弱ではあるが，2θ=42° に Cu のピークのみが確認されたものの，ピーク高が低いことから薄膜はアモルファス構造を有していることが考えられる．また，X 線入射角度 α=1.0 よりも高角度の α=2.0 での X 線回折パターンにみられる Cu のピーク高が低くなっていることから，X 線は基板にまで達しており，そのためピークが低くなったとも考えられる．

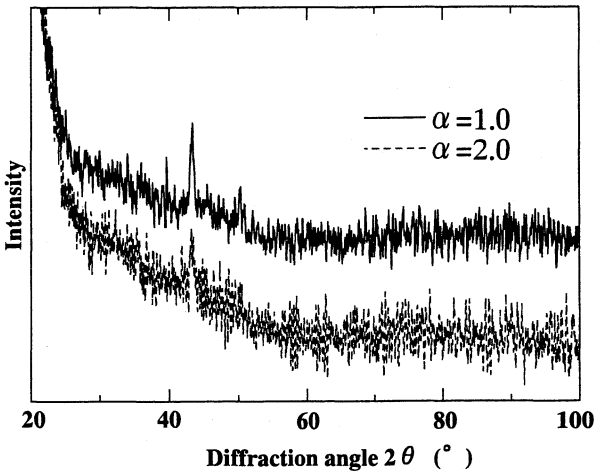

Fig. 10 X-ray diffraction patterns of Cu thin film.

3.5 XPS による深さ方向への薄膜構成元素分布の把握

Cu 薄膜の深さ方向に対する元素分布について評価するために，X 線光電子分光分析を行った．結果を Fig. 11 に示す．同分析に用いた薄膜付与材は，XD の分析に適用した同様の条件(d)下で製膜を行った薄膜付与材を用いた．測定結果より，薄膜と基板との界面において，濃度傾斜を示す混合層(Mixing layer)が形成されていることが明らかとなった．この混合層の存在により，薄膜の密着性が向上したものと考えられる．

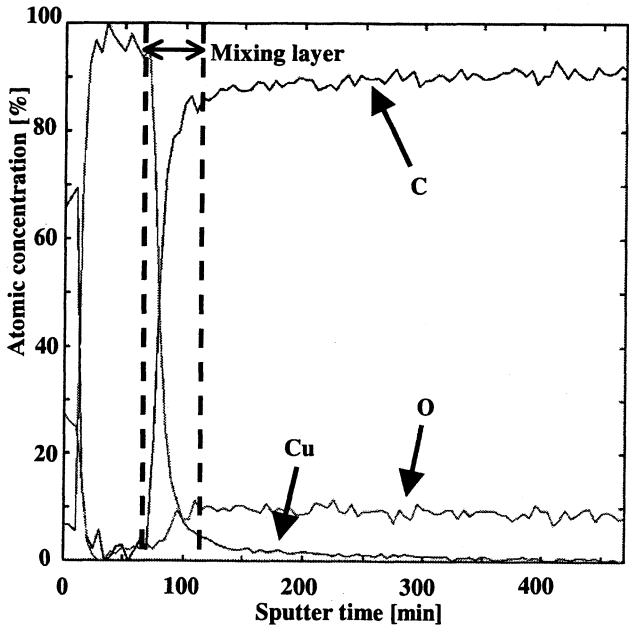

Fig. 11 XPS patterns of Cu thin film.

3.6 電気特性評価

薄膜の機能評価として，絶縁抵抗計を用いて，薄膜の表面抵抗率，体積抵抗率とを測定した．その結果を Fig. 12～15 に示す．結果より，LACEA の薄膜未付与材では 2.0×10^{15}[Ω]の表面抵抗率を示したのに対し，Cu 薄膜を付与した薄膜付与材では $1.2\sim1.6\times10^{3}$[Ω]と表面抵抗率の低下が認められた．また，製膜方法の違い，及び前処理の違いによる有意差はなかった．

一方，体積抵抗率を測定した結果については，体積抵抗率は薄膜未付与材，付与材共に $1.5\sim4.3\times10^{9}$[Ω・m]と高い体積抵抗率を示した．また，表面抵抗率と同様に，製膜方法の違い，また前処理の違いによる有意差は認められなかった．

これらの結果より，これらの薄膜付与材について，電気・電子部材への適用の可能性が明らかとなった．

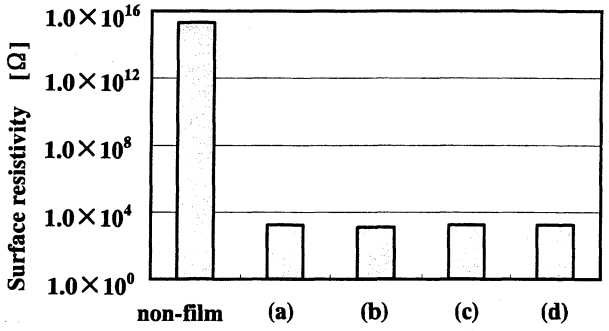

Fig. 12 Surface resistivity of LACEA coated with Cu pretreated by beam irradiation. (a), (b), (c) and (d) correspond to the conditions of film formation shown in Table 1.

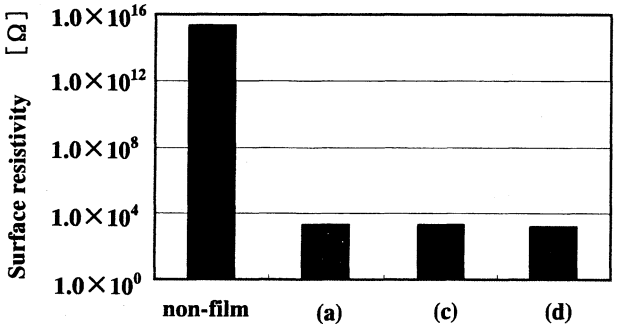

Fig. 13 Surface resistivity of LACEA coated with Cu pretreated by buff polish and beam irradiation. (a), (c) and (d) correspond to the conditions of film formation shown in Table 1.

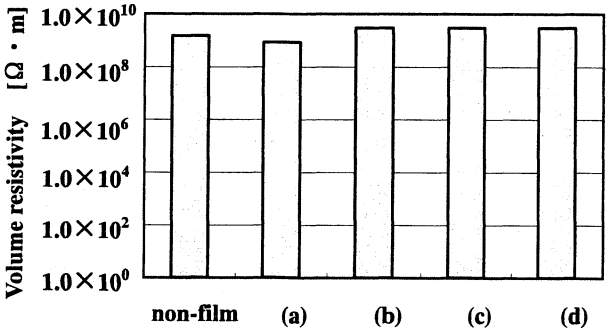

Fig. 14 Volume resistivity of LACEA coated with Cu pretreated by beam irradiation. (a), (b), (c) and (d) correspond to the conditions of film formation shown in Table 1.

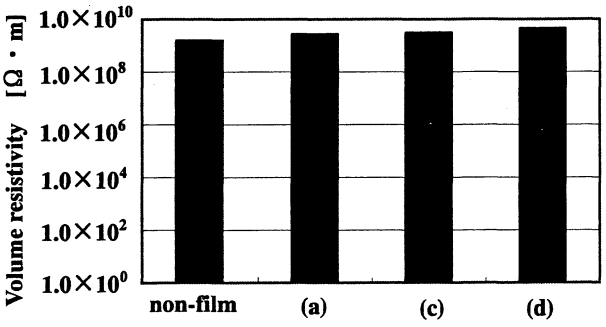

Fig. 15 Volume resistivity of LACEA coated with Cu pretreated by buff polish and beam irradiation. (a), (c) and (d) correspond to the conditions of film formation shown in Table 1.

4. 結論

本研究では，生分解性プラスチックへの金属薄膜付与による最適な条件を確立し，更には，この薄膜付与材の電気・電子部材への適用を想定し研究を遂行した．それらの結果より，以下に示す事柄が明らかとなった．

(1) 基板表面の前処理として実施したバフ研磨は，基板表面の微細な凹凸を除去することから，膜接着強度の低下をもたらす可能性のあることが明らかとなった．

(2) 前処理としてバフ研磨により，基板最表面の除去を施し製膜した薄膜では，基板であるプラスチック内部から熱によるガス発生，及び脱泡が生じ，薄膜にき裂やはく離等の欠陥をもたらす可能性のあることが明らかとなった．

(3) 基板表面の前処理として実施したビーム照射は，膜接着強度の向上をもたらす有用な方法であることが確認された．

(4) 耐熱性の低い生分解性プラスチックであっても，ビーム照射時間を短くすることなどによって基板への熱影響を軽減でき，良好な薄膜形成が可能であることが明らかとなった．

(5) Cu 薄膜は，電気・電子部材として適する導電性を有し，その適用が期待できることが明らかとなった．

(6) ビーム照射を先行させるイオンビームミキシング法による混合層の形成と，その後の真空蒸着による堆積の組み合わせによる製膜法は，耐熱性の低い生分解性プラスチックへの良好な薄膜形成手法となることが明らかとなった．

謝辞

本研究を遂行するに際し，三井化学株式会社及び長野技研株式会社には，それぞれ供試材料のご提供を頂いた．また，薄膜の形成に際し，工学院大学工学研究科博士課程の佐々木道子氏(現　独立行政法人理化学研究所)の助力を得た．尚，本研究は，主として文部科学省ハイテク・リサーチ・センター整備事業による「AMC」，「Post AMC」の研究プロジェクト研究助成，及び工学院大学総合研究所プロジェクト研究助成により遂行された．ここに記して謝意を表す．

参考文献

1) 矢ケ崎隆義，木村雄二，鷹野一朗，伊藤紀子，高分子材料のイオンビームミキシング法による薄膜付与と多機能化，平成 7 年～9 年度科学研究費補助金(基礎研究(c)(2))研究成果報告書，(1998)
2) 久保田宏，松田智：廃棄物工学，培風館，49 (1998)
3) 木内正人，茶谷原昭義，堀野裕治，木野村淳，杢野由明，藤井兼栄，大阪工業技術試験所季報，**44-1**，25 (1993)
4) 鷹野一朗，高森浩太郎，竹本正勝，関口勇，磯部昭二，工学院大学研究報告，**58**，101 (1985)
5) 岩木正哉，磯部昭二，下條哲男，竹下正勝，鷹野一朗：イオン応用機器概論，開発社，57 (1994)
6) 鷹野一朗，中村勲，沢田芳夫，溶接，**71**，4 (2002)
7) 山田香織，矢ケ崎隆義，木村雄二，鷹野一朗，材料，**54-1**，79 (2005)
8) 矢ケ崎隆義，木村雄二，材料，**47**，84 (1998)
9) 表面技術協会：PVD・CVD 皮膜の基礎と応用，槇書店，48 (1994)
10) 矢ケ崎隆義，木村雄二，材料，**45**，328 (1996)
11) 筏義人：生分解性高分子の基礎と応用，アイピーシー，292 (1999)
12) 土肥義治：生分解性プラスチックハンドブック，エヌ・ティー・エス，281 (1995)
13) 日本機械学会：Standard Method for Evaluating the Defects in the Coatings Made by Dry Processing，日本機械学会，6 (1996)

Available online at www.sciencedirect.com
ScienceDirect
Electrochemistry Communications xxx (2008) xxx–xxx
electrochemistry communications
www.elsevier.com/locate/elecom

Site-selective chemical etching of GaAs through a combination of self-organized spheres and silver particles as etching catalyst

Yukiko Yasukawa [a], Hidetaka Asoh [a,b], Sachiko Ono [a,b,*]

[a] *Research Institute for Science and Technology, Kogakuin University, Japan*
[b] *Department of Applied Chemistry, Kogakuin University, 2665-1 Nakano-cho, Hachiouji, Tokyo 192-0015, Japan*

Received 30 January 2008; received in revised form 14 February 2008; accepted 15 February 2008

Abstract

Microfabrication of the *n*-GaAs substrate surface was investigated by a combination of colloidal crystal templating, electroless plating and subsequent metal-assisted etching using noble metals as a catalyst. Ag and Cu nanosized particles were deposited site selectively to form metal-honeycomb patterns on GaAs using self-organized polystyrene spheres as a mask. By Ag-assisted etching, GaAs was effectively etched into a convex-array structure. Different anisotropic etching patterns were observed throughout the substrate after Ag-assisted etching, by changing the crystal-face orientation of *n*-GaAs from (100) to (111).

Keywords: Compound semiconductor; Metal-assisted chemical etching; Self-organized structure; Electroless plating; Colloidal crystals

1. Introduction

To fabricate multifunctional porous Si, "metal-assisted chemical etching" was proposed as a useful technique [1]. The method utilizes the catalytic ability of noble-metal thin films/particles in an etchant composed of a mixture of HF and H_2O_2 solutions without the use of any electrical connections or strong oxidizing agents [2]. Thus, the effects of metal-assisted etching with Au, Pt, Ag and Pd were systematically investigated for Si(100) [2,3]. However, the investigation of this etching method in group III–V compound semiconductors is rare in contrast to the case of Si, so it is less understood. Therefore, we describe here the effectiveness of metal-assisted etching for the most widely utilized group III–V compound semiconductor, GaAs, as a function of crystal-face orientations, i.e., (100) and (111) possessing a resistivity level of 10^{-3} Ω cm order. The morphological control of the GaAs surface is of interest from the standpoint of fundamental science, and further, the application to devices in the future.

A templating technique based on self-organized polystyrene (PS) spheres has been reported for the fabrication of Si hole arrays [4], dot arrays [4], disk arrays [5], pillar arrays [5] and porous alumina possessing 2D/3D composite structures [6] by means of anodization as well as the control of pit initiation sites on aluminum [7]. Here, PS spheres can be dissolved easily by ultrasonic cleaning in toluene after the experimental processes. Therefore, PS spheres forming the self-organized structure were selected as a mask, aiming for the "site-selective" etching of GaAs. As a result of previous studies [8,9], electroless Cu plating on Si has been clarified and the technique was well established. Also, deep cylindrical nanoholes have been generated by etching the *p*-Si substrate by depositing Ag particles [10], however, there is no report on successful electroless Cu and Ag plating of GaAs. Thus, Cu and Ag were chosen as metal sources for the metal-assisted etching in the present study.

* Corresponding author. Address: Department of Applied Chemistry, Kogakuin University, 2665-1 Nakano-cho, Hachiouji, Tokyo 192-0015, Japan. Tel.: +81 426 28 4843; fax: +81 426 25 8982.
E-mail address: sachiono@cc.kogakuin.ac.jp (S. Ono).

1388-2481/$ - see front matter © 2008 Published by Elsevier B.V.
doi:10.1016/j.elecom.2008.02.024

2. Experimental

A GaAs wafer was cleaved to 1 cm × 1 cm in size and used as a substrate. Before forming a mask on the substrate, the native-oxide film was removed by immersing the substrate in 46 wt% HF solution for 15 min. Schematic explanation of the present experimental procedure and site-selective chemical etching of GaAs was shown in Fig. 1. A solution with PS spheres of 1 μm diameter was adjusted to the suspension concentration of 0.25%, supplied dropwise onto the substrate, and then dried in air. After the complete evaporation of the solvent, PS spheres forming a close-packed structure were obtained as a mask. To fix the mask on the substrate, a heat treatment was carried out at 100 °C for 1–2 h (Fig. 1a). Subsequently, electroless Cu plating was proceeded in a solution consisting of 0.01 wt% $CuSO_4 \cdot 5H_2O$ and 46 wt% HF without any reductants [8,9], with the bath temperature maintained at 25 °C for 12 ~ 20 min. Immersion plating in an aqueous solution containing 10^{-4} mol dm^{-3} $AgClO_4$ and 10^{-3} mol dm^{-3} NaOH at room temperature was conducted for 20 min [10] for Ag deposition (Fig. 1b). It was immediately followed by chemical etching in a mixture of 5 mol dm^{-3} HF and 1 mol dm^{-3} H_2O_2 solutions at room temperature (Fig. 1c–e). Finally, ultrasonic cleaning in toluene was carried out to remove the mask. The obtained surface morphologies of GaAs were observed by scanning electron microscopy (SEM, Hitachi S-4200) and atomic force microscopy (AFM, Digital Instrument Nano Scope IIIa).

3. Results and discussion

Fig. 2 represents a SEM image of a Cu-honeycomb pattern formed on the *n*-GaAs(100) substrate by electroless plating for 16 min. Cu particles were deposited site selectively only on the exposed areas of the substrate, i.e., the apertures between PS spheres, whereas essentially no Cu particles were deposited at the contact areas of the PS sphere and the underlying GaAs substrate. It was found that the Cu-honeycomb pattern consists of an aggregation of Cu particles of ~75 nm on average, though the size of particles is somewhat scattered. The present study could be the first report on Cu plating of GaAs without bias because the surface processing technique of GaAs has not

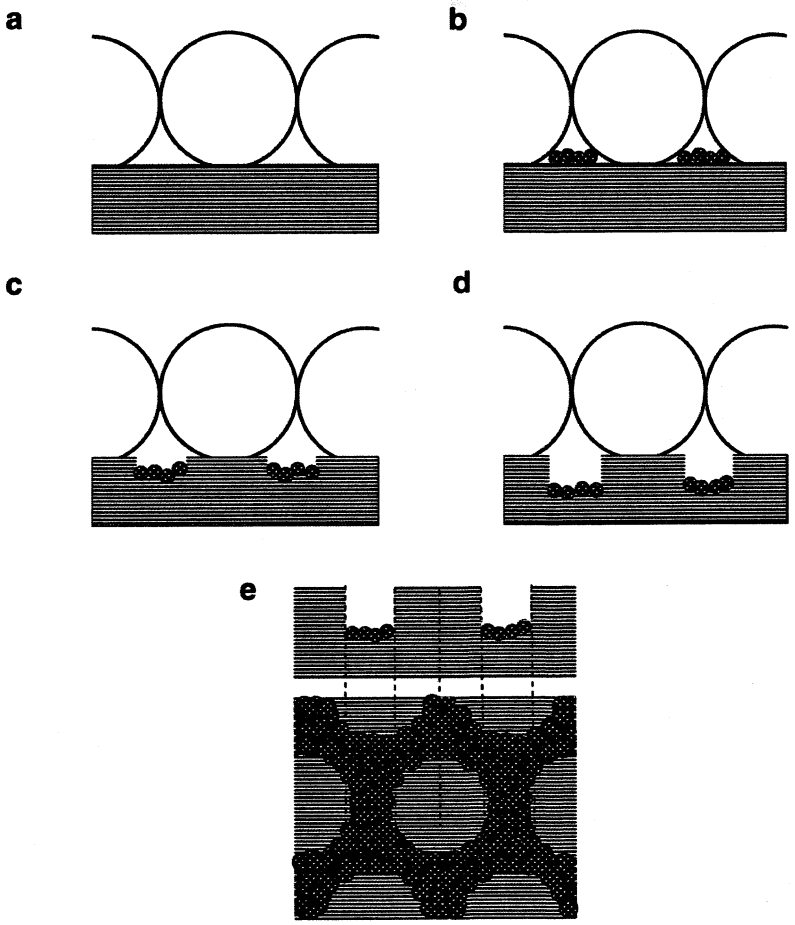

Fig. 1. Schematic explanation of site-selective chemical etching of GaAs. (a) Colloidal crystals formed on substrate as a mask, (b) deposition of noble-metal particles, (c) the initial stage of chemical etching of GaAs using a metal catalyst, (d) after completion of chemical etching, and (e) obtained cross section and corresponding top view after removal of the mask.

Please cite this article in press as: Y. Yasukawa et al., Site-selective chemical etching of GaAs through a combination ..., Electrochem. Commun. (2008), doi:10.1016/j.elecom.2008.02.024

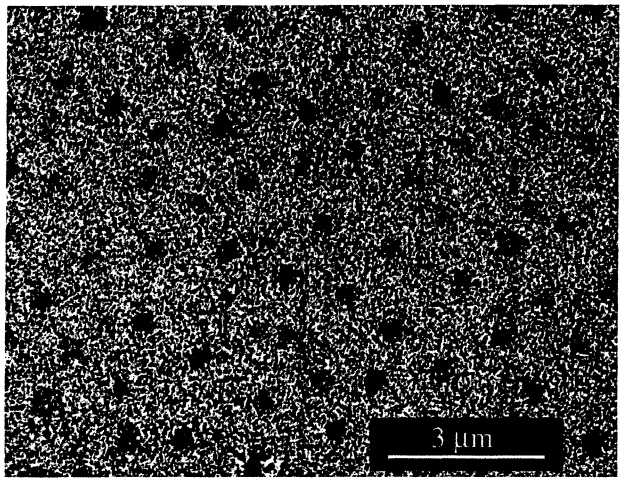

Fig. 2. SEM micrograph of Cu-honeycomb pattern formed on present *n*-GaAs(100) substrate. PS spheres of 1 μm diameter were utilized as a direct mask.

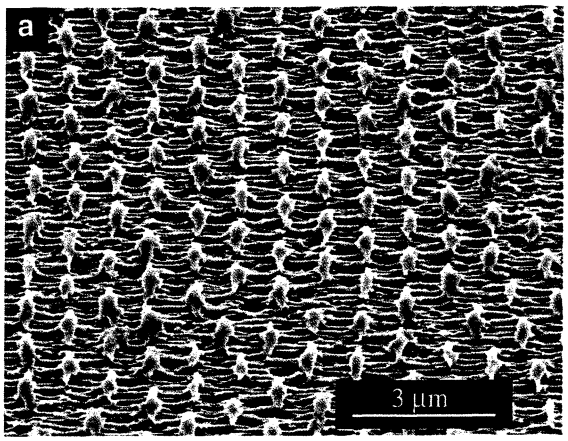

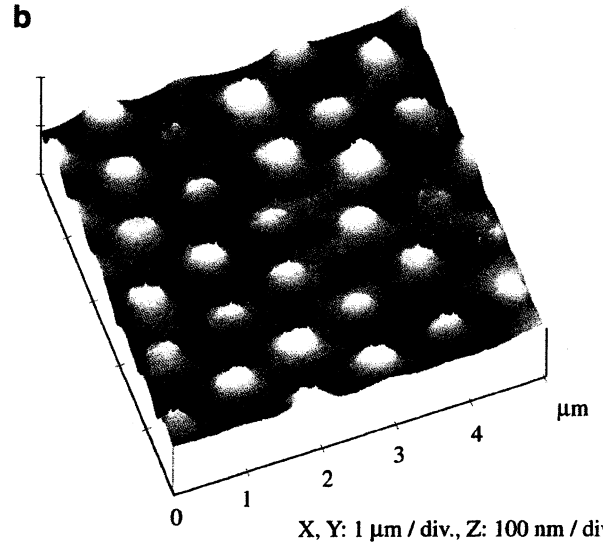

Fig. 3. Surface structures of *n*-GaAs(100) substrate obtained by a combination of self-organized structural mask consisting of PS spheres (∅1 μm), electroless plating and metal-assisted etching. Typical patterns obtained from (a) SEM micrograph observed from 45° to the surface, and (b) AFM image.

been sufficiently established and the removal of the native-oxide film from the surface is difficult [11]. A similar honeycomb pattern and particle size of Ag were obtained by Ag immersion plating. Afterward, the Cu- and Ag-plated substrates were exposed to an etching solution for 60 s. Fig. 3a shows a GaAs substrate after Ag plating and subsequent etching. Upon etching, the anisotropic GaAs convex arrays were formed. In the preliminary set of experiments, the etching behavior of the GaAs(100) substrate possessing colloidal crystals as the mask but without any metal catalysts, i.e., the conventional "chemical etching", was first investigated. As a result, GaAs was etched by the present HF-based etching solution itself. By comparing the chemically etched specimen described above with the specimen etched with Ag assistance represented in Fig. 3a, the difference in etching structures between the two specimens is clearly revealed. Therefore, it was confirmed that the obtained GaAs convex structure shown in Fig. 3a is due not to chemical etching but is originated from "metal-assisted" chemical etching with Ag. Essentially, the structure shown in Fig. 3a has an inverse relation to the Ag-honeycomb pattern exhibiting a pattern similar to that in Fig. 2. Note that the etching structure originated from the use of PS "spheres" with 1 μm diameter, though the achieved pattern showed an anisotropic shape. On the other hand, effective metal-assisted etching was not achieved for the Cu-plated specimen because Cu is less noble compared with Ag. An AFM image of the corresponding GaAs convex structure is shown in Fig. 3b. The average etching depth of 35 nm is much shallower than that of *p*-Si(100) [*ca.* 100 nm] etched with Ag assistance [12] under identical experimental conditions. *p*-Si(100) exhibited an isotropic etching structure with an etching rate of ~1.7 nm/s by Ag-assisted etching [12], while the present *n*-GaAs(100) shows an anisotropic configuration, and the average etching velocity was estimated to be ~0.6 nm/s on the bases of a line analysis of the AFM image shown in Fig. 3b. Concerning the mechanism for the Ag-assisted chemical etching of Si, Li and Bohn reported as follows [2]: (I) When the oxidants (H_2O_2) are reduced on the surfaces of Ag particles, positive holes (h^+) are generated as cathode reaction. (II) The oxidative dissolution of Si occurs in HF-containing etchant as anode reaction. (III) Finally, porous silicon can be generated as a localized electrochemical process. The fundamental mechanism of metal-assisted etching of GaAs might be somewhat analogous to that of Si, but underlying mechanisms must be more complicated for GaAs since GaAs is composed of two different constituents. Also, chemical reactivities [11] and valences of Ga and As are different so that the contributions of Ga and As elements to metal-assisted etching might not be identical at the atomic level. Thus, Si and GaAs exhibit dissimilar etching configurations and etching rates even when the same experimental conditions and the same catalytic metal are utilized.

Please cite this article in press as: Y. Yasukawa et al., Site-selective chemical etching of GaAs through a combination ..., Electrochem. Commun. (2008), doi:10.1016/j.elecom.2008.02.024

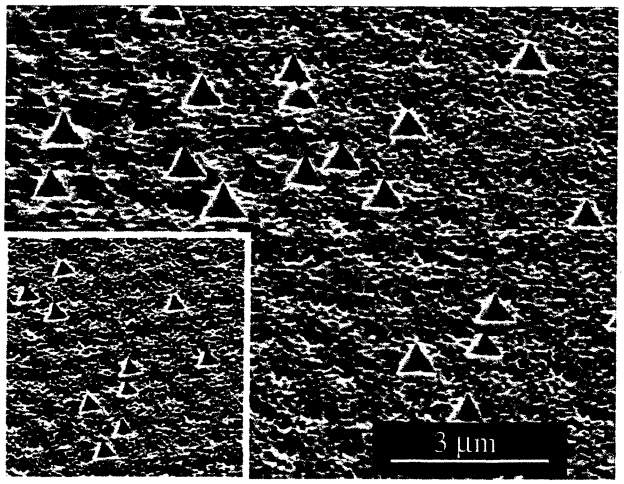

Fig. 4. SEM micrograph of Ag-assisted etching for *n*-GaAs(1 1 1) substrate observed from 45° to the surface. All the experimental conditions were the same as in the case of Fig. 3 Inset shows low-magnification view of obtained specimen.

Ag-assisted etching was also studied on the *n*-GaAs(1 1 1) substrate under the same experimental conditions. Although it is not confirmed, the obtained structure seems to be etched with Ag assistance and form convex configurations. On the other hand, the contact areas between the PS sphere and the substrate were etched owing to the removal of the mask during etching, i.e., traces of chemical etching at the convex portion are seen in Fig. 4. Therefore, the SEM image shows two different types of etching effects simultaneously. In contrast to the (1 0 0) substrate, the observed convex arrays imply that Ag-assisted etching proceeds relatively isotropically and at a shallow depth on the (1 1 1) substrate. According to a previous report [10], no marked difference between *p*-Si(1 0 0) and *p*-Si(1 1 1) substrates was seen in the electroless-deposited Ag particles. However, subsequent Ag-assisted etching generated different patterns on the two planes, i.e., etched holes tended to be generated on the surface of Si(1 1 1), but much deeper holes in the direction perpendicular to the substrate surface were formed on Si(1 0 0). Thus, the present result is consistent with that for Si. In addition, the shape of Ag particles is one of the dominant factors in the control of the orientation and the depth of etched holes in Ag-assisted Si etching [3]; the deeper cylindrical holes in the direction perpendicular to the surface originated as a consequence of the more spherical shape of Ag particles and the subsequent etching. Therefore, the shallower etching structure seen in GaAs(1 1 1) implies that the (1 1 1) substrate is chemically inactive compared with the (1 0 0) substrate in terms of Ag-assisted etching, or deformed Ag particles [3] were generated on (1 1 1). Although a reason for the generation of triangular pits seen in Fig. 4 is not yet confirmed, they could be composed of {1 1 2} pit walls because {1 1 2} is the most stable plane enveloping directions of <1 1 1> [13].

4. Conclusion

In conclusion, we demonstrated that electroless Cu and Ag plating yielded patterned structures reflecting the self-organized structural mask, and consequently, Ag-assisted etching was accomplished on the *n*-GaAs substrate. In the present etching method, the crystal-face orientation, i.e., *n*-GaAs(1 0 0) and (1 1 1), considerably affect the resultant etching structure and the etching rate. As a suggestion of future work, we will try to fabricate novel surface structures by using the difference in etching patterns between the crystal-face orientations of *n*-GaAs.

References

[1] S. Yae, Y. Kawamoto, H. Tanaka, N. Fukumuro, H. Matsuda, Electrochem. Commun. 5 (2003) 632.
[2] X. Li, P.W. Bohn, Appl. Phys. Lett. 77 (2000) 2572.
[3] K. Tsujino, M. Matsumura, Electrochim. Acta 53 (2007) 28.
[4] H. Asoh, A. Uehara, S. Ono, Jpn. J. Appl. Phys. 43 (2004) 5667.
[5] H. Asoh, A. Oide, S. Ono, Electrochem. Commun. 8 (2006) 1817.
[6] H. Asoh, S. Ono, Appl. Phys. Lett. 87 (2005) 103102.
[7] H. Asoh, K. Nakamura, S. Ono, Electrochem. Acta 53 (2007) 83.
[8] H. Asoh, S. Sakamoto, S. Ono, J. Colloid Interface Sci. 316 (2007) 547.
[9] S. Ono, A. Oide, H. Asoh, Electrochem. Acta 52 (2007) 2898.
[10] K. Tsujino, M. Matsumura, Adv. Mater. 17 (2005) 1045.
[11] I. Shiota, K. Motoya, T. Ohimi, N. Miyamoto, J. Nishizawa, J. Electrochem. Soc. 124 (1977) 155.
[12] H. Asoh, F. Arai, S. Ono, Electrochem. Commun. 9 (2007) 535.
[13] S. Langa, J. Carstensen, M. Christophersen, H. Föll, I. Tiginyanu, Appl. Phys. Lett. 78 (2004) 1074.

Please cite this article in press as: Y. Yasukawa et al., Site-selective chemical etching of GaAs through a combination ..., Electrochem. Commun. (2008), doi:10.1016/j.elecom.2008.02.024

Available online at www.sciencedirect.com
ScienceDirect
Electrochimica Acta 53 (2007) 83–86
ELECTROCHIMICA Acta
www.elsevier.com/locate/electacta

Control of pit initiation sites on aluminum foil using colloidal crystals as mask

Hidetaka Asoh *, Koji Nakamura, Sachiko Ono

Department of Applied Chemistry, Faculty of Engineering, Kogakuin University, 1-24-2 Nishi-shinjuku, Shinjuku-ku, Tokyo 163-8677, Japan

Received 8 December 2005; received in revised form 13 January 2007; accepted 15 January 2007
Available online 27 January 2007

Abstract

The electrochemical etching of aluminum foils using a physical mask of colloidal spheres was studied to directly control the initiation sites of pits independent of the surface activation state of the substrate. A two-dimensional array of colloidal spheres used as a mask was prepared by self-assembly on an aluminum substrate. The transfer of the hexagonally ordered pattern of self-assembled colloidal spheres to the aluminum substrate could be achieved by the selective electrochemical etching of an exposed aluminum surface. That is, etch pits were generated only in the triangular void space among the three spheres on the aluminum surface. Based on this process, the dispersibility of the initiation sites of pits was improved clearly in comparison with that for the conventional method. The density of pits could also be controlled by changing the diameter of spheres used as a mask.

Keywords: Electrochemical etching; Aluminum; Electrolytic capacitor; Physical mask; Colloidal crystal

1. Introduction

In the field of aluminum electrolytic capacitors, a high-power capacitor has attracted growing interest due to the demand for their utilization as power supplies and in several inverter applications. To obtain a high-power capacitor, dc etching is typically carried out in a hot chloride solution containing electrolyte under constant-current or constant-voltage conditions, and results in the formation of tunnel pits following the selective dissolution of (1 0 0) faces [1–3]. From the standpoint of high-power capacitors, it is important to maximize the surface area of an electrode because the surface area of etched aluminum basically determines the capacitance of electrolytic capacitors. However, the ideal enlargement of the surface area by electrochemical etching is difficult due to a disorderly pit distribution and the growth of merged pits by laterally directed dissolution. Therefore, improvements in pit distribution density and the homogeneity of pit sizes, while avoiding an excessive dissolution of the aluminum surface, are essential for maximizing the surface area of etched aluminum. Although the dispersibility of the initiation sites of pits has been improved generally by changing the chemical compositions of the substrate [4,5], an other approach to directly controlling the initiation sites of pits independently of the surface activation state of the substrate has been expected recently [6]. For applications to high-voltage electrolytic capacitors, it should also be added that a certain interval between adjacent pits is required by considering the thickness of oxide films as dielectrics. In this report, we describe a novel control method for pit initiation sites on aluminum using a direct physical mask of colloidal spheres for etching. The methods used here are based on the pattern transfer of regular arrays of micrometer-sized colloidal spheres to an aluminum substrate using electrochemical etching.

2. Experimental

Fig. 1 shows the schematic of etching using a colloidal crystal as a mask. High-purity (>99.99%) aluminum foils predominantly composed of (1 0 0) faces were used in dc etching. A monodisperse suspension solution of polystyrene (PS) spheres (Nissin EM Co., Ltd Tokyo, 0.2% solids) was dropped onto the aluminum foil to prepare the physical mask. The suspension drop was dried in air, and the spheres self-assembled into a

* Corresponding author. Tel.: +81 3 3340 1486; fax: +81 3 3340 0147.
E-mail address: asoh@cc.kogakuin.ac.jp (H. Asoh).

0013-4686/$ – see front matter © 2007 Elsevier Ltd. All rights reserved.
doi:10.1016/j.electacta.2007.01.021

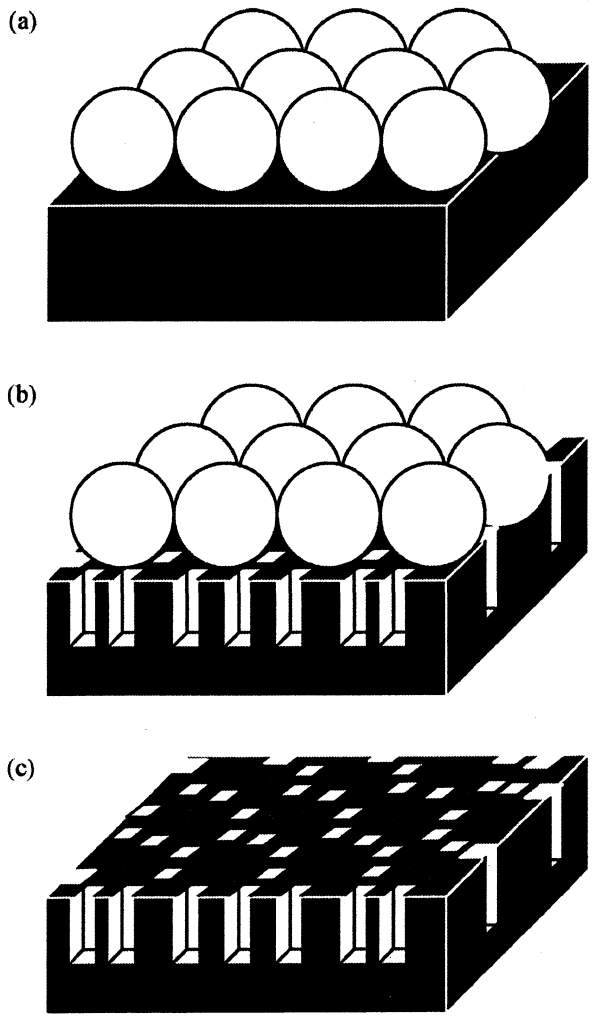

Fig. 1. Schematic for etching process using colloidal crystal as mask: (a) self-assembled PS spheres on aluminum substrate; (b) electrochemical etching of aluminum coated with colloidal crystals; (c) removal of spheres.

closely packed structure with three-dimensional ordered lattices via attractive capillary forces (Fig. 1a) [7,8]. After the complete evaporation of the solvent, the aluminum foils coated with colloidal crystals were heated in a muffle furnace at 100 °C, which is higher than the glass-transition point (T_g: ~93 °C) of the PS spheres [9], for 1 h to fix each sphere to the underlying aluminum foil. Note that self-assembled PS spheres crystallized into the cubic closely packed structure or the face-centered cubic lattice with a large number of layers. In this etching, however, the formation of closely packed two-dimensional arrays of colloidal spheres with long-range ordering in the first layer on the aluminum substrate and their binding force are essential.

Aluminum foils with colloidal crystals were anodically etched at a constant current density of 2000 A m^{-2} in a mixture of 1 mol dm^{-3} hydrochloric acid and 4 mol dm^{-3} sulfuric acid solutions at 70 °C (Fig. 1b). To control the morphology of tunnel pits, the changes in voltage transient during the initial stage of dc etching were measured using a digital multimeter with a data acquisition system. The surface morphology of the etched aluminum foil was observed by scanning electron microscopy (SEM) after the removal of the mask in toluene (Fig. 1c). To investigate the etching morphology of each sample in the depth direction, oxide replicas were formed in a mixture of 0.5 mol dm^{-3} boric acid and 0.05 mol dm^{-3} sodium tetra-borate solutions at a constant current density of 5 A m^{-2} up to 40 V at 20 °C. After anodization, the aluminum substrate was stripped away in a saturated mercuric chloride solution.

3. Results and discussion

3.1. Effect of physical mask on control of initiation sites of pits

Fig. 2 shows typical SEM images of the aluminum surface after ordinary electrochemical etching. In the case without a physical mask, a large number of pits were generated irregu-

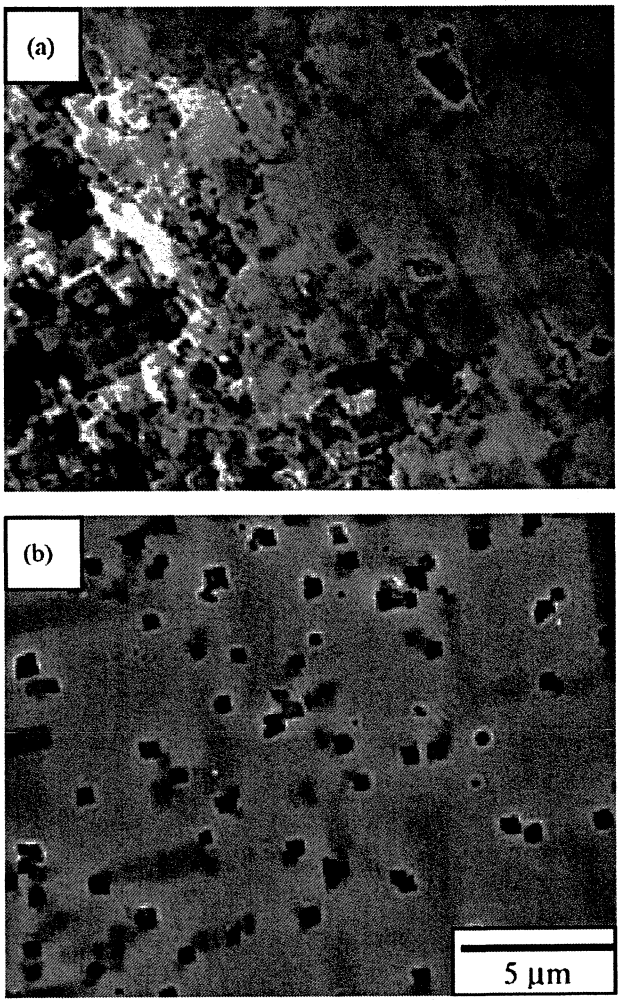

Fig. 2. SEM images of aluminum surfaces after etching: (a) without mask and (b) with mask. Etching was carried out in a mixture of 1 mol dm^{-3} hydrochloric acid and 4 mol dm^{-3} sulfuric acid solution at 70 °C for 5 s. The PS spheres used as a mask were 3 μm in diameter.

larly, which merged by laterally directed dissolution, as shown in Fig. 2a. Consequently, some areas were overetched or unetched because electrochemical etching proceeded locally.

On the other hand, when colloidal crystals were used as a direct mask during electrochemical etching, evenly distributed pits of uniform sizes were generated under the triple points of spheres (3 μm in diameter), as shown in Fig. 2b. In this case, the size of etched pits was approximately 0.6 μm. The pit distribution was different from the random distribution, shown in Fig. 2a. The pit arrays were arranged like a network over the entire area of the specimen. This result indicates that PS spheres can act as a physical mask for electrochemical etching. That is, etch pits are generated only in the exposed aluminum surface. In other words, etching can proceed only in the conductive area, which was located in the triangular void space among three spheres on the aluminum surface. This templating mechanism is somewhat similar to "natural lithography" proposed by Deckman and Dunsmuir [10]. However, our approach is different from "natural lithography" based on a dry process, in that the underlying aluminum substrate can be fabricated directly by a wet process in electrolytes.

In the proposed process, it is important to fix the position of PS spheres onto an aluminum foil by appropriate heat treatment. Fig. 3 shows the SEM image of the aluminum foil coated with colloidal crystals after electrochemical etching. To clearly show the structure of the heat-treated PS spheres, the specimen was observed before the complete removal of PS spheres. Although some deformation of the spherical shape was observed, it was confirmed that PS spheres could play the role of a mask in restricting the position of the pits generated during electrochemical etching. When the sample had been annealed below the T_g of polystyrene, the fixation of PS spheres on the aluminum substrate was insufficient. For the sample annealed above the T_g, the binding force between the spheres and the aluminum substrate was improved by enlarging the contact area between them as a result of the viscoelastic deformation of PS spheres. Therefore, the exposed aluminum area might be adjusted precisely. A detailed study on the effect of heat treatment conditions such as temperature and period is now in progress.

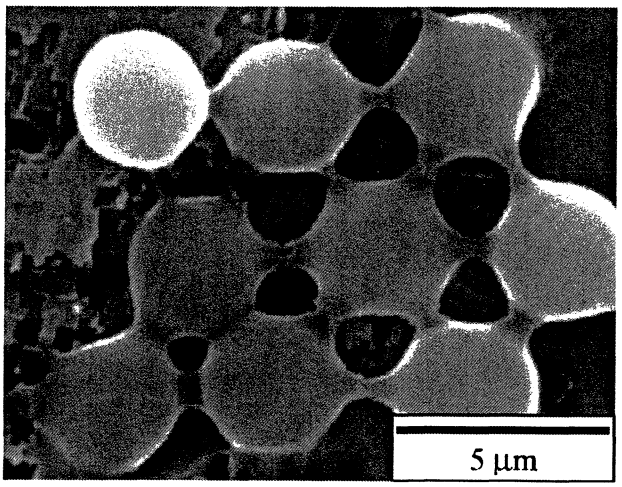

Fig. 3. SEM image of etched aluminum surface before removal of spheres. Etching conditions were the same as those in Fig. 2b.

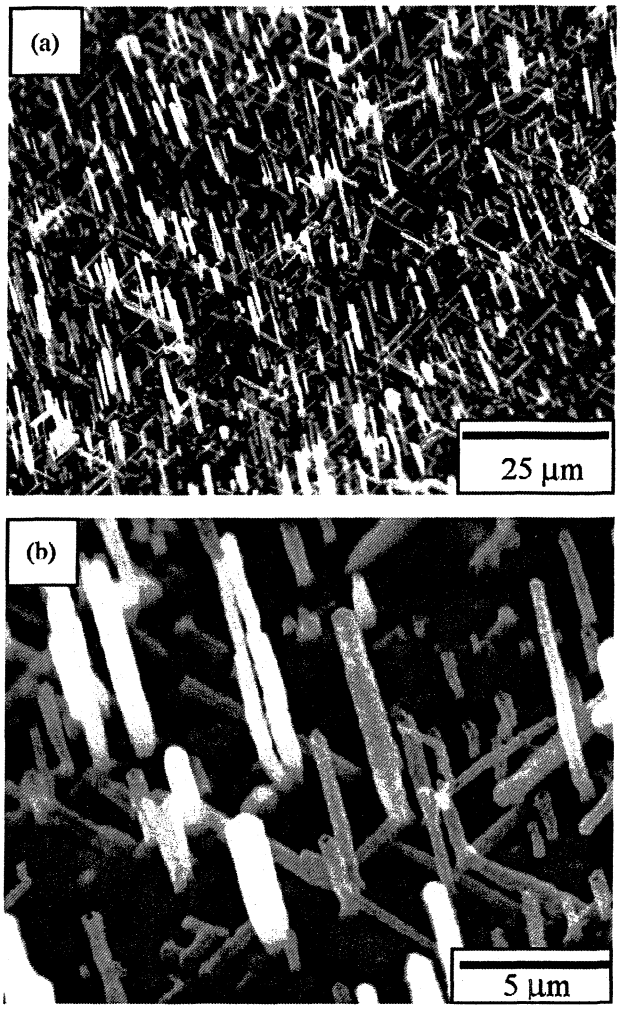

Fig. 4. SEM images of oxide replica formed in neutral solution under constant-current condition: (a) low-magnification and (b) high-magnification views. Etching conditions were the same as those in Fig. 2b. A specimen was observed at an angle of 45° to the surface.

3.2. Morphology of tunnel pits

Tunnel pit morphology, which depends on etching conditions, directly affects the capacity of an electrolytic capacitor. Fig. 4 shows typical SEM images of an oxide replica. From an oblique SEM image, the depth of the tunnels was estimated to be approximately 10 μm. Although the inherent tunnel morphology was quite similar to that of industrial aluminum etched foil, the pit positions were obviously different from those obtained for the conventional method.

3.3. Effect of diameter of PS spheres on pit density

To modulate the capacity of an electrolytic capacitor, it is necessary to control pit size and pit density arbitrarily. In the

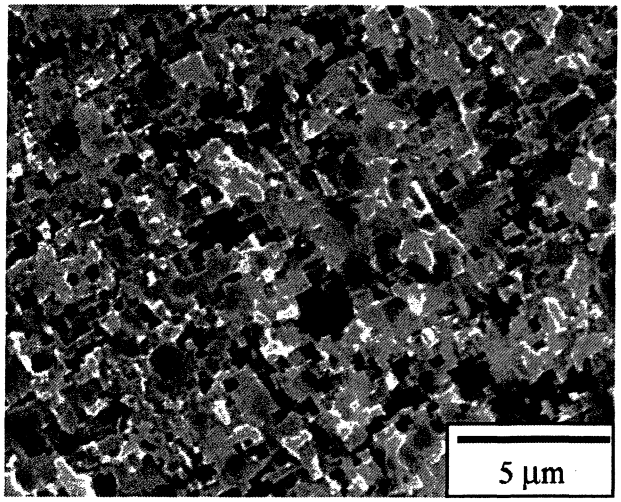

Fig. 5. SEM image of etched aluminum surface after removal of spheres. The PS spheres used as a mask were 1 μm in diameter. Electrochemical etching was performed under the same conditions as those in Fig. 2b.

present method, pit density, that is, the number of initiation sites for pit generation, can be adjusted arbitrarily by changing the diameter of the PS spheres used as a physical mask. When the diameter of PS spheres decreases, the triangular void space among the three spheres, which can act as an initiation site for pit generation, also decreases. However, the exposed aluminum spots can be increased in comparison with the case of Fig. 2b. Fig. 5 shows the SEM image of the etched aluminum surface using small PS spheres (1 μm in diameter). If the spheres are sufficiently robust to protect aluminum from dissolution during electrochemical etching, regular arrays of isolated pits can be obtained. As shown in Fig. 5, although the etched aluminum surface was coarser than that shown in Fig. 2b, pit density increased clearly. The overetching at the aluminum surface seemed to be insufficient for explaining protection using the mask against aluminum dissolution. Colloidal spheres used as a mask may be desorbed from the substrate by laterally directed dissolution at the mask/aluminum interface during electrochemical etching. Therefore, it is necessary to perform etching under optimum conditions.

4. Conclusions

We have described the electrochemical etching of aluminum using colloidal spheres as a physical mask to control the number of pit initiation sites. The method proposed here was based on the pattern transfer of regular arrays of micrometer-sized colloidal spheres to an aluminum substrate using electrochemical etching. That is, etch pits were generated only in the exposed aluminum surface, located in the triangular void space among the three spheres on the aluminum substrate. Using this process, improvements in pit distribution density and the homogeneity of pit sizes, while avoiding excessive dissolution of aluminum surface, could be achieved easily by changing the diameter of spheres in comparison with that used in the conventional method. Further research on the capacity of the samples obtained would clarify the association of etching conditions and the enlargement of the surface area of an aluminum electrode.

Acknowledgements

Parts of this work were financially supported by a Grant-in-Aid for Scientific Research from the Japan Society for the Promotion of Science and the Light Metal Education Foundation of Japan. Thanks are also due to the "High-Tech Research Center" Project for Private Universities: matching fund subsidy from the Ministry of Education, Culture, Sports, Science and Technology.

References

[1] C.G. Dunn, R.B. Bolon, A.S. Alwan, A.W. Stirling, J. Electrochem. Soc. 118 (1971) 381.
[2] R.S. Alwitt, H. Uchi, T.R. Beck, R.C. Alkire, J. Electrochem. Soc. 131 (1984) 13.
[3] K. Hebert, R. Alkire, J. Electrochem. Soc. 135 (1988) 2146.
[4] K. Arai, T. Suzuki, T. Atsumi, J. Electrochem. Soc. 132 (1985) 1667.
[5] W. Lin, G.C. Tu, C.F. Lin, Y.M. Peng, Corros. Sci. 38 (1996) 889.
[6] H. Masuda, M. Tajima, K. Nishio, Chem. Lett. 31 (2002) 1150.
[7] N.D. Denkov, O.D. Velev, P.A. Kraichevsky, I.B. Ivanov, H. Yoshimura, K. Nagayama, Nature 361 (1993) 26.
[8] Y. Xia, B. Gates, Y. Yin, Y. Lu, Adv. Mater. 12 (2000) 693.
[9] B. Gates, S.H. Park, Y. Xia, Adv. Mater. 12 (2000) 653.
[10] H.W. Deckman, J.H. Dunsmuir, Appl. Phys. Lett. 41 (1982) 377.

— Article —

結晶性アノード酸化アルミナ皮膜の誘電特性に対する電解液種の影響

奥平 浩平, 阿相 英孝, 小野 幸子*

*工学院大学工学部応用化学科（〒163-8677 東京都新宿区西新宿1-24-2）

Effect of Electrolyte Species on Dielectric Property of Crystalline Anodic Alumina Film

Kohei OKUDAIRA, Hidetaka ASOH, and Sachiko ONO*

Department of Applied Chemistry, Faculty of Engineering, Kogakuin University (1-24-2, Nishi-Shinjuku, Shinjuku-ku, Tokyo 163-8677, Japan)

Received June 7, 2007 ; Accepted September 10, 2007

Dielectric properties of crystalline anodic barrier films formed on aluminum by multiple step anodizing were evaluated with focusing on the effects of each processing stage and electrolytes species. An aluminum sheet was first immersed in a boiling water to form a hydrated oxide and subsequently anodized up to 350 V in a mixture of boric acid - sodium borate solution or ammonium adipate solution. After the first anodizing, the leakage current of the film formed in borate was much higher than that of the film formed in adipate. After the subsequent heating in air at 500℃, the leakage current of the film formed in borate showed few change although that of adipate remarkably increased. These results suggest that the degree of crystallization accompanied by defects formation after the first anodizing of the film formed in adipate is lower than that in borate. The leakage current after the second anodizing of both films in the borate was effectively suppressed; however, it is still high in the film formed in borate. TEM observation indicated that the film formed in adipate was thinner than the other; despite their same withstand voltage, suggesting higher permittivity of the film formed in adipate. In accordance to that, the capacitance of the film formed in adipate was higher than that of borate. These differences in dielectric properties between the films would be attributed to the difference in anion incorporation depth into the films, particularly incorporation depth of borate.

Key Words : Aluminum, Anodic Oxide Film, Dielectric Property, Anion Incorporation, Leakage Current

1 緒 言

アルミニウムをホウ酸塩，有機酸塩などの中性溶液中でアノード酸化すると，孔のないバリヤー型のアノード酸化アルミナ皮膜が生成する．形成される皮膜は生成電圧に比例して成長し，高い耐電圧を付与できることから，電解コンデンサの誘電体皮膜として工業的に利用されてきた．近年，大型産業用インバータを始め，ハイブリッドカー，燃料電池自動車などのインバータ回路でアルミニウム電解コンデンサの需要が高まり，さらなる高電圧化・長寿命化が要求されている．アルミニウムのバリヤー型アノード酸化皮膜の厚さは生成電圧にほぼ比例し，単位電圧当りの厚さ（Anodizing ratio）は1.4～1.6 nm V^{-1}程度である[1]．静電容量は皮膜の誘電率と表面積に比例し膜厚に反比例するから，求められる耐圧で静電容量をより増加させるためには，誘電率の向上と基板面積の増大が重要である．後者の目的のためには，アルミニウム基板に電解エッチングを施し，基板の表面積を拡大する手法で大容量を得てきた[2,3]．誘電特性の向上のためには，アノード酸化の前処理として水和処理や熱処理を行い，γアルミナから成る結晶性のバリヤー型皮膜を形成させることで，より高い誘電率，耐電圧を得る手法が用いられている[4-9]．

著者らの研究グループは，既報において，皮膜の厚さや誘電特性に電流密度が大きく影響すること，その原因に電解質アニオンの封入が挙げられることを報告した[1,10]．また，5～20 Vの低電圧領域で作製した薄い誘電体皮膜を対象とし，皮膜作製時の電流密度と皮膜厚さの関係[11]，生成電圧と皮膜厚さの関係，低電圧ほどAnodizing ratioが高くなり，Al^{3+}の輸率は低電圧ほど減少し皮膜構造が異なることなど，高電圧領域で作製した皮膜と低電圧領域で作製した皮膜の性質の違いについて検討してきた[12]．

中高圧用の電解コンデンサ誘電体皮膜の製造工程は，先に述べたようにアルミニウム基板の水和処理，アノード酸化，加熱処理など特性向上のために多段階で行われている．また電解液としては一般に高電圧を保持できるホウ酸塩溶液が多用されるが，誘電体皮膜生成時の各処理工程や皮膜に封入される電解質アニオンが皮膜の誘電特性，構造に与える影響に関しては不明な点が多い．そこで，本研究では，種々の処理工程が皮膜の構造と誘電特性に及ぼす影響を検討すると共に，ホウ酸塩電解液と有機酸塩電解液であるアジピン酸塩電解液

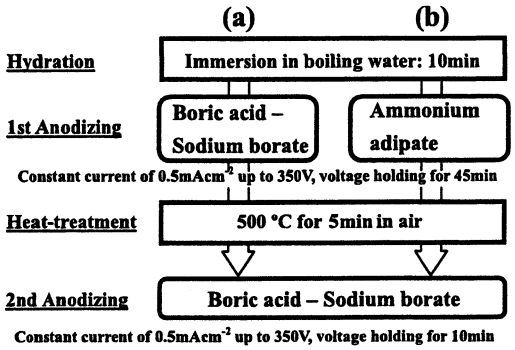

Fig. 1 Formation procedure of crystalline anodic films using two types of electrolytes for the first anodizing. (a) 1.6 mol dm^{-3} Boric acid –0.008 mol dm^{-3} Sodium borate (b) 0.01 mol dm^{-3} Ammonium adipate.

を用いた場合のそれぞれの誘電特性を比較することで，電解液成分である電解質アニオンが皮膜の結晶化や静電容量に及ぼす影響を明らかにすることを目的とした．

2 実験方法

試料には99.99％アルミニウム板（面積10 cm^2）を用い，前処理として5 wt％NaOH溶液（85℃）中に20秒浸漬した後，30 vol％HNO_3に60秒浸漬するアルカリ脱脂処理を行い，イオン交換水で十分に洗浄し冷風乾燥したものを実験に供した．

Fig. 1に試料作製フローチャートを示す．アルミニウム基板を沸騰蒸留水中に10分間浸漬し，1.6 mol dm^{-3}ホウ酸–0.008 mol dm^{-3}ホウ酸ナトリウム，または0.01 mol dm^{-3}アジピン酸アンモニウム電解液を用い，85℃，0.5 mA cm^{-2}で定電流電解し，350 Vに到達後，45分間の定電圧保持電解を行った．その後，大気中500℃で5分間の熱処理を行い，再度，1.6 mol dm^{-3}ホウ酸 –0.008 mol dm^{-3}ホウ酸ナトリウム電解液中で同条件での定電流電解を行い，350 V到達後，10分間の定電圧保持電解を行った．

生成した皮膜の漏れ電流を評価する為に，0.5 mol dm^{-3}ホウ酸 –0.05 mol dm^{-3}ホウ酸ナトリウム（20℃）中で，生成電圧の75％（262 V）を印加する定電圧印加法（一般に15分後の電流を漏れ電流とする），及び，電圧を1 V s^{-1}で掃引した際の電流の変化を測定する電圧掃引法を用いた．耐圧評価としては，0.1 mA cm^{-2}の微小電流で試料を再アノード酸化する定電流印加法を用いた[13]．アノード酸化によりあらかじめ生成された皮膜が抵抗となるため，電圧は皮膜厚さに応じて急激にジャンプする．その後，0.1 mA cm^{-2}で素地をアノード酸化した時と同じ電圧上昇勾配（生成速度）で皮膜は成長する．電圧－時間（V-t）曲線の電圧ジャンプ後の直線部分を時間ゼロに外挿し，その電圧値を耐圧Vjとした．なお，漏れ電流や耐圧測定の際に，測定液に試料を浸漬保持することによって皮膜中に生じているボイド状の欠陥に液が浸透し，孤立ボイドが開封され連結することで漏れ電流が増加することが予想された．しかし実際には浸漬時間60分程度までの漏れ電流や耐圧の変化が今回の2種の電解液による違いを明らかにするための測定結果に与える影響は少なかったため，浸漬直後に測定したデータを採用した．また測定はいずれも5回以上行い，平均的データを求めた．

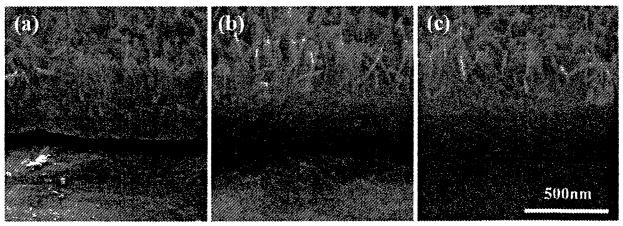

Fig. 2 SEM images of fracture section of aluminum specimens (a) after hydration, (b) after first anodizing in boric acid -sodium borate and (c) after second anodizing in boric acid -sodium borate.

生成した皮膜の静電容量はLCRメーター（HIOKI, 3511-50）を用い，150 g l^{-1}アジピン酸アンモニウム溶液中，周波数120 Hzで測定を行った．対極には大面積の白金板を用いた．皮膜の比誘電率は（1）式から求めた．ここで，C：容量，ε_r：比誘電率，S：電極面積，d：皮膜厚さ，8.855×10^{-8}：真空の誘電率，である．

$$C = 8.855 \times 10^{-8} \frac{\varepsilon_r S}{d} \qquad (1)$$

皮膜の結晶性評価は薄膜X線回折（TFXRD, MXP-18AHF22）を用い，X線入射角度0.3°で測定を行った．皮膜に含まれる深さ方向の元素分布はグロー放電発光分光分析装置（GDOES, Jobin-Yvon JY7500RF）を用いて測定した．皮膜構造の観察は，電界放射走査型電子顕微鏡（FESEM, HITACHI S-4200型）を用いた．また，二次化成後の皮膜についてはFIBにより断面サンプリングを行い，走査透過電子顕微鏡（STEM, JEOL JEM2100F）を用いて検討した．

3 結果および考察

3．1 SEMによる皮膜構造観察

Fig. 2に，(a) アルミニウムを沸騰水浸漬した水和処理後，(b) ホウ酸－ホウ酸ナトリウムでの一次化成後，(c) 二次化成後，のそれぞれの皮膜破断面のSEM像を示す．水和処理後に生成する水和酸化物は，外層に薄片状の酸化物層：約300 nm，内層に緻密な酸化物層：約200 nmを持つ構造であった．内層は粒状構造で結晶性を持つと考えられる．一次化成後には，水和酸化物の外層の薄片層はそのまま残り，内層の緻密な層は約370～400 nmに厚く成長した．水和酸化物存在下の皮膜生成過程においては，高電場による水和酸化物の脱水による相転移によってγ-Al_2O_3（またはγ'-Al_2O_3）が生じ，また，電解液温度が85℃以上の場合，皮膜は全て結晶化することが知られている[4]．しかし，(b)，(c) に示すように，SEM観察から一次化成後，二次化成後の構造上の変化を見出すことは困難だった．同様に，一次化成にアジピン酸アンモニウムを用いた皮膜および熱処理後の皮膜においても，SEM観察による皮膜構造の差異は明らかでなかった．

3．2 定電圧印加法および電圧掃引法による漏れ電流評価

Fig. 3 (a) にホウ酸－ホウ酸ナトリウム，(b) にアジピン酸アンモニウムの一次化成，熱処理，二次化成の各処理工程

後に対して定電圧印加法を用い漏れ電流測定を行った結果を示す．ホウ酸－ホウ酸ナトリウムの場合は，一次化成後と熱処理後の漏れ電流値は，ほぼ同じであった．これに対し，アジピン酸アンモニウムは一次化成後の漏れ電流値はホウ酸塩より低い値をとるが，熱処理をする事でホウ酸－ホウ酸ナトリウムの一次化成，および熱処理後と同程度の電流値に増加した．熱処理は酸化皮膜の脱水や結晶化を促進するが，結晶化に伴う体積収縮によるボイド・クラック生成を促して欠陥量が増加すると考えられる．さらに二次化成を行うことで欠陥が修復され，両電解液共に漏れ電流値は最も低い値となった．このように，一次化成後の皮膜の漏れ電流が異なることから，両者の結晶性に違いがあることが推察される．ホウ酸－ホウ酸ナトリウムの一次化成では，欠陥生成を伴う結晶化がアジピン酸アンモニウムよりも進行していると考えられる．両電解液共に，二次化成後，漏れ電流値は低下するが，ホウ酸－ホウ酸ナトリウムにおいて，欠陥の存在に起因する電流上昇がしばしば見られるのに対して，アジピン酸アンモニウムには見られなかった．このことから，一次化成時にアジピン酸アンモニウムを用いることで，欠陥がより少ない皮膜が生成されると推定される．

Fig. 4 (a) にホウ酸－ホウ酸ナトリウム，(b) にアジピン酸アンモニウムの一次化成，熱処理，二次化成の各処理工程後に対して電圧掃引法を用い漏れ電流測定を行った結果を示す．ホウ酸－ホウ酸ナトリウムの一次化成後の漏れ電流は，150 V付近から急激に上昇する挙動が見られる．ホウ酸－ホウ酸ナトリウムの熱処理後は，電圧印加直後から電流値が高い値を示し，一次化成と同様に150 V付近からさらに電流上昇が見られた．二次化成を行うと，定電圧印加法と同様に，漏れ電流値は最も低い値となった．アジピン酸アンモニウムの場合は，一次化成時の漏れ電流が最も低くなり，熱処理後はホウ酸－ホウ酸ナトリウム同様，電圧印加直後の電流値がかなり高い値を示した．二次化成を行うと，一次化成に近い電流値に漏れ電流が抑えられた．

電圧掃引に伴う電流上昇の挙動が皮膜の欠陥量に関連すると考えると，両電解液共に熱処理後は欠陥が大きく増加している．ホウ酸－ホウ酸ナトリウムでは，一次化成後も熱処理後も低い電圧領域から電流上昇が見られ，アジピン酸アンモニウムより耐圧が低く，皮膜中の欠陥が多いことがわかる．これらの漏れ電流測定結果から，電圧掃引法は定電圧印加法と比較し，より詳細に皮膜の耐圧や欠陥量を推定することが

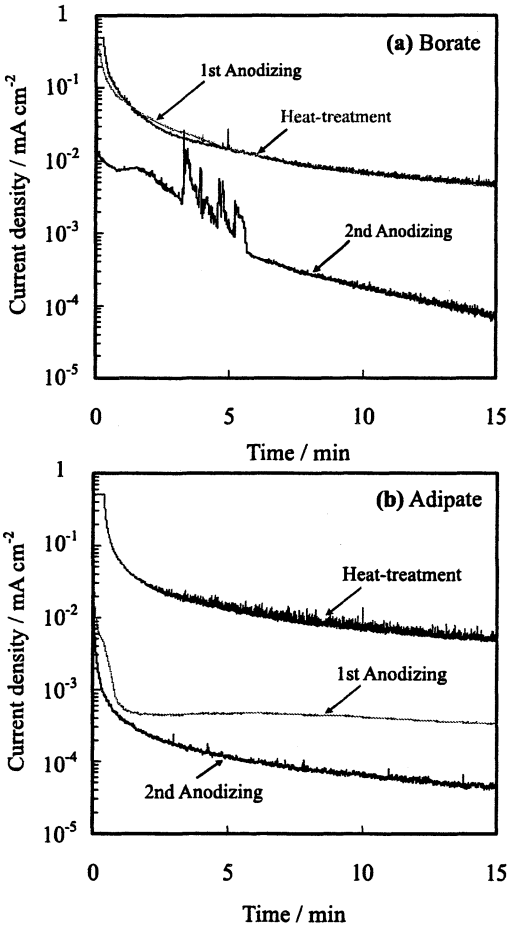

Fig. 3 Leakage current measurement by applying 75% of the formation voltage, *i.e.*, 262 V, to the anodic film obtained after each processing stage. The first anodizing was performed in (a) boric acid-sodium borate and (b) ammonium adipate.

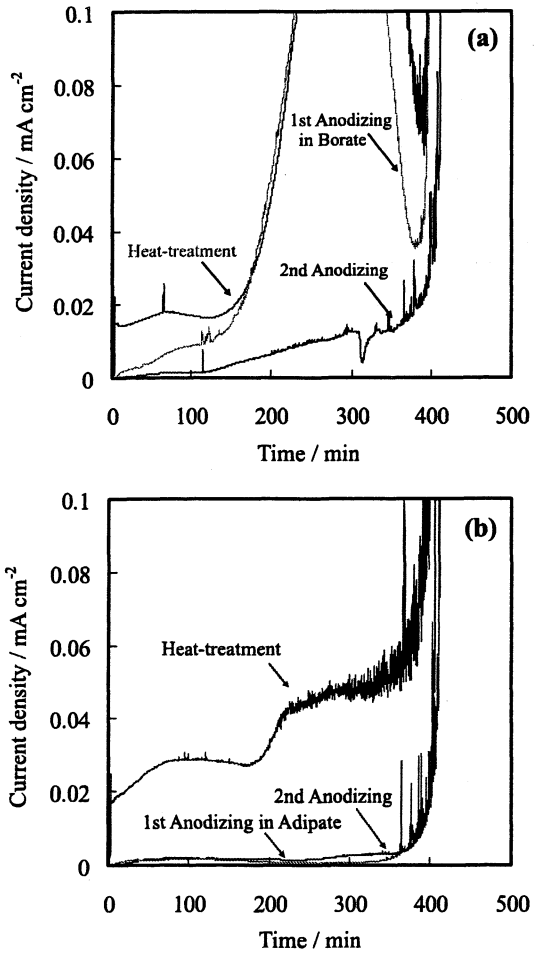

Fig. 4 Leakage current measurement by voltage sweep method applying to the anodic film obtained after each processing stage. The first anodizing was performed in (a) boric acid-sodium borate and (b) ammonium adipate.

可能であると考えられる．

3．3　再アノード酸化法による耐圧測定

Fig. 5 (a) にホウ酸－ホウ酸ナトリウム，(b) にアジピン酸アンモニウムの一次化成，熱処理，二次化成の各処理工程後に対して0.1 mA cm^{-2}で再アノード酸化したときのV-t曲線を示す．ホウ酸－ホウ酸ナトリウムの一次化成後は，200 Vまで急激に電圧が立ち上がるが，それ以降，電圧上昇速度は著しく低下する．熱処理後は，初期電圧から緩やかに立ち上がり，一次化成同様，200 V付近から電圧上昇速度は低下した．二次化成を行うことで，380 V付近まで急激に電圧が立ち上がった．このような電圧の立ち上がりの遅れは皮膜中の欠陥修復のためと考えられる[14]．一方，アジピン酸アンモニウムでは，一次化成後は370 V付近まで急激に電圧が立ち上がるが，熱処理後，ホウ酸－ホウ酸ナトリウムと同様に，電圧上昇に遅れが現れた．しかし二次化成後は，ホウ酸－ホウ酸ナトリウム同様，380 V付近まで急激に電圧が立ち上がる挙動を示した．この電圧上昇挙動は，皮膜の欠陥量に関連していると考えられ，先に述べた電圧掃引法の電流挙動で示された結果と類似している．すなわち，両者の一次化成後の比較から，ホウ酸－ホウ酸ナトリウムの場合はアジピン酸アンモニウムの場合より欠陥の多い皮膜が生成され，熱処理後には耐圧が失われて0 Vから電流が立ち上がるが，200 V付近で電圧上昇速度が低下する傾向もアジピン酸アンモニウムの場合より顕著であり，欠陥量の多さを示唆している．最終的に両電解液の二次化成後の耐圧は，ホウ酸－ホウ酸ナトリウムは384 V，アジピン酸アンモニウムは382 Vとほぼ同等の値を示した．定電圧印加，電圧掃引，定電流印加の3種類の酸化皮膜に対する特性評価法を比較すると，定電圧印加法は漏れ電流値という数値としての評価が可能な利点を持つが，後者の2手法においてはより詳細な皮膜の構造と対応した特性評価が可能であった．

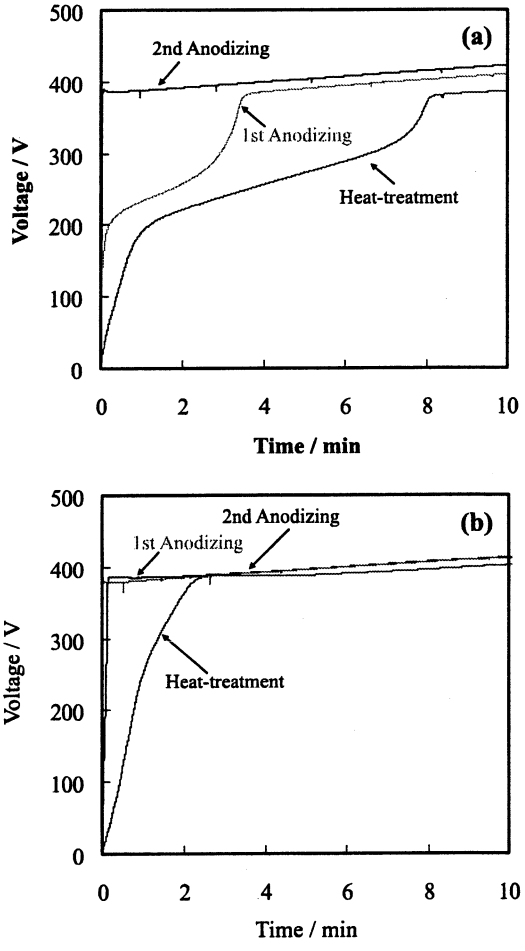

Fig. 5 Change in voltage-time curves obtained at re-anodizing of anodic film after each processing stage. The first anodizing was performed in (a) boric acid-sodium borate and (b) ammonium adipate.

3．4　TEMによる二次化成後の皮膜断面観察

Fig. 6に，(a) ホウ酸－ホウ酸ナトリウム，(b) アジピン酸アンモニウムで一次化成を行い，二次化成まで行った皮膜をFIBにより断面試料を作製し観察したTEM像を示す．皮膜は外層部の薄片状の水和酸化物層と，内層部の緻密な結晶性酸化物の2層から成る．また，暗いコントラストを示す結晶性酸化物の大きさから，内層の上部側は結晶粒径が小さく，内層の素地側は結晶粒径が大きいことが確認できる．これは，アノード酸化皮膜の生成時に，Al^{3+}イオンの溶液側への移動により酸化物が成長する際に，図1 (a) のSEM像の内層に見られた水和酸化物の緻密な層が脱水により結晶性酸化物に相転移することで結晶粒径の小さい層を形成し，一方，O^{2-}イオンの移動により皮膜/素地界面で生成した無定形皮膜が水和酸化物の脱水によって生じたγ-Al_2O_3を核に相転移することで，結晶粒径の大きい層になっていると考えられる[6]．両皮膜の結晶性やボイド（欠陥）量の違いは明らかでないが，皮膜厚さはホウ酸－ホウ酸ナトリウムが375 nm，アジピン酸アンモニウムが350 nmであり，アジピン酸アンモニウムの方が約6.8％薄いことがわかった．

3．5　XRDによる各処理工程後の結晶性評価

Fig. 7 (a) にホウ酸－ホウ酸ナトリウム，(b) にアジピン酸アンモニウムの一次化成，熱処理，二次化成の各処理工程後におけるXRDスペクトルを示す．低角度側21，27°のピークは擬似ベーマイト（Al_2O_3-xH_2O）のピークであり，46，67°のピークはγ-Al_2O_3である．両電解液共に一次化成後は水

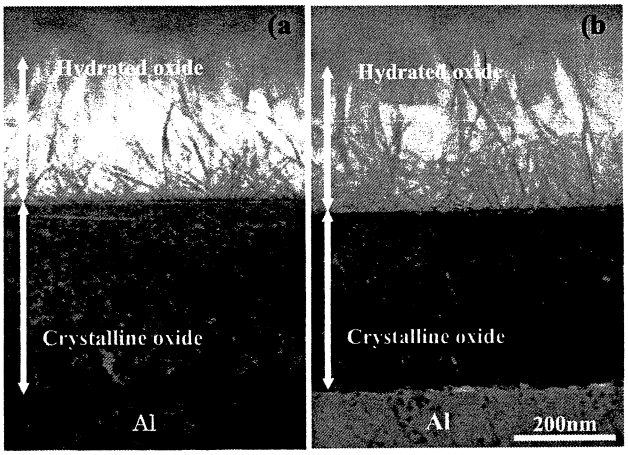

Fig. 6 TEM images of cross section prepared by FIB after 2nd anodizing. The first anodizing was performed in (a) boric acid-sodium borate and (b) ammonium adipate.

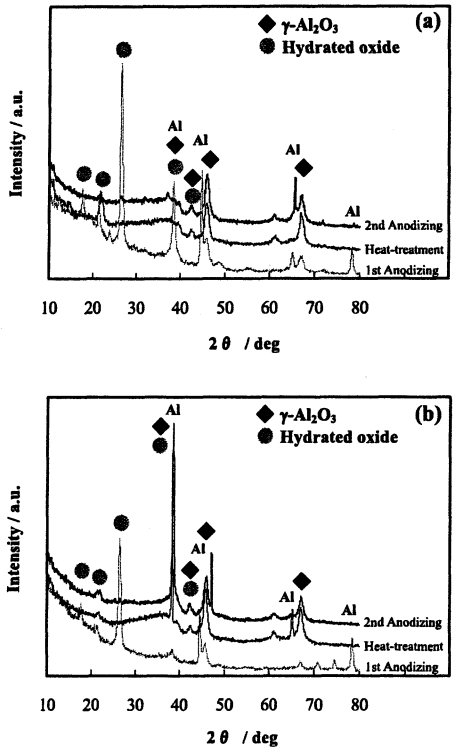

Fig. 7 X-ray diffraction spectra of the anodic films obtained at each processing stage. The first anodizing was performed in (a) boric acid-sodium borate and (b) ammonium adipate.

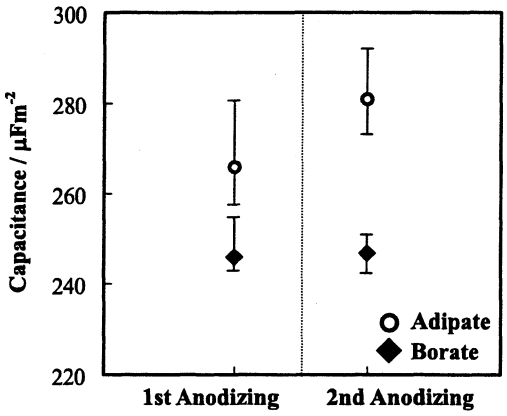

Fig. 8 Comparison of capacitance of the anodic films obtained after the first anodizing and second anodizing. The first anodizing was performed in (◆) boric acid-sodium borate and (○) ammonium adipate.

和酸化物の強度が高いのに対して，γ-Al_2O_3の強度は低い．熱処理後にはγ-Al_2O_3の強度が高くなり，水和酸化物のピークが低くなっていることから，皮膜の結晶化が顕著に進行していることがわかる．また，二次化成後のγ-Al_2O_3の強度は熱処理後からさほど変化しておらず，二次化成による結晶化の進行は低いことがわかる．一次化成後のγ-Al_2O_3のピーク強度を両皮膜で比較すると，ホウ酸－ホウ酸ナトリウムの方が高い値を示し，アジピン酸アンモニウムを用いることで一次化成でのγ-Al_2O_3への結晶化が抑制されたと考えられる．

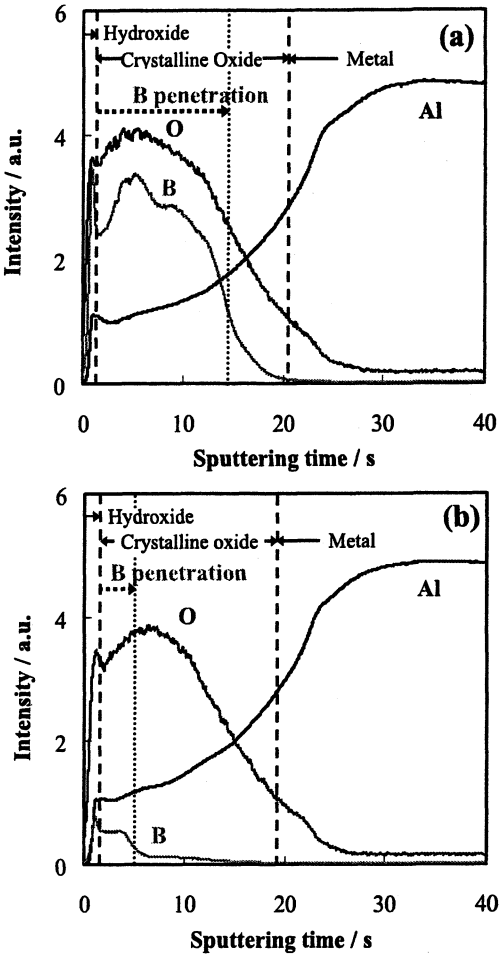

Fig. 9 GDOES depth profiles of Al, B and O in the anodic films formed after 2nd anodizing. Dotted arrows indicate boron penetration depth in the films. The first anodizing was performed in (a) boric acid-sodium borate and (b) ammonium adipate.

しかし，二次化成後における両皮膜の結晶性の違いは明瞭でない．

3．6　一次化成，二次化成後の静電容量測定と誘電特性のまとめ

Fig. 8にホウ酸－ホウ酸ナトリウム，アジピン酸アンモニウムの一次化成および二次化成後の静電容量を示す．両者の静電容量は，一次化成，二次化成後共に，アジピン酸アンモニウムの方が高い値を示した．また，アジピン酸アンモニウムは二次化成後の静電容量が一次化成後よりも若干上昇しているのに対して，ホウ酸－ホウ酸ナトリウムは，ほぼ一定である．二次化成後の静電容量は，アジピン酸アンモニウムが14.3％高い値を示した．XRDによって評価した結晶性は，少なくとも一次化成後はホウ酸－ホウ酸ナトリウムの方が高いにも関わらず，静電容量はアジピン酸アンモニウムの場合が高い．このことは，静電容量が皮膜の結晶性のみでなく，皮膜中に封入される電解質アニオンにも依存することを示唆している．

Table 1にホウ酸－ホウ酸ナトリウムおよびアジピン酸アンモニウムを一次化成に用いた，二次化成後の皮膜の静電容量，再アノード酸化法により測定した耐電圧，CV積（容

Table 1 Dielectric properties of the anodic films formed after second anodizing. The first anodizing was performed in boric acid-sodium borate or ammonium adipate. Capacitance: *C* Withstand voltage: *Vj* Film thickness: d Relative permittivity: ε_r

First anodizing	$C/\mu Fm^{-2}$	*Vj*/V	$CV/mFVm^{-2}$	d/nm	ε_r	Anodizing ratio/nmV^{-1}
Borate	245	384	94.1	375	10.4	1.07
Adipate	280	382	107	350	11.1	1.00

量×耐圧)，皮膜厚さ，比誘電率，Anodizing ratioをまとめて示す．静電容量が高く，皮膜が薄いアジピン酸アンモニウムの誘電率はホウ酸－ホウ酸ナトリウムよりも約7.8%高い値を示した．皮膜の結晶性のみではこの結果は説明できず，一次化成で形成される皮膜に封入される電解質アニオンの違いが影響している可能性が考えられる．

3．7 二次化成後の皮膜のGD-OESによる深さ方向の元素分析

皮膜の静電容量に影響すると考えられる皮膜中の元素分布を解析した結果をFig. 9に示す．(a) ホウ酸－ホウ酸ナトリウムと (b) アジピン酸アンモニウムの二次化成後の皮膜に対し，GD-OESによる深さ方向の元素分布測定を行った結果である．生成した皮膜の構造は，上部に薄片状の水和酸化物層，内部に緻密な結晶性酸化物層を持つ．皮膜に含まれる電解質アニオンとして検出される元素は，ホウ酸－ホウ酸ナトリウムの場合はホウ素，アジピン酸アンモニウムでは炭素であるが，炭素のGDOESによる分布解析は困難であるため，二次化成時の電解液に用いたホウ酸の混入深さに注目して検討した．ホウ酸－ホウ酸ナトリウムの場合，ホウ素は表層側から皮膜の約70%深さまで混入していた．次に，アジピン酸アンモニウムの場合は，ホウ素が皮膜表層側から皮膜の約18%深さまで含まれていた．また，発光強度からもホウ素混入量がホウ酸－ホウ酸ナトリウムの方が多いことがわかる．一次化成を異なる電解液で作製した皮膜は，二次化成後に結晶性に大きな差異が無く，含まれるホウ素の混入深さと混入量が大きく異なることから，Table 1に示した両皮膜の誘電特性の違いは主としてホウ素量に起因すると考えられる．

以上の実験結果から，アノード酸化皮膜中にホウ素が多く含有される場合，誘電率の低下と膜厚の増加がもたらされることが強く示唆された．

4 結 論

多段電解で生成する結晶性アノード酸化皮膜の誘電特性に対して一次化成に用いる2種の電解液が及ぼす影響について検討した結果，以下の結論を得た．

1) 一次化成後の皮膜の結晶性はアジピン酸アンモニウムを用いた場合よりホウ酸－ホウ酸ナトリウムを用いた場合が高く，欠陥生成による漏れ電流も高い．結晶性は両皮膜とも熱処理で顕著に進行し，漏れ電流が増加するが，二次化成後は漏れ電流も低下し両皮膜に大きな結晶性の違いは見出だせない．
2) 一次化成にアジピン酸アンモニウムを用いた場合，ホウ酸－ホウ酸ナトリウムを用いた場合より二次化成後の皮膜の静電容量が高く，漏れ電流は低い．また耐圧は同一であるが皮膜の誘電率は高く，膜厚は薄い．
3) 二次化成後の皮膜中に分布するホウ素は両皮膜で大きく異なり，ホウ酸－ホウ酸ナトリウムでは皮膜の70%深さまで，アジピン酸アンモニウムでは20%以下である．これから，ホウ素が皮膜の誘電率を低下させる主な要因であると推定される．
4) 定電圧印加，電圧掃引，定電流印加の3種類の酸化皮膜に対する特性評価法を比較すると，定電圧印加法は漏れ電流という数値としての評価が可能な利点を持つが，後の2手法においてより詳細な皮膜の欠陥量などの構造評価が可能である．

文 献

1) S. Ono, F. Mizutani, M. Ue, and N. Masuko, The ECS Meeting, Corrosion and Corrosion Protection, Proceeding of the International Symposium, The Electrochemical Society, Inc. PV**2001-22**, 1129 (2001).
2) R. S. Alwitt, H. Uchi, T. R. Beck, and R. C. Alkire, *J. Electrochem. Soc.*, **131**, 13 (1984).
3) H. Uchi, T. Kanno, and R. S. Alwitt, *J. Electrochem. Soc.*, **148**, B17 (2001).
4) R. S. Alwitt, *J. Electrochem. Soc.*, **114**, 843 (1967).
5) K. Shimizu, K. Kobayashi, and H. Nishibe, *J. Jpn. Inst. Light Metals*, **35**, 553 (1985)[in Japanese].
6) H. Takahashi, Y. Umehara, T. Miyamoto, N. Fujimoto, and M. Nagayama, *J. Surf. Finish. Soc. Jpn.*, **38**, 67 (1987) [in Japanese].
7) R. S. Alwitt, *J. Surf. Finish. Soc. Jpn.*, **32**, 226 (1981) [in Japanese].
8) C. Crevecoeur and H. J. de Wit, *J. Electrochem. Soc.*, **134**, 808 (1987).
9) N. Osawa and A. Hibino, *Sumitomo Light Metal Technical Reports*, **45**, 73 (2004) [in Japanese].
10) S. Ono, T. Osaka, and N. Masuko, *Denki Kagaku (Electrochemistry)*, **64**, 819 (1996) [in Japanese].
11) C. Wada, H. Asoh, and S. Ono, *Electrochemistry*, **73**, 145 (2005) [in Japanese].
12) S. Ono, C. Wada, and H. Asoh, *Electrochim. Acta*, **50**, 5103 (2005).
13) H. Takahashi and M. Nagayama, *Corrosion Sci.*, **18**, 911 (1978).
14) S. Ono and N. Masuko, *J. Jpn. Inst. Light Metals.*, **43**, 447 (1993) [in Japanese].

[事例・トピックス]

タンタル代替ニオブコンデンサ誘電体皮膜の成長挙動と特性

工学院大学　小野 幸子*1　阿相 英孝*2

電子機器の小型高密度化への要求がますます高まる中、現在、電解コンデンサの誘電体としてTa_2O_5皮膜が広く利用されている。しかし、希少金属であるタンタルは価格も不安定で、その代替研究が推進される状況にある。ニオブはタンタルと性質が類似し埋蔵量はタンタルの10倍以上と見込まれているため、タンタル代替素材として注目されている。本稿では、ニオブアノード酸化皮膜の構造と特性高度化に関する筆者らの研究を述べる。

はじめに

アルミニウムやタンタルなど、バルブ金属の緻密なアノード酸化皮膜を誘電体として利用した電解コンデンサは、比較的安価に種々の用途に適応した特性を提供することが可能なため、古くから実用化が進んだ。昨今、電子機器の小型高密度化への要求が高まり、コンデンサ用誘電体酸化膜の特性改善は重要な課題で、誘電特性の制御因子の解明が待たれている。中でも、タンタル電解コンデンサの誘電体として、ペレット状に成形した焼結粉末のアノード酸化により成長するTa_2O_5皮膜が、小型コンデンサに広く利用されてきた。

しかしながら、タンタルの資源と供給は十分でなく、価格の安定性にも不安があり、希少な金属であるレアメタルの代替研究が、政府の科学技術政策における元素戦略の対象として推進される状況となった。

タンタルと周期表の同族で性質が類似したニオブは、地殻中の埋蔵量がタンタルの10倍以上と見込まれて安価であり、タンタルコンデンサ代替の新たなコンデンサ素材として注目されている。筆者らはAl、Nb、Taなどの酸化皮膜の生成条件が幾何学的形態や組成、結晶性などの構造に及ぼす影響と、それらの構造と誘電特性の関係について基礎的な立場から検討を進めてきた。まだ特性制御因子の完全な理解には至っていないが、本稿では、ニオブアノード酸化皮膜の構造と特性の高度化に関する筆者らの最近の研究を中心に解説する。

*1おの　さちこ：工学部 応用化学科　教授
*2あそう　ひでたか：同科　講師
〒163-8677　東京都新宿区西新宿1-24-2
03-3340-2732

皮膜厚さ、アニオン封入量、誘電特性の電解条件による変化[1)-3)]

AlとTa、Nbなどのアノード酸化皮膜の化学的および誘電的特性は、当然ながらかなり異なる。例えば、比誘電率はそれぞれ約10、23、40であり、ニオブ酸化物が顕著に高いことが分かる。単位生成電圧あたりの厚さ(Anodizing ratio、電場強度の逆数)はそれぞれ1.5nm、1.6nm、2.5nm、絶縁破壊電圧は(電解液により多少異なるが)約500V、300V、250V程度である。しかし、電流密度、電解液温度、電圧保持などの電解条件が、皮膜厚さや封入される電解質アニオン量と分布などの皮膜の形態や、組成、誘電特性に対して及ぼす影響は金属種が異なってもその傾向は同一である。

酸化皮膜の厚さは静電容量に直接影響するため重要である。すなわち、静電容量は誘電体面積と誘電率に比例し、膜厚に反比例する。

図1にリン酸中で60Vで皮膜を生成し、微小電流で再アノード酸化したときのジャンプ電圧(V_j、耐圧)から電気化学的に評価した、膜厚の電圧依

存性と電流密度依存性を示す。電圧に比例して膜厚は変化するが、所定の電圧で定電圧保持し電流を減衰した皮膜はさらに成長し、保持時間が長いほど膜厚は厚くなる。透過電子顕微鏡で観察した結果、膜厚は139nmでAnodizing ratioとして2.3(nm/V)、60Vのまま20分間電圧を保持し電流減衰した皮膜の厚さは161nm(Anodizing ratio は2.7)であった。

図1の菱形(◇)のプロットで明らかなように、異なる電流密度で一定電圧まで生成した皮膜の厚さは、その電流密度の対数に反比例する。さらに、定電圧保持して電流減衰を行った場合、Vjを電解の最終電流値の対数に対してプロットすると、四角(□)は上記の直線に乗る。つまり、皮膜厚さは皮膜の生成過程によらず、最終電流密度で決まり、電流密度の対数と直線関係を持つことが分かる。アルミニウムのバリヤー型皮膜でも同様な挙動が確かめられている[3]。

図2に、リン酸電解液でNbをアノード酸化した場合の電流密度と温度が諸特性に及ぼす効果をモデル的にまとめて示す。この結果はどのバルブ金属に対しても共通である[1)-3)]。すなわち、電流密度が低いほど、電解液温度は高いほど皮膜は厚く、アニオンの混入量と深さは減少する。皮膜の厚さ、アニオン混入量、侵入深さ、誘電率がいずれも電流の対数に対して直線的に変化することが確かめられたが、これは皮膜構造や成長挙動が電場強度に強く依存していることを示唆する。このことはGüntherschultzeとBetzにより見出され[4]、その後理論的に確立された電流iと電場強度Eの関係$i = A\exp(bE)$[5]からも説明できる。誘電率自体はアニオン混入量が少なく純粋な酸化物に近いほど高いが、電場保持性は逆にアニオン混入量が多いほど高い[3]。コンデンサとしての両特性はともに高いことが望まれるが、皮膜の組成変化により相互に逆な変化を示すのである。

Nb^{5+}とO^{2-}の輸率と皮膜へのアニオン封入

皮膜中には電解質アニオンが封入されるが、その皮膜中での分布と混入量の電

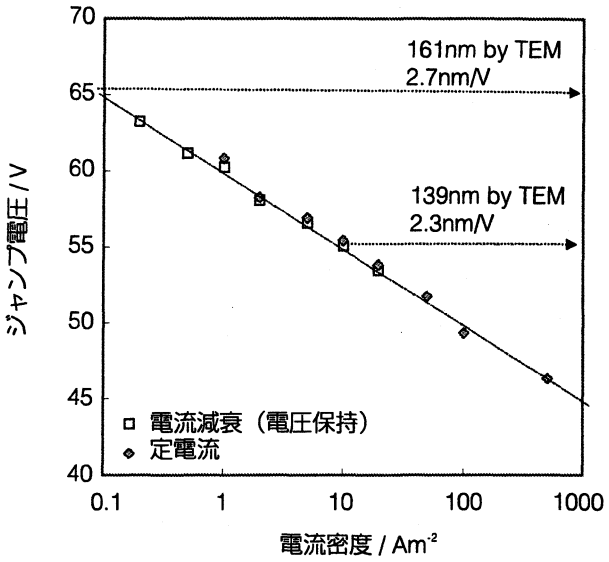

図1　ジャンプ電圧により評価した皮膜厚さと生成電圧の関係(電流減衰：50Am^{-2}で60Vまで定電流電解したあと電圧保持し電流減衰、定電流：60Vまで種々の電流で電解)

解条件依存性は、グロー放電発光分光分析(GD-OES)で測定できる。また、あらかじめNb試料をケイ酸ナトリウム中で5Vまでアノード電解し、封入するSiをマーカーとして使うことにより、ニオブイオンおよび酸化物イオンの輸率を知ることができる。Siはアノード電解時の電場の影響下でも皮膜中を移動しないからである。

リン酸電解液で生成する皮膜について得られた結果を**図3**に示す。リン酸電解液で生成した皮膜へのPの封入は、皮膜厚さの0.46までほぼ一定濃度であり、またSiのピーク位置からNb^{5+}の輸率は約0.26であることが分かる。すなわち、ニオブイオンの移動により皮膜／溶液界面で成長する酸化皮

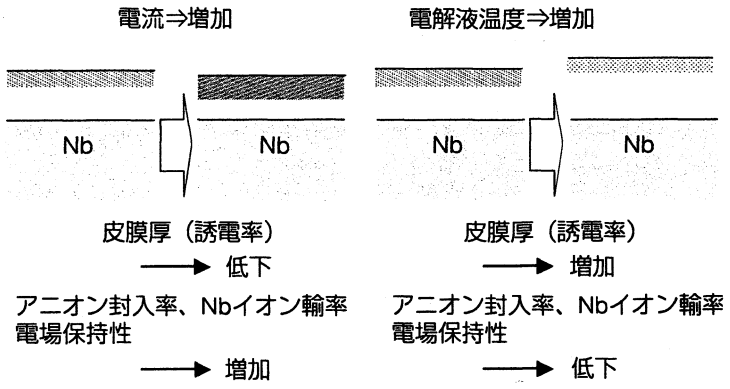

図2　アノード酸化皮膜の厚さ、アニオン混入挙動、誘電特性に及ぼす電流密度と電解液温度の効果

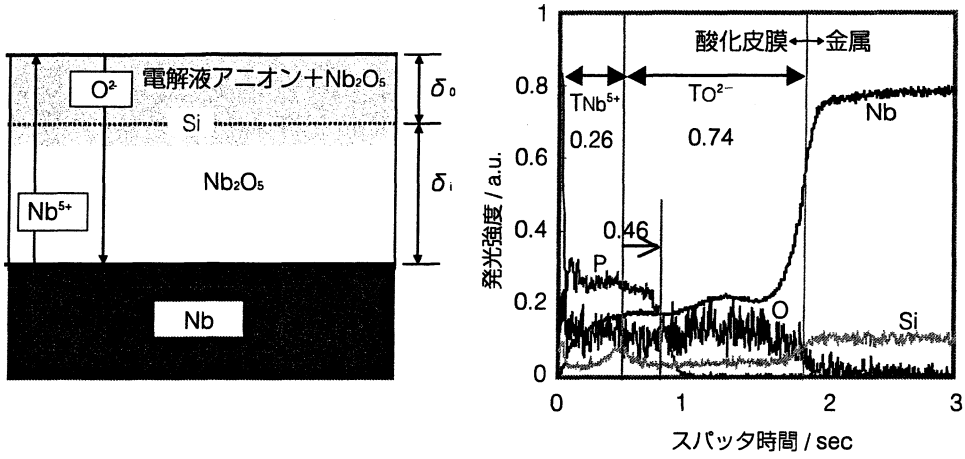

図3 (左)ニオブアノード皮膜の構造とSiをマーカーとしたNb⁵⁺およびO²⁻イオンの輸率の推定モデル図、(右)GD-OESによるニオブアノード酸化皮膜中の深さ方向元素分布とSiをマーカーとしたイオンの輸率の推定(リン酸中で60Vまで電解)

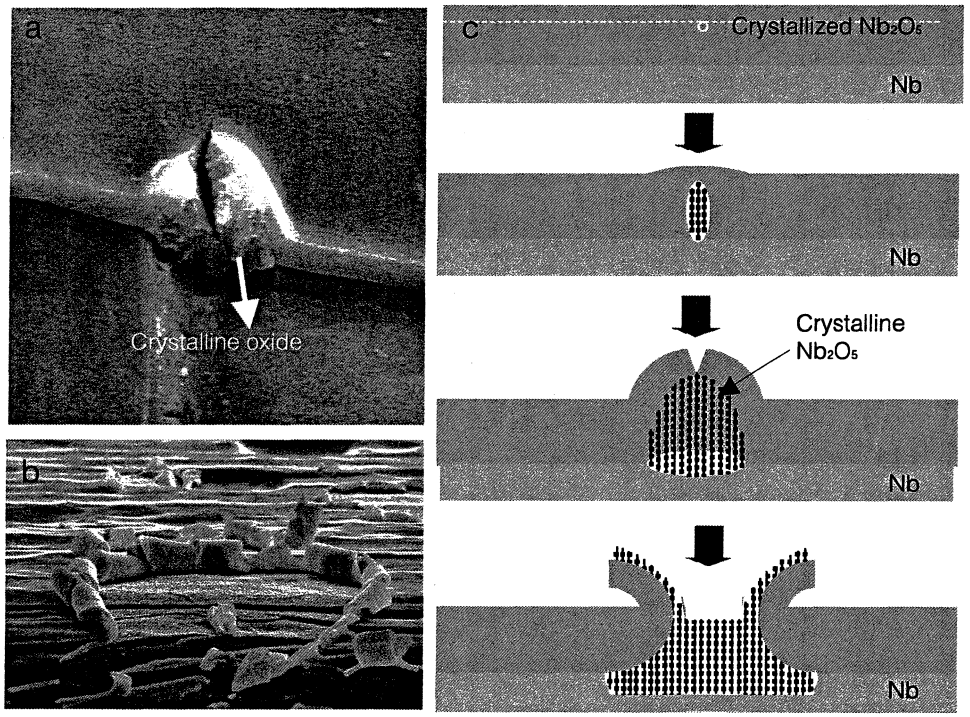

図4 (a)ニオブアノード酸化皮膜に生ずる結晶化を伴う欠陥、(b)結晶化の進行により花びら状に拡大した欠陥、(c)素地に由来した結晶核の発生と欠陥成長モデル図

膜の割合が0.26、酸化物イオンの移動により皮膜/素地界面で成長する割合が0.74である。このNb^{5+}の輸率は電圧を保持して電流減衰させても変わらないが、電解液温度の上昇により直線的に低下し、80℃で1.6となった。皮膜中に封入されたリン(リン酸アニオンにもとづく)は、誘電特性に強く影響するが、その封入量と封入深さは電流密度の対数に直線的に比例して増加する。

化成破壊の原因となる皮膜の欠陥生成とその抑制[6)-8)]

皮膜の内部構造を評価するため、アルカリに浸漬溶解した時の溶解挙動(耐圧の変化)を再アノード酸化法で測定した。皮膜を熱処理すると、加熱温度が高いほど溶解されにくくなる。しかし、皮膜が1/2程度の厚さまで溶解されると不均一な溶解(皮膜中の欠陥)が現れ、その程度は熱処理温度が高いほど顕著であった。すなわち、皮膜の何らかの質的な不均一性が加熱によって顕著になると考えられる。

一般的に皮膜の化成破壊は皮膜の微小部からの結晶化から開始し、結晶の成長に伴って酸化皮膜は花びら状に剥離していく。結晶化が開始する初期段階を皮膜断面から捉えたのが、**図4**(a)に示すSEM像であり、結晶化が皮膜の内部を起点としていることが分かる。すなわち、図4(c)に示す

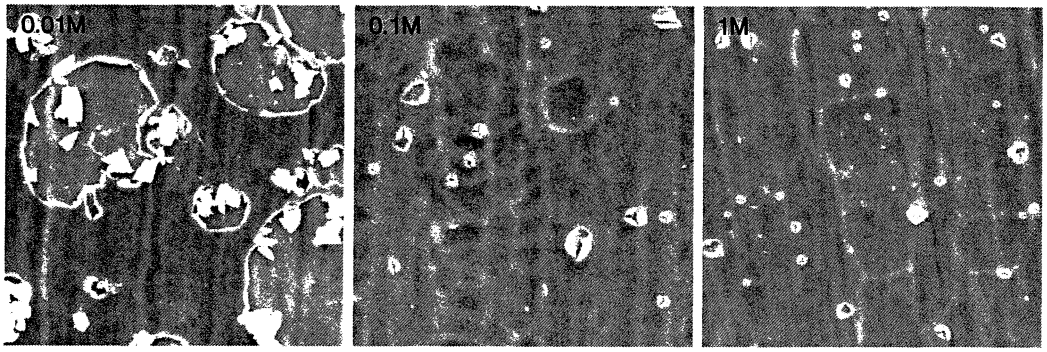

写真
リン酸中で電解した皮膜に生成する欠陥と電解液濃度の関係（電解液が薄いほど欠陥の成長が顕著である）

ように、皮膜生成初期に素地に由来して結晶核が生じ、皮膜の成長と共に急激に増大して皮膜の割れに至り、ついには素地／皮膜界面で連続的に結晶化が進行すると考えられる。図4(b)に示すように、非晶質皮膜と素地界面に結晶性酸化物が成長し、皮膜は花びら状に剥離する。

欠陥生成と結晶化は、**写真**に示すように、電解質アニオンの濃度に強く依存し、高濃度では抑制されることが分かった。そこで、素地に由来する結晶核の生成と成長を抑制するために、電解質アニオンの封入を利用することを試みた。はじめに高濃度のリン酸で10Vまで電解し、その後は結晶化が顕著に生じる0.01モルの低濃度リン酸で電解した結果、1段目の電解液が高濃度ほど、また電流密度が高いほど、結晶の成長が抑制された。いずれもリンの封入量が増加する条件である。このように、電解条件や電解液条件を変えることで化成破壊を抑制することが可能である。

酸化皮膜の静電容量に及ぼす電解液種とpHの影響[9)-11)]

リン酸や有機酸電解液をアルカリ領域にpH調製して生成したアノード酸化皮膜の静電容量は、アンモニア水を用いた場合に顕著に増加することが、最近明らかになった。皮膜の厚さをTEMにより測定し比誘電率を求めると、pH10のクエン酸＋アンモニアの場合は223であり、クエン酸単独の63、リン酸単独の33に比較して著しく高い値となる。また、高容量を示す皮膜はインピーダンス測定で電気特性の異なる2層構造を示すが、皮膜外層を60%程度溶解すると1層構造になる[11)]。これはアンモニアの封入位置にほぼ一致する。また、皮膜の内層の静電容量は外層より著しく高い。これらの結果は、皮膜に封入される電解質アニオンが皮膜の誘電特性を強く支配していることを示唆している。

まとめ

ニオブのアノード酸化誘電体皮膜の構造と特性を制御する因子に関する基礎的な知見を、筆者らの結果を中心に解説した。誘電体の質は、皮膜の緻密性や結晶性と同時に電解質アニオンなど皮膜組成により強く制御される。今後の詳細な検討と改質への努力によって、タンタル代替品としてのみならず、ニオブコンデンサへのいっそう高度な機能の付与が期待される。

NbOコンデンサや合金組成を変えた素材に関する研究も開始されており、元素戦略に則って高機能性ニオブコンデンサの開発研究の更なる活性化が待たれている。

参考文献

1) S. Ono, M. Baba, M. Shimoyama and H. Asoh, in Surface Oxide Films/2003, The Electrochemical Society Proceedings Series, PV 2003-25, p.133, Pennington, NJ (2004)
2) 小野幸子、表面技術、**54**、447 (2003)
3) S. Ono, F. Mizutani, M. Ue and N. Masuko, in Corrosion and Corrosion Protection/2001, The Electrochemical Society Proceedings Series, PV 2001-22, p.1129, Pennington, NJ (2001)
4) A.Günther schulze and H.Betz, Z.Phys. **92**, 736 (1934).
5) C.J.Del' Oca, L.Young, J. Electrochem. Soc. **117**, 1548 (1970).
6) 小野幸子、 金属のアノード酸化皮膜の機能化部会 第22回津軽コンファレンス(2005/11/1-2 海扇閣、青森) p.17-22
7) 小野幸子、表面技術、**58**、342 (2007)
8) 阿相英孝、大舘広和、小野幸子、表面技術、**55**、202 (2004)
9) 倉持健、阿相英孝、望月隆、小野幸子、表面技術 **55**、218 (2004)
10) 小野幸子、電気化学会 第74回大会特別講演(2007/3/29-31 東京理科大学、野田)講演要旨集p.441
11) 板谷浩丘、長原和宏、高橋英明、阿相英孝、小野幸子、表面技術協会第115回講演会講演論旨集p.190

第4章
新しい機能性膜，新しい表面処理法

4-2 新しい表面処理法

チタン，スズ，亜鉛およびニオブのアノード酸化によるナノポーラス酸化膜の作製

工学院大学 工学部 応用化学科
小野 幸子，阿相 英孝

TiO_2，SnO_2，ZnOなどの酸化物半導体は，光触媒，ガスセンサや色素増感太陽電池への応用の期待が高まっています。アノード酸化では簡便に高比表面積を持つナノポーラス酸化物を得ることが可能で，高度な機能発現を求めて研究も活発化しています。

金属のアノード酸化により酸化皮膜を素地表面に生成し，これを実用的に利用することは，アルミニウムを初めとしてマグネシウム，チタン，タンタル，ステンレスなど多くの例があります。アノード酸化による皮膜は素地自体が酸化物として成長するため密着性に優れており，アルミニウムやマグネシウムでは優れた耐食性・装飾性を付与する目的で古くから広く実用に供されてきました。またアノード酸化皮膜は電解条件によって皮膜構造や特性を制御することが可能なため，孔のないバリヤ型皮膜はコンデンサの誘電体皮膜や液晶のゲート絶縁膜などに，ポーラス(多孔質)型皮膜は分離膜(メンブレン)，種々のナノ構造作製のための鋳型(テンプレート)，触媒担持体など酸化皮膜の機能性に着目した応用例が多くみられます。アノード酸化で絶縁性のある酸化皮膜が成長する金属を特にバルブ金属と呼び，Al，Ta，Ti，Nb，Zr，W，V，Bi，Y，Mo，Hfなどが研究されてきました。しかし，これらは主として緻密なバリヤ型皮膜の生成に注目したもので，ポーラス皮膜の成長は火花放電を伴う絶縁破壊によっており，溶岩状の不規則な多孔質構造が得られます。チタンにおいては絶縁破壊により得られるアナターゼ型の酸化物がチタニア粒子と同様に光触媒活性を示すことが知られていますが，規則的なセル構造を持つ多孔質膜の作製についてはAl，Mg以外にはあまり報告されていませんでした。

TiO_2の他にSnO_2，ZnOは酸化物半導体であるため，光触媒，ガスセンサ，発光デバイス，リチウム電池などへの応用の他，昨今特に透明電極や色素増感太陽電池の半導体電極としての期待が高まっています。これらの作製法は現在主としてゾルゲル法や，CVD，PVDなどの気相蒸着法に拠っています。一方，最近になって従来アノード酸化では限られた厚さの皮膜のみが得られていたTi，InP，Nb，Taなど種々の金属および半導体基板上に，アノード酸化により表面積の高いポーラス酸化皮膜を作製する検討が新たな機能の発現を期待して試みられるようになりました[1～3]。ランダムな堆積酸化物ではなく，素地／皮膜界面での酸化膜成長を電解条件で制御できるような，シリンダ状セル構造を持つ皮膜が成長する場合を「自己規則化皮膜」と呼び，ドイツのSchmukiのグループをはじめとして研究が活発化してきました。一方スズや亜鉛のアノード酸化挙動に関する検討は大変少ないのが現状です[4,5]。本稿ではアノード酸化という簡便でかつ構造や特性の制御性が高い手法を用いてチタ

ンやスズ，亜鉛，ニオブ上に生成させたポーラス酸化皮膜の構造と成長挙動を，電解液の種類および電解条件の影響とともに紹介します。

チタンの場合，フッ化物を含む電解液（たとえば1mol・dm^{-3} $(NH_4)H_2PO_4$ ＋ 0.5wt％ NH_4F，20V）を用いると図1に示すようなチューブ状のポーラス皮膜が得られます[2, 6]。これらは非晶質のTiO_2ですが，加熱により結晶化が可能です。最近，このようなチタニアナノチューブを$TiCl_4$で処理して用いた高い変換効率を示す色素増感太陽電池への適用例が報告されました[7]。現在では数十μmを超える皮膜の作製も可能で，粒状チタニアに比較して高比表面積のみならず形状異方性の効果も期待されます。また，基板として球状チタン焼結体（商品名タイボラス）を用いることで，より高い表面積や機能性を付与することが可能と思われます[6]。

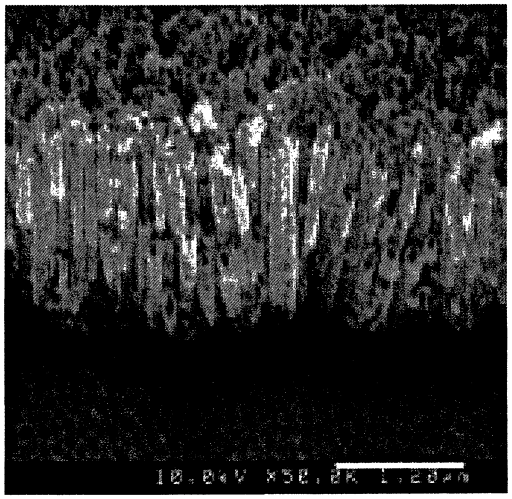

図1　アノード酸化により20Vで生成したチタニアナノチューブの構造

スズを種々の電解液でアノード酸化すると，電解液の種類やpHによらず，ポーラス皮膜を生成することができます[8]。図2に1mol・dm^{-3}水酸化ナトリウムで10分間定電圧電解を行った後の試料破断面のSEM像を，図3にSTEM像を示します。これらの像から，アルミニウムのアノード酸化ポーラスアルミナと類似したセル構造を持つ皮膜が生成することが確認されます。aは生成電圧5Vの場合で，セル径は50～100nmです。しかしbcに示すように生成電圧が15Vに上昇してもセル径は大きく変化しません。生成電圧の上昇に伴い電流は直線的

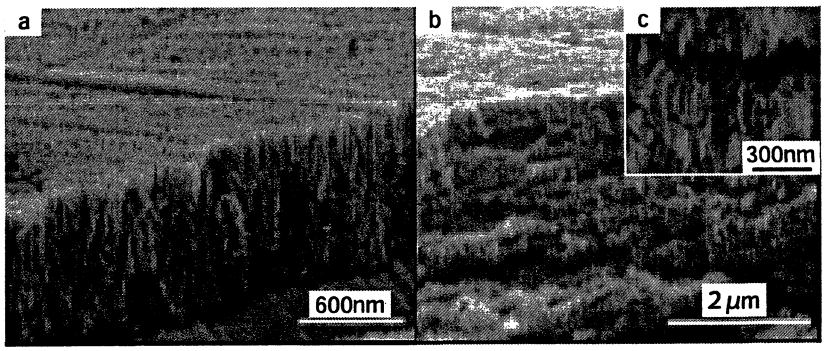

図2　水酸化ナトリウム中でa5Vおよび（b, c）15Vで生成したスズのアノード酸化皮膜の破断面SEM像

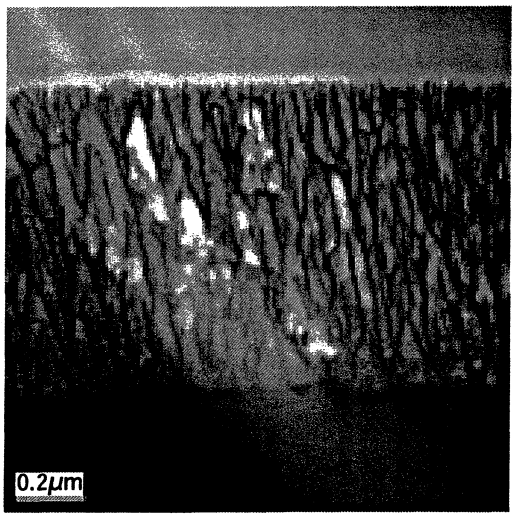

図3　NaOH中，5Vで生成したスズのアノード酸化皮膜の破断面STEM像

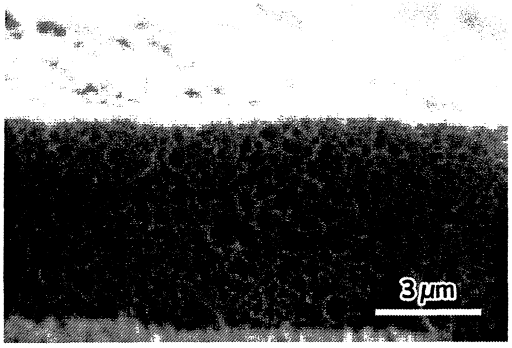

図4　シュウ酸中，20Vで生成したスズの網目状アノード酸化皮膜のSEM像

に増加して酸化皮膜は厚くなりますが，これらの傾向は水酸化ナトリウム，ホウ酸アンモニウム，シュウ酸，リン酸など電解液によらず同じです。絶縁性皮膜が生成するAlでは電圧上昇で電流が指数関数的に増加しますが，これと異なるのは酸化物が半導体のためと考えられます。電流密度がある値を超えると得られる皮膜の孔形状は直管状から網目状に変化します（図4）。表1に各種電解液を用いて皮膜を生成したときの電流と得られる皮膜構造の特徴をまとめました。硫酸電解液中では特異な角型やチューブ状

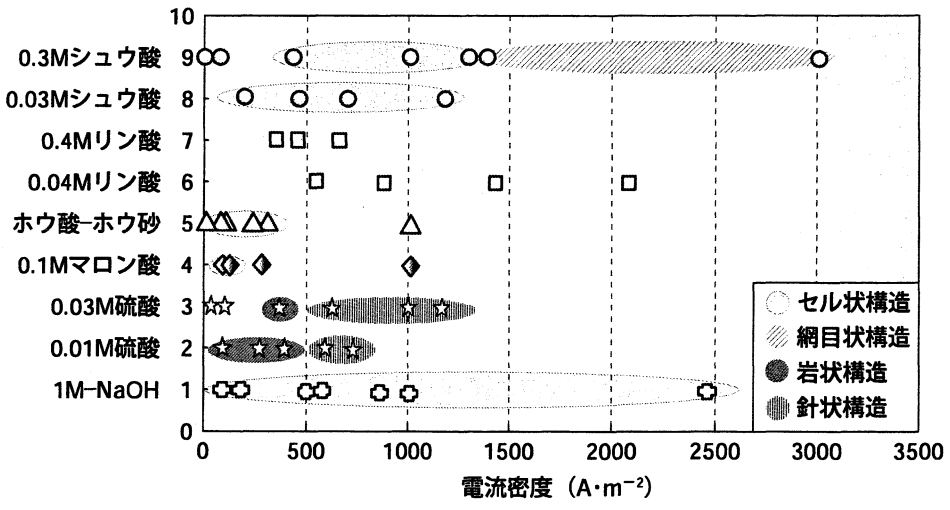

表1　スズのアノード酸化電流密度と生成する皮膜構造の関係

を示す皮膜が得られます。

図5ａに亜鉛を0.1mol・dm^{-3}水酸化ナトリウム中，電流密度100A・m^{-2}で形成した皮膜の断面SEM像を示しますが，皮膜は表層の粒状層と内部のセル状構造との二層構造のように観察されます[9]。一方，電解液がシュウ酸の場合，酸化皮膜は白色を呈しており，主として$Zn(OH)_2$結晶からなる角型構造皮膜が生成します（図5ｂ）。硫酸中では亜鉛は溶解し，酸化皮膜の成長は見られません。

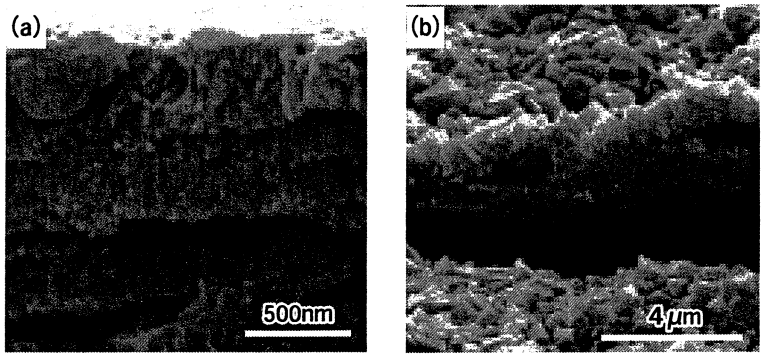

図5　亜鉛のアノード酸化皮膜
ａ水酸化ナトリウム中，20V
ｂシュウ酸中，100Am^{-2}

ニオブは高い耐食性を持ち，電解液のpHによらずバリヤ型皮膜が生成しますが，フッ化物を含む電解液中ではポーラス皮膜が成長します。皮膜はフッ素の影響により層状に剥離しやすく，ミクロン単位での皮膜成長は特殊な電解条件を要します。図6は超厚膜化したニオブアノード酸化皮膜の破断面ですが，皮膜はNb_2O_5の結晶性を示します[3]。

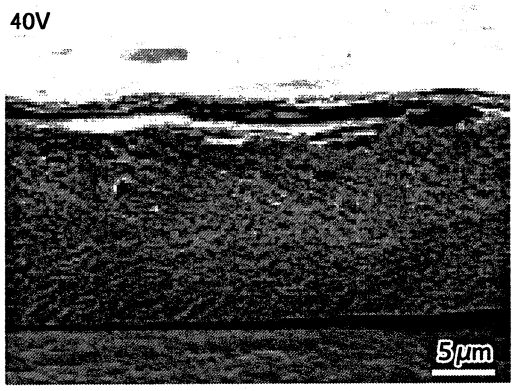

図6　超厚膜化したニオブのアノード酸化皮膜

ここに紹介したナノポーラスアノード酸化皮膜の作製は緒についたところといえ，今後の発展が大いに期待できる分野です。現在は見出されていない，種々の金属や半導体のポーラス皮膜作製における進展と応用の成功を期待したいと思います。

参考文献

1) Zwilling, V., E. Darque-Ceretti, A. Boutry-Forveille, D. David, M. Y. Perrin and M. Aucouturier : Surf. Interface Anal., **27**, 629(1999)
2) A. Ghicov, H. Tsuchiya, J. M. Macak, P. Schmuki : Electrochem. Commun., **7**, 505(2005)
3) 長坂匠，阿相英孝，小野幸子，表面技術協会　第113回講演大会　講演要旨集p. 102(2006/03　東洋大学，川越)
4) H-C. Shin, J. Dong, and M. Liu, Advanced Materials **16**, 237,(2004)
5) 山口靖英，山崎正敏，吉原左知雄，白樫高史：DENKI KAGAKU, **64**, 373(1996)
6) 阿相英孝，吉嗣一貴，小野幸子：電気化学会　第73回大会　講演要旨集p. 79(2006/4　首都大学東京，八王子)
7) G. K. Mor, K. Shankar, M. Paulose, O. K. Varghese, C. A. Grimes : Nano Letters **6**, 215(2006)
8) 小野幸子，小林良平，阿相英孝：電気化学会　第73回大会　講演要旨集p. 79(2006/4　首都大学東京，八王子)
9) 小林勇太，阿相英孝，小野幸子：金属のアノード酸化皮膜の機能化部会　第23回有明コンファレンス(2006/11　九州)

Design of two-dimensional/three-dimensional composite porous alumina by colloidal crystal templating and subsequent anodization

Hidetaka Asoh[a] and Sachiko Ono
Department of Applied Chemistry, Kogakuin University, 1-24-2 Nishi-shinjuku, Shinjuku-ku, Tokyo 163-8677, Japan

(Received 24 February 2005; accepted 12 July 2005; published online 29 August 2005)

The unique two-dimensional/three-dimensional composite porous alumina structure, which consisted of the outer inverse opal structure and the inner parallel channel array structure formed on an Al substrate, has been fabricated using a combination process involving colloidal crystal templating and subsequent multistep anodization. The pore periodicity and film thickness of the sophisticated porous structure presented here can be easily controlled by changing the diameter of spherical colloidal particles used as templates and adjusting the anodization conditions, such as voltage and time. The resulting porous materials can potentially find applications as catalytic supports, separation media, optical devices, and sensors. © *2005 American Institute of Physics.* [DOI: 10.1063/1.2037199]

Anodic porous alumina, a typical self-ordered nanochannel material formed by the anodization of Al in an appropriate acidic solution, has recently been widely applied as a starting material for the fabrication of several types of nanodevice, such as photonic,[1,2] electronic,[3,4] and magnetic devices,[5,6] because of its potential applications based on a unique solid geometry and its so-called honeycomb structure on the nanometer scale. To expand the application field of the ordered channel array structure of anodic porous alumina, it is necessary to improve the regularity of the channel arrangement, to control the size and position of the channels, and to constitute sophisticated structures with three-dimensional (3D) periodicity.

In this letter, we propose an approach to the fabrication of the 2D/3D composite porous alumina structure, which is based on a combination of a templating process of colloidal crystals and subsequent multistep anodization. The 2D/3D composite porous alumina consists of an outer inverse opal structure and an inner parallel channel array structure formed on Al substrate. Such composite porous materials with controlled morphologies may overcome some of the limitations of the 2D bulk channel structure.

Figure 1 shows the schematic of the fabrication of the 2D/3D composite porous alumina structure on an Al substrate. The templating process used to fabricate the 3D porous structure was carried out as described previously.[7] A monodisperse suspension of polystyrene (PS) beads (Nissin EM Co., Ltd Tokyo, 0.2% solids) was dropped onto the Al substrate. The suspension drop was dried in air, and the nanospheres were self-assembled into a closely packed structure with 3D ordered lattices via attractive capillary forces [Fig. 1(a)].[8] After the complete evaporation of the solvent, the Al substrate with the colloidal crystal structure of PS beads was anodized in a neutral solution under the constant current condition [Fig. 1(b)]. After the first anodization, the sample was immersed in 97% toluene to dissolve the PS beads used as a template [Fig. 1(c)]. Then, the second anodization was conducted under a different condition to the first anodization. Specifically, the sample was anodized to form the channel arrays underneath the outer 3D porous structure at a constant voltage condition in oxalic acid solution [Fig. 1(d)]. The ordered geometric structure formed on the Al substrate was evaluated by means of field-emission scanning electron microscopy (SEM, Hitachi S-4200). In addition, a transmission electron microscope (TEM, JEOL JEM-2100F) operating at 200 kV in conjunction with an energy dispersion x-ray spectrometer (EDX, JEOL JEM-2300T) was utilized to examine the microstructures and the chemical composition. The cross section of anodic films was prepared by using focused ion beam (FIB, SSI SMI2050MS) techniques.

Figure 2 shows the typical SEM image of a composite layer composed of PS beads and alumina filled in the void space between the spheres. These images indicate that anodization products can be grown through the gaps in the self-assembled PS beads from the bottom surface during anodization. The thickness of the composite layer was approximately 2 μm. The number of stacked layers was 6–10, taking into account the diameter of the PS beads (204 nm). In the present experiment, we adopted a constant current condition to control the film thickness with a selected voltage. The voltage-time curve at a constant current density for the anodization of the Al substrate with the colloidal crystals was almost the same as that for a conventional electropolished Al substrate in a neutral solution.

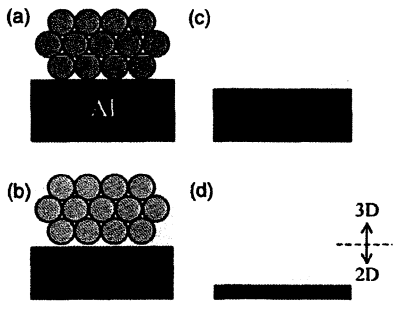

FIG. 1. Scheme for fabricating 2D/3D composite anodic porous alumina by templating process involving colloidal crystals and multistep anodization. (a) Self-assembly of PS beads [template]; (b) first anodization [PS beads/alumina composite]; (c) removal of beads [3D-porous alumina]; (d) second anodization [2D/3D porous alumina composite].

[a]Electronic mail: asoh@cc.kogakuin.ac.jp

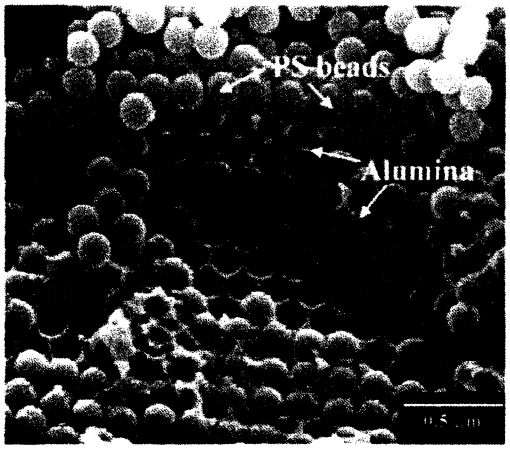

FIG. 2. SEM images of the surface and cross section of the anodized Al before removal of PS beads. Anodization was conducted in a mixture of 0.5 mol dm^{-3} boric acid and 0.05 mol dm^{-3} sodium tetra-borate solution at constant current density of 10 Am^{-2} up to 50 V at 20 °C.

Figure 3(a) shows a cross-sectional TEM image of the 3D porous structure after dissolving the PS beads in toluene. The TEM image of the resulting porous structure shows an ordered hexagonal pattern of air spheres in the solid framework. The framework of this sample was confirmed to be amorphous by electron diffraction patterns. To identify the chemical composition of this solid material, EDX analysis was performed. Figure 3(b) shows the typical EDX spectrum taken at the wall of the honeycomb networks. It was found from the spectrum that the framework basically consisted of aluminum and oxygen because the strong K α peak of O at 0.5 keV and the K α peak of Al at 1.5 keV were detected. The other peaks of Ga, Cu, C, and Si seem to originate from Ga ion beams of FIB, a copper grid and contamination elements incorporated during sample preparation, respectively. These results clearly indicate that the as-anodized honeycomb networks are basically amorphous and composed of alumina.

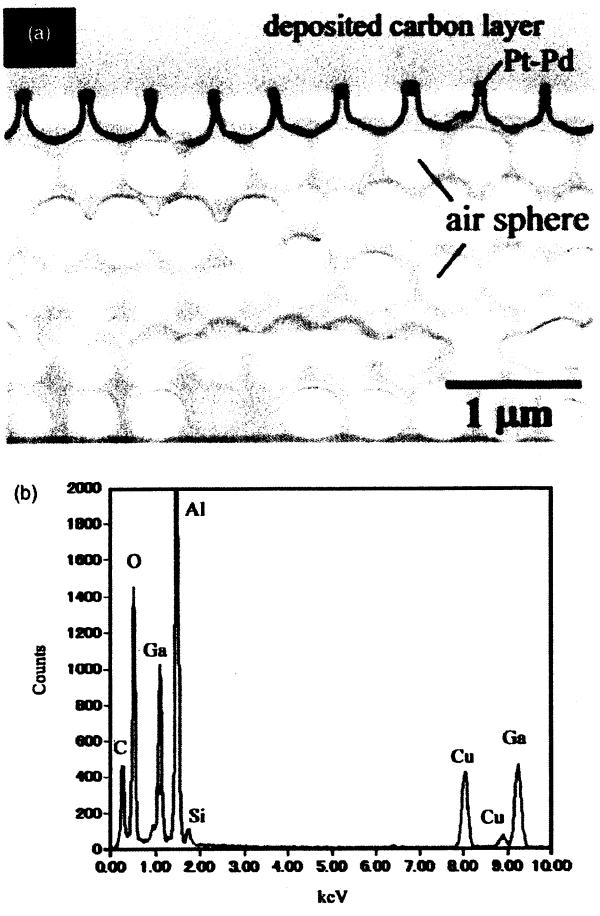

FIG. 3. (a) TEM image of the cross-section of the 3D porous alumina after removal of PS beads. No crystalline oxide was detected by electron diffraction. (b) Typical EDX spectrum obtained from the framework.

To determine the mechanism of the formation of alumina in the nanospace between particles, further detailed study is now in progress.

This proposed templating process using the electrochemical reaction is somewhat similar to the electrodeposition technique for colloidal assemblies on a conductive glass substrate reported by Braun and Wiltzius[9] although the electrodeposition is a cathodic reaction. However, our approach has some characteristic points of interest: (i) the underlying Al substrate can be anodized directly in aqueous solutions and the void can be filled with anodization products, that is, alumina; (ii) the level of the unoxidized Al surface is shifted inward in the sample with anodization time; and (iii) this process makes it possible to modulate the 3D porous structure by additional multistep anodization, as described below.

An important advantage of the process proposed here is that it is possible to connect the structures with different dimensional characters by applying additional anodization. Figure 4 shows the typical 2D/3D composite porous alumina structures. The anodized specimens were bent into a V-shape, producing cracks in the oxide film. These composite structures consisted of the outer inverse opal structure and the inner parallel channel array structure formed on an Al substrate. The periodicity of the pores in the outer 3D porous structure was fundamentally determined by the diameter of the PS beads. In the case of Fig. 4(a), the PS beads of 204 nm diameter were used as templates. To change the periodicity of the pores in 3D porous alumina, the PS beads of 474 nm diameter were applied in the case of Fig. 4(b). The anodization conditions used were the same in both cases. In addition, the magnification of both images was the same. This indicates that the formation of the 2D/3D composite structure could be achieved by a combination of a templating process of colloidal crystals and subsequent multistep anodization, that is independent of the PS bead diameter.

Moreover, the interval of the pores in the outer 3D porous alumina was in good agreement with the diameter of the PS beads used as a template. According to a previous report on a study using PS beads as templates, the center-to-center distance between the pores is reduced by approximately 30% less than the initial size of the PS beads owing to the shrinkage during the drying and heat treatment process.[10] The decrease in pore distance in our process is small in comparison with that achieved using high-temperature processes such as polymerization, sol-gel hydrolysis, thermal decomposition, and calcination.[11–13]

Concerning the periodicity of the inner 2D channel array structure, it is recognized that the channel periodicity has a good linear relationship with the anodization voltage, where the proportionality constant of periodicity for a specific volt-

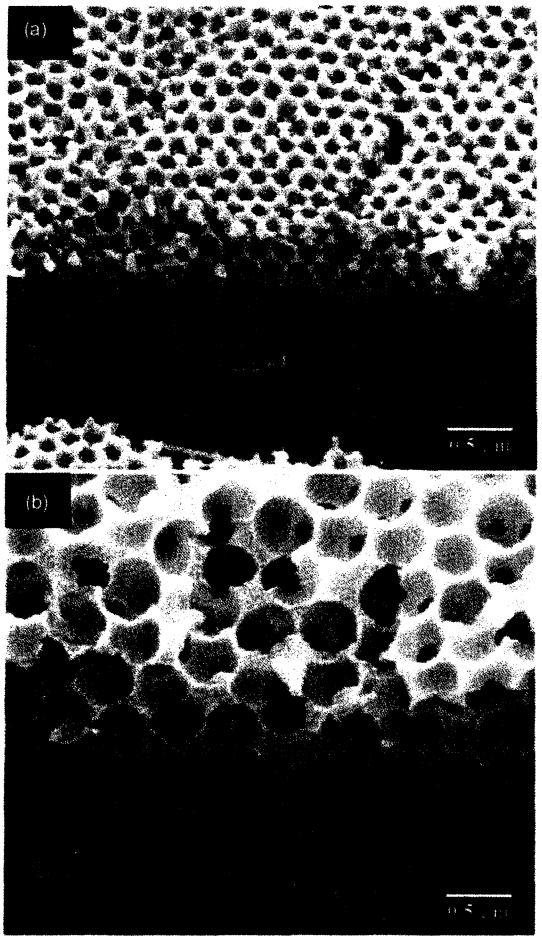

FIG. 4. Cross-sectional SEM image of anodized Al with 2D/3D composite structures. The first anodization conditions were the same as those in Fig. 2. After removal of PS beads, the second anodization was performed in 0.05 mol dm^{-3} oxalic acid at 80 V for 10 min at 20 °C. The PS beads used as templates were (a) 204 nm and (b) 474 nm in diameter.

age is approximately 2.5 nm/V. In addition, the depth of the 2D channels can also be adjusted from the nanometer scale to several hundreds micrometer scale by adjusting the anodization period. In the case of Fig. 4(a), the periodicity of the pores of the outer inverse opal alumina was almost in agreement with that of the underlying straight parallel channels on which anodization was conducted under a constant voltage of 80 V to adjust the channel interval to approximately 200 nm. Therefore, the growth of straight parallel channels perpendicular to the substrate could be observed underneath each hollow space. Figure 5 demonstrates the ordered channel configuration with 200 nm interval in the inner 2D porous alumina. To show clearly the arrangement of 2D straight channel, the outer 3D porous alumina was removed prior to additional anodization. This result indicates that the hemispherical scalloped pattern of the bottom layer in inverse opal alumina can initiate pore development and can guide the growth of the channel in the film thickness direction. This fabrication process using scalloped pattern formed on an Al substrate is somewhat similar to the previous work.[14,15] However, this proposed method has an advantage in that it

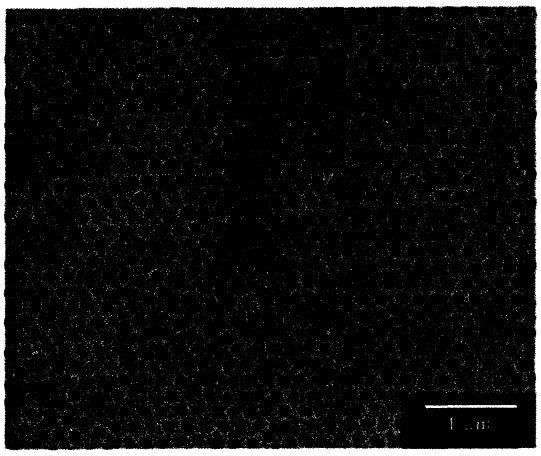

FIG. 5. SEM image of the surface of the inner 2D channel array structure. The first anodization condition was the same as that in Fig. 2. After removal of the outer 3D porous alumina, the second anodization was performed under the same condition as that in Fig. 4. To facilitate the observation, pore-widening treatment was carried out in 5 wt% phosphoric acid at 30 °C for 60 min.

can be used for large-area patterning using a simple electrochemical process with a high throughput and a low cost without special tools, including molds for imprinting.

In summary, we have described the fabrication of 2D/3D composite porous alumina structures by using a combination of a templating process of colloidal crystals and subsequent multistep anodization. The obtained unique anodic porous alumina, which consists of an outer inverse opal structure and an inner parallel channel array structure formed on an Al substrate, has potential technological and scientific applications as catalytic supports, separation media, large-surface-area adsorbants, optical devices, and sensors that require a tailored space of controlled periodicity.

[1]H. Masuda, M. Ohya, H. Asoh, M. Nakao, M. Nohtomi, and T. Tamamura, Jpn. J. Appl. Phys., Part 2 **38**, L1403 (1999).
[2]I. Mikulskas, S. Juodkazis, R. Tomasiunas, and J. G. Dumas, Adv. Mater. (Weinheim, Ger.) **13**, 1574 (2001).
[3]N. Kouklin, L. Menon, and S. Bandyopadhyay, Appl. Phys. Lett. **80**, 1649 (2002).
[4]X. Mei, D. Kim, H. E. Ruda, and Q. X. Guo, Appl. Phys. Lett. **81**, 361 (2002).
[5]D. Al-Mawlawi, N. Coombs, and M. Moskovits, J. Appl. Phys. **70**, 4421 (1991).
[6]K. Nielsch, R. B. Wehrspohn, J. Barthel, J. Kirschner, U. Gösele, S. F. Fischer, and H. Kronmüller, Appl. Phys. Lett. **79**, 1360 (2001).
[7]H. Asoh, A. Uehara, and S. Ono, Jpn. J. Appl. Phys., Part 2 **43**, L1159 (2004).
[8]Y. Xia, B. Gates, Y. Yin, and Y. Lu, Adv. Mater. (Weinheim, Ger.) **12**, 693 (2000).
[9]P. V. Braun and P. Wiltzius, Nature (London) **402**, 26 (1999).
[10]J. E. G. J. Wijnhoven and W. L. Vos, Science **281**, 802 (1998).
[11]G. Subramania, K. Constant, R. Biswas, M. M. Sigalas, and K.-M. Ho, Appl. Phys. Lett. **74**, 3933 (1999).
[12]A. Richel, N. P. Johnson, and D. W. McComb, Appl. Phys. Lett. **76**, 1816 (2000).
[13]B. T. Holland, C. F. Blanford, and A. Stein, Science **281**, 538 (1998).
[14]H. Masuda, H. Yamada, M. Satoh, H. Asoh, M. Nakao, and T. Tamamura, Appl. Phys. Lett. **71**, 2770 (1997).
[15]H. Asoh, K. Nishio, M. Nakao, T. Tamamura, and H. Masuda, J. Electrochem. Soc. **148**, B152 (2001).

Available online at www.sciencedirect.com
SCIENCE DIRECT®
Electrochimica Acta 50 (2005) 5103–5110
ELECTROCHIMICA Acta
www.elsevier.com/locate/electacta

Structure and property of anodic barrier films formed on aluminum in low voltage range

Sachiko Ono *, Chieko Wada, Hidetaka Asoh

Department of Applied Chemistry, Faculty of Engineering, Kogakuin University, 1-24-2 Nishi-shinjuku, Shinjuku-ku, Tokyo 163-8677, Japan

Received 9 December 2004; received in revised form 14 April 2005; accepted 14 April 2005
Available online 25 July 2005

Abstract

The structure and properties of anodic films formed in a relatively low voltage range in ammonium adipate solution have been investigated focusing on the effect of formation voltage. When anodization voltage was identical, the linear relationship of film thickness with the log of the final current density during film growth could be ascertained for all the films formed even at low voltages such as 5 V. The anodization ratio determined from the transmission electron microscopy (TEM) cross section of the film formed at 5 mA cm^{-2} until voltage increased to 5 V was 1.8 nm/V suggesting a lower electric field strength during anodization than that for the film formed at the voltage higher than 20 V. Furthermore, the transport number of Al^{3+} ions and amount of incorporated anions decreased with decreasing formation voltage, particularly at the voltage lower than 10 V. Changes in chemical dissolution rate in the depth of the films in an acid solution indicated that the films formed in the voltage range from 20 to 80 V were composed of one layer and the films formed at voltages lower than 10 V were composed of two layers with different dissolution rates. However, when applied voltage was kept constant following current decay, the film formed one layer, implying the inward migration of the incorporated anions to the film/metal interface. It was suggested that the outer layer with the higher dissolution rate contains electrolyte anions and the inner layer with the lower dissolution rate consists of pure alumina. Thus, it is clarified that the structure and properties of anodic film change with increasing anodization voltage because of the change in electric field strength, even if anodization is conducted at a constant current density.

Keywords: Anodic film; Aluminum; Transport number; Electric field strength; TEM

1. Introduction

The growth of anodic oxide films in neutral electrolytes proceeds at both film/electrolyte and film/substrate interfaces giving a duplex structure [1,2]. The oxide layer formed at the former interface includes electrolyte anions, while a pure-alumina layer is formed at the latter interface. The thickness ratios of each layer, respectively, represent the transport numbers of Al^{3+} and O^{2-} if the incorporated anions are immobile in the film. It is suggested [3] that borate is immobile in the film but phosphate migrates inward after incorporation. Species such as chromate, tungstate and molybdate migrate outward. The depth and content of incorporated anions must affect the dielectric properties of anodic oxide films as a capacitor material as well as film thickness [4].

Concerning the thickness of anodic films, it is generally taken to be proportional to applying voltage. However, the classical theory of ionic conduction at high field strengths for various metals [1,5–7] indicates that film thickness must be inversely proportional to the logarithm of ionic current, when a film is formed at an identical voltage. The precise clarification of the factors determining film thickness is essential in the capacitor industry because film thickness directly affects capacitance.

Recently, one of the present authors [4,8–10] reported that the changes in current density and electrolyte temperature induce notable changes in film structure as well as in composition, which were evaluated by the transmission electron microscopy (TEM), secondary ion mass spectroscopy

* Corresponding author.

0013-4686/$ – see front matter © 2005 Elsevier Ltd. All rights reserved.
doi:10.1016/j.electacta.2005.04.047

(SIMS) and glow discharge optical emission spectroscopy (GD-OES). Namely, the thickness of the film formed in a borate solution at a constant current density up to an identical voltage decreases with increasing current density and markedly increases with temperature. The thickness ratio of the boron incorporated in the outer layer is 0.4 at a current density of 2 mA cm^{-2} and increases to 0.45 at 20 mA cm^{-2} at an anodization voltage of 80 V. A porous cell structure is developed when the film is formed at a current density higher than 10 mA cm^{-2}. Boron content in the outer layer increases 1.5 times when current density increases 10 times [4].

The main purpose of this work is to evaluate the effect of anodization voltage, particularly at the voltages lower than 80 V as well as current density on film thickness and microstructure. Since capacitance is inversely proportional to film thickness, precise information on the nature of the films formed in the low voltage range must be beneficial to obtain high-capacitance and high-quality dielectric films.

2. Experimental

High-purity (99.99%) aluminum sheets were electropolished in a 4:1 mixture of ethanol–perchloric acid solution before anodization. Anodic films were formed in 0.1 mol dm^{-3} ammonium adipate, which is generally used in the capacitor industry in a low voltage range, at 20 °C at various constant current densities up to 80 V. The iR-drop at various anodization current densities induced by electrolyte resistance, which was 3.7 V in maximum at 10 mA cm^{-2} at 20 °C, was compensated by applying voltage [11]. Galvanostatic polarization was conducted to prevent the iR-drop induced by solution resistance when the anodization voltage was lower than 10 V. An electrochemical measurement called the "pore-filling (PF)" technique [12–14], i.e. re-anodization of an anodized specimen, was adopted in evaluating the thickness and imperfections of anodic oxide films. For this evaluation, voltage–time (V–t) curves were measured during re-anodization at 0.1 mA cm^{-2} in 0.1 mol dm^{-3} ammonium adipate at 20 °C, where voltage jump (V_j) is suggested to be proportional to film thickness. Details were described in our previous paper [4]. Anodic film structures were observed by TEM (Hitachi H-9000) operated at 300 kV. The cross sections of films with a thickness of 30–50 nm were prepared using an ultramicrotome with a diamond knife attached. Glow discharge optical emission spectroscopy (Jobin-Yvon JY5000RF) was used for measuring the depth profiles of constituent elements in the films accompanied by argon ion sputtering at 40 W.

3. Results and discussion

3.1. Relation between current density and film thickness

Anodic films were formed in 0.1 mol dm^{-3} ammonium adipate solution at 20 °C at various constant current densities

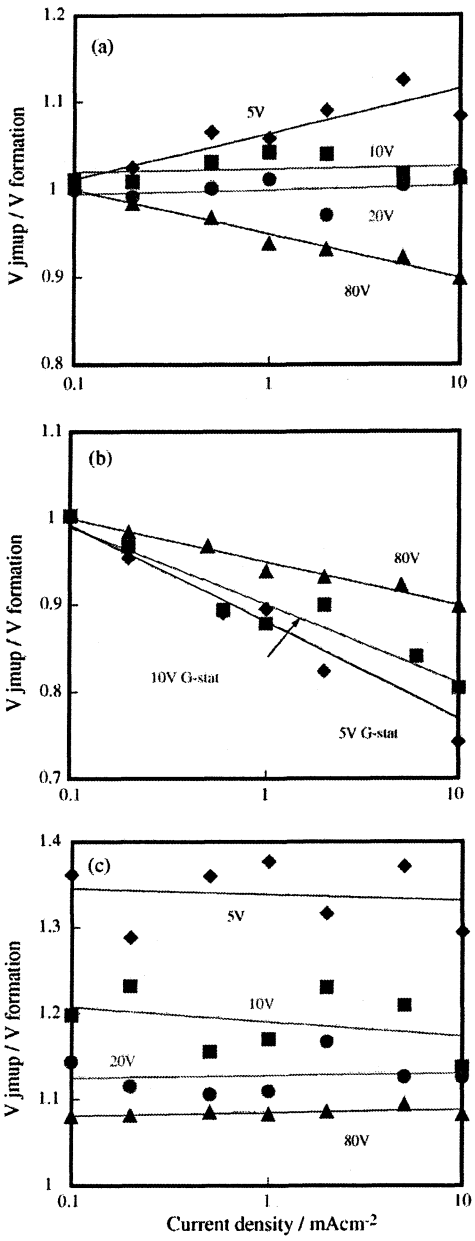

Fig. 1. Relationship between ratio of voltage jump V_j to formation voltage V_f and log of current density: (a) constant current; (b) constant current and re-anodization was conducted by Galvanostatic polarization at the voltage lower than 10 V; (c) constant voltage followed by current decay for 20 min.

of 0.1–10 mA cm^{-2} up to an identical voltage ranging from 5 to 80 V. Galvanostatic polarization was used for anodization at a voltage lower than 10 V. The thickness of the films was evaluated from the voltage jump V_j in re-anodization in a mixed borate solution as described above. As shown in Fig. 1a, the voltage jump V_j, namely, the thickness of the films had a linear relationship with the log of current density and decreased with increasing current density if the formation voltage was higher than 40 V, as we previously reported

for the films formed in a borate solution [4]. However, concerning the voltage range lower than 20 V, V_j was identical or increased with increasing log of current density. To compare all the results, the ratios of voltage jump V_j to formation voltage V_f are plotted on the *Y*-axis. Then, re-anodization was conducted also at the Galvanostatic polarization using three electrodes. As shown in Fig. 1b, V_j decreased with increasing current density for all the films formed even at low voltages such as 5 V. The cause of the deference between two re-anodizing methods of the Galvanostatic and the conventional two electrodes polarization is unknown. Furthermore, when the anodization voltage was sustained for 20 min associated with current decay, the film thickness became the same for each formation voltage independent of current density (Fig. 1c).

Subsequently, the effect of current decay during voltage holding on film thickness was examined. Fig. 2 shows the current–time transient during anodization at 80 V, voltage was kept constant followed by exponential current decay. The first anodization was performed at 1 mA cm^{-2} until voltage reached 80 V. The V_j of the films formed until each anodization point specified in Fig. 2 is plotted in Fig. 3a against its final current density. Furthermore, the total electricity passed was also plotted against its final current density in Fig. 3b. As is clearly shown, the thickness of the films formed at both constant current density and constant voltage followed by current decay was identical and lied on a straight line. In the case of total electricity, it has a roughly linear relationship with the log of current density although the values are rather scattered. This reveals that film thickness is determined by the final current density without relying on the early formation process when the applied voltage is constant. The result also implies a reduction in the extent of the iR-drop induced by the oxide film itself caused by a decrease in current density.

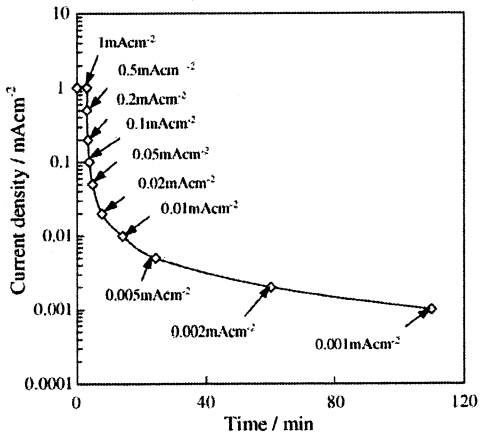

Fig. 2. Current–time transient for anodization at 80 V and kept the voltage constant associated with exponential current decay. The first anodization was performed at 1 mA cm^{-2} until the voltage increased to 80 V.

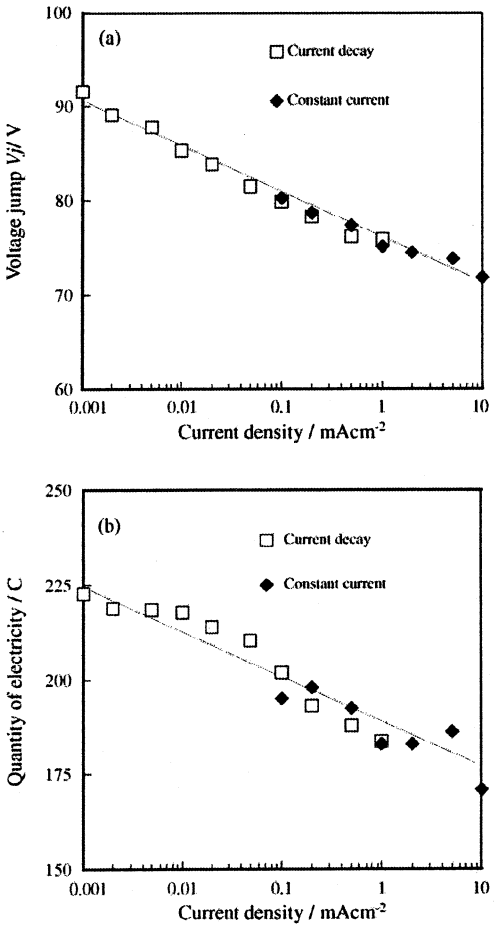

Fig. 3. Changes in: (a) voltage jump and (b) total electricity with log of current density. Anodization was conducted at a constant current or a constant voltage followed by current decay.

3.2. *In-depth structure of films evaluated from acid dissolution behavior*

For the clarification of in-depth film structure, the change in the chemical dissolution rate of the films was measured. The films were dipped in 2 mol dm^{-3} sulfuric acid at 60 °C for a certain period and re-anodized to estimate the change in film thickness by measuring voltage jump. Anodic films were formed at constant current density of 5 mA cm^{-2} until voltage reached in the voltage range 5–80 V. Fig. 4 shows the change in voltage–time curve with dissolution time when anodized specimens were re-anodized in boric acid–borate solution at 0.1 mA cm^{-2} up to 80 V (Fig. 4a) and kept the voltage of 80 V followed by current decay for 20 min (Fig. 4b). V_j was determined by extrapolating the linear part of *V–t* curves to an anodization time of zero. The similar dissolution behavior was measured for the films formed at 5 V as shown in Fig. 5. The delay in the initial voltage increase appeared in the films formed at 80 V, which is more noticeable than that in the films formed after current decay as shown in Fig. 4b and also the films formed at 5 V, indicates the less compact structure of

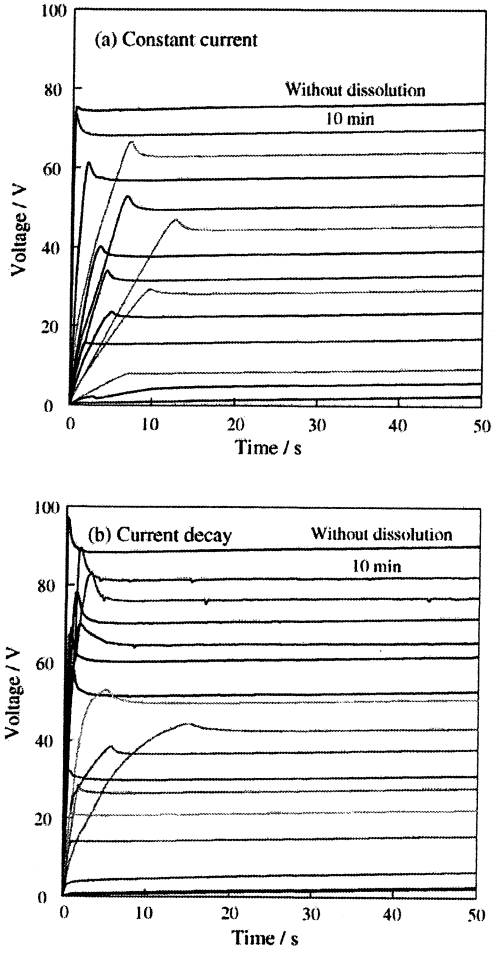

Fig. 4. Changes in voltage–time curves with dissolution time (10 min each) when anodized specimens were re-anodized in boric acid–borate solution at 0.1 mA cm^{-2}: (a) anodic films were formed at 5 mA cm^{-2} up to 80 V and (b) at 80 V followed by current decay for 20 min. Voltage jump (V_j) was determined by extrapolation of the linear part of V–t curves to an anodization time of zero.

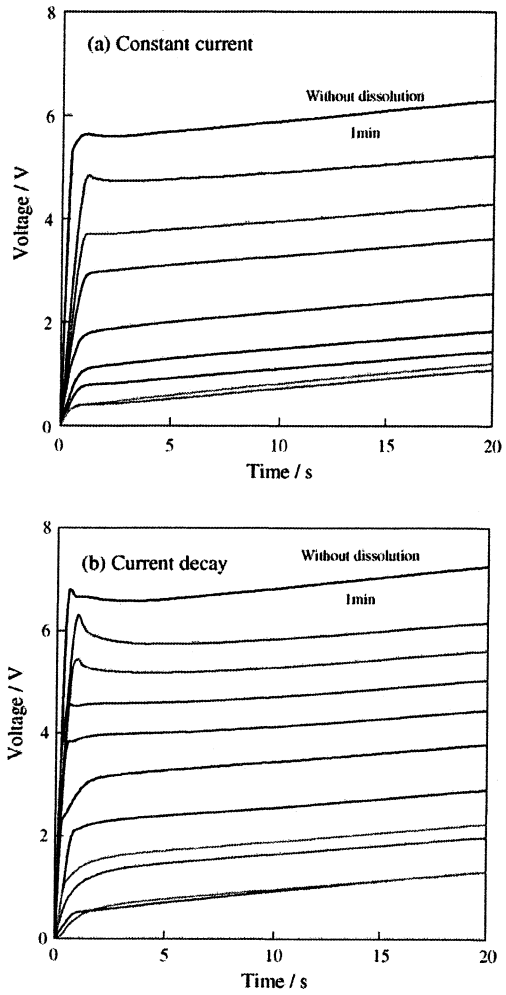

Fig. 5. Changes in voltage–time curves with dissolution time (1 min each) when anodized specimens were re-anodized in boric acid–borate solution at 0.1 mA cm^{-2}: (a) anodic films were formed at 5 mA cm^{-2} up to 5 V and (b) at 5 V followed by current decay for 20 min.

the film. The porosity of the defect observed after dissolution for 60 min was estimated to be 0.01 from the first voltage slope. As we reported previously, defect content presented at the barrier layer of anodic films increases with increasing formation voltage [14,15]. These small defects would be produced by minute breakdown events at the higher anodization voltage range more than the lower voltage range. However, the defects in the films could be partly repaired during voltage hold followed by current decay.

Changes in voltage jump with dissolution time are summarized in Fig. 6. The results suggest that the films formed in the higher voltage range from 20 to 80 V show no change in dissolution rate (Fig. 6a), so that they seem to be composed of one layer. On the other hand, the films formed at 5 and 10 V are composed of two layers with different dissolution rates as shown in Fig. 6b. It is assumed that the outer layer with a high dissolution rate contains electrolyte anions and the inner layer with a low dissolution rate consists of pure alumina. We reported that the layer of high anion content shows a high dissolution rate for the barrier layer of porous anodic films formed in various electrolyte such as phosphoric, chromic, oxalic and sulfuric acid solutions [14,15]. Electrolyte anions migrate into anodic films under a high electric field and anion content increases with increasing electric field strength [16]. Therefore, the electric field strength must be low during anodization at a voltage lower than 10 V. When the anodization voltage was kept constant for 20 min, the dissolution rate of all films showed almost no change with time suggesting anion migration into the full depth of the film to form one layer (Fig. 7).

When the anodization voltage is as low as 5 V, the effect of the thin oxide layer formed by electropolishing, which is suggested to be approximately 3 nm thick and relatively resistant to acid dissolution, on dissolution rate has to be taken into account. Fig. 7 shows changes in voltage jump with the dissolution time of the films formed on electropolished and

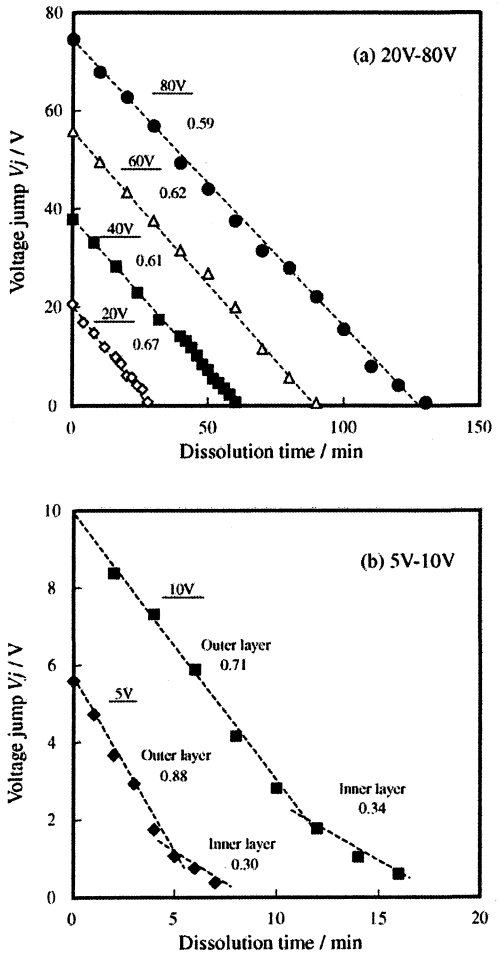

Fig. 6. Changes in voltage jump V_j with dissolution time in sulfuric acid. The figures indicate the slope of voltage against time (V min^{-1}): (a) 20–80 V and (b) 5–10 V.

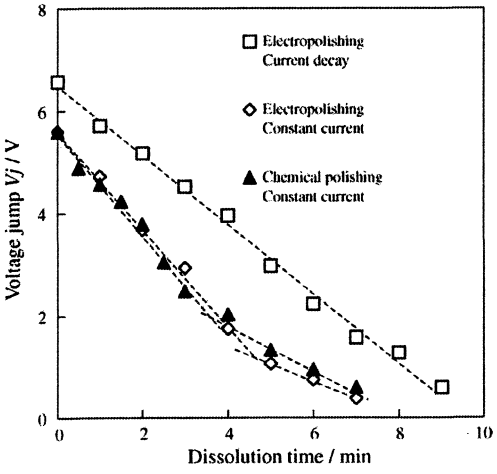

Fig. 7. Dependence of pretreatments of substrates and anodization conditions on changes in voltage jump V_j with dissolution time in sulfuric acid.

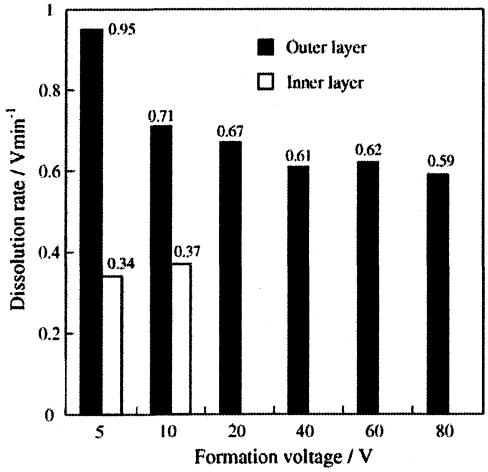

Fig. 8. Effect of formation voltage on dissolution rate. The films formed at low voltages consist of two layers.

alkaline-degreased aluminum substrates at 5 mA cm^{-2} until voltage reach 5 V to evaluate the effect of pretreated substrate surface. Dissolution curves of both films are almost same. Therefore, it is considered that the surface oxide film formed by electropolishing has no significant effect on dissolution behavior, although the surface film formed by electropolishing is resistant to acid dissolution unlikely to that formed by alkaline-degreasing [17]. It is noteworthy that the dissolution rate of the film after voltage holding was between those of the outer and inner layers of the two-layer film.

The dissolution rates of the films in sulfuric acid solution formed in the voltage range from 5 to 80 V are summarized in Fig. 8. They were almost the same in the voltage range from 40 to 80 V but gradually increased with decreasing voltage, particularly at 5 V.

3.3. *Effect of formation voltage on anodization ratio evaluated by TEM*

The TEM images of the cross sections of the anodic films formed at 5 mA cm^{-2} until voltage reached 80, 20 and 5 V shown in Fig. 9 indicate thickness of 120, 32 and 9 nm giving anodization ratios of 1.5, 1.6 and 1.8 nm/V, respectively. Thus, the anodization ratio of the film, that is, the reciprocal of electric field strength, increased with decreasing formation voltage. This indicates that the film formed at a low voltage is grown at low electric field strength. Such low electric field strength during anodic film growth must have a large effect on film properties because most factors of anodic film structure including anion incorporation are controlled by electric field strength. According to our previous study [10,14], the boron content in the film, as well as the ratio of boron-incorporated depth, increases linearly with increasing log of current density and decreasing electrolyte temperature in the case of borate solution. It was shown that the changes in current density and temperature, which were associated with

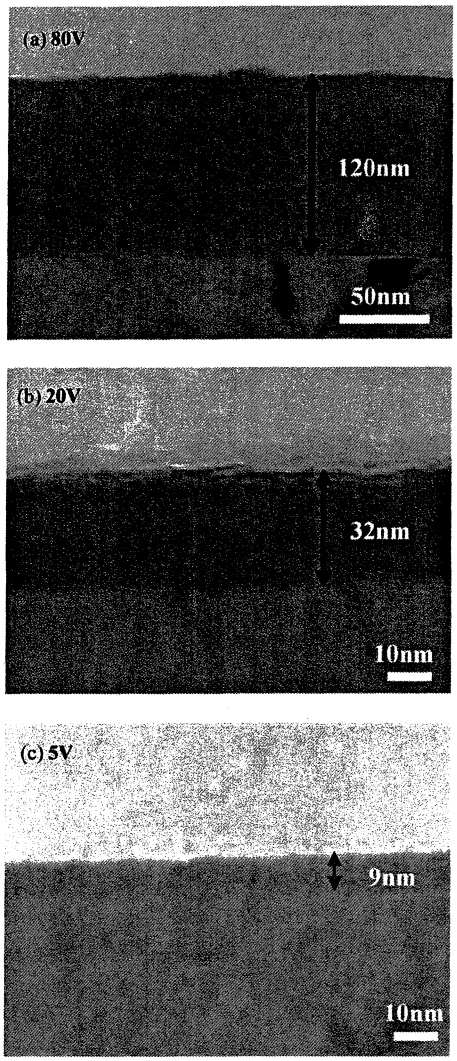

Fig. 9. TEM images of cross sections of anodic films formed at 5 mA cm^{-2} up to: (a) 80 V, (b) 20 V and (c) 5 V indicating the anodizing ratios of 1.5, 1.6 and 1.8 nm/V, respectively.

the change in electric field strength assumed by the thickness change, induced the notable change in electric properties. Namely, the relative permittivity of anodic alumina decreases with increasing anion content, while voltage sustainability increases with increasing anion content [10,14]. However, the reason why electric field strength is lower at the lower voltage range even though anodic current was constant in the present case has been still unresolved.

3.4. Transport number of Al^{3+} and anion content measured by GD-OES

The GD-OES depth profiles shown in Fig. 10 were measured to evaluate the distribution of constituent elements in the film in relation to anodization voltage. To measure the transport number of Al^{3+} ions, Si was used as an immobile marker. An aluminum substrate was pre-anodized in 20% sodium silicate at 0.1 mA cm^{-2} until voltage reached 2 V before anodic film formation in ammonium adipate. The transport number of Al^{3+} ion appears to be 0.44 as indicated by the position of the Si marker (Fig. 10a). The relatively high intensities of C, O and N detected at the outer part of the film suggest the enrichment of organic anion species in contrast to the constant value of Al spectrum intensity. The enrichment of those elements was also observed slightly near the film/substrate interface (Fig. 10a and b). When the formation voltage is 20 V, the spectrum position of the Si marker is spread into the film indicating the transport number of Al^{3+} ions to be 0.30. However, the spectrum peak of the Si marker was detected at the very surface of the film formed at 5 V, indicating the transport number of Al^{3+} ions to be approximately 0.1. The spread of Si in the film formed at 5 V is very low, namely, 0.4 of the film thickness. It is just the same thickness to that of the primal Si containing layer formed at 2 V. This implies that anodic film growth proceeds mostly at the film/substrate interface when the formation voltage is as low as 5 V.

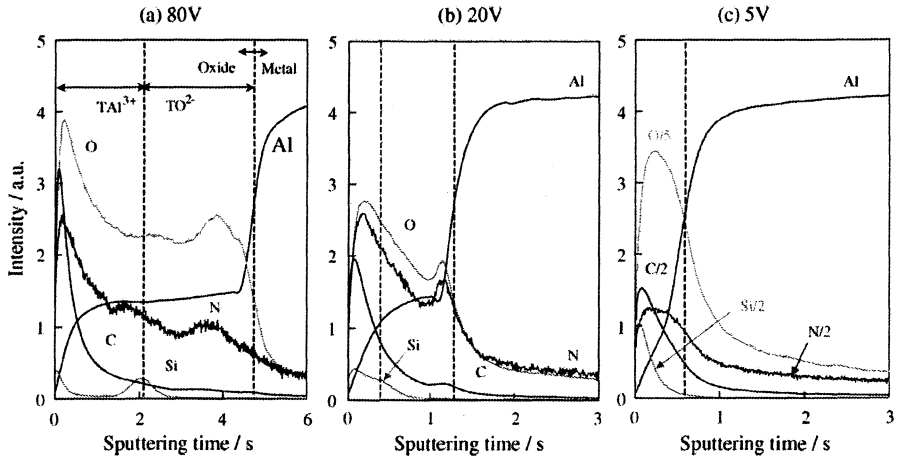

Fig. 10. (a–c) GD-OES depth profiles of constituent elements in the films and estimated transport numbers of Al^{3+} and O^{2-} ions in relation to anodization voltage. Si was used as an immobile marker by pre-anodization of the substrate at 2 V in silicate solution.

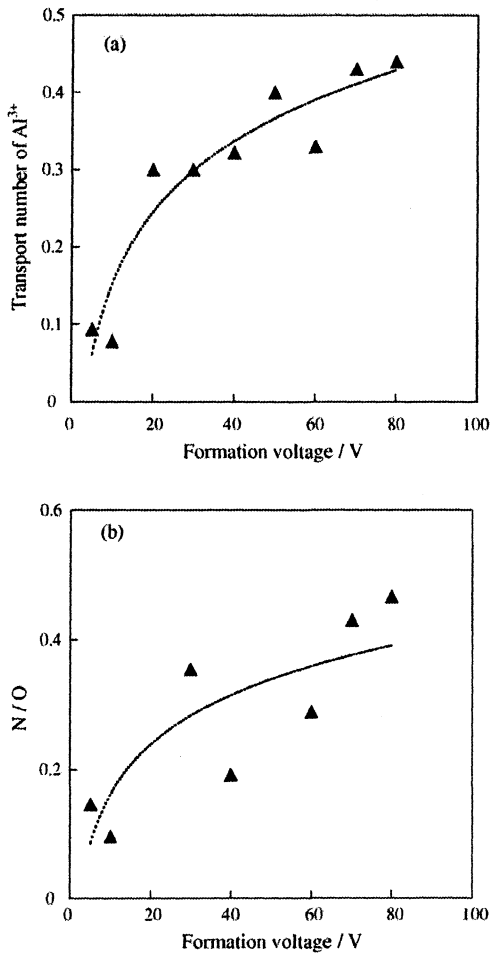

Fig. 11. Relationship of formation voltage with: (a) transport number of Al^{3+} ions and (b) relative electrolyte anion content evaluated from the spectrum intensity ratio of nitrogen to oxygen (N/O).

From the results obtained by the GD-OES measurement, the relationship of formation voltage with transport number of Al^{3+} ions and electrolyte anion content are summarized in Fig. 11. The relative anion content was evaluated from the spectrum intensity ratio of nitrogen to oxygen (N/O). Both the transport number and N/O ratio decreased with decreasing formation voltage particularly at voltages lower than 10 V. These results clearly show that electric field strength gradually decreases with decreasing formation voltage and significantly drops at voltages lower than 10 V.

4. Conclusions

(1) The thickness of the anodic films formed in ammonium adipate solution at an identical voltage decreases with increasing current density and is linearly related to the log of current density. This relation was verified even at voltages lower than 10 V.

(2) The thickness of the films obtained during current decay at a constant anodization voltage is also proportional to the log of the final current density. These results indicate that the film thickness is determined by the final current density during anodization regardless of first anodization process.

(3) Changes in chemical dissolution rate in-depth of the films in acid solution indicate that the films formed in the voltage range from 20 to 80 V are composed of one layer and the films formed at voltages lower than 10 V are composed of two layers having different dissolution rates. However, when the applied voltage was kept constant following current decay, the film becomes one layer because of the inward migration of anions. It is suggested that the outer layer with the higher dissolution rate contains electrolyte anions and the inner layer with the lower dissolution rate consists of pure alumina.

(4) The anodization ratio determined from the TEM cross section of the film formed at 5 mA cm^{-2} at a voltage of 5 V is 1.8 nm/V suggesting a lower electric field strength during anodization compared with that (1.5 nm/V) obtained for the film formed at 80 V, even though anodization is conducted at a constant current.

(5) The transport number of Al^{3+} ions and anion content decrease with decreasing voltage. In particular, they dropped significantly at voltages lower than 10 V indicating a low electric field strength, which acts as an important factor for controlling film properties. Thus, it is clarified that the structure and property of anodic film changes with increasing voltage because of the change in electric field strength in spite of the same current density.

Acknowledgements

Parts of this work were financially supported by grant-in-aids from the Ministry of Education, Science, Sports and Culture, Japan and the Light Metal Education Foundation of Japan.

References

[1] J.A. Davies, B. Domeij, J.P. Pringle, F. Brown, J. Electrochem. Soc. 112 (1965) 675.
[2] J.W. Diggle, T.C. Downie, C.W. Goulding, Chem. Rev. 69 (1969) 365.
[3] G.E. Thompson, Y. Xu, P. Skeldon, K. Shimizu, S.H. Han, G.C. Wood, Philos. Mag. B 55 (1987) 651.
[4] S. Ono, F. Mizutani, M. Ue, N. Masuko, Proceedings of The Electrochemical Society, PV. 2001–22, Pennington, NJ, 2001, p. 1129.
[5] A. Güntherschulze, H. Betz, Z. Phys. 92 (1934) 736.
[6] N. Cabrera, N.F. Mott, Rep. Prog. Phys. 12 (1948) 163.
[7] C.J. Dell'Oca, L. Young, J. Electrochem. Soc. 117 (1970) 1548.
[8] S. Ono, T. Osaka, N. Masuko, Denki Kagaku 64 (1996) 819.
[9] S. Ono, N. Masuko, Proceedings of Processing Materials for Properties, TMS, US, 2000, p. 297.

[10] S. Ono, S. Yamashita, N. Masuko, Proceedings of the Second International Symposium on Aluminium Surface Science and Technology, Benelux Metallurgie, 2000, p. 163.
[11] C. Wada, H. Asoh, S. Ono, Electrochemistry 73 (2005) 145.
[12] A. Dekker, A. Middelhoek, J. Electrochem. Soc. 117 (1970) 440.
[13] S. Ono, N. Masuko, J. Jpn. Inst. Light Met. 43 (1993) 447.
[14] S. Ono, K. Takeda, Proceedings of Eighth International Symposioum on Passivity of Metals and Semiconductors, 2000, p. 931.
[15] S. Ono, H. Ichinose, T. Kawaguchi, N. Masuko, J. Jpn. Inst. Light Met. 40 (1990) 780.
[16] S. Ono, H. Ichinose, T. Kawaguchi, N. Masuko, Corros. Sci. 31 (1990) 249.
[17] S. Ono, M. Saito, H. Asoh, Electrochim. Acta (in press).

Available online at www.sciencedirect.com
SCIENCE DIRECT
ELSEVIER
Electrochimica Acta 51 (2005) 827–833
ELECTROCHIMICA Acta
www.elsevier.com/locate/electacta

Self-ordering of anodic porous alumina formed in organic acid electrolytes

Sachiko Ono *, Makiko Saito, Hidetaka Asoh

Department of Applied Chemistry, Faculty of Engineering, Kogakuin University, 1-24-2 Nishi-shinjuku, Shinjuku-ku, Tokyo 163-8677, Japan

Received 19 November 2004; received in revised form 6 May 2005; accepted 16 May 2005
Available online 8 August 2005

Abstract

New self-ordering porous alumina films were fabricated in organic acid electrolytes. Highly ordered cell arrangements of porous alumina films were realized in malonic acid at 120 V and tartaric acid at 195 V having 300 nm and 500 nm pore intervals, respectively. Self-organization was achieved at the maximum voltage required to induce high-current-density anodization while preventing burning, i.e., an extremely high-current flow concentrated at local points. The cells of the film grown at a high field must be pressed against each other, so that the self-ordering proceeds with the porous layer growth. When the self-ordering of cell arrangement proceeds, the cells became smaller. To improve the regularity of the cell configuration, a low electrolyte temperature and a relatively high electrolyte concentration were effective for maintaining a high-current-density to prevent burning. Surface flatness was an essential factor for self-ordering, however, the surface oxide film produced by electropolishing an aluminum substrate prevented quick pore growth in the organic acids having a low dissociation constant. It is confirmed that electropolishing followed by alkaline treatment was most appropriate as the pre-treatment in preparing flat surfaces.

Keywords: Anodic porous alumina; Self-ordering; High-current-density; Organic acid; Pre-treatment

1. Introduction

Because of its self-ordered and nanosized-pore arrangements in addition to the ease in the control of its pore interval by changing anodization voltage, anodic porous alumina is a promising candidate starting material for the nanofabrication of various devices [1–5]. Except for the pre-texturing methods for an aluminum substrate, such as an imprinting process [6,7] and other nanoindentation processes using scanning probe microscopy [8,9] or focused ion beam lithography [10], highly ordered self-organizing porous alumina is suggested to be obtained only in three types of electrolyte at specified self-ordering voltages: sulfuric acid at 25 V, oxalic acid at 40 V and phosphoric acid at 195 V, giving 63 nm, 100 nm and 500 nm pore intervals, respectively [11–13]. To expand the application field of anodic porous alumina, the fabrication of ordered porous alumina with arbitrary pore intervals is highly required.

Recently, we have found that the homogeneity of cell size and cell configuration increases with increasing formation voltage accompanied by an exponential increase in current density [14]. The self-ordering of the pore arrangement of anodic porous alumina can be achieved at the maximum voltage required to induce high-current-density anodization while preventing "burning", i.e., an extremely high-current flow concentrated at local points leading to local film thickening or electric breakdown at the entire surface accompanying vigorous gas evolution [14,15]. Such a maximum voltage was identical with the previously established self-ordering voltage. In addition, barrier layer thickness as well as cell size of the center of the burnt film is significantly thinner than that of the standard film. Thus, it is suggested that the condition inducing film growth

* Corresponding author. Tel.: +81 3 3340 2732; fax: +81 3 3340 2732.
E-mail address: sachiono@cc.kogakuin.ac.jp (S. Ono).

0013-4686/$ – see front matter © 2005 Elsevier Ltd. All rights reserved.
doi:10.1016/j.electacta.2005.05.058

under the high-current-density, namely the high electric field strength is the key factor determining the self-ordering of porous alumina rather than the self-ordering voltage itself.

With the above background, we have studied the self-ordering conditions of anodic porous alumina grown in solutions of various organic acids, such as citric acid, malonic acid, maleic acid and tartaric acid. In these acid electrolytes, a relatively large cell is available upon application of a high anodization voltage due to their low acidity. These organic acids are all carbonic acid, which is the same to oxalic acid.

Recently, Singubara et al. [16] have reported on the formation of self-ordering porous anodic alumina in a mixture of sulfuric acid and oxalic acid solutions at a voltage between 25 V and 40 V. However, little information is available for the porous alumina formed at a voltage between 40 V and 195 V and higher than 200 V. We have also reported on the formation of self-ordered porous alumina in concentrated phosphoric acid solutions in the voltage range from 160 V to 195 V [17]. In the present paper, we describe the detailed self-ordering behavior realized in malonic acid and tartaric acid solutions at high voltages giving a pore interval from 200 nm to 500 nm.

2. Experimental

High-purity (99.99%) aluminum sheets were pre-treated by four different methods. To compare the effects of surface characteristics on the subsequent anodization behavior: (1) electropolishing in a 4:1 mixture of ethanol and 60% perchloric acid at 10 °C for 3 min; (2) alkaline degreasing in 5% sodium hydroxide at 60 °C for 20 s; (3) chemical polishing in a mixture of 70% phosphoric acid, 25% sulfuric acid and 5% nitric acid at boiling temperature for 60 s; (4) electropolishing followed by chemical treatment in an alkaline mixture of 0.7% NaOH and 1.4% $NaNO_3$ at 60 °C for 30 s. We called the fourth treatment as "alkaline treatment". Anodization was performed at a constant voltage in malonic acid and tartaric acid solutions. The surface morphology of the aluminum substrate after various pre-treatments was evaluated by atomic force microscopy (AFM; Digital Instruments Nano Scope IIIa). Cell arrangement was evaluated by field-emission scanning electron microscopy (FESEM; HITACHI S-4200) of the oxide–substrate interface after removing the anodic film by immersion in a boiling solution of 6% phosphoric acid and 2% chromic acid for 10 min, in which the selective dissolution of the oxide ensued. This is the most simple and accurate method for the evaluation of cell homogeneity. The level of self-ordering can be assessed by an ordering index, namely the fraction of regular hexagonal cells, which neighboring to six cells individually. When self-ordering progresses, the size of the domain consist of only regular hexagonal cells increases.

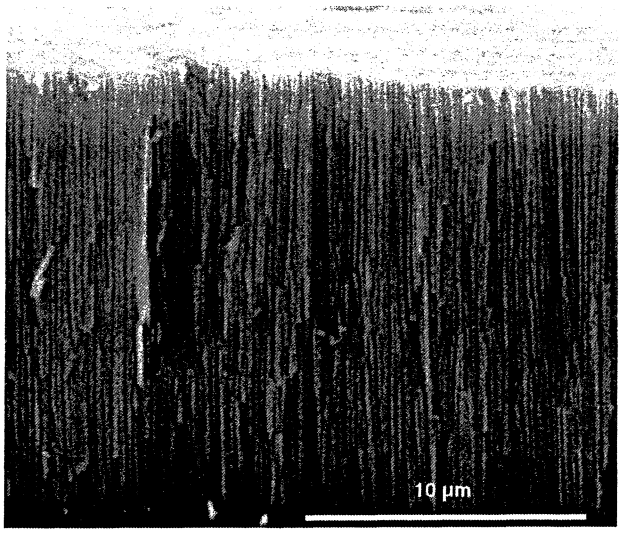

Fig. 1. SEM image of cross-section of film formed in 5 mol dm^{-3} malonic acid solution at 100 V for 1 h at 20 °C.

3. Results and discussion

3.1. Effect of pre-treatment on self-ordering of cell arrangement in malonic acid

Formation of porous anodic alumina in malonic acid solution was carried out on alkaline degreased aluminum substrates at first. As shown in Fig. 1, the cross-section of the anodic porous alumina formed in 5 mol dm^{-3} malonic acid solution at 20 °C on an alkaline degreased specimen at 100 V for 1 h has a regularly arranged cell configuration. However, when the cell arrangements of the anodic aluminas formed on an alkaline degreased substrate and a chemically treated substrate in an alkaline mixed solution after electropolishing were compared, it was found that the latter pre-treatment notably improves the homogeneity of the cell arrangement (Fig. 2). No cell domains consist of only regular hexagonal cells were found in the former case. Therefore, it is clear that surface flatness is an essential factor for self-ordering.

3.2. Effect of pre-treatment on surface morphology of substrate and pore initiation

To improve cell arrangement, the effects of pre-treatments on film structure was examined. Fig. 3 shows current–time transients during the anodization of the aluminum substrates in 5 mol dm^{-3} malonic acid solution at 100 V for 1 h at 20 °C after various pre-treatments. When an aluminum specimen was pre-treated by alkaline degreasing in 5% sodium hydroxide, a large current increase caused by initial pore nucleation immediately occurred. In contrast, such a current increase notably delayed in the case of electropolishing. Chemical polishing and electropolishing followed by alkaline treatment gave a sufficiently quick increase in current indicating quick pore initiation. When the electrolyte temperature was lower

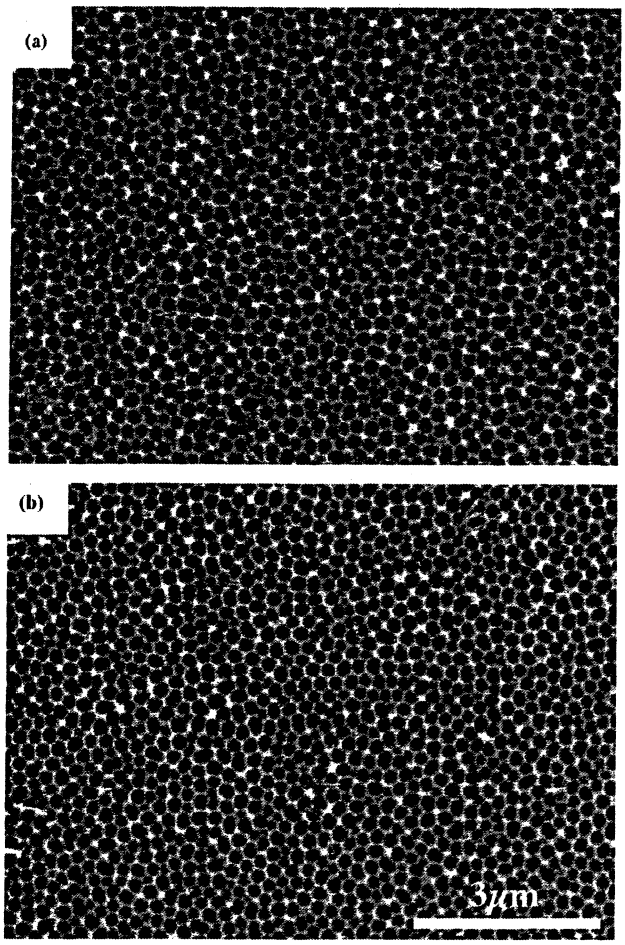

Fig. 2. SEM images of oxide–substrate interface of porous alumina formed in 5 mol dm^{-3} malonic acid at 100 V for 6 h at 20 °C. The pre-treatment was carried out in: (a) 5% NaOH solution and (b) a mixture of phosphoric acid, sulfuric acid and nitric acid solutions.

or the electrolyte concentration was lower than those in the present cases, the current increases were more retarded. Similar phenomena were also observed in tartaric acid. Thus, in some organic acid electrolytes having a low dissociation

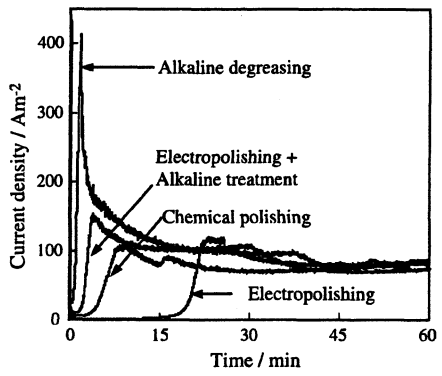

Fig. 3. Current–time transients during anodization of aluminum substrate in 5 mol dm^{-3} malonic acid solution at 100 V for 1 h at 20 °C after various pre-treatments.

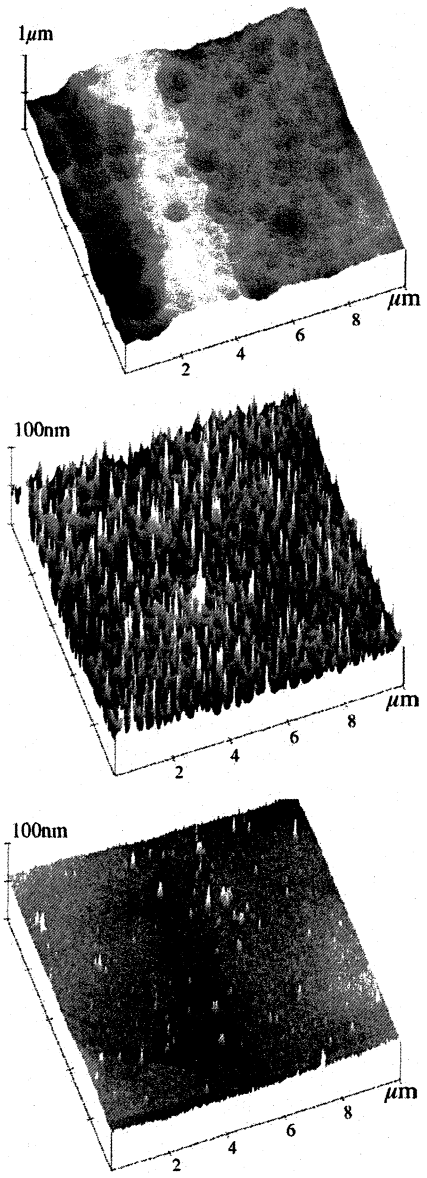

Fig. 4. AFM images of aluminum substrate after various pre-treatments: (a) alkaline degreasing; (b) chemical polishing; (c) electropolishing followed by alkaline treatment. The scale of the z-axis in (a) is 10 times that of the others.

constant, electropolishing could not be adapted because the thin and probably dense oxide film formed by polishing prevented pore initiation because of the low dissolution ability of the electrolytes although the film thickness was as small as approximately 3 nm. However, a flat and smooth surface of an aluminum substrate is essentially required to realize a regular cell arrangement.

The AFM of aluminum surfaces pre-treated by various methods was performed. As shown in Fig. 4a, the alkaline degreasing gave a roughness higher than 2–3 μm caused by the rolling process of aluminum sheets in addition to the presence of etched concaves approximately 0.5 μm. Although the

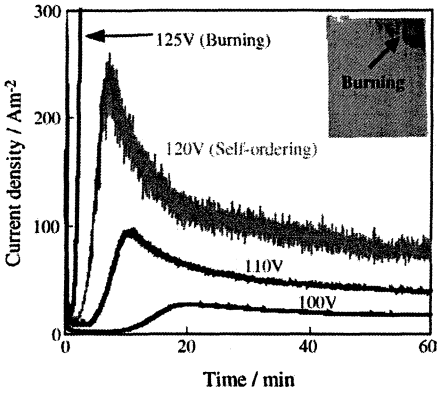

Fig. 5. Current–time curves for anodization in 5 mol dm^{-3} malonic acid at different voltages for 1 h at 5 °C. The SEM image in the panel shows a burnt specimen surface formed at 125 V.

chemical polishing attained a specular surface, the surface flatness was inferior to that of the electropolished surface as indicated in Fig. 4b. Flatness similar to that of the electropolished surface could be achieved by the electropolishing followed by the alkaline treatment, as shown in Fig. 4c. As demonstrated in Fig. 3, this treatment enables the quick current increase followed by a quick pore growth. Therefore, we utilized this pre-treatment in the preceding experiments with the aim of improving the regularity of the cell configuration.

3.3. Confirmation of self-ordering voltage

Concerning the effect of electrolyte temperature, we previously suggested that a low temperature under 5 °C is essential in improving homogeneity to attain high-current-density anodization while preventing burning in the case of phosphoric acid [14]. Therefore, optimum self-ordering voltage was investigated in the electrolyte of 5 mol dm^{-3} malonic acid at 5 °C by applying different voltages. Fig. 5 shows the dependence of current density on formation voltage. Current density increased with increasing formation voltage. The oxide film obtained was opaque and golden. At 125 V, current density markedly increased followed by the formation of a dark area at the edge of the specimen shown in the frame as a SEM image. The oxide film formed by burning became black because of the local thickening of the film. As we reported previously [15], a burnt porous film formed in phosphoric acid or malonic acid exhibits a highly ordered cell arrangement, which is induced by a high-current-density resulting in high electric field [14,15]. Therefore, we performed anodization at the critical voltage just below that for burning, i.e., a self-ordering voltage of 120 V in this electrolyte to maintain stable and uniform growth of anodic porous alumina.

SEM images of the cell arrangement of the aluminum specimens after removal of porous alumina formed in 5 mol dm^{-3} malonic acid solution at 5 °C are shown in Fig. 6 in relation to the effects of anodization time and burning.

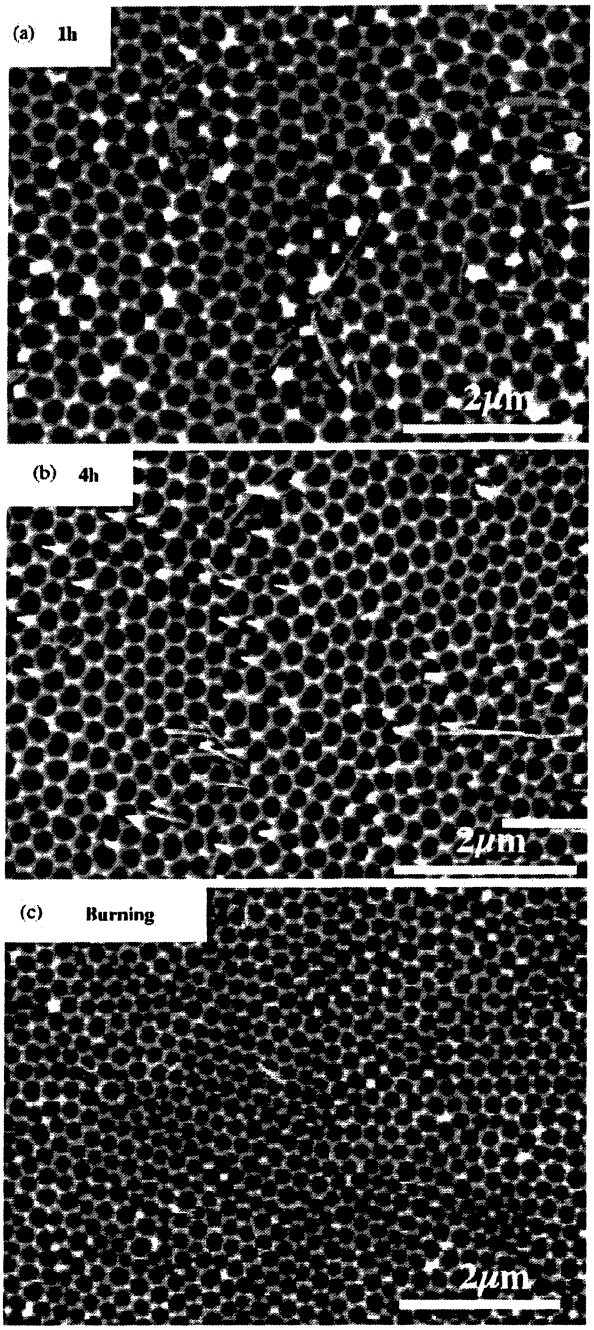

Fig. 6. SEM images of cell arrangement of aluminum specimens after removal of porous alumina formed in 5 mol dm^{-3} malonic acid solution at 5 °C, demonstrating the effects of anodization time and high-current-density; (a) 1 h; (b) 4 h; (c) a burnt spot indicated in the panel of Fig. 5. Aluminum pillars are found in (b) at the domain boundaries because this SEM image was taken from an inclined angle.

Domains of ordered cell arrays were clearly found in the film formed for 1 h (Fig. 6a), which was much superior to that formed at 20 °C, as shown in Fig. 2. Furthermore, the homogeneity of the cell configuration improved after prolonged anodization (Fig. 6b), as described in previous studies

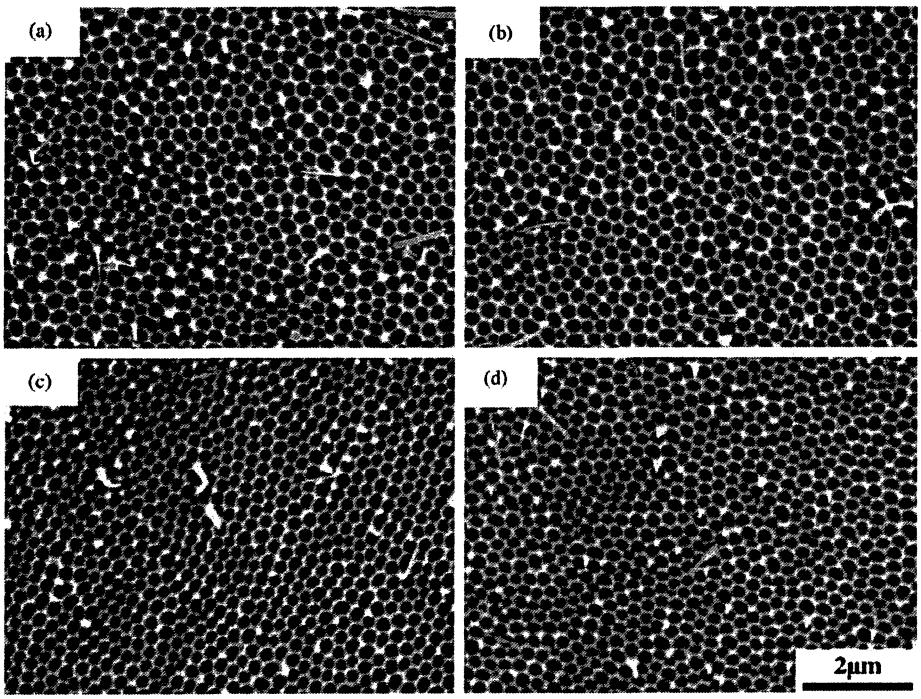

Fig. 7. SEM images of cell arrangement of aluminum specimens after removal of porous alumina formed in: (a) 2 mol dm^{-3}; (b) 3 mol dm^{-3}; (c) 4 mol dm^{-3}; (d) 5 mol dm^{-3} malonic acid solutions at 120 V for 6 h at 5 °C demonstrating the effect of electrolyte concentration.

[12,14], namely the domain size increased with increasing anodization time. Since the SEM image in Fig. 6b was taken from a declined angle fine aluminum pillars are distinguishable between cell junctions. They are necessarily formed at the fourth or fifth points of cell junctions but not at the regular triple points of adjacent hexagonal cells, namely the pillars were formed at irregular cell junctions and at the domain boundaries. Similar to the films formed in phosphoric acid, the burnt spot shown in the panel of Fig. 5 indicated highly ordered cell arrangements (Fig. 6c), which is caused by high electric field associated with high-current-density [14,15,17].

3.4. Effect of electrolyte concentration

The SEM images in Fig. 7 indicate the effect of electrolyte concentration on cell configuration. Anodic films were individualy formed in malonic acid solutions of different concentrations of 2 mol dm^{-3} to 5 mol dm^{-3} at 120 V for 6 h at 5 °C. With increasing electrolyte concentration up to 4 mol dm^{-3}, cell ordering improved as clearly shown in Fig. 7c. The ordering indices were approximately 30 for (a and b), 71 for (c) and 66 for (d). This can be explained by the higher current density consumed during anodization in the concentrated electrolyte. However, the ordering of the cell configuration became inferior when electrolyte concentration increased to 5 mol dm^{-3}. This seems to be partly caused by the high viscosity of the concentrated 5 mol dm^{-3} electrolyte used.

3.5. Self-ordering of anodic porous alumina formed in tartaric acid solution

Current–time curves obtained by anodization in 3 mol dm^{-3} tartaric acid at different voltages for 1 h at 5 °C are shown in Fig. 8. When formation voltage increased, current density increased. When the formation voltage reduced 197 V, burning occurred followed by the occurrence of an extremely high-current-density. SEM image of the burnt specimen surface formed at 197 V revealed a predominant film growth along with rolling lines, as shown in the panel of Fig. 8.

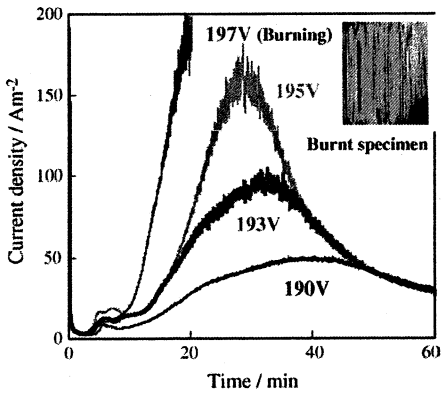

Fig. 8. Current–time curves for anodization in 3 mol dm^{-3} tartaric acid at different voltages for 1 h at 5 °C. The SEM image in the panel shows the burnt specimen surface formed at 197 V.

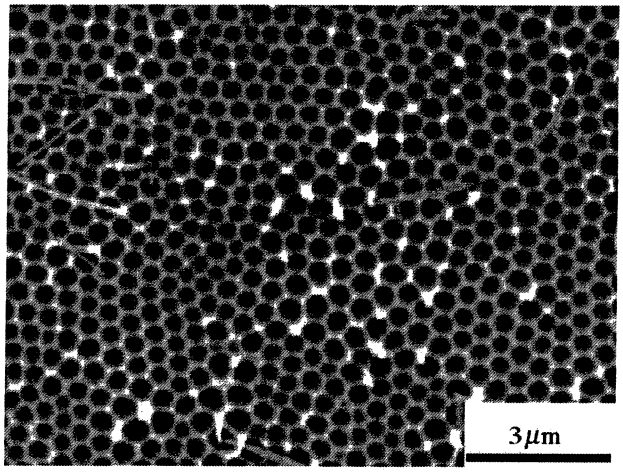

Fig. 9. SEM image of self-organized cell arrangement of aluminum specimens after removal of porous alumina formed at 195 V in 3 mol dm^{-3} tartaric acid solution at 5 °C for 35 min. Long aluminum fibers were formed at irregular cell junctions.

When the cell arrangement was verified by SEM, the high self-organization of the cell arrangement was observed in the film (Fig. 9) formed at the maximum voltage of 195 V for preventing burning, i.e., a high electric field in tartaric acid solution. This self-ordering behavior was similar to those observed in the other acid solutions, such as malonic acid and in previously reported self-organized electrolytes [14].

3.6. *Mechanism and confirmed conditions of self-ordering of anodic porous alumina*

Thus, new self-ordering conditions were confirmed in organic acid electrolytes using the previously suggested mechanism of anodization at a high electric field at a barrier layer [14,15,17]. The electric field strength is an impressed voltage per unit thickness of the oxide layer. According to the classical theory of ionic conduction at the high field strength

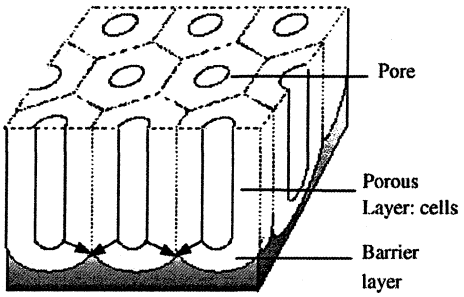

Fig. 10. Honeycomb model structure of anodic porous alumina. Arrows indicate a force generated by rapid oxide growth associated with high-current flow at the barrier layer, which induces a compressive force between cell boundaries.

for the anodic barrier film grown on various metals [18,19], the film thickness of each metal is inversely proportional to the logarithm of ionic current when the film is formed up to the same voltage. Thus, it is indicated that the log of current density $\log i$ is proportional to the electric field strength E, i.e., the formation voltage/film thickness ratio at the barrier layer. As we reported earlier, the high electric field strength E at the barrier layer of porous films is a strong controlling factor of the self-ordering [14,15,17].

Fig. 10 indicates a honeycomb model structure of anodic porous alumina. It has to be bare in mind that the porous oxide layer is only formed at the bottom of the barrier layer as a result of inward migration of oxygen ions associated with the oxide dissolution at the top of the barrier layer under the certain electric field. When a current density is high, rapid oxide growth induces a compressive force at the barrier layer between each cell boundary as shown in arrows in Fig. 10. Therefore, the bottom of cells grown at the barrier layer under a high field must be pressed against each other, so that the self-ordering proceeds with the growth of porous film.

Fig. 11 illustrates the schematic model of the self-organization of the cell arrangement under a high-current-density, i.e., a high electric field compared with the case of a

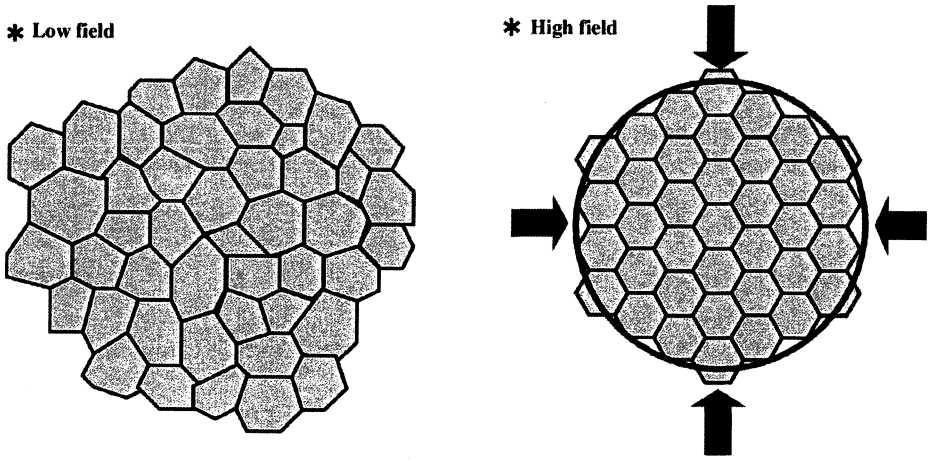

Fig. 11. Schematic representation of self-organization of cell arrangement at high-current-density, i.e., high electric field.

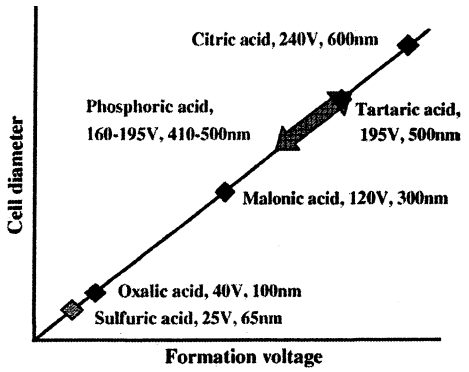

Fig. 12. Result view of self-ordering voltages and corresponding cell diameters reported until now.

low electric field. Therefore, the bottom of cells grown at the barrier layer under a high field must be pressed against each other, so that the self-ordering proceeds with the growth of porous film. When the self-ordering of cell arrangement proceeds, the cells become smaller [14,15] although the applying voltage is maintained to be the same, as it is also shown in Fig. 7. This is because of a high electric field that produces a thinner barrier layer and smaller cells.

The self-ordering voltages reported until now and the corresponding cell diameters are summarized in Fig. 12. In addition to the conventional self-ordering conditions formed in sulfuric, oxalic and phosphoric acid solutions, new self-ordering conditions realized in citric acid [15], concentrated phosphoric acid [17], malonic acid [20] and tartaric acid solutions are shown. Further, we have reported the self-ordering conditions of anodic porous alumina formed in a mixture of sulfuric acid and malonic acid solutions in the voltage range from 25 V to 195 V [21]. The details of these conditions will be published elsewhere.

4. Conclusions

New self-ordering porous aluminas having 300 nm and 500 nm pore intervals were fabricated in organic acid electrolytes, such as malonic and tartaric acid solutions. Each self-ordering voltage was observed as the maximum voltage required for maintaining a high-current-condition in the entire specimen area in the electrolytes used, while preventing an extremely high-current flow at a local spot, which leads to burning. To improve the regularity of the cell configuration, a low electrolyte temperature and a relatively high electrolyte concentration were effective for maintaining a high-current-density while preventing burning. In addition, excellent surface flatness and evenness, which were crucial to achieve the linear growth of pores, were attained by the alkaline treatment after electropolishing. Therefore, it is concluded that the self-ordering of arbitrary pore intervals can be realized by choosing an adequate electrolyte and electrolytic conditions at the appropriate formation voltage required for maintaining a high-current condition, i.e., a high electric field, as we suggested in our previous papers [14,15,17].

References

[1] S. Shingubara, O. Okino, Y. Sayama, H. Sakaue, T. Takahagi, Solid State Electron. 43 (1999) 1143.
[2] T. Iwasaki, T. Motoi, T. Den, Appl. Phys. Lett. 75 (1999) 2044.
[3] Y. Kanamori, K. Hane, H. Sai, H. Yugami, Appl. Phys. Lett. 78 (2001) 142.
[4] X. Mei, D. Kim, H.E. Ruda, Q.X. Guo, Appl. Phys. Lett. 81 (2002) 361.
[5] H. Asoh, M. Matsuo, M. Yoshihama, S. Ono, Appl. Phys. Lett. 83 (2003) 4408.
[6] H. Masuda, H. Yamada, M. Satoh, H. Asoh, M. Nakao, T. Tamamura, Appl. Phys. Lett. 71 (1997) 2770.
[7] H. Asoh, S. Ono, T. Hirose, M. Nakao, H. Masuda, Electrochim. Acta 48 (2003) 3171.
[8] H. Masuda, K. Kanezawa, K. Nishio, Chem. Lett. 31 (2002) 1218.
[9] S. Shingubara, Y. Murakami, K. Morimoto, T. Takahagi, Surf. Sci. 532–535 (2003) 317.
[10] C.Y. Liu, A. Datta, Y.L. Wang, Appl. Phys. Lett. 78 (2001) 120.
[11] H. Masuda, K. Fukuda, Science 268 (1995) 1466.
[12] H. Masuda, F. Hasegawa, S. Ono, J. Electrochem. Soc. 144 (1997) L127.
[13] H. Masuda, K. Yada, A. Osaka, Jpn. J. Appl. Phys. 37 (1998) L1340.
[14] S. Ono, M. Saito, M. Ishiguro, H. Asoh, J. Electrochem. Soc. 151 (2004) B473.
[15] S. Ono, M. Saito, H. Asoh, Electrochem. Solid State Lett. 7 (2004) B21.
[16] S. Shingubara, K. Morimoto, H. Sakaue, T. Takahagi, Electrochem. Solid State Lett. 7 (2004) E15.
[17] S. Ono, N. Kato, M. Saito, H. Asoh, The Electrochemical Society Proceedings Series, Pennington, NJ, in press.
[18] A. Güntherschulze, H. Betz, Z. Phys. 92 (1934) 367.
[19] N. Cabrera, N.F. Mott, Rept. Prog. Phys. 12 (1948) 163.
[20] M. Saito, H. Muto, H. Asoh, S. Ono, 204th Meeting of Electrochemical Society, Orlando, USA, Oct 12–16, 2003 (abstract 30).
[21] S. Tamura, H. Asoh, S. Ono, 111th Meeting of Surface Finish Society of Japan, Matsushima, Japan, September 13, 2004, p. 121 (abstracts).

「溶射技術」第26巻／第２号　別刷

日本溶射協会秋季大会受賞論文集

論文賞

超音速フリージェットPVDによる金属膜の形成と密着性評価

湯本　敦史・廣木　富士男・塩田　一路・丹羽　直毅

2007年１月

工学院大学工学部 機械システム工学科

論文賞

超音速フリージェットPVDによる金属膜の形成と密着性評価

湯本　敦史・廣木　富士男・塩田　一路・丹羽　直毅
工学院大学工学部 機械システム工学科

1　はじめに

現在，構造材料・機能材料を問わずコーティング技術が材料の特性の向上，新機能の開発において重要な材料技術の一つであるとの位置付けが認知されつつある。

コーティング技術は基材に不足する特性を皮膜により補完する技術であり，必要諸特性をコンパクトな複合体で実現することが可能であるが，総てのコーティング技術に共通する課題は，皮膜特性の向上と高い界面強度を確保し基材との剥離を防ぐことである。この問題点の解決に向け，さまざまな角度からのアプローチが試みられており，半導体，MEMS等の機能材料の分野では従来からある固定観念に囚われない柔軟な発想を取り入れた新規のプロセスを開発することで，多くのブレークスルーを達成し[1]，さまざまな製品として工業化に寄与している。

翻って，構造材料の分野に目を向けてみると，Cold Spray[2] やショットコーティング[3] などのいくつかの新しいプロセスが提案されてはいるが，構造材料の分野におけるコーティング技術の研究や工業化はごく限られた分野のみ突出しており，コーティング技術が本来持つ可能性を勘案すると必ずしも幅広い適用用途であるとは言い難い。

近年，構造材料に対し高い成膜速度で良好な皮膜特性および密着性を有する皮膜が得られるプロセスが模索されている。しかし，高い成膜速度を有する既存のコーティング技術には，個々のプロセスに起因する種々の技術的課題や制約が存在し，次世代コーティングとして高い性能を達成する新しい原理によるコーティング法の開発が切望されている[4]。

著者らは，高い成膜速度で緻密な皮膜形成を達成する新しいコーティング技術として，超音速フリージェットPVD（Supersonic Free-Jet PVD; SFJ-PVD）を提案・開発している[5]。本法は，不活性ガス雰囲気中で皮膜となる原料を加熱蒸発させることにより生成されるnmサイズの粒子（ナノ粒子）を超音速のガス流により加速，基板上にナノ粒子を堆積させることにより皮膜形成させる新しい原理による技術である。

本法を用い，膜厚数百 μmのTiおよびAl金属膜[6]，TiとAlのナノ粒子を基板上で混合させることにより，TiAl金

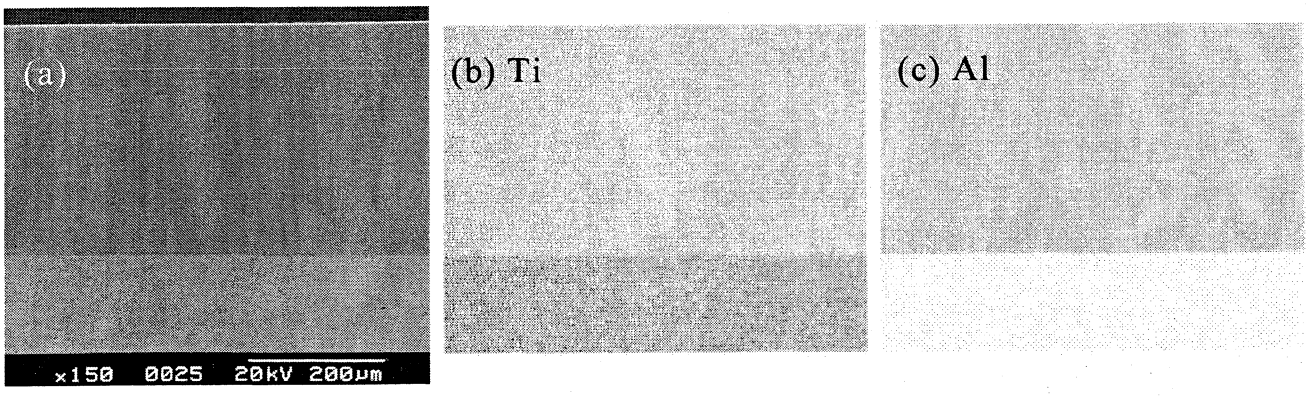

(a) SE像　(b) Tiマップ　(c) Alマップ

図1　Ti基板上に成膜させたTiAl膜断面のSEM-EDS写真

属間化合物をその場合成させた皮膜[7]，本法に活性金属-プラズマ反応[8)~13)]を組み込み，Ti/TiN膜[14]の形成に成功している。図1[15]はTi基板上にTiとAlのナノ粒子を1：1の割合で混合，形成させたTiAl膜断面写真である。図1からTi基板上に約320 μ mmの膜厚の緻密な皮膜が形成されていること，また，同軸対向噴流自励振動型フルイディックミキサー[16]を本PVD装置に取り付けることにより，TiとAlのナノ粒子を均一に混合させることが可能でありことが明らかとなっている[17]。

一般的に高い成膜速度を有する成膜法による皮膜では成膜プロセスが起因した積層組織と呼ばれる皮膜組織を呈することや，膜中のき裂，空隙の存在により膜特性の不足が懸念されている。図1および既報の研究成果は，本法が高い成膜速度と緻密な膜形成を両立すること，および金属，金属間化合物，窒化物セラミックスなど幅広い素材の成膜に対応できることを示しており，新しいコーティング技術として本法の優れた可能性を示唆している。

本稿では，超音速フリージェットPVDの概略と，新しいコーティング技術法において最重要検討課題の一つである膜の耐剥離性に関する基礎的検討として金属膜の密着性について報告し，本法の特徴を示す。

2　超音速フリージェットPVD

図2に超音速フリージェットPVD装置の概略図を示す。本装置は二つのナノ粒子生成室と一つの膜形成室，合計三つのチャンバおよび排気システムで構成されている。各ナノ粒子生成室は膜形成室と搬送管によって連結されている。あらかじめすべてのチャンバを真空排気し，その後チャンバ内に不活性ガスを導入する。不活性ガス雰囲気に置換させたナノ粒子生成室内では，膜素材となる材料の加熱による蒸発およびそれにともないナノ粒子の生成が行われる。

生成室1（図2右下のチャンバ）は抵抗加熱方式，生成室2（左のチャンバ）はアーク加熱方式を採用している。抵抗加熱方式は加熱量の制御性に優れ，アーク加熱方式は高融点の素材を蒸発させることが可能である。

各々の生成室で生成させたナノ粒子は，生成室と膜形成室（右上のチャンバ）の差圧により発生するガスの流れにより搬送管を通じ膜形成室内に搬送される。搬送管の先端にはガスの流れを超音速に加速する超音速ノズルが接続されており，ナノ粒子は高速に加速されたガスの流れによって基板上に堆積され，基板を固定しているX-Yステージの移動により，任意のパターンに皮膜を形成する。ノズルによって加速されたガス流はノズル内の急

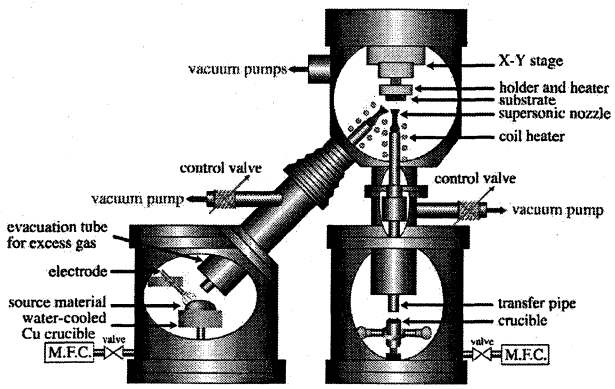

図2　超音速フリージェットPVD装置概略図

激な断熱膨張によりガス温度が低下，ガス流速の低下を招く。そのため，本装置ではノズル外周にヒータが設けられており，ノズル内のガスを間接加熱することでガス温度を制御している。

また，生成室内で粒子が滞留することにより粒子の肥大化が起こる。そこで，本装置には生成室内で搬送管に吸い込みきれないガスや粒子を排出するための余剰粒子排除機構が設けられており，搬送される粒子の粒径制御を行っている。

ナノ粒子を搬送するガスとしてはHeを選択している。その理由は，He雰囲気下で生成するナノ粒子の粒径分布が他の不活性ガスの場合に比べもっとも小さいこと[18]，さらに他の不活性ガスと比較して音速がもっとも速いためである。

使用する超音速ノズルは，大別すると6種類のノズルについて検討しており，当グループでは以下のような名称で区別している。

・一次元矩形ノズル
・一次元軸対称ノズル
・二次元（矩形）ノズル
・軸対称ノズル
・ベル形矩形ノズル
・ベル形軸対称ノズル

圧縮性流体力学の一次元流れの基礎式[19),20)]を用い，任意に決定したスロート部の面積とノズル長さのノズルでノズル断面が矩形のものを一次元矩形ノズル，ノズル断面が円形のものを一次元軸対称ノズルと称している。

二次元ノズルと軸対称ノズルは，特性曲線法を用いて設計したノズルである。ベル形ノズルは，一次元ノズルを放物線近似法により特性曲線法を用いて設計したノズルに近い形状[21]に改良したノズルである。

以上のノズルの設計には，設計したいノズルのタイプ，

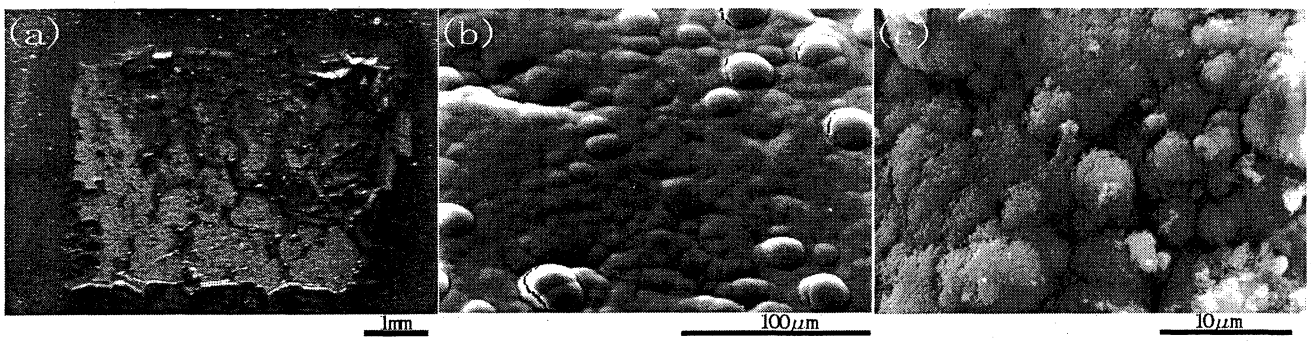

(a) 肥大化した粒子により皮膜は黒色を呈し，皮膜に無数のき裂，剥離が確認される

(b) 皮膜表面拡大写真。10～20μmのき裂を有する肥大した粒子が確認される

(c) 図(b) の肥大粒子表面の拡大写真。図(b) の肥大した粒子はナノ粒子が2～5μm程度に凝集したナノ粒子がさらに凝集して形成されていることが確認される

図3　余剰粒子排除機構が十分機能せずにナノ粒子生成室内のガスの流れが乱れ，生成室内にガスが滞留した場合に得られた皮膜

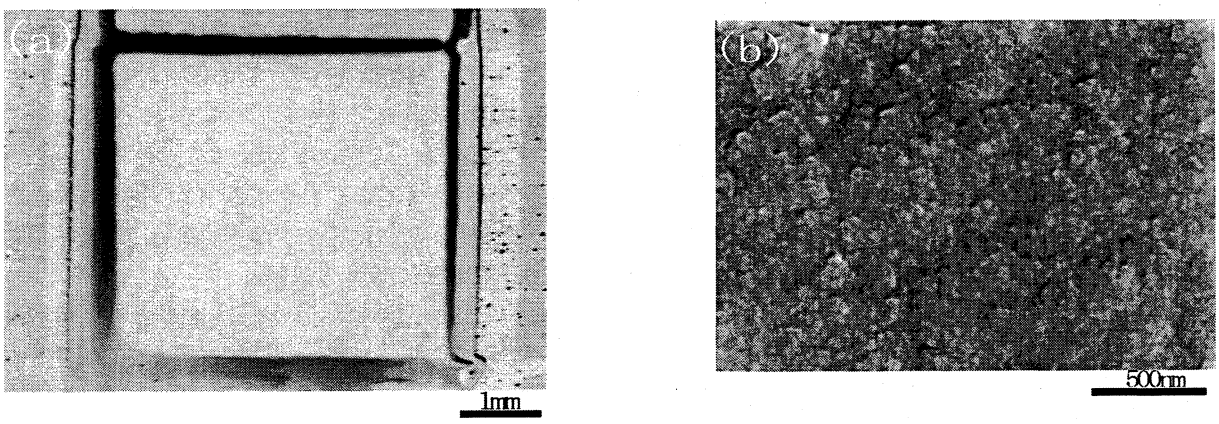

(a) 基板上に生成させたTi皮膜の全体像

(b) Ti皮膜表面の拡大写真。ナノ粒子が凝集せずに成膜されていることが確認される

図4　余剰粒子排除機構を機能させ成膜させた金属光沢を有するTi膜

スロート面積とガス組成を決定することで半自動的にCAD/CAM図面化するノズル設計支援ソフトをすでに開発しており，ノズル製作期間の短縮化と研究を効率的に進められるような体制を整えている。

しかし，ノズルに関しては基礎的な検討段階であり，まだ最適なノズルタイプや形状は明らかとなっていない。研究の途中ではあるが現時点では，マッハ数とスロート後のノズル内での噴流の加速度が膜性状へ影響を及ぼしているようである。また，金属膜と窒化物膜の比較において，金属膜の成膜にはスロート後の長さが比較的長いノズルの方が再現性の良いデータが取れ，窒化物では逆に短いノズルの方が再現性の良いという傾向が得られている。

超音速ノズルは，本法において良好な膜特性を得るもっとも重要なパラメータであることがこれまでの基礎検討で明らかとなっており，詳細なノズル性能の評価とともに本法における最適なノズル選定について今後も継続して検討する。

3　結　果

3.1　成膜因子の検討

3.1.1　粒子径の影響

図3および**図4**は，成膜条件を変えたTi膜の表面写真である。20mm角，板厚1mmのTi基板（JIS-1種純チタン）を使用し，皮膜原料は純Tiを使用した。基板の前処理はアセトン中で1分間超音波洗浄のみ行った。原料のTiは水冷銅ハース上に設置，W電極によるアーク加熱により蒸発させた。超音速ノズルはマッハ3.6の一次元軸対称ノズルを用いた。

本法においては，ナノ粒子生成室内のガスの流れの状態は重要である。すなわち，ナノ粒子生成室内においてガスが滞留した場合と，余剰粒子排出のための真空ポンプを作動させ，搬送管に吸い込みきれないガスおよび粒子が生成室内で滞留することなく排出される場合とでは，皮膜の形態が大きく異なる。

図3に余剰粒子排除機構が十分機能せずにナノ粒子生成室内のガスの流れが乱れ，生成室内にガスが滞留した場合に得られた皮膜の顕微鏡写真を示す。図3(a)では基板上に黒色の粉体状のTiが観察され，また積層時の剥離により一部基板表面の露出が確認される。図3(b)は，黒粉状Tiの高倍率のSEM観察結果である。図3(b)には肥大化した粒子およびクラックの存在が確認される。図3(b)に示した肥大粒子表面をさらに高倍率で観察した結果を図3(c)に示す。これらの写真を比較すると，まず図3(b)より，皮膜は10～20μmm程度の粒子で構成されていることが分かる。その1つの粒子の表面を高倍率で観察したものが図3(c)であるが，図3(b)で1つの粒子と見えるものが，直径2～5μmmの小粒から構成されており，さらにその小粒は1mm以下の直径の微細粒子で構成されていることがわかる。すなわち，図3(b)に見られる肥大粒子は，ナノ粒子が2次的あるいは3次的に凝集して形成されていることが明らかである。

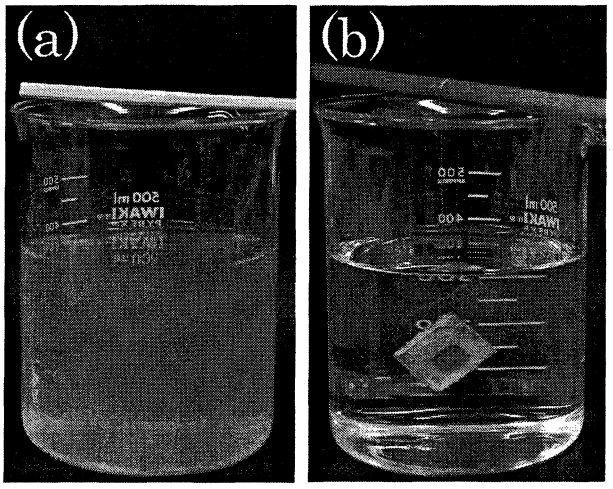

(a) S45C基板のみ　　(b) Ti膜／S45C基板

図5　3%NaCl水溶液に200時間浸漬後の外観写真

これに対し図4(a)は，余剰粒子排除機構を機能させてナノ粒子生成室内のガスの滞留を抑制した場合であり，Ti膜は金属光沢を有している。その表面をさらに高倍率で観察した結果を図4(b)に示す。図4(b)ではこのような高倍率においても図3(b)に見られるような肥大粒子が認められず，ナノ粒子が緻密に積層されていることが確認される。

図3と図4に示したTi皮膜の成膜状況の差異はAl膜を形成させる場合でも同様の傾向を示し，基板温度やノズ

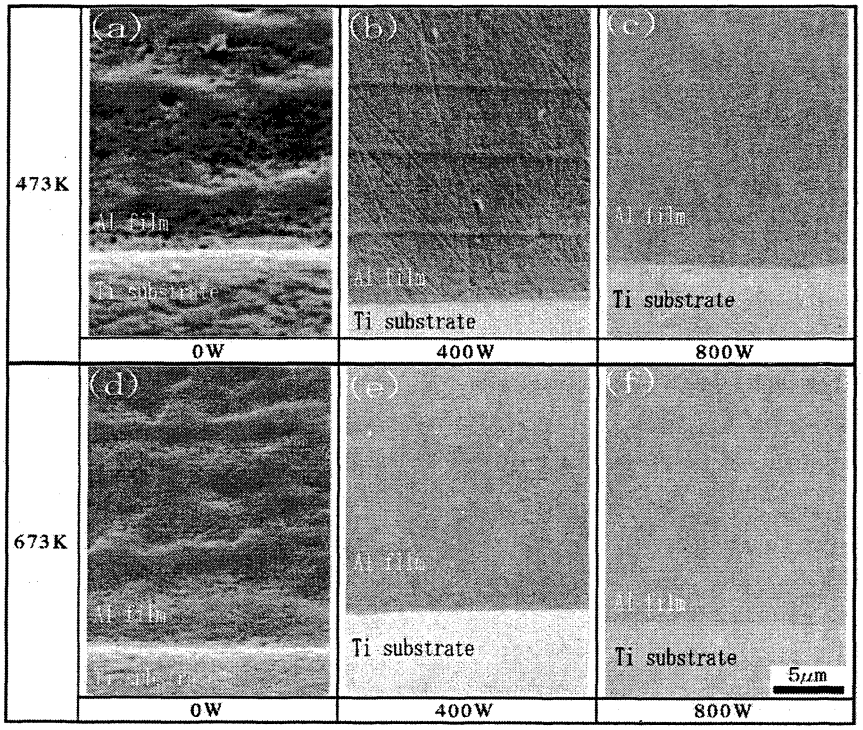

図6　基板温度（473K，673K）とノズル加熱電力（0W，400W，800W）によるAl膜断面SEM写真

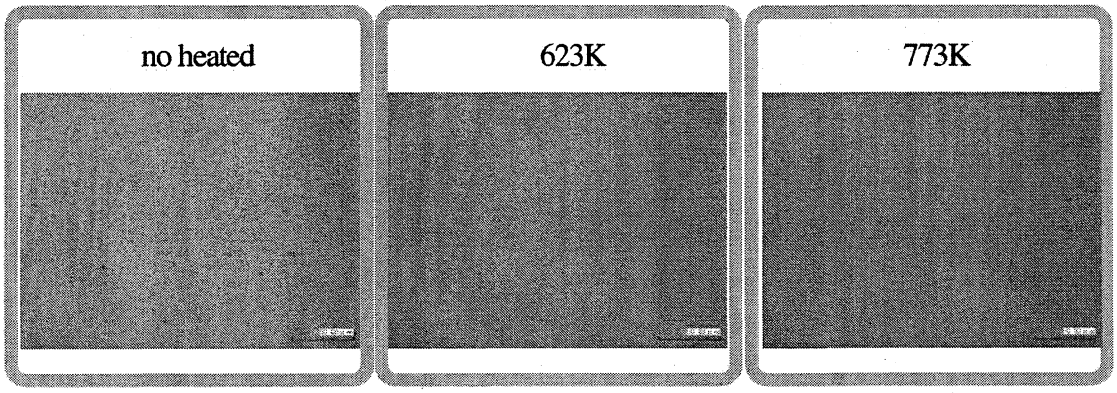

図7　超深度カラー3D形状測定顕微鏡によるAl膜表面写真

ル加熱電力など，他の作成条件を変えても成膜状況は改善されなかった。

また，余剰粒子排除機構を機能させS45C基板上にTi膜を形成させたものを3％NaCl水溶液による200時間の浸漬を行い，膜の緻密さを評価した。Ti膜の成膜条件は，基板温度523K，ノズル加熱電力量900W，ノズルはマッハ4.2の一次元軸対称ノズルを用いた。**図5**に200時間浸漬後の外観写真を示す。図5（a）は，比較のためTiを成膜せずに基板のみを浸漬させたものである。Ti膜/S45C基板を浸漬させた図5（b）はNaCl水溶液に変色が無く基材の腐食も観察されないのに対し，S45C基板のみの図5（a）では基材の腐食により水溶液が変色していることが観察される。浸漬後の試験片断面SEM観察では，S45C基材のみの試験片は基材表面に錆の発生が確認されたが，Ti膜/S45C基板の試験片は基材の腐食は観察されなかった。以上の結果から，本法により膜中にき裂などの欠陥が無い緻密なTi膜の形成が達成されたと判断した。

緻密な皮膜には，肥大化した粒子およびクラックが観察されないことから，本法において肥大した粒子の有無が成膜の可否を決定するもっとも重要な因子であると考えられる。すなわち，余剰粒子排除機構を用いナノ粒子生成室内のガスの滞留を抑制し，粒子の肥大化を防ぐことが金属光沢を有する緻密な皮膜の形成に有効であると考えられる。

3.1.2　基板温度とノズル加熱の影響

図6は，Ti基板上に基板温度を473K，673K，ノズル加熱電力を0W，400W，800Wと変えてAl膜を形成させた場合の断面の状態を観察した写真である。

図6（a）に見られる5～10 μm間隔の基板と平行な縞模様は，試料作製時の積層によるものである。またこの写真には，縞模様の間に直径が0.5～1 μm程度のボイドが認められる。しかし，ノズル加熱電力が400Wの場合は，図6（b）に示すように縞模様が淡くなると同時にボイドもほとんど認められなくなる。ノズルの加熱電力が800Wと増加すると，図6（c）に示すように，縞模様もボイドも認められない。

基板温度が673Kと高くなると，図6（a）と（d）を比較して明らかなように，縞模様が淡くなり，ボイドの平均直径が小さくなる傾向が認められる。また，ノズル加熱電力の増加とともに，（e），（f）に示すように縞模様もボイドも完全に認められなくなる。Ti膜の場合もAl膜と同様の傾向が認められた。

以上の結果より，本法においては，基板加熱温度よりノズル加熱量が皮膜性状に大きく影響を及ぼしていることが明らかとなっている。また，Al膜，Ti膜ともにこれらの条件において膜中のクラックの存在は確認されなかった。

図7はノズル加熱電力量を900W一定，基板加熱のみを無加熱，623K，773Kと変えて，単結晶Si（100）基板上にマッハ3.6-ベル形軸対称ノズルを用いて成膜させたAl膜の表面写真である。表面観察において，基板温度によらずき裂などの欠陥は確認されず，表面粗さ（Ra）は150nm程度であり，金属光沢を有する緻密な皮膜が形成されていることが明らかとなった。また，各成膜条件による膜の結晶性を評価するためXRD分析を行ったが，基板温度によらず特定の面に配向することはなく，多結晶膜となっていることも確認された。

以上の結果は，本法において基板温度に比べノズルを加熱する温度，すなわちガス温度が膜形成に有効に作用していることを示唆しているものと考えられる。

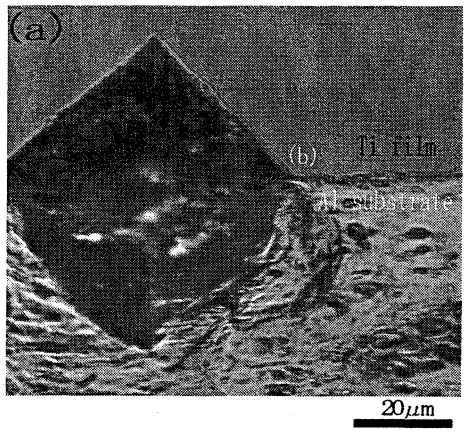

(a) 界面に打ち込まれた圧痕の形状

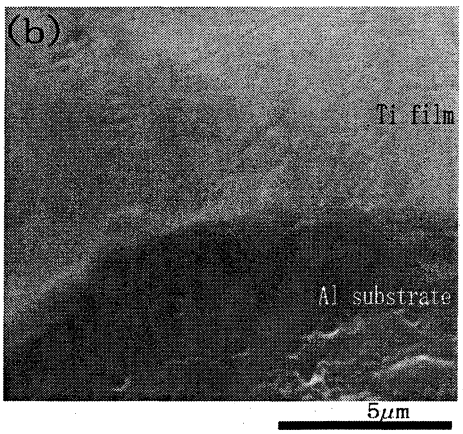

(b) 界面上の圧痕の綾先端拡大写真

図8　Ti膜／Al基板界面にビッカース圧子（荷重4.9N）を打ち込んだ圧痕形状

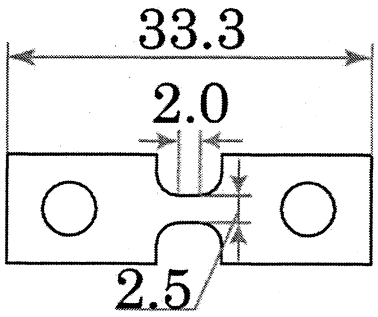

図9　引張試験片形状

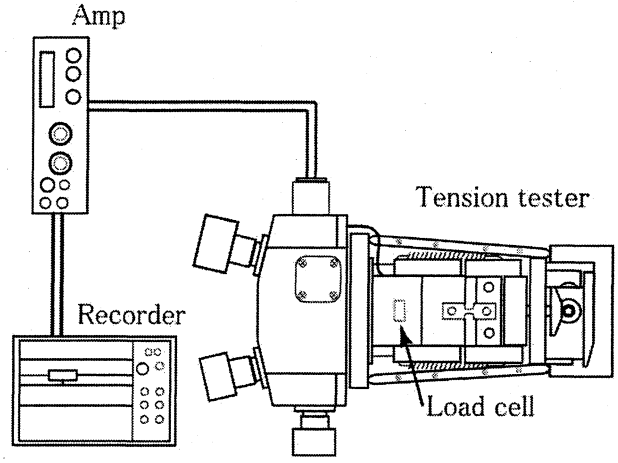

図10　微小引張試験装置概略図

3.2　密着性評価

Al膜/Ti基板，Ti膜/Al基板の界面に荷重4.9Nでマイクロビッカース圧子（対面角136°）を打ち込み，界面を観察した。**図8**（a）は基板温度473K，ノズル加熱電力800Wの条件で作製したTi膜／Al基板界面のビッカース圧痕の写真であり，四角錐圧子の稜先端が打ち込まれた界面にクラックが発生していない。図8（b）は界面における圧痕先端の拡大写真である。図8（b）の高倍写真においてもクラックは発生していないことが確認できる。Al膜/Ti基板においても膜中および界面にビッカース圧子を打ち込んだことによりクラックは発生しなかった。このことはAlおよびTi膜と基材との界面において4.9Nのビッカース荷重に十分耐えられる界面強度を有していることを示すものであり，良好な接合状態にあると考えられる。

また，**図9**に示す引張試験片形状としたS45C基材上にTi膜を形成させ，**図10**に示すSEMステージ上に設けた微小引張試験機により引張試験中の連続観察を行った。成膜はマッハ4.2のベル形軸対称ノズル，基板温度473K，ノズル加熱電力900W，膜厚が80μmとなる条件とした。

図11は破断後の試験片のSEM写真とEDS分析結果である。図11からTi膜は破面近傍まで残存していることが確認でき，試験中の観察からも引張試験による基板の変形にともないTi膜も塑性変形する様子が観察され，Ti膜の基材からの離脱は見られなかった。

Ti膜/Al基板，Al膜/Ti基板の異種界面へのビッカース圧子による打ち込み試験，Ti膜/S45C基板の微小引張試験の結果から，本法によるTiおよびAlの金属膜は良好な密着性を有しているものと考えている。

4　おわりに

超音速フリージェットPVDは，不活性ガス雰囲気中で膜素材を蒸発・生成させたナノ粒子を，超音速のガス流により加速，基材に積層，成膜させる新しいコーティン

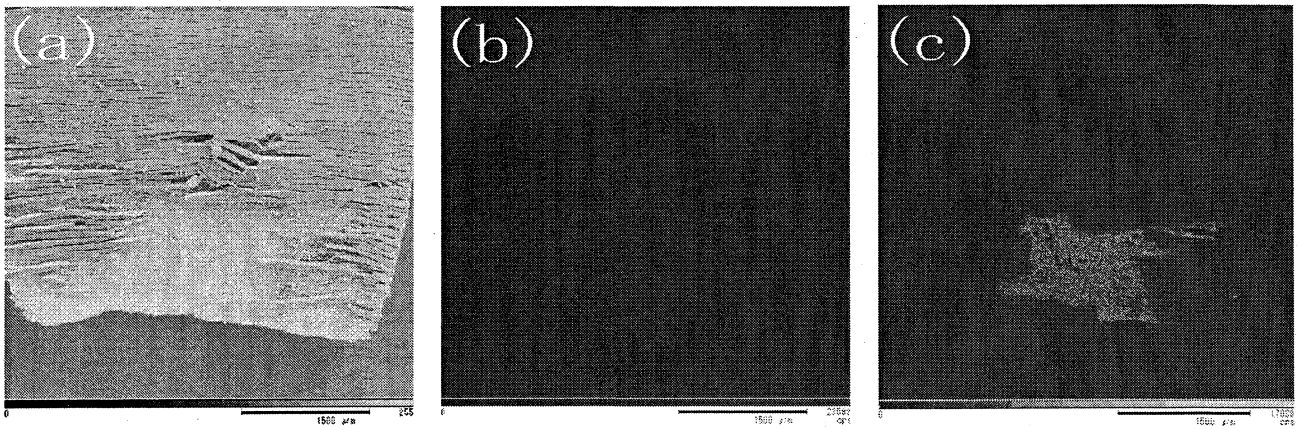

(a) SE像　　(b) Tiマップ　　(c) Feマップ

図11　Ti膜／S45C引張破面近傍のSEM-EDS写真

グ法である。

本法は，ナノ粒子の緻密な積層，蒸発させた原子の高い捕集効率を特徴とし，高い成膜速度で高密度の皮膜を形成させることが可能である。さらに，異種素材のナノ粒子を基板上で物理的に混合させることができるため皮膜素材の自由度が広く，また，皮膜組成を制御し傾斜組成とすることが可能であるなど他のコーティング法に比べ優れた特徴を有している。

本法に関するこれまでの研究の中で，Ti，Al，Cr，Al-Si，Fe-Crなどの緻密な金属膜の形成が可能であることを示し，さらに，TiとAlナノ粒子を基板上でその場合成させたTiAl金属間化合物膜，TiN，TiAlNの窒化物の形成も達成している。また，新しいコーティング法の開発段階において避けては通れない界面の密着性評価に関しては，基礎的評価としてTiおよびAlの金属膜に対しビッカース圧子による打ち込み試験と引張試験において良好な密着性を示すことを明らかとした。

本法におけるナノ粒子の低温基板上での膜形成および化合物のその場合成は，一般的な溶融-凝固過程などと異なるナノ領域の特異な現象との関連も考えられ学術的にも興味深く，また，工業的にも本法の今後の発展を期待している。

謝　辞

本研究は，文部科学省科学研究補助金（若手B 17760586），笹川科学研究助成および工学院大学アドバンストマテリアルセンタ（AMC）の援助により行われた。これらの援助に対し，深く謝意を表する。また，実験に協力して頂いた工学院大学大学院生稲石智氏，佐々木博成氏，清水崇行氏にも謝意を表します。

参 考 文 献

1）例えば，日亜化学工業（株）中村修二，特願平2-288665（1990）.
2）A.P.Alkimov, A.N.Papyrin, V.F.Kosarev and M.M.Shushpanav: U.S.Patent 5,302,414（1994）
3）伊藤義康，須山章子，新藤尊彦，安藤秀泰：日本金属学会誌，65，p443-448（2001）.
4）吉田豊信，まてりあ，40，p.322（2001）.
5）湯本敦史，丹羽直毅，廣木富士男，塩田一路，山本剛久（出願タマティーエルオー株）：特願2004-300122（2004）.
6）湯本敦史，廣木富士男，塩田一路，丹羽直毅，日本金属学会誌，65，p.635（2001）.
7）A. Yumoto, F. Hiroki, I. Shiota and N. Niwa, Surf. Coat. Technol., 169-170, p.499（2003）.
8）宇田雅広，大野悟，日本化学会誌，6，p.862（1984）.
9）宇田雅広，大野悟，表面科学，5，p.426（1984）.
10）宇田雅広，日本金属学会会報，22，p.412（1983）.
11）宇田雅広，化学と工業，36，p.72（1983）.
12）大野悟，宇田雅広，日本金属学会誌，48，p.640（1984）.
13）大野悟，奥山秀男，本間一廣，高木一徳，本庄俊夫，尾澤正也，日本金属学会誌，59，p.408（1995）.
14）A. Yumoto, T. Yamamoto, F. Hiroki, I. Shiota and N. Niwa, Mater. Trans., 43, p.2932（2002）.
15）A. Yumoto, T. Yamamoto, F. Hiroki, I. Shiota and N. Niwa, Trans. Mater. Res. Soc. jpn, 29, p.1889（2004）.
16）廣木富士男，湯本敦史，丹羽直毅，山本圭治郎（出願タマティーエルオー株）：特願2004-173484（2004）.
17）H. Takahashi, F. Hiroki, A. Yumoto and K. Yamamoto: 8th International Symposium on Fluid Control, Measurement and Visualization, CD-ROM（2005）.
18）横山誠二，小久保貞男，斎藤己由，伊藤光允，川上正博：日本金属学会誌，57，p.54（1993）.
19）松尾一泰：「圧縮性流体力学」理工学社（1994）.
20）H.W.Liepmann and A. Roshko（玉田玳）：「Elements of Gasdynamics」，吉岡書店（1960）.
21）木村逸郎：「ロケット工学」養賢堂（1993）.

Materials Science Forum Vols. 492-493 (2005) pp. 341-345
online at http://www.scientific.net

Fabrication of Nanostructure Composites in Functionally Graded Coatings with Supersonic Free-Jet PVD

Atsushi Yumoto[1,a], Takahisa Yamamoto[2,b], Fujio Hiroki[1,c], Ichiro Shiota[1,d] and Naotake Niwa[1,e]

[1]Faculty of Engineering, Kogakuin University, Tokyo 163-8677, Japan

[2]Graduate School of Frontier Sciences, University of Tokyo, Tokyo 113-8656, Japan

[a]a_yumoto@nifty.com, [b]yamataka@k.u-tokyo.ac.jp, [c]at94296@ns.kogakuin.ac.jp, [d]i-shiota@cc.kogakuin.ac.jp, [e]niwa@cc.kogakuin.ac.jp

Keywords: Nanoparticle. Supersonic gas flow. Nano-indentation hardness test. Titanium-aluminides. Aluminum-silicon alloy.

Abstract. Graded Al/AlTi and Al/Al-Si coatings are prepared by depositing nanoparticles with supersonic free-jet PVD (SFJ-PVD). The SFJ-PVD has been developed as a new coating method in which a coating film is formed by depositing nanoparticles with very high velocity onto a substrate. The high velocity of nanoparticles is produced by the supersonic gas flow of inert gas. A smooth, compact and defect-free microstructure is formed both at the interface between substrates and coating films and inside the coating films. The microstructures of Al/AlTi and Al/Al-Si coating films have very fine grain size. Mixing Ti and Al nanoparticles by depositing them onto a substrate produces *in-situ* syntheses of γ-TiAl and α_2-Ti_3Al intermetallic compounds on the substrate. It is confirmed with nano-indentation hardness tester that graded coatings have graded hardness corresponding to the gradation of composition.

Introduction

Aluminum alloys attract much attention due to their excellent mechanical properties, and wide potential application in the fields of transport such as automobiles and aerospace. However, aluminum alloy usually exhibit low heat-resistant and poor hardness. Generally, heat and/or wear resistances are often required only at the surface of the materials. Thus, a coating process is one of the most promising methods to achieve the requirements. However, conventional coating processes generally have following major technical problems; low adhesive strength at the interface, the difficulty of controlling structure and grain size in coating film especially in case of high deposition rate methods and the difficulty to suppress defects such as voids, cracks and columnar boundaries [1].

We developed supersonic free-Jet PVD (SFJ-PVD) [2-4] as a new coating method in which the coating film is formed by depositing nanoparticles onto a substrate at very high velocity. SFJ-PVD provides a high deposition rate and thick film coating. The two evaporation chambers of the SFJ-PVD apparatus make possible to produce two different nanoparticles in the respective chambers and to mix them onto a substrate in the deposition chamber with desired composition by controlling the deposition rates of the nanoparticles respectively. This advantage is very beneficial for fabricating graded-composition coatings.

In this paper, graded Al/AlTi and graded Al/Al-Si coatings on Al alloy substrates are prepared by depositing nanoparticles with SFJ-PVD.

Experimental Procedure

An A1050 aluminum alloy plate with the dimension of 20mm ×20mm×1mm was used as a substrate. Also, pure Ti, pure Si or pure Al were used as evaporation sources.

The schematic diagram of SFJ-PVD is illustrated in Fig. 1, showing the two stages in SFJ-PVD, "gas evaporation" and "vacuum deposition". In the gas evaporation stage, a source material is evaporated to form nanoparticles in an inert gas atmosphere. The nanoparticles are then carried to a substrate with the inert gas through a transfer pipe where a gas flow is generated by the pressure difference between the evaporation and the deposition chambers. The gas flow is accelerated to supersonic velocity (Mach number 3.6) by a specially designed supersonic nozzle joined to the tip of the transfer pipe. In the vacuum deposition stage, the nanoparticles are deposited onto the substrate in the deposition chamber. The evaporation source material of Al was placed in a graphite crucible then heated and evaporated by the surrounding Ta ribbon heater in the evaporation chamber 1. The evaporation source material of Ti or Si was placed in a water-cooled copper crucible then heated and evaporated by arc plasma in the evaporation chamber 2. The substrate was fixed on a stage that was driven in X-Y directions, and the coated area was 7mm square on the substrate in the deposition chamber. The stage and the nozzle are heated by electric resistance heating systems. The temperature of the substrate was measured at a point close to the coated area of the substrate by a thermocouple, and the substrate temperature was controlled. Main control-parameters of the SFJ-PVD apparatus are electric power for evaporation source heating, carrier gas flow rate, electric power for nozzle heater and substrate temperature. Preparation conditions are shown in Table 1. The further experimental details of the deposition technique were reported in previous papers [2-4]. To form graded coating films on the Al050 substrates, we began evaporating only Al in the evaporation chamber 1, and gradually increased the evaporation rate of Ti or Si in the evaporation chamber 2. The composition of the coating film was controlled by electric power for heating applied to each evaporation source.

Cross sections of the coated specimens were observed by SEM equipped with an EDX analyzer. Specimens for the observation were mechanically polished with up to 0.3μm Al_2O_3. The microstructures of the coated specimens were observed by a TEM. Phases of the graded Al/AlTi specimens were identified by XRD. The hardness of the coated specimens was measured using a nano-indentation hardness tester (ENT-1040a) at Elionix Inc. with applied load of 9.8mN.

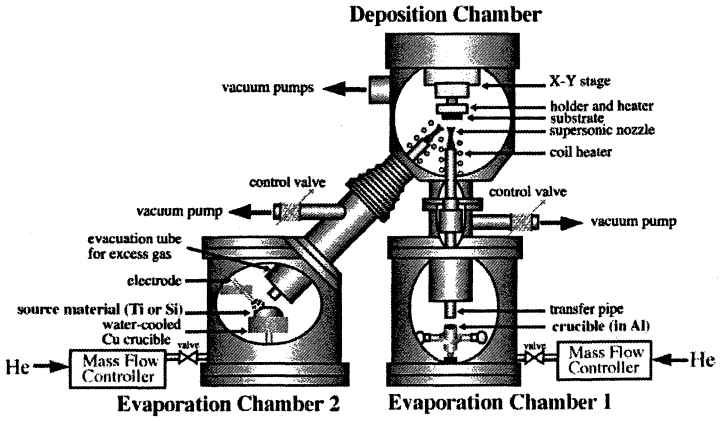

Fig. 1: Schematic diagram of a supersonic free-jet PVD apparatus.

Table 1: Preparation conditions of a graded Al/AlTi film and a graded Al/Al-Si film.

	Al/AlTi		Al/Al-Si	
Evaporation chamber	1	2	1	2
Source materials	Al	Ti	Al	Si
Evaporation power (kW)	4.0 -3.5	0 -0.4	3.8 -3.1	0 -0.4
He gas flow rate (l/min)	7.0			
Substrate materials	A1050			
Substrate temperature (K)	non-heated		523	
Nozzle heater (W)	900			

Results and Discussion

Figure 2 presents SEM images and EDX analysis of the cross sections of the graded Al/AlTi film and the graded Al/Al-Si film. Figures 2 (a) and (c) indicate that smooth, compact, and defect-free interfaces and coating films had formed. No large Ti or Si particles were visible in the specimens. No obvious interface was observed between the A1050 substrate and the graded coating films in Fig. 2 (a) and (c). The EDX in Fig. 2(b) reveals that the coating started with pure Al, the Ti content gradually increased, and the composition was Ti-43.7at%Al at the film surface. Fig. 2(d) reveals that the coating started with pure Al, the Si content gradually increased, and the composition was Al-57.8at%Si at the film surface. Figure 3 shows TEM image of the graded Al/Al-Si coating film. In the figure, some typical grains of Al or Si are indicated. As shown in Fig. 3, nano-meter sized Si phases are dispersed uniformly in the Al matrix. The Si phases in the coating film were nearly spherical with 10nm to 20nm in diameter and uniformly dispersed in the matrix. Those results suggest the SFJ-PVD was able to control the composition of the graded coating film, and to disperse nano-meter sized Si phases in the graded Al/Al-Si coating film. Similar results were obtained in all the coated specimens of Ti, Al, graded Ti/TiAl and graded Ti/TiN films by our previous study.

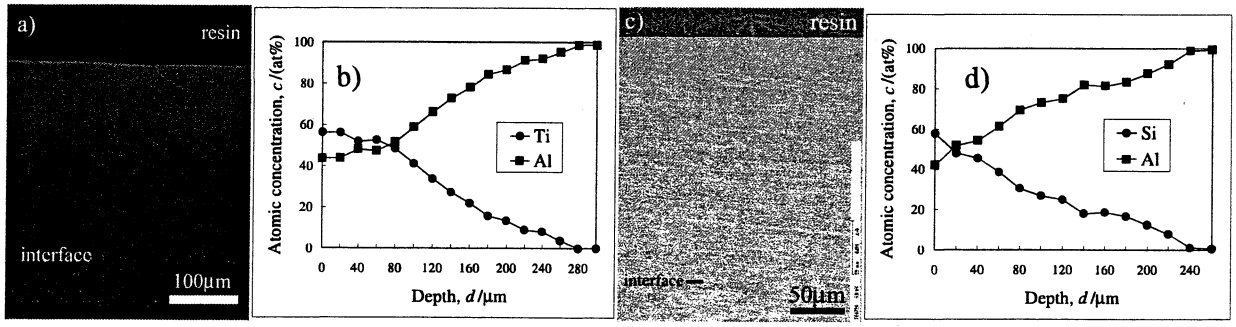

Fig. 2: SEM image and EDX analysis of cross-sections of a) and b) the graded Al/AlTi film on the A1050 substrate, c) and d) the graded Al/Al-Si film on the A1050 substrate

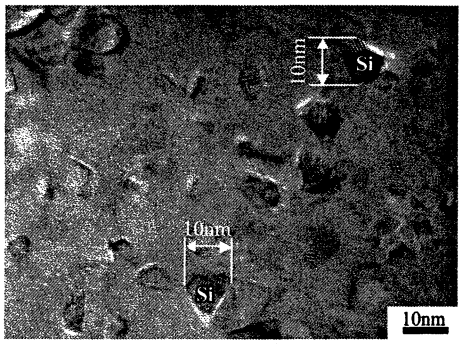

Fig. 3: TEM microstructure of the graded Al/Al-Si coating film.

XRD profiles of the graded Al/AlTi film is provided in Fig. 4. Figure 4 reveals that the γ-TiAl phase and α_2-Ti_3Al phase coexist in the graded Al/AlTi film. It is notable that mixing Ti and Al nanoparticles by depositing them onto the substrate produces *in-situ* syntheses of titanium-aluminides intermetallic compounds on the substrate.

Figure 5 shows the relation between the nano-indentation hardness and the composition of the Al/Al-Si coating film graded from pure Al to Al-57.8at%Si. In Fig.5, the hardness gradually increases from 0.65GPa to 5.9GPa as the Si content increase in the graded composition of the coating film. The nano-indentation hardness of A1050 substrate with the same measuring condition was about 0.62GPa that is almost the same hardness of 0.65GPa of the film near the interface between the substrate and the film. Hardness increase in the Al-Si composites coating film should be due to the strengthening effect of the increase of Si content by the graded coating. Kojima *et al.* [5] reported that the hardness of the Al-20mass%Si, Al-30mass%Si and Al-50mass%Si coating films produced by low-pressure plasma spray process were about 80Hv, 100Hv and 200Hv, respectively. Mori *et al.* [6] reported that the hardness of the Al-20mass%Si and Al-40mass%Si coating films produced by plasma spray process were about 150Hv and 200Hv, respectively. According to the study on the conversion of Vickers hardness into nano-indentation hardness [7] the hardness values of these sprayed Al-Si coating films are much lower than those of the Al-Si coating film with Si phase from 10nm to 20nm in the present study, that might be due to the difference of Si phase size and also of porosity of films. We have succeeded in obtaining compact and thick graded Al/Al-Si coating film with the dispersed nano-meter sized Si phase by the SFJ-PVD. The result in this study suggests this process has excellent potential for the fabrication of nano-composite coatings.

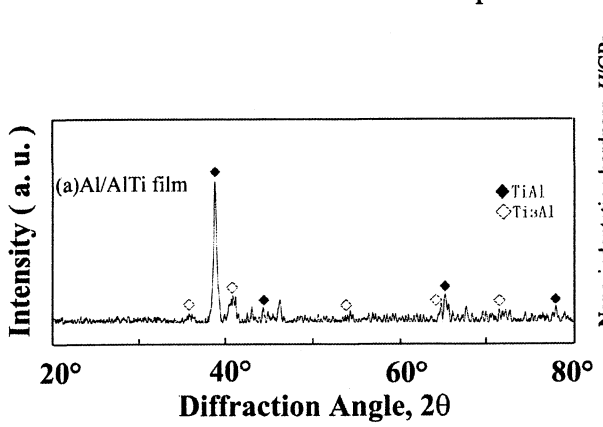

Fig. 4: XRD profiles of (a) the graded Al/AlTi film.

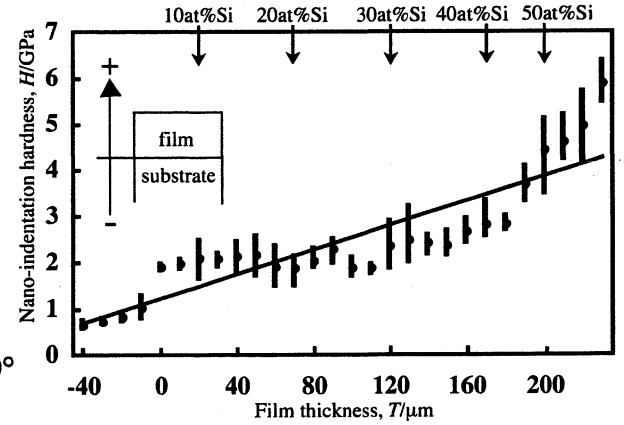

Fig. 5. Relation between the hardness and the composition of the Al/Al-Si coating film.

Conclusions

Graded Al/AlTi and Al/Al-Si nano-composite coatings on A1050 substrates by depositing Al and Ti or Si nanoparticles were produced with the SFJ-PVD. The results obtained are as follows,

(1) By controlling the deposition rate of Al and Ti or Si nanoparticles respectively through the control of evaporation rate in two different evaporation chambers, it is possible to produce the graded Al/AlTi and Al/Al-Si coating films without voids or cracks.

(2) Si phases in the film were nearly spherical with 10nm to 20nm in diameter and uniformly dispersed in the coating film.

(3) Mixing Ti and Al nanoparticles produced *in-situ* syntheses of γ-TiAl and α_2-Ti_3Al intermetallic compounds on the substrate.

(4) Nano-indentation hardness gradually increases from 0.65GPa to 5.9GPa as the Si content in the graded coating film increase from 0 to 57.8 percent.

Acknowledgments

The authors gratefully thank Mr. T. Itoh, and Mr. T. Uematsu of Elionix Co., Ltd. for the nano-indentation hardness test. This work was partly supported by the JFE 21st Century Foundation and the Advanced Materials Center (AMC) of Kogakuin University.

References

[1] A. C. Raghuram and R.F. Bunshah: J. Vac. Sci. Technol. A Vol. 9 (1972), p.1389.
[2] A. Yumoto, F. Hiroki, I. Shiota and N. Niwa: J. Japan Inst. Metals Vol. 65 (2001), p.635.
[3] A. Yumoto, T. Yamamoto, F. Hiroki, I. Shiota and N. Niwa: Mater. Trans., JIM Vol. 43(2002), p. 2932.
[4] A. Yumoto, F. Hiroki, I. Shiota and N. Niwa: Surf. Coat. Technol. Vol. 169-170 (2003), p.499.
[5] Y. Kojima, A. Mebata, M Sakamoto and N. Onaka: J. Japan Thermal Spraying Soc. vol. 24 (1988), p. 21.
[6] H. Mori, K. Nakanishi and H. Tachikawa: J. Japan Inst. Metals Vol. 65 (2001), p. 707.
[7] K. Miyahara, N. Nagashima, S. Matsuoka and T. Ohmura: Trans. Jpn. Soc. Mech. Eng. Vol. A64 (1998), p. 2567.

FLUCOME '05 Chengdu

Mixing chamber utilizing oscillation phenomena of coaxial impinging jets

Hisanobu TAKAHASH [1], Fujio HIROKI[2], Atushi YUMOTO[3] and Keijiro YAMAMOTO[4]

1. Graduate Student, Kogakuin University Telephone and Fax number: 81-426-28-4483
e -mail: am04031@ns.kogakuin.ac.jp

2. Kogakuin University e-mail: at94296@ns.kogakuin.ac.jp

3. Kogakuin University e-mail: a_yumoto@nifty.com

4. Kanagawa Institute of Technology e-mail:yamakei@we.kanagawa-it.ac.jp

Abstract

The aim of our product work to confirm the mixing method of two fluids utilizing the oscillation phenomena of two opposing jets in mixing system and to investigate using it. In the case of open space, the conditions suitable for the mixing of two jets are specified as Reynolds number, rectangular nozzle aspect ratio, rectangular nozzle spacing. Cardinal factor for the oscillation phenomena is two-dimensionality of jet velocity distribution. In the case of mixing system, the jets' oscillation phenomena depend on Jet's Reynolds number, rectangular nozzle aspect ratio, rectangular nozzle spacing and the space of mixing system. In this study, the oscillation phenomena in mixing system utilized in the mixing chamber are examined.

The results obtained are as follows: (1) The oscillating frequency of the jets became the maximum in the case of the ratio, rectangular nozzle spacing l / rectangular nozzle width w, was about 15.(2) The oscillation phenomena was generated in the case of $l \geq 2\,l^*$, where l^* is the length of the jet's potential core. In this case, the impingement plane of the jets becomes easy to rotate. (3) In the case of the space of mixing system, the jet's oscillation phenomena were generated in the condition of the diameter of the space of mixing system over $9.6\,w$. (4) Deposition of mixture different kind of source nanoparticles produces high-density compact coatings without voids and cracks with SFJ-PVD using mixing system.

Keyword: coaxial impinging jets, jet's oscillation phenomena, mixing chamber

1. Introduction

Fluid mixers are required in various industrial technology fields. However, all of the fluid mixers need energy supply such as electric power and have mechanical moving parts, so that the breakdown occurs in the mixers. If the mixers employing the technology of fluidic oscillator realized, the energy supply and mechanical moving parts become unnecessary so that the breakdown does not occur. No mechanical moving part in the device enables to miniaturize the device, since the structure of the device becomes simple.

This paper presents the development of a mixing chamber utilizing the oscillation phenomena of two coaxial opposing impinging jets. The oscillation phenomena are cyclic phenomena that tow opposing jets repeat passing each other. In order to develop the jets' impinging type mixing chamber, it is necessary to clarify the major parameters which have the effect to generate the oscillation phenomena. The parameters generating the jets' oscillation phenomena estimated the jet Reynolds number, rectangular nozzle aspect ratio, two rectangular nozzle spacing.

It is possible to utilize this mixing method in the small space. So this mixing method will be applied in various industrial technology fields, i.e., μ-TAS, biochemistry analysis system and so on. This study attached mixing system at supersonic free-jet physical vapor deposition (SFJ-PVD) [2, 3], and investigated the effect of composition in coating film by two fluids utilizing the oscillation phenomena of two opposing jets in mixing system using mixing system.

2. Experiments

Experimental equipments are shown in Fig.1. The mixing system is shown in Fig.2(a). Working fluid was air and supplied to mixing chamber as shown in Fig.2(b). Experiments were carried out with large size Model 1 and real size Mode 2. Large size Model 1 had 10 times size of Model 2. Model 2 was installable for SFJ-PVD apparatus.

Supersonic free-jet physical vapor deposition (SFJ-PVD) has been developed as a new coating method in which a coating film is produced by depositing nanoparticles with very high velocity onto a substrate. The schematic diagram of SFJ-PVD is illustrated in Fig. 3, showing the two stages in SFJ-PVD, "gas evaporation" and "vacuum deposition". In the gas evaporation stage, a source material is evaporated to form nano-meter sized particles (nanoparticles) in an inert gas atmosphere. The nanoparticles are then carried to a substrate with the inert gas through a transfer pipe where a gas flow is generated by the pressure difference between the evaporation and deposition chambers. The gas flow is accelerated to supersonic velocity (Mach 3.6) by a specially designed supersonic nozzle joined to the tip of the transfer pipes. In the vacuum deposition stage, the nanoparticles are deposited onto the substrate. In the evaporation chamber 1, the evaporation source material was placed in a graphite crucible then heated and evaporated by the surrounding Ta ribbon heater. In the evaporation chamber 2, the evaporation source material was placed in a water-cooled copper crucible then heated and evaporated by arc plasma. The substrate was fixed on a stage that was driven in X-Y directions, and the coated area was 5mm square on the substrate. In this method, the deposition rates of various evaporation sources can be controlled independently using heating systems.

In Fig.4(a), Supersonic nozzles were placed at the angle of 45 degrees in deposition chamber. Supersonic nozzle was attached transfer pipe by the joint, nut and ferrule attached/non-attached mixing system. In Fig.4(b), Supersonic nozzle of M=3.6 was attached at outlet of the mixing system. In the case of Model l, the supersonic of M=1.7 was attached at the outlet of the mixing system. Transfer tube was made to be the coaxially opposing each other when the transfer tube was attached with mixing system.

In the experiments, the distances between the opposing rectangular nozzles l and the rectangular nozzle aspect ratio a_s(= rectangular nozzle depth h / rectangular nozzle width w) were selected as a parameter. Phenomena of the jet's oscillation were analyzed by using FFT spectrum analyzer.

Experiments on Model 1 were carried out in the two case i.e., the mixing chamber was installed in free space in the atmosphere or the mixing chamber was installed in the mixing system.

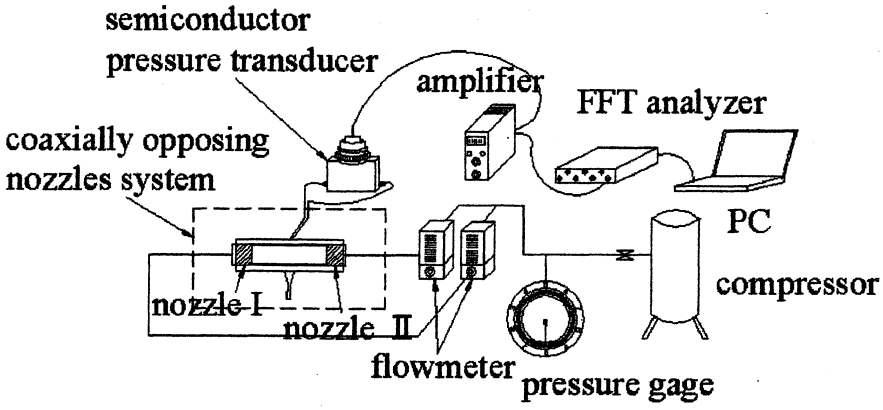

Fig. 1 Test set-up

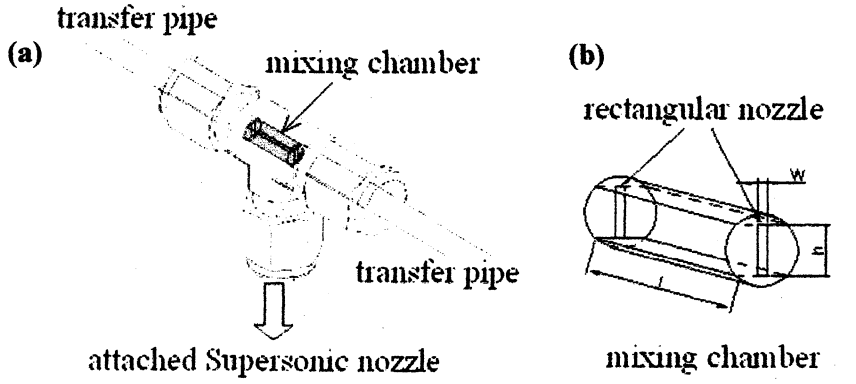

Fig.2 Coaxially opposing mixing system

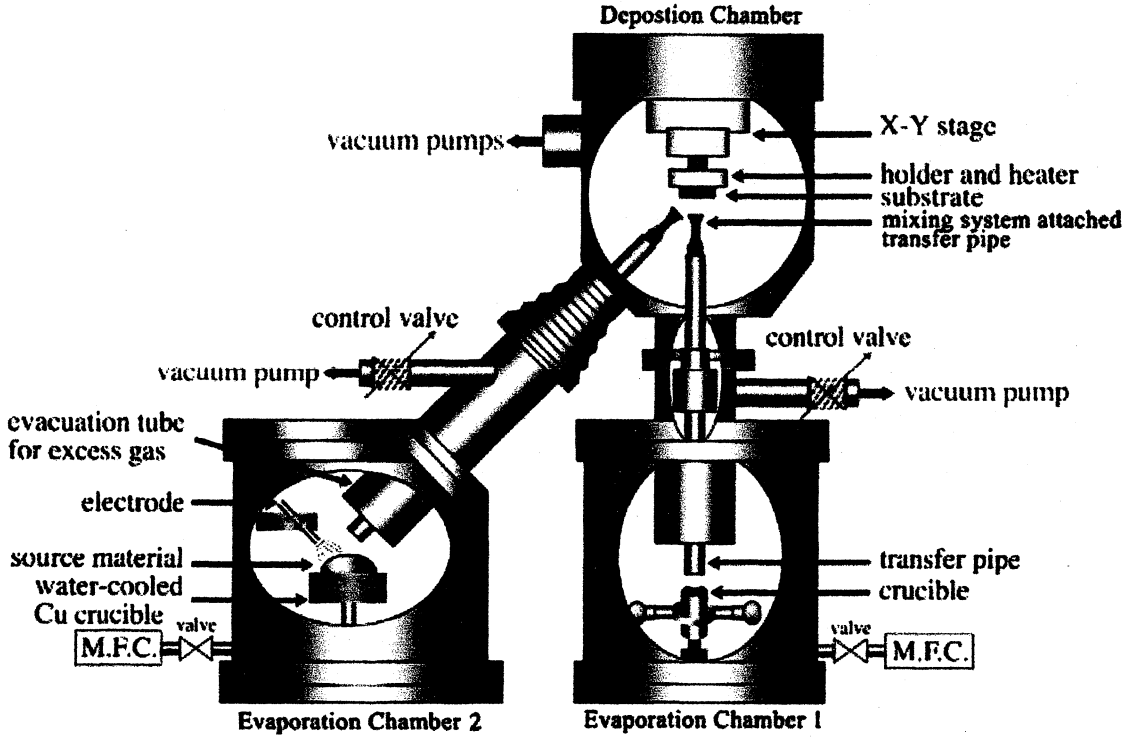

Fig.3 Schematic diagram of the supersonic free-jet PVD apparatus

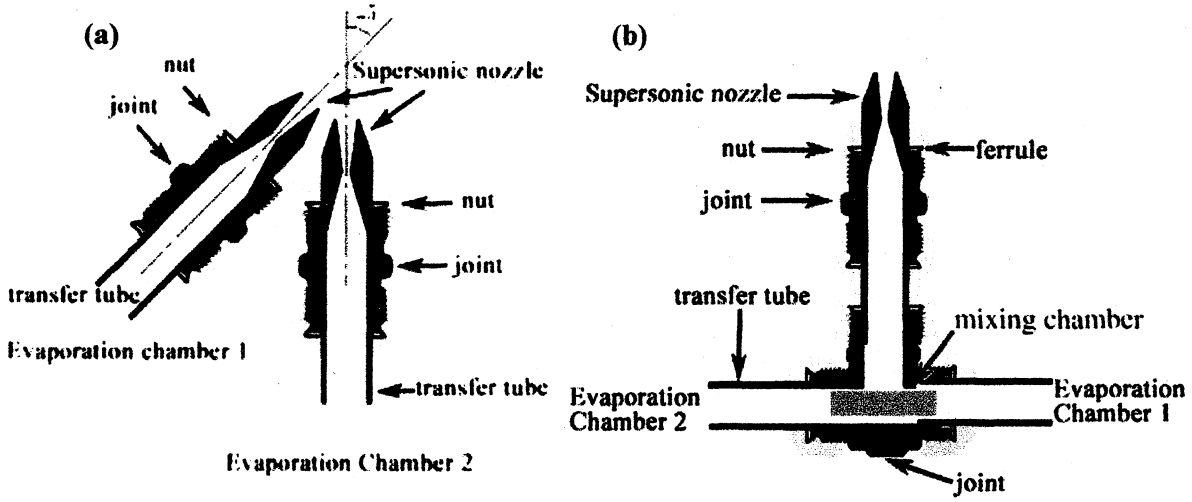

Fig.4 SFJ-PVD attached/non-attached mixing system

3. Result

3.1 Potential core length of jet from rectangular nozzle of Model 1

The measured centerline velocity distribution of the jet from the rectangular nozzle of the aspect ratios 4 and 8 are shown in Fig.5. Jet flow rate was 40[m^3/h]. The measured potential core lengths of jets from these rectangular nozzles are shown in Table 1.

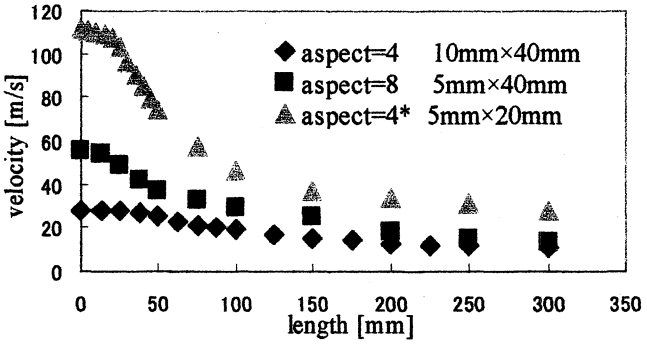

Fig.5 Centerline velocity distribution

Table 1 potential core length

aspect	potentialcore[mm]
$a_s = 4$	≒ 50mm
$a_s = 8$	≒ 25mm
$a_s = 4^*$	≒ 25mm

3.2 Oscillation phenomena of Model 1

The frequency of the jet's oscillation was measured by measuring the pressure fluctuation of the jets flow from the mixing chamber. The relationship between the oscillation frequency and jet flow velocity in the case of a_s= 4 is shown in Fig.6. The Strouhal number of the oscillating jet vs. jet's Reynolds number is shown in Fig.7.

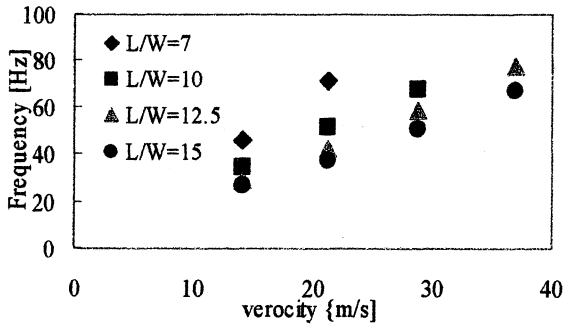

Fig.6 Frequency of oscillation vs. jet velocity

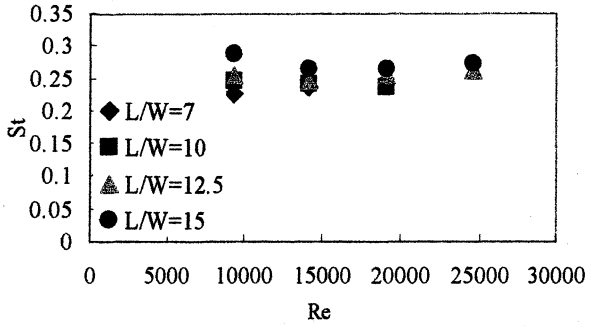

Fig.7 Strouhal number vs. jet's Reynolds number

In the atmospheric condition, the frequency of impinging jet's oscillation was proportional to jet flow velocity and inversely proportional to the distances between the opposing rectangular nozzles. The amplitude and the frequency of the oscillating pressure have the maximum value at the condition of $l/w \fallingdotseq 15$.

The main condition causing the jets' oscillation was regarded as the two-dimensionality of jet velocity distribution i.e., flatness of it along the height direction of the rectangular nozzle and the roundness of the jet velocity distribution along the width direction of the rectangular nozzle at the jets' collision plane [1].

The oscillation phenomena was not appeared in the case of $l \leq 2\,l^*$, l^* is the length of the jet's potential core. This results show that the collision plane does not rotate in the case of impinging of the jet's with flat velocity distribution.

The effects of the supply flow rate balance on the oscillation range were examined. This is the important characteristics for realizing a useful mixing chamber, because it is difficult to control the two supply flow rate producing the opposing jets in the same flow rate in a real miniaturized mixing chamber. The experiments were carried out in the manner that one of the jet supply flow rate was fixed, and the other one was changed. Strong sound pressure signals were produced in the mixing chamber under the condition of the jet supply flow difference within about ±20% of the fixed supply flow rate, i.e., the oscillation phenomena appeared.

The effects of the constrained plates on the oscillation phenomena were examined. The same oscillation phenomena were observed under the condition of the width of the constrained plates over that of the rectangle nozzle.

Recirculating flow reflected from the side wall of the mixing system make the oscillation steady [1]. Then, the effect of the space of the mixing system on the oscillation phenomena was examined. The results show that the steady oscillation was obtained by the mixing system of the diameter over $9.6w$.

3.3 Stable phenomenon of Model 1

The impingement phenomena of opposing cylindrical jets in mixing system were examined. The pressure fluctuations were observed, but the intensity of them was very smaller than that by the opposing rectangular nozzles, so that the frequency could not be measured.
It was considered that the impingement plane of opposing cylindrical jets kept perpendicular position.

3.4 Stable phenomenon and Oscillation phenomena of Model 2

The impingement phenomena of opposing cylindrical jets were examined in Model 2. The relationship between pressure fluctuation and rectangular nozzles spacing is shown in Fig.8. The results were same as that of Model 1. The results show that the impingement plane of opposing cylindrical jets kept perpendicular position.

In case of the rectangular nozzles of a_s= 4, the relationship between l/w and amplitude of the pressure fluctuation is shown in Fig9. Fluctuating pressure changes with the rectangular nozzles spacing. It becomes largest at l/w = 15.

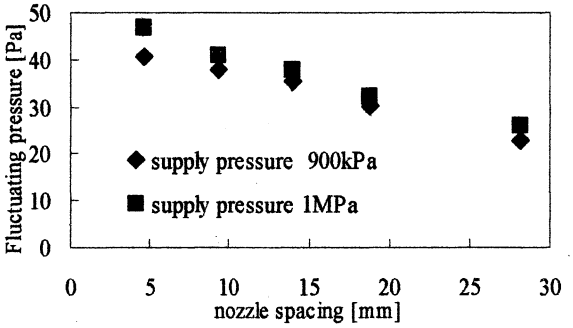

Fig.8 Fluctuating pressure as a function of rectangular nozzles spacing

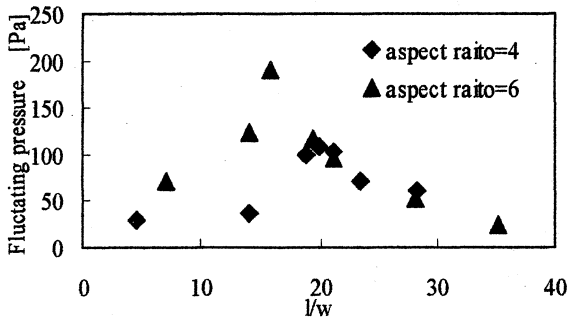

Fig.9 Fluctuating pressure as a function of l/w

3.5 Visualization experiments

Visualization experiments were carried out on Model 1 and Model 2. In model 2, He gas was used as the working fluid. The Powders of Ti and Al were mixed in the He gas and supplied to the opposing rectangular nozzles. In model 1, air was used as the working fluid and as a tracer for the visualization, the powder of bread was mixed. The visualization results in two cases i.e., used the mixing chamber and without mixing chamber, are shown in Fig.10 and Fig.11, respectively.

Microstructure of cross-sections of coated specimens were observed by scanning electron microscope (SEM) equipped with an energy dispersive X-ray (EDX) analyzer. Specimens of the observation were polished with SiC paper up to #2000, and then mechanical polished with up to 0.3mm Al_2O_3.

Figure 10 and 11 shows SEM image and the characteristic X-ray mappings of Al and Ti elements taken from the cross-sections of TiAl coating films on Ti substrate with SFJ-PVD attached/ non-attached mixing system. The specimen was produced by mixing Ti and Al nanoparticles from the two evaporation chambers with the same deposition rate. The result of non-attached mixing system is shown in Fig. 10. In Fig. 10(a), SEM image of TiAl coating on Ti substrate. The lower side of Fig. 10 is Ti substrate. Fig. 10(b) and (c) were corresponding mappings of Ti and Al. These images agree becoming dark in the part of the coating film, indicating the increase of Ti or Al content. Thus, the substrate is pure Ti, it is clearly dark part in Ti element map. These element maps shows obvious layered structure of Ti, Al, Ti rich mixed layer and Al rich mixed layer was observed in coating film.

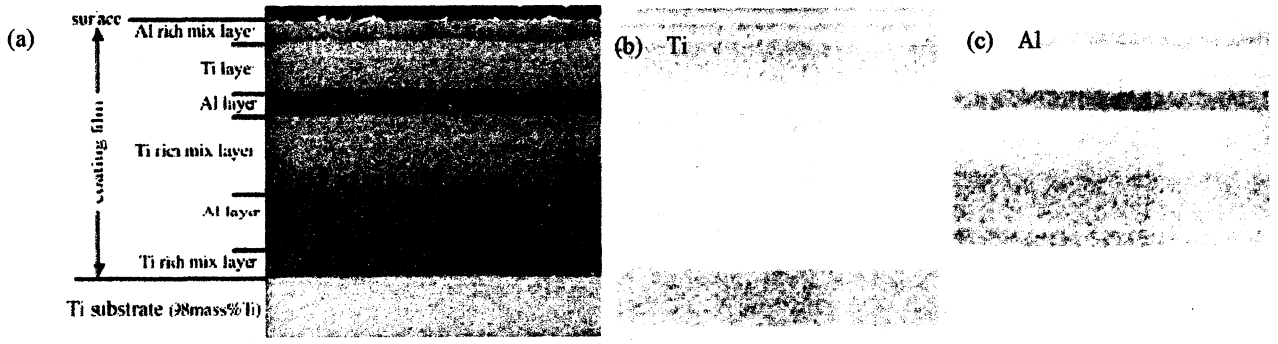

Fig.10 SEM image of Ti-Al coating on Ti substrate and the corresponding X-ray mappings of Al and Ti elements (Non-attached mixing system)

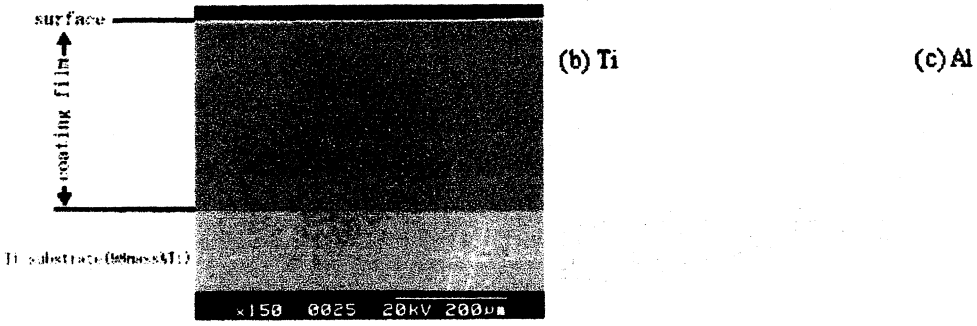

Fig.11 SEM image of Ti-Al composite coating on Ti substrate and the corresponding X-ray mappings of Al and Ti elements (attached mixing system)

film have been formed. Large Al or Ti particle is invisible in Fig. 11(b) and (c). Figure 11 indicates the same atomic fraction of Al and Ti nanoparticles is mixed without crack and defect.

In Fig. 11(a), lower side is Ti substrate. Upper side is coating film of mixture of Ti and Al. Fig. 11(b) and (c) were corresponding mappings of Ti and Al. No obvious layered structure was observed between interface and the surface of coating film in Fig. 11 (b) and (c). In Fig. 11(c), lower side is bright zone, there is no Al element in substrate. Al of Fig. 11(c) exists from the position on Ti substrate of Fig. 11(b).

Those results suggest that SFJ-PVD attached mixing system may have controlled the composition of Ti and Al in the coating film.

Fig.12. Image of bread crumb coating on board

The powder of bread was mixed in one supply jet in Model 1 and was sprayed over the board. As shown in Fig 12, the bead powder was scattered in a uniform way, this result shows that the opposing jets could be fully mixed by the mixing chamber utilizing jets' impinging fluidic oscillator.

4. Conclusion

This study aims to confirm the mixing method of two fluids utilizing the oscillation phenomena of two opposing impinging jets. Fluid mixing chamber of this study was developed in order to set at the SFJ-PVD(Supersonic Free-Jet PVD), etc..

The mixing chamber utilizing the jets' impinging fluidic oscillator was realized. The results obtained in this paper are as follows

(1) The maximum oscillating frequency obtained with the condition that rectangular nozzle spacing l / rectangular nozzle width $w \fallingdotseq 15$,

(2) The oscillation phenomena were not appeared in the case of $l \geq 2l^*$. l^* is the length of the jet's potential core,

(3) The oscillation phenomena were appeared in the condition of the diameter of the chamber over $9.6w$,

(4) Deposition of mixture different kind of source nanoparticles produces high-density compact coatings without voids and cracks with SFJ-PVD using mixing system.

References

[1] keijiro Yamamoto, Akira Nomoto, Tadao Kawashima, and Yoshiaki Nakatsuchi: Oscillatory Phenomena in Coaxial Impingement of Opposing jets, Journal of the Japan Hydraulics and Pneumatic Society, 6-6, 68/77 (1975)

[2] Atushi Yumoto, Takahisa Yamamoto, Fujio Hiroki, Ichiro Shiota and Naotake Niwa: Al/Al-Si Nano-Composite Graded Coating Prepared by Supersonic Free-Jet PVD, Mater. Trans. Vol.45.(2004), pp.2740-2743.

[3] Atushi Yumoto, Takahisa Yamamoto, Fujio Hiroki, Ichiro Shiota and Naotake Niwa Nano-Composite Coatings by Supersonic Free-Jet PVD, Trans. Mater. Res. Soc. Jpn, Vol.29(2004), pp1889-1892.

The 8TH International Symposium on Fluid Control, Measurement and Visualization, 2005

FLUCOME '05
Chengdu

Development of Micro Fluidic Devices

Takahiro TANAKA[1], Fujio HIROKI[2], Atushi YUMOTO[3] and Keijiro Yamamoto[4]

1. Graduate Student, Kogakuin University Telephone and Fax number: 81-426-28-4483
e-mail: am04033@ns.kogakuin.ac.jp
2. Kogakuin University e-mail: mailto:at94296@ns.kogakuin.ac.jp
3. Kogakuin University e-mail: a_yumoto@nifty.com
4. Kanagawa Institute of Technology e-mail:yamakei@we.kanagawa-it.ac.jp

Abstract

A micro fluid device utilizing coaxial impinging jets phenomena which has no mechanical moving part was developed. This device consists of two identical nozzles coaxially opposing each other, i.e., extremely simple structure. The opposing nozzles are sandwiched with flat plates, so the opposing jets have two-dimensional structure. This device had two functions, i.e., the micro fluidic valve controlled by the opposed impinging jet and the micro fluidic mixer employing the opposing jets' oscillation phenomenon generated in the mixing chamber. The oscillation phenomenon is undesirable for the micro fluid device, however, it is essential for the micro fluid mixture.

In this research, it was proved that the micro fluidic valve could modulate the flow rate ranging from 6% to 100% of full admission flow rate and the micro fluidic mixer could mix fluids under the condition of the flow rate over 4ml/min.

KEYWORDS: micro fluidic device, fluidic valve, fluidic mixer, impinging jets

1. Introduction

Recently, the development of the miniaturized biochemistry analysis system that is called μ-TAS (Total Analysis System) is paid to attention. The advantages of μ-TAS are the measurable of liquids with very little amount of samples and very shout time required to the reaction between the liquids. The μ-TAS needs micro fluidic elements which carry out the mixing, the reaction, separation, detection, and the adjustment of flow rate of reagents. The abilities needed by the micro fluidic elements are heat proof against high temperature generated by exothermic reaction, and structural simplicity for facilitate production. Moreover, μ-TAS needs the micro valve for adjusting the reacting time of the reagent in the micro reactor.

Fluidic devices have these abilities. But almost all of the fluidic devices utilize jet's interaction with the another jets or walls, therefore the Reynolds number of the jet must be over around 30 which needed for forming jet flow. Reynolds number of a micro elements was very low, in this case, the viscous effect of fluid dominates over inertia one. A micro valve, Microfluidic Turn-down Valve in which a jet flow rate control by an impinging jet had been developed [1].

In this research, we developed the micro fluidic device. The micro fluidic valve developed was based upon an impinging jets idea, i.e., the flow rate of the jet changes according to the opposing jet and the sensitivity of the change [2]. We focused to the oscillation phenomenon which happens when two nozzles have been arranged coaxially opposing each other [3], and we investigated the condition to operate as the micro fluidic mixer using the oscillation phenomenon of the jets.

2. Experiment procedure

The experiment was carried out by using the equipment shown in Fig.1. The water was used as the working fluid. Water flows to the model from a head tank through flow adjusting valves and flow meters. A liquid pump was used when the high supply pressure was required. Jet flows were visualized by coloring the working fluid, the dye injection method.

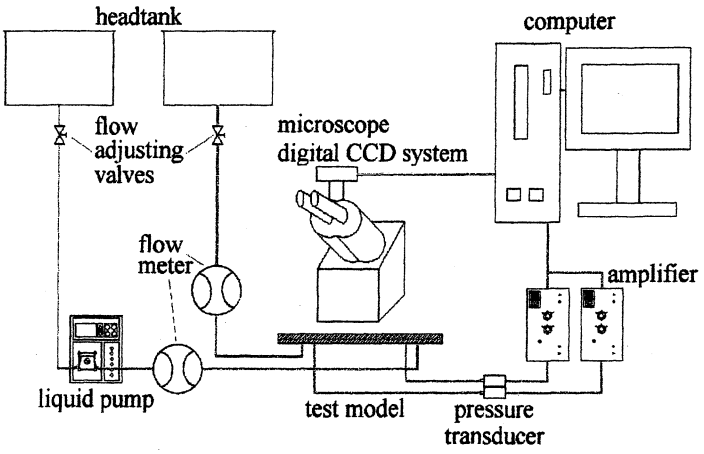

Fig.1. schematic diagram of experimental equipment

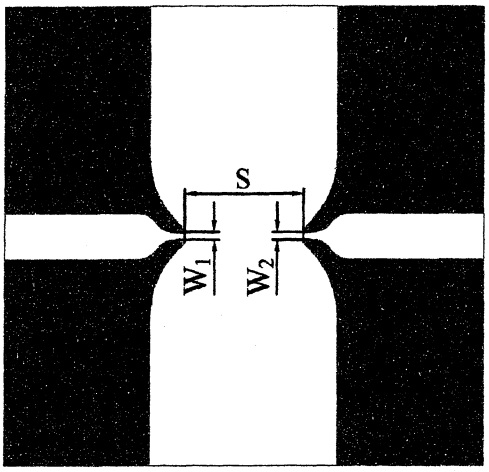

Fig.2. schematic diagram of test model

The test model used in this research is a kind of a jet impingement type fluidic device with very simple structure as shown in Fig.2. Two nozzles placed coaxially opposing each other. The widths of these opposing nozzles are represented by W_1 and W_2. The depth of the opposing nozzles and the distance between these nozzles are represented by d and S, respectively. Test models are classified as shown in Table.1. In Models A, C, D, and E, the width of the control nozzle and the reactor nozzle were different. But, these were equal width in Model B.

The pressure taps holed in the cover plat on the supply ports, and pressure transducers were inserted in the pressure taps.

Table.1. Classification of the Model

Model name	A	B	C	D	E	F	G
Nozzle width W_1	240 [μm]	240 [μm]	1. 75 [mm]	1. 75 [mm]	200 [μm]	200 [μm]	200 [μm]
Nozzle width W_2	240 [μm]	350 [μm]	1. 75 [mm]	1. 75 [mm]	200 [μm]	200 [μm]	200 [μm]
Distance between nozzles S	1.13 [mm]	1.13 [mm]	5. 63 [mm]	26. 25 [mm]	5.25 [mm]	5.25 [mm]	5.25 [mm]
Depth d	180 [μm]	180 [μm]	0. 86 [mm]	6 [mm]	600 [μm]	700 [μm]	800 [μm]

3. Results

3.1 Micro valve

The micro fluidic valve employing the impingement type fluidic device was made for realizing a flow control valve for adjusting reaction time of the reagent in micro reactors. The one nozzle of the device was connected with the reactor, so this nozzle called as the reactor nozzle. The other nozzle was connected with the adjusting valve which controls the supply flow of the liquid into this nozzle, and the jet flow from this nozzle acts as the control flow, so this nozzle called as the control nozzle. The impingement plane of the opposing jets could be shifted by changing in the control flow, and then the

flowing out resistance of the reactor nozzle could be changed. As a result, the adjustment of reactor flow rate was possible by the adjusting the control flow.

Models A and Model B could be used as a micro valve. This experimental conditions were carried out in Reynolds number Re_r=375 or 75 of the reactor nozzle.

$$Re = \frac{UW}{v} \tag{1}$$

In case of Re_r, U was taken as the maximum flow velocity at reactor nozzle U_{rmax} when control flow doesn't flow, and nozzle width $W=W_2$, and v is kinematic viscosity of the water. In case of Reynolds number Re_c of the control nozzle flow, $U=U_c$, and $W=W_1$.

Figure.3. shows the relation between the control flow rate and the flow rate through the reactor nozzle. It was possible that the micro valves, Model A and B, could modulate the flow ranging from 6% to 100% of initial reactor flow rate Q_{ri} in either model. Under the 6% of Q_{ri}, the control flow flows into the reactor nozzle, i.e., the reactor flow run back. Almost equal characteristics could be seen though there is a difference in the width of the nozzles of Models A and B. Similar characteristics were obtained even when the initial flow rate of the reactor differs, i.e., same amount of the control flow was required. The control flow did not reach the reactor nozzle to under Re_c=200. After steep decreasing of flow rate occurred the control flow reached reactor nozzle.

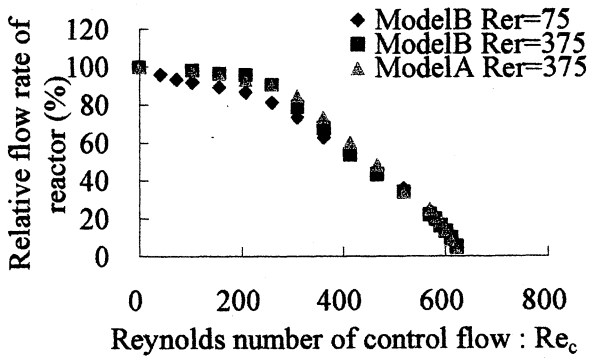

Fig.3. Relative flow rate of reactor vs. Reynolds number of control flow

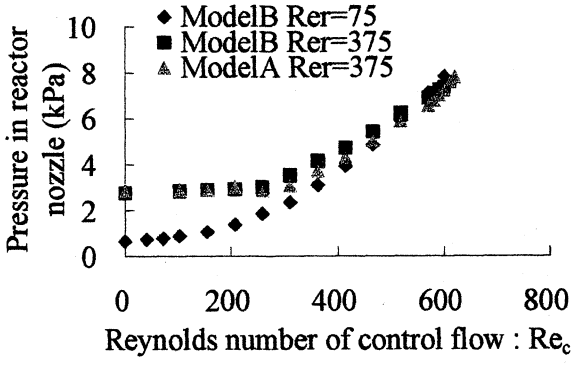

Fig.4. Pressure in reactor nozzle vs. Reynolds number of control flow

The difference in the characteristics appeared on the pressure in the reactor nozzle, i.e., back pressure of the nozzle, as shown in Fig.4. There was no difference between Model A and Model B, but different Re_r's produced different characteristics in lower Re_r region under 300. The pressure generated in the reactor nozzle for Re_r=75 was lower than that for Re_r=375 in the range of low control flow. However, the difference decreased in the larger range of the control flow rate. In large control flow range over Re_r=500, the control flow reached the reactor nozzle and these pressures were nearly same volume.

3.2 Micro fluidic mixer

The micro fluid mixer developed was for mixing two kinds of reagents. This micro fluidic mixer utilized the oscillation phenomenon of opposing impingement jets. The oscillation phenomena of opposing impingement jets were investigated for two-dimensional plane jet and for three dimensional axisymmetric jet and found that two dimensional jets' impingement produce the oscillation phenomenon [2]. In this study, this phenomenon applied to miniature device of sub-millimeters.

Then, we carried out the pre- experiment in the millimeter meter order. And the oscillation phenomenon was confirmed in Model C and D. Visualization image of Model C is shown in Fig. 5-(a)-1 ~ Fig.5-(a)-5, and Model D is shown in Fig. 5-(b)-1 ~ Fig.5-(b)-5.

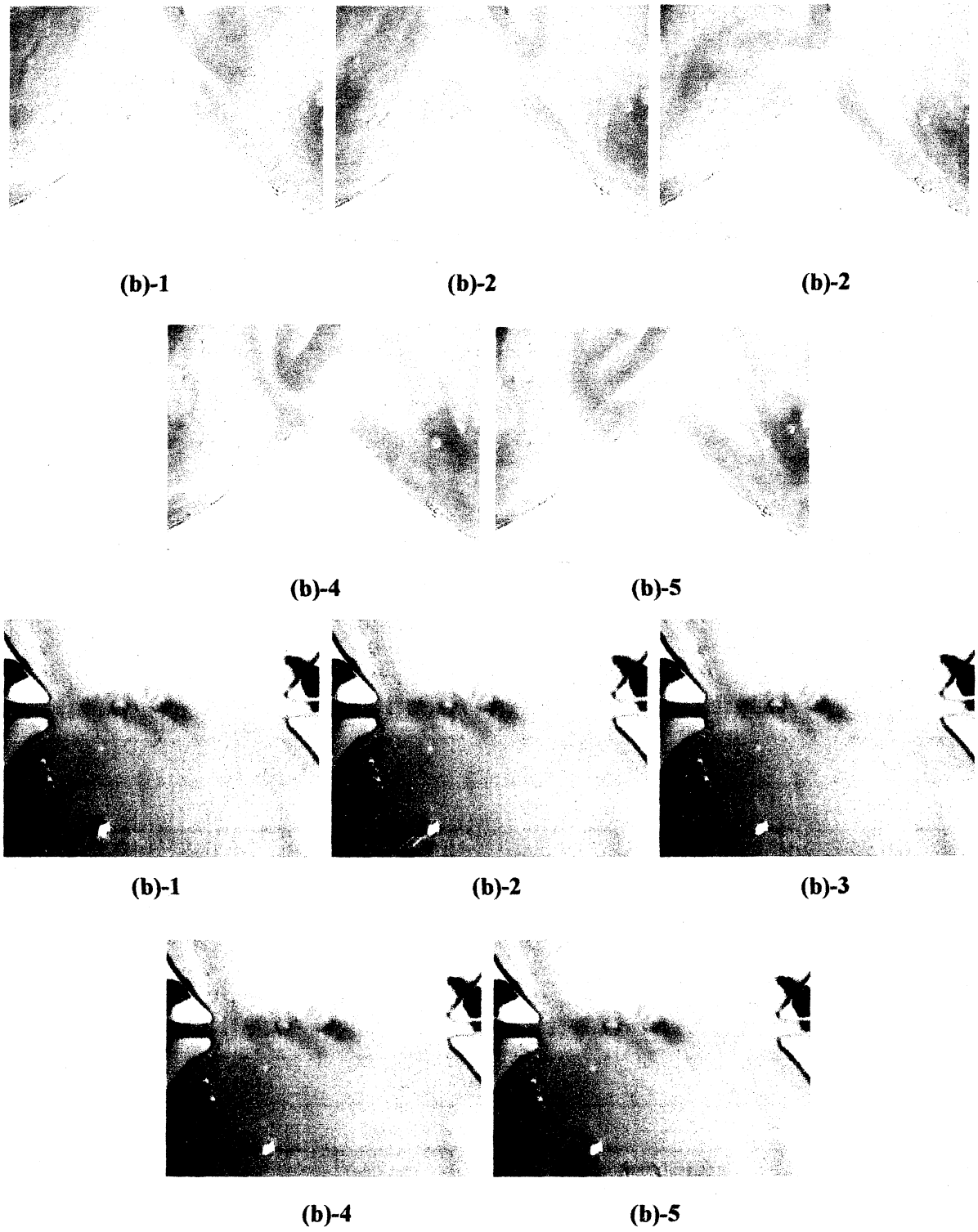

Fig.5. Visualized images of oscillation phenomenon
(a) model C, (b) model D

Next, experiments were carried out under the condition of Re up to about 250 in Model E, F and G. The control flow velocity and the reactor flow velocity were set equal. The flow field was visualized by the dye injection method and the oscillation frequency was measured.

The width of the nozzles, W_1 and W_2, was equal to 200 μm, and the distance between nozzles S was fixed at 5.23 mm. This distance was sufficient distance for producing the jets's oscillation. In order to keep the two-dimensionality of jets' velocity distribution, the depth of the nozzles d was fixed deeper than that of Model A and Model B. The nozzle aspect ratio As ($=d/W$) of Model E, F and G were 3, 3.5 and 4, respectively.

Relation between frequency and Reynolds number is shown in Fig.6. The frequency increased proportionally as increase in Reynolds number within 100 for each models. However, over 100, the inclination of the curves decreased. The oscillation generated at slower flow velocity as shallower nozzle. The oscillation began at Reynolds number of around 40~60, which correspond to the flow rate of around 4ml/min.

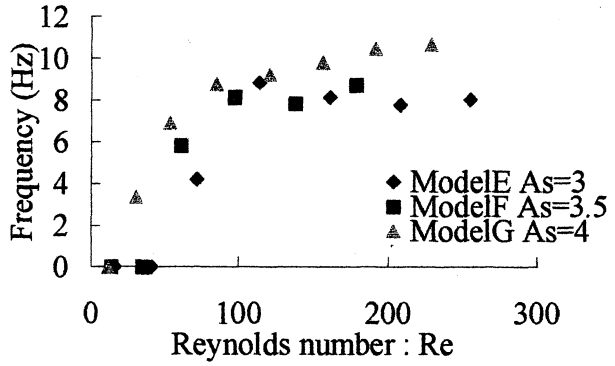

Fig.6. Relation between f and Reynolds number

Visualized flow fields in Model F are shown in Fig.7. Figure.7-(a) shows the flow pattern in Re=35. Two fluids flow separately and steady. The oscillation was confirmed in around Re=60, as shown in Fig. 7- (b). Figure.7- (c) show the flow pattern in Re=100, there were no difference between Fig. 7- (b). Figure.7-(c) and Fig. 7-(d) show the flow patterns for Re=140 and Re=220, respectively. Irregularity in color decreased comparing with the Figs.7 - (a) and (b). This result suggested that the micro fluidic mixer may have mixed the two fluids.

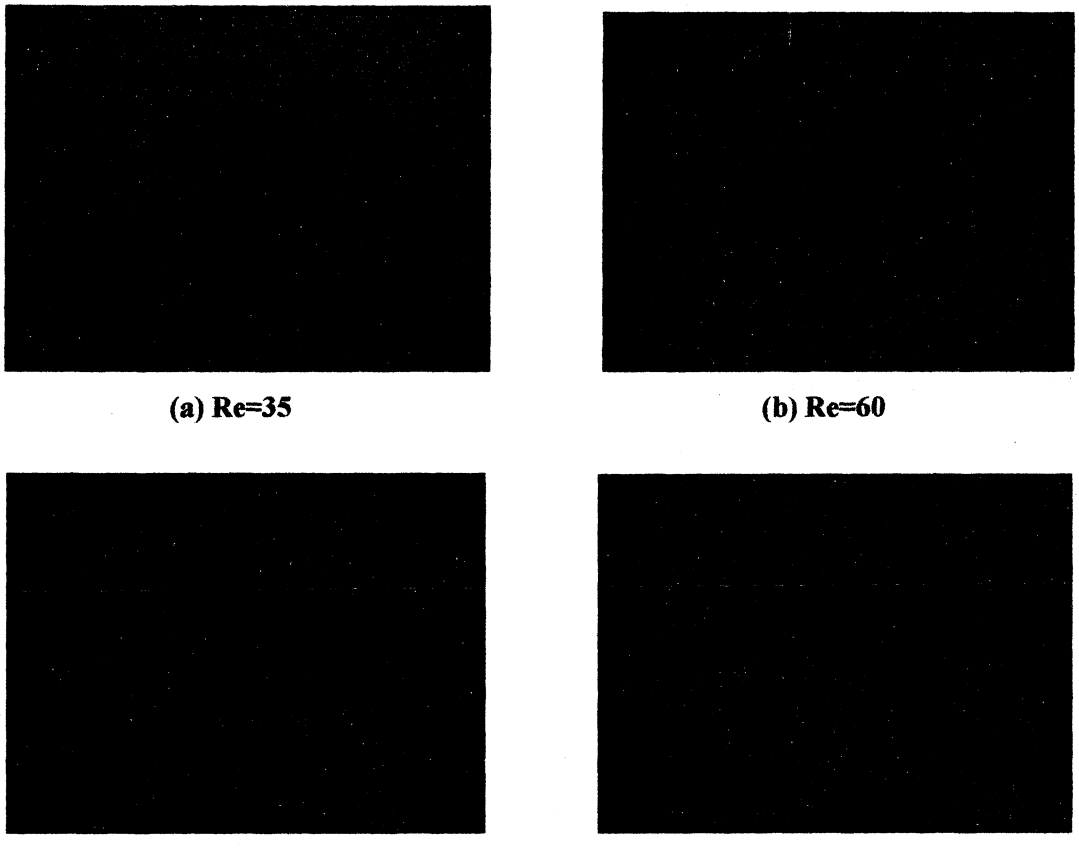

(a) Re=35 **(b) Re=60**

(c) Re=140 **(d) Re=220**

Fig.7. Visualized images of oscillation phenomenon in model F

4. Conclusions

Micro fluidic devices were developed. The devices had two functions of a valve and a mixer.
As the micro fluidic valve,
(1) The valve could modulate the flow rate ranging from 6% to 100% of full admission flow rate,
(2) Almost same characteristics obtained even if the widths of opposing nozzles were different.

As the micro fluidic mixer,
(1) The oscillation phenomenon began from about Re = 40 ~ 60, and could mix fluids at the flow rate over 4ml/min,
(2) The frequency increased proportionally to Reynolds number within 100, however, over 100, the inclination of the curves decreased.

References

[1] Tesar, V, "Microfluidic Turn-down Valve", Journal of Visualization, Vol.5, No.3 pp.301-307, (2002)
[2] Keijiro Yamamoto, Takashi Ishida, Shin Kawamachi, and Akira nomoto, "Impingement type fluid amplifier", Proceedings of 2nd International Symposium on Fluid Control and Measurement, (1988), pp 516-520.
[3] keijiro Yamamoto, Akira Nomoto, Tadao Kawashima, and Yoshiaki Nakatsuchi, "Oscillatory Phenomena in Coaxial Impingement of Opposing jets", Journal of the Japan Hydraulics and Pneumatic Society, 6-6, (1975), pp 68-77.

超音速フリージェットPVDによる傾斜組成皮膜の形成

湯本敦史[1)]，山本剛久[2)]，廣木富士男[1)]，塩田一路[1)]，丹羽直毅[1)]

1）工学院大，2）東大

Formation of Functionally Graded Coatings with Supersonic Free-Jet PVD

Atsushi YUMOTO[1)], Takahisa YAMAMOTO[2)], Fujio HIROKI[1)],

Ichiro SHIOTA[1)], Naotake NIWA[1)]

1) Kogakuin University, Shinjuku-ku, Tokyo, Japan

2) University of Tokyo, Bunkyo-ku, Tokyo, Japan

Compositional graduation is produced by depositing nanoparticles with supersonic free-jet PVD (SFJ-PVD). The SFJ-PVD has been developed as a new coating method in which a coating film is formed by depositing nanoparticles with very high velocity onto a substrate. The high velocity of nanoparticles is produced by the supersonic gas flow of inert gas. Graded Al/AlTi films, graded Ti/TiAl films and graded Al/Al-Si films are produced by depositing nanoparticles of Al, Ti or Si formed in different evaporation chambers with controlling evaporation rate. A smooth, compact and defect-free microstructure is formed both at the interface between substrates and coating films and inside the coating films. It is confirmed from nano-indentation hardness testing that the hardness of the graded coatings corresponds to the compositional graduation.

1. 緒　言

基材に不足する特性の補完を目的としたコーティング技術に注目が集まるなか，更なる皮膜特質の向上と共に遮熱・耐熱，耐摩耗など一部の用途では，基材保護の観点から数十から数百μmの膜厚を確保する必要性が高まっている．特に熱遮蔽コーティング（Thermal Barrier Coatings: TBC）においては，熱効率向上に伴うタービンブレードの高温化はブレードの基材となるNi基超合金をイットリア部分安定化ジルコニアによるTBCによって数100Kの温度低下が求められており，200～300μmの膜厚が必要だと言われている[1)]．現在，これら要請の下，高い成膜速度で良好な皮膜特性および密着性を有する皮膜が得られるプロセスが模索されている．しかし，高い成膜速度を有する既存のコーティング技術には，個々のプロセスに起因する種々の技術的課題や制約が存在し，次世代コーティングとして高い性能を達成する新しい原理によるコーティング法の開発が切望されている[2)]．

傾斜機能材料は，異種材料間の組成を連続的に変化させることにより異種材料間の物性差を連続的に変化させることが可能であり[3)]，本材料設計を用いた傾斜組成膜（Functionally Graded Coatings: FGC）は，基材と皮膜間の熱応力の緩和など，基材からの皮膜の剥離を抑制するのに有効であることが知られている[4,5)]．

著者らは，高い成膜速度で緻密な皮膜形成を達成する新しいコーティング技術として，超音速フリージェットPVD（Supersonic Free-Jet PVD; SFJ-PVD）を提案，開発している．本法は，不活性ガス雰囲気中で皮膜となる原料を加熱蒸発させることにより生成されるnmサイズの粒子（ナノ粒子）を超音速のガス流により加速，基板上にナノ粒子を堆積させることにより皮膜形成させる新しい原理による技術である．本法を用い，膜厚数百μmのTiおよびAl金属膜[6]，TiとAlのナノ粒子を基板上で混合させることによりTiAl金属間化合物をその場合成させた皮膜[7]，本法に活性金属-プラズマ反応[8-13]を組み込みTi/TiN膜[14]の形成に成功している．Fig. 1[15]は，Ti基板上にTiとAlのナノ粒子を1：1の割合で混合，形成させたTiAl膜断面写真である．Fig. 1よりTi基板上に約320μmの膜厚の緻密な皮膜が形成されていること，また，本法によりTiとAlのナノ粒子を均一に混合させることが可能でありことが明らかとなっている．一般的に高い成膜速度を有する溶射法やCold Sprayなどによる皮膜では，成膜プロセスが起因した積層組織と呼ばれる皮膜組織を呈することや膜中のき裂，空隙の存在により膜特性の不足が懸念されている．Fig. 1および既報の研究成果は，本法が高い成膜速度と緻密な膜形成を両立すること，および金属，金属間化合物，窒化物セラミックスなど幅広い素材の成膜に対応できることを示しており，新しいコーティング技術として本法の優れた可能性を示唆している．

本研究は，超音速フリージェットPVDにより，基板上に堆積させる異種ナノ粒子の混合比を連続的に変化させることにより，基材成分から連続的に組成が傾斜したAl/AlTi，Ti/TiAl，Al/Al-Si傾斜組成皮膜の形成を試みた．

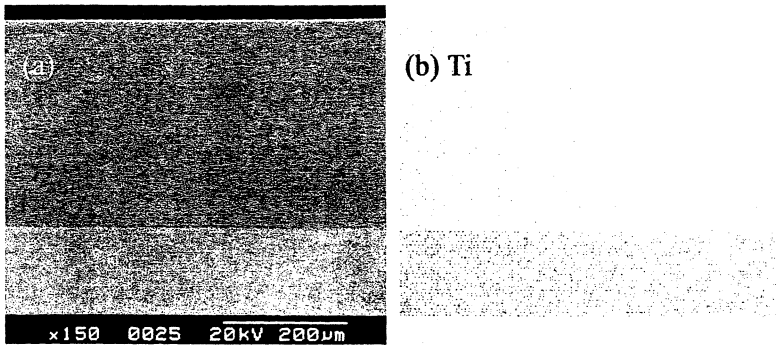

Fig. 1 SEM image of TiAl coating film on Ti substrate and the corresponding X-ray mappings of Ti and Al elements.

2. 実験方法

Fig. 2に超音速フリージェットPVD装置の概略図を示す．本装置は二つのナノ粒子生成室と一つの膜形成室，合計三つのチャンバ，および排気システムで構成されている．各ナノ粒子生成室は膜形成室と搬送管によって連結されている．あらかじめ全てのチャンバを真空排気し，その後チャンバ内に不活性ガスを導入する．不活性ガス雰囲気に置換させた

ナノ粒子生成室内では，膜素材となる材料の加熱による蒸発およびそれに伴いナノ粒子の生成がおこなわれる．生成室 1（Fig. 2 右下のチャンバ）は抵抗加熱方式，生成室 2（左のチャンバ）はアーク加熱方式を採用している．抵抗加熱方式は加熱量の制御性に優れ，アーク加熱方式は高融点の素材を蒸発させることが可能である．

各々の生成室で生成させたナノ粒子は，生成室と膜形成室（右上のチャンバ）の圧力差により発生するガスの流れにより搬送管を通じ膜形成室内に搬送される．搬送管の先端にはガスの流れをマッハ数 3.6 の超音速に加速するノズルが接続されており，ナノ粒子は高速に加速されたガスの流れによって基板上に堆積され，基板を固定している X-Y ステージの移動により，任意のパターンに皮膜を形成する．超音速ノズルによって加速されたガス流はノズル内の急激な断熱膨張によりガス温度が低下，ガス流速の低下を招く．そのため，本装置ではノズル外周にヒータが設けられており，ノズル内のガスを間接加熱することでガス温度を制御している．

基板は 20mm 角，板厚 1mm の Ti 基板（JIS-1 種純チタン），Al 基板（A1050）を使用し，皮膜原料は純 Al，純 Ti および純 Si を使用した．基板の前処理はアセトン中で 1 分間超音波洗浄のみおこなった．原料の Al はグラファイト坩堝に入れ生成室 1 に設置し，Ta ヒータによって加熱した．また，Ti もしくは Si は水冷銅ハース上に設置，W 電極によるアーク加熱により蒸発させた．皮膜の組成制御は，生成室内の皮膜原料を加熱する電力量のみを制御することにより試みた．なお，他の成膜条件は，既報 [6,7,14,15] と同様とした．形成させた皮膜は断面切断後，機械研磨し，SEM 観察および皮膜組成を分析した．また，皮膜の硬度は対稜角 115° のダイヤモンド圧子を装着したエリオニクス製ナノインデンテーション（ENT-1040a）装置，荷重 9.8mN で測定した．

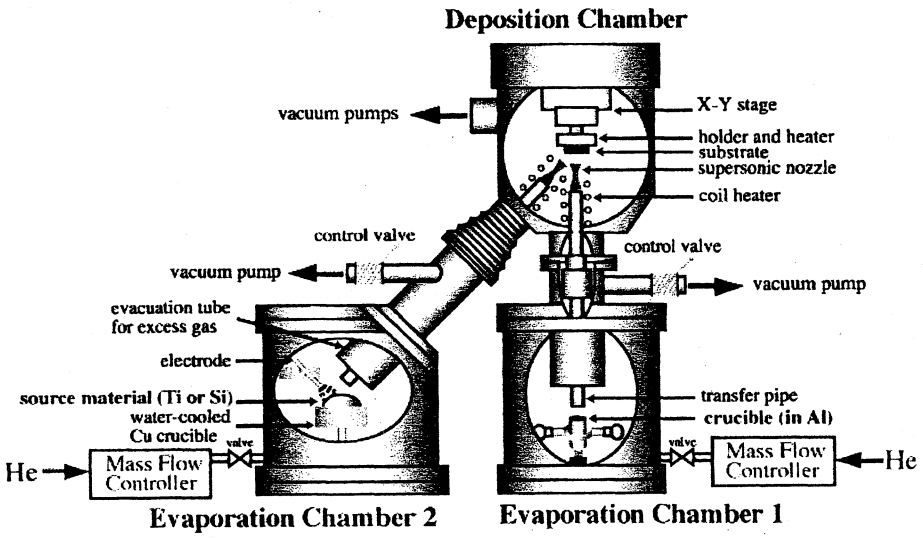

Fig. 2. Schematic diagram of a supersonic free-jet PVD apparatus.

3. 結　果

3.1. 傾斜組成 TiAl 膜の形成

基板を Al とし連続的に Ti 組成を増加させた傾斜組成 Al/AlTi 膜と，基板を Ti とし皮膜中の Al 組成を連続的に増加させた傾斜組成 Ti/TiAl 膜を形成させた．皮膜組成の制御は，生成室 1 の Al の加熱電力量と生成室 2 の Ti の加熱電力量を制御することにより基板上での Al および Ti の混合比を連続的に制御した．傾斜組成 Al/AlTi 膜は，生成室 1 の Al 加熱電力量を 4.0～3.5kW，生成室 2 の Ti の 0～0.4kW に，Ti/TiAl 膜は，Al の加熱電力量を 0.8～3.1kW，Ti の加熱電力量を 0.7kW 一定とした．

Fig. 3(a)および(c)の SEM 写真から皮膜中にき裂やボイドなどの欠陥は確認されず緻密な皮膜が形成されていること，また Fig. 3 (b) および(d)の組成分析結果から，Al/AlTi 膜および Ti/TiAl 膜の表面組成はそれぞれ Ti-43.7at%Al，Ti-52.2at%Al であり，基板から皮膜表面に向かって Al および Ti 組成が連続的に傾斜化していることが明らかとなった．

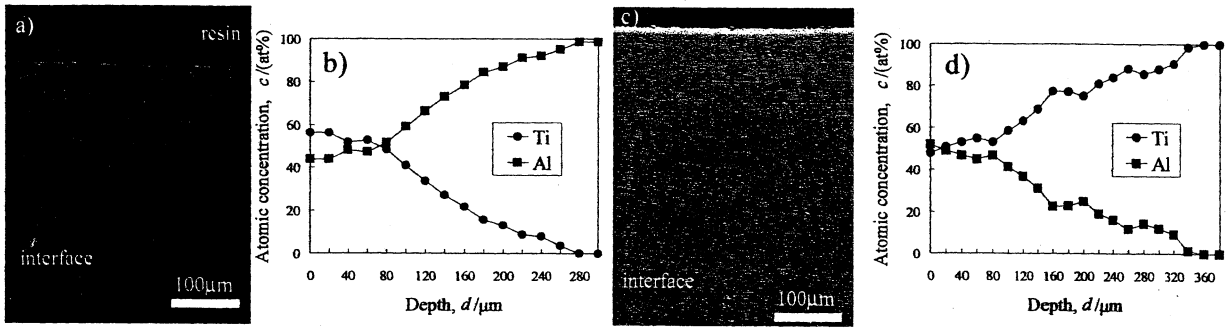

Fig. 3. SEM image and EDX analysis of cross-sections of a) and b) the graded Al/AlTi film on the A1050 substrate, c) and d) the graded Ti/TiAl film on the Ti substrate.

3.2. 傾斜組成 Al-Si 膜の形成

Al の加熱電力量を 3.8～3.1kW，Si の加熱電力量を 0～0.4kW とし，A1050 基板から連続的に Si 組成を増加させた傾斜組成 Al/Al-Si 膜を形成させた．Fig. 4 および Fig. 5 は，形成させた皮膜断面の SEM-EDX と TEM 写真である．Fig. 4(a)の SEM 写真から皮膜中にき裂やボイドなどの欠陥は確認されず緻密な皮膜が形成されていること，また界面にも欠陥が無く基板-皮膜間界面おいて明瞭なコントラストの差も無いため良好な界面性状であると判断された．さらに皮膜中に肥大した Si 粒は確認されず TEM 観察の結果，Al マトリックス中に 10～20nm の Si 粒が分散されていることが確認された．

Fig. 4(b)からは，皮膜表面の Si 組成は 57.8at%であり，基板から連続的に Si 組成が傾斜化していることが明らかとなった．

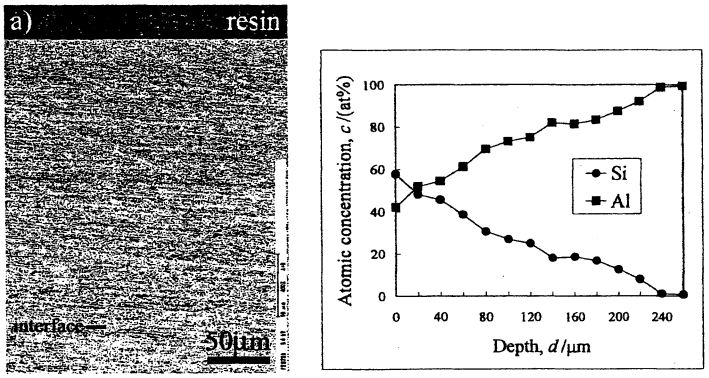

Fig. 4. SEM image and EDX analysis of cross-sections of a) and b) the graded Al/Al-Si film on the A1050 substrate.

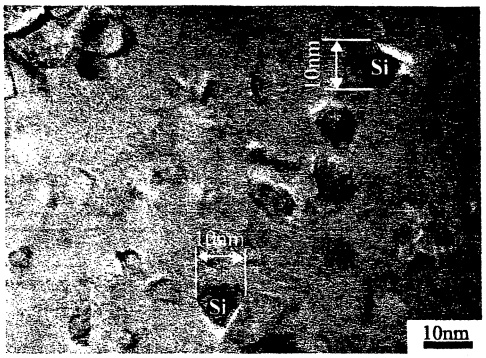

Fig. 5. TEM microstructure of the graded Al/Al-Si coating film.

3.3. ナノインデンテーション硬さ

皮膜組成の変化に伴う硬度の変化を測定するため，皮膜断面を基板から表面に向かって10μm 間隔で硬さ測定した．基準試料として純 Ti（JIS-1 種）と A1050 を同測定装置，同条件で測定した結果，それぞれ 3.14GPa と 0.63GPa であった．Fig. 6 は，Al/Al-Si 膜の断面の圧痕 FE-SEM 写真である．Fig. 6 より，基板から皮膜表面に向かい圧痕の大きさが連続的に小さくなっていることが判り，硬度は0.65GPaから5.9GPaまで連続的に変化していた．なお，Ti/TiAl 膜，Ti/TiN 膜も同様に測定し，皮膜断面の組成分析結果と対応させ各皮膜組成と硬度の関係をまとめたものが Fig. 7 である．Fig. 7 より，各々の傾斜組成皮膜は，組成の変化に対応し，硬度が変化していることが明らかとなった．

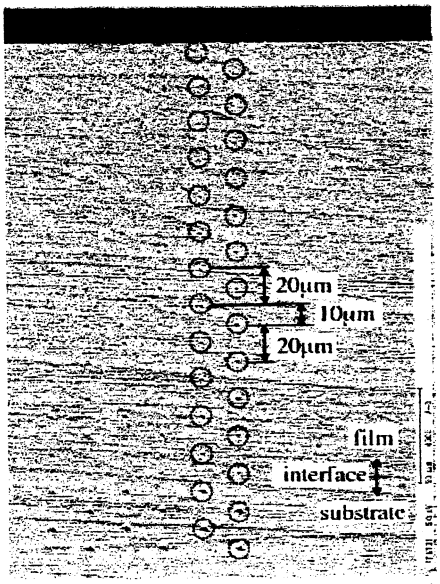

Fig. 6. Cross-sectional micrograph of Al/Al-Si film with the indents of nano-indentation.

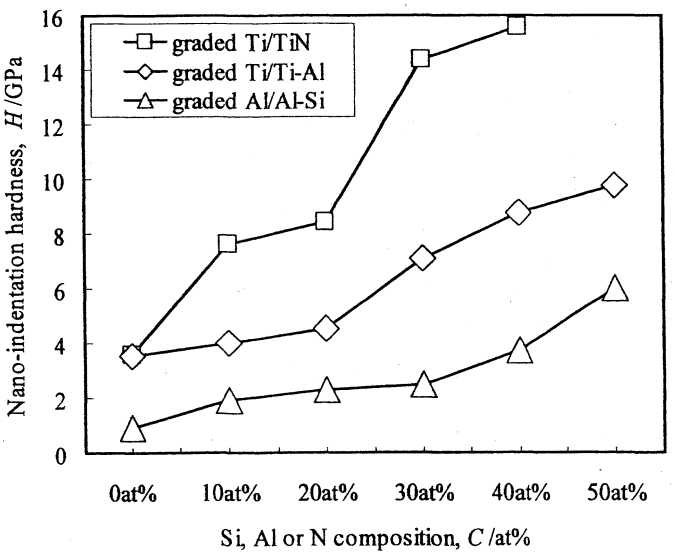

Fig. 7. Nano-indentation hardness variation with gradation of content in the graded composite coating films.

4. 結　言

超音速フリージェットPVDにより，基板上に混合させる異種ナノ粒子の混合比を連続的に制御することにより傾斜組成皮膜の形成を試み，以下の知見が得られた

1） 本法を用い，皮膜原料の蒸発加熱電力を連続的に変化させることにより，皮膜原料の蒸発量を制御することで，皮膜組成を傾斜化させた皮膜が得られた．

2） Al/AlTi膜，Ti/TiAl膜，Al/Al-Si膜中および界面においてき裂やボイドなどの欠陥は確認されず緻密な皮膜が得られた．

3） Al/Al-Si膜をTEM観察した結果，皮膜のAlマトリックス中に10ー20nmの微細Si粒が分散していることが確認された．

4） 皮膜硬度をナノインデンテーションにより測定した結果，皮膜組成の変化に対応し，硬度が連続的に変化していることが明らかとなった．

謝辞

ナノインデンテーション硬さ測定は，株式会社エリオニクスの伊藤拓嗣氏，植松卓彦氏にご協力いただいた．ここに深く謝意を表する．

文献

1） 後藤孝，まてりあ，43，p.585(2004).

2） 吉田豊信，まてりあ，40，p.322(2001).

3） C. Lei, H. Jiandong, G. Zuoxing, L. Qihong and W. Zhijiang, Mater. Trans., 45, p.2791(2004).

4） 未踏科学技術協会編，傾斜機能材料，工業調査会，p.1(1993).

5） A. Kawasaki, R. Watanabe, M. Yuki, Y. Nakanishi and H. Onabe, Mater. Trans. JIM, 37, p.788(1996).

6） 湯本敦史，廣木富士男，塩田一路，丹羽直毅，日本金属学会誌，65，p.635(2001).

7） A. Yumoto, F. Hiroki, I. Shiota and N. Niwa, Surf. Coat. Technol., 169-170, p.499(2003).

8） 宇田雅広，大野悟，日本化学会誌，6，p.862(1984).

9） 宇田雅広，大野悟，表面科学，5，p.426(1984).

10） 宇田雅広，日本金属学会会報，22，p.412(1983).

11） 宇田雅広，化学と工業，36，p.72(1983).

12） 大野悟，宇田雅広，日本金属学会誌，48，p.640(1984).

13） 大野悟，奥山秀男，本間一廣，高木一徳，本庄俊夫，尾澤正也，日本金属学会誌，59，p.408(1995).

14） A. Yumoto, T. Yamamoto, F. Hiroki, I. Shiota and N. Niwa, Mater. Trans., 43, p.2932(2002).

15） A. Yumoto, T. Yamamoto, F. Hiroki, I. Shiota and N. Niwa, Trans. Mater. Res. Soc. jpn, 29, p.1889(2004).

研究業績

3. ナノ界面・粒子

Microsyst Technol (2007) 13:1047–1053
DOI 10.1007/s00542-006-0303-z

TECHNICAL PAPER

Self-assembly of three dimensional micro mechanisms using thermal shrinkage of polyimide

Kenji Suzuki · Hideaki Yamada · Hirofumi Miura · Hideaki Takanobu

Received: 15 July 2006 / Accepted: 23 October 2006 / Published online: 15 November 2006

Abstract This paper describes three-dimensional microstructures fabricated using a simple self-assembly process involving the thermal shrinkage of polyimide. The proposed method enables hinged structures to be automatically rotated out of the wafer plane and to remain bent without the need to use any interlocking mechanisms. The hinged structures were fabricated using surface micromachining techniques involving heating in a furnace. An increase in the bending angle due to the shrinkage of polyimide was observed with increasing heating temperature, heating time, and length of the polyimide hinge. Of these three parameters, the heating time was found to be the most suitable for precise control of the bending angle. Furthermore, microcubes were fabricated by this method and the self-assembly process was successfully visualized using a CCD camera.

1 Introduction

Recently, many three-dimensional (3D) micro mechanisms have been developed in the MEMS field. Bulk micromachining techniques including anisotropic wet etching and deep reactive ion etching, and micromachining techniques using thick-layer photoresists and electroforming are capable of producing a wide variety of high-aspect-ratio structures. However, only quasi-3D structures can be produced using two-dimensional (2D) lithography. One way to fabricate truly 3D structures is to use out-of-plane rotation of hinged structures. Many kinds of fully 3D structures, including optical mirrors and lenses, have been assembled from surface-micromachined planar structures by rotating the hinged components out of the wafer plane.

There are two kinds of assembly processes for producing hinged structures, namely manual assembly and self-assembly. Manual assembly is usually performed using probing equipment under a microscope (Suzuki et al. 1994). However, it is not suitable for high-density integration or batch fabrication since it is complicated, time-consuming and requires large areas for probing. To automate the assembling process, actuators integrated in the hinged structures, including pneumatic balloon actuators (Jeong et al. 2005; Lu et al. 2005), scratch drive actuators (Akiyama et al. 1994) and electromagenetic actuators (Shimoyama et al. 1998), have been developed. Although these methods enable dynamic adjustment of the rotation angle, they require complex mechanisms and the use of many wires for actuation. Self-assembly methods using external magnetic fields (Iwase and Shimoyama 2005), the surface tension of liquids (Syms et al. 2003) and thermal shrinkage of V-groove polyimide joints (Ebefors et al. 1998) have also been developed. Three-dimensional structures assembled using external magnetic fields and the surface tension of liquids are mechanically interlocked making dynamic actuation after assembly

K. Suzuki (✉) · H. Yamada
Department of Mechanical Systems Engineering,
Kogakuin University, 2665-1, Nakano-machi, Hachioji-shi,
Tokyo 192-0015, Japan
e-mail: ksuzuki@cc.kogakuin.ac.jp

H. Miura · H. Takanobu
Department of Mechanical Systems Engineering,
Kogakuin University, 1-24-2, Nishi-shinjuku, Shinjuku,
Tokyo 163-8677, Japan

difficult. Structures assembled using the thermal shrinkage of V-groove polyimide joints permit dynamic actuation after assembly by making use of the thermal expansion of the polyimide joints. However, the bending angle is limited to 5° per V-groove joint. In addition, the structural materials that can be used are limited by fabrication processes using crystalline anisotropic etching.

The objective of this study is to develop a simple self-assembly method using the thermal shrinkage of polyimide. A schematic illustration of the 3D microstructure of a polyimide hinge is shown in Fig. 1. Two rigid plates are connected by an elastic hinge. A 3D structure can be assembled from this planar structure by bending the hinge. In this study, PIX-1400 (HD Micro System Corp.) was used as the hinge material. PIX-1400 has a low Young's modulus and a high elongation at room temperature, and its Young's modulus increases and thermal shrinkage occurs when it is heated at 500°C (Naka et al. 2004). These properties of polyimide enable the hinged plates to be rotated out of the wafer plane by using a simple heating process and their configuration can be maintained without the need to use any interlocking mechanisms.

Since the assembly process makes use of the mechanical properties of the polyimide hinge, there are few restrictions on the material of the rigid plates that can be used. The polyimide hinge can undergo large elastic deformation of greater than 38° after assembly, which enables wide-ranging dynamic actuation using various methods such as the application of magnetic and electrostatic forces.

2 Self-bending mechanism

The self-bending mechanism is shown in Fig. 2. When the hinged structure is heated, the Young's modulus and the shrinkage ratio of the polyimide increase considerably at temperatures above 500°C (Naka et al. 2004). However, the shrinkage of the hinge in the longitudinal direction is constrained by the bottom plate. Therefore, this shrinkage is greater on the top surface of the film and an internal stress is generated in the polyimide film, resulting in rotation that bends the freestanding structure out of the wafer plane. The structure can be bent over a wide range of angles by varying the heating conditions for polyimide. The structure retains its configuration even after the hinge has been cooled and can undergo large elastic deformation due to the change in mechanical properties of the polyimide hinge.

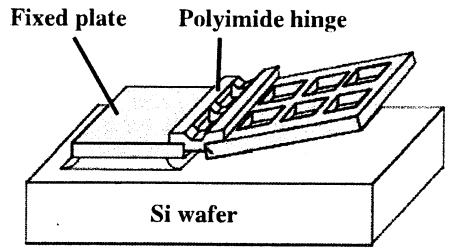

Fig. 1 Schematic illustration of 3D microstructure of a polyimide hinge

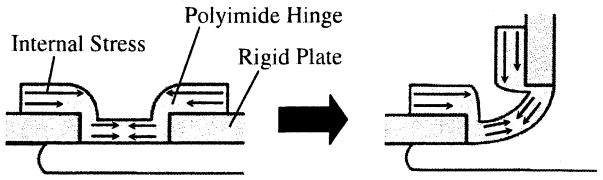

Fig. 2 Schematic illustration of principle of self-assembly

3 Fabrication process

The fabrication process of the hinged structure is shown in Fig. 3. First, a 3-μm-thick SiO_2 layer is deposited by sputtering (Fig. 3a), and is patterned by electron-beam (EB) lithography using masks of a 0.5-μm-thick aluminum film and EB resist (ZEP7000, Nippon Zeon Corp.). The aluminum film mask is used to improve the resistance of the plasma etching. The SiO_2 layer is etched by reactive ion etching (RIE) using a CF_4 plasma (RF power: 200 W, etching time: 60 min) (Fig. 3b). After removing EB resist and the aluminum mask, a polyimide film (PIX-1400, HD Micro System

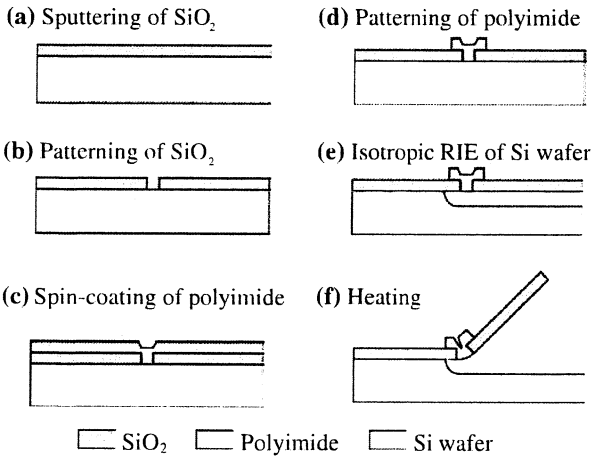

Fig. 3 Fabrication process of the hinged structure

Corp.) is spin-coated and soft-baked for 60 s at 140°C (Fig. 3c). In order to cover the steps between the SiO_2 plates and to provide sufficient strength, the minimum thickness of the polyimide film was determined to be 3 μm. Then, the polyimide film is patterned by EB lithography using masks of a 0.15-μm-thick aluminum film and EB resist and is etched by RIE using an O_2 plasma (RF power: 100 W, etching time: 70 min) (Fig. 3d). After post-baking for 30 min at 200°C and 60 min at 350°C, the movable plate is released from the silicon wafer by isotropic RIE of the silicon using an SF_6 plasma (RF power: 50 W, etching time: 50 min) (Fig. 3e). Finally, the polyimide hinges are heated in a furnace in a N_2 atmosphere to rotate the hinges out of the wafer plane (Fig. 3f). The self-assembled structure is shown in Fig. 4.

4 Properties of polyimide hinges

Precise control of the final bending angle is necessary to assemble 3D microstructures. The bending angle depends on the heating temperature (T), the heating time (t), the hinge length (L_h) and the polyimide film length (L_p) including the overlap length with the rigid plates. The definitions of L_h and L_p are shown in Fig. 5. The effects of these parameters on bending angles were investigated experimentally.

4.1 Effect of heating temperature

The heating temperature was varied from 400 to 700°C under the conditions of constant t, L_h and L_p. The results show that the optimal heating temperature is 500°C because the polyimide hinge exhibited little shrinkage below 500°C and was easily broken by cracking above 500°C.

4.2 Effect of heating time

The shrinkage of polyimide film proceeds gradually when the film is heated at 500°C. In order to investigate the time dependence of the shrinkage, the thickness variation of a polyimide film on heating was measured. The polyimide film was spin-coated on a silicon wafer and some square patterns were etched before heating to form edges of the film. The heating time was varied between 30 and 120 min at 500°C, and the thicknesses of the polyimide film before (h_1) and after heating (h_2) were measured at nine points using a surface profiler. The averaged values of the rate of change of the thickness, which is defined as $\alpha = (h_1 - h_2)/h_1$, are plotted against the heating time in Fig. 6. The rate of change of the thickness is almost proportional to the heating time and reaches –3.2% after heating for 120 min.

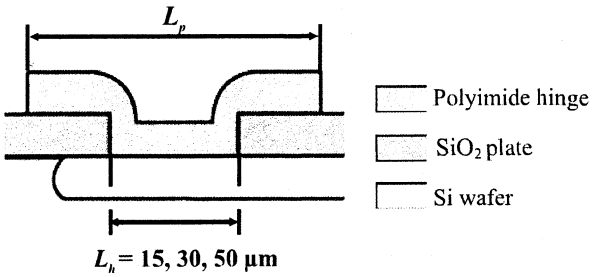

Fig. 5 Definitions of hinge length (L_h) and polyimide film length (L_p)

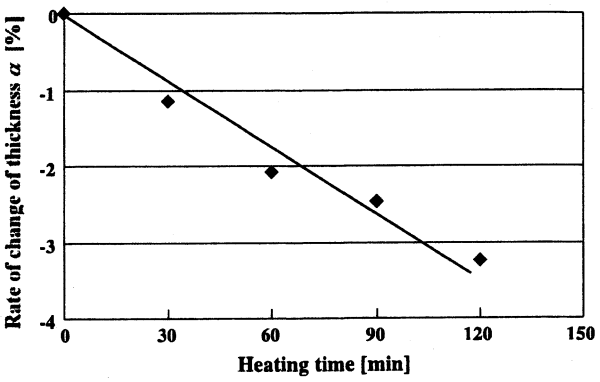

Fig. 6 Rate of change of thickness as a function of heating time

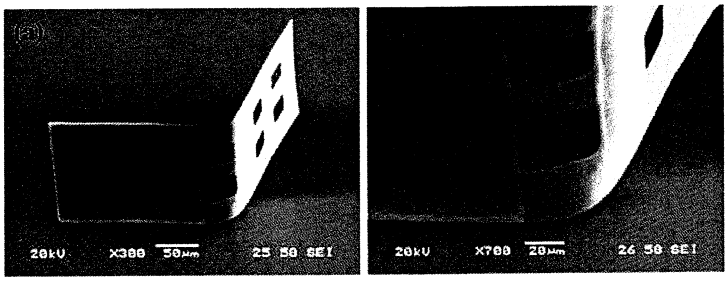

Fig. 4 SEM photographs of self-assembled structures. **a** After producing self-assembled structure. **b** A close-up view of the polyimide hinge

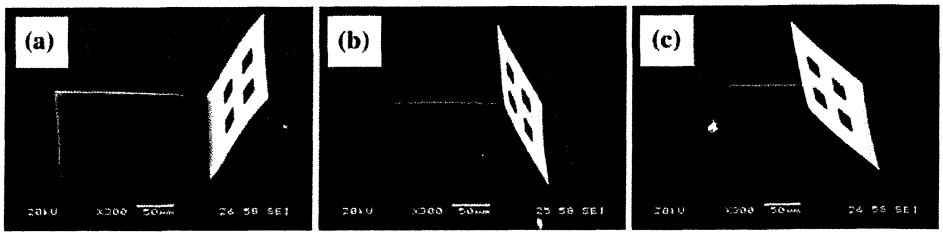

Fig. 7 SEM photographs of the hinged structures. L_h 30 μm, heating time **a** 30 min, **b** 45 min, **c** 60 min

Next, the effect of the heating time on the bending angle of the hinges was investigated. The heating time was varied between 10 and 60 min at 500°C. Figure 7 shows SEM photographs of the self-assembled hinges for various heating times. The bending angle of the hinge is plotted as a function of the heating time in Fig. 8. The bending angle increases almost linearly with heating time, and varies over a wide range from 30 to 170°. Thus, the heating time is a suitable parameter for achieving precise control of the bending angle over a wide range.

4.3 Effect of hinge length

The effect of hinge length on the bending angle was investigated. Structures were prepared that had hinge lengths in the range from 15 to 50 μm and a constant L_p of 90 μm, as shown in Fig. 7. L_h is limited to 50 μm because hinges longer than 50 μm adhered to the wafer plane during heat treatment. The bending angle increased as the hinge length increased, as shown in Fig. 8.

4.4 Effect of polyimide film length

The effect of polyimide film length was investigated. Hinged structures were prepared that had different polyimide film lengths and a constant L_h of 30 μm, as shown in Fig. 9. Bending angles for various lengths of polyimide films are plotted as a function of heating time in Fig. 10. The bending angle increased as L_p increased. This is probably due to an increase in the internal stress in the polyimide hinge as the overlap area of the polyimide film and the plates increased.

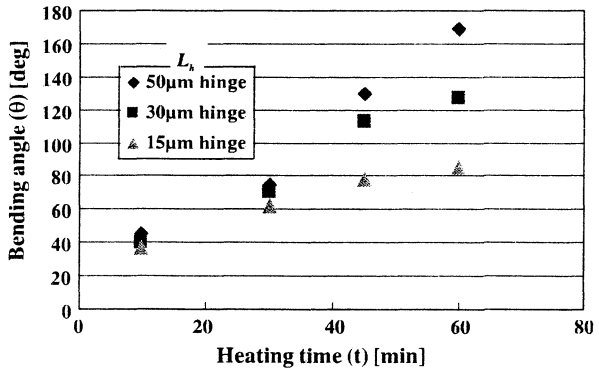

Fig. 8 Variation of bending angle with heating time for three different hinge lengths

4.5 Effect of number of plates

In order to realize practical 3D microstructures having out-of-plane motion, it is necessary to produce

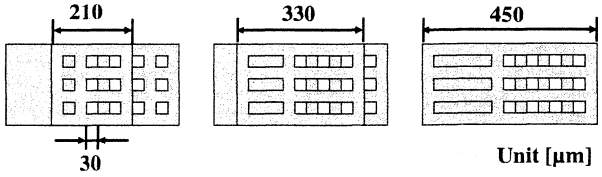

Fig. 9 Variation of polyimide film length (Lp)

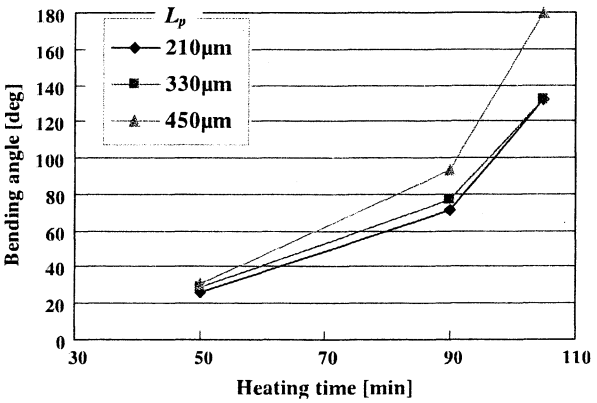

Fig. 10 Variation of bending angle with heating time for various lengths of the polyimide film (L_p)

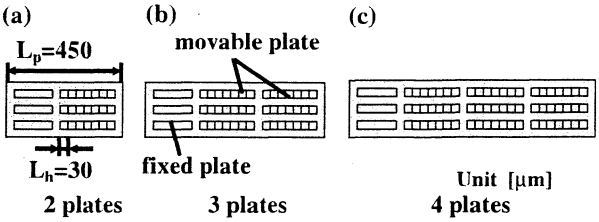

Fig. 11 Serial connection of various numbers of plates. The plates are fully coated with a polyimide film

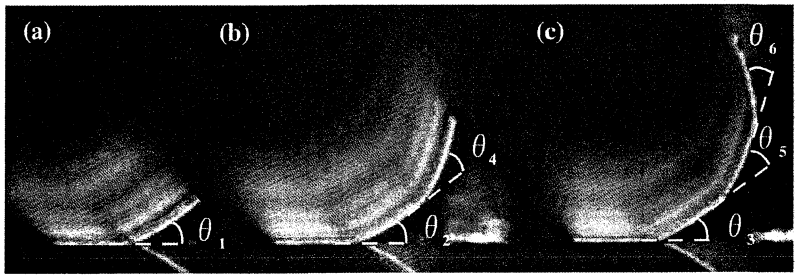

Fig. 12 Side profile of serially connected plates by polyimide hinges

structures having multiple plates connected in series. So, the effect of the number of plates on bending angle of each hinge was investigated. The structures having different numbers of plates were prepared, as shown in Fig. 11. The plate length was 210 μm and the hinge length was 30 μm. The plates were completely coated with polyimide film since longer lengths of polyimide film result in larger bending angles.

Figure 12 shows the side profile of several plates connected by polyimide hinges after 90 min heating at 500°C. The measured bending angles $\theta_1 - \theta_6$ are shown in Fig. 13. The results show that the bending angles are almost the same regardless of the number of plates. The average bending angle is 35.2° and the standard deviation is 2.6°.

5 Self-assembly of a microcube

By utilizing the properties of the polyimide hinges ascertained by these experiments, microcubes were assembled to demonstrate this self-assembly method. Figure 14 shows a schematic view of a planar structure for assembling a microcube, which consists of five movable plates and a fixed plate connected by polyimide hinges. It was heated for 90 min at 500°C in a furnace to produce 90°C rotation of each plate.

Furthermore, the assembly process was observed using the experimental set up shown in Fig. 15. For visualization, the hinged structure was heated locally using a far infrared heater so that a CCD camera could be set up in close proximity to the structure. The heat treatment was performed in a N_2 atmosphere to prevent degradation of the polyimide film and crack formation caused by thermal oxidation. The time variation of the heating temperature is shown in Fig. 16. First, the temperature was raised to 300°C, which is around the glass-transition temperature of polyimide, at a rate of 60°C/min (polyimide is stable

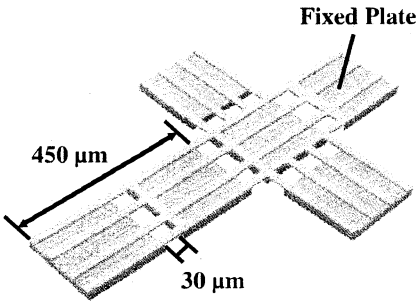

Fig. 14 A planar structure for assembling a microcube

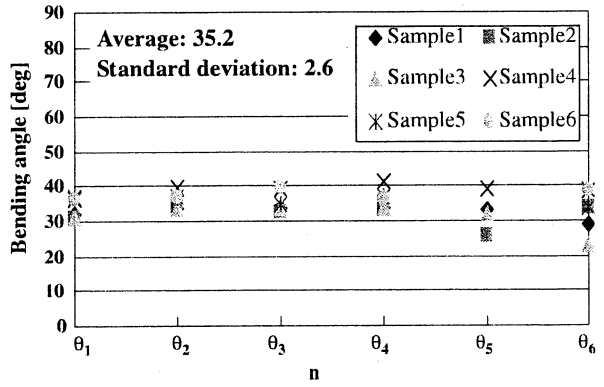

Fig. 13 Bending angles of polyimide hinges connecting various numbers of plates in series

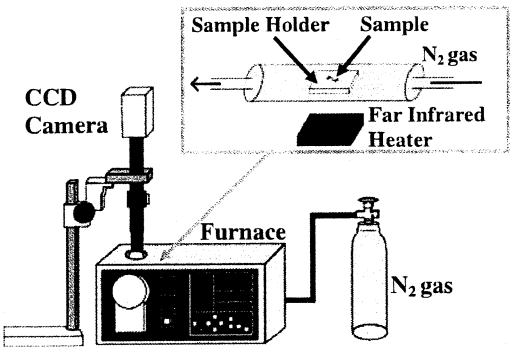

Fig. 15 Schematic illustration of experimental set-up for visualizing assembly process

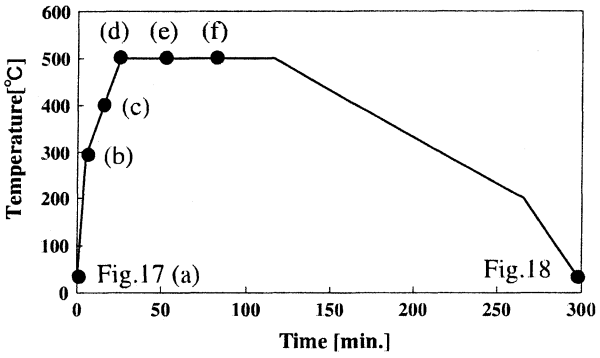

Fig. 16 Time variation of curing temperature

below its glass-transition temperature). The temperature was then raised to 500°C at a slow rate of 10°C/min since the mechanical properties of the polyimide hinges begin to change. And then, the temperature was maintained at 500°C for 90 min to bend the hinges to 90°. After the assembly had been formed, the temperature was lowered to 200°C at a very slow rate of –2°C/min.

Figure 17 shows the images obtained which illustrate the sequential assembly process. The initial state prior to heating is shown in Fig. 17a. Each hinge is bent slightly out of the wafer plane due to the residual stress during the fabrication process. Figure 17b shows the image taken at 300°C. It should be noted that the structure became flat at one point between 200 and 300°C. This is because the polyimide changes into a rubber-like material and the internal stress is relieved around the glass transition temperature. Subsequently, each plate began to rotate at approximately 400°C, as shown in Fig. 17c. When the temperature was maintained at 500°C, all the hinges were gradually bent at almost the same rate, as shown in Fig. 17d–f, and finally, a microcube was completely assembled after 90-min heating. The shape of the cube remained unchanged during the cooling stage. Figure 18 shows SEM photographs of the self-assembled microcubes. Many cubes were assembled simultaneously on the same wafer, as shown in Fig. 18a.

6 Conclusion

A simple self-assembly method for producing a hinged structure using the thermal shrinkage of polyimide is proposed. The effects of the heating conditions and the dimensions of the polyimide hinge on the bending

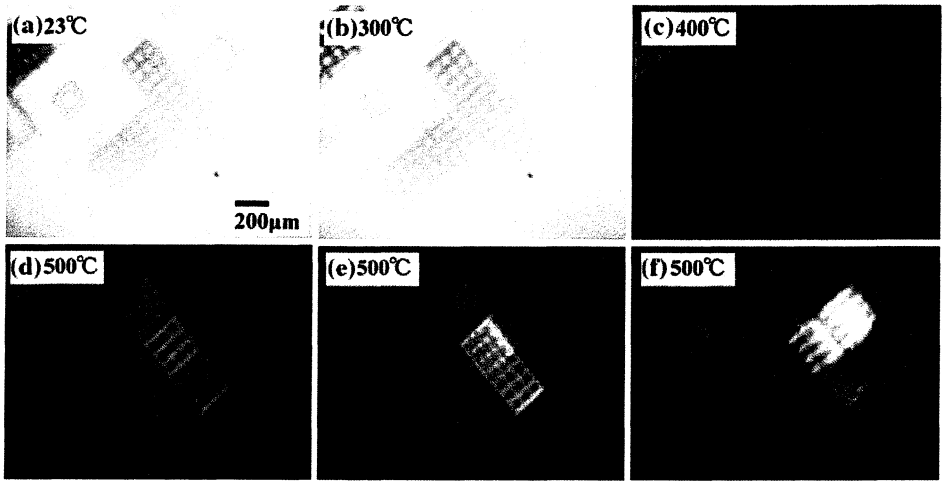

Fig. 17 Captured images showing the self-assembly process of a microcube

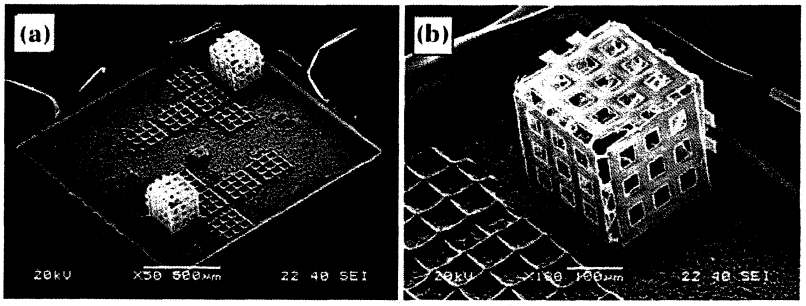

Fig. 18 SEM photographs of the microcubes. **a** Two out-of-plane microcubes assembled simultaneously on a chip. **b** Close-up view of a microcube

angle were investigated experimentally. The results show that the final bending angle of the polyimide hinge can be controlled over a wide range from 30 to 170° by varying the heating time at a temperature of 500°C. The bending angle also depends on the hinge length and the overlap length of the hinge and the plate. The bending angles of multiple hinges are almost the same and are independent of the number of plates. By utilizing these properties of polyimide hinges, many microcubes were simultaneously assembled on a wafer. Furthermore, the assembly process of the cubes was successfully visualized using a CCD camera. These results demonstrate that this assembly process is a promising technique for batch fabrication of truly 3D microstructures.

Acknowledgments This research was supported by the Smart Machine and Micro-Bio Systems Research Center (SMBC) at Kogakuin University, which is one of the "High-Tech Research Center" projects for private universities, matching funding received from the Ministry of Education, Culture, Sports, Science and Technology, 2003–2007.

References

Akiyama T, Collard D, Fujita H (1994) Scrach drive actuator with mechanical links for self-assembly of three-dimensional MEMS. IEEE J Microelectromech Syst 3(1):4–9

Ebefors T, Mattsson J, Kalvesten E, Stemme G (1998) Dynamic actuation of polyimide V-groove joints by electrical heating. Sens Actuators A67:199–204

Iwase E, Shimoyama I (2005) Multistep sequential batch assembly of three-dimensional ferromagnetic microstructures with elastic hinges. IEEE J Microelectromech Syst 14(6):1265–1271

Jeong OC, Kusuda S, Konishi S (2005) All PDMS Pneumatic balloon actuators for bidirectional motion of micro finger. In:Proceedings of the 18th international conference on micro electro mechanical systems, pp 407–410

Lu Y, An Z, Kim CJ (2005) A microhand: modeling, manufacturing, and demonstration. In:Proceedings of the 18th international conference on micro electro mechanical systems, pp 650–653

Naka K, Nagase H, Ichiyanagi M, Konishi S (2004) Pyrolyzed-polyimide for MEMS application. In:Proceedings of the 21st sensor symposium, pp 461–464

Shimoyama I, Kano O, Miura H (1998) Three-dimensional microstructures folded by Lorentz force. In:Proceedings of the 11th international conference on micro electro mechanical system, pp 24–28

Suzuki K, Shimoyama I, Miura H (1994) Insect-model based microrobot with elastic hinges. IEEE J Microelectromech Syst 3(1):4–9

Syms RA, Yeatman M, Bright VM, Whitesides GM (2003) Surface tension-powered self-assembly of microstructure—the state-of-art. IEEE J Microelectromech Syst 12(4):387–417

Xia L, Wu W, Xu J, Hao Y, Wang Y (2006) 3D nanohelix fabrication and 3D nanometer assembly by forced ion beam stress-introducing technique. In:Proceedings of the 19th international conference on micro electro mechanical systems, pp 118–121

Proceedings of the 2007 IEEE/RSJ International
Conference on Intelligent Robots and Systems
San Diego, CA, USA, Oct 29 - Nov 2, 2007

Water Strider Robots with Microfabricated Hydrophobic Legs

Kenji Suzuki, Hideaki Takanobu, Kota Noya, Hiroyuki Koike, and Hirofumi Miura

Abstract— **This paper discusses biomimetic water strider robots that have microfabricated hydrophobic legs. Various kinds of supporting legs with hydrophobic microstructures on their surfaces were developed using MEMS (micro electromechanical systems) techniques. The lift and pull-off forces of these supporting legs were analyzed theoretically and then measured. The experimental results were in good agreement with the calculations. Two different mechanisms for autonomous water strider robots were developed. One robot with twelve microfabricated legs driven by a vibration motor successfully moved on a water surface and also made left/right turns by exploiting differences in the resonant frequencies of the legs. The other robot, with six microstructured legs, moved on water through elliptical motion of its middle legs, which is similar to the motion of actual water striders.**

I. Introduction

In recent years, there has been considerable interest in insect-inspired miniature robots. Through evolutionary processes, numerous species of insects have adapted themselves to diverse environments. Based on scaling effects, some insects have acquired unique locomotive abilities, such as hexapod walking, jumping, and flapping flight, which markedly extend their field of activity. The working principles behind these behaviors are considered to be highly efficient and optimized for microscale systems. They, therefore, provide alternate design rules for developing smart and advanced microrobotic mechanisms. For example, insect flight is well-suited for micro flapping mechanisms [1],[2] and MAV (micro air vehicles) [3],[4]. The present paper focuses on the surface-tension dependent locomotion of water striders. Recent studies have revealed the mechanisms that enable insects to stay, as well as walk, on water [5]-[11]. Various kinds of miniature robots, which are able to move on water, have been developed. Hu et al. [5] identified the mechanism of the momentum transfer that was responsible for water strider locomotion and proposed a mechanical water strider driven by elastic thread. Gao et al. [6] showed that the legs of water striders are covered with thousands of tiny hairs that have fine nanoscale grooves. These hierarchical micro- and nanostructures create super hydrophobic surfaces. Suhr et al. [9] developed a water strider robot that is driven in one of its resonant modes using unimorph piezoelectric actuators. Song et al. [10]-[11] analyzed the statics of the supporting leg and developed a non-tethered water strider robot using two miniature DC motors and a lithium-polymer battery. In the present study, to understand the effects of surface tension, a more detailed analysis of the supporting leg, including the lift and the pull-off force, was carried out both theoretically and experimentally. Hydrophobic supporting legs with microstructured surfaces were developed using MEMS (micro electromechanical systems) techniques. Furthermore, two non-tethered mechanisms for water strider robots with microfabricated legs were created, and wireless locomotion on water was demonstrated. Locomotion that depends on surface tension provides miniature robots with efficient mobility on shallow water. In the near future, such robots could potentially be used for entertainment or water quality monitoring.

Manuscript received April 9, 2007. This work was supported in part by the Smart Machine and Micro-Bio Systems Research Center (SMBC) in Kogakuin University, which is one of the private universities' "High-Tech Research Center" projects, and a matching fund subsidy from MEXT (Ministry of Education, Culture, Sports, Science and Technology), 2003-2007. This work was also partially supported by the MEXT Grant-in-Aid for Scientific Research (C), 17510108, 2005-2006.

K. Suzuki and H. Koike are with the Department of Mechanical Systems Engineering, Kogakuin University, 2665-1, Nakano-machi, Hachioji-shi, Tokyo 192-0015, Japan (Phone: +81-42-628-4905; Fax: +81-42-627-2360; e-mail: ksuzuki@cc.kogakuin.ac.jp).

H. Takanobu, K. Noya and H. Miura are with the Department of Mechanical Systems Engineering, Kogakuin University, 1-24-2 Nishi-shinjuku, Shinjuku, Tokyo 163-8677, Japan (e-mail: takanobu@ieee.org).

II. Numerical Model of the Supporting Leg

The loading capacity of the supporting leg is an important design parameter. In this section, a numerical model of the forces acting on the supporting leg is proposed.

A. Lift force

Figure 1 shows a two-dimensional model of the supporting leg. We assume that the leg is a unit-length, long, rigid cylinder with radius r, and is made of a material with contact angle θ_c. The vertical lift force F acting on the leg consists of a buoyancy force F_b and a force due to surface tension F_s.

$$F = F_b + F_s \tag{1}$$

The buoyancy force F_b is deduced by integrating the vertical component of the hydrostatic pressure p over the body area in contact with the water. The force due to surface tension F_s is the vertical component of the surface tension γ along the contact perimeter. Keller [12] showed that F_b and F_s are equal to the weights of the fluid displaced inside and outside of the contact perimeter, respectively. That is, F_b is proportional to the area S_1, shown in Fig. 1, and F_s is proportional to the area S_2.

$$F_b = \int_0^{\phi_0} p\cos\phi \cdot r\, d\phi = \rho g S_1$$

$$= \rho g\,(-2 z_0 r \sin\phi_0 - r^2 \sin\phi_0 \cos\phi_0 + r^2 \phi_0) \quad (2)$$

$$F_s = 2\gamma \sin\theta_0 = \rho g S_2 \quad (3)$$

where the definitions of ϕ_0 and θ_0 are shown in Fig.1. The relationship between them is:

$$\phi_0 = \pi + \theta_0 - \theta_c \quad (4)$$

From the Young-Laplace equation, hydrostatic pressure on the water surface is

$$p = -\rho g z = \frac{\gamma}{R} \quad (5)$$

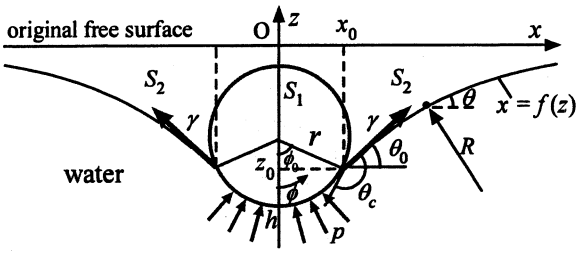

Fig. 1 2D model of a supporting leg

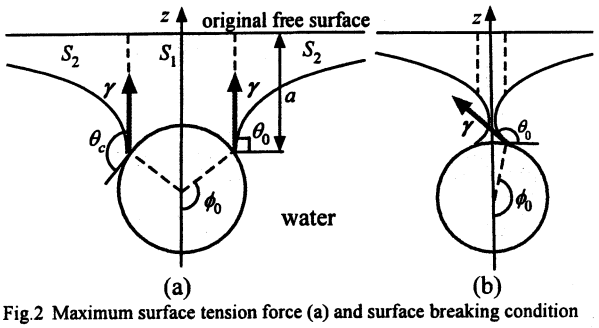

Fig.2 Maximum surface tension force (a) and surface breaking condition (b)

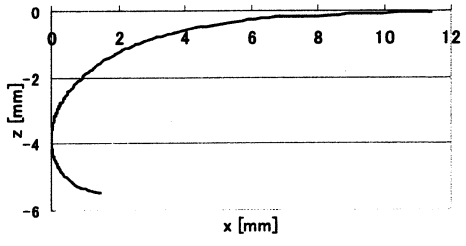

Fig. 3 Water surface profile calculated by (11).

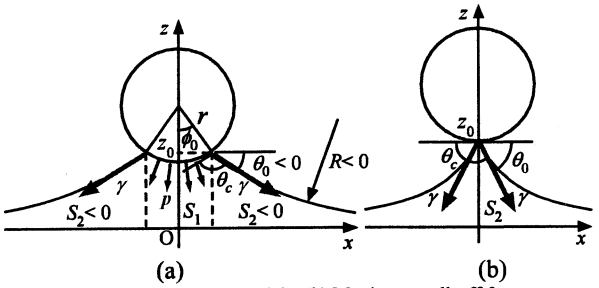

Fig. 4 Pull-off force. (a) 2D model , (b) Maximum pull-off force.

where R is the radius of curvature of the water's surface. The governing equation of the water's surface profile, $x = f(z)$, is given by

$$\frac{\rho g z}{\gamma} = -\frac{1}{R} = -\frac{f''(z)}{\left(1 + f'(z)^2\right)^{\frac{3}{2}}} \quad (6)$$

The boundary conditions for $f(z)$ are

$$f(0) = \infty \ , \ f(z_0) = x_0 \quad (7)$$

By integrating (6) from 0 to z, the following equation is obtained

$$\frac{\rho g z^2}{2\gamma} = 1 - \frac{f'(z)}{\sqrt{1 + f'(z)^2}} = 1 - \cos\theta \quad (8)$$

where θ is the slope of the water surface ($f'(z) = \cot\theta$). Then, the following equations can be derived from (8).

$$z = \pm a\sqrt{1 - \cos\theta} \ , \ a = \sqrt{\frac{2\gamma}{\rho g}} \quad (9)$$

$$f'(z) = \frac{a^2 - z^2}{-z\sqrt{2a^2 - z^2}} \quad (10)$$

By integrating (10), the equation of the water's surface profile is:

$$x = f(z) = \frac{a}{\sqrt{2}} \cosh^{-1}\left(\frac{\sqrt{2}\,a}{|z|}\right) - \sqrt{2a^2 - z^2} + C \quad (11)$$

The constant C can be determined from the boundary conditions (7). Figure 3 shows the water surface profile given by (11). From (3), the force due to surface tension F_s reaches a maximum value at $\theta_0 = \pi/2$. Under this condition, the depth of the contact perimeter becomes a, as shown in Fig.2 (a).

$$(F_S)_{\max} = 2\gamma \quad (12)$$

$$z_0 = -a = -\sqrt{\frac{2\gamma}{\rho g}} \quad (13)$$

Substituting the values of material constants at 20°C ($\gamma = 7.28\times10^{-2}$, $g = 9.81$ m/s^2 and $\rho = 9.98\times10^2$ kg/m^3) into (13), a is obtained as 3.86 mm. It is noted that both the maximum surface tension force and the value of a do not depend on the diameter of the leg or the contact angle θ_c if the surface is hydrophobic ($\theta_c > \pi/2$). On the other hand, the buoyancy force F_b does depend on the diameter of the supporting leg. When the diameter is much smaller than a, the force due to surface tension dominates over the buoyancy force.

As the depth of the contact perimeter exceeds a, θ_0 becomes greater than $\pi/2$, and the surface tension force decreases with increasing depth. Figure 2 (b) shows the water surface profile just before the surface is broken.

B. Pull-off force

When the leg is lifted out of the water, the water rises with the leg, as shown in Fig. 4(a). The buoyancy force and the force due to surface tension, given by (2) and (3) respectively, both

become negative, that is, downward forces. In this paper, the force needed to lift the leg from water is defined as the pull-off force. Figure 4 (b) shows the water surface profile just before the leg is completely pulled off. In this situation, the buoyancy force becomes zero, and the maximum pull-off force is given by:

$$F = -2\gamma\cos\theta_0 = 2\gamma\cos\theta_c \qquad (14)$$

Equation (14) shows that a leg with a large contact angle can be easily lifted from the water surface. Therefore, water striders' super hydrophobic legs reduce the pull-off force rather than generating a strong supporting force.

C. *Results of the simulation*

Figure 5 shows the calculated lift force and the pull-off force for 30-mm-long legs as a function of the height of the leg *h*, in the z-direction measured from the bottom of the leg, as shown in Fig.1. The pull-off force is shown as a negative lift force. Figure 5 (a) shows the effect of the leg surface's contact angle on the pull-off force. The lift force is almost independent of the contact angle, while the pull-off force depends on the contact angle. Figure 5 (b) shows the effect of the leg's diameter on the lift force. The maximum lift force increases with increasing leg diameters, due to the increase in buoyancy. However, if the density of the leg is equal to or greater than that of water, the buoyancy is roughly canceled by the weight of the leg itself. The net load is thus supported by the force due to surface tension, which is independent of the diameter

III. Fabrication of the Microstructured Legs

According to Wenzel's law, micro structures on a surface enhance hydrophobicity. Mechanical structures, as well as chemical properties, also play an important role in creating super hydrophobic surfaces. In the present paper, three kinds of hydrophobic supporting legs with micro structures fabricated using MEMS processes, are proposed. They are shown in Fig. 6.

Figure 6 (a) shows a PDMS (polydimethlysiloxane) hair-like structure formed on a 0.5-mm-diameter brass wire. A comb-shaped PDMS film, shown in Fig. 7 (a), is wrapped around this wire. The fabrication process for the PDMS structure is shown in Fig. 7 (b). First, the comb-shaped mold was patterned using SU-8, a photoresist that enables the creation of thick patterns by UV lithography. PDMS was poured into the grooves of the mold by capillary action. The

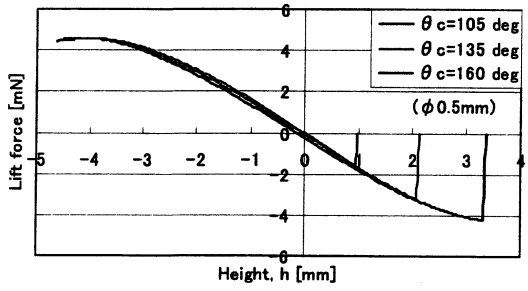

(a) Effect of contact angle. The diameter of the leg is 0.5 mm.

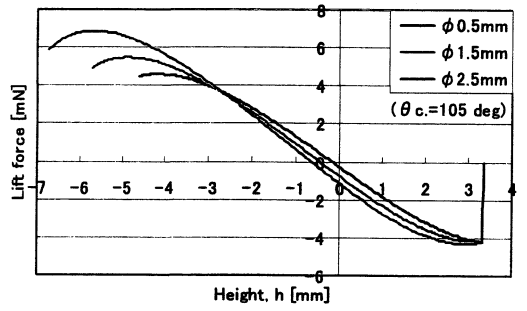

(b) Effect of diameter. The contact angle is 105 degrees.

Fig. 5 Calculated lift force. The leg length is 30 mm.

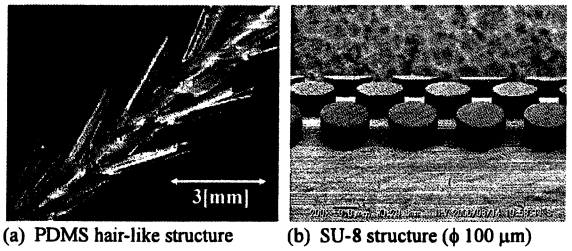

(a) PDMS hair-like structure (b) SU-8 structure (φ 100 μm)

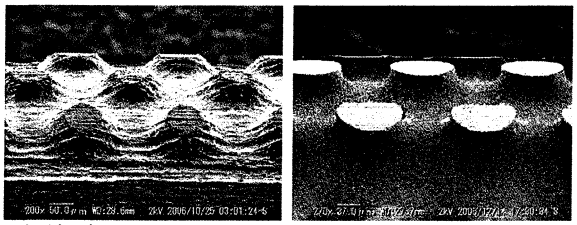

(c) Aluminum structure (d) Brass structure

Fig. 6 Microstructures on cylindrical supporting legs.

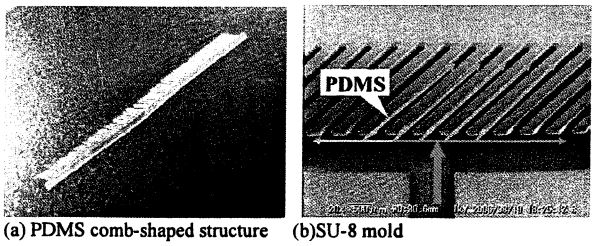

(a) PDMS comb-shaped structure (b)SU-8 mold

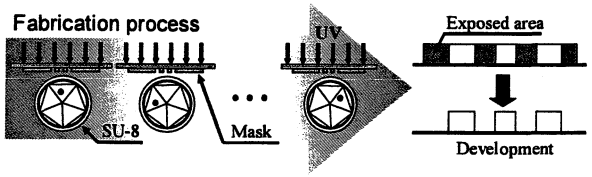

(c) Patterning of SU-8 structure

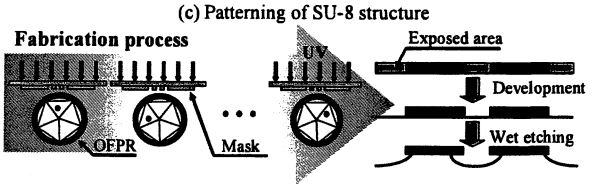

(d) Patterning and etching of metal wires

Fig.7 Fabrication processes.

PDMS structure was then cured and released from the mold. Finally, the structure was wrapped around the wire, dipped into, and coated by a fluorinated hydrophobic agent (FS-1010).

The second structure, shown in Fig. 6(b), consists of SU-8 patterns fabricated by photolithography on a 1-mm-diameter cylindrical brass wire. The diameters of the circular patterns are 100 μm. The fabrication process is shown in Fig. 7 (c). First, SU-8 was coated on the wire by dipping. The surface of the SU-8 layer was divided into 5 faces, with each face being patterned separately.

The third structure was formed on the surface of a metal wire by wet etching. Figures 6 (c) and (d) show the aluminum and brass structures, respectively. As shown in Fig. 7 (d), the photolithography was carried out on the cylindrical wire in the same manner as the SU-8 structure. The OFPR resist was used instead of SU-8. The wires were then patterned by wet isotropic etching. Compared with aluminum wire, the brass wire has structures with sharper edges.

IV. Measurement of the Lift and Pull-off Forces

A. Experimental setup

To investigate the performance of the supporting legs with microstructures, the lift and pull-off forces of the legs were measured. The experimental setup for these measurements is shown in Fig. 8. The geometry and the contact angles of the specimen are shown in Fig. 9 and Table I. The water surface was moved vertically using a z stage to immerse and pull out the specimen. The lift force and the pull-off force were obtained by using a laser displacement gauge to detect the deformation of a parallel leaf spring fixed to the specimen. Using two laser displacement gauges, the relative distance between the water's surface and the specimen was also measured.

B. Experimental results

The experimental lift force results obtained for various kinds of legs are shown in Fig.10. HIREC1450 is a fluorinated hydrophobic agent that was sprayed on the leg surface. As the leg depth increases, the lift force initially increases, reaches a maximum, and then decreases slightly; finally, the water's surface is broken.

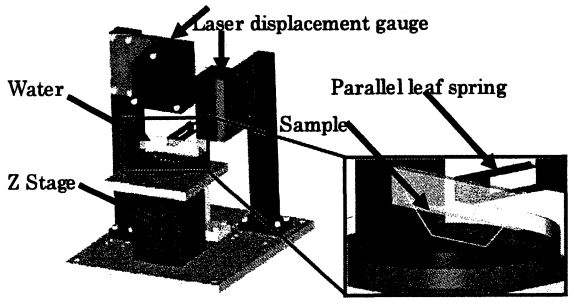

Fig. 8 Experimental setup for measurements

TABLE I
Material, Diameter, and Contact Angle of the Legs

Material	Diameter [mm]	Contact angle [deg]
PDMS	2.5	117
SU-8	1.1	128
Aluminum	1.4	123
Brass	1.0	123
Hirec 1450	0.5	138

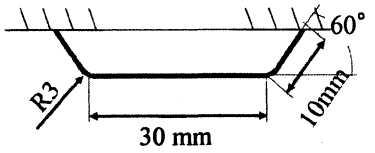

Fig. 9 Specimen's geometry

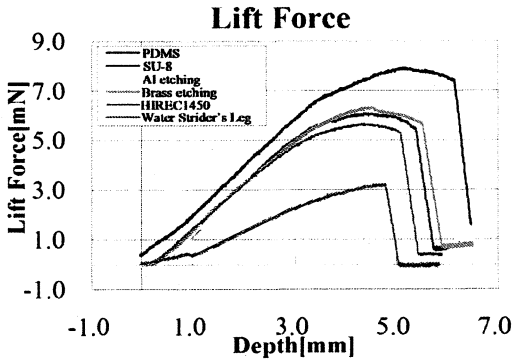

Fig.10 Lift forces for various microfabricated legs

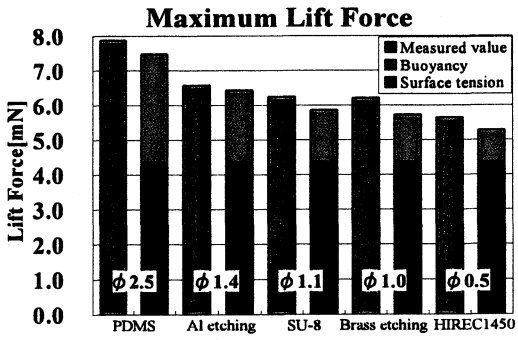

Fig. 11 Comparison between measured and calculated maximum lift forces.

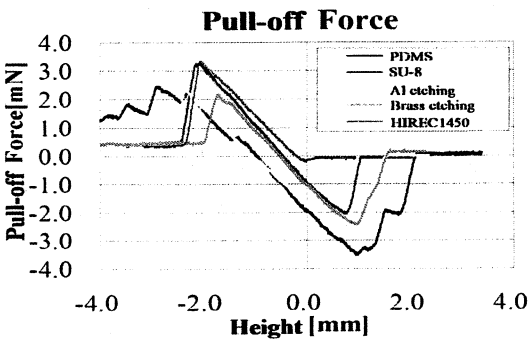

Fig. 12 Pull-off forces for various microfabricated legs

A comparison between the measured and calculated maximum lift forces is shown in Fig. 11. The orange and blue bars represent the calculated buoyancy force and the force due to surface tension, respectively. The effects of the specimen's angled ends were ignored in the calculations. Nonetheless, the experimental results are in good agreement with the calculations. The surface tension forces are the same, regardless of the material used, since the maximum surface tension force is 2γ per unit length if the surface of the leg is hydrophobic. The differences in lift force are derived from the differing buoyancy forces that depend on the leg's diameter.

The pull-off forces for the microfabricated legs are shown as negative forces in Fig. 12. The legs were first submerged completely in the water, and then the water's surface was lowered gradually by using the z stage. The force acting on the legs is plotted as a function of height between the leg and the water's surface. It was found that the maximum pull-off force decreases as the contact angle increases. The theoretical predictions shown in Fig. 5 were verified by the experiments.

V. Development of Water Strider Robots

A. Water strider robot using a vibration motor

Two different mechanisms for locomotion on water were developed. Figure 13 shows a water strider robot that uses a vibration motor with an eccentric weight. Twelve micropatterned brass legs, shown in Fig.6 (d), support the robot's body. The roles and specifications of the legs are shown in Table II. Each leg has a different length and consequently a different resonant frequency. When the rotational speed of the motor is varied, different legs resonate, enabling the robot to move forward, left, and right. A vibration motor, a lithium polymer battery, and electrical circuits for PWM (pulse width modulation) were mounted on the robot. In this manner, non-tethered actuation was achieved. The robot weighed 7.85 g and could therefore be supported by the hydrophobic legs without breaking the water's surface. Photographs of the robot moving on the water surface are shown in Fig. 15. The velocity of the forward motion was about 70 mm/s, while both the velocities of left and right turns were 50 mm/s. The radii of the left and right turns were 700 mm and 800 mm, respectively. These differences are due to the differences in the number and the length of the activated legs.

B. Hexapod water strider robot

The other mechanism developed in the present study was a hexapod robot, as shown in Fig. 16. The forelegs and hind legs support the body, while the middle legs generate the elliptical motion required for propulsion. This locomotion mechanism is similar to that of an actual water strider. The supporting legs were 135 mm in length and had PDMS hair-like structures. The loading capacity of the four supporting legs was predicted to be 7.5 g, which was sufficient to support the weight of the robot (5.4 g). A DC

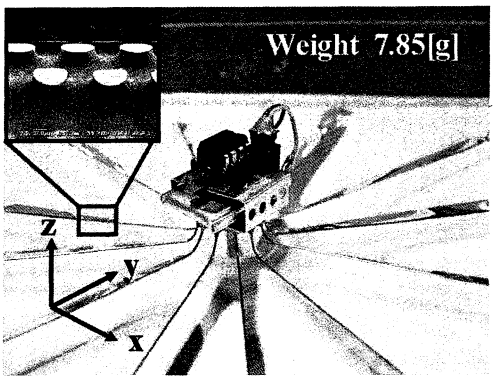

Fig. 13 Water strider robot with a vibration motor

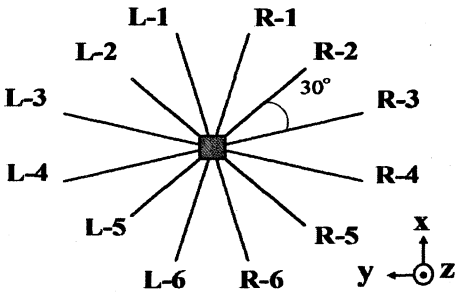

Fig. 14 Design of the supporting legs

TABLE II
Role, Length, and Resonant Frequency of the Leg

Leg No.	Role	Length	Resonant Frequency	Duty cycle of input pulse
L-1,6 R-1,6	Support	85 mm	-	-
L-3,4 R-3,4	Straight motion	95 mm	109 Hz	32 %
L-2,5	Right turn	80 mm	115 Hz	34 %
R-2,5	Left turn	70 mm	132 Hz	39 %

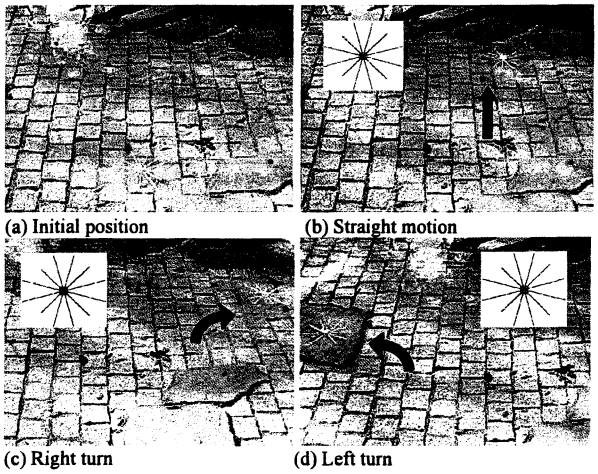

(a) Initial position (b) Straight motion

(c) Right turn (d) Left turn

Fig. 15 Locomotion on the water surface.

motor and a lithium polymer battery were mounted on the body, and wireless actuation was achieved. As shown in Fig. 17, a slider-crank mechanism was used for creating the elliptical motion of the middle legs. The simulated trajectory of the middle leg is shown in Fig. 18. The velocity of the locomotion on a water surface was determined from the images of a high-speed camera, and the experimental results are shown in Fig. 19. Forward locomotion using surface tension was successfully achieved. The middle legs were driven at 2 Hz. A maximum speed of 90 mm/s and an average speed of 40 mm/s were achieved.

VI. Conclusion

Various kinds of supporting legs with microstructured surfaces were fabricated using MEMS techniques. The lift and pull-off forces of the legs were investigated theoretically and experimentally, and the experimental results were in good agreement with the theoretical predictions.

An autonomous water strider robot with a vibration motor was developed. Forward motion and left/right turns were achieved by using the legs' different resonant frequencies.

A hexapod water strider robot was also developed. Locomotion on the surface of water was achieved by the elliptical motion of the middle legs, which is similar to that of an actual water strider.

References

[1] K. Suzuki, I. Shimoyama and H. Miura, "Insect-Model Based Microrobot with Elastic Hinges," *IEEE J. Microelectromecanical Systems*, Vol. 3, No. 1, March, 1994, pp. 4-9.

[2] M. Sitti, "Piezoelectrically Actuated Four-Bar Mechanism with Two Flexible Links for Micromechanical Flying Insect Thorax," *IEEE/ASME Trans. on Mechatronics* , Vol. 8, No. 1, March 2003, pp.26-36.

[3] N. Pornsin-Sirirak, M. Liger, Y.-C. Tai, S. Ho and C.-M. Ho, "Flexible Parylene-Valved Skin for Adaptive Flow Control," in *Proc 15th IEEE Int. Conf. on MEMS* 2002, pp.101-104.

[4] T. N. Pornsin-Sirirak, S.W. Lee, H. Nassef, J. Grasmeyer, Y.-C. Tai, C. -M. Ho, M. Keennon, "MEMS Wing Technology for a Battery-Powered Ornithopter," in *Proc 13th IEEE Int. Conf. on MEMS* 2000, pp. 799-804.

[5] D. L. Hu, B. Xhan and J. W. M. Bush,"The hydrodynamics of water strider locomotion," *Nature*, Vol.424, 7 August 2003, pp.663-666.

[6] Xuefeng Gao and Lei Jiang, "Water-repellent legs of water strider," *Nature*, Vol. 432, 4 November 2004, p.36.

[7] R. B. Suter and H. Wildman, "Locomotion on the Water Surface: Propulsive Mechanisms of the Fisher Spider *DOLOMES TRITON*," *J. Experimental Biology*, Vol. 200, 1997, pp. 2523-2538.

[8] R. B. Suter, O. Rosenberg, S. Loeb, H. Wildman and J. H. Long, Jr., "Locomotion on the Water Surface: Hydrodynamic Constraints on Rowing Velocity Require a Gait Change," *J. Experimental Biology*, Vol. 202, 1999, pp. 2771-2785.

[9] S. H. Suhr, Y. S. Song, S. J. Lee, and M. Sitti, "Biologically Inspired Water Strider Robot," *Robotics: Science and Systems*, MIT, Boston, June 2005.

[10] Y. S. Song, S. H. Suhr and M. Sitti, "Modeling of the Supporting Legs for Designing Biomimetic Water Strider Robots," in *Proc. IEEE Int. Conf. on Robotics and Automation*, Orlando, 2006, pp.2303-2310.

[11] Y. S. Song and M. Sitti, "STRIDE: A Highly Maneuverable and Non-Tethered Water Strider Robot," in *Proc. of IEEE Int. Conf. on Robotics and Automation*, Roma, 2007, pp.980-984

[12] J. B. Keller, "Surface tension force on a partly submerged body," *Physics of Fluids*, Vol. 10, No. 11, Nov. 1998, pp.3009-3010.

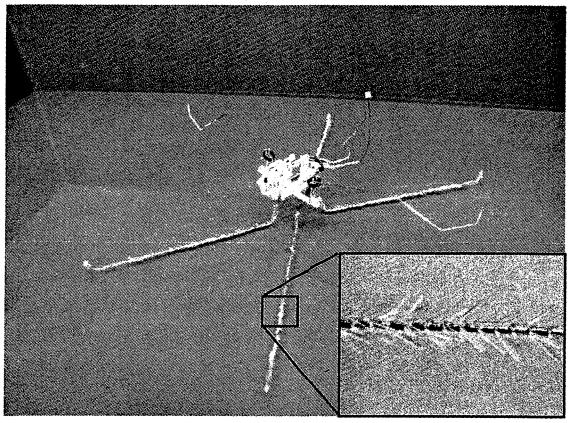

Fig. 16 Hexapod water strider robot

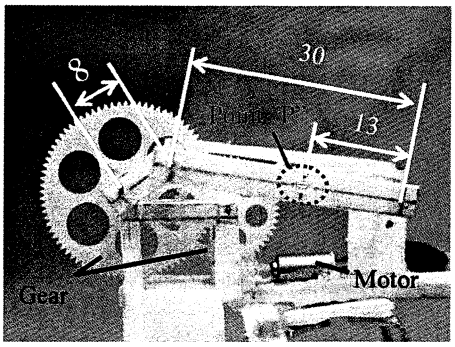

Fig. 17 Slider-crank mechanism for creating the elliptical motion of the middle leg.

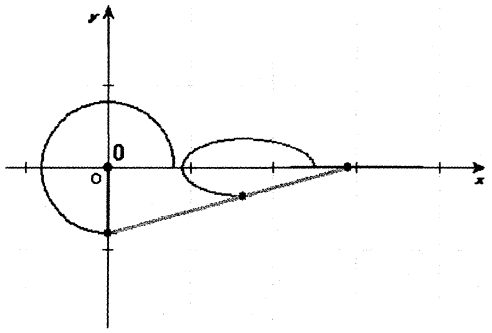

Fig. 18 Elliptical trajectory of the middle leg

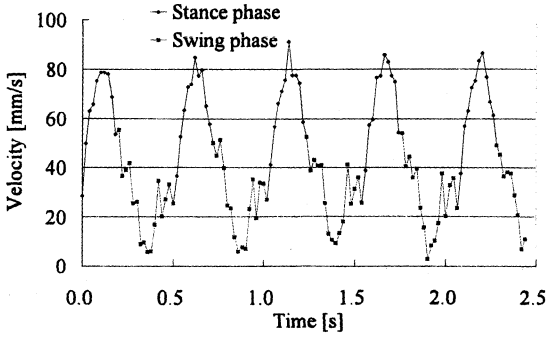

Fig. 19 Experimental results

Study on Insect-Model-Based Adhesive Robot on Vertical Wall

Y. Fujigaki*, T. Aizawa, K. Suzuki, H. Takanobu, H. Miura

Abstract This paper describes adhesive robot that walks on a vertical wall based on adhesion mechanism of ants. First, adhesion mechanism of ants was investigated experimentally. It was found that the adhesion was responsible for surface tension of liquid secreted from the end of the leg. Then an adhesive pad based on an adhesive organ of ant was fabricated by using microfabrication techniques of PDMS and adhesive properties of the pad were measured. Furthermore, a hexapod microrobot with the adhesive pads on its soles was developed. The robot successfully walked on a vertical wall.

Keywords : Insect-Model-Based Robot, Adhesion, Meniscus force, Surface tensity

1. INTRODUCTION

As size of a mechanical element decreases, ratio of the surface area to the volume increases and surface forces including van der Warals force and meniscus force become dominant compared to the gravity force. The surface forces often causes increase in friction and wear of moving parts of microdevices. Consequently reduction of surface forces is important.to design the microsystems. On the other hand, insects can move freely on a vertical wall and a ceiling. It is considered that insects take advantage of surface forces such as van der Warals force and meniscus force to adhere to walls[1]-[4]. The adhesion is specific characteristics of small living things and may provide a new design guidline for microsystems The purpose of this study is to clarify the adhesion mechanism of insects and apply it to microrobots.

2. ADHESION MECHANISM OF ANTS

In this study, we focused on the adhesion mechanism of ants and ovserved a sole of ant walking on various surfaces under a microscope. When the ant walked on the smooth glass surface (Ra=0.25μm), a flexible "adhesive pad" came out from the end of the foot and liquid was secreated from the adhesive pad, as shown in Fig.1. The foot adhered to the vertical glass surface without slip. On the contrary, when the ant walked on a vertical smooth teflon surface (Ra=0.25μm), the leg slipped on the surface and falled down, although the liquid was secreted from the adhesive pad. In the case of rough teflon surface (Ra = 2.97 μm), the ant can walk by hooking the claws on the asperity of the surface. These obserevations indicate that the adhesion to the smooth surface is responsible for the secreted liquid, not for hooking of the claws. A small amount of liquid confined between two hydrophilic surfaces such as glass surface generates an attractive force caused by surface tension of the liquid, which is called "meniscus force". The results of ovservations suggest that ants adhere to smooth surfaces by meniscus force of the liquid secreted from the adhesive pad.

* Department of Mechanical Systems Engineering, Kogakuin University 2665-1 Nakanomachi, Hachioji-shi Tokyo

3. FABRICATION OF ADHESIVE PAD

The adhesive pad based on the adhesion mechanism of ant was fabricated using microfabrication techniques. Required functions of the adhesive pad are to supply the liquid from the holes in the surface, and flexibility to contact any surface closely. PDMS (Polydimethylsiloxane) was used as a material of the adhesive pad.. The adhesive pad consists of two PDMS layers. In the bottom layer, many holes was formed to supply the liquid. In the top layer, a flow channel connecting to the holes was fabricated The fabrication sequence of the adhesive pad is shown in Fig. 2.
First, The SU-8 resist was spin-coated on a silicon wafer and patterned to form the mold for the holes and the flow channel. Then PDMS was puored in the mold. Next, the top layer was peeded off from the wafer and bonded to the bottom layer. A tube for supplying the liquid is joined with the flow channel. Finally, the pad is peeled off from the wafer.

The fabricated adhesive pad is shown in fig. 3. The dimension of the adhesive pad is 4mm×7mm. The diameter of the holes is 0.1mm.

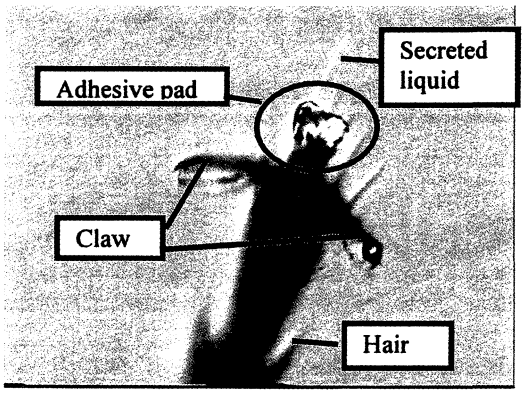

Fig.1 Adhesive pad at the end of ant's leg

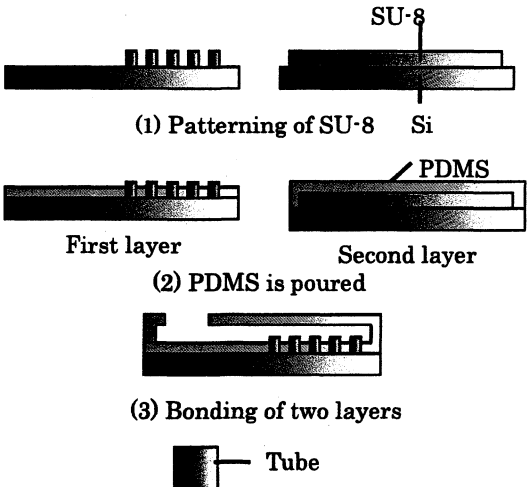

Fig.2 Process Sequence of adhesion pad

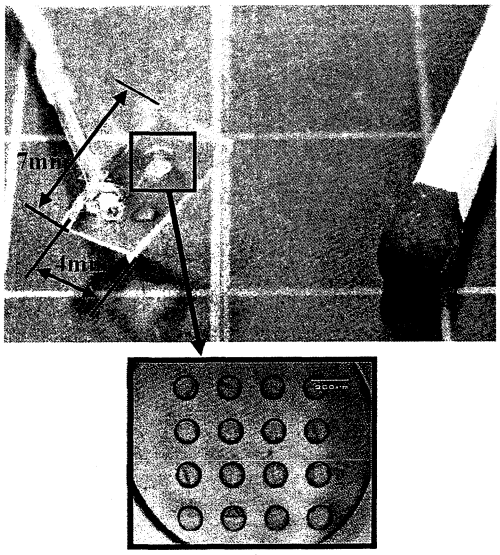

Fig. 3 Fabricated adhesive pad

4. MEASUREMENT OF ADHESIVE FORCE

Pull-off force of the adhesive pad from a quartz glass substrate was measured. Experimental setup for the measurement is shown in Fig.4. Double cantilever springs are used for the measurement. The deflection of the cantilever is measured with the laser displacement sensor, and the pull-off force is calculated from the displacement of cantilever.

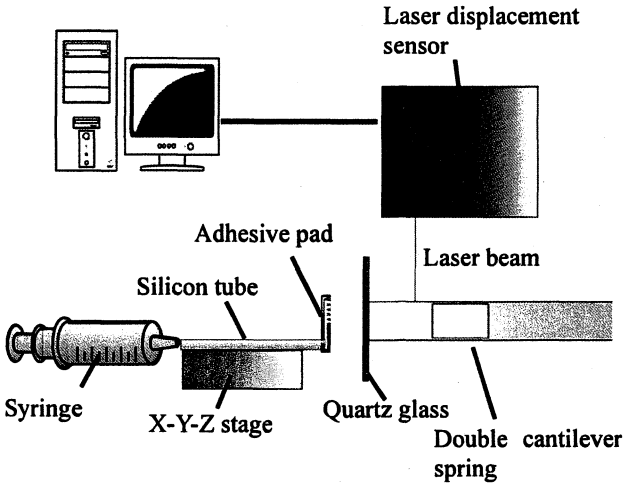

Fig. 4 Measurement of adhesive force

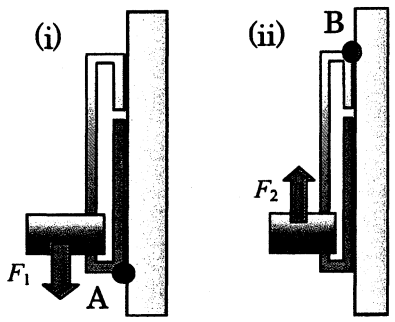

Fig. 5 Measurement of pull-off force

Table 1 Results of the measurements

	F_1	F_2
Water	408 mN	46.2 mN
Ethanol	314 mN	6.6 mN

Water and ethanol were tested as liquid. Pull-off force was applied by pulling the tube in two directions, F_1 and F_2, as shown in Fig.5. When F_1 is applied, the moment is acted to the adhesive pad around the heel (Point A) and the pad is peeled from the tiptoe side, while F_2 causes the moment around the tiptoe (point B) and the pad is peeled from the heel side. Results of the measurement are shown in Table 1. There was a great difference between F_1 and F_2, Peeling from the heel side is much easier than that from the tiptoe side. This phenomenon is dependent on the distribution of liquid, deformation of the pad, and geometry of contact surface, and the detailed mechanism has been not clarified. In regard to the supplied liquid, water generates larger adhesive force than ethanol. This is responsible for the larger surface tension of water.

5. FABRICATION OF ADHESIVE ROBOT

A hexapod robot that walks on vertical walls was fabricated by using the adhesive pads on the soles. The robot is required to adhere to the wall strongly enough to support its weight. However, when the robot detachs the leg from the wall, the adhesive force must be small. In order to meet these requirements, the robot was designed to apply the moment of the gravity force around the heel and to pull off the adhesive pad from the heel side to detach the leg. The mechanism of the leg is shown in Fig.6. The leg consists of an ABS (Acrylonitrile Butadiene Styrene) pipe, an adhesive pad, SMA (shape-memory alloy) actuators, and a spring. Adhesive pad was attached to the bottom surface of the leg and the tube for supplying the liquid was put through the pipe. The leg is contracted by two SMA wires in front and rear of the leg, and extended by the spring. Fig.7 shows the movement of the leg. When the leg is detached from the wall, the rear SMA wire is contracted first by passing an electric current to pull off the pad from the heel side. Then both sides of the SMA wires are contracted to detach the pad completely. When the leg is attached to the wall, the rear SMA wire is first extended by turning off the current to touch the wall from the heel side. Then the front SMA wire is extended.

The photograph of the adhesive robot is shown in Fig. 8. The dimension of the robot is 35mm in length, 25mm in width, and 25mm in height. The weight of the robot is 11g. The robot was controlled to walk in the "alternating tripod gait," which is one of the typical gaits of insects. Fig. 9 shows the alternating tripod gait. A filled circle represents a leg touching the wall and an open circle represents a leg in the air. Control system of the robot is shown in Fig. 10. The six legs were divided into two groups of diagonal three legs and the legs in each group were moved together so that each leg could move as shown in Fig. 7. Fig. 11 shows the adhesive robot attached to a vertical quartz glass surface. The robot walked successfully in alternating tripod gait on the vertical wall of quartz glass.

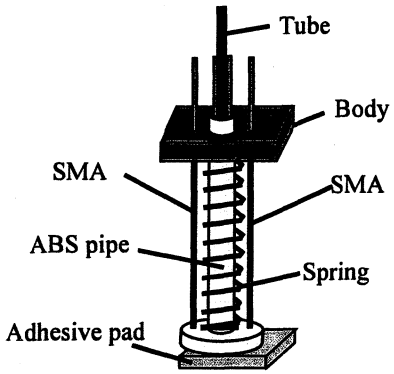

Fig.6 Mechanism of a leg

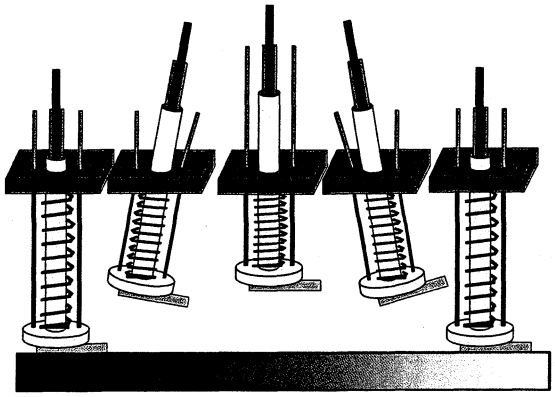

Fig. 7 Movement of a leg

Fig.9 Alternating tripod gait of an insect

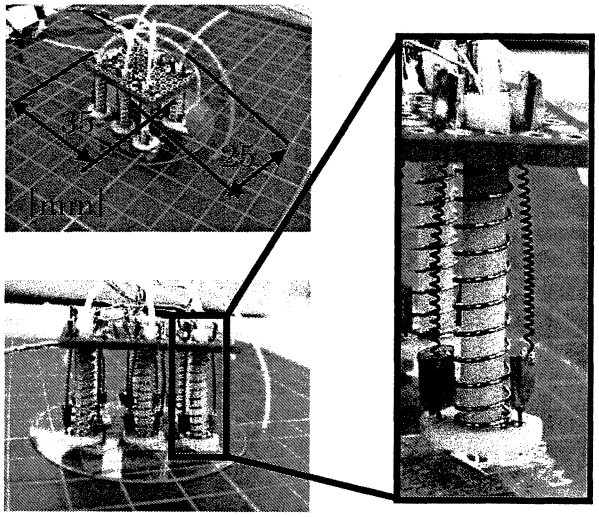

Fig.8 Adhesive robot

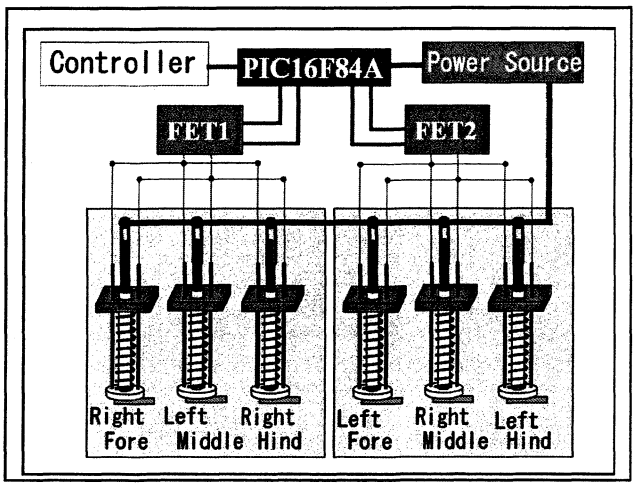

Fig.10 Control system

6. CONCLUSION

Adhesion mechanism of ants was investigated experimentally and the adhesion was found to be caused by meniscus force of liquid secreted from the end of the leg. Then an adhesive pad was fabricated based on an adhesive organ of ant. The pull off force of the adhesive pad was measured .Adhesive force was considerably small when the adhesive pad is peeled from the heel side. Then adhesive robot using the adhesive pad as a sole of each leg was fabricated. The robot was attached to the vertical wall and actuated by SMA so that the pull off force of the leg could be minimized. The robot successfully walked on a vertical wall of quartz glass.

Acknowledgments

This research was supported by Smart Machine and Micro-Bio Systems Research Center (SMBC) in Kogakuin University, which is one of the "High-Tech Research Center" projects for private universities: matching fund subsidy from MEXT (Ministry of Education, Culture, Sports, Science and Technology), 2003-2007.

References

[1] Walter Federle, Elizabeth L. Brainerd, Thomas A.McMahon, and Bert olldobler:"Biomechanics of the movable pretarsal adhesive organ in ants and bees", PNAS, Vol. 98, No.11.PP6215-6220

[2] N. E. Stork, "Experimental Analysis of Adhesion of Chrysolina Polita (Chrysomelidae: Coleoptera) on a Variety of Surfaces," J. exp. Biol. 88 (1980) pp.91- 107.

[3] G. Walker, A. B. Yule and J. Ratcliffe, "The Adhesive Organ of the Blowfly, Calliphora Vomitoria: a functional approach (Diptera: Calliphoridae)," J. Zoological Society of London, (A) 205 (1985) pp.297-307.

[4] M. Scherge, S.Gorb, Biological Micro- and Nano- tribology, Nature's Solutions, Springer (2001).

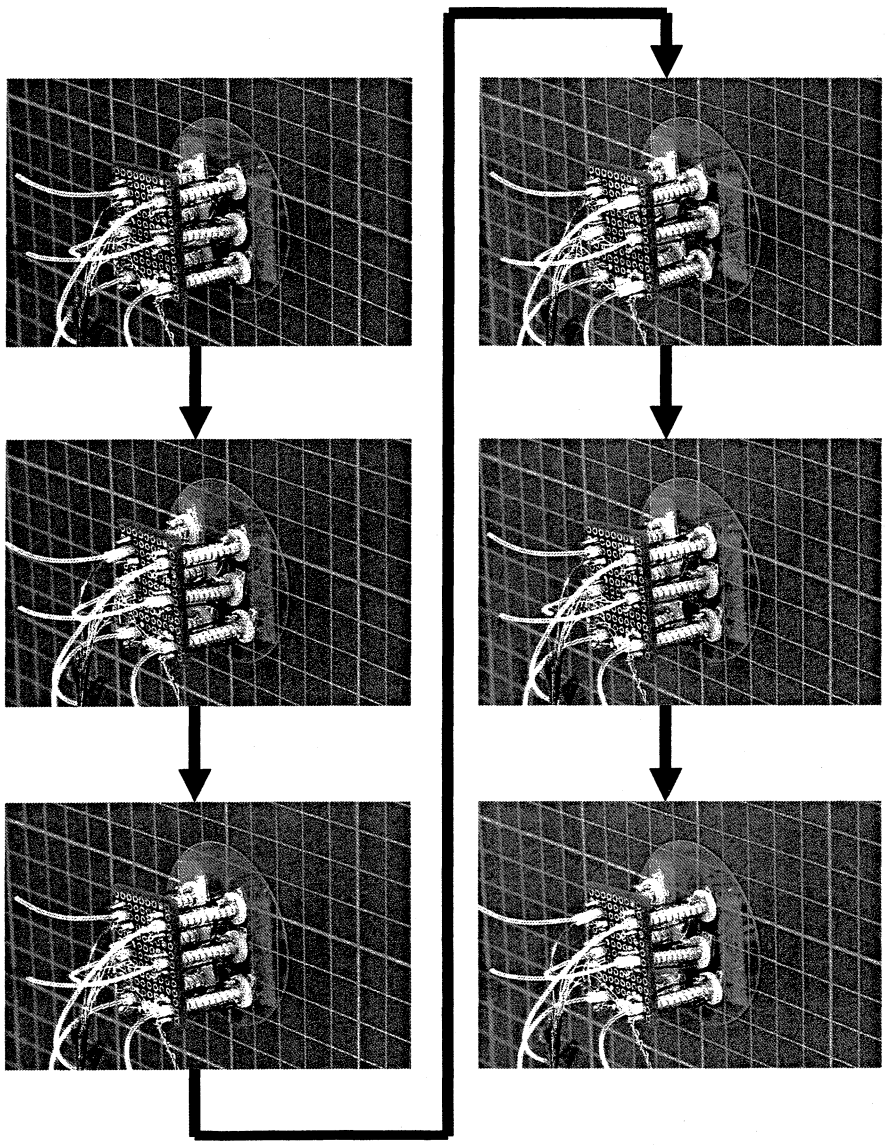

Fig. 11 Adhesive robot walking on a vertical wall

Available online at www.sciencedirect.com
ScienceDirect
Vacuum 81 (2007) 1003–1011
VACUUM
SURFACE ENGINEERING, SURFACE INSTRUMENTATION & VACUUM TECHNOLOGY
www.elsevier.com/locate/vacuum

Kinetic process of phase separation in Co–SiO_2 thin films and preparation of mesoporous SiO_2 thin films with mesopore channels aligned perpendicularly to substrate surfaces

Junichiro Otomo*, Ryo Kurokawa, Hiroshi Takahashi, Hidetoshi Nagamoto

Department of Environmental Chemical Engineering, Faculty of Engineering, Kogakuin University, 2665-1 Nakanomachi, Hachioji, Tokyo 192-0015, Japan

Received 26 July 2006; received in revised form 10 November 2006; accepted 23 December 2006

Abstract

A physical co-sputter deposition process under a relevant working gas pressure condition was used to produce a multi-component thin film with a longitudinally self-organized microstructure. In this paper, Co–Si–O thin films were prepared by radio frequency (RF) magnetron sputtering, and their growth structures were studied by means of SEM, TEM, XRD and XPS. The microstructural changes in the Co–Si–O thin film and their dependence on Ar working gas pressure were investigated; the formation of Co–Si–O thin films, having a regular array of needle-like Co columns aligned perpendicularly to the substrate surfaces, was observed with appropriate Ar working gas pressure, and the diameter of the columns increased with increasing Ar pressure. Mesoporous silica thin films having perpendicular mesopore channels were obtained by chemical etching of the columnar Co parts in the Co–Si–O thin films. Through experimental observations, we propose that the phase separation and resultant microstructures in the thin films are determined by the surface mobility of the two components (Co and silica) on the film surface. A simple model, incorporating a diffusion process in the simultaneous deposition of two components, is presented. The model demonstrates the general trends of a kinetically self-organized microstructure in a two-component thin film.

Keywords: Sputter deposition; Co–Si–O thin film; Phase separation; Mesoporous silica; Self-organization; Kinetic Monte Carlo simulation

1. Introduction

Mesoporous materials have many potential applications in catalysis, separation technology, and electronic and energy devices [1–6]. The advance of their synthetic methods is quite important. In this work, we investigate a preparation technique of mesoporous silica thin films by using radio frequency (RF) sputter deposition. The characteristic feature of the present mesoporous silica thin film is its mesopores oriented perpendicularly to the substrate surface.

In general, the preparation of mesoporous films having mesopores oriented perpendicularly to a substrate surface in conjunction with high pore volume and high specific surface area is quite difficult. Kondoh et al. previously reported mesoporous thin films with one-dimensional channels perpendicular to the substrate surface, which also have high specific surface areas (600–1000 $m^2 g^{-1}$) [7,8]. In Ref. [8], the authors used a co-deposition technique to prepare mesoporous films; a mixture of Co/TiO_2 was co-deposited on a substrate using RF sputter deposition to obtain a precursor Co–TiO_2 thin film. Under suitable conditions, needle-like Co surrounded by a titania matrix was formed in the thin film. Mesoporous titania films were successfully obtained by chemical etching of the needle-like Co parts (template method). Recently, the same authors also applied the template method for the preparation of mesoporous silica films from a precursor Co–SiO_2 thin film [9]. This method is very interesting in terms of its self-organization and applications, but the mechanism has not been clarified sufficiently.

Recently, we also prepared mesoporous silica films having mesopores oriented perpendicularly to the substrate

*Corresponding author. Tel./fax: +81 426 28 4523.
E-mail address: otomo@cc.kogakuin.ac.jp (J. Otomo).

0042-207X/$ - see front matter © 2007 Elsevier Ltd. All rights reserved.
doi:10.1016/j.vacuum.2006.12.007

surface from precursor FeO–SiO_2 thin films using the template method, and found that their microstructures were strongly dependent on the working gas (Ar gas) pressure during sputter deposition [6]. Thus, comprehension of the correlation between the microstructures in the thin films and the working gas pressure will bring an understanding to the self-organization mechanism in the template method. In this work, we investigated the longitudinally self-organized growth structure of sputter-deposited Co–SiO_2 thin films, and prepared the corresponding mesoporous silica thin films. We also discuss the mechanism of self-organization in Co–SiO_2 thin films through observation of the influence of working gas pressure on their microstructure. In a latter part of this paper, we attempt to explain self-organized film growth using a kinetic Monte Carlo simulation.

2. Experimental

The template method was applied to prepare mesoporous silica thin films, i.e. Co–Si–O thin films (we denote sputter-deposited thin films as Co–Si–O thin films, hereafter) were deposited on substrates using an RF magnetron sputterer, and then mesoporous silica thin films were obtained by removing the Co components from the Co–Si–O thin films in an HNO_3 aqueous solution. The detailed experimental procedure is as follows. First, the desired amounts of Co powder (Nilaco Co., Tokyo, Japan, purity >99.9%, 10 μm) and SiO_2 powder (Sigma-Aldrich Co., USA, purity >99.6%, 325 mesh) were mixed by ball milling and the resultant Co/SiO_2 powdered mixture was then pressed and set in a quartz plate to be used as a target. The Co:SiO_2 molar ratio of the Co/SiO_2 target was fixed at 83:17 (Co:SiO_2 volume ratio ≅ 6:4). Next, Co–Si–O thin films were deposited on suitable substrates such as glassy carbon (Tokai Carbon Co. Ltd., Tokyo, Japan) sheets and silica glass sheets under Ar-flow conditions (purity >99.99%) using an RF magnetron sputterer. Before deposition, these substrates were boiled in an HNO_3 aqueous solution (HNO_3 conc. 30 wt%) at 90 °C for 1 h, and then rinsed with Milli-Q water. To investigate the correlation between the growth structures of Co–Si–O thin films and sputter conditions, the Ar working gas pressure was changed between 10 and 100 mTorr. The target power density was fixed at 4.7 W cm^{-2}. The substrate temperature was not controlled during deposition. The typical size of the Co–Si–O thin films was ca. 5 mm × 5 mm × 2 μm thickness. The obtained Co–Si–O thin films were characterized by X-ray diffraction (XRD) (Rigaku Rint 2500VHF), field emission scanning electron microscopy (FE-SEM) (Hitachi S-4200), transmission electron microscopy (TEM) (Hitachi H-9000NAR) and X-ray photoelectron spectroscopy (XPS) (Physical Electronics Quantum 2000). The deposition rate was determined from the thickness of the obtained Co–Si–O thin films using FE-SEM. Finally, the Co component, which plays the role of template in the mesoporous silica thin film, was removed by wet etching in an HNO_3 aqueous solution (HNO_3 conc. 0.1–1 wt%) to obtain mesoporous silica thin films. After wet etching, the resultant samples were placed in methanol, and dried at approximately 5–10 °C. The microstructures of the mesoporous silica thin films were observed by FE-SEM, and the components in the thin films were examined by SEM-energy dispersive X-ray (EDX) analysis (Horiba EMAX-7000). Also, the N_2 adsorption–desorption isotherms were measured (Micrometrics ASAP 2010 system) to estimate the pore size distributions in the mesoporous silica thin films by using the Barrett–Joyner–Halenda (BJH) model [10]. The SEM, TEM, XRD and XPS characterizations for the Co–Si–O thin films and resultant mesoporous silica thin films were conducted using sputter-deposited thin films on glassy carbon substrates while the N_2 adsorption–desorption isotherm measurements were conducted using sputter-deposited thin films on silica glass substrates.

3. Results and discussion

3.1. Microstructures of Co–Si–O thin films and porous SiO_2 thin films

The color of the Co–Si–O thin films formed on silica glass substrates was black. Typical characterization results are given for the thin films in Figs. 1 and 2. The XRD patterns of the Co/SiO_2 target and Co–Si–O thin films are shown in Fig. 1. The XRD peak profile of the Co–Si–O thin film indicates that a crystalline Co hexagonal phase coexists with its cubic phase, but the Co peaks have a broadened feature, suggesting that the obtained Co–Si–O thin film includes small Co particles. Also, the XRD pattern of the Co–Si–O thin film has a broad peak between 15° and 25°, suggesting that amorphous SiO_2 forms in the

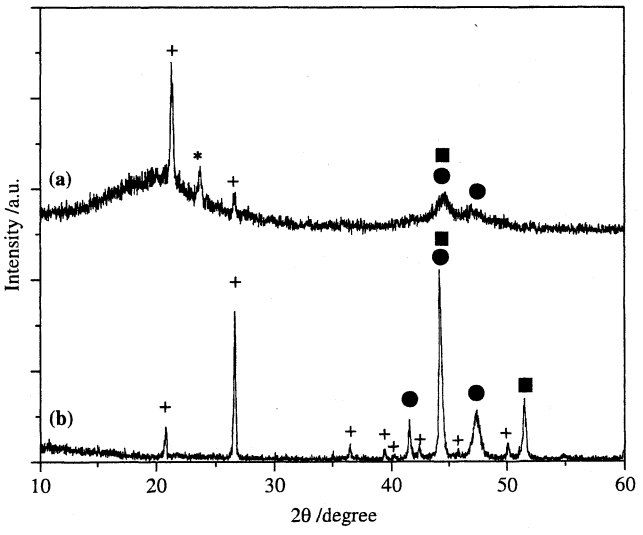

Fig. 1. XRD patterns of a Co–Si–O thin film and Co/SiO_2 target: (a) Co–Si–O thin film, (b) Co/SiO_2 target; ●: Co (hexagonal phase); ■: Co (cubic phase); +: SiO_2 (hexagonal phase); *: undefined peak.

Co–Si–O thin film, but an additional hexagonal SiO_2 phase is also observed (Fig. 1a). The composition of the Co–Si–O thin films was estimated from SEM–EDX analyses. The Co/Si atomic ratios in the Co–Si–O thin films were approximately identical to the initial molar ratios of the Co/SiO_2-target powder. The XPS profile of the Co–Si–O thin film is shown in Fig. 2. The binding energy of the Co–Si–O thin film at the Co $2p_{3/2}$ peak maximum was around 777.8 eV. According to previous reports, which gave the Co $2p_{3/2}$ peak position in Co as 778.1 eV [11], in CoO as 780.4 eV [12], in Co_3O_4 as 780.2 eV [13], and in Co_2O_3 as 779.9 eV [14], we conclude that the present Co–Si–O thin film consists primarily of Co and amorphous SiO_2, with a partial amount of hexagonal SiO_2.

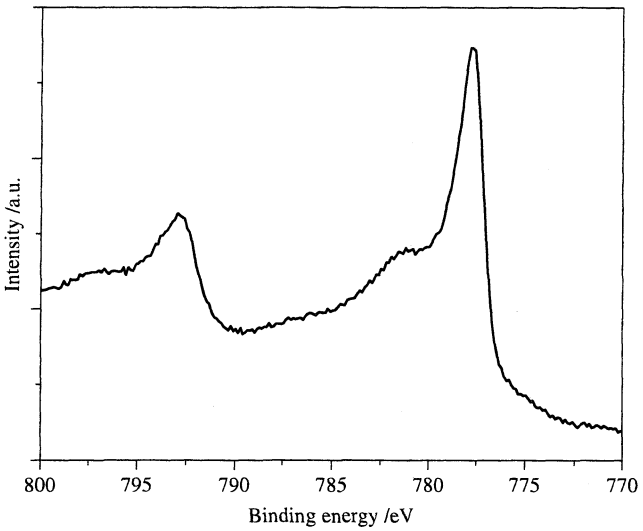

Fig. 2. X-ray photoelectron spectra of a Co–Si–O thin film (Co–Si–O-15 mTorr).

The growth structures of the Co–Si–O thin films deposited on glassy carbon substrates formed under different Ar pressures (10–100 mTorr) before etching were observed using FE-SEM. The Co–Si–O thin films deposited under different Ar pressures are designated as Co–Si–O (x) mTorr. The deposition rates of the thin films decreased monotonously with increasing Ar pressure between 10 and 100 mTorr. The cross-sectional images show that crack-free Co–Si–O thin films form on substrates. The microstructural textures of the Co–Si–O thin films were strongly dependent on the Ar pressure. At Ar pressures of 10 and 15 mTorr (deposition rates of Co–Si–O 10 mTorr and Co–Si–O 15 mTorr are ca. 940 and 890 nm h^{-1}, respectively), the cross-sectional images have no characteristic features (Fig. 3a and b). On the other hand, the microstructural textures of the Co–Si–O thin films revealed obvious changes at higher Ar pressures; the cross-section of Co–Si–O 80 mTorr (deposition rate: ca. 390 nm h^{-1}) shows a columnar microstructure (Fig. 3c). It was observed that similar columnar microstructures formed in Co–Si–O 100 mTorr (deposition rate: ca. 300 nm h^{-1}), as shown in Fig. 3d. The columnar microstructure, therefore, tends to grow with increasing Ar pressure.

Next, we conducted the wet etching of Co–Si–O thin films with non-columnar and columnar microstructures, i.e. SiO_2 thin films were prepared from Co–Si–O 15 mTorr

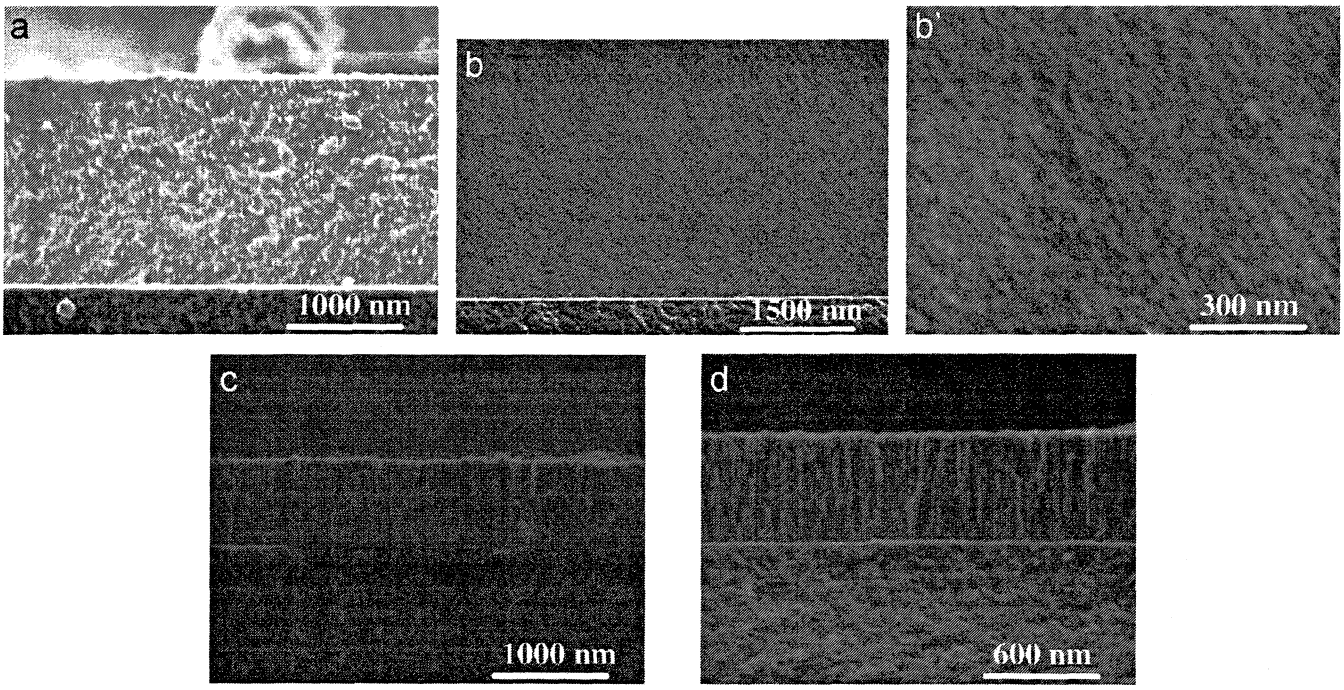

Fig. 3. SEM micrographs of cross-sections of Co–Si–O thin films on glassy carbon substrates at different Ar pressures. Deposition time: 2 h. (a) 10 mTorr; (b) 15 mTorr; (b′) enlarged view of (b); (c) 80 mTorr; (d) 100 mTorr.

and Co–Si–O 100 mTorr by wet etching. The obtained SiO_2 thin films are referred to hereafter as SiO_2 (x) mTorr-E. The SEM-EDX analysis of the films was again carried out and no Co was detected, suggesting that the Co component had been sufficiently removed from the Co–Si–O thin films such that only SiO_2 thin films remained. The microstructures of the obtained SiO_2 thin films were observed using FE-SEM. The SEM images of the SiO_2 thin films are shown in Fig. 4. The cross-sectional images of SiO_2 15 mTorr-E are shown in Fig. 4a, but no characteristic feature in the microstructural texture was observed. On the other hand, it was found that meso- and macro-pores formed in SiO_2 100 mTorr-E from the interface of the substrate and the surface of the SiO_2 thin film; the pores were oriented approximately perpendicular to the surface of the film (Fig. 4b). The top view of SiO_2 100 mTorr-E indicates that the pores having diameters in the order of 10^1–10^2 nm distribute randomly (Fig. 4b′).

In order to further investigate the microstructure of SiO_2 15 mTorr-E, an N_2 adsorption–desorption isotherm was measured. Fig. 5a shows the N_2 adsorption–desorption isotherm of SiO_2 15 mTorr-E, whose pattern has a hysteresis loop. This fact strongly suggests that SiO_2 15 mTorr-E consists of mesopores. The N_2 desorption volumes were plotted against the pore diameter in Fig. 5b. A sharp distribution of the pore diameters was obtained; the N_2 desorption peak was located at around 4 nm (Fig. 5b), and the N_2 adsorption peak was located at around 5 nm. The specific surface area of SiO_2 15 mTorr-E was estimated to be ca. 800 $m^2 g^{-1}$ from the total surface area and weight of the thin film; the film weight was not measured directly, but approximately estimated from the film volume (deposited area × film thickness) and film porosity (ca. 0.6) calculated from the Co–Si–O thin film composition.

To identify the microstructure of the thin film, we again observed the cross-section of a Co–Si–O thin film before etching (Co–Si–O 15 mTorr) by TEM observation (Fig. 6). The dark parts in the cross-sectional TEM images indicate Co parts. The formation of needlelike Co nanowires or cylindrical Co particles (ca. 5 nmϕ × ca. 10 nm height) was observed; the cylindrical Co parts connect together to form a needlelike array of Co columns aligned along the direction from the substrate to the surface of the thin film, as shown in Fig. 6b. Based on the above data, therefore, we can estimate the microstructure of a porous SiO_2 thin film; mesopores form in SiO_2 15 mTorr-E with a pore diameter of about 5 nm. Furthermore, the mesopores are oriented

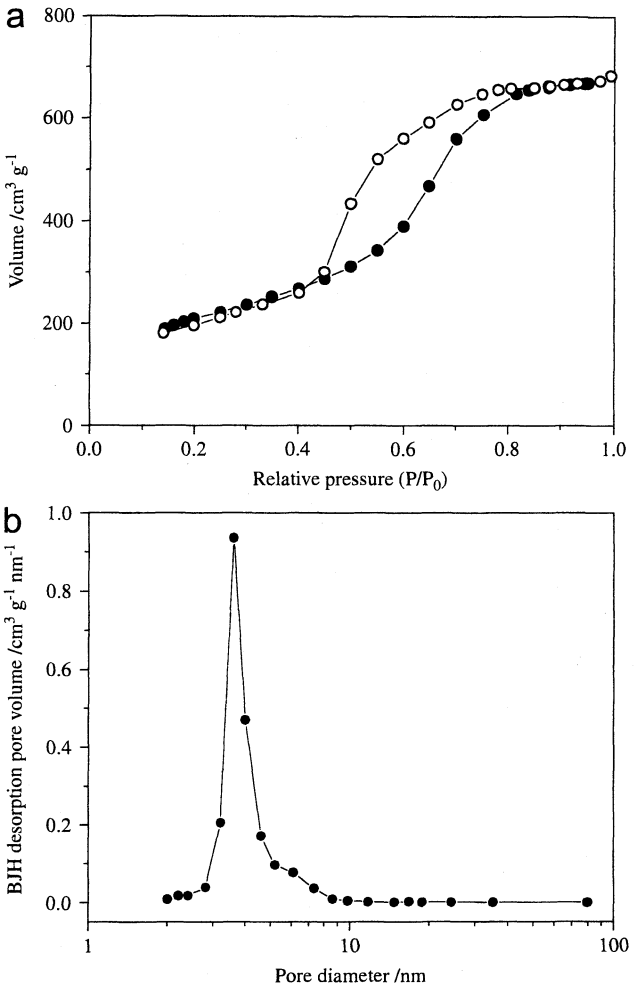

Fig. 5. (a) N_2 adsorption–desorption isotherm of SiO_2 15 mTorr-E; ○: adsorption; ●: desorption, (b) pore diameter distribution of SiO_2-15 mTorr-E (calculated from the desorption process).

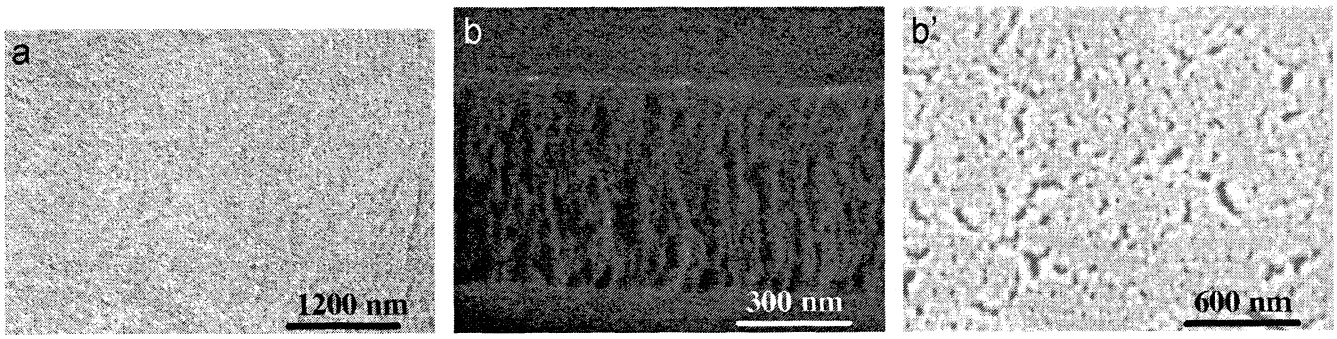

Fig. 4. SEM micrographs of SiO_2 thin films: (a) cross-sectional view of SiO_2 15 mTorr-E; (b) cross-sectional view of SiO_2 100 mTorr-E; (b′) top view of SiO_2 100 mTorr-E.

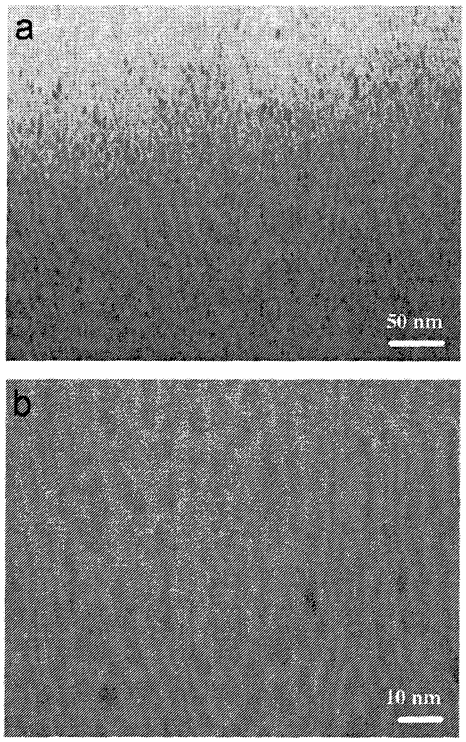

Fig. 6. TEM micrographs of a Co–Si–O thin film on a glassy carbon substrate. (a) cross-sectional view of Co–Si–O 15 mTorr; (b) enlarged view of (a). The upper direction of the images corresponds to the direction to the surface of the thin film, and the lower direction of the images corresponds to the direction to the substrate of the thin film.

approximately perpendicular to the surface of the film, although branch connections and meanderings exist.

As shown above, the sputtering conditions influence the microstructure of the deposited thin films. The transport step in the sputter deposition is controlled by certain deposition parameters, such as the apparatus geometry and working gas pressure, while the diffusion steps of the adatoms on the surface and in the bulk are controlled by the substrate temperature, but may also be influenced by energetic particle bombardment [15–17]. In the present study, the substrate temperatures were not controlled, but monitored during deposition, and found to be approximately 373–393 K, which is relatively low. Thus, the diffusion in the bulk can be negligible, while the influence of energetic particle bombardment on the surface diffusion step is considerable; the energetic particle bombardment will induce the surface diffusion of adatoms. Ar plays the main role of energetic particle bombardment, and thus the Ar pressure is more likely to influence the film structures. The present SEM observations of the thin films before and after etching show a strong dependence of the microstructures on Ar pressure. The TEM observations of the Co–Si–O thin film show direct evidence of the phase separation between Co and SiO_2 and their orientational microstructures. In addition, the TEM images suggest a relationship between the growth structures of the Co–Si–O thin films and the Ar pressure. At relatively low Ar pressures such as 15 mTorr, a longitudinally long shape of Co, i.e. regular array of Co columns, forms (see Fig. 6: TEM pictures). The formation of the regular array of Co columns suggests that surface diffusion of adatoms and the resultant nucleation of Co and SiO_2 during deposition govern the film structure. Because the bulk diffusion is negligible under the present condition, the ratio of surface diffusion length to deposition rate will be a key factor in the formation of the regular array of Co columns. The SEM pictures in Fig. 4 suggest that the surface diffusion length of the adatoms increases and greater Co nucleation occurs with further increasing Ar pressure up to 100 mTorr. The resultant formation of a needlelike regular array of Co columns proceeds with a one-dimensional alignment toward the surface of the substrate. Thus, we conclude that the surface diffusion length and deposition rate are important parameters for controlling the growth structures of Co–Si–O thin films. Next, we try to discuss the self-organized growth structures of deposited thin films using a kinetic Monte Carlo simulation.

3.2. Kinetic modeling of a co-deposition process

In order to discuss a self-organized growth structure having a regular array of mesoscale columns perpendicularly arraigned to a substrate, we employed a simple model for phase separation in a thin film that consists of two kinds of particles; A-particles and B-particles. Although the deposition process or trajectories of the adatoms in a Co–Si–O thin film cannot be exactly reproduced by the two particles (A and B), here we focus on the discussion of the relationship between the phase separation of the growth structure and the control parameters, such as surface diffusion length and deposition rate; the formation of A- and B-domains in the model will reflect the phase separation of Co and silica in a Co–Si–O thin film, which can then be used to help understand the present phenomenon. Since we deal with deposition, diffusion and diffusional phase separation in our model, the growth mechanism of thin films can be modeled with a kinetic Monte Carlo simulation [18–27]. The present experimental results suggest that phase separation during deposition is governed by the surface diffusion of adatoms. We therefore, assume that the diffusion process occurs on the film surface, and is negligible in the bulk phase in this model (solid-on-solid model), where the crystal is treated as a simple cubic lattice, with the requirement that no vacancy sites exist within the crystal and overhangs are not permitted. The solid-on-solid model has been used for molecular-beam epitaxial growth [19,20], and it has helped to elucidate basic physical mechanisms that influence growth structures [24–27]. In our study, the solid-on-solid model is extended to two components to describe phase separation (a kinetic phase separation model) [27]. The cross-sectional structure of a thin film reflects the history of the stacked layers formed via the deposition and diffusive jump steps on the film surface; the cross-sectional structure

will be determined from the deposition rate and surface diffusion length of the adatoms.

An $N \times N$ cell lattice, being mapped on a surface using discrete square lattice sites, was employed with periodic boundary conditions. Typically, the lattice dimension, $N = 100$, was applied in this model. At first, 10 layers of A- and B-particles ($N \times N \times 10$) were deposited randomly on the surface. The ratio of the average particle numbers of A-particle per volume, R_A, defined as $R_A = n_A/(n_A + n_B)$, where n_x represents the particle number of x-particle per volume, was set as a parameter value. Then, the deposition step and diffusive jump step for A- and B-particles were simulated according to their rates using a kinetic Monte Carlo method. We employed the Maksym algorithm [19]. The calculation procedure was continued until over 80 stacking layers were formed.

At each deposition step, one surface site was randomly selected, and then one A- or B-particle was attached on the selected site according to the value of R_A. In this study, we control the total deposition rate of A- and B-particles through the number of deposition steps per second, using v_{ad} as parameter values. Thus, the velocity of the addition of a new random monolayer (ML), I_{ad} (ML s^{-1}), is given by $I_{ad} = v_{ad}/a_0$, in which a_0 represents the lattice constant of the $N \times N$ cell lattice, and the time elapsed in the addition of a new random ML, τ_{ML}, is given by $\tau_{ML} = 1/I_{ad}$. In addition, in order to avoid the formation of vacancy sites or overhangs in the crystal thorough deposition steps, we employed so-called 'downward funneling scheme' at each deposition step [21,22]. One surface site is randomly selected as an original site at each deposition step, as already described above. Then, one site surrounded with the maximum number of nearest-neighbor particles within a square with a side of three lattice constants centered upon the original site is chosen as the final deposition site. In other words, relaxation to a lower neighboring site of a deposited particle occurs at each deposition step. Such a 'downward funneling' scheme seems artificial, but it has been observed in the molecular dynamics of simple Lennard–Jones systems [28,29], and has also been employed in previous solid-on-solid model simulations [21,22].

At each diffusive jump step, a particle is allowed to diffuse across the surface according to its jump rate, which depends on the local environment; jumps are allowed on the four nearest-neighbor sites in-plane, and allowed up or down the edge of a terrace having only one height step [21]. The jump rate for diffusion, r_d, includes a jump probability, P_d, and a frequency factor, ν. The corresponding jump rate and jump probability are given by

$$r_d = \nu P_d, \tag{1}$$

and

$$P_d = \exp\left(-\frac{\Delta E}{k_B T}\right), \tag{2}$$

where k_B and T are Boltzmann's constant and the simulation temperature, respectively, and ΔE corresponds to an activation barrier expressed by the energy function of the particle–particle bonds. T was fixed at 400 K in this study. The activation barrier, ΔE, is given by

$$E = n_s e_s + n_d e_d, \tag{3}$$

where n_s is the number of the same kind of neighbor particles (substrate and in-plane nearest neighbor: $n_s = 0$–5), e_s is the bonding energy between the same kind of neighbor particles (A-particle–A-particle or B-particle–B-particle), n_d is the number of different kinds of neighbor particles (substrate and in-plane nearest neighbor: $n_d = 0$–5), and e_d is the bonding energy between the different kinds of neighbor particles (A-particle–B-particle). The typical value of e_s ($e_s = e_{A-A} = e_{B-B}$) was set to 0.05 eV, and e_d ($= e_{A-B}$) was set to 0 eV. Thus, we assumed that there was no interaction between the different kinds of neighbor particles in this model. The values of the bonding energy do not correspond exactly to real values, but this is not a key issue. As discussed later, a considerable matter in our model is the correlation between the surface diffusion length and the self-organized growth structure. In addition, the Ehrlich–Schwoebel barrier [30,31] is not employed in our model to simplify the discussion of phase separation phenomena, i.e. there is no activation barrier for hopping up or down steps at the edges of a terrace in our model.

The surface diffusion length of the adatoms, L_{dif}, is determined by the frequency number of adatom jump steps until the adatoms become buried by the new ML. L_{dif}, is given by:

$$L_{dif} = \sqrt{D_{dif}\tau_{ML}}, \tag{4}$$

where D_{dif} is the surface diffusion coefficient, which equals $a_0^2/4\tau_j$ if a two-dimensional surface diffusion (in-plane diffusion) is assumed. Here, τ_j is the time constant of the jump rate ($\tau_j = 1/r_d$). L_{dif} is, therefore, transformed to

$$L_{dif} = \frac{1}{2}\sqrt{\frac{r_d}{I_{ad}}}a_0. \tag{5}$$

Note that L_{dif} in Eq. (5) is a minimal length if diffusion over the edge of a terrace is considered besides in-plane diffusion. According to the description above, we should focus on the L_{dif} value as a control parameter to determine the growth-structure in this model. L_{dif} ranged from $0.2a_0$ to $10a_0$ (equivalent to $r_d/I_{ad} = 0.2$–400) in this study.

Visualization of the surfaces in the stacked layers was examined under the conditions of various parameter values, as shown in Fig. 7. As L_{dif} increases with the constant value of $R_A = 0.2$, the domain size of the A component increases (Fig. 7a and b). At the higher values of L_{dif}, the domain of the A component connects to form a longitudinal columnar structure (Fig. 7c), and the diameter of the longitudinal columns also increases (Fig. 7d). The uniformity of the columnar structure in terms of size and spatial configuration appears with increasing L_{dif}. Also, the influence of R_A (0.1–0.5) was examined at a constant value

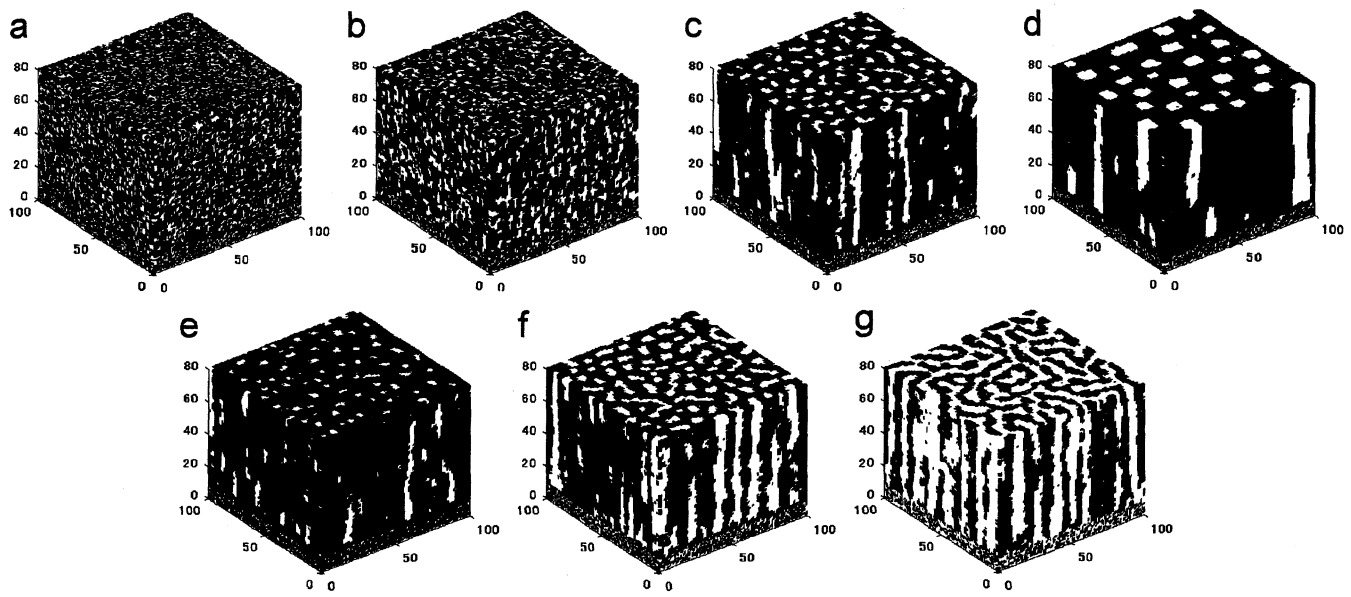

Fig. 7. Visualization of surfaces in stacked layers. White part: A-particle, black part: B-particle. (a) $R_A = 0.2$, $L_{dif} = 0.60a_0$, (b) $R_A = 0.2$, $L_{dif} = 1.43a_0$, (c) $R_A = 0.2$, $L_{dif} = 3.60a_0$, (d) $R_A = 0.2$, $L_{dif} = 10.0a_0$, (e) $R_A = 0.1$, $L_{dif} = 3.66a_0$, (f) $R_A = 0.3$, $L_{dif} = 3.57a_0$, (g) $R_A = 0.5$, $L_{dif} = 3.55a_0$. (a)–(d): $L_{dif} = 0.60a_0$–$10.0a_0$ at the constant value of R_A, (e)–(g): $R_A = 0.1$–0.5 at the constant value of L_{dif}.

of L_{dif} (Fig. 7e–g). When the value of $R_A = 0.5$ is applied, a bicontinual structure appears (Fig. 7g).

The properties of the domains (number, volume and area of domains) were evaluated as a function of L_{dif}. Three-dimensional domain (3D) and two-dimensional domain (2D) were defined, respectively, as follows. If nearest neighbor-particles (nearest neighbor-sites occupied by A- or B-particles: in-plane sites, top site and bottom site) were the same kind of particle in the center site, these sites were regarded as connecting sites (A–As and B–Bs). Thus, a 3D-domain consists of a group of the three-dimensionally connecting sites. Meanwhile, a 2D-domain was defined as a group of the connecting sites among in-plane sites, i.e. 2D-domains were evaluated at each stacked layer. The 3D-domains and 2D-domains were counted with consideration of the periodic boundary conditions. As a typical example, the properties of the 2D- and 3D-domains with $R_A = 0.2$ are presented in Fig. 8. An average 2D-domain area at each stacked layer is plotted against the number of stacked layers (Fig. 8a). With an increasing number of stacked layers, the average 2D-domain area reaches equilibrium immediately. An overall average 2D-domain area, calculated from the 2D-domain areas at every stacked layer, increases with increasing L_{dif} (Fig. 8b), while the number of 3D-domains decreases with increasing L_{dif} (Fig. 8c). The visual examinations in Fig. 7 and domain counting in Fig. 8 describe the present experimental results qualitatively; as stated in the experimental part, the surface diffusion length will not be so long at relatively low Ar pressures. The relatively short surface diffusion length of the adatoms results in the formation of a longitudinally long shape of Co. With further increasing Ar pressure, the surface diffusion length of the adatoms increases and greater nucleation of Co occurs.

Finally, we evaluated longitudinal connectivity through the stacked layers as a function of L_{dif}. An average domain height, $H^{(x)}$, for x-particle (= A-particle or B-particle), is defined as follows:

$$H^{(x)} = \sum_i h_i^{(x)} \left(\frac{V_i^{(x)}}{V_{sum}^{(x)}} \right), \tag{6}$$

where $h_i^{(x)}$ is the height of a 3D-domain i that consists of x-particles. $V_i^{(x)}$ is the volume of the 3D-domain i, and $V_{sum}^{(x)}$ is the total volume of the x-particle. Thus, we define a percolation probability, $P_L^{(x)}$, (i.e. a probability for longitudinal penetration through L stacked layers by 3D-domains of x-particles) as follows:

$$P_L^{(x)} = \frac{H^{(x)}}{L}. \tag{7}$$

As shown in Fig. 9, $P_L^{(A)}$ is plotted as a function of L_{dif} at $L = 70$ stacked layers ($= 70a_0$), because the 2D-domain areas at each stacked layer achieve equilibrium adequately through 70 layers (Fig. 8a). The $P_L^{(A)}$ demonstrates S-curves when applied to the values of $R_A = 0.1$ and 0.2; as increasing L_{dif}, the longitudinal growth of 3D-domains occurs abruptly. At values of $R_A = 0.3$ and 0.5, $P_L^{(A)}$ converges in the unity immediately, because the site percolation threshold in a cubic lattice is around $R_A = 0.31$ [32].

The present kinetic phase separation model (two-component solid-on-solid model) demonstrates the formation of a longitudinal columnar structure, taking into

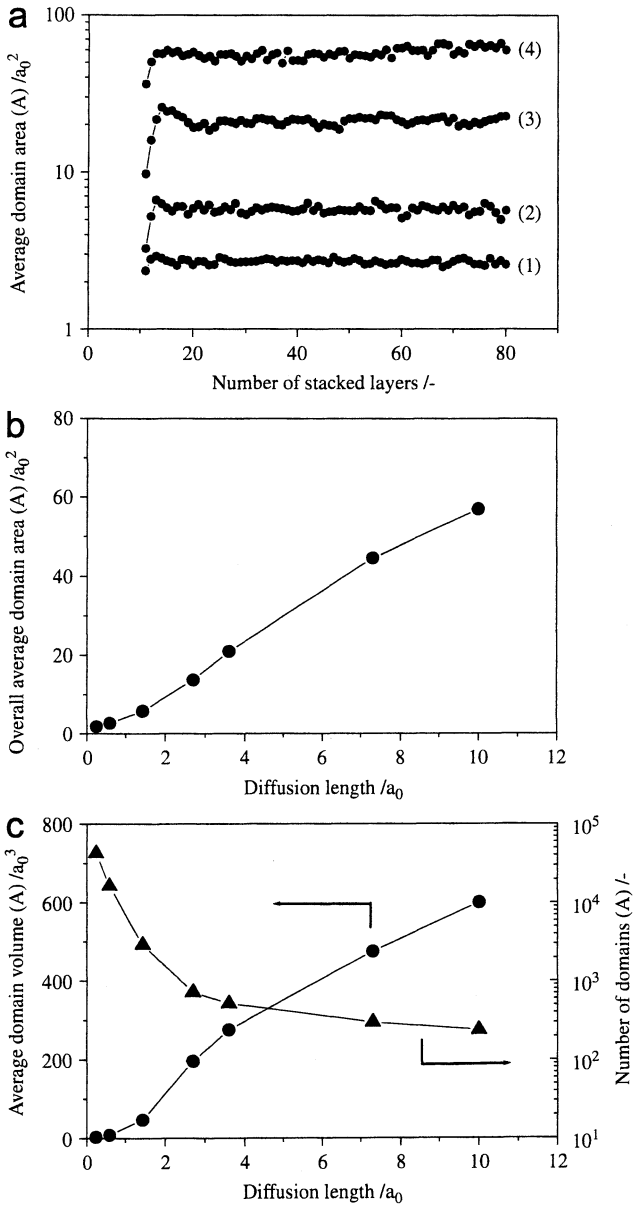

Fig. 8. Properties of the 2D- and 3D-domains of A-particles ($R_A = 0.2$). (a) Average 2D-domain areas of A-particles plotted against stacked layers, (1) $L_{dif} = 0.60a_0$, (2) $L_{dif} = 1.43a_0$, (3) $L_{dif} = 3.60a_0$, (4) $L_{dif} = 10.0a_0$; (b) Overall average 2D-domain areas of A-particles plotted against L_{dif}; (c) Average 3D-domain volume of A-particles and number of 3D-domains of A-particles plotted against L_{dif}.

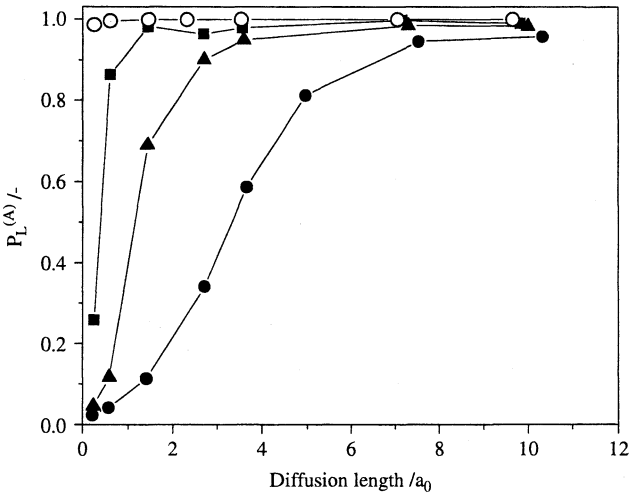

Fig. 9. Percolation probability of A-particles, $P_L^{(A)}$, as a function of diffusion length, L_{dif}. ● $R_A = 0.1$; ▲ $R_A = 0.2$; ■ $R_A = 0.3$; ○ $R_A = 0.5$.

consideration the surface diffusion process of the first layer. Adams et al. [26] have investigated phase separation in a two-component thin film using the Ising model (Kawasaki spin exchange dynamics), and obtained a longitudinal columnar structure. Recently, Fukutani and co-researchers have also discussed phase separation in a two-component thin film (phase-separated Al–Si film) using a continuum model (modified Cahn–Hilliard model), and demonstrated the formation of a longitudinal columnar structure in the Al–Si film [33]. The longitudinal columnar structure appears in our model without reference to the magnitude of the bonding energy, and it is significantly dependent on the diffusion length. In fact, when the magnitude of an activation barrier is changed, a longitudinal columnar structure is still obtained. Thus, the surface diffusion process plays an essential role in the formation of longitudinal columnar structures. Under the present experimental conditions, the diffusion length of the Co particles is unknown. Judging from the present, TEM and SEM images (Figs. 6 and 4b′), the distance of Co columns is estimated to be between ca. 5 and 100 nm. Thus, the diffusion distance can well be in the orders of 10^0–10^2 nm. Although the exact correspondence of the model length to a real length cannot be realized in our simple model, the model will roughly correspond to the description using the parameter of diffusion lengths within the orders of 10^{-1}–10^0 nm if a site length of 0.25 nm (that corresponds to interatomic distance for Co) is assumed. Nevertheless, it is to be noted that the model fails to demonstrate the formation of longitudinal columnar structures when a relatively high value of R_A (~0.5) is applied. In this model, a bicontinual structure forms with $R_A = 0.5$ (Fig. 7g), while the longitudinal columnar structures of Co–SiO_2 form in the experiment (Co:SiO_2 volume ratio ≅ 5:5–6:4). A condensation process should be further improved.

4. Conclusion

We have investigated the correlation between the growth structure in co-deposited Co–Si–O thin films and the Ar working gas pressure for RF magnetron sputtering. The observation of microstructures in the thin films suggests that a mesoscale needlelike array of Co columns aligned perpendicularly to a substrate surface, forms in Co–Si–O

thin films when relevant Ar working gas pressures are applied ($\cong$15 mTorr); the diameter of the Co columns increases with increasing Ar pressure up to 100 mTorr. Taking into account, energetic particle bombardment, the surface diffusion process is considerable in self-organized microstructures with a regular array during deposition; the surface diffusion length of the adatoms may increase with increasing Ar pressure due to the energetic particle bombardment, and thus the surface diffusion length will determine the microstructures of the deposited thin films.

A simple model, incorporating a diffusion process in the simultaneous deposition of two components (A-particles and B-particles), is presented. This model reproduces the general trends of a kinetically self-organized microstructure in a two-component thin film; a longitudinal regular array of columns (domains of A-particles) forms in a stacked film with increasing adatom diffusion length. A percolation probability defined as a probability for longitudinal penetration through stacked layers, demonstrates the formation of the longitudinal regular array of columns as a function of diffusion length.

In addition, we have successfully prepared mesoporous silica thin films having mesopore channels aligned perpendicularly to the substrate surface, formed by chemical etching of the Co parts in the Co–Si–O thin films (template method). This method can achieve high pore volume and high specific surface area in concurrence with the formation of a regular array of mesopore channels.

Acknowledgments

This work was financially supported by the "Research and Development of Polymer Electrolyte Fuel Cell" program of the New Energy and Industrial Technology Development Organization (NEDO) of Japan and the Nippon Sheet Glass Foundation for Materials Science and Engineering. The authors would like to express their gratitude for valuable discussions with Dr. Shinji Kondoh (Asahi Techno Glass Company).

References

[1] Martin CR. Chem Mater 1996;8:1739.
[2] Kresge CT, Leonowicz ME, Roth WJ, Vartuli JC, Beck JS. Nature 1992;359:710.
[3] Yanagisawa T, Shimizu T, Kuroda K, Kato C. Bull Chem Soc Jpn 1990;63:988.
[4] Sun T, Ying JY. Nature 1997;389:704.
[5] Abe T, Tachibana Y, Uematsu T, Iwamoto M, Chem. Soc. J. Chem Commun 1995;16:1617.
[6] Otomo J, Wang S, Takahashi H, Nagamoto H. J Membrane Sci 2006;279:256.
[7] Kondoh S, Iwamoto Y, Kikuta K, Hirano S. J Am Ceram Soc 1999; 82:209.
[8] Kondoh S, Shinichi H. Kotai Butsuri 2001;36:827.
[9] Kondoh S, Katori S. Seramikkusu 2004;39:185.
[10] Barrett EP, Joyner LG, Halenda PP. J Am Chem Soc 1951;73:373.
[11] Wagner CD, Riggs WM, Davis LE, Moulder JF, Mullenberg GE. Handbook of X-ray photoelectron spectroscopy. Eden Prairie, MN 55344: Perkin-Elmer Co., Physical Electronics Division; 1979.
[12] Nefedov VI, Firsov MN, Shaplygin IS. J Electron Spectrosc Relat Phenom 1982;26:65.
[13] Oku M, Hirokawa K. J Electron Spectrosc Relat Phenom 1976;8:475.
[14] McIntyre NS, Cook MG. Anal Chem 1975;47:2208.
[15] Thornton JA. J Vac Sci Technol 1974;11:666.
[16] Thornton JA. J Vac Sci Technol A 1986;4:3059.
[17] Eltoukhy AH, Greene JE. J Appl Phys 1980;51:4444.
[18] Weeks JD, Gilmer GH, Jackson KA. J Chem Phys 1976;65:712.
[19] Maksym PA. Semicond Sci Technol 1988;3:594.
[20] Clarke S, Vvedensky DD. J Appl Phys 1988;63:2272.
[21] Smilauer P, Wilby MR, Vvedensky DD. Phys Rev B 1993;47:4119.
[22] Schinzer S, Sokolowski M, Biehl M, Kinzel W. Phys Rev B 1999; 60:2893.
[23] Ishii A, Kawamura T. Appl Surf Sci 1998;130–132:403.
[24] Ratsch C, Wheeler MC, Gyure MF. Phys Rev B 2000;62:12636.
[25] Murty MVR, Cooper BH. Surf Sci 2003;539:91.
[26] Adams CD, Srolovitz DJ, Atzmon M. J Appl Phys 1993;74:1707.
[27] Eisenmenger-Sittner C, Bangert H, Bergauer A. J Cryst Growth 1998; 186:151.
[28] Evans JW, Sanders DE, Thiel PA, DePristo AE. Phys Rev B 1990; 41:5410.
[29] Yue Y, Ho YK, Pan ZY. Phys Rev B 1998;57:6685.
[30] Ehrlich G, Hudda FG. J Chem Phys 1966;44:1039.
[31] Schwoebel RL, Shipsey EJ. J Appl Phys 1966;37:3682.
[32] Stauffer D, Aharony A. Introduction to percolation theory, revised 2nd ed. Philadelphia, PA: Taylor & Francis Inc; 1994 [chapter 2].
[33] Fukutani K, Tanji K, Saito T, Den T. J Appl Phys 2005;98:033507.

Journal of the Society of Inorganic Materials, Japan 13, 448–455 (2006)

特集　無機材料と環境技術

ガラスによる高レベル放射性廃棄物の固化処理*

大　倉　利　典**

1　はじめに

原子力発電所から発生する使用済核燃料には，再び燃料として使用できるウランやプルトニウムが含まれている．これらの元素を発電用原子炉で再利用するための使用済燃料再処理工程で，高レベル放射性廃液（以下，高レベル廃液）が分離される（図1）．また，再処理工程からは，低レベルの放射性液体，固体廃棄物も発生する．高レベル放射性廃棄物とは，再処理施設で使用済燃料からウランやプルトニウムを分離・回収した後に残る，核分裂生成物を主成分とする廃棄物で放射能濃度が高い廃棄物のことをいう．この高レベル放射性廃棄物は，低レベル放射性廃棄物に比べてその発生量自体は少量であるが，放射線の管理に注意が必要なアクチニド元素などの半減期の長い核種も比較的多く含まれているため，長期間にわたり人間環境から隔離する必要がある．このため，高レベル放射性廃棄物は，ガラスと混ぜて溶かし，キャニスターと呼ばれるステンレス製の容器に注入したあと，冷やして固めるという方針が採られており，この状態のものをガラス固化体という．ガラスはほかの物質に比べて化学的耐久性に優れ，機械的強度が大きく，放射性成分を多量に溶かしこむことができるので，現在，各国ともガラス固化処理方式を採用している．

本稿では，はじめに，日本の高レベル放射性廃棄物処理処分に関する方策を概説し，次いで，ガラス固化技術の現状と問題点について述べる．さらに，リン酸マグネシウムガラスを用いた筆者らの最新の研究結果を紹介する．

2　日本の高レベル放射性廃棄物処理処分方策

日本の高レベル廃液固化については，（旧）動力炉・核燃料開発事業団（動燃，現：日本原子力研究開発機構）が中心になって，国の研究機関，大学，民間企業，海外研究機関などの協力の下に，国の方針にしたがって研究開発が行われた．研究開発が始まったのは

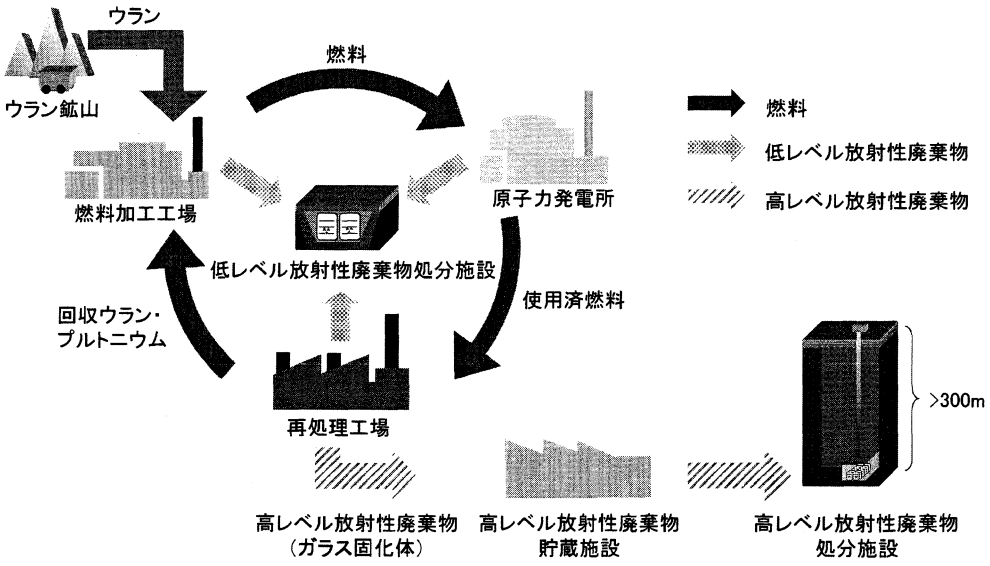

図1　原子燃料サイクル

* Immobilization of High Level Nuclear Wastes with Glasses
** Toshinori OKURA

1970年代中頃であるが，実際の高レベル廃液を取り扱う研究は，動燃の高レベル放射性物質研究施設(CPF; Chemical Processing Facility，動燃東海)および(旧)日本原子力研究所(原研，現：日本原子力研究開発機構)の廃棄物安全試験施設(WASTEF; Waste Safety Test Facility，原研東海)が稼働し始めた1980年代初めからである．日本の高レベル放射性廃棄物処理処分の具体的方策等は，1980年10月に原子力委員会放射性廃棄物対策専門部会で「放射性廃棄物処理処分方策について」にとりまとめられた．以下に，同報告書の主旨概要を示す．「高レベル廃液の固化処理技術開発は，ホウケイ酸ガラスによる固化に重点を置く．この技術開発の成果は，海外委託再処理にともなう返還廃棄物対策(1990年以降)および民間再処理事業者の行う固化処理(原子炉施設や再処理施設から発生する低レベルおよび高レベル廃液を蒸発処理した濃縮廃液，フィルター・脱塩基に使用された廃樹脂などをより安定な形態にするために固体状に処理すること)への活用を図る．使用済燃料として原子炉から取り出された後，再処理を経てガラス固化された固化体は，それに含まれる放射性核種の崩壊熱が深地層の岩盤に与える影響を緩和するため，深地層中に搬入されるまでの間，30～50年間程度，冷却のため貯蔵される．」というものである．1992年4月に東海ガラス固化・貯蔵施設(TVF; Tokai Vitrification Facility，動燃東海)が完成した．

3　ガラス固化技術の現状と問題点

高レベル廃液のガラス固化技術は，日本を含め各国でプラント規模のガラス固化施設が廃液処理運転に入っている段階にある．ガラス固化するのには，高レベル廃液を約600℃で加熱して酸化物粉末とし，ガラス形成剤を混入し高温で熱溶解してガラスにする．Ru, Csなどの放射性成分の揮発を防ぐため，溶融温度は低い方が望ましい．このガラス固化体は崩壊熱を出すため，30～50年間一時貯蔵して冷却(空冷)することにより，発熱量は約1/3から1/5に減少し，安全な処分ができるようになる．そして，最終的には地下300 mより深い安定な深地層中に処分される．現在は，ガラス固化体が450℃以下の状態になったら地層処分が可能となっている．長期間にわたっての安全性を予測・評価する場合，処分場を包むまわりの地層(天然バリア)と緩衝材(人工バリア)を組み合わせた多重バリアの機能についての検討が必要である(図

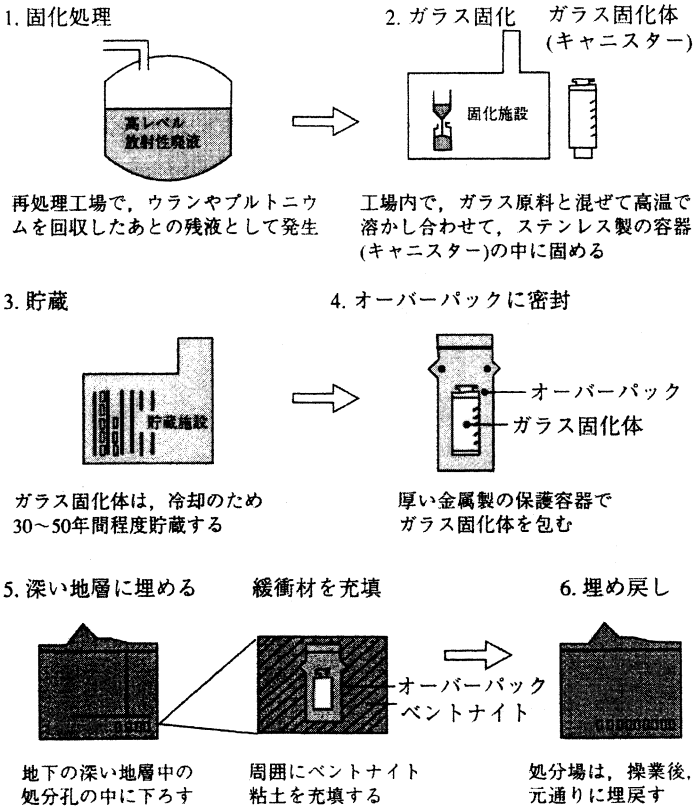

図2　地層処分の概略

2)．なかでも，地層処分後の地下水との接触による固化ガラスからの放射性物質の浸出が最も重要となり，次いでガラスの安定性および固化ガラス中の放射性物質の崩壊熱による結晶化や分相現象が問題となる．

高レベル放射性廃棄物には多種類の放射性物質が含まれる．したがって特定の放射性物質のみでなく，すべての放射性物質を化学的に安定な物質にする必要がある．ガラス組成としては，ホウケイ酸系，アルミノケイ酸系，リン酸系が候補として検討され，固化プロセスの実現性，廃棄物含有量，熱的安定性，化学的耐久性(浸出率)，耐放射線性などの比較評価の結果，現在では主としてホウケイ酸系が選択されている．その理由として，化学薬品に対する耐食性に優れていること，ガラス溶融温度を比較的低くできるため，プロセス材(溶融炉材，電極材)に対する負担が軽減できること，廃棄物成分の許容含有量が比較的高く，熱や放射線に対する抵抗も高いことなどがあげられる．ホウケイ酸ガラスの構造は，おもにケイ酸とホウ酸が網目構造を形成するので，結晶性の物質と違い，イオン半径が異なる多種類の放射性物質が網目の中に入り均質で安定な一種類の物質になる．放射性物質はガラス成分の一つとしてガラスそのものになる．ガラスは容積の小さい固化体にすることができ，取り扱いが容易である．また，ガラスは本来水に対して非常に溶け難い安定な物質である．古代遺跡から多くのガラス製品が出土しているが，いずれも製造当時の色彩や輝きがほとんど失われていない．廃棄物中の成分は燃料のタイプや再処理法によりわずかに異なり，それに応じてガラスの組成も異なる．たとえば廃棄物中に Na_2O が多い場合はガラスの溶融温度が低くなり，耐食性，放射線に対する耐久性，水に対する耐浸出性などの低下をもたらすことになる．また，MoO_3 はガラスへの溶解度がほかの成分に比べて低く，Na_2MoO_4，Cs_2MoO_4 などのモリブデン酸アルカリとして，溶融物から分離しやすい．分離・析出した相は「イエローソリッド」と呼ばれ，^{90}Sr，^{137}Cs などの非常に危険な核種を固溶し，しかも水に溶けやすいため，この相の分離・析出は極力避けなければならない．さらに，MoO_3 はガラスの機械的強度を弱めるので，ガラス中の廃棄物の量は制限されることになる．ガラス固化体中の放射性廃棄物の量としては，質量割合で10～20%が含まれている．ガラス固化体の組成の一例を**表1**に示す．これは廃棄物の含有量が酸化物で15%である．この場合，ガラス固化体はウラン1tあたり約1101(約300kg)発生する．代表的な100万kWの原子力発電所1基あたり，年間これの30倍程度のガラス固化体ができることになる．

表1　ガラス固化体の組成

ガラス組成/mass%	
SiO_2	43～47
B_2O_3	14
Al_2O_3	3.5～5
Na_2O	10
その他	9～12.5
廃棄物酸化物(Na_2O を除く)	15

4　リン酸マグネシウムガラスによる固化処理[1)～3)]

現在，固化ガラスにはホウケイ酸ガラスが使用されており，放射性廃棄物の含有量は最大で25 mass%となっている．しかし，このガラスは再処理工程で含有する P_2O_5 の濃度が増加すると分相してしまうことが報告されており，P_2O_5 濃度が最大で1～3 mass%になるように廃棄物含有量を制限しなければならない．これにより，ガラス固化体自体の量が増えてしまうという問題がある．そこで，筆者らは，高レベル放射性廃棄物固化のベースガラスとして，ホウケイ酸ガラス同様融点が低く，より多く様々な種類の元素を取り込める特性をもつリン酸塩ガラスに着目した．そのなかでも，リン酸マグネシウムガラスは，メタ組成(モル比で $MgO/P_2O_5=1$)付近で組成-物性間にリン酸異常現象と呼ばれる非線形性を示し，anomalous タイプに分類されている．多くのリン酸塩ガラスは鎖状構造を有することが知られているが，リン酸マグネシウムガラスは組成により二つのタイプの構造を含むと考えられており，一つは $MgO/P_2O_5<1$ のときでテトラメタリン酸構造を含むもの，もう一つは $MgO/P_2O_5>1$ のときでピロリン酸構造を含むものである．この構造の変化が異常現象を引き起こしていると考えられる[4)]．本研究では，リン酸マグネシウムガラスを用いて模擬放射性廃棄物を固化させたガラス固化体について，熱的安定性や耐水性の評価，振動スペクトルを用いた構造変化の検討を行い，さらに γ 線を照射させたときの影響についても検討した．また，鎖状構造をもつ normal タイプのリン酸カルシウムガラスを用いた固化体についても同様の検討を行った．

$AO:P_2O_5$ (A=Mg, Ca)=40:60, 50:50, 55:45(モル比)のガラスを粉砕し，**表2**に示した組成の模擬廃棄物[5)]を固化ガラス中の含有率が25および45 mass%になるように混合し，1250℃で2時間溶融

後，急冷して固化ガラスとした．この固化ガラスについて，X線回折(XRD)測定によりガラス状態を，走査型電子顕微鏡(SEM)により微細構造を，フーリエ変換赤外吸収(FT-IR)およびLaser Raman測定により結合状態を評価した．また，示差熱分析(DTA)によりガラス転移点(Tg)と結晶化開始温度(Tc)を求め，その差(Tg-Tc)から固化ガラスの熱的安定性を検討した．耐水性の評価は，MCC-2法[6](純水50 mlに粉砕した試料約1 gを浸し，90℃で20日間保持後，試料全体の重量減少より浸出率を求める．)を用いた浸出試験により行った．さらに，γ線(Co-60)照射試料(全線量で10 μR)に対しても同様の評価を行った．

表2　模擬放射性廃棄物の組成

廃棄物元素	原　料	mass%
Na	$NaNO_3$	64.8
Sr	SrO	2.9
La	La_2O_3	16.1
Mo	MoO_3	7.5
Mn	MnO_2	1.2
Fe	Fe_2O_3	6.6
Te	TeO_2	0.9

表3　XRD測定の結果

組成比/mol%	模擬廃棄物含有量/mass%	ガラス固化体	密度/g·cm^{-3}	500℃·2時間加熱処理 前	500℃·2時間加熱処理 後
$MgO:P_2O_5=40:60$	0	40M60P 0W	2.45	○	○
	25	40M60P25W	2.67	○	○
	45	40M60P45W	2.91	○	○
$MgO:P_2O_5=50:50$	0	50M50P 0W	2.25	○	○
	25	50M50P25W	2.73	○	×
	45	50M50P45W	2.89	○	×
$MgO:P_2O_5=55:45$	0	55M45P 0W	2.51	○	○
	25	55M45P25W	2.76	×	×
	45	55M45P45W	3.02	○	×
$CaO:P_2O_5=40:60$	0	40C60P 0W	2.67	○	×
	25	40C60P25W	2.85	○	×
	45	40C60P45W	2.99	×	×
$CaO:P_2O_5=50:50$	0	50C50P 0W	2.75	○	×
	25	50C50P25W	2.93	×	×
	45	50C50P45W	3.04	×	×
$CaO:P_2O_5=55:45$	0	55C45P 0W	2.91	○	×
	25	55C45P25W	2.96	×	×
	45	55C45P45W	3.14	×	×

M：MgO，C：CaO，P：P_2O_5，W：Waste(模擬廃棄物)
○：非晶質状態，×：結晶状態

表3に固化ガラスのXRD結果を示す．$MgO-P_2O_5$系では，廃棄物含有量が増加しても均一なガラス状態の試料を作製することができた．しかし，$CaO-P_2O_5$系では，廃棄物を含有させると，どの組成においても結晶化する傾向を示した．**表4**に$MgO-P_2O_5$系固化ガラス，**表5**に$CaO-P_2O_5$系固化ガラスのDTA結果をそれぞれ示す．すべての組成において，TgおよびTcは廃棄物含有量が増加すると低下する傾向にあった．固化ガラスの安定性は廃棄物含有量が増加すると低下したが，$MgO:P_2O_5=40:60$以外の$MgO-P_2O_5$系ガラスと$CaO:P_2O_5=50:50$の$CaO-P_2O_5$系ガラスは，廃棄物含有量にあまり影響を受けないことがわかった(**図3**)．このことから，$MgO-P_2O_5$系ガラスにおいては，ピロリン酸構造を多く含む組成のほうが安定性は高くなるのではないかと考えられる．

図4に示した浸出試験の結果から，$MgO-P_2O_5$系

表 4　$MgO-P_2O_5$ 系固化ガラスの DTA 測定結果

固化ガラス	40M60P			50M50P			55M45P		
	0W	25W	45W	0W	25W	45W	0W	25W	45W
Tg/℃	519	492	490	528	506	495	547	508	490
Tc/℃	754	658	609	772	635	617	683	617	596

表 5　$CaO-P_2O_5$ 系固化ガラスの DTA 測定結果

固化ガラス	40C60P			50C50P			55C45P		
	0W	25W	45W	0W	25W	45W	0W	25W	45W
Tg/℃	496	453	400	526	474	386	541	389	377
Tc/℃	666	623	491	609	580	484	618	529	472

Tg：ガラス転移点　Tc：結晶化開始温度

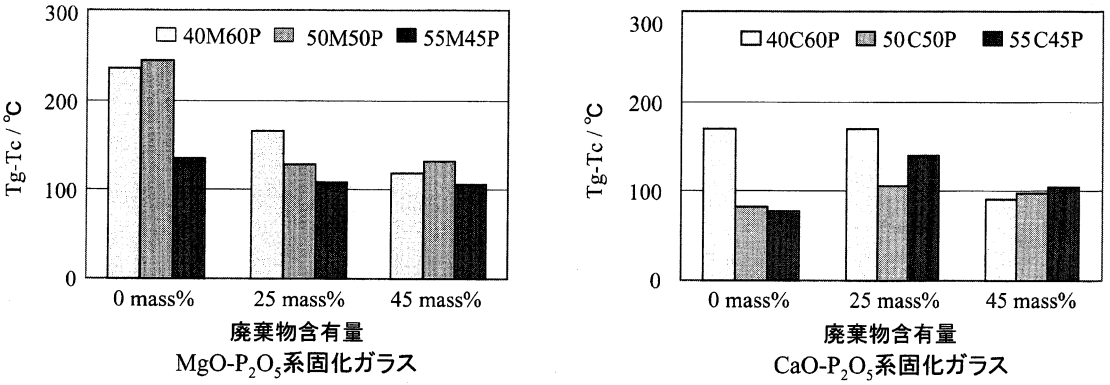

図 3　固化ガラスの安定性

ガラスと $CaO-P_2O_5$ 系ガラスのどちらの場合も，模擬廃棄物を含まない場合はそれほど値に変化はなく，耐水性も悪いが，模擬廃棄物含有量が増加するにつれ，耐水性は高くなった．全体的に比較して，$MgO-P_2O_5$ 系のほうが $CaO-P_2O_5$ 系よりも明らかに浸出率が低い結果になった．$MgO-P_2O_5$ 系においては，$MgO:P_2O_5=50:50$ で廃棄物含有量が 45 mass%の固化ガラスの浸出率は 10^{-6} g/cm^2·day オーダーとなり，現在使用されているホウケイ酸ガラス固化体(廃棄物含有量 25 mass%)の浸出率 2.5×10^{-5} g/cm^2·day と比べてかなり低い値となった．この結果から，今回の実験においては，この組成が固化ガラスとして適していると考えられる．$CaO-P_2O_5$ 系においては，$CaO:P_2O_5=50:50$ で廃棄物含有量が 45 mass%の固化ガラスの浸出率が低い値を示したが，6.85×10^{-5} g/cm^2·day とホウケイ酸ガラス固化体よりも高い値となった．

図 5 に $MgO-P_2O_5$ 系固化ガラスの SEM 観察結果を示す．XRD で結晶性のピークが確認でき，浸出率も悪かった $MgO:P_2O_5=55:45$ で廃棄物含有量が 25 mass%の固化ガラスでは結晶の生成が，他の試料では均質なガラス状態が確認できた．しかし，浸出率が悪かった $MgO:P_2O_5=40:60$ で廃棄物含有量が 25 mass%の固化ガラスでは分相(バイノーダル分相)が見られた．

固化ガラスの Laser Raman スペクトルを**図 6** に，その結果をまとめたものを**表 6** に示す．$MgO-P_2O_5$ 系および $CaO-P_2O_5$ 系のどちらのガラスにおいても，環状や鎖状の構造が模擬廃棄物元素によって切断されるために，$P_2O_7^{4-}$ や PO_4^{3-} などのピークの増加が観察された．しかし，**図 7** に示した固化ガラスの FT-IR スペクトルにおいては，$MgO-P_2O_5$ 系では PO_3^- や PO_4^{3-} の吸収ピークは減少していた．これは，模擬廃棄物含有量が増加すると環状構造や鎖状構造は切断され，PO_3^- や PO_4^{3-} の構造単位は増加するが，非対称の架橋酸素 M-O-P(M＝廃棄物元素)の構

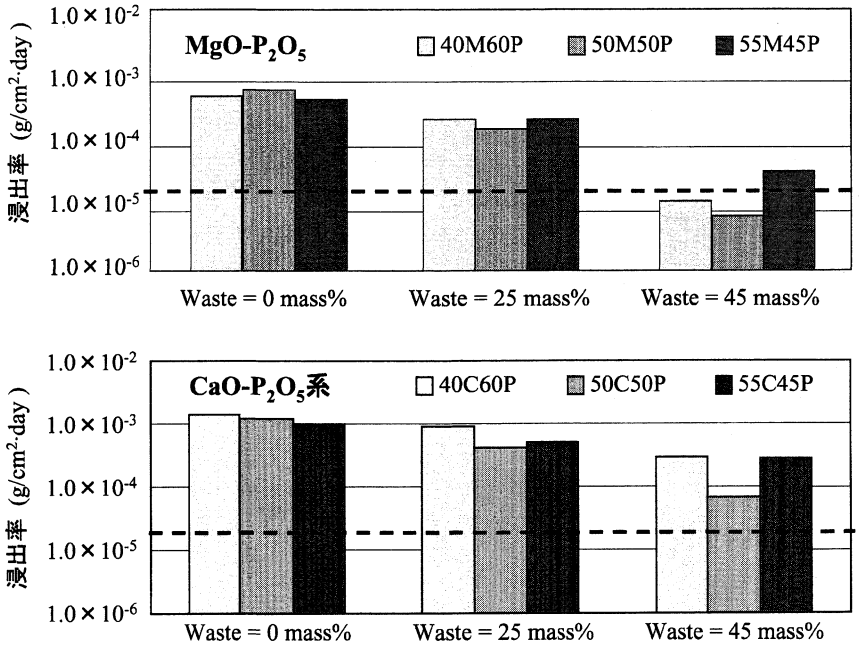

図4　ガラス固化体の浸出率

------：ホウケイ酸系ガラス固化体(waste＝25 mass%)，2.5×10^{-5} g/cm²·day

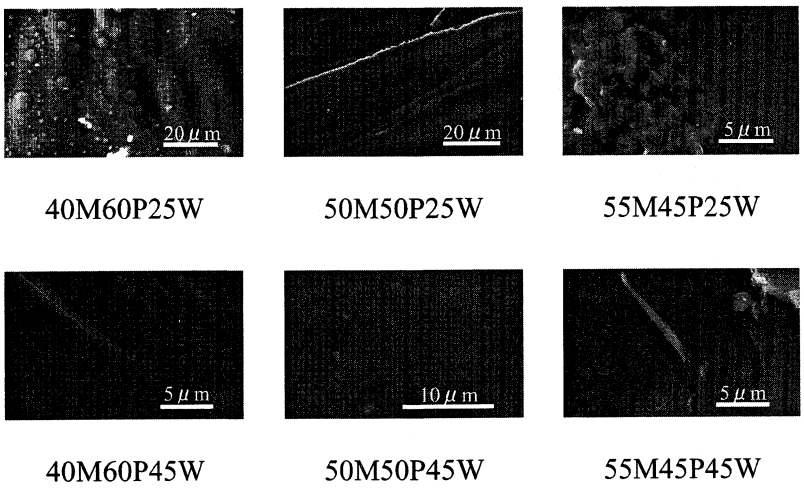

図5　$MgO–P_2O_5$ 系固化ガラスの SEM 像

造が増加したため，見かけ上吸収ピークは減少したものと考えられる．このような構造が増加すると，ガラスネットワーク中のクロス・リンケージの密度が増加したことになり，このことが固化ガラスの耐水性を向上させたものと考えられる．しかし，$CaO–P_2O_5$ 系においては，PO_3^- や PO_4^{3-} も増加していたため，ガラスネットワーク中のクロス・リンケージの密度が耐水性に大きく影響するのではないかと考えられる．**表7**に FT-IR スペクトルの結果をまとめたものを示す．

γ線を照射することによって，浸出率は一桁近く悪くなったが，FT-IR, Laser Raman どちらのスペクトルにも照射前後に変化が見られず，大きな構造的変化は起きないことがわかった．

5　おわりに

現在では，ホウケイ酸ガラスに対する基礎的検討はほぼ完了しており，ガラス固化体そのものが放出する放射能の影響を調べるために，γ線やα線などの放射線および He などのイオンをガラス固化体に照射させる実験が多くなってきている．リン酸ガラスの最大の難点は，溶解物が非常に腐食性であるということであるが，それにもかかわらず，多くの工学的問題を克服して，1980 年代にかなりの量の廃棄物(およそ 1000 m^3)がリン酸ガラスで固定された．リン酸ガラスはそ

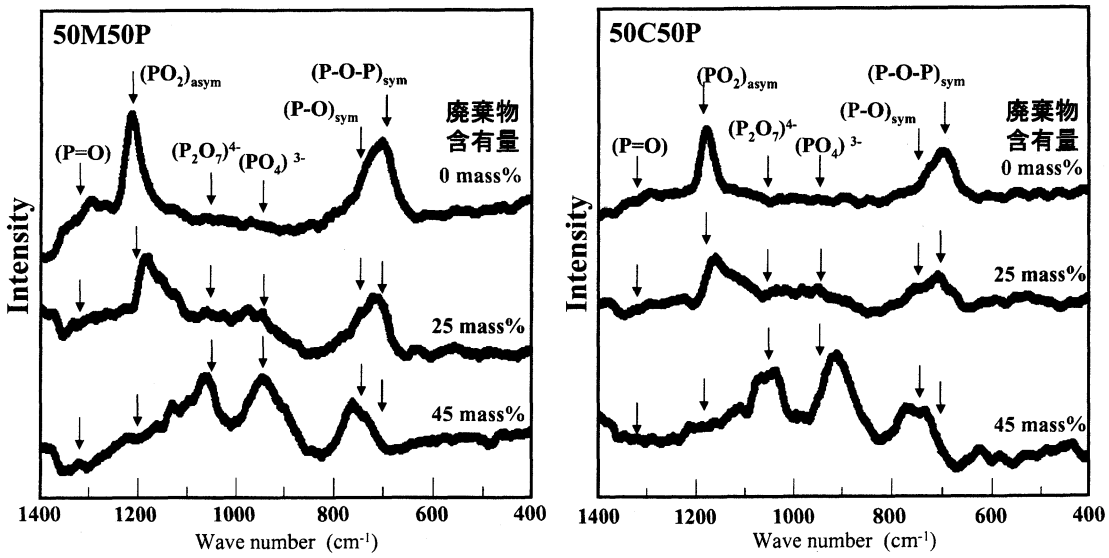

図 6　ガラス固化体の Laser Raman スペクトル

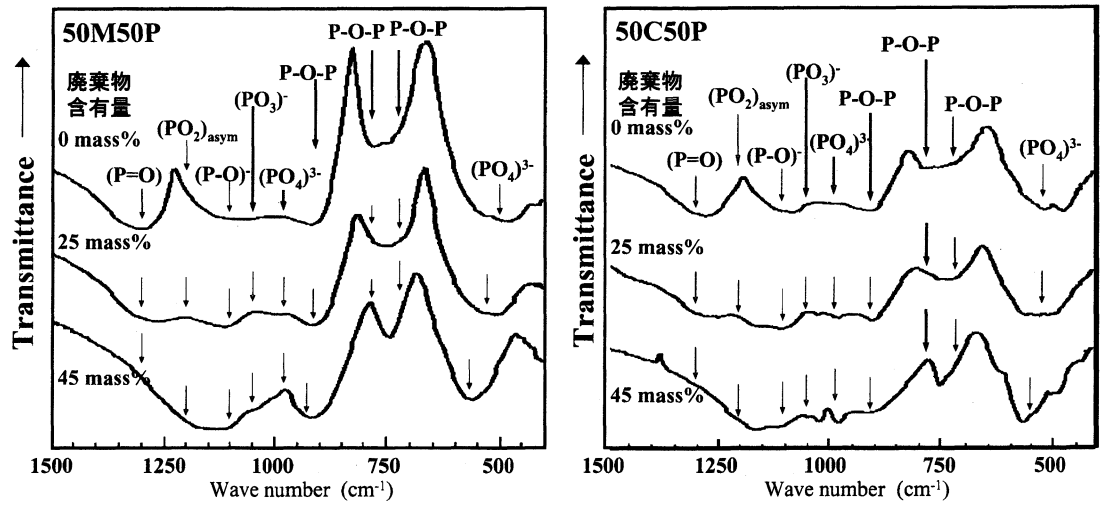

図 7　ガラス固化体の FT-IR スペクトル

表 6　廃棄物含有量の増加に対する Laser Raman 測定結果

Wave number /cm^{-1}	1300	1200	1050	950	760	700
	(P=O)	$(PO_2)_{asym}$	$(P-O)_{sym}$	$(PO_4)^{3-}$	$(P-O-P)_{sym}$	$(P-O-P)_{sym}$
M-P glass	減少	減少	増加	増加	増加	減少
C-P glass	減少	減少	増加	増加	増加	減少

表 7　廃棄物含有量の増加に対する FT-IR 測定結果

Wave number /cm^{-1}	1300	1200	1100	1050	980	920	720-790	480-570
	(P=O)	$(PO_2)_{asym}$	$(P-O)^-$	$(PO_3)^-$	$(PO_4)^{3-}$	$(P-O-P)_{asym}$	$(P-O-P)_{sym}$	$(PO_4)^{3-}$
M-P ガラス	減少	増加	増加	減少	減少	シフト*	減少	シフト*
C-P ガラス	減少	増加	変化なし	増加	増加	変化なし	変化なし	シフト*

*：高波数側にシフト

のポテンシャルの高さから現在でも米国を中心に多くの研究が行われており，様々なデータが蓄積されている．その中にはリン酸ナトリウム-アルミニウムガラスやリン酸鉄-鉛ガラスなどがあり，いずれもホウケイ酸ガラスに匹敵する化学的耐久性があることが報告されている．現在は，リン酸鉄-鉛ガラスの開発に焦点が当てられている[7),8)]．

文　献

1) T. Okura, T. Miyachi, H. Monma, *Trans. Mater. Res. Soc. Japan*, **29**, 2175 (2004).
2) 大倉利典，特開 2005-207885.
3) T. Okura, T. Miyachi, H. Monma, *J. Eur. Ceram. Soc.*, **26**, 831 (2006).
4) T. Okura, K. Yamashita, T. Kanazawa, *Phys. Chem. Glasses*, **29**, 13 (1988).
5) M. Ishida, T. Yanagi, R. Terai, *J. Nucl. Sci. Technol.*, **24**[5], 404 (1987).
6) D. M, Strachan, "Scientific Basis for Nuclear Waste Management", Vol. 3, Ed. by J. D. Moor, Plenum Press, New York (1980) p. 347.
7) S. T. Reis, M. Karabulut, D. E. Day, *J. Nucl. Mater.*, **304**, 87 (2002).
8) P. Y. Shin, *Mater. Chem. Phys.*, **80**, 299 (2003).

筆者紹介

大倉利典　工学院大学工学部マテリアル科学科助教授　工学博士

1990 年東京都立大学大学院工学研究科工業化学専攻博士課程修了，同年東陶機器㈱(TOTO)基礎研究所，1993 年工学院大学助手，1995 年講師，2002 年助教授，現在に至る．1997 年 9 月より 1998 年 8 月まで米国マサチューセッツ工科大学(MIT)客員研究員．

連絡先　〒192-0015 東京都八王子市中野町 2665-1(勤務先)

(2006. 6. 27 受付)
(2006. 8.　1 受理)

Available online at www.sciencedirect.com
SCIENCE DIRECT®
ELSEVIER
Journal of the European Ceramic Society 26 (2006) 831–836
ECERS
www.elsevier.com/locate/jeurceramsoc

Properties and vibrational spectra of magnesium phosphate glasses for nuclear waste immobilization

Toshinori Okura*, Tomoko Miyachi, Hideki Monma

Department of Materials Science and Technology, Faculty of Engineering, Kogakuin University, 2665-1, Nakano, Hachioji, Tokyo 192-0015, Japan

Available online 8 August 2005

Abstract

The leaching behavior and structure of magnesium phosphate glasses containing 45–55 mol% MgO incorporated with simulated high level nuclear wastes (HLW) were studied. The leach rate of the waste glasses decrease with increasing of the simulated HLW content. The gross leach rate of the glass waste form containing 50 mol% MgO and 45 mass% simulated HLW is of the order of 10^{-6} g/cm^2 day at 90 °C, which is small enough as compared with the corresponding release from a currently used borosilicate glass waste form. The isolated ions such as dimeric $(P_2O_7)^{4-}$ and monomeric $(PO_4)^{3-}$ ions increase upon as increasing the incorporating amount of the simulated HLW. The changes in properties can be attributed to the structure changes owing to the incorporation of the simulated HLW.

Keywords: Thermal properties; Vibrational spectra

1. Introduction

The disposal of radioactive waste generated by the nuclear fuel cycle is among the most pressing and potentially costly environmental problems. The high level nuclear wastes (HLW) are immobilized in a stable solid state and completely isolated from the biosphere.

Nuclear waste glasses are typically borosilicate glasses, and these glass compositions can experience phase separation at elevated concentrations of P_2O_5. The maximum P_2O_5 concentrations must be limited to between 1 and 3 mass%. For some waste streams, this can require considerable dilution and a substantial increase in the volume of the waste glass produced. Hence, there has been a continuing interest in developing phosphate glasses as waste forms. Furthermore, typical borosilicate glasses are limited to no more than 5 mass% actinides (2 mass% for plutonium). In contrast, iron phosphate glass with up to 15 mass% P_2O_5 can accommodate up to 40 mass% of simulated HLW.[1,2]

Phosphate glasses have some advantages over borosilicate glasses, such as a lower melting temperature and higher solubility for problematic elements, such as sulfur, and were investigated as early as the 1960s. Later work on sodium–aluminum phosphate glass[3] and iron–aluminum phosphate glass[4] showed that some of these glasses have comparable or better chemical durability than the borosilicate glasses. Present efforts are focused on the development of lead–iron phosphate glasses.[1,5–10] The main disadvantage of phosphate glass is that the melts are highly corrosive. Still, a number of the engineering problems were overcome and in the 1980s at Mayak in the Urals, considerable amounts of waste, approximately 1000 m^3, were immobilized in a phosphate glass.[11] Vitrification of wastes with Na–Al phosphate glass matrix continues today at the Mayak Production Association in Chelyabinsk where 300 million Curies of activity of HLW have been immobilized in glass. There have been studies to investigate the immobilization of Cs,[12] CsCl and SrF_2,[13] mixed-waste sludge[14] and spent nuclear fuel[2] in iron phosphate glass compositions.

Magnesium phosphate glasses are classified as 'anomalous phosphate glasses', which exhibit anomalies in the relationship between physical properties, such as density and

* Corresponding author. Tel.: +81 426 28 4149; fax: +81 426 28 4149.
E-mail address: okura@cc.kogakuin.ac.jp (T. Okura).

0955-2219/$ – see front matter © 2005 Elsevier Ltd. All rights reserved.
doi:10.1016/j.jeurceramsoc.2005.07.031

refractive index, and MgO/P_2O_5 (M/P) molar ratio around the metaphosphate composition (M/P = 1). The structures of M–P glasses have been studied.[15] Most of the phosphate glasses form high polyphosphate consisting of chains of phosphate ions, while the structures of M–P glasses are of two types, one includes four membered rings of PO_4 tetrahedra at M/P < 1 (type T) and the other contains dimers of PO_4 tetrahedra at M/P > 1 (type P).

In this study, M–P glasses are chosen as the base glass.[16] Simulated HLW (radioactive isotopes were not employed)[17] was incorporated into the base glass to study its effects on the properties of the glasses. The present article reports on the leach rates to water and some thermal properties. The variations of the glass structure due to the incorporation of the simulated HLW are also examined by Fourier-transformed infrared (FT-IR) and Raman spectra.

2. Experimental procedure

2.1. Sample preparation

The M–P glass frit that is used to produce glass waste form can be prepared by combining appropriate amounts of magnesium oxide and phosphoric acid and by heating at 1250 °C for 1 h. The powder mixtures of the glasses containing 0, 25 and 45 mass% of simulated HLW were melted at 1250 °C for 2 h. The melt waste glass was poured into a stainless plate. The composition of the simulated HLW is shown in Table 1.

2.2. Leach test

According to the technique of MCC-2,[18] the leach test for the glass waste forms was conducted in distilled water. About 1 g of each sample crushed to 10–20 mesh was dipped into 50 ml of water in a Teflon mini-autoclave beaker within an oven kept at 90 °C for 20 days. The total surface area of the grains was estimated by the following:

$$S = \frac{WS_0}{\rho} \quad (1)$$

where W and ρ are the mass in g and the density in g/cm^3 of sample, and S_0 the specific surface of crushed specimen, respectively. The leach rates of gross and each constituent element were determined from the total weight loss of the specimen and the leachate analysed by inductively coupled argon plasma spectroscopy (ICP).

Table 1
Composition of simulated nuclear wastes

Waste element	Raw material	mass%
Na	$NaNO_3$	64.8
Sr	SrO	2.9
La	La_2O_3	16.1
Mo	MoO_3	7.5
Mn	MnO_2	1.2
Fe	Fe_2O_3	6.6
Te	TeO_2	0.9

2.3. Density, XRD and DTA

The density of the waste forms was measured at room temperature using the Archimedes method with kerosene as the immersion fluid. Powder X-ray diffraction (XRD) analysis of the as-quenched melt was used to verify the amorphous state of the samples. The differential thermal analyses (DTA) were performed in flowing air at a heating rate of 20 °C/min.

2.4. FT-IR and Raman spectra

The FT-IR spectra were measured using the KBr pellet technique in the frequency range 400–4000 cm^{-1} at room temperature. The Raman spectra were measured using a double grating spectrometer with an argon ion laser, scattered radiation being collected at 90° to the incident beam. The spectra were recorded over the 400–1400 cm^{-1} range at room temperature.

3. Results and discussion

3.1. Vitrification of wastes with M–P glass matrix

The composition and density of the M–P glass waste forms prepared in this study are listed in Table 2, where the structure of 45M55P0W (M/P < 1) glass is referred to as the type T, and that of 50M50P0W (M/P = 1) and 55M45P0W (M/P > 1) glass is referred to as the type P. The density increases with increase in simulated HLW content. The glass states were confirmed by the absence of XRD peaks. Only the 55M45P25W glass waste form partially crystallized during cooling. The appearance of the base glass is colorless and transparent. The colors of the glasses, which contain the simulated HLW, are dark brown and turn darker with increasing the simulated HLW content. The borosilicate glasses are limited to no more than 5 mass% actinides. In contrast, M–P glass with up to 55 mol% P_2O_5 can accommodate up to 45 mass% of simulated HLW.

Table 2
Composition and density of glass waste forms prepared in this study

Composition (mol%)	Simulated waste content (mass%)	Waste form	Density (g/cm^3)
$MgO:P_2O_5 = 45:55$	0	45M55P0W	2.45
	25	45M55P25W	2.67
	45	45M55P45W	2.91
$MgO:P_2O_5 = 50:50$	0	50M50P0W	2.25
	25	50M50P25W	2.73
	45	50M50P45W	2.89
$MgO:P_2O_5 = 55:45$	0	55M45P0W	2.51
	25	55M45P25W	2.76
	45	55M45P45W	3.02

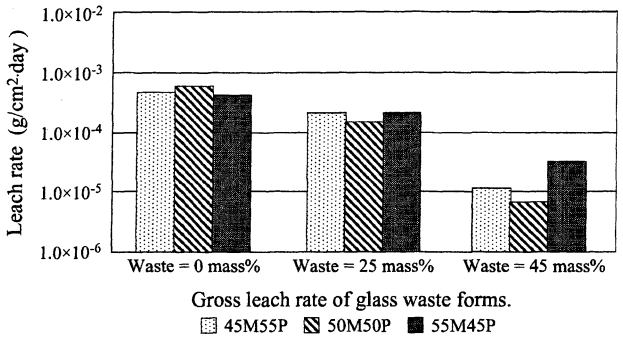

Fig. 1. Gross leach rate of glass waste forms.

Table 3
Leach rate of each constituent element of 55M45P45W glass waste form

Element	55M45P45W (g/cm^2 day)
Mg	4.79×10^{-7}
P	1.08×10^{-6}
Na	7.35×10^{-7}
Sr	1.00×10^{-9}
La	n.d.
Mo	1.80×10^{-7}
Mn	2.00×10^{-9}
Fe	1.60×10^{-8}
Te	1.00×10^{-9}

3.2. Leach rates of samples in water

The gross leach rates and the leach rates of each constituent element of the sample in water at 90 °C were determined from the total weight loss of the specimen and chemical analysis of leachate solution. The results are summarized in Fig. 1 and Table 3. The chemical durability of the glasses was greatly improved as the addition of simulated HLW. Fig. 1 shows that 50M50P45W has the gross leach rate of the order of 10^{-6} g/cm^2 day, which is fairly low as compared with that of the borosilicate waste glass. Of the elements in most phosphate glasses, Na shows higher leach rate than others, probably because of rather higher solubility of its polyphosphate consisting of chains of phosphate ions. No effect of Na in the M–P glass waste form on its leachability was found. These results can be attributed to the glass structure.

3.3. Thermal properties of glass waste form

It is important to obtain information about the thermal stability of the glass waste form, since the crystallization of glass

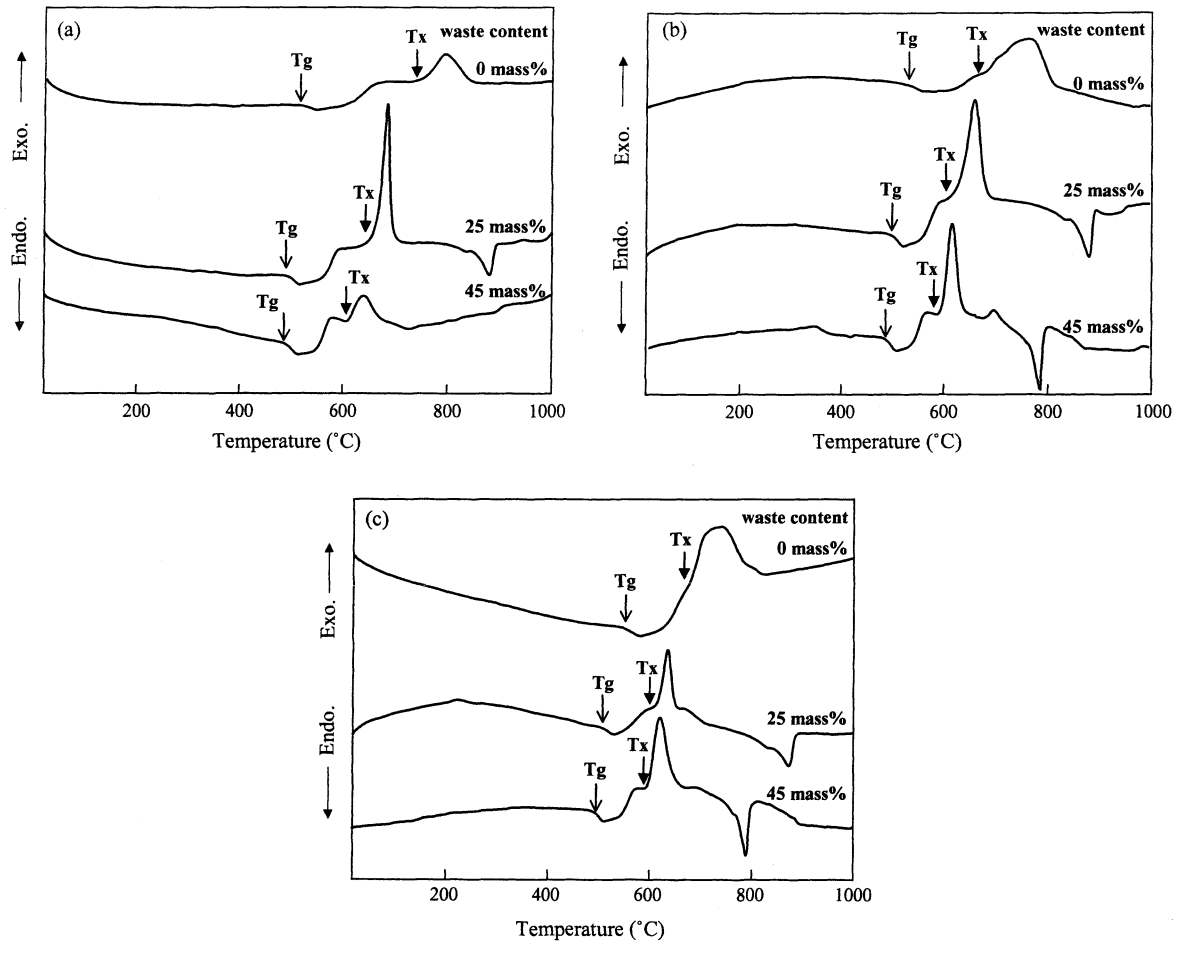

Fig. 2. DTA curves for samples with simulated waste content (0, 25 and 45 mass%). (a) 45M55P, (b) 45M55P, (c) 45M55P.

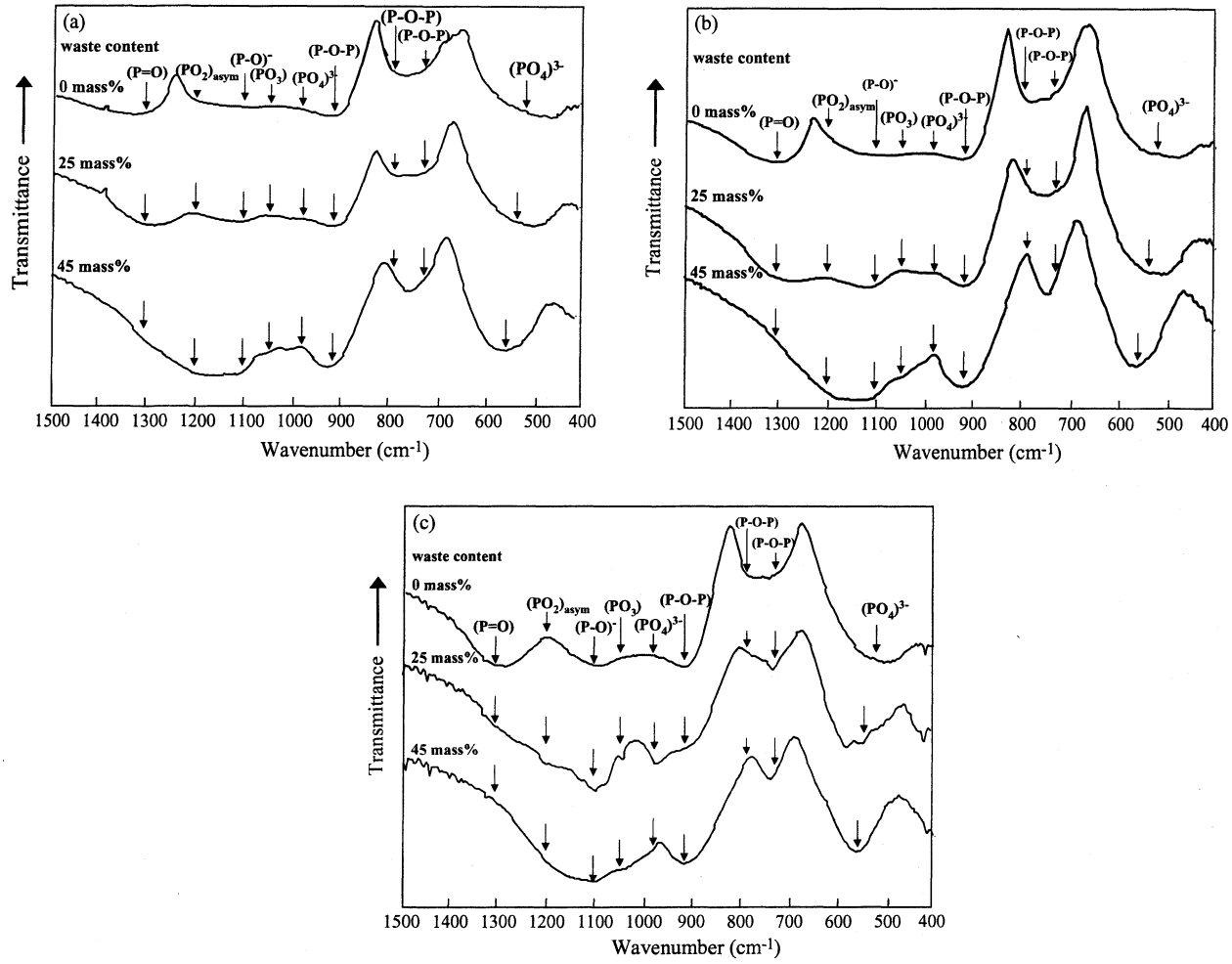

Fig. 3. FT-IR spectra of glass waste forms. (a) 45M55P, (b) 50M50P, (c) 55M45P.

waste can mostly increase the undesirable aqueous corrosion rate of the form, probably due to the formation of somewhat more soluble crystals or the increase in surface area.

Fig. 2 shows the DTA curves of the samples. The starting temperature of the crystallization peaks (Tx) and glass transition temperature (Tg) determined from the DTA curves and the stability of the waste forms (Tx – Tg) are listed in Table 4. The stability of the waste forms with the type P glass matrix does not change with increasing the simulated HLW content.

3.4. FT-IR spectra of glass waste form

The FT-IR spectra of the samples listed in Table 2 are shown in Fig. 3. The strong band near 1300 cm^{-1} is attributed to (P=O) stretching mode. The band obviously becomes smaller indicating a decrease in the double bond character and in the effective force constant of the (P–O) bond as found in ultraphosphates with increasing the simulated HLW content.

The band near 1200 cm^{-1} is assigned to asymmetric stretching modes of the two non-bridging oxygen atoms bonded to phosphorus atoms, $(PO_2)_{asym}$ or Q^2 units, in the phosphate tetrahedra. Their amplitudes obviously increase with increasing waste content. This result indicates that the phosphate linkages are shortened as the simulated HLW incorporate into the glass structure and leading to increase the relative content of the Q^2 units.

The absorption bands near 1100 cm^{-1} have been assigned to $(P–O)^-$ groups and its amplitudes increase with increasing waste content. It is suggested that the absorption bands of (M–O–P) (M = waste element) also locate at near 1100 cm^{-1}, and the relative content of these bonds increase with increasing waste content leading to increased intensity of 1100 cm^{-1} band.

The intensity of the band near 1050 cm^{-1}, which is assigned to (PO_3) end groups (Q^1), tends to decrease with increasing waste content. The absorption bands near 980 and 480–570 cm^{-1} are assigned to the stretching and deformation modes of $(PO_4)^{3-}$ groups (Q^0), respectively. It is shown that the absorption bands of the deformation modes of $(PO_4)^{3-}$ group shift to higher frequencies, and the amplitudes of $(PO_4)^{3-}$ group's absorption bands near 980 cm^{-1} decrease with increasing waste content. The Q^1 and Q^0 groups decrease with increasing waste content. These results indicate

Table 4
The results of DTA measurement of glass waste forms

	Waste forms								
	45M55P			50M50P			55M45P		
	0 W	25 W	45 W	0 W	25 W	45 W	0 W	25 W	45 W
Tg (°C)	519	492	490	553	509	495	541	506	489
Tx (°C)	754	658	609	684	617	596	681	614	598
Tx – Tg	235	166	119	131	108	101	140	108	109

Tg: glass transition temperature, Tx: starting temperature of crystallization.

that the relative content of non-bridging oxygen (P–O$^-$), which may be replaced by the formation of (M–O–P) bonds, decreases as the incorporation of the simulated HLW.

The absorption bands near 920 and 720–790 cm^{-1} are assigned to the asymmetric and symmetric stretching modes of the (P–O–P) linkages, respectively. The asymmetric stretching band of (P–O–P) near 920 cm^{-1} initially shifts to higher frequencies as the amount of the waste increases. The larger wavenumber of the (P–O–P) band is a result of the smaller (P–O–P) bond angle, which results from shorter phosphate linkages or smaller metal cation size. The phosphate linkages of the glasses with higher waste content are shorter due to the depolymerization of the glass structure.

The formation of asymmetric bridging oxygen (M–O–P) would increase the cross-link density of the glass network, improving the chemical durability of the glasses.

3.5. Raman spectra of glass waste form

The Raman spectra of the samples listed in Table 2 are shown in Fig. 4. The band near 1300 cm^{-1} is assigned to the symmetric stretching mode of terminal oxygen (P=O).

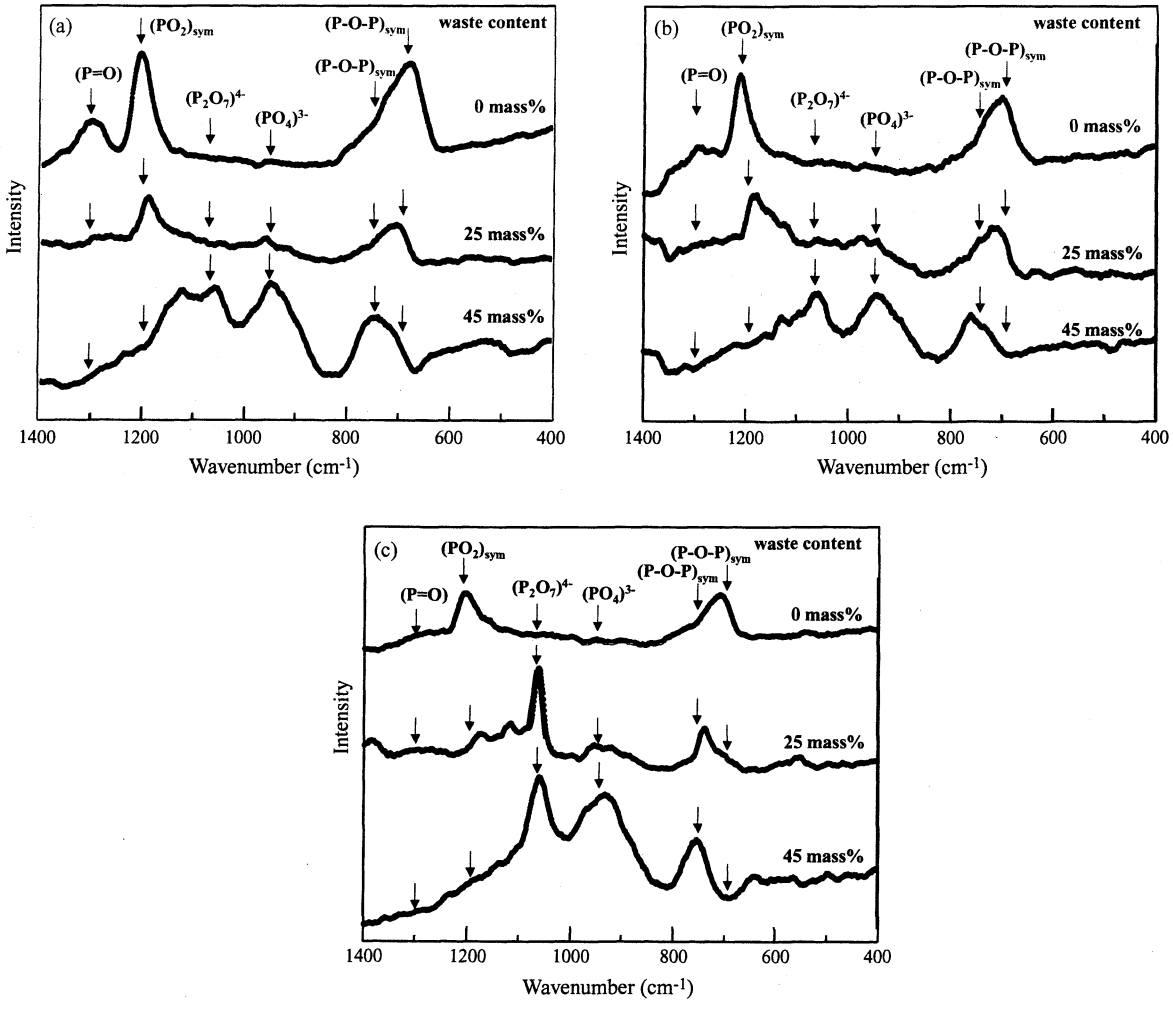

Fig. 4. Raman spectra of glass waste forms. (a) 45M55P, (b) 50M50P, (c) 55M45P.

The bands near 1200 and 700 cm^{-1} are due to the symmetric stretching mode of non-bridging oxygen $(PO_2)_{sym}$ on each tetrahedron and to the symmetric stretching mode of bridging oxygen between two tetrahedral $(P–O–P)_{sym}$, respectively. The bands near 1050 and 760 cm^{-1}, which are characteristic of pyrophosphate groups, are attributed to (P–O) symmetric stretching mode of non-bridging oxygen and (P–O–P) symmetric stretching mode of bridging oxygen, respectively. There are also some traces of orthophosphate groups $(PO_4)^{3-}$ as indicated by the band near 950 cm^{-1}. With increase waste content, the (P=O) stretching mode bands becomes smaller indicating a decrease in the double bond character and in the effective force constant of the (P–O) bond as found in ultraphosphates. Also, with increasing waste content, the bands near 1200 and 700 cm^{-1} have disappeared from the spectrum and the bands near 1050, 760 and 950 cm^{-1} are predominate, that is, the bands characteristic of the pyrophosphate dimer $(P_2O_7)^{4-}$ and orthophosphate monomer $(PO_4)^{3-}$ species increased.

4. Conclusions

M–P glasses are proposed as the potential nuclear waste glasses. The leach rates and structure of M–P glasses loaded with the simulated HLW were examined. The main features of this work are as follows:

(1) Up to 45 mass% loading of the simulated HLW can be incorporated into the base M–P glasses.
(2) The leach rate of the waste glasses decreases with increasing the simulated HLW content. The gross leach rate of the 50M50P45W waste form with the type P glass matrix is of the order of 10^{-6} g/cm^2 day at 90 °C, which is fairly low as compared to that of the borosilicate waste glass.
(3) The stability of the waste forms with the type P glass matrix does not change with increasing the simulated HLW content.
(4) With increasing waste content, the bands characteristic of the pyrophosphate dimer $(P_2O_7)^{4-}$ and orthophosphate monomer $(PO_4)^{3-}$ species increase.
(5) The formation of asymmetric bridging oxygen (M–O–P) increases the cross-link density of the glass network, improving the chemical durability of the glasses.
(6) The type P50M50P glass with low density is most suitable for vitrification of wastes.

References

1. Day, D. E., Wu, Z., Ray, C. S. and Hrma, P., Chemically durable iron phosphate glass waste forms. *J. Non-Cryst. Solids*, 1998, **241**, 1–12.
2. Mesko, M. G. and Day, D. E., Immobilization of spent nuclear fuel in iron phosphate glass. *J. Nucl. Mater.*, 1999, **273**, 27–36.
3. Geel, J., Van Eschrich, H., Heimerl, W. and Grziwa, P., Solidification of high-level liquid wastes to phosphate glass-metal matrix blocks. *IAEA, Vienna*, 1976, 22–26.
4. Grambow, B. and Lutze, W., *Scientific Basis for Neuclear Waste Management, Vol. 2*, ed. CJM, Jr. Plenum Press, New York, 1979, pp. 109–116.
5. Sales, B. C. and Boatner, L. A., Lead-iron phosphate glass: a stable storage medium for high-level nuclear waste. *Science*, 1984, **226**, 45–48.
6. Sales, B. C. and Boatner, L. A., In *Radioactive Waste Forms for the Future*, ed. W. Lutze and R. C. Ewing. North-Holland, Amsterdam, 1988, pp. 193–231.
7. Yanagi, T., Yoshizoe, M. and Nakatsuka, N., Leach rates of lead-iron phosphate glass waste forms. *J. Nucl. Sci. Technol.*, 1988, **25**, 661–666.
8. Yanagi, T., Yoshizoe, M. and Kuramoto, K., Leach rates and thermal properties of lead-iron phosphate glass waste forms. *J. Nucl. Sci. Technol.*, 1989, **26**, 948–954.
9. Reis, S. T., Karabulut, M. and Day, D. E., Structural features and properties of lead-iron-phosphate nuclear waste forms. *J. Nucl. Mater.*, 2002, **304**, 87–95.
10. Shin, P. Y., Properties and FTIR spectra of lead phosphate glasses for nuclear waste immobilization. *Mater. Chem. Phys.*, 2003, **80**, 299–304.
11. Lutze, W., In *Radioactive Waste Forms for the Future*, ed. W. Lutze and R. C. Ewing. North-Holland, Amsterdam, 1988, pp. 1–159.
12. Reis, S. T. and Martinelli, J. R., Cs immobilization by sintered lead iron phosphate glasses. *J. Non-Cryst. Solids*, 1998, **247**, 241–247.
13. Mesko, M. G., Day, D. E. and Bunker, B. C., Immobilization of CsCl and SrF2 in iron phosphate glass. *Waste Manag.*, 2000, **20**, 271–278.
14. Spence, R. D., Gilliam, T. M., Mattus, C. H. and Mattus, A. J., Laboratory stabilization/solidification of surrogate and actual mixed-waste sludge in glass and grout. *Waste Manag.*, 1999, **19**, 453–465.
15. Okura, T., Yamashita, K. and Kanazawa, T., A structural explanation for the phosphate glass anomaly. *Phys. Chem. Glasses*, 1988, **29**, 13–17.
16. Okura, T., Miyachi, T. and Monma, H., Immobilization of simulated high level nuclear wastes with magnesium phosphate glasses. *Mater. Res. Soc. Jpn.*, 2004, **29**(5), 2175–2178.
17. Ishida, M., Yanagi, T. and Terai, R., Leach rates of composite waste forms of monazite-and zirconium phosphate-type. *J. Nucl. Sci. Technol.*, 1987, **24**, 404–408.
18. Strachan, D. M., In *Scientific basis for nuclear waste management*, ed. J. D. Moor. Plenum Press, New York, 1980, pp. 347–348.

研究業績

4. デバイスへの応用

電子デバイス微細接合部の熱サイクル信頼性評価

実装継手用鉛フリーはんだの力学特性評価

立野昌義，後藤芳樹，小久保邦雄（機械工学科）

Abstract

The forces of this study is to clarify mechanical properties of lead-free solder, Sn-Ag-Cu alloy system. Indentation method was used to obtain mechanical properties including elastic modulus E, and Vickers hardness HV in the led-free solder at room temperature.

The results show that dependences of Elastic modulus E and Vickers hardness HV on the indentation load P and holding time t. Vickers hardness is independent on the indentation load in ranges over 0.9807 mN$\leq P\leq$9.81 N, but depends on the holding time. The Elastic modulus E also depends on the holding time. Aging effect on the mechanical properties for solder system is found experimentally.

1. はじめに

高密度実装電子部品には従来から Sn-Pb 共晶はんだが用いられてきた. Sn-Pb 共晶はんの融点が低いことや濡れ性が優れているため，高密度実装に適した材料としてコンピュータや家電製品の基板に組み込まれてきた．しかしながら，酸性雨によりプリント基板を含む家電製品の廃棄物から鉛が溶出するため環境に著しく悪影響を及ぼす．このことから，高密度実装電子部品には鉛フリーはんだが用いられるようになった[(1)–(3)].

高密度電子デバイスのはんだ接合部の熱疲労に対する信頼性は，実際に機器に温度変化を繰返し与える温度サイクル試験により評価されている[(4)]．ただし，製品開発における設計・試作および品質評価を繰り返すことにより，開発期間が長期化するなどの問題がある．そのため，はんだ接合部に生ずる熱ひずみを解析的に評価し，熱疲労特性を設計段階で予測する手法の開発が求められている[(4)]．しかしながら，はんだの接合部の数値解析に必要となる鉛フリーはんだの力学的特性データが少ないのが現状である．

本研究では Sn－Ag－Cu 系はんだ合金を対象として，硬さおよび弾性係数を硬さ試験より求め，これらの力学的特性に及ぼす圧子圧入荷重および保持時間の影響を明らかにした．

2. 試験方法

2. 1 供試材料および試験片

供試材にはニホンハンダ製 Sn-Ag-Cu 系はんだ合金素材 (96.5wt%Sn－3.0%Ag－0.5%Cu, 22×7×400mm 板材：溶融凝固後に圧延)，融点 218℃)を用いた．この板状素材を組織安定

化のため，恒温槽にて 130℃×2 時間保持後に徐冷した．この熱処理温度は融点の絶対温度のおよそ 82%に相当する．熱処理後に機械加工および放電加工にて所定の大きさの試験片に切り出し，硬さ試験および引張試験用試験片材料に用いた．

硬さ試験に用いる試験片は，熱処理後の素材を 10mm×5mm の試験片形状に製作し，耐水研磨紙（～#2500）で研磨後，バフ研磨によって鏡面加工仕上げ加工を施した．

硬さ試験に用いた試験機は，㈱島津製作所製微小硬さ計(マツザワ製) 0.9807 N≤P≤9.81 N，および超微小硬さ試験機(株式会社エリオニクス製 ENT-1100a)　0.98 mN≤P≤98 mN を用いた．硬さ試験の圧子にはビッカース圧子を取り付けて行った．硬さの圧子圧入荷重依存性を評価する際の荷重保持時間を t=30s に設定した．硬さ試験はすべて室温 25℃±3℃の条件にて，各条件にて最低 5 回の実験を行った．レーザー顕微鏡を用いて鏡面に仕上げたはんだ表面に導入した圧痕を観察した．

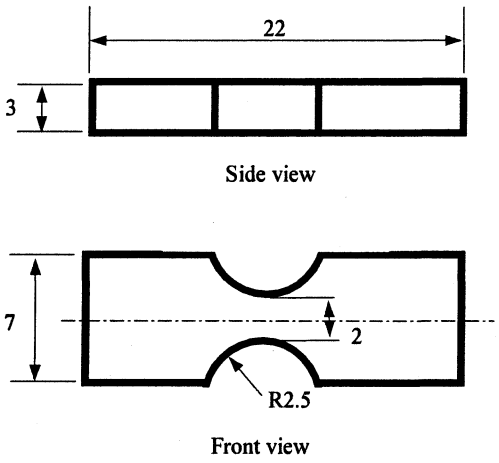

Fig.1 Configuration of specimen for tensile test

2．2　弾性係数算出法

圧子圧入試験の除荷過程における圧子圧入荷重 P と変位 h との関係を用いて縦弾性係数 E を予測する方法については，既報[(1),(2)]にて提案されている．

本方法では，除荷曲線における除荷開始直後荷重 P_{max} から $P_{max}/2$ までの P と h との関係を 2 次曲線近似し，その 2 次曲線における P_{max} における接線を用いて，塑性変形硬さと複合弾性率を求めている．ここで，複合弾性係率とは硬さ試験対象となる試料と圧子の両方の弾性率を含むパラメータである．算出された複合弾性率から，ダイヤモンド圧子の弾性率を 1050GPa，ポアソン比を ν=0.07，およびはんだのポアソン比を ν=0.39 として仮定して，はんだの弾性係数を算出した．

本実験では 0.9807 mN≤P≤9.81 mN において，荷重保持時間を 5 s, 20 s, 60 s に設定して弾性係数に及ぼす圧子荷重および荷重保持時間依存性を明らかにした．

この結果と比較する目的で，図 1 に示す板状試験片（くびれ部断面 2×3mm）をフライス盤とワイヤーカットを用いて作製し，引張試験を行った．試験片のくびれ部には歪ゲージを市販の瞬間接着剤で貼り付け，ひずみと荷重を同時計測した．実験に用いた装置は JT トーシ製引張試験機（ロードセル最大耐荷重 2000 N）を使用する．

ロードセルで求めた荷重とひずみゲージで計測したひずみデータを同期させPCに読み込せ，応力－ひずみ曲線を作図した．応力はロードセルの荷重を断面最小部の断面積で除した値とした．

3. 実験結果

3.1 硬さの荷重依存性および時間依存性

図2には，はんだ鏡面仕上げ面における硬さの圧子圧入荷重依存性を示す．圧子圧入荷重条件毎の平均硬さは圧子荷重(0.9807 mN≤P≤9.81 N)によらずほぼ一定の値を示した．硬さの平均値はHV=14.1を得た．この計測結果は，既報[(1)(2)]における凝固後に組織安定化を目的として熱処理(熱処理温度：融点の89%×1時間保持後に徐冷)した材料の硬さと試験条件は異なるがほぼ同等である．

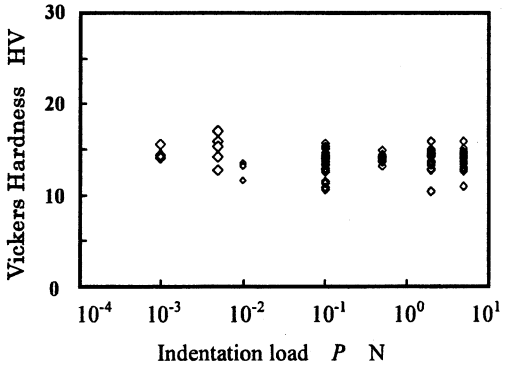

Fig.2 Dependence of Vickers Hardness on indentation load

はんだは低融点材料であるため，室温環境下でクリープ挙動を示す．このことから，硬さを評価する際，圧子の押し込み荷重保持時間tが硬さの計測結果に影響を及ぼす．

このため，硬さ試験における計測データを整理するためには，圧子押し込み保持時間および荷重との関係を充分把握する必要がある．

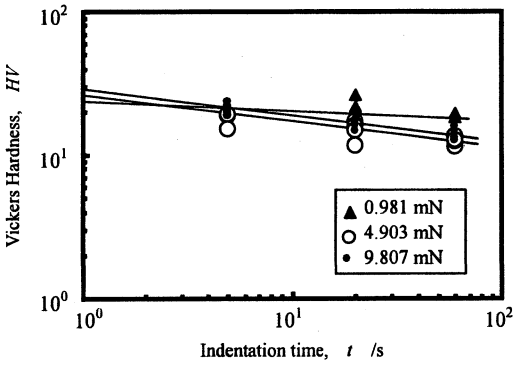

Fig.3 Relationship between Vickers hardness and indentation time

宮本ら[(1)(2)]は，両者の関係にはクリープが関与し，硬さが荷重保持時間に伴い減少する現象を式(1)で近似でき，整理できることを示した．

$$HV=HV_0 \cdot t^{c} \cdots\cdots\cdots\cdots\cdots\cdots\cdots\cdots\cdots\cdots(1)$$

ここで，式(1)内のHV_0はクリープの関与が比較的少ない硬さ，cはクリープに関与する材料定数として評価している．ただし，この結果が荷重範囲について適用できるかの検討は行われていないのが現状である．したがって，圧子圧入荷重の異なる条件での評価結果を式(1)に基づいて評価を行った．

図3には硬さの荷重保持時間の依存性を示す．この結果から，HV_0=22～30となり,圧子圧入荷重の増加に伴いHV_0が減少する.クリープに関与する材料定数はc=-0.13～-0.18となり，圧子圧入荷重の増加に伴い減少する傾向が確認できた．

上記のモデルの適用範囲に関しては今後，実験的に明らかにする方針である．

3.2 弾性係数の評価

図4には，硬さ試験により得た弾性係数の荷重保持時間依存性を示した．実験より得た弾性係数は荷重保持時間の増大により減少する．硬さ試験機で得られた弾性係数と引張試験から得た弾性係数とを比較した．

応力－ひずみ曲線内弾性域の直線の傾きは 54.5 GPa となり，硬さ試験から得た弾性係数 E とほぼ同等である．

今後は，鉛フリーはんだを対象として，試験片材料および引張試験におけるひずみ速度依存性ならびにクリープ特性とを対比させ，本結果の妥当性を明らかにする．

4. 結言

鉛フリーはんだは，低融点材料であるため，常温でもクリープ現象が発生し，試験機の荷重負荷条件や荷重保持時間の依存する可能性が高い．このことから，硬さ試験では荷重および荷重保持時間の影響を，引張試験では引張負荷時のひずみ速度の依存性を把握する必要がある．得られた結果を以下に要約する．

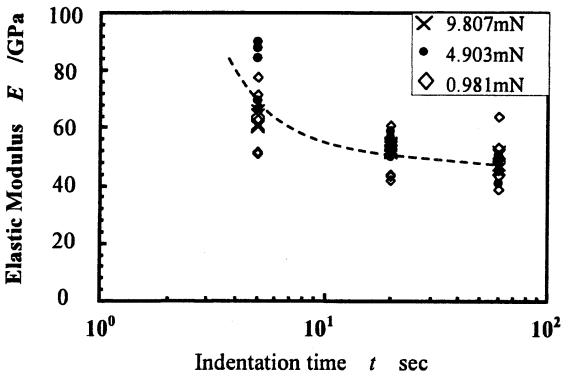

Fig.4 Relationship between Elastic modulus and indentation time

(１)はんだ表面硬度は圧子圧入荷重によらずほぼ一定値を得る．本実験で適用した圧子圧入荷重条件(0.9807 mN≤P≤9.81 N)における平均硬さは HV=14.1 である．

(２)はんだ表面の硬さは荷重保持時間に依存する．HV_0=22～30 となり，圧子圧入荷重の増加に伴い HV_0 が減少する．クリープに関与する材料定数は c=-0.13～-0.18 となり，圧子圧入荷重の増加に伴い減少する傾向が確認できた．

(３)硬さ試験で得た弾性係数値は圧子圧入時間の依存性がある．ただし，計測値は応力－ひずみ線図の弾性域から得られる直線の傾きとほぼ同等な値となる．

今後の課題

鉛フリーはんだを対象として，試験片材料および引張試験におけるひずみ速度依存性ならびにクリープ特性とを対比させ，本結果の妥当性を明らかにする．

引用文献

(1) 宮本　輝，小川武史，大澤　直，圧子圧入法による鉛フリーはんだの力学的特性の予測：材料，Vol.51,No.4，pp.445-450，(2002).

(2) 小川武史，宮本　輝，大清水和憲，大澤　直：Sn-Pb 系および Sn-Ag 系共晶はんだの硬さ試験による力学的特性評価，材料，Vol.49,No.6，pp.666-671(2000).

(3) 高温強度部門委員会，日本材料学会，はんだの引張強度試験法標準，(2000)

(4) 山田春彦，小川一義，電子部品はんだ接合部の熱疲労寿命解析，豊田中央研究所 R&D レビュー，Vol.31，No.4，pp.43-51.(1996).

材料試験技術

JOURNAL OF MATERIAL TESTING
RESEARCH ASSOCIATION OF JAPAN

マイクロサイズ材料の引張試験と強度評価

Tensile Testing and Strength Evaluation for Micro-sized Materials

後藤芳樹　Yoshiki GOTOH
新井裕介　Yusuke ARAI
宮坂勝利　Katsutoshi MIYASAKA
立野昌義　Masayoshi TATENO
小林光男　Mitsuo KOBAYASHI
小久保邦雄　Kunio KOKUBO

材料試験技術　Vol. 53　No. 1　2008年1月号別刷

日本材料試験技術協会

文部科学省　学会番号：30079
日本学術会議指定学術団体：1744

材料試験技術 Vol. 53 No. 1 2008年1月

資 料

20−2160

マイクロサイズ材料の引張試験と強度評価

Tensile Testing and Strength Evaluation for Micro-sized Materials

後藤芳樹* 新井裕介** 宮坂勝利*
立野昌義* 小林光男*** 小久保邦雄*

Abstract

The development of the technique of micro-fabrication enabled the reduction of the weight and size of the industrial products. The size of the components used in such products is considered to be in the order of microns, and the mechanical properties of such micro-sized materials are considered to be different from those of bulk (ordinary sized) materials.

Micromechanical evaluation of micro-sized materials including static and fatigue behavior is an important issue for developing a reliable machine in service operation. But, there has been an absence of the Standards for the test procedure in order to micro-sized materials, and the evaluation of mechanical properties including reliability and durability has not been performed.

We designed a tensile tester of capacity 500 mN for micro-sized materials. Tension tests were performed for Au bonding wire specimen in a constant speed test , and the stress-strain behavior was obtained in the range of 0.1〜0.5 μm/sec.

Key words: Micro-sized materials, Tensile test, Au bonding wire, Stress-strain behavior

1. はじめに

近年，マイクロ加工技術の発達により，携帯電話やパソコンをはじめとする工業製品の小型軽量化が進んでいるが，これらの設計においては，構成する微小寸法材料の基本的な静的強度や疲労特性などの機械的性質を知る必要がある。しかし，このような機器を構成する部材はマイクロやナノメートル領域の寸法となり，現時点では，このようなスケールの材料の機械的性質を評価する方法が確立されていないため，手探りの状態で設計ならびに製造が行われており，製作された機器の信頼性・耐久性は予測ができない状態である。

材料の機械的特性の中で，設計上まず必要になるのは，降伏点や引張強さなどの静的強度である。静的強度を求めるためには引張り，曲げ，ねじりなどの試験があるが，そのなかでも重要なのは引張試験である。引張試験は単純で均一な応力を負荷することができ，試験片の内部に応力勾配を生じる曲げやねじり試験とは異なり，延性材料を評価することができるという優れた特徴があるため，マイクロサイズであることによる試験片のチャッキングの難しさや，微小な伸びの測定の難しさがあるにもかかわらず，その試験法を確立する必要がある。

これまでに行われた微小寸法材料の引張試験は，小川ら[1),2)]が摩擦の影響を受けない構造を用いた横型引張試験機を用いて，50 μm の薄板の引張試験を行っ

※ 原稿受付 2007年10月16日
* 工学院大学工学部機械工学科
Yoshiki GOTOH, Katsutoshi MIYASAKA, Masayoshi TATENO and Kunio KOKUBO
(Department of Mechanical Engineering, Kogakuin University, Tokyo)
** 工学院大学大学院
Yusuke ARAI
(Graduate school of Mechanical Engineering, Kogakuin University, Tokyo)
*** 工学院大学工学部機械システム工学科
Mitsuo KOBAYASHI
(Department of Mechanical System Engineering, Kogakuin University, Tokyo)

た。試験片は平行部を補強するための補強部を有するもので，チャッキング後に補強部を除去して試験するものである。また，箕島ら[3),4)]は引張りおよび曲げの静的試験と疲労試験の可能な縦型の試験機を用いて細線の引張試験と疲労試験を行なっている。試験はプラスチックタブに試験片を接着し，試験開始時にタブを切断して試験片に荷重を負荷する方式である。砂田ら[5)]も横型の引張試験機を用い，プラスチックタブに試験片を接着する方法を用いて行っている。このように，タブを用い，試験片をタブに接着して引っ張る試験方法は，細線の場合にはチャッキングの難しさを避けることができる点で有利であり，簡便であることから，将来有望な試験方法であると考えられる。我々は，まずタブを用いて引っ張る方法で試験を試みることとし，引張試験機の製作を行った[6),7)]。また，微小な伸びの計測には CCD カメラを用いた画像センサにより，試験片の標点間の伸びを非接触で測定する方法を採用し，25 μm の金線の引張試験を行なったのでその結果について報告する。

2．引張試験機と試験システム

2.1　引張試験機

Fig. 1 に示すようなマイクロサイズ材料のための引張試験機を製作した。試験機は，駆動部分にサブミクロンフィードバック移動装置（シグマテック㈱）を用い，専用コントローラをパソコンで制御することにより速度 0.1 μm～10 mm/sec の範囲で一定速度試験が可能であり，ストロークは 20 mm である．ロードセルは容量±500 mN（㈱共和電業）とし，試験片の下部に取り付けた。試験片の中心軸の方向に正確に荷重が加わるよう，試験片を取付けた後，ロードセルを取付けた台の位置の微調整を可能にするため，XY 方向に移動可能なテーブルと，初期荷重が加わらぬようにZ 方向に移動可能なテーブルを組み合わせて用いた。

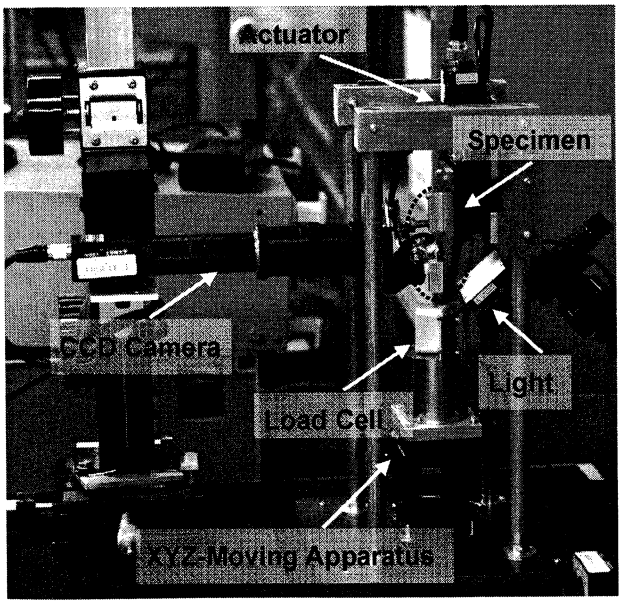

Fig. 1　Tensile Tester

2.2　伸びの計測

伸びの計測にはデジタル画像センサ（㈱KEYENCE, CV－3500）を用いた。この画像センサは 200 万画素の CCD カメラにより，試験片上の 2 点に予め標点をマーキングしておき，パターンサーチ計測モードにより，このマークの画像を認識させ，指定した範囲内でサーチし，2 点間の距離を計測するもので，この方法により試験片を取り付けたタブの伸びの如何に拘わらず，試験片の標点間の伸びだけを非接触で測定することができるのが特徴である。伸びの測定精度は，CCD カメラにエクステンションチューブを取り付けて画像を拡大し，1 画素の大きさは 2.0 μm である。画面上のデジタル表示は 1／1000 画素までの表示が可能である。

2.3　システム概要

本装置のシステムの概要を Fig. 2 に示す．試験片には，パソコンによりサブミクロンフィードバック移動装置を制御して引張速度一定で引張変位を加える。試験片に加わる荷重は，試験片の下部に置かれたロードセルで検出し，その信号はセンサーインターフェイス PCD 300 A（㈱共和電業）を介してパソコンに取り込まれる。また，CCD カメラで測定した試験片の変位信号は，一旦アナログデータに変換した後，センサーインターフェイス PCD 320 A（㈱共和電業）を介してパソコンに取り込まれる。つまり，これらのシステムにより，試験開始から試験片が破断するまで，ロードセルの荷重データと CCD カメラによる伸びデータは同期させて同時にパソコンに取り込まれ，そのデー

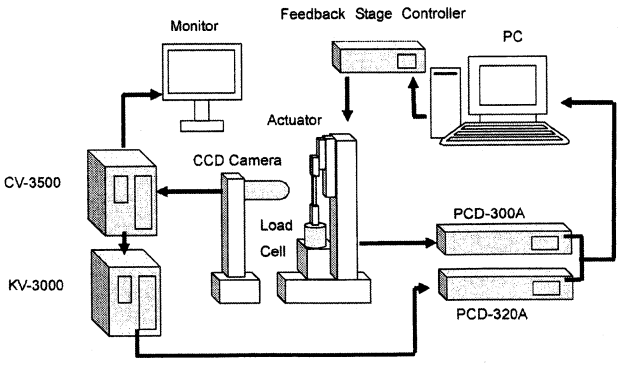

Fig. 2　Schematic diagram of tensile testing system

タから荷重－伸び線図を描くことができる。また，試験中の試験片の変形の様子はモニターで確認され，ビデオレコーダに記録することもできる。

3．試験方法

3.1　供試材料および試験片

供試材料は Kulicke & Soffa, Ltd. 製，直径 25 μm のワイヤーボンディング用金線（種類：AW 14，Au：99.99%）を用いた。この金線のカタログデータは引張強度 210 MPa である。この材料を適当な長さに切断して試験片とし，タブに取り付けた。タブは，厚さ 0.2 mm のポリプロピレンシートから Fig. 3 に示すような形状に切り出す。次に，タブの中心部分に金線試験片を瞬間接着剤で接着するのであるが，その取り付け方は，まず，金線を二つの三角穴に通し，金線の片側を接着剤で接着して固定する。そして，金線のもう一方に 0.1 gf の錘を吊るして金線のねじれやたわみを除去した後に接着する。最後に，金線の余分な部分を除去する。

3.2　試験方法

引張試験は，タブの両端のピン穴にピンを挿入し，Fig. 4(a)に示すような試験機の上下のホルダー部に装着して固定した上でタブの左右の枠の部分を熱したカッターで焼き切り，試験片にのみ荷重が加わる状態にして試験を実施する。

試験中の防振・防風の対策として，試験機は防振台（シグマ光機㈱）の上に設置し，周囲をアクリル板で囲んでいる。試験片の評点間距離は 1 mm とし，試験速度は 0.1，0.2，0.3，0.4，0.5 μm/s の 5 種類で試験を行い，引張速度の違いが，金線の引張特性にどのような影響を及ぼすのか調べた。

4．試験結果及び考察

引張試験の結果，得られた金線の荷重－伸び線図を Fig. 5 に，Fig. 6 に応力－ひずみ曲線を示す。引張速度は 0.1，0.2，0.3，0.4，0.5 μm/s の 5 種類で行った。荷重－伸び線図は引張り速度に依存し，引張り速度が遅いほど伸びは大きく，速度が速いほど伸びは小さくなる傾向を示した。金線が極めて延性に富む材料であることを確認する結果となった。得られた荷重－伸び線図を見ると，荷重については計測値のばらつきは少ないが，伸びについては，ところどころ計測値がばらついている部分が見られる。つまり，画像センサにより CCD カメラを用いて計測する場合，測定精度を上げるために画像を拡大して倍率を上げて計測するため，周囲の振動や風による微小なノイズの影響が現れているものと思われる。このノイズの影響を少なくするためには，さらに，防振や防風の対策が必要と考えられる。また，今後，さらに伸びの測定精度を向上させるためには，CCD の解像度を上げる必要があるが，そのためには一層，周囲の振動等によるノイズの影響を減らすことが必要と考えられる。

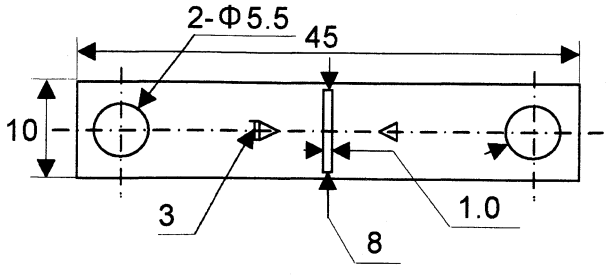

Fig. 3　Dimension of Polypropylene tab（t＝0.2 mm）

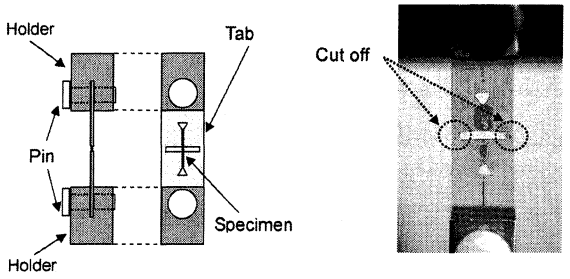

(a) Specimen mounted in the holder　　(b)Cut off the side of tab

Fig. 4　Procedure to mount a specimen in the holder

また，引張り強さについては，Fig. 7 に示すように，これまでに行った 28 本の試験の結果では，193 MPa ～219 MPa の範囲に分散しており，引張り強さ 205～207 MPa の範囲のものが最も度数が多いという結果となった。

Fig. 8 に示すように，光学顕微鏡により破断した試験片を観察したところ，試験片はほぼ中央部分から破断している。試験を始めた初期の頃は，接着部から破断することが多く見られたが，ホルダー部の改良や，金線の取り付け方を工夫することにより，現在では約 80% の試験片が中央部付近で破断するようになった。また，破断後の径は，破断前の 25 μm よりも小さくなっており，試験片がくびれている様子が確認でき，十分に塑性変形した後に破断していることが分かる。

4．結　言

本研究では，マイクロ材料の引張特性を評価する方法を確立するために，引張試験機を自作し，引張試験

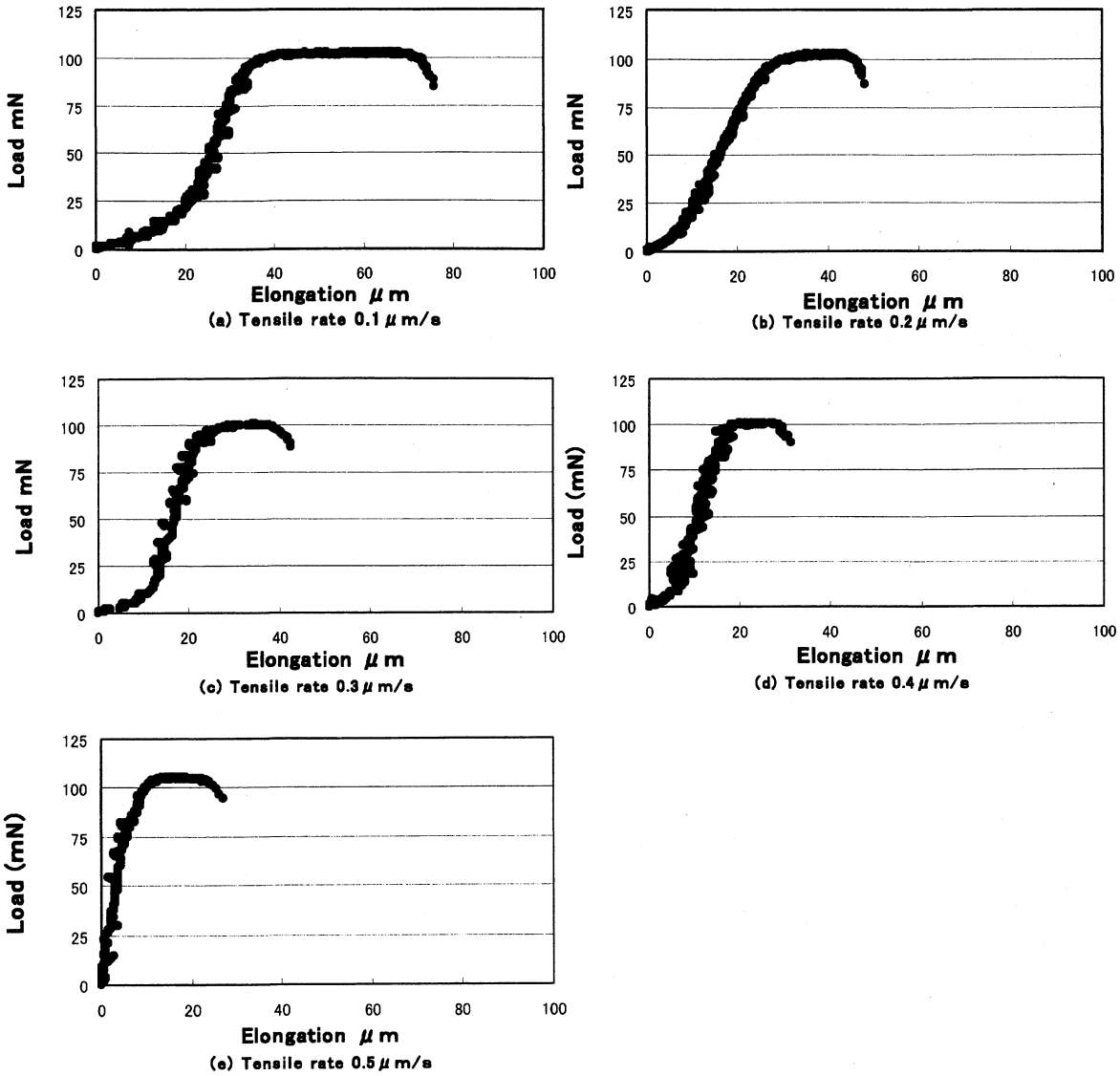

Fig. 5 Load–Elongation diagram of gold wire for each tensile rate

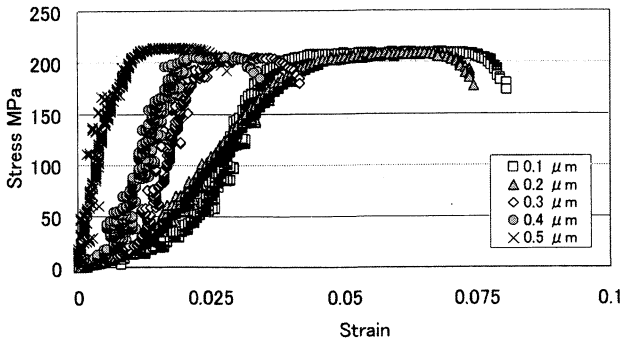

Fig. 6 Stress–Strain diagram of gold wire for each tensile rate

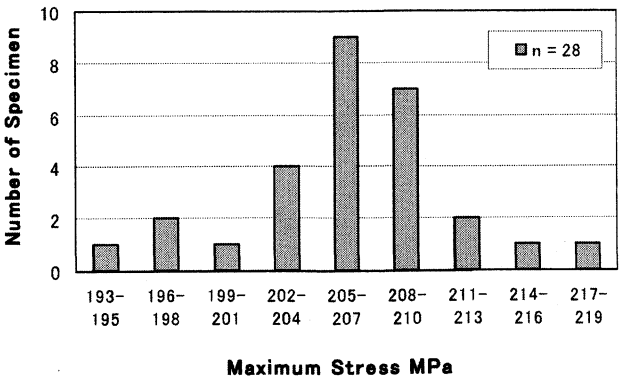

Fig. 7 Number of specimen v.s. Maximum Stress

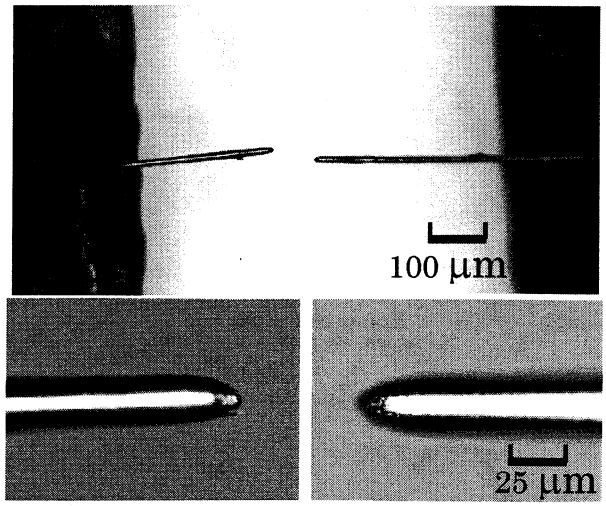

Fig. 8 Fracture part of gold wire. (observation by optical microscope)

を行った結果，以下のことが明らかとなった。

1）直径25 μmのワイヤーボンディング用金線の荷重と標点間の伸びを自動で計測し，荷重－伸び曲線を描くことができた。

2）得られた荷重－伸び線図から，荷重については計測値のばらつきは少ないが，伸びについては，計測値がばらついている部分が見られる。これは，画像センサによりCCDカメラを用いて計測する場合，測定精度を上げるために画像を拡大して倍率を上げて計測するため，周囲の振動や風による微小なノイズの影響が現れることが分かった。

参考文献

1）小川，石川，北原：機械技術研究所所報，Vol. 49, No. 2, pp. 57－62（1995）

2）H.Ogawa, K.Suzuki, S.Kaneko, Y.Nakano, Y.Ishikawa and T.Kitahara : Pro IEEE Micro Electro Mechanical Systems '97, pp 430－435（1997）

3）箕島，田中，石田：日本材料学会　第269回疲労部門委員会　第27回マイクロマテリアル部門委員会研究討論資料，p. 44－45（2004－5）

4）K.Minosima, Y.Maekawa, K.Komai：日本材料学会第269回疲労部門委員会第27回マイクロマテリアル部門委員会研究討論資料，p. 35－43（2004－5）

5）砂田，松村，浅田，木之本，越智，政木：日本機械学会2005年度年次大会講演論文集（1），p. 315－316（2005－9）

6）後藤，立野，小久保：工学院大学総合研究所「マイクロ先進スマート機械・マイクロバイオシステム研究センター」中間研究成果報告会　第2回，pp. 40－41（2005－3）

7）後藤，立野，小久保：工学院大学総合研究所「マイクロ先進スマート機械・マイクロバイオシステム研究センター」中間研究成果報告会　第3回，pp. 77－80（2006－3）

＜研究業績＞

1. Ken-ichi Isono, Eiichiro Niikura, Koichi Murakawa, Fumio Hasegawa, and Hideo Kawanishi, "Improvement of Crystal Quality of n-AlGaN by Alternate-Source-Feeding Metal Organic Vapor Phase Epitaxy", Japan J. Appl. Phys., Vol.46, No.9A, 5711-5714 (2007.09)
2. Kouichi Murakawa, Eiichiro Niikura, Fumio Hasegawa, and Hideo Kawanishi, "Reduction of Threading Dislocations in AlGaN/AlN/SiC Epitaxial Layers by Controlled Strain with (AlN/GaN) Multibuffer-layer Structure", Japan. J. Appl. Phys., Vol.46, No.6A, 3301-3304 (2007.06)
3. Hideo Kawanishi, Masanori Senuma, and Takeaki Nukui, "Tm-mode lasing and anisotropic polarization properties of AlGaN multiple quantum well lasers in deep-ultraviolet spectral region", Proceeding of SPIE Photonics West 2007, Vol.6473, 64731D (2007.2)
4. Eiichiro Niikura, Kouichi Murakawa, Fumio Hasegawa, and Hideo Kawanishi, "Improvement of crystal quality of AlN and AlGaN epitaxial layers by controlling the strain with the (AlN/GaN) multi-buffer layer", Journal of Crystal Growth, Vol.298, 345-348. (2007.01)
5. Hideo Kawanishi, Eiichiro Niikura, Mao Yamamoto, and Shoichiro Takeda, "Experimental energy difference between heavy- or light-hole valence band and crystal-field split-off-hole valence band in $Al_xGaN_{1-x}N$", Appl. Phys. Lett., Vol.89, No.25, 251107-1 - 251107-3 (2006.12)
6. Hideo Kawanishi, Masanori Senuma, Mao Yamamoto, Eiichiro Niikura, and Takeaki Nukui, "Extremely weak surface emission from (0001) c-plane AlGaN multiple quantum well structure in deep-ultraviolet spectral region", Appl. Phys. Lett, Vol.89, No.8, 081121-1 - 081121-3 (2006.08)
7. Hideo Kawanishi, Masanori Senuma, and Takeaki Nukui, "Anisotropic polarization characteristics of lasing and spontaneous surface and edge emissions from deep-ultraviolet (λ ≈240 nm) AlGaN multiple-quantum-well lasers", Appl. Phys. Lett., Vol.89, No.4, 041126-1 - 041126-3 (2006.7)
8. 川西英雄、瀬沼正憲、貫井猛晶、「深紫外AlGaN多重量子井戸半導体レーザー光の光学的異方特性」、日本光学会(応用物理学会)光学、35巻、5号、265-267 (2006. 05)
9. Naoyuki Obinata, Koichi Sugimoto, Kazuyuki Ijima, Masaya Ishibiki, Shinichi Egawa, Tohru Honda, and Hideo Kawanishi, "Relationship between Excess Ga and Residual Oxides in Amorphous GaN Films Deposited by Compound Source Molecular Beam Epitaxy", Japan. J. Appl. Phys. Vol.44, No.12, 8432-8434 (2005.12)
10. 川西英雄、高野隆好、瀬沼正憲、貫井猛晶、「光励起によるAlGaN多重量子井戸型深紫外レーザーの発振特性-発振波長域240～360nm」応用物理、第74巻、第11号、1458-1462 (2005.11)
11. Tohru Honda, Yohta Aoki, Miwako Akiyama, Naoyuki Obinata, Shinichi Egawa, and Hideo Kawanishi, "GaN films deposited at low temperature on (111) Si by compound-source molecular beam epitaxy technique", J. Vac. Sci. Technol, B23(4) (2005.07)

Japanese Journal of Applied Physics
Vol. 46, No. 6A, 2007, pp. 3301–3304

Reduction of Threading Dislocations in AlGaN/AlN/SiC Epitaxial Layers by Controlled Strain with (AlN/GaN) Multibuffer-Layer Structure

Kouichi MURAKAWA, Eiichirou NIIKURA, Fumio HASEGAWA, and Hideo KAWANISHI

Department of Electronic Engineering, Kogakuin University, 2665-1 Nakanno-machi, Hachioji, Tokyo 192-0015, Japan

(Received December 7, 2006; accepted February 24, 2007; published online June 6, 2007)

AlGaN/AlN layers were grown on SiC substrates with an (AlN/GaN) multibuffer-layer structure (MBLS). The tensile strain in the *a*-axis of the grown layer was controlled by changing the structure of the (AlN/GaN) MBLS. It was found that the crystal quality of the grown layers was improved by increasing the strain. It was also confirmed by transmission electron microscopy (TEM) observation that the dislocation density of the AlN layer decreased with increase of the tensile strain in the *a*-axis. The screw dislocations decreased more rapidly with the distance from the substrate for the same tensile strain than the edge dislocations did. [DOI: 10.1143/JJAP.46.3301]

KEYWORDS: AlN, AlGaN, TEM, tensile strain, dislocation density, multibuffer-layer structure, FWHM

1. Introduction

Control of the crystal quality of AlN and AlGaN is very important for the development of ultraviolet (UV) and deep-UV light-emitting diodes (LEDs) and laser diodes (LDs). These layers are generally grown on lattice-mismatched substrates such as sapphire or SiC. The lattice mismatch is one of the origins of the crystal defects in the epitaxial layer. It is reported that the misfit dislocations, the main defects due to the lattice mismatch, and other threading dislocations can be reduced by various kinds of buffer layers and crystal growth techniques.[1] Our group reported that the residual strain of the AlN grown layer can be controlled by changing the structure of the (AlN/GaN) multibuffer-layer structure (MBLS)[2,3] and as a result the crystal quality of the grown layer can be improved for low pressure metal-organic vapor phase epitaxy (LP-MOVPE).[4] By combining this AlN/GaN MBLS and alternate-source-feeding epitaxy (ASFE)[5] for the growth of the AlN template and AlGaN multi-quantum well (MQW), our group has achieved lasing at the shortest wavelength reported so far (241 nm), although it was under optical excitation.[6] Unfortunately, crystal quality has been evaluated only by the full width at half maximum (FWHM) of the X-ray rocking curve (XRC) of both (0002) plane for the tilting (ω-scan) and of ($10\bar{1}2$) plane for the twisting (φ-scan). How the misfit dislocations can be reduced by the AlN/GaN MBLS has, therefore, not necessarily been clarified yet.

The purpose of this work is to measure directly the threading dislocations of the AlGaN/AlN/SiC samples with different strains by transmission electron microscopy (TEM), and to find whether the threading dislocations are really reduced by introduction of strain in the grown layer with the AlN/GaN MBLS.

2. Experimental Procedure

The AlN template and AlGaN epitaxial layers with an Al composition of 0.6–0.8 were grown by LP-MOVPE on (0001) 6H- or 4H-SiC substrates using the (AlN/GaN) MBLS as shown in Fig. 1. The AlN template and the (AlN/GaN) MBLS were grown by conventional simultaneous-source-feeding epitaxy, but the AlGaN cladding layer was grown by the alternate-source-feeding (ASF) MOVPE.[4] Trimethylgallium (TMGa), trimethylaluminum (TMAl), and ammonia (NH_3) were used as source materials for gallium,

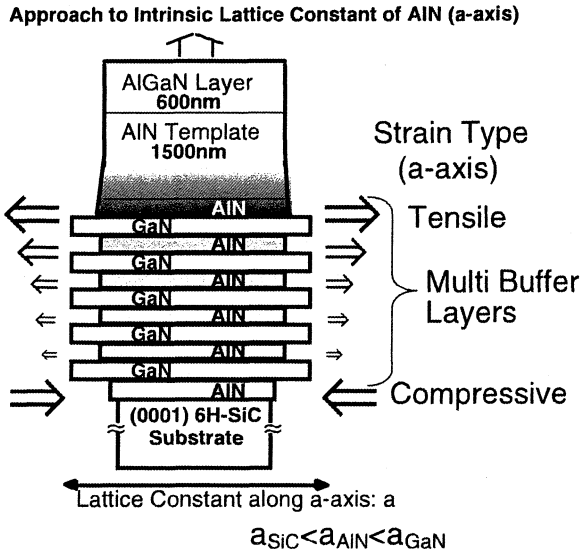

Fig. 1. Structure of the grown samples and model of the strain introduction. The basic structure of the MBLS is a superlattice structure (SL).

aluminum, and nitrogen, respectively. The source materials were introduced into the reactor through the flow channel with a hydrogen carrier gas. The residual strain of the AlN template was changed by changing the structure of the (AlN/GaN) MBLS.[2,3] Basic structure of MBLS is a superlattice (SL) structure as shown Fig. 1. As the thickness of the GaN layer increases, the tensile strain in the *a*-axis of the AlN template increases, because the *a*-axis lattice constant of GaN is larger than that of AlN. The thicknesses of the AlN template and AlGaN layer (which is used as a cladding layer of the laser structure) were about 1500 and 600 nm, respectively. Details of the growth method are described in our previous paper.[4] The grown layers were characterized by 2θ–ω X-ray diffraction (XRD) for both *a*- and *c*-planes to determine the strain in the grown layer, a ω-scan of the (0002) plane to see the tilting (probably related to screw and mixed dislocations) and φ-scan of ($10\bar{1}2$) plain of AlN layers to observe the twisting (probably related to edge dislocation).

Threading dislocations of the grown layers were observed by TEM (JEM 2100) with an incident axis of [210]. Both

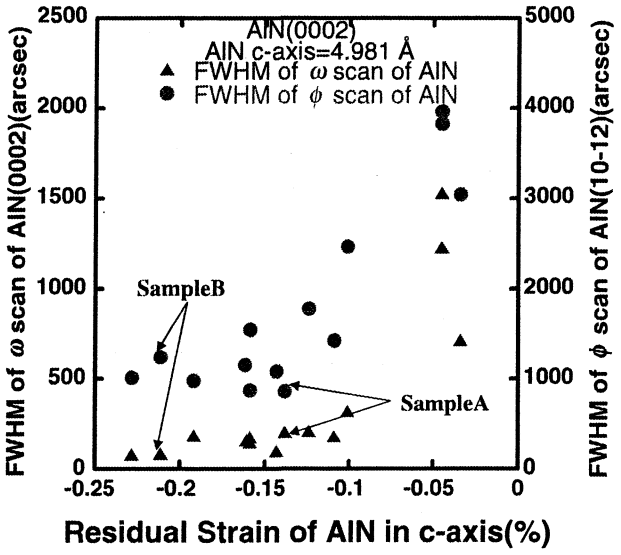

Fig. 2. FWHM of both (0002) ω-scan and $(10\bar{1}2)$ ϕ-scan XRCs for the AlN template against the residual strain of the AlN layer expressed as $[(c - c_0)/c_0 \times 100]$. The FWHM decreases with increasing strain.

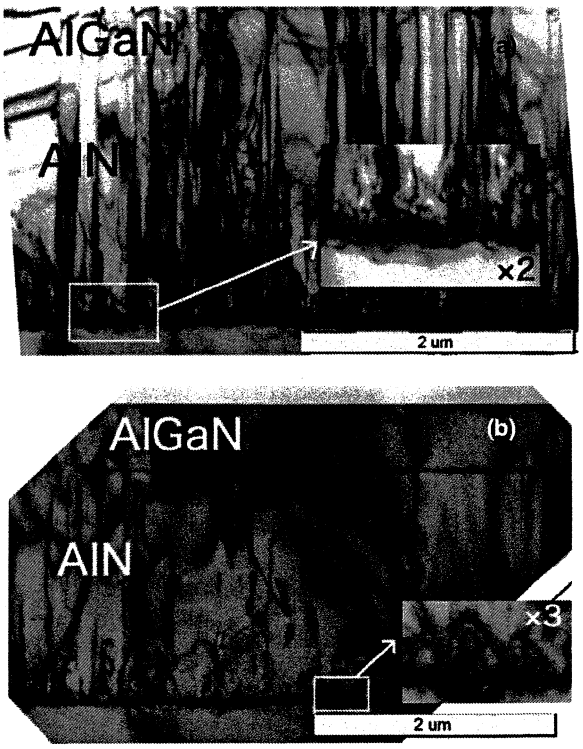

Fig. 3. Bright-field TEM images of (a) sample A with smaller tensile strain in a-axis and (b) sample B with larger tensile strain in the a-axis. Whole dislocations including edge, screw and mixed dislocations can be seen in these images.

bright-field and dark field patterns of 0002 and $11\bar{2}0$ spots were obtained to observe whole dislocations and to distinguish between edge and screw dislocations, respectively.

3. Results and Discussion

The FWHM of the ω-scan XRC for the AlGaN cladding layer was nearly equal to that of the AlN template underneath, therefore, the evaluation of the AlN template is reasonable for the evaluation of all the layers.[7] The dependence of the FWHM of the XRC of both the (0002) ω-scan and the $(10\bar{1}2)$ φ-scan on the residual strain expressed as $[(c - c_0)/c_0]$ is shown in Fig. 2. The results indicate that the more the AlN layer is tensile strained in the a-axis, the more the crystal quality is improved, suggesting that fewer dislocations are introduced. This tendency is the same for the FWHM of both the ω-scan (tilt) and φ-scan (twist). Cracks were observed in the periphery of the 10 mm square wafer, particularly for the strongly strained samples. There is, however, few crack in the central part of the wafer and in fact optically pumped lasers have been obtained with those strongly strained wafers.[6] In order to confirm the reduction of the dislocations, TEM observations were performed on the samples with less strain [sample A in Fig. 2: $[(c - c_0)/c_0 = -0.14\%]$ and more strain [sample B in Fig. 2: $[(c - c_0)/c_0 = -0.22\%]$. The results are shown in Figs. 3–5. Figure 3 shows bright-field TEM images of samples A and B. As it is well known, the bright field TEM image shows whole dislocations including edge, screw and mixed dislocations. As can be seen in the enlarged part of the interface in Fig. 3, there are many dislocations induced at the interface because of the lattice mismatch between AlN and SiC, but most of them are terminated inside the MBL, as it has been reported that other superlattices terminate the threading dislocations.[8] In addition, however, some of the dislocations in the AlN adjacent to the MBL form loops to terminate each other for sample B with the larger tensile strain in the AlN template [see the enlarged part of the interface in Fig. 3(b)]. On the other hand, such dislocation loops can not be seen in the AlN adjacent to the MBL for sample A with less strain [see the enlarged part of the interface in Fig. 3(a)]. As a result, the total dislocation density of sample B with the larger tensile strain in the a-axis is much smaller than that of sample A with smaller tensile strain in a-axis. This bending and coalescence of the dislocations is probably the main reason why the more strained samples have fewer dislocations, although the bending is not well observed by TEM in the AlN template except in the vicinity of the MBL [the inset of Fig. 3(b)].

We can distinguish edge and screw dislocations by dark-field TEM images. Figure 4 shows the dark-field TEM image of a $[g = (000\bar{2})]$ diffraction spot. White lines include both screw and mixed dislocations. The dislocation density of the less strained sample [A; Fig. 4(a)] is from 7.5×10^9 to $4.5 \times 10^9\,\mathrm{cm}^{-2}$, decreasing from the interface (bottom of the photo) to the top of the AlN template. On the other hand, the dislocation density of the more strained sample [B; Fig. 4(b)] is from 5.8×10^8 to $7.5 \times 10^7\,\mathrm{cm}^{-2}$, indicating that the dislocation density (screw + mixed) of the AlN template decreases with increasing the tensile strain in the a-axis.

Similar results for the edge and mixed dislocations are shown in Fig. 5. The diffraction spot observed by TEM is $[g = (\bar{1}\bar{1}20)]$ in this case. The number of edge dislocations is much larger than that of screw dislocations as generally reported.[9] Still, the density of the more strained sample [B; Fig. 5(b)] is about one order of magnitude lower than that of the less strained sample [A; Fig. 5(a)]. Figure 5(c) shows the

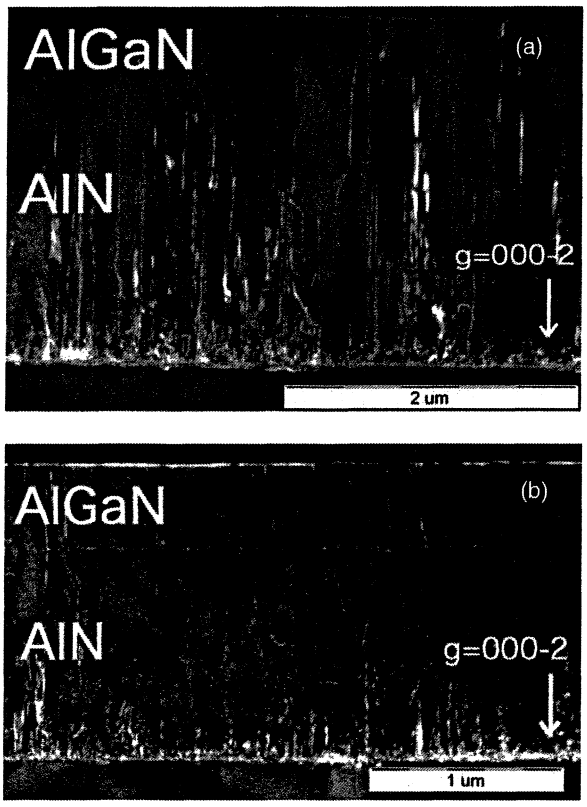

Fig. 4. Dark-field TEM image of $g = 000\bar{2}$ diffraction spot. White lines include both of screw and mixed dislocations. (a) Less strained sample A [$(c - c_0)/c_0 \times 100 = -0.14\%$]. The dislocation density decreases from 7.5×10^9 to 4.5×10^9 cm^{-2}. (b) More strained sample B [$(c - c_0)/c_0 \times 100 = -0.22\%$]. The dislocation density decreases from 5.8×10^8 to 7.5×10^7 cm^{-2}.

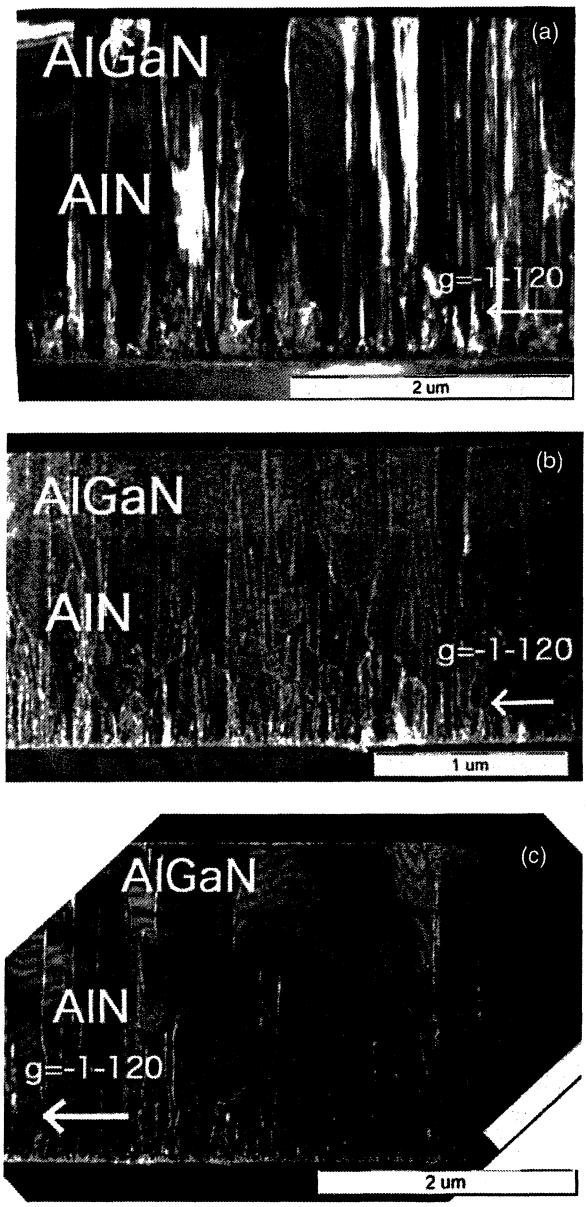

Fig. 5. Dark-field TEM image of $g = \bar{1}\bar{1}20$ diffraction spot. White lines include both edge and mixed dislocations. (a) Less strained sample A [$(c - c_0)/c_0 \times 100 = -0.14\%$]. (b) More strained sample B [$(c - c_0)/c_0 \times 100 = -0.22\%$], (c) Most strained sample C whose tensile strain in the a-axis is much larger [$(c - c_0)/c_0 \times 100 = -0.38\%$] than that of sample B [$(c - c_0)/c_0 \times 100 = -0.22\%$].

dark-field TEM image of sample C, whose tensile strain in the a-axis was much larger [$(c - c_0)/c_0 \times 100 = -0.38\%$] than that of sample B [$(c - c_0)/c_0 \times 100 = -0.22\%$]. This large strain was performed by other series of the growth on the 4H–SiC substrates. The (edge + mixed) dislocation density of this highly strained sample (C) is one order less than that of sample B, suggesting that the more strained in the a-axis, the less dislocations are induced. More cracks were observed in the periphery of wafer C, but laser operation has also been achieved using this wafer. Since the edge dislocation density is about one order of magnitude higher than the screw dislocation density, more strain must be needed to reduce the dislocation density to a reasonable level for the lasing.

Figure 6 shows the dislocation densities in the AlN epitaxial layer plotted against the distance from the SiC substrate: Figure 6(a) shows decrease of the (screw + mixed) dislocations and Fig. 6(b) shows decrease of the (edge + mixed) dislocations. It can be seen easily that the gradient of the decrease of the dislocation density is larger for the larger tensile strain in the a-axis. Two other facts are also confirmed: 1) A increase of the strain about 0.1% decreases the dislocation density by about one order. The edge dislocation density is about one order of magnitude larger than that of screw dislocations as previously reported.

Recently Amano reported that the dislocation density in AlN on sapphire decreases with increasing AlN thickness, and that this is due to the built-in tensile strain in the AlN layer.[10] The same phenomenon should occur in our case: The (AlN/GaN) MBLS is introduced between the AlN and the SiC substrate, and the AlN layer is tensile strained in the a-axis during the growth in our case, therefore, the dislocations introduced at the MBLS/SiC interface are bent by the strain [as can be seen in the enlarged part of the interface in Fig. 3(b)] during the growth of AlN, and as a result the number of threading dislocations is reduced.

4. Conclusions

It was demonstrated by TEM observation that the dislocation density of an AlN template decreases with increasing tensile strain in the a-axis. The tensile strain in

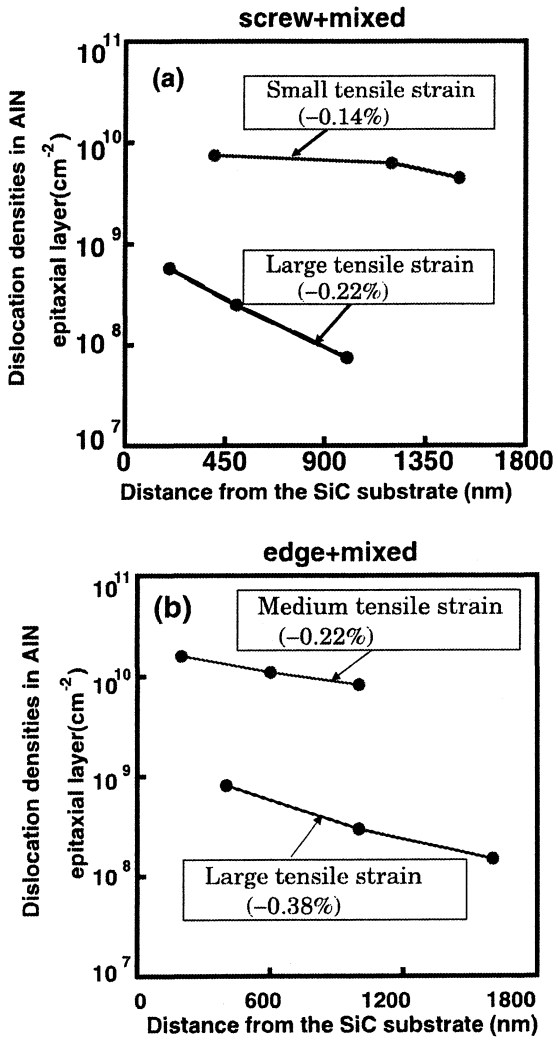

Fig. 6. Dislocation densities in the AlN epitaxial layer plotted against the distance from the SiC substrate. (a) (Screw + mixed) dislocations. (b) (Edge + mixed) dislocations.

the *a*-axis was introduced by the (AlN/GaN) multibuffer-layer structure. Since the edge dislocation density is about one order of magnitude higher than the screw dislocation density, more strain must be needed to reduce the dislocation density to $10^8/cm^2$ level.

Acknowledgements

The authors express their thanks to Mr. T. Nukui for his help on the TEM observation and to Mr. M. Senuma for his help on the MOVPE growth. They are also very grateful to professor Emeritus Y. Suematsu and professor Emeritus K. Iga of Tokyo Institute of Technology for their encouragement regarding our work. This work is supported by the Japan Society for the Promotion of Science and the Ministry of Education, Culture, Sports, Science and Technology, a Grant-in-Aid for Scientific Research (S) No. 17106005 and a Grant-in-Aid for Scientific Research on Priority Areas No. 18069009.

1) D. Cherns, S.-L. Sahonta, R. Liu, F. A. Ponce, H. Amano, and I. Akasaki: Appl. Phys. Lett. **85** (2004) 4923.
2) M. Kurimoto, T. Nakada, Y. Ishihara, M. Shibata, T. Takano, J. Yamamoto, T. Honda, and H. Kawanishi: Phys. Status Solidi A **176** (1999) 665.
3) M. Kurimoto, T. Nakada, Y. Ishihara, M. Shibata, T. Honda, and H. Kawanishi: Jpn. J. Appl. Phys. **38** (1999) L551.
4) Y. Ishihara, J. Yamamoto, M. Kurimoto, T. Takano, T. Honda, and H. Kawanishi: Jpn. J. Appl. Phys. **38** (1999) L1296.
5) M. Kurimoto, M. Shibata, J. Yamamoto, M. Tsubamoto, T. Honda, and H. Kawanishi: J. Cryst. Growth **189–190** (1998) 189.
6) T. Takano, Y. Narita, A. Horiuchi, and H. Kawanishi: Appl. Phys. Lett. **84** (2004) 3567.
7) E. Niikura, K. Murakawa, F. Hasegawa, and H. Kawanishi: to be published in J. Cryst. Growth (2006).
8) W. H. Sun, J. P. Zhang, J. W. Yang, H. P. Marusaka, M. A. Khan, R. Liu, and F. A. Ponce: Appl. Phys. Lett. **87** (2005) 211915.
9) T. Hino, S. Tomiya, T. Miyajima, K. Yanashima, S. Hashimoto, and M. Ikeda: Appl. Phys. Lett. **76** (2000) 3421.
10) H. Amano: private communication; presented at 1st Int. Symp. Growth of III–Nitrides (ISGN-1), June 2006, Linkping, Sweden.

Japanese Journal of Applied Physics
Vol. 46, No. 9A, 2007, pp. 5711–5714

Improvement of Crystal Quality of n-AlGaN by Alternate-Source-Feeding Metal Organic Vapor Phase Epitaxy

Ken-ichi ISONO, Eiichiro NIIKURA, Koichi MURAKAWA, Fumio HASEGAWA, and Hideo KAWANISHI

Department of Electronic Engineering, Kogakuin University, Hachioji, Tokyo 192-0015, Japan

(Received April 18, 2007; accepted June 7, 2007; published online September 7, 2007)

The crystal quality of AlGaN layers was improved using alternate-source-feeding epitaxy (ASFE) in low-pressure (LP) metal organic vapor phase epitaxy (MOVPE). The green emission of photoluminescence (PL) from the AlGaN clad layer was reduced, indicating that point defects such as Ga or Al vacancy were reduced by ASFE. On the other hand, the full width at half maximum (FWHM) of the X-ray rocking curve was not improved at all and the dislocation density observed by transmission electron microscopy (TEM) was not reduced by ASFE. Furthermore, the yellow emission from GaN/AlGaN multi-quantum well (MQW) grown by conventional-simultaneous source-feeding epitaxy (SSFE) on the ASFE AlGaN clad layer was also reduced. This indicates that the improvement of the crystal quality of the AlGaN clad layer influences the crystal quality of the MQW grown on it. [DOI: 10.1143/JJAP.46.5711]

KEYWORDS: AlGaN, point defect, green emission, alternate-source-feeding epitaxy, XRC

1. Introduction

After the commercialization of blue and green light emitting diodes (LEDs) and violet laser diodes (LDs) with an InGaN active layer, interest in nitride research has shifted to the growth of high-quality AlGaN layers for ultraviolet (UV)-LEDs and UV-LDs. The development of such UV devices, however, has not been achieved as quickly as expected. Although the shortest wavelengths reported so far for AlGaN-based LEDs and LDs are 250 and 343 nm, respectively,[1,2] their efficiency and output power are not yet sufficiently high. The main difficulty is in the growth of crack-free, thick and high-crystal-quality AlGaN layers. Since the optimum growth temperature of AlGaN is higher than that of GaN, and a higher crystal quality is needed for UV-LED and LD materials, various growth techniques have been investigated.[3] Our group has proposed an alternate-source-feeding epitaxy (ASFE)[4] for low-pressure metal organic vapor phase epitaxy (LP-MOVPE), and by combining with the (AlN/GaN) multi-buffer-layer structure (MBLS),[5,6] we have achieved lasing at the shortest wavelength reported so far (241 nm), though it was under optical excitation.[7]

As for ASFE, similar growth methods have been reported from several groups. Khan's group reported that crystal quality was improved markedly by migration-enhanced (ME)-MOVPE and obtained UV-LEDs with good performance.[8] Historically, however, they changed its name as switched atomic layer epitaxy (S-ALE),[9] pulsed ALE,[10] and ME-MOCVD,[11] and their growth sequence and applied layers were also slightly changed. Other groups call it flow-modulation epitaxy (FME)[12] and alternating pulsative supply (APS).[13] This fact indicates that it is not well understood what is essential for the growth and what kind of crystal quality is improved by ASFE in our term. It is certainly not atomic layer epitaxy because several to 10 mono-layers are grown in one cycle in our case, and there is no evidence of enhanced migration, therefore, we call it alternate-source-feeding epitaxy (ASFE) for the present.

The purpose of this work is to make clear what is improved by alternate-source-feeding MOVPE and how it affects the UV-LED performance.

It was indicated that dislocation density was not reduced, whereas point defect density was reduced by ASFE, and that the reduced point defects in the n-AlGaN clad layer affect the conventional simultaneous source-feeding epitaxy (SSFE) grown, multi-quantum-well (MQW) active layer to improve LED performance.

2. Experimental Procedure

The growth of an n-$Al_{0.15}Ga_{0.85}N$ clad layer and a GaN/$Al_{0.1}Ga_{0.9}N$ MQW structure on it was carried out by LP-MOVPE. The sample structures and growth sequence are schematically shown in Fig. 1. Firstly, an AlN/GaN MBLS was grown on a 6H–SiC substrate.[5,6] Then, a 500-nm-thick n-$Al_{0.15}Ga_{0.85}N$ clad layer was grown by ASFE: 2 s trimethylgallium (TMG) and trimethylaluminum (TMA) supply and 2 s NH_3 supply without a sweep-out interval. An n-$Al_{0.15}Ga_{0.85}N$ clad layer was also grown by conventional SSFE for comparison. A three-layer quantum-well (QW) structure consisting of 3-nm-thick GaN wells and 7-nm-thick $Al_{0.1}Ga_{0.9}N$ barriers was grown by conventional SSFE on both the ASFE- and SSFE-grown n-$Al_{0.15}Ga_{0.85}N$ clad layers. A 20-nm-thick $Al_{0.25}Ga_{0.75}N$ blocking layer was also grown on top of the MQW by SSFE.

The crystal quality of the n-$Al_{0.15}Ga_{0.85}N$ clad layer was evaluated using the full width at half maximum (FWHM) of the $(10\bar{1}5)$ plane X-ray rocking curve (XRC), after finding the $(10\bar{1}5)$ plane diffraction peak by reciprocal lattice mapping. The twist is thought to reflect edge and mixed dislocations. To confirm the effect of ASFE on the dislocation directly, transmission electron microscopy (TEM) was performed on another sample grown in another growth system; ASFE grown $Al_{0.7}Ga_{0.3}N$ on a conventional SSFE grown AlN template. Photoluminescence (PL) measurements to see yellow or green emission were performed by changing the excitation power of an ArF exima laser, because the relative yellow or green emission intensity against the edge emission changes with excitation intensity.

3. Results and Discussion

The $(10\bar{1}5)$ plane XRCs of both the ASFE- and SSFE-grown n-$Al_{0.15}Ga_{0.85}N$ clad layers are shown in Fig. 2(a) and a comparison of the resultant FWHM values of both the symmetric (0002) plane and the asymmetric $(10\bar{1}5)$ plane XRCs are shown in Fig. 2(b). The $(10\bar{1}5)$ plane XRCs, and

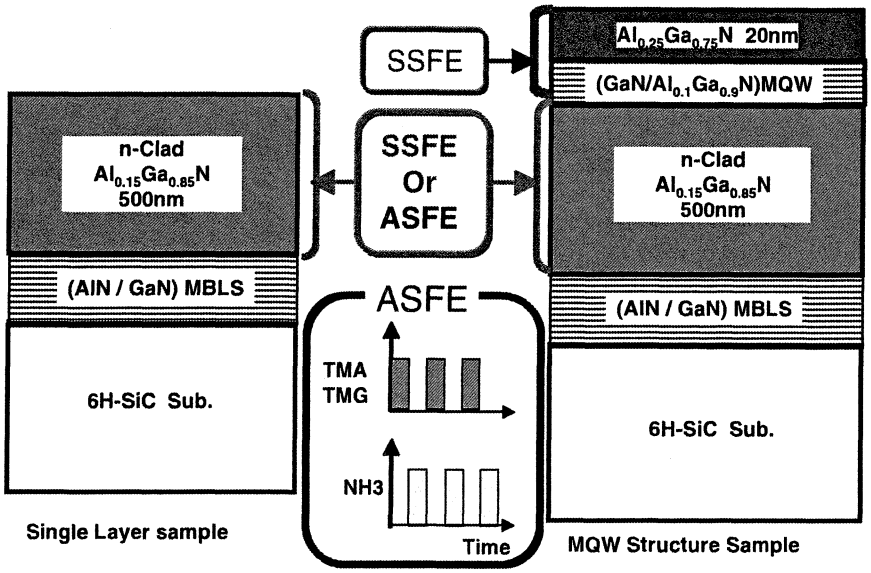

Fig. 1. Structure and growth sequence of measured samples.

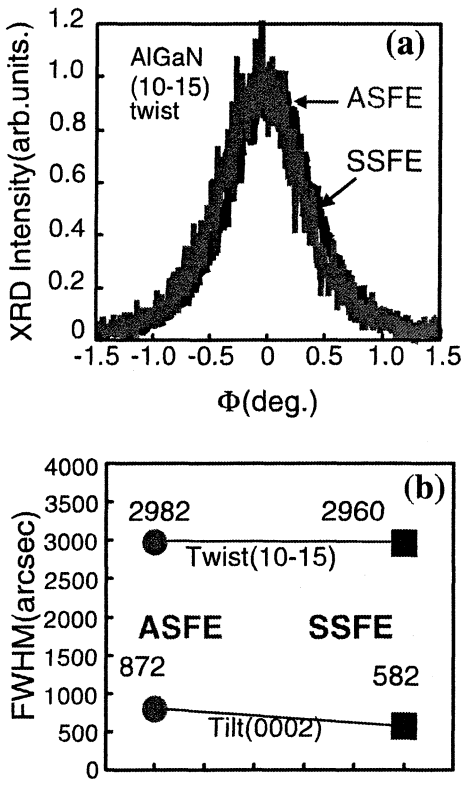

Fig. 2. $(10\bar{1}5)$ plane phi scan rocking curves of both ASFE- and SSFE-grown n-$Al_{0.15}Ga_{0.85}N$ clad layers (a) and comparison of resulting FWHM values of both symmetric (0002) plane omega scan and asymmetric $(10\bar{1}5)$ plane phi scan rocking curves (b).

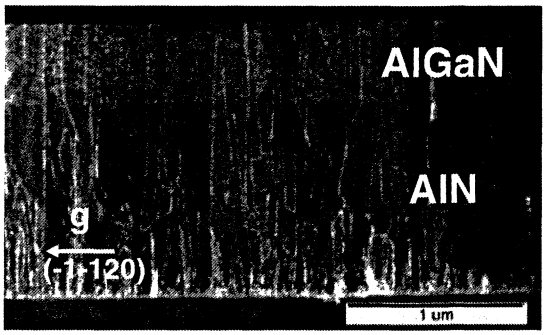

Fig. 3. Dark-field TEM image of $g = \bar{1}\bar{1}20$ diffraction spot. The $Al_{0.7}Ga_{0.3}N$ layer was grown by ASFE on a conventional SSFE-grown AlN template continuously in a different growth apparatus from the one used for the PL measurement samples. White lines include both edge and mixed dislocations.

thus also the FWHMs, are almost the same for the both samples grown by ASFE and SSFE as can be seen in Fig. 2. As it is well known, FWHM of XRC reflects dislocation density well;[14] the FWHM of so-called phi scan XRC of asymmetrical planes such as $(10\bar{1}5)$ generally indicates the magnitude of the twisting of the crystal, reflecting the (edge + mixed) dislocation density of the grown layer. The omega scan XRC of symmetrical plane such as (0002) is for tilting, reflecting (screw + mixed) dislocation density of the sample. Although the FWHM of the XRCs shown in Fig. 2 is relatively large (about 3000 arcsec for twisting), it can be seen that there is no difference between the ASFE- and SSFE-grown $Al_{0.15}Ga_{0.85}N$ clad layers. As for the omega scan XRC (screw and mixed dislocations), the FWHM of the ASFE-grown $Al_{0.15}Ga_{0.85}N$ clad layer (about 850 arcsec) was slightly larger than that of SSFE-grown $Al_{0.15}Ga_{0.85}N$ clad layer (about 600 arcsec). These XRC results indicate that the dislocation densities are almost the same for both AlGaN layers, i.e., that ASFE does not reduce dislocation density.

This fact was confirmed more directly by TEM observation on another structure and a better quality sample grown by another growth apparatus with which deep UV optically pumped lasers were successfully fabricated. An $Al_{0.7}Ga_{0.3}N$ clad layer was grown by ASFE onto a conventional SSFE-grown AlN template. A dark field TEM image of a [$g = (\bar{1}\bar{1}20)$] diffraction spot is shown in Fig. 3. The white lines show edge and mixed dislocations. All dislocations in the

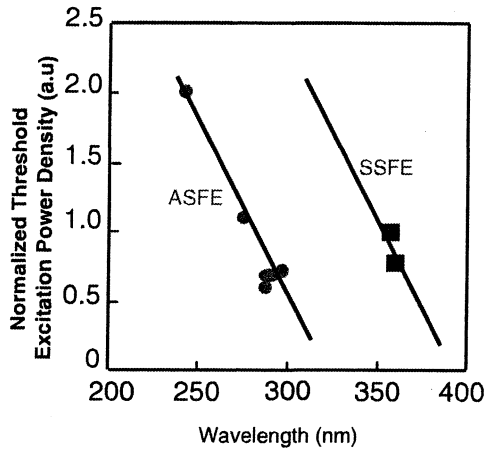

Fig. 4. Comparison of threshold pumping power densities of optically pumped UV-LDs grown by ASFE and SSFE.

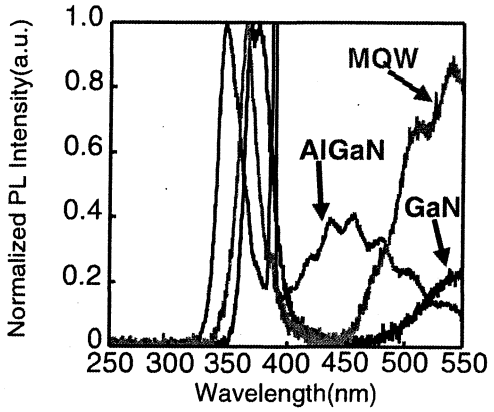

Fig. 5. PL spectra of GaN, AlGaN, and GaN/AlGaN MQWs. Yellow emission (about 550 nm) is observed for the GaN and GaN/AlGaN MQWs. whereas blue emission (about 450 nm) is observed for the AlGaN sample. The 386 nm peak is a stray light from the ArF exima laser, and it was eliminated with a filter for the GaN and GaN/AlGaN MQW samples.

SSFE-grown AlN template go through into the ASFE-grown $Al_{0.7}Ga_{0.3}N$ clad layer, indicating that ASFE cannot stop or reduce any dislocations.

On the other hand, it is fact that device performance is really improved by ASFE, as we reported previously.[15] Figure 4 shows a comparison of the threshold pumping power densities of optically pumped UV-LDs grown by ASFE and SSFE. The threshold pumping power density increases with a decrease in the lasing wavelength, however, for the same threshold pumping power density, the available lasing wavelength is much shorter for the sample grown by ASFE (denoted as flow-rate modulation epitaxy in ref. 15) than for the sample grown by conventional SSFE.

To find the difference in crystal quality between layers grown by ASFE and those grown by SSFE, PL measurements were performed, by changing the excitation power. Generally, GaN and AlGaN show yellow or green emission in addition to the band edge emission as shown in Fig. 5, namely, yellow emission (about 550 nm) for GaN and blue-green emission (450–530 nm) for AlGaN. (The 386 nm peak is a stray light of the ArF exima laser. It was not eliminated with a filter for the AlGaN samples.) The MQW sample gave

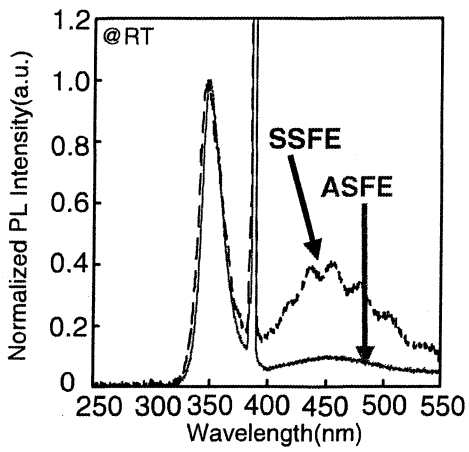

Fig. 6. Comparison of PL spectra of n-$Al_{0.15}Ga_{0.85}N$ clad layers grown by ASFE and SSFE. The 386 nm peak is a stray light from the ArF exima laser.

a yellow emission as shown in Fig. 5, indicating that the longer wavelength emission of this sample is from the GaN quantum well rather than from the AlGaN clad layer.

A comparison of the PL spectra between the n-$Al_{0.15}Ga_{0.85}N$ clad layers grown by ASFE and those grown by conventional SSFE MOVPE is shown in Fig. 6. It can be seen that the blue or green emission normalized by the band edge emission is greatly reduced by ASFE MOVPE. As is well known, the relative PL intensity of the yellow or green emission to the band edge emission depends on excitation intensity; therefore, excitation dependence of the relative PL intensity of the blue or green emission was compared between both samples. The curves were parallel and the blue or green emission from the ASFE-grown $Al_{0.15}Ga_{0.85}N$ was less than half that from the conventional SSFE-grown sample, independent of the excitation intensity.

There have been many reports on the yellow, green or blue emission from GaN or AlGaN, and there is still controversy over the origin of these longer wavelength emissions than the band edge emission.[16,17] A common idea for these emissions, however, is that these emissions are related to point defects such as Ga vacancy and Al vacancy, although one report says it is related to dislocations.[18] Therefore, it is reasonable to think that an epitaxial layer with a weak yellow or green emission will have fewer point defects than a sample with a strong yellow or green emission.

It was also found that the SSFE-grown MQW grown on the ASFE-grown $Al_{0.15}Ga_{0.85}N$ clad layer gave a weaker yellow emission than that grown on the conventional SSFE-grown $Al_{0.15}Ga_{0.85}N$ clad layer. The results are shown in Fig. 7. The normalized intensity of the yellow emission (about 550 nm) of the ASFE sample is much lower than that of the SSFE sample. One might suspect that this longer wavelength emission is from the $Al_{0.15}Ga_{0.85}N$ clad layers. If it were from the $Al_{0.15}Ga_{0.85}N$ clad layers, the wavelength should have been about 450 nm; however, it was about 550 nm. The longer wavelength emission from these samples is, therefore, certainly from the GaN/$Al_{0.1}Ga_{0.9}N$ MQW, not from the $Al_{0.15}Ga_{0.85}N$ clad layers. The difference between these two samples is only the method used to grow the

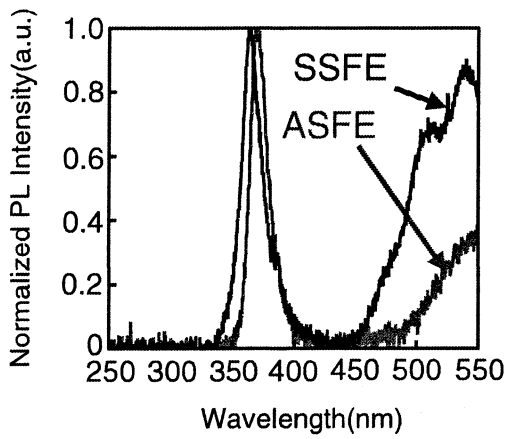

Fig. 7. PL spectra of SSFE-grown MQWs grown on both ASFE- and SSFE-grown $Al_{0.15}Ga_{0.85}N$ clad layers. The PL is from the GaN/$Al_{0.1}$-$Ga_{0.9}N$ MQWs, not from the $Al_{0.15}Ga_{0.85}N$ clad layer.

$Al_{0.15}Ga_{0.85}N$ clad layers, by ASFE or SSFE. The MQW active layers were grown in the same way by conventional SSFE for both samples. Therefore, it should be concluded that the MQW grown on the $Al_{0.15}Ga_{0.85}N$ clad layer with a lower point defect density also had a fewer point defects. Absolute intensity of the band edge emission was much stronger for the ASFE sample than for the SSFE sample, probably because there were fewer nonradiative point defects in the ASFE sample. The fewer nonradiative point defects in the MQW is probably the reason why we could reduce the threshold excitation density of the optically pumped deep UV lasers by applying the ASFE to grow the clad layer,[10] and why Kahn's group obtained good performance for UV LEDs fabricated by ME-MOVPE.[6]

The reason why point defects are reduced by ASFE is considered to be as follows: ASFE is not actually an atomic layer epitaxy because 5–7 monolayers are grown by one cycle of ASFE. However, the Ga and Al deposited during the III column source supply period must be completely nitrified during the NH_3 supply as in the case of atomic layer epitaxy. This must be the reason why point defects, generally assumed to be a Ga or Al vacancy, are reduced by ASFE. It is known that vacancies can be moved easily via dislocations, therefore, it is speculated that point defects in the SSFE-grown MQW diffused into the ASFE-grown n-AlGaN clad layer underneath during the growth, and as a result, the yellow emission from the SSFE-grown MQW was also reduced.

4. Conclusions

It was found that the blue or green emission of PL from the AlGaN clad layer grown by ASFE MOVPE was much weaker than that from the AlGaN clad layer grown by conventional SSFE. Since the FWHMs of both the (0002) and ($10\bar{1}5$) plane XRCs were comparable, and it is well recognized that yellow, green, and blue emissions from nitrides are related to some point defects such as Ga vacancy or Al vacancy, it was concluded that the point defect density was reduced by ASFE MOVPE. It was also found that the MQW grown on an AlGaN clad layer with a lower point defect density also has a lower point defect density than the MQW grown on an AlGaN clad layer with a higher point defect density.

Acknowledgements

The authors express their thanks to Mr. Y. Ohtaki, who graduated from our laboratory, for the growth of some of the samples. They are also very grateful to Professor Emeritus Y. Suematsu and Professor Emeritus K. Iga of Tokyo Institute of Technology for their encouragement regarding our work. This work was partially supported by a Grant-in-Aid for Scientific Research (S) (No. 17106005) from the Japan Sciety for the Promotion of Science and a Grant-in-Aid for Scientific Research in Priority Areas "Optoelectronics Frontier by Nitride Semiconductor" (No. 18069009) from the Ministry of Education, Culture, Sports, Science and Technology, Japan.

1) V. Adivarahan, W. H. Sun, A. Chitnis, M. Shatalov, S. Wu, H. P. Maruska, and M. Asif Khan: Appl. Phys. Lett. **85** (2004) 2175.
2) K. Iida, T. Kawashima, A. Miyazaki, H. Kasugai, S. Mishima, A. Honshio, Y. Miyake, M. Iwaya, S. Kamiyama, H. Amano, and I. Akasaki: Jpn. J. Appl. Phys. **43** (2004) L499.
3) H. Amano, S. Takanami, M. Iwaya, S. Kamiyama, and I. Akasaki: Phys. Status Solidi A **195** (2003) 491.
4) M. Kurimoto, M. Shibata, J. Yamamoto, M. Tsubamoto, T. Honda, and H. Kawanishi: J. Cryst. Growth **189–190** (1998) 189.
5) M. Kurimoto, T. Nakada, Y. Ishihara, M. Shibata, T. Takano, J. Yamamoto, T. Honda, and H. Kawanishi: Phys. Status Solidi A **176** (1999) 665.
6) M. Kurimoto, T. Nakada, Y. Ishihara, T. Takano, M. Shibata, T. Honda, and H. Kawanishi: Jpn. J. Appl. Phys. **38** (1999) L551.
7) T. Takano, Y. Narita, A. Horiuchi, and H. Kawanishi: Appl. Phys. Lett. **84** (2004) 3567.
8) J. P. Zhang, X. Hu, Yu. Bilenko, J. Deng, A. Lunev, M. S. Shur, R. Gaska, M. Shatalov, J. W. Yang, and M. A. Khan: Appl. Phys. Lett. **85** (2004) 5532.
9) M. Asif Khan, J. N. Kuznia, D. T. Olson, T. George, and W. T. Pike: Appl. Phys. Lett. **63** (1993) 3470.
10) J. P. Zhang, M. Asif Khan, W. H. Sun, H. M. Wang, C. Q. Chen, Q. Fareed, E. Kuokstis, and J. W. Yang: Appl. Phys. Lett. **81** (2002) 4392.
11) V. Adivarahan, S. Wu, J. P. Zhang, A. Chitnis, M. Shatalov, V. Mandavilli, R. Gaska, and M. Asif Khan: Appl. Phys. Lett. **84** (2004) 4762.
12) M. Hiroki and N. Kobayashi: Jpn. J. Appl. Phys. **42** (2003) L2305.
13) J. S. Hwang, S. Tanaka, S. Iwai, Y. Aoyagi, and S. Seong: J. Cryst. Growth **200** (1999) 63.
14) P. Gay, P. B. Hirsch, and A. Kelly: Acta Metall. **1** (1953) 315.
15) T. Takano, Y. Ohtaki, Y. Narita, and H. Kawanishi: Jpn. J. Appl. Phys. **43** (2004) L1258.
16) M. A. Reshchikov, H. Morkoc, S. S. Park, and K. Y. Lee: Appl. Phys. Lett. **78** (2001) 3041.
17) R. Armitage, W. Hong, Q. Yang, H. Feick, J. Gebauer, E. R. Weber, S. Hautakangas, and S. Saarinen: Appl. Phys. Lett. **82** (2003) 3457.
18) D. G. Zhao, D. S. Jiang, H. Yang, J. J. Zhu, Z. S. Liu, S. M. Zhang, J. W. Liang, X. Li, and H. M. Gong: Appl. Phys. Lett. **88** (2006) 241917.

Anisotropic polarization characteristics of lasing and spontaneous surface and edge emissions from deep-ultraviolet ($\lambda \approx 240$ nm) AlGaN multiple-quantum-well lasers

Hideo Kawanishi,[a] Masanori Senuma, and Takeaki Nukui
Department of Electronic Engineering, Kohgakuin University, Nakano-machi 2665-1, Hachioji-shi, Tokyo 192-0015, Japan

(Received 24 January 2006; accepted 8 June 2006; published online 27 July 2006)

The authors report on their experimental discovery of a transverse-magnetic-field (TM)-mode polarization of lasing and spontaneous edge emissions (anisotropic polarization emissions) above and below the lasing threshold from the AlGaN multiple-quantum-well (MQW) laser at 240.8 nm. The deep ultraviolet MQW emitted very weak or no surface emission (anisotropic polarization emission) below the threshold. On the other hand, the AlGaN multiple-quantum-well laser at 355.1 nm operated in the transverse-electric-field (TE) mode above the threshold, and homogeneous high-intensity spontaneous surface emission and both TE- and TM-mode edge emissions (isotropic emissions) were observed below the threshold. © *2006 American Institute of Physics.*
[DOI: 10.1063/1.2236792]

Wurtzite-type BN, AlN, GaN, and related semiconductors are attractive materials for the production of laser diodes and light-emitting diodes with emission in the spectral range from ultraviolet (UV) to deep UV. The band structures and optical characteristics of GaN and AlN have been theoretically analyzed.[1–3] Unique optical properties of AlGaN have been pointed out experimentally in a few studies.[4,5] The theoretical laser mode gain of AlGaN multiple quantum wells (MQWs) has also been investigated, which led to the conclusion that TE-mode gain is dominant in the spectral range from about 270 to 340 nm.[6]

The room temperature lasing of an AlGaN MQW laser was demonstrated in the spectral region from about 240 to 355 nm under optical pumping.[7,8] In addition, we have recently achieved lasing at the shortest recorded wavelength of 228.9 nm at a lower temperature than 170 K.[9] To produce such lasers, high-quality AlGaN MQW structures, and cladding and guide layers were grown on 6*H* and 4*H*-SiC substrates using an epitaxial growth technique called alternate source-feeding epitaxy or flow-rate modulation epitaxy.[8,10] The shortest lasing wavelengths of AlGaN and AlGaInN lasers had been 350 nm under current injection[11] and 258 and 305 nm under optical pumping, respectively,[12,13] before our report.

In this study, the optical polarizations of lasing and spontaneous surface and edge emissions from AlGaN MQW grown on a SiC substrate were experimentally investigated in the spectral region from about 240 to 360 nm.

An AlGaN MQW laser was built on a freestanding AlN template grown on a 6*H* or 4*H*-SiC substrate by adopting an AlN/GaN multibuffer layer between the AlN template and the substrate. The purpose of this AlN/GaN multibuffer layer was to control residual strain and decrease threading dislocation density (TDD) in AlN (TDD $\approx 10^8$–10^9 cm^{-2} by transmission electron microscopy) and $Al_xGa_{1-x}N$ cladding, $Al_yGa_{1-y}N$ guide (TDD $\approx 10^7$–10^8 cm^{-2}), and $Al_zGa_{1-z}N$ MQW (TDD $\approx 5\times10^6$–5×10^7 cm^{-2}) layers.[14,15]

The AlN template used was 1.5 μm thick. The bottom $Al_yGa_{1-y}N$ guide (0.1 μm thick and $y=0.76$ for 240.8 nm lasing) and cladding $Al_xGa_{1-x}N$ (0.6 μm thick and $x=0.84$ for 240.8 nm lasing) layers were grown on the AlN template but not on top of the AlGaN MQW active region to achieve an effective optical pumping of the active region using the 193 nm line of the ArF excimer laser. The quantum well and barrier thicknesses were 10 and 15 nm, and the Al compositions were $z=0.67$ and $z=0.76$ for 240.8 nm lasing, respectively.

The optical measurement system used for edge and surface emissions is schematically illustrated in Fig. 1. The Glan-Taylor deep-UV polarizer or conventional sheet-type polarizer was used for the spectral region from 190 to 400 nm or from 320 nm to the visible wavelength, respectively. This measurement system was carefully cali-

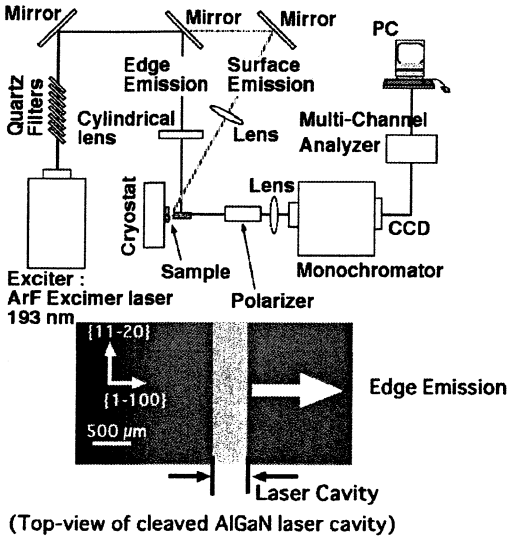

FIG. 1. (Color online) Schematic diagram of UV and deep-UV optical measurement systems. The inset indicated the top view of cleaved AlGaN laser with cavity (≈500 μm long).

[a]Electronic mail: kawanisi@cc.kogakuin.ac.jp

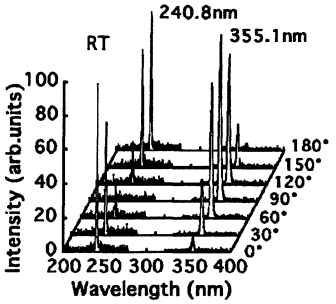

FIG. 2. Polarization behaviors of lasing light of AlGaN MQW lasers operating at 240.8 and 355.1 nm. The polarizer angles of 0° and 180° indicate TM-mode polarization ($E \| c$ axis), whereas that of 90° indicates TE-mode polarization ($E \perp c$ axis).

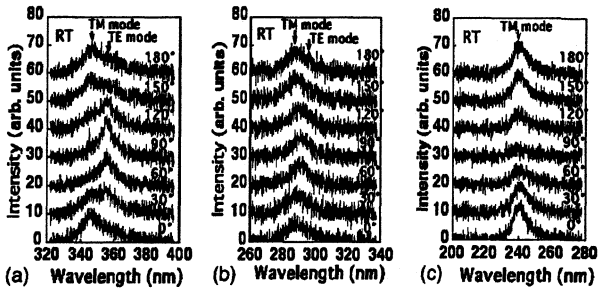

FIG. 3. Polarization behaviors of spontaneous edge emission of AlGaN MQW lasers below threshold at room temperature. (a) TE- and TM-mode emissions, (b) TM- and weak TE-mode emissions, and (c) mostly TM-mode emission for AlGaN MQW lasers at 355.1, 289.8, and 240.8 nm, respectively.

brated using laser radiation (wavelength of 350–360 nm) from an UV AlGaN MQW laser and also a visible light source. By this measurement system, optical polarization behaviors of the edge and surface emissions from the same AlGaN MQW laser samples could be detected both above and below the threshold.

The experimental results for the optical polarization behavior of the lasing light (edge emissions) are summarized in Fig. 2 for the AlGaN MQW lasers operating at 240.8 and 355.1 nm. Lasing and spontaneous edge emissions were detected through cleaved facets ($\{1,-1,0,0\}$ m plane; see top-view inset of Fig. 1), whereas spontaneous surface emission was detected parallel to the c axis through the c-plane surface.

The lasing output of the AlGaN MQW laser operating at 355.1 nm was strongly polarized into the transverse-electric-field mode (TE mode), as shown in Fig. 2, whereas the lasing radiation at 240.8 nm was strongly polarized into the transverse-magnetic-field mode (TM mode). A laser structure with a Fabry-Pérot resonator has weak lasing-mode selectivity in the TE mode, because of the higher reflectivity of cleaved facets in the TE mode than in the TM mode.[16] As a result, conventional semiconductor lasers made of an isotropically emitting material usually oscillate in the TE mode.

On the other hand, TM-mode lasing at 240.8 nm was a result of anisotropic emission due to the anisotropic dipole moment in the AlGaN MQW active layer having high Al content. This indicates that the laser gain was weak or zero for TE-mode lasing. However, it was expected that there was sufficient lasing gain for TM-mode lasing in AlGaN MQW lasers having a high Al content. As a result, TM mode was the main lasing mode in the AlGaN MQW laser at 240.8 nm. In this case, the dipole moment was formed only along the c axis, so that TE-mode surface emission and optical gain are not expected for AlGaN MQW having a high Al content.

To further clarify lasing polarization characteristics, the polarization behaviors of spontaneous edge emission from AlGaN MQW lasers below the threshold were carefully investigated through cleaved facets at room temperature for 355.1, 289.8, and 240.8 nm lasing samples and are summarized in Figs. 3(a), 3(b), and 3(c), respectively.

Spontaneous edge emission was weakly polarized in the TM mode for the shorter emission at ≈347 nm, but strongly polarized in the TE mode for the longer emission at ≈355 nm, as shown in Fig. 3(a), where the energy difference between the TE and TM modes was ≈80 meV. Lasing occurred in the TE mode at 355.1 nm when pumping level increased above the threshold, as shown in Fig. 2. These experimental results were the same as those obtained at 20 K.

TE-mode edge emission approached TM-mode emission at ≈290 nm [as shown in Fig. 3(b)], where the energy difference between the TE and TM modes was as small as 21 meV. In addition, lasing occurred at 289.8 nm in the TE mode of this sample. It is probable that this sample was nearly an intermediate AlGaN MQW laser sample between 355.1 and 240.8 nm samples (but lasing at a slightly longer wavelength than that of spontaneous TM-mode emission). This experimental result suggests that the lasing polarization changed from the TM mode to the TE mode at the intermediate AlGaN MQW sample. The intermediate lasing wavelength was estimated to be approximately 280–290 nm for the AlGaN MQW laser; the estimated Al contents x of $Al_xGa_{1-x}N$ were ≈0.41–0.36.

Spontaneous edge emission was strongly polarized in the TM mode for the shortest emission at ≈240 nm below the threshold, as shown in Fig. 3(c). Lasing occurred in the TM mode at 240.8 nm, as pumping level increased above the threshold.

We also attempted to detect spontaneous surface emission through the c plane, along the c axis (through the surface of a wafer, parallel to the c axis), for the two typical AlGaN MQW lasers at 240.8 nm (sample A) and 355.1 nm (sample B) below the threshold, as shown in Fig. 4. Very weak or no spontaneous surface emission was detected below the threshold for sample A.

The optical polarization behavior of spontaneous surface emission at ≈355 nm was also analyzed using a deep-UV polarizer. Strong and homogeneous spontaneous surface emission (no optical polarization) from sample B was ob-

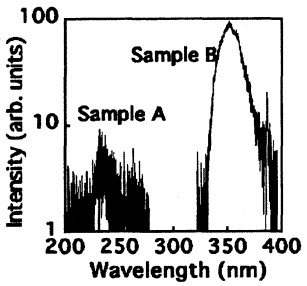

FIG. 4. Spontaneous surface emission from two different AlGaN MQW lasers at 240.8 nm (sample A) and 355.1 nm (sample B) below threshold.

served. This means that the homogeneous and isotropic dipole moment, which is associated with surface and edge emissions, was formed in the wurtzite AlGaN MQW with a low Al content.

The band structures of GaN and AlN have been discussed in several papers.[1–4] The valence band structure of wurtzite GaN is split into three bands named *A*, *B*, and *C* bands, in order from the conduction band side. The *A* and *B* bands are active only in the TE mode. This means that dipole moments associated with the *C* bands are polarized in the direction parallel to the *c* axis (perpendicular to the *c* plane).

Our experimental results partly differ from previous results.[1,3–5] For example, the spontaneous edge emission intensities in the TE and TM modes at ≈355 nm were nearly the same below the threshold, as shown in Fig. 3(a). Thus, lasing occurs in the TE mode above the threshold because the TE-mode reflectivity of cleaved facets is higher than the TM-mode reflectivity. However, lasing occurred in the TM mode for the AlGaN MQW laser at 240.8 nm because the *C* band is active only in the TM mode,[4] even if the TE-mode reflectivity were higher than the TM-mode reflectivity.

One reason for some of the differences between the experimental results and the theoretical results might be the residual strain in the AlGaN MQW system. The residual strain caused by lattice mismatch can be eliminated using the BAlGaN quaternary lattice-matching system.[17–19] However, further investigation of the residual strain effect on the polarization behavior of the lasing light and the spontaneous emission is necessary for the AlGaN MQW lasers.

In summary, the polarization behaviors of lasing light and spontaneous edge and surface emissions were experimentally investigated for an AlGaN MQW laser. A TM-mode polarization of lasing and spontaneous emissions from a deep-UV AlGaN MQW laser at 240.8 nm was observed under optical pumping. On the other hand, TE-mode polarized lasing was detected for the UV AlGaN MQW at 355.1 nm above the threshold, and homogeneous and high-intensity spontaneous surface and edge emissions in the TE and TM modes (isotropic emission) were observed below the threshold. These experimental results will be useful for the design of high-performance UV to deep-UV AlGaN MQW lasers.

The authors are very grateful to Professor Emeritus Y. Suematsu of the Tokyo Institute of Technology for encouragement, Professor Emeritus K. Iga of the Tokyo Institute of Technology for fruitful discussion, and Professor F. Hasegawa of Kohgakuin University (who is also a professor emeritus of Tsukuba University) for his helpful suggestion. This work is supported by a Grant-in-Aid for Scientific Research [Grant-in-Aid for Scientific Research (S) No. 17106005] from the Japan Society for the Promotion of Science.

[1] R. Dingle, D. D. Sell, S. E. Stokowski, and M. Ilegems, Phys. Rev. B **4**, 1211 (1971).
[2] M. Suzuki, T. Uenoyama, and A. Yanase, Phys. Rev. B **52**, 8132 (1995).
[3] J. Li, K. B. Nam, M. L. Nakarmi, J. Y. Lin, H. X. Jiang, P. Carrier, and S. H. Wei, Appl. Phys. Lett. **83**, 5163 (2003).
[4] K. B. Nam, J. Li, M. L. Nakarmi, J. Y. Lin, and H. X. Jiang, Appl. Phys. Lett. **84**, 5264 (2004).
[5] J. Shakya, K. Knabe, K. H. Kim, J. Li, J. Y. Lin, and H. X. Jiang, Appl. Phys. Lett. **86**, 091107 (2005).
[6] W. W. Chow and M. Kneissl, J. Appl. Phys. **98**, 114502 (2005).
[7] T. Takano, Y. Narita, A. Horiuchi, and H. Kawanishi, Appl. Phys. Lett. **84**, 3567 (2004).
[8] T. Takano, Y. Ohtaki, Y. Narita, and H. Kawanishi, Jpn. J. Appl. Phys., Part 2 **43**, L1258 (2004).
[9] H. Kawanishi, M. Senuma, T. Nukui, Y. Ohtaki, and Y. Yamamoto (unpublished).
[10] M. Hiroki and N. Kobayashi, Jpn. J. Appl. Phys., Part 1 **42**, 2305 (2003).
[11] K. Iida, T. Kawashima, A. Miyazaki, H. Kasugai, S. Mishima, A. Hoshino, Y. Miyake, M. Iwata, S. Kamiyama, H. Amano, and I. Akasaki, Jpn. J. Appl. Phys., Part 2 **43**, L499 (2004).
[12] S. Bidnyk, J. B. Lam, B. D. Little, Y. H. Kwon, J. J. Song, G. E. Bulman, H. S. Kong, and T. J. Schmidt, Appl. Phys. Lett. **75**, 3905 (1999).
[13] R. Gaska, C. Chen, J. Yang, E. Kupkstis, A. Khan, G. Tamulaitis, I. Yilmaz, M. S. Shur, J. J. Rojo, and L. J. Schowalter, Appl. Phys. Lett. **81**, 4658 (2002).
[14] M. Kurimoto, T. Nakada, Y. Ishihara, M. Shibata, and H. Kawanishi, Jpn. J. Appl. Phys., Part 2 **38**, L551 (1999).
[15] Y. Ishihara, J. Yamamoto, M. Kurimoto, T. Takano, T. Honda, and H. Kawanishi, Jpn. J. Appl. Phys., Part 2 **38**, L1296 (1999).
[16] T. Ikegami, IEEE J. Quantum Electron. **QE-8**, 470 (1972).
[17] M. Haruyama, T. Shirai, H. Kawanishi, and Y. Suematsu, *Proceedings of the International Symposium on Blue Laser and Light Emitting Diodes* (Ohmsha Ltd., Tokyo, Japan, 1996), p. 106.
[18] T. Takano, M. Kurimoto, J. Yamamoto, Y. Ishihara, M. Horie, and H. Kawanishi, *Proceedings of the International Workshop on Nitride Semiconductors* [IPAP Conf. Ser. **1**, 147 (2000)].
[19] T. Takano, M. Kurimoto, J. Yamamoto, and H. Kawanishi, J. Cryst. Growth **237–239**, 972 (2002).

Extremely weak surface emission from (0001) *c*-plane AlGaN multiple quantum well structure in deep-ultraviolet spectral region

Hideo Kawanishi,[a] Masanori Senuma, Mao Yamamoto, Eiichiro Niikura, and Takeaki Nukui
Department of Electronic Engineering, Kohgakuin University, Nakano-machi 2665-1, Hachioji-shi, Tokyo 192-0015, Japan

(Received 9 February 2006; accepted 3 July 2006; published online 24 August 2006)

We studied the anisotropic optical properties of *c*-plane $Al_xGa_{1-x}N$ multiple quantum wells and *m*-plane $Al_xGa_{1-x}N$ single layer grown on a SiC substrate. Very weak surface emission was detected from *c*-plane samples with $x=0.66-0.76$ (emission wavelength of 228–240 nm), although strong surface emission was detected from *c*-plane samples with $x=0-0.41$ (280–365 nm) and *m*-plane samples with $x=0-0.76$ (240–365 nm). These results indicate that crystal-field splitoff hole valence band plays an important role in $(E\|c)$ polarization and isotropic emissions from $Al_xGa_{1-x}N$ with $x\geqq 0.5$. © *2006 American Institute of Physics*. [DOI: 10.1063/1.2338543]

AlGaN and BAlGaN are becoming promising semiconductors for developing deep-ultraviolet (UV) light-emitting semiconductor devices. The theoretical shortest wavelengths of photoluminescence, light-emitting diodes (LEDs) and laser diodes (LDs) of AlGaN and BAlGaN are 200, and 210 nm, respectively. On the other hand, the shortest emission wavelengths that have been experimentally demonstrated are 250 nm for LED,[1] 305.9 nm for UV laser under current injection,[2] and 241.5 nm (at room temperature) and 228.9 nm (at low temperature) for deep-UV laser under optical pumping,[3,4] respectively. The quantum efficiency of an AlGaN LED operating at wavelengths shorter than about 300 nm becomes low, and the highest quantum efficiencies were 0.01% and 1.5% at emission wavelengths of 250 and 280 nm, respectively.[1,5] However, the reason for this low quantum efficiency of AlGaN LEDs in the deep-UV spectral region is still not understood well.

Recently, the high quality AlGaN and AlN epitaxial layers have been grown by improved growth techniques, such as migration-enhanced epitaxy,[1] alternate source-feeding epitaxy,[4,6] and high-temperature metal-organic vapor phase epitaxy.[7] The smallest full-width at half maximum for the x-ray rocking curve [(0002) plane x-ray rocking curve for ω scan] was as small as ≈50 arcsec for the AlN.[8] Experimental anisotropic optical polarization for the luminescence of the *m*- and *c*-plane InGaN, GaN, AlGaN, and AlN have been reported.[9–18] Recently, anisotropic optical polarization has also been discovered in the *c*-plane AlGaN multiple quantum well (MQW) laser.[19]

In this letter, we report extremely weak surface emission and anisotropic emission from a (0001) *c*-plane $Al_xGa_{1-x}N$ ($x=0.66-0.76$) MQW in the spectral region from 228 to 240 nm under optical pumping, although a definite intensity of edge emission was still observed from the (1–100) cleaved *m*-plane facet. In addition, the optical characteristics of AlGaN single layer with *m*-plane surface were investigated under optical pumping to determine the origins of the extremely weak surface emission and the anisotropic optical properties from the *c*-plane AlGaN MQW structure.

The sample structure was the same as that of AlGaN MQW lasers lasing in the 240–355 nm spectral region.[3,4] A detailed description of the growth conditions and layer structure of the AlGaN MQW laser can be found in Refs. 3 and 6.

The AlGaN MQW structure was optically pumped through the *c*-plane surface. Figure 1 shows the relationship between the optical pumping power density and light output of the deep-UV AlGaN MQW laser at room temperature. Light output through the cleaved *m*-plane facet was considerably increased above the lasing threshold. The threshold pumping power density was ≈2.0 mJ/cm^2, and lasing oscillation was obtained at 241.5 nm for this sample. Typical light output spectra through the cleaved facet, above and below the threshold, are shown in the inset.

Figure 2 shows a summary of the surface (through the *c* plane) and edge (through the *m* plane) emission intensities as functions of emission wavelength for four different samples of *c* plane $Al_xGa_{1-x}N$ ($x=0-0.76$) MQWs, in which the optical pumping power density was below the threshold and was fixed at ≈1.6 mJ/cm^2. The solid and dashed lines indicate surface emissions (circle) and edge emissions (square), respectively.

The surface emission intensity (through the *c* plane) was 30–40 times higher than the edge emission intensity at 287 nm, and decreased in the region of wavelengths shorter than 287 nm. Only extremely weak surface emissions were

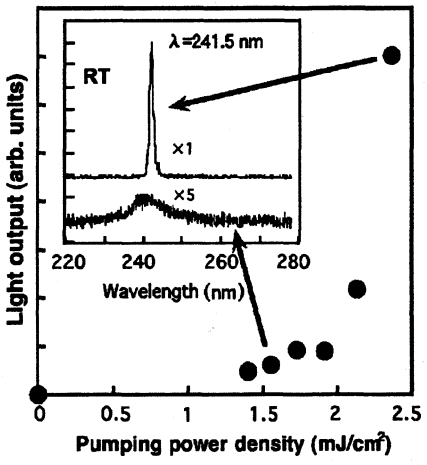

FIG. 1. Light output as function of optical pumping power density for deep-UV AlGaN MQW laser at 241.5 nm (measured at room temperature).

[a]Electronic mail: kawanisi@cc.kogakuin.ac.jp

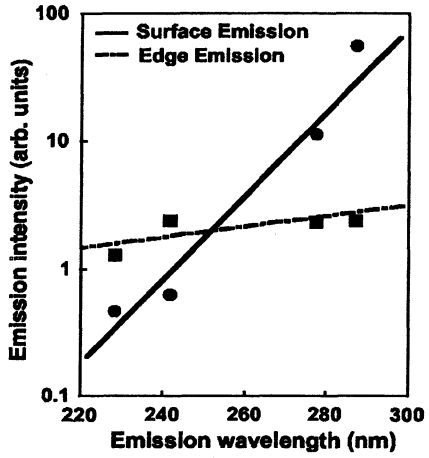

FIG. 2. Surface [through (0001) c plane] and edge [through (1–100) m plane] emission intensities as functions of emission wavelength from (0001) c-plane $Al_xGa_{1-x}N$ (x=0–0.76) MQWs (below threshold).

detected at 228 and 240 nm, and the emission intensities at 228 and 240 nm were nearly two orders of magnitude smaller than that at 287 nm. On the other hand, the edge emission (through the cleaved m-plane facets of the c-plane AlGaN MQW) slightly decreased in the spectral region shorter than 287 nm, as shown in Fig. 2. This small decrease in edge emission intensity is probably due to the low crystalline quality of the $Al_xGa_{1-x}N$ MQWs with high Al content. This difference between the surface emission and edge emission intensities is evidence of the anisotropic optical properties of the c-plane AlGaN MQW with a relatively high Al content.

In a previous study,[19] we have carefully investigated the optical polarization behavior of the spontaneous surface and edge emissions from the UV and deep-UV AlGaN MQW structures by inserting a UV polarizer in our measurement system. As a result, symmetric and isotropic TE-mode ($E\|c$) and TM-mode ($E\perp c$) emissions were observed for both the surface and edge emissions at 355.1 nm from the c-plane $Al_xGa_{1-x}N$ MQW (x=0.04) below the lasing threshold. However, only TM-mode emission was observed for the spontaneous edge emission at 240.8 nm from the c-plane $Al_xGa_{1-x}N$ MQW structure (x=0.66). This fact indicates that the spontaneous surface and edge emissions from the c-plane $Al_xGa_{1-x}N$ MQW structure (x=0.66) were polarized anisotropically.

The mechanism of the extremely weak surface emission becomes clearer by measuring the optical polarization behavior of the lasing light. Figure 3 shows a summary of the optical polarization characteristics of the lasing light from the c-plane $Al_xGa_{1-x}N$ MQW deep-UV laser operating at 240.77 nm (solid line, x=0.66) and 355.12 nm (dashed line, x=0.04). The lasing light from the c-plane AlGaN MQW, which was detected through the cleaved m-plane facet, was optically polarized into the TM mode ($E\|c$) for the c-plane laser operating at 240.77 nm, but into the TE mode ($E\perp c$) for the c-plane laser operating at 355.12 nm.

In addition, we have examined the optical characteristics of the m-plane $Al_xGa_{1-x}N$ (x=0–0.76) single epitaxial layers (1.5 μm thick) grown on the (1–100) m-plane 6H-SiC substrate to clarify the mechanism of the anisotropic optical properties. Figure 4 shows the intensity variation of the surface (through the m plane, in this case) spontaneous emission from the m-plane AlGaN layers for the spectral region from 230 to 320 nm. The surface emission intensity from the c-plane surface $Al_xGa_{1-x}N$ (x=0–0.76) is also plotted in Fig. 4 for comparison. As expected, strong surface emission was obtained from the m-plane $Al_xGa_{1-x}N$ (x=0–0.76) epitaxial single layers in the spectral region from 240 to 365 nm, but surface emission from the m-plane AlGaN decreased for wavelengths shorter than 240 nm, which is probably due to the poor crystalline quality of our m-plane AlGaN single layer compared with the c-plane AlGaN MQW.

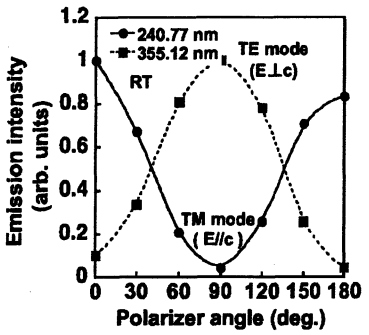

FIG. 3. Optical polarization characteristics of the lasing light from AlGaN MQW laser operating at 355.12 nm (dotted line) and at 240.77 nm (solid line).

Our experimental results on the optical properties, such as the polarization of laser light and the anisotropic surface emission from the c-plane AlGaN MQWs grown on the (0001) c-plane 4H or 6H-SiC substrate, and the strong surface emission from the m-plane AlGaN (x=0–0.76) single layers grown on the (1–100) m-plane 6H-SiC substrate, suggest that the crystal-field splitoff hole (CH) valence band (VB) becomes the nearest VB to the conduction band rather than the heavy-hole VB and light-hole VB, then $E\|c$ polarization and anisotropic characteristics of emission are detected, because the CH band is active only to the polarized emission of $E\|c$. Therefore, the dipole moment is formed only in parallel to the c axis. This characteristic of the CH band is the origin of the weak surface emission from the c-plane AlGaN MQWs in the spectral region from 228 to 290 nm. However, more detailed investigations are needed to determine the physical origins of the anisotropic polarization, extremely weak emission, band structure of the $Al_xGa_{1-x}N$ with Al contents of x=0.67–1 (emission wavelength shorter than 240 nm), and dipole moment related to

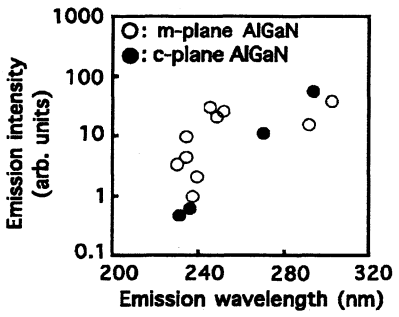

FIG. 4. Surface emission intensity (through m plane, plotted as open circles) as function of emission wavelength from m-plane AlGaN single epitaxial layers grown on (1–100) m-plane 6H-SiC substrate.

the light emission of ternary AlGaN and of the MQW lasers. This extremely weak surface emission is possibly related to the low quantum efficiency of deep-UV LEDs with emission wavelengths shorter than about 300 nm.

In summary, extremely weak surface emission was observed from (0001) *c*-plane AlGaN MQWs (x=0.66–0.76) grown on a (0001) *c*-plane 4*H* or 6*H*-SiC substrate in the spectral region from 228 to 240 nm. The origin of this extremely weak surface emission was partly clarified by examining specific characteristics, such as the optical polarization characteristics of the laser light, the intensity variation of the spontaneous surface and edge emissions from the (0001) *c*-plane deep-UV and UV AlGaN MQWs as functions of the emitting wavelength, and the strong surface emission from the (1–100) *m*-plane $Al_xGa_{1-x}N$ (x=0–0.76). As a result, the CH band plays an important role in the deep-UV emission and anisotropic polarization properties of the AlGaN with high Al content.

The authors are very grateful to Y. Suematsu and K. Iga of the Tokyo Institute of Technology for encouragement in their work, and to F. Hasegawa of Kohgakuin University for useful suggestions for their research. This work is supported by a Grant-in-Aid for Scientific Research [Grant-in-Aid for Scientific Research (S) No. 17106005] from the Japan Society for the Promotion of Science.

[1]V. Adivarahan, W. H. Sun, A. Chitnis, M. Shatalov, S. Wu, H. P. Maruska, and M. A. Khan, Appl. Phys. Lett. **85**, 2175 (2004).
[2]K. Iida, T. Kawashima, A. Miyazaki, H. Kasugai, S. Mishima, A. Honshio, Y. Miyake, M. Iwaya, S. Kamiyama, H. Amano, and I. Akasaki, Jpn. J. Appl. Phys., Part 2 **43**, L499 (2004).
[3]T. Takano, Y. Narita, A. Horiuchi, and H. Kawanishi, Appl. Phys. Lett. **84**, 3567 (2004).
[4]H. Kawanishi, M. Senuma, T. Nukui, Y. Ohtaki, and Y. Yamamoto (unpublished).
[5]V. Adivarahan, S. Wu, J. P. Zhang, A. Chitnis, M. Shatalov, V. Mandavilli, R. Gaska, and M. A. Khan, Appl. Phys. Lett. **84**, 4762 (2004).
[6]T. Takano, Y. Ohtaki, Y. Narita, and H. Kawanishi, Jpn. J. Appl. Phys., Part 2 **43**, L1258 (2004).
[7]Y. Ohba, H. Yoshida, and R. Sato, Jpn. J. Appl. Phys., Part 2 **36**, L1565 (1997).
[8]N. Onojima, J. Suda, and H. Matsunami, Jpn. J. Appl. Phys., Part 2 **42**, L445 (2003).
[9]Y. J. Sun, O. Brandt, S. Cronenberg, S. Dhar, H. T. Grahn, K. H. Ploog, P. Waltereit, and J. S. Speck, Phys. Rev. B **67**, 041306(R) (2003).
[10]N. F. Gardner, J. C. Kim, J. J. Wierer, Y. C. Shen, and M. R. Kramer, Appl. Phys. Lett. **86**, 111101 (2005).
[11]H. Masui, A. Chakraborty, B. A. Haskell, U. K. Mishra, J. S. Speck, S. Nakamura, and S. P. DenBaars, Jpn. J. Appl. Phys., Part 2 **44**, L1329 (2005).
[12]R. Dingle, D. D. Sell, S. E. Stokowski, and M. Ilegems, Phys. Rev. B **4**, 1211 (1971).
[13]K. Domen, K. Horino, A. Kuramata, and T. Tanahashi, Appl. Phys. Lett. **71**, 1996 (1997).
[14]B. Rau, P. Waltereit, O. Brandt, M. Ramsteiner, K. H. Ploog, J. Puls, and F. Henneberger, Appl. Phys. Lett. **77**, 3343 (2000).
[15]E. Kuokstis, C. Q. Chen, M. E. Gaevski, W. H. Sun, J. W. Yang, G. Simin, M. A. Khan, H. P. Maruska, D. W. Hill, M. C. Chou, J. J. Gallagher, and B. Chai, Appl. Phys. Lett. **81**, 4130 (2002).
[16]K. B. Nam, J. Li, M. L. Nakarmi, J. Y. Lin, and H. X. Jiang, Appl. Phys. Lett. **84**, 5264 (2004).
[17]J. Shakya, K. Knabe, K. H. Kim, J. Li, J. Y. Lin, and H. X. Jiang, Appl. Phys. Lett. **86**, 091107 (2005).
[18]J. Li, K. B. Nam, M. L. Nakarmi, J. Y. Lin, H. X. Jiang, Pierre Carrier, and Su-Huai Wei, Appl. Phys. Lett. **83**, 5163 (2003).
[19]H. Kawanishi, M. Senuma, and T. Nukui, Appl. Phys. Lett. **89**, 041126 (2006).

Experimental energy difference between heavy- or light-hole valence band and crystal-field split-off-hole valence band in $Al_xGa_{1-x}N$

Hideo Kawanishi,[a] Eiichiro Niikura, Mao Yamamoto, and Shoichiro Takeda
Department of Electronic Engineering, Kohgakuin University, Nakano-machi 2665-1, Hachioji-shi, Tokyo 192-0015, Japan

(Received 8 September 2006; accepted 19 November 2006; published online 19 December 2006)

The energy difference between heavy- or light-hole (HH or LH) and crystal-field split-off-hole (CH) valence bands of *m*- and *c*-plane $Al_xGa_{1-x}N$ was experimentally investigated as the peak-energy difference between ($\boldsymbol{E} \perp C$)- and ($\boldsymbol{E} \| C$)-polarized emissions. The energy difference was zero at $x \approx 0.73-0.78$. However, this value was significantly larger than $x \approx 0.36-0.41$, at which the spontaneous surface-emission intensities of $\boldsymbol{E} \perp C$ and $\boldsymbol{E} \| C$ polarizations from the $Al_xGa_{1-x}N$ were equal. These results suggest a shorter carrier lifetime (larger optical gain) in the CH than in the HH and/or LH. © *2006 American Institute of Physics*. [DOI: 10.1063/1.2410242]

The band structure of AlGaN is very important for obtaining efficient and mode-stabilized ultraviolet (UV) and deep-UV optical devices such as light emitting diodes and laser diodes. The polarization behaviors of spontaneous emission from GaN, AlN, and AlGaN were experimentally studied and reported in literature.[1–7] $\boldsymbol{E} \perp C$-axis emission dominated from GaN.[2–4] However, the $\boldsymbol{E} \| C$-axis emission intensity from AlGaN increased with increasing Al composition,[6] and $\boldsymbol{E} \| C$-axis emission dominated from AlN.[5] Transverse-magnetic-field mode (TM mode, such as $\boldsymbol{E} \| C$-axis) lasing was experimentally demonstrated in deep-UV AlGaN multiple quantum well (MQW) lasers at wavelengths shorter than 250–260 nm under optical pumping.[8] Extremely weak or no surface emission from *c*-plane AlGaN was detected in the deep-UV spectral region.[9]

The band structures of GaN and AlN have been theoretically studied.[10–12] According to the studies, the valence bands (VBs) of GaN, AlN, and AlGaN are separated into three VBs, namely, heavy-hole (HH), light-hole (LH), and crystal-field split-off-hole (CH) VBs, respectively. These VBs have different emission and absorption properties, where HH and LH, and CH VBs are related dominantly to $\boldsymbol{E} \perp C$-axis, and $\boldsymbol{E} \| C$-axis emissions, respectively. However, the Al composition at which the energy difference between HH or LH and CH becomes zero has not been clarified yet. The laser gain properties of AlGaN quantum wells were theoretically investigated only in the wavelength range from 270 to 340 nm.[13]

Our previous experimental results suggested that the cross point of the HH or LH VB and CH VB was significantly larger than cross point $x \approx 0.36-0.41$ ("cross point A"), at which spontaneous emission intensities related to HH or LH and CH VBs were nearly equal.[8,9]

In this study, we try to determine the Al composition x, at which energy difference between the HH or LH and CH VBs becomes zero, both for *m*- and *c*-plane AlGaN, by measuring the energy difference between $\boldsymbol{E} \perp C$-axis and $\boldsymbol{E} \| C$-axis emissions. We call this cross point "cross point B." We compare cross points A and B for *c*- and *m*-plane AlGaN to determine clearly the emission mechanisms from the CH VB and lasing-mode behavior of UV and deep-UV AlGaN lasers.

m- or *c*-plane AlGaN epitaxial layers were grown on (1–100) or (0001) SiC substrate by low-pressure metal-organic vapor phase epitaxy. The detailed layer structure and growth conditions of the *m*- and *c*-plane AlGaN are explained in Refs. 14 and 15. The optical measuring setup (for measuring optical polarization and emission intensity) in the UV and deep-UV spectral regions is explained in Ref. 8.

The low temperature emission spectra at room temperature are summarized in Figs. 1(a) and 1(b) for *m*-plane GaN and $Al_{0.32}Ga_{0.68}N$ single layers (≈ 1 μm thick) grown on a (1-100) 6*H*-SiC substrate. $\boldsymbol{E} \perp C$-axis emission dominated from the *m*-plane GaN, but weak $\boldsymbol{E} \| C$-axis emission was

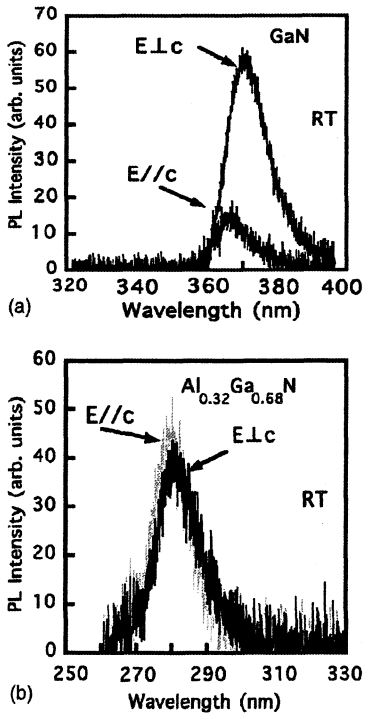

FIG. 1. Polarized photoluminescence emissions from *m*-plane (a) GaN and (b) $Al_{0.32}Ga_{0.68}N$ single layer, at room temperature.

[a]Electronic mail: kawanisi@cc.kogakuin.ac.jp

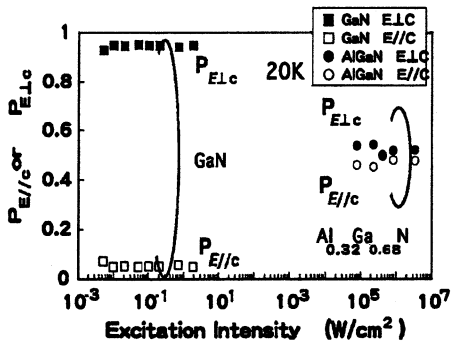

FIG. 2. Stability of normalized polarizations $P_{E\perp C}$ and $P_{E\|C}$ for both m-plane GaN and $Al_{0.32}Ga_{0.68}N$ single layers at low temperature (20 K).

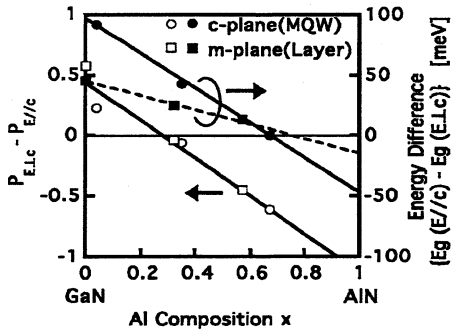

FIG. 3. Normalized polarization difference $(P_{E\perp C}-P_{E\|C})$ and emission energy difference $\{E_g(E\|C)-E_g(E\perp C)\}$ as functions of Al composition x for c-plane $Al_xGa_{1-x}N$ MQWs and m-plane $Al_xGa_{1-x}N$ single layers. All data were taken at room temperature.

also detected. The $E\perp C$-axis emission originates in HH and/or LH VBs, because these VBs are active only for $E\perp C$-axis emission.[10] On the other hand, $E\|C$-axis emission originates in the CH VB.

The energy difference between $E\perp C$-axis and $E\|C$-axis emissions was 45 meV for the m-plane GaN single layer, as shown in Fig. 1(a). The energy difference was larger than $\approx$18–23 meV, which was determined for unstrained GaN,[12] but smaller than 80–90 meV, which was measured using the photoluminescence peak energy for the strained c-plane GaN single layer and GaN/AlGaN MQW structure grown on SiC or Al_2O_3.[2,6,8,9] On the other hand, the $E\perp C$-axis and $E\|C$-axis emission intensities were nearly the same for the m-plane $Al_{0.32}Ga_{0.68}N$ (the same as in Refs. 6 and 8), as shown in Fig. 1(b).

The dependences of optical polarization on optical-excitation intensity for the m-plane GaN and $Al_{0.32}Ga_{0.68}N$ single layers are summarized in Fig. 2 (measured at 20 K), where the normalized polarizations $P_{E\perp C}$ and $P_{E\|C}$ are defined, respectively, by

$$P_{E\perp C}=I_{E\perp C}/(I_{E\perp C}+I_{E\|C}),$$

$$P_{E\|C}=I_{E\|C}/(I_{E\perp C}+I_{E\|C}),$$

where $I_{E\perp C}$ and $I_{E\|C}$ are emission intensities for $E\perp C$-axis and $E\|C$-axis emissions, respectively. The optical excitation intensity changed from 0.05 W/cm^2 (weak excitation) to 2 W/cm^2 (medium excitation) in the case of the He–Cd ion laser (for GaN excitation under continuous-wave operation) and from 0.01 to MW/cm^2 (strong excitation) in the case of the excimer laser (for $Al_xGa_{1-x}N$ excitation under pulsed operation with a pulse width of $\approx$2.5 ns and repetition rate of 100 Hz). $P_{E\perp C}$ emission dominated from GaN, but nearly the same emission intensities for both $P_{E\perp C}$ and $P_{E\|C}$ were detected for the m-plane $Al_{0.32}Ga_{0.68}N$. The normalized polarizations $P_{E\perp C}$ and $P_{E\|C}$ for the GaN and $Al_{0.32}Ga_{0.68}N$ were stable with changes in excitation intensity, as shown in Fig. 2.

On the other hand, a strong temperature dependence of the polarizations was detected. For example, $P_{E\perp C}$ and $P_{E\|C}$ for the GaN were $\approx$0.6 and 0.4 at room temperature, respectively. However, $P_{E\perp C}$ and $P_{E\|C}$ were $\approx$0.82 and $\approx$0.18 at 20 K, respectively. As a result, $P_{E\perp C}$ and $P_{E\|C}$ for the GaN and AlGaN depend strongly on sample temperature.

Figure 3 is a summary of our experimental results at room temperature for the ($E\perp C$-axis)- and ($E\|C$-axis)-polarized emissions from m-plane $Al_xGa_{1-x}N$ single layers (x=0–0.58) grown on a (1-100) m-plane SiC substrate and c-plane $Al_xGa_{1-x}N$ MQW (x=0–0.67) grown on a (0001) c-plane SiC substrate. Closed circles and squares represent the energy differences for the c-plane AlGaN MQWs and the m-plane AlGaN single layers, respectively, where Al compositions in the AlGaN were determined from lattice constant or the peak wavelength of spontaneous emission. The absolute value of the energy difference and dependence of the energy difference on Al composition x for m-plane $Al_xGa_{1-x}N$ were significantly smaller than those for c-plane $Al_xGa_{1-x}N$, as shown in Fig. 3. These changes of absolute values and dependence on Al composition originate in the strain included in c- and m-plane AlGaN epitaxial layers. Experimentally obtained residual strains ($\Delta c/c$) for c- and m-plane GaN were –0.3% [by conventional (0002) x-ray diffraction, tensile strain along the a axis] and –0.1% [by in-plane (0002) x-ray diffraction, tensile strain], respectively. However, the energy difference was zero at nearly same Al composition for c- and m-plane $Al_xGa_{1-x}N$ (cross point B is at $x\approx0.73$ for c-plane AlGaN MQWs and at $x\approx0.78$ for m-plane AlGaN single layer, and the corresponding emission wavelength was $\approx$240–260 nm).

The difference between normalized polarizations $(P_{E\perp C}-P_{E\|C})$ is also plotted as open circles and squares for the c-plane AlGaN MQWs and m-plane AlGaN single layer in Fig. 3. The difference was zero at $x\approx0.36$–0.41 (cross point A is at $x\approx0.36$–0.41 for c- and m-plane AlGaN, and the corresponding emission wavelength was $\approx$280–290 nm). Cross point A is significantly smaller than cross points B for the m-plane AlGaN single layer and for the c-plane AlGaN MQWs.

Cross point A is strongly related to the carrier lifetime in the HH, LH, and CH VBs. A shorter carrier lifetime leads to higher emission intensity and higher optical gain in the AlGaN. Estimation of optical gain for UV AlGaN (at 355.6 nm) and deep-UV AlGaN (at 240.0 nm) MQW lasers was carefully examined by Hakki and Paoli method.[16] Spontaneous emission intensities of $E\perp C$ axis (smaller energy the emission) and $E\|C$ axis (larger energy emission) were nearly the same for the UV AlGaN MQW, but $E\|C$ axis emission was the main part for the deep-UV AlGaN MQW, below the threshold. Then significantly higher optical gain was obtained only for $E\perp C$ axis in the UV AlGaN MQW laser and only for $E\|C$ axis in the deep-UV AlGaN MQW laser, respectively, above threshold. Therefore, our experimental results on UV and deep-UV AlGaN suggest a shorter

carrier lifetime in the CH VB than in the HH and/or LH VBs, by considering energy levels of HH, LH, and VC VBs (CH VB is located below or equal to HH and LH VBs). This indicates that the shorter carrier lifetime of the CH VB is related to the larger optical gain in this CH VB than in the HH and/or LH VBs. As a result, the TM mode lasing becomes the main mode in the AlGaN MQW laser at wavelengths shorter than 280–290 nm.

We conclude that the energy difference between HH or LH VB and CH VB was zero at $x \approx 0.73-0.78$ (cross point B) for *c*- and *m*-plane $Al_xGa_{1-x}N$. Cross point B is significantly larger than cross point A for the *m*-plane AlGaN single layer and for the *c*-plane AlGaN MQWs. This difference between cross points A and B proposes a shorter carrier lifetime in the CH VB than in the HH and/or LH VBs. It is expected that the optical gain related to the CH VB is much larger than to the HH and/or LH VBs. As a result, deep-UV AlGaN MQW lasers (at wavelengths shorter than 280–290 nm) show a tendency to lase in the TM mode.

The authors are very grateful to Y. Suematsu and K. Iga of the Tokyo Institute of Technology and to F. Hasegawa of Kohgakuin University for fruitful comments and discussions. This work is supported by JSPS and MEXT, Grant-in-Aid for Scientific Research [Grant-in-Aid for Scientific Research (S) No. 17106005 and Grant-in-Aid for Scientific Research on Priority Areas No. 18069009].

[1] R. Dingle, D. D. Sell, S. E. Stokowski, and M. Ilegems, Phys. Rev. B **4**, 1211 (1971).
[2] K. Domen, K. Horino, A. Kuramata, and T. Tanahashi, Appl. Phys. Lett. **71**, 1996 (1997).
[3] E. Kuokstis, C. Q. Chen, M. E. Gaevski, W. H. Sun, J. W. Yang, G. Simin, M. Asif Khan, H. P. Maruska, D. W. Hill, M. C. Chou, J. J. Gallagher, and B. Chai, Appl. Phys. Lett. **81**, 4130 (2002).
[4] B. Rau, P. Waltereit, O. Brandt, M. Ramsteiner, K. H. Ploog, J. Puls, and F. Henneberger, Appl. Phys. Lett. **77**, 3343 (2000).
[5] J. Li, K. B. Nam, M. L. Nakarmi, J. Y. Lin, H. X. Jiang, Pierre Carrier, and Su-Huai Wei, Appl. Phys. Lett. **83**, 5163 (2003).
[6] K. B. Nam, J. Li, M. L. Nakarmi, J. Y. Lin, and H. X. Jiang, Appl. Phys. Lett. **84**, 5264 (2004).
[7] J. Shakya, K. Knabe, K. H. Kim, J. Li, J. Y. Lin, and H. X. Jiang, Appl. Phys. Lett. **86**, 091107 (2005).
[8] H. Kawanishi, M. Senuma, and T. Nukui, Appl. Phys. Lett. **89**, 041126 (2006).
[9] H. Kawanishi, M. Senuma, M. Yamamoto, E. Niikura, and T. Nukui, Appl. Phys. Lett. **89**, 081121 (2006).
[10] M. Suzuki, T. Uenoyama, and A. Yanase, Phys. Rev. B **52**, 8132 (1995).
[11] I. Vurgaftman and J. R. Mayer, J. Appl. Phys. **94**, 3675 (2003).
[12] P. Misra, U. Behn, O. Brandt, H. Grahn, B. Imer, S. Nakamura, S. P. DenBaars, and J. S. Speck, Appl. Phys. Lett. **88**, 161920 (2006).
[13] W. W. Chow and M. Kneissl, J. Appl. Phys. **98**, 114502 (2005).
[14] T. Takano, Y. Narita, A. Horiuchi, and H. Kawanishi, Appl. Phys. Lett. **84**, 3567 (2004).
[15] T. Takano, Y. Ohtaki, Y. Narita, and H. Kawanishi, Jpn. J. Appl. Phys., Part 2 **43**, L1258 (2004).
[16] B. W. Hakki and T. L. Paoli, J. Appl. Phys. **46**, 1299 (1975).

深紫外 AlGaN 多重量子井戸型半導体レーザー光の光学的異方特性

川西　英雄・瀬沼　正憲・貫井　猛晶

光　　学　35巻5号（2006）　別刷

深紫外 AlGaN 多重量子井戸型半導体レーザー光の光学的異方特性

川西　英雄・瀬沼　正憲・貫井　猛晶

Optical Anisotropic Characteristics of Deep-Ultraviolet AlGaN Multiple-Quantum-Well Lasers

Hideo KAWANISHI, Masanori SENUMA and Takeaki NUKUI

End of October 1993, room temperature deep-UV lasing was demonstrated at around 240 nm by AlGaN multiple-quantum-well laser under optical pumping, for the first time. The unique optical anisotropic polarization of laser output was discovered in the AlGaN MQW lasers lasing shorter than 280-290 nm. The anisotropic polarization is the reflection of an anisotropic dipole moment, which directly related in laser gain, in the AlGaN active layer with high Al content.

Key words: deep-UV laser, AlGaN MQW, optical polarization, TE and TM modes, anisotropic polarization

2003年10月の末，AlGaN多重量子井戸型半導体レーザーで，深紫外波長域240 nm近傍での室温レーザー発振をはじめて実現した[1]．その大きな理由のひとつは，「交互供給法」とよぶ高品質なAlGaNのエピタキシャル成長の新技術が提案されたことによる[2]．その方法を，「ASFE法」(alternate source-feeding epitaxy) とよんでいる．

もうひとつの理由は，常識にとらわれず研究を進めてきたからではないだろうか．すなわち，発光波長が約280～290 nm以下で発光するAlGaNエピタキシャル層では，表面（c面）側からの発光はほとんど観測されなかった．しかし，その試料を励起し，レーザー発振の可能性を確かめたからである．

このことは，AlGaN活性領域における発光過程が「非等方的」であるとすると容易に理解できる．すなわち，新しい「謎」が生まれたのである．

その「謎」を解明すべく，深紫外域でのAlGaN多重量子井戸型半導体レーザーの光学的偏波特性など，最近筆者らが行った研究成果の一部をここで紹介したい．なお，ここでの研究成果は，深紫外域発光デバイスの高効率化にも直接関係する可能性があり，この分野の研究者の皆さんに興味をもっていただけると幸いである．

1. AlGaN多重量子井戸型半導体レーザーの構造

深紫外域でレーザー発振が得られたAlGaN多重量子井戸型半導体レーザーの断面構造を図1に示す[3]．(0001)面SiC基板（すなわちc面基板）を用いている．

特に，発光過程に直接影響を与える可能性のある結晶の品質は，X線回折により，c軸のティルト角の変位およびc軸を中心とした結晶のツイスト角の変位をそれぞれ，ωおよびϕに関するXRC（X線ロッキングカーブ）半値幅で評価した．ωとϕには高品質領域で強い相関があることもわかり，ωスキャン特性を改善することで，ϕスキャン特性も改善した．現在，最も狭いもので$\Delta\omega=78$ arcsecおよび$\Delta\phi=800$ arcsecとなった．すなわち，今後さらなる改善も必要であるが，半導体レーザーを構成するAlGaNエピタキシャル層はc軸に強く配向し，その品質は現時点で得られている最も高品質なAlGaN結晶であろう．

2. 深紫外レーザー光の光学的偏波特性

AlGaN多重量子井戸型半導体レーザーの，①表面発光および，②端面発光の偏波特性は，図2に示した光学系で測定した．試料は固定したまま，光学系を簡単に変更することによって，表面発光および端面発光が測定できるよう工夫している．励起光源にはArFエキシマーレーザーの193 nmの発振線を用い，励起光強度は，直列に並べた

工学院大学電子工学科（〒192-0015 八王子市中野町2665-1）　E-mail: kawanisi@cc.kogakuin.ac.jp

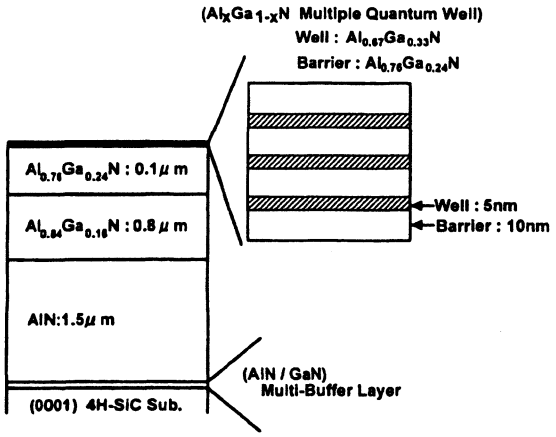

図1　深紫外 AlGaN 多重量子井戸型半導体レーザーの断面構造．このときの各層の Al 組成は，発振波長が 240.8 nm の場合の例を示している．

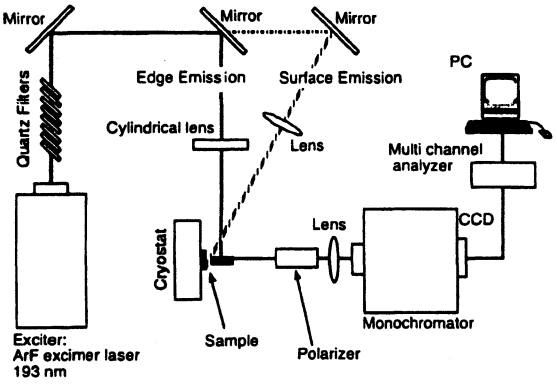

図2　偏波面特性を測定するための光学系．表面発光特性では，励起光は斜め入射．一方，端面発光およびレーザー発振特性の測定では，垂直入射．

石英板の枚数を変えて変化させた．なお，偏波特性の測定では，深紫外域を含む 190～400 nm の波長域で有効なグラン・テイラー型偏光器を利用し，その特性は，300 nm 以上の波長域で有効な通常型の平板型偏光板と，355 nm 域のレーザー発振光とで精密に注意深く校正した．

図 3 は，組成の異なる 2 種類の AlGaN 多重量子井戸型半導体レーザーで得た紫外域レーザー光（発振波長：355.1 nm），および深紫外域レーザー光（発振波長：240.8 nm）の偏波特性をまとめたものである（いずれも室温）．測定結果は，紫外域レーザー光は TE モードで発振しているのに対し，深紫外域レーザー光は TM モードで発振している．TE モードでのレーザー発振は，GaAs 系，InP 系などの半導体レーザーでよく知られている通りである．すなわち，発光強度およびレーザー利得は等方的であり，TE モードに対する等価屈折率（伝搬定数を真空の波数で除し

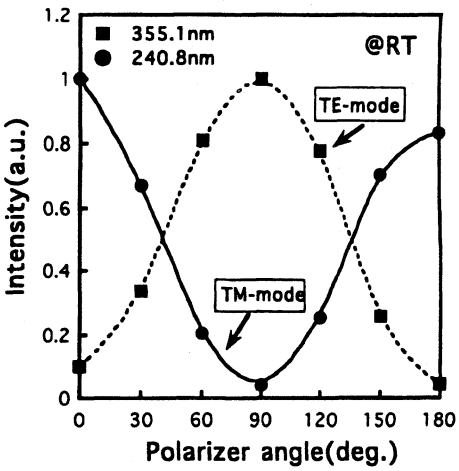

図3　発振波長が，355.1 nm および 240.8 nm の代表的な 2 種類の紫外および深紫外 AlGaN 多重量子井戸型半導体レーザーからの出力光の偏波特性（室温）．横軸の偏光角は 0° および 180° で，結晶の c 軸方向に一致．

たもので，屈折率の分散項は含まれていない）が，TM モードのそれに比べわずかに大きいために，TE モードに対する端面の「モード反射率」がわずかに大きくなる．すなわち，閾値利得の面から，レーザー発振モードの選択が起こっている．なお，このときの表面発光強度の異方性はほとんど観測できなかった．

一方，深紫外域 AlGaN では，発光特性および利得は非等方的であり，TE モード方向の利得はないか，あるにしてもきわめて小さく，TM モードに対するレーザー利得のみしか確保されない．その結果，深紫外域 AlGaN では，レーザー利得の面から，TM モードでのレーザー発振モードの選択が起こっている．

このことは，図 4 に示した測定結果のように，2 種類の試料で，表面からの自然放出光強度が大きく違うことで明らかになる[4]．図 4 は，AlGaN 多重量子井戸型半導体レーザーのそれぞれの試料を変えることなく，図 3 の測定の励起強度を下げ（レーザー発振をしない励起強度）測定した．ただし，励起強度は，それぞれの試料での測定でほぼ同じとした．その結果，AlGaN の c 軸方向から検出した深紫外域の表面発光強度（波長，約 240.8 nm）は，極端に微弱であった．他方，紫外域の自然放出発光強度（波長，約 355.1 nm）では，表面発光強度は端面発光強度に比べ，逆転し，約 1 桁強かった[4]．

この実験事実から，以下のことが推定できる．すなわち，Al 組成の大きな AlGaN 活性層内には，深紫外域の発光にかかわる「電気双極子モーメント」が c 軸方向に偏っているため，c 軸方向への光の放出が観測できない，

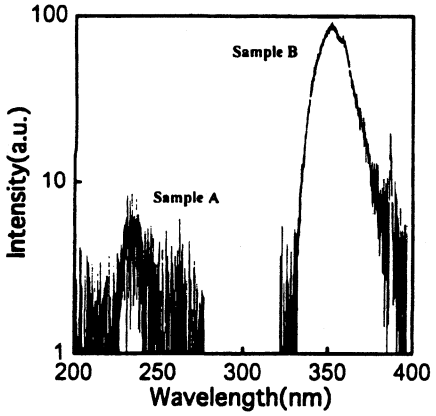

図4　図3の測定に用いた2種類の試料の表面発光強度．励起強度を上げたときSample AおよびBは，それぞれ240.8 nmおよび355.1 nmでレーザー発振した．

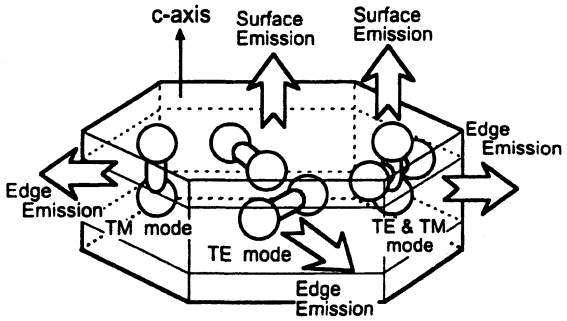

図5　AlGaN活性層内に形成される「電気双極子モーメント(光の周波数に対応)」の概念図．この「電気双極子モーメント」がc軸に平行にのみ形成されるとき，表面発光不可能か，きわめて微弱（観測系の開口数による）となる．一方，c軸に垂直な方向（c面内）に形成される場合，表面発光は観測可能．なお，端面発光は，いずれの場合も観測可能．

と古典的に考えるのが妥当である．

上に示した2つの実験事実を理解しやすくするために，図5に，紫外域および深紫外域で発光するAlGaNに関する「電気双極子モーメント」の形成方位と発光強度との関係をまとめてみた．

紫外域発光のAlGaN量子井戸型半導体レーザーでは，「電気双極子モーメント」は，c面内に等方的に形成されるとともに，それと垂直なc軸方向にも形成されている．その結果，TEモードおよびTMモードいずれの場合にも，レーザー利得が確保されている．一方，深紫外域発光のAlGaN量子井戸型半導体レーザーでは，「電気双極子モーメント」は，c軸方向に偏り形成されるために，TMモードに対するレーザー利得のみしか確保できない．

以上述べた実験結果に対する筆者らの主張は，別の測定結果からも確認できている．ページ数の関係で割愛するが，端面からの自然放出光の偏波面依存性を測定することで明らかになった[4]．このような現象が顕著に表れるのが，発光波長として280～290 nm以下の波長域である．AlGaNのAlの組成にして約40%のあたりからであった．

GaNおよびAlNのバンド構造が，第一原理計算によりすでに求められている．バンド構造に関する詳しい議論は参考文献を参照願いたい[5]．結論として，筆者らの実験結果は，この理論計算と，紫外域に発光波長を有するGaNにおいても，その光学的偏波特性とともに，それぞれのバンドのエネルギー差においても，いずれも一致しないようである．ここでは，問題点を指摘するだけにとどめておく．より詳しい議論は，今後の皆さんの精密な測定と，実験・理論両面からの詳細な検討に任せるとする．

3. 深紫外AlGaN多重量子井戸半導体レーザーの今後に期待すること

深紫外域で動作する半導体レーザーの実現は，ひとつの技術的な夢である．このとき，常識にとらわれることなく，この分野の研究を進めることがきわめて重要ではないか，そのような体験をしたように思う．また，電流注入ではなく，光励起でレーザー発振を試みる，そんな実験・研究は決してしないだろう．それを愚直に試みたことで，常識では理解できない実験結果が，突然現れてきた．たくさんの「謎」が出現したことになる．

ここでの議論は，より詳細な追跡と，今後の詳細な考察が必要であろう．この分野の研究に興味をもつ研究者・技術者の人たちにそれを委ねたい．

本研究は，文部科学省・科学研究補助金，基盤研究（S）（課題番号：17106005）として実施しているものである．研究を進める機会を与えていただいたことに感謝する．また，日ごろから貴重な議論をいただいている，本学・特別専任教授・長谷川文夫教授，また，結晶内の歪み解析と，AlN・AlGaN結晶の高品質化を手伝っていただいている本学・新倉栄一郎君および村川浩一君に感謝する．

文　献

1) T. Takano *et al.*: Appl. Phys. Lett., **84** (2004) 3567-3569.
2) T. Takano *et al.*: Jpn. J. Appl. Phys., **43** (2004) L1258-L1260.
3) 川西英雄ほか：応用物理，**74** (2005) 1458-1462.
4) H. Kawanishi *et al.*: "Anisotropic polarization characteristics of lasing and spontaneous surface and edge emissions from deep-UV AlGaN MQW lasers," submitted.
5) M. Suzuki *et al.*: Phys. Rev. B, **52** (1995) 8132-8139.

(2005年1月12日受理)

Japanese Journal of Applied Physics
Vol. 44, No. 12, 2005, pp. 8432–8434

Relationship between Excess Ga and Residual Oxides in Amorphous GaN Films Deposited by Compound Source Molecular Beam Epitaxy

Naoyuki OBINATA, Koichi SUGIMOTO, Kazuyuki IJIMA, Masaya ISHIBIKI, Shinichi EGAWA, Tohru HONDA* and Hideo KAWANISHI

Department of Electronic Engineering, Kogakuin University, 2665-1 Nakano-machi, Hachiohji, Tokyo 192-0015, Japan

(Received February 10, 2005; accepted July 27, 2005; published December 8, 2005)

Amorphous GaN (a-GaN) films were deposited at a low temperature below 500°C by compound-source molecular beam epitaxy (CS-MBE). The relationship between excess Ga and its oxidation in the deposited GaN films is reported. X-ray photoelectron spectroscopy (XPS) revealed that the excess Ga in deposited films was oxidized in the air and converted to gallium oxide. By increasing the substrate temperature, the total amount of gallium oxide in the deposited films decreased due to the reduction of the excess Ga. Cathodoluminescence (CL) intensity from the UV to the blue spectral regions increased with as the amount of gallium oxide in the deposited films decreased. [DOI: 10.1143/JJAP.44.8432]

KEYWORDS: GaN, oxidation, XPS, CL, MBE

1. Introduction

Group III nitride semiconductors such as GaN and related materials have been attracting much attention for applications in light-emitting devices operating in the visible and UV spectral regions.[1,2] Producing low-cost GaN-based light-emitting devices on a large scale requires low-temperature fabrication processes.[3] If compound-source molecular beam epitaxy (CS-MBE) is used, a low substrate temperature is expected for the deposition of GaN films, because the deposition temperature is lower with CS-MBE than that with conventional MBE.[4] The epitaxial growth of ZnSe-based materials by CS-MBE at low temperatures has previously been reported.[5] Amorphous GaN (a-GaN) films on low-cost substrates, for example, borosilicate glass deposited at a low temperature by CS-MBE, are effective for the fabrication of low-cost light emitters on a large scale. For example, a-GaN-based UV detectors have been produced.[6] Using a-GaN films, UV/blue light emission was observed from electrically operated electroluminescent devices (ELDs), the lifetime of which is still short.[7] The short lifetime is due to excess Ga, which was included in the a-GaN films as an emission layer of the ELDs. Reduction the amount of this excess Ga affects device lifetime. In this paper, we report that the a-GaN films on $BaTiO_3$/Cr/borosilicate glass[8] were deposited at different substrate temperatures by CS-MBE. The relationship between excess Ga and its oxidation in a-GaN films was investigated.

2. Experiments

a-GaN films were deposited by CS-MBE. Annealed GaN powder, which was synthesized using the reaction between gallium metal and ammonia, was used as a source material. The GaN powder was kept at 850–860°C in a Knudsen cell (K-cell) during the deposition. During the deposition, no additional nitrogen sources such as ammonia were introduced. Because the GaN source contained hydrogen,[9] the source was annealed in vacuum at 800°C up to 5 h. The color of GaN powder used as a source was yellow before annealing but changed to white after annealing. $BaTiO_3$/Cr/borosilicate glass substrates were used in this study. Cr metal was used for electrodes. For the fabrication of a-GaN-based ELDs, $BaTiO_3$ as an insulator material was prepared by spin coating. Prior to the deposition, chemical cleaning with ultrasonication and thermal cleaning in vacuum for 1 h at 500°C were carried out. The a-GaN films were deposited for 5 h at substrate temperatures of 350–500°C. The deposition rates of the a-GaN films deposited using CS-MBE technique as a function of substrate temperature is shown in Fig. 1. After the deposition, the a-GaN films were placed in air prior to being measured with X-ray photoelectron spectroscopy (XPS). The depth profiles of XPS measurements were observed using Ar^+ ion beam etching (IBE). The etching rate using IBE was 2.4 nm/s.

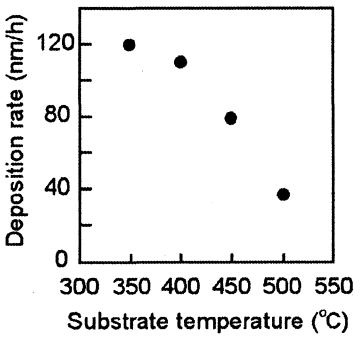

Fig. 1. Deposition rate of amorphous GaN films deposited using CS-MBE as a function of substrate temperature.

3. Results

The Ga 2p XPS spectra of a-GaN films as obtained by XPS with Ar^+ IBE are shown in Fig. 2. In this figure, three spectra drawn with black lines show etching for 0, 5, and 30 s and the gray lines show the fitted curves. Two peaks of the Ga 2p XPS spectra were observed at 1119 and 1121 eV, which correspond to the Ga–N and Ga–O bonds, respectively.[10] No signals corresponding to the metallic gallium were observed in the Ga 2p XPS spectra. In Figs. 2(a) and 2(b), the peak intensity corresponding to Ga–N bonding was higher than that corresponding to Ga–O bonding after etching. Thus, the surface concentration of gallium oxide was higher than in the deposited films. This observation is consistent with the surface oxidation of a-GaN films. The relationship between the atomic concentration ratio of Ga–

*Corresponding author. E-mail address: c+11761@ns.kogakuin.ac.jp

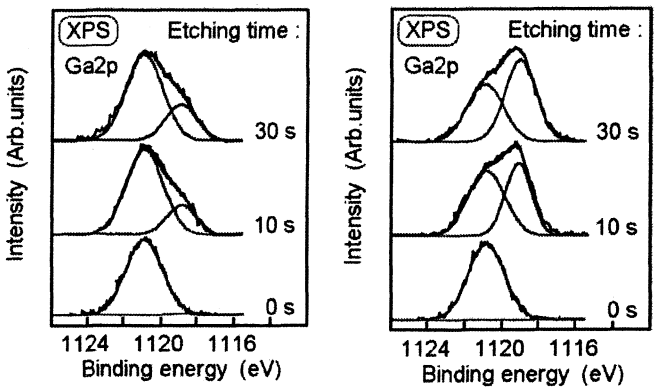

Fig. 2. Ga 2p XPS spectra of amorphous GaN films: (a) at 350°C and (b) at 500°C. Gray lines show the fitting curve. The depth profile of Ga 2p XPS measurements used Ar^+ ion beam etching with etching times of 0, 5 and 30 s.

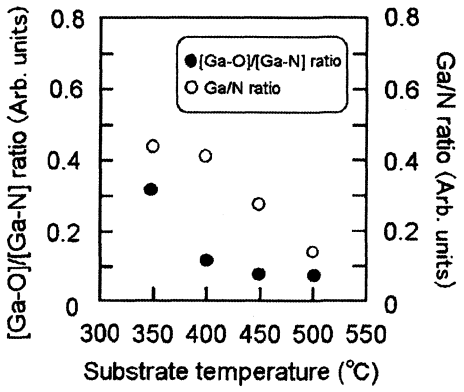

Fig. 3. Atomic concentration ratios of Ga–O/Ga–N in amorphous GaN films at different substrate temperatures.

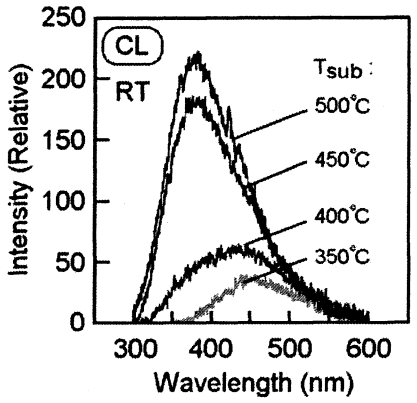

Fig. 4. CL spectra of amorphous GaN films deposited at different substrate temperatures.

O/Ga–N in a-GaN films and the substrate temperature is summarized in Fig. 3. Ga/N ratio as a function of substrate temperature is also shown in Fig. 3. As substrate temperature increased, the atomic concentration ratio of Ga–O/Ga–N decreased. On the other hand, Ga/N ratio also decreased, indicating that excess Ga decreased with increasing substrate temperature. The Ga/N ratio of the GaN layer grown by metal organic vapor phase epitaxy (MOVPE)[11] is 0.15, although we cannot compare the ratio of a-GaN with that of GaN crystals because the ordering conditions of a-GaN are different from those of GaN crystals. The Ga–O/Ga–N ratio of the GaN layer grown by MOVPE was approximately 0.01. Cathodoluminescence (CL) spectra of a-GaN films deposited at different substrate temperatures are shown in Fig. 4. The spectra were measured at room temperature (RT). The spectra started from the near-band edge of GaN. The CL intensity from the UV to blue spectra region increased with substrate temperature.

4. Discussion

Usually, observation of CL or photoluminescence (PL) spectra from the semiconductor films including excess metals at RT is rare. The remarkable point is the observation of the luminescence from the deposited films, although they include excess Ga metal. It was previously reported that excess Ga in a-GaN films deposited by CS-MBE was observed by Auger electron spectroscopy (AES).[7] However, in this study the peak corresponding to metallic gallium was not observed by XPS measurements. The peak from Ga–O bonds as a substitute for metallic gallium was observed in XPS measurements. Thus, these XPS results indicate that the excess Ga metal in a-GaN films oxidized in air and was converted to gallium oxide after deposition.

Furthermore, the surface concentration of gallium oxide was higher than that in the deposited GaN films. We consider that the excess Ga in deposited GaN films creates a wetting layer on the surface of the deposited films. The wetting layer consists of excess Ga that is oxidized in air and converted to gallium oxide. On the other hand, gallium oxide also exists in the inner part of the deposited GaN films. The GaN powder used as a source material contains gallium oxide.

As substrate temperature increased, the amount of excess Ga metal in the deposited GaN films decreased, because the vapor pressure of the excess Ga in the deposited films was higher than that of the GaN in the deposited films.[12] Thus, as substrate temperature increased, the deposition rate of the films decreased. CL intensity increased with decreasing gallium oxide in the deposited films. These results indicate that the reduction of excess Ga leads to the

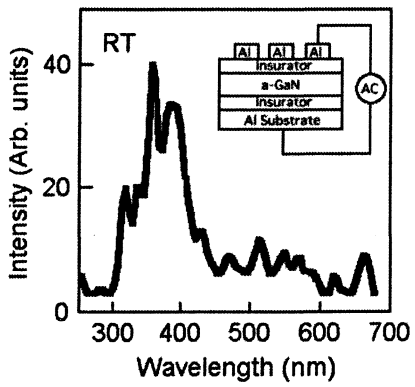

Fig. 5. Electroluminescence spectra of GaN deposited on Al substrate.

reduction of Ga–O bonds in the deposited layer. Reducing the amount of excess Ga is effective in realizing the UV ELDs based on a-GaN.

ELDs were fabricated using a-GaN films. The films were deposited on glass insulators covered on one side with an Al substrate, which was used as the back-surface contact. The deposition temperature was 500°C. After deposition, insulator layers were fabricated on the films and Al electrodes were evaporated on them. We adopted a double-insulator structure as the device structure, which is a capacitor as shown in the inset of Fig. 5. The devices were operated using AC voltage, whose peak-to-peak voltage (V_{pp}) was 350 V; its frequency was 200 Hz. We observed UV light emission from the devices at RT; as shown in Fig. 5. The results indicate that the a-GaN films deposited by CS-MBE are candidates for applications to light-emitting devices operating in the UV spectral region. At present, the detailed characteristics of these devices are under integration. Although the quantum efficiency of the devices is under integration, the UV light emission from the devices indicated that the a-GaN film is a candidate for the low-cost fabrication of UV light emitters.

5. Summary

We have deposited a-GaN films at a low temperature of 350–500°C by CS-MBE. The XPS spectra reveal that excess Ga metal was oxidized in air and converted to gallium oxide. With increasing substrate temperature, the total amount of gallium oxide in the deposited films decreased. The CL intensity of light-emission bands from the UV to the blue spectral regions increased as the total amount of gallium oxide in the deposited films decreased. We demonstrated UV light emission from devices using the a-GaN films. This indicates that the a-GaN film is a candidate for the low-cost fabrication of UV light emitters.

Acknowledgements

We thank Professor Emeritus Y. Suematsu of the Tokyo Institute of Technology for his encouragement. We also thank Professor Emeritus K. Iga, Professor F. Koyama and T. Sakaguchi for their helpful discussions.

1) S. Nakamura, T. Mukai and M. Senoh: Appl. Phys. Lett. **64** (1994) 1687.
2) I. Akasaki and H. Amano: Jpn. J. Appl. Phys. **36** (1997) 5393.
3) T. Honda, K. Sato, T. Hashimoto, M. Shinohara and H. Kawanishi: Phys. Status Solidi A **188** (2001) 587.
4) T. Honda, K. Sato, T. Hashimoto, M. Shinohara and H. Kawanishi: J. Cryst. Growth **237** (2002) 1008.
5) K. Ohkawa, A. Tujimura, T. Nishikawa, S. Yoshii, T. Yokogawa, M. Kubo and Y. Sasai: J. Cryst. Growth **159** (1996) 632.
6) S. Yagi: Jpn. J. Appl. Phys. **38** (1999) L792.
7) T. Honda, Y. Inao, K. Konno, K. Mineo, S. Kumebe and H. Kawanishi: Phys. Status Solidi A **192** (2002) 461.
8) T. Minami, T. Miyata, K. Kitamura, H. Nanto and S. Takata: Jpn. J. Appl. Phys. **27** (1988) L876.
9) K. Nishino and S. Sakai: in *Gallium Nitride and Related Semiconductors*, eds. J. H. Edgar, S. Stride, I. Akasaki, H. Amano and C. Wetzel (INSPEC, London, 1999) p. 367.
10) S. D. Wolter, B. P. Luther, D. L. Waltemyer, C. Önneby, S. E. Mohney and R. J. Molnar: Appl. Phys. Lett. **70** (1997) 2156.
11) M. Kurimoto, M. Shibata, J. Yamamoto, M. Tsubamoto, T. Honda and H. Kawanishi: J. Cryst. Growth **189–190** (1998) 189.
12) A. Koukitu and H. Seki: Jpn. J. Appl. Phys. **36** (1997) L750.

光励起によるAlGaN多重量子井戸型深紫外レーザーの発振特性

―発振波長域240～360 nm―

川西英雄・高野隆好
瀬沼正憲・貫井猛品

応用物理　第74巻　第11号（2005年）抜刷

研究紹介

光励起によるAlGaN多重量子井戸型深紫外レーザーの発振特性
―発振波長域240～360 nm―

川西英雄*・高野隆好**
瀬沼正憲*・貫井猛晶*

最近実現されたAlGaN系深紫外半導体レーザーの光励起による室温レーザー発振についてまとめる．AlGaNはGaNからAlNまでの広いバンドギャップを有し，紫外から深紫外域の波長域で発光可能な半導体である．新しく開発した「交互供給法」により，高Al組成AlGaNの高品質エピタキシャル結晶成長が可能になったことから，AlGaN多重量子井戸型半導体レーザーを製作し，光励起によりレーザー発振が達成された．そのときの最短波長は，室温で241 nmであった．

Keywords : deep-UV, AlGaN-MQW laser, multi buffer layer, alternate source-feeding epitaxy, metal organic vapor phase epitaxy

1. まえがき

最近，紫外線（Ultra Violet : UV）の波長域の光を，ワイドバンドギャップ半導体から効率よく発生しようとする研究が注目されてきている．このような背景のもとで，これまで，インコヒーレント光の短波長化への多くの挑戦が試みられ，発光効率，発光出力が大幅に向上するとともに，265 nm域で発光する発光ダイオードが報告され，研究段階での最短波長の発光ダイオードとなった[1]．

これに対し，日本におけるUVで動作する半導体レーザーの開発研究は，産業界があまり興味を示さなかったこともあり，進展はみられず，停滞気味で今日に至っている．一方，海外では，特に米国では，この分野の研究に重点配分し，それを機に活発な研究が進んでいる．

半導体レーザーとして，これまでに達成された最短発振波長は，電流注入型半導体レーザーでは350.9 nmおよび354.7 nmであった[2,3]．これに対し，光励起型半導体レーザーでは328 nmであった[4]．

最近，筆者らは，反応管内に導入した材料ガス間の中間反応を防ぐために「交互供給法（Alternate Source-Feeding Epitaxy : ASFE）」を新しく開発することで，高品質AlGaN半導体結晶を成長し，世界で最短波長の光励起レーザー発振することに成功した[5]．

この「交互供給法（ASFE）」は，その前に廣木・小林が報告していた「フロー・レート・モジュレーション・エピタキシー」[6]とよく似てはいるが，その基本的な考え方が異なる．すなわち，高品質なAlNおよびAlGaNエピタキシャル層を得るために，①供給原料の中間反応を積極的に抑制すること，および②1サイクルに成長できるエピタキシャル成長層厚は，5～9分子層あるいはそれ以上の任意の厚さに調整でき，結晶成長速度が大きく設定できるなどの特長がある．この技術を開発したことで，紫外から205～210 nmまでの深紫外域（Deep-Ultra Violet : Deep-UV）での高効率発光実現の可能性が，視野に入りつつある．その一例として，この方法によって成長したAlGaN多重量子井戸型半導体レーザーで，241.5 nmの深紫外域でのレーザー発振が達成され，また，発振しきい値も大幅に低下した[5,7]．

今後，「半導体ダイオード」とし，電流注入型半導体レーザーダイオードを実現するためには，多くの研究課題が残されているが，この分野の研究の発展を願い，最近得た研究成果をまとめた．

2. 紫外・深紫外半導体レーザーに適合する混晶半導体

図1は，紫外から深紫外域に対応するワイドバンドギャップ半導体のバンドギャップE_gと格子定数（六方晶系半導体ではa軸の格子定数）との関係を示している．

図1に示すように，この波長域に対応できる（ダブルヘテロ構造を実現可能な半導体のみを記した）半導体は，AlNとGaN，およびBNからなるBAlGaN四元混晶半導体が中心的役割を果たすことになる．ここでは，AlNとGaNと

* 工学院大学工学部電子工学科　〒192-0015　八王子市中野町2665-1．e-mail : kawanisi@cc.kogakuin.ac.jp
** 松下電工(株) 新規商品創出技術開発部　〒571-8686　門真市大字門真1048．
分類番号　7.7, 1.8
Deep-UV lasing (240-360 nm) of AlGaN multi-quantum well lasers under optical pumping. Hideo KAWANISHI*, Takayoshi TAKANO**, Masanori SENUMA* and Takeaki NUKUI*.
* Department of Electronic Engineering, Faculty of Engineering, Kohgakuin University (2665-1 Nakano-machi, Hachioji 192-0015)
** New Product Technologies Development Department, Matsushita Electric Works, Ltd. (1048 Ooaza Kadoma, Kadoma 571-8686)

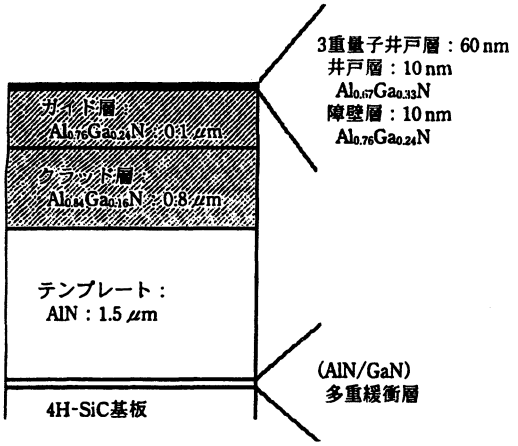

図3 AlGaN多重量子井戸型深紫外半導体レーザーの構造(室温において241.5 nmでレーザー発振した試料).

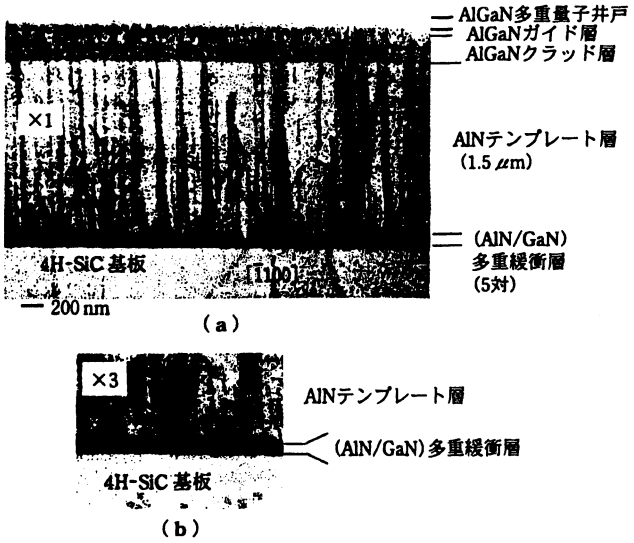

図4 AlGaN多重量子井戸型深紫外半導体レーザーの断面TEM写真. 観察は[$\bar{1}$100]面方位から行った. (a)基板およびテンプレートを含む広域での断面TEM写真(このときの倍率を基準とし, ×1と図中に表記). 最上部の量子井戸に至るまで, 貫通転位の大幅な減少が見て取れる. (b)基板および(AlN/GaN)多重緩衝層付近の拡大断面TEM写真((a)の断面をさらに3倍に拡大. ×3と表記). この緩衝層の界面において, 貫通転位の減少がみられる.

4. AlGaN多重量子井戸型半導体レーザー

①(AlN/GaN)-MBLS構造と, ②ASFE法による減圧・有機金属気相エピタキシャル成長法(Low Pressure Metal Organic Vapor Phase Epitaxy: LP-MOVPE)とを利用し, AlGaN多重量子井戸型半導体レーザーを製作した. その基本的な構造を, 図3に示している. 量子井戸層のAl組成を変化させることで半導体レーザーの発振波長を変えるが, 障壁層のAl組成は, 以下のように決定した. すなわち, 量子井戸と障壁層との間のバンドギャップ差 ΔE_g は約0.32 eV以上, 活性層とクラッド層の間の比屈折率差 Δ が Δ=6%と設計した.

SiC(4Hおよび6H)基板上に(AlN/GaN)-MBLSを成長後, 厚さ約1.5 μmのAlNテンプレートを成長, その上にAlGaNクラッド層, AlGaNガイド層, その上にAlGaN多重量子井戸(3対の量子井戸, 井戸層10 nm, 障壁層10 nm)を成長した. 上部のガイド層およびクラッド層は半導体レーザーの活性領域の励起効率をよくするために除いた. ここで, AlNテンプレートは, 基本的にバルクの格子定数に一致させるか, 若干の圧縮ひずみを加える程度にする.

こうすることで, その上に成長した結晶の ω および ϕ に対するXRC半値幅が最小値をとり, 結晶品質が向上するからである[8]. なお, クラッド層, ガイド層および量子井戸のAl組成は, それぞれ異なっており, 光閉じ込め, およびキャリア閉じ込めを考慮して決定した. また, クラッド層以降を「交互供給法」で成長し, それ以外の層は, 通常の同時供給法で成長した.

図4(a), (b)には, このようにして成長した結晶の断面透過電子顕微鏡写真(Transparent Electron Microscope: TEM)を示している. 基板と多重緩衝層の境界領域では, 貫通転位が急激に減少し, さらに, AlNテンプレートで転位が減少, また, クラッド層, およびガイド層の界面でも, この貫通転位は減少していることがわかる. 量子井戸活性層における貫通転位密度は, おおよそ 10^7〜10^8 cm^{-2} と見積もられた. また, 表面のエッチピット密度を別途求めたが, ほぼ同じ値の範囲にあった. したがって, このMBLSは貫通転位をその界面で停止し, GaNの結晶品質を向上させるだけでなく, AlNの結晶品質を向上させるのに有効な方法であり, 今後のさらなる研究の発展を望みたい.

一方, 図5(a), (b)には, AlNとBAlN, およびGaNとBGaNの各波長域での屈折率分散特性をそれぞれまとめた[14]. また, AlGaNのバンドギャップ E_g は, フォトルミネッセンス測定から測定したバンドギャップをもとにして求めた次式で計算した(室温).

$$E_g(\mathrm{AlGaN}) = 3.4057 + 2.293x + 0.5x^2$$

ここに, x はAlGaNにおけるAlの固相比である.

5. AlGaN多重量子井戸型半導体レーザーの発振特性

光励起用の半導体レーザーは,「劈開法」によって製作した. SiC基板上に成長した六方晶系窒化物半導体では, 基板の劈開面と, その上に成長した窒化物半導体の「劈開面」は一致しており, 容易にファブリー・ペロー共振器が構成できる[15].

なお, 劈開で製作した反射鏡の電力反射率は, 図5に示すように, AlGaNの屈折率が紫外, 深紫外域で可視域に比較して小さく, 反射率はこの波長域では約19%程度以下と小さい.

図6は, 発振波長の異なるAlGaN多重量子井戸型半導体レーザーの室温での発振スペクトルをまとめたものである. 発振波長は, それぞれ, 359.5 nm, 300.6 nm, 270.4 nmと241.5 nmである. ここで, 300.6 nmで, レーザー発振

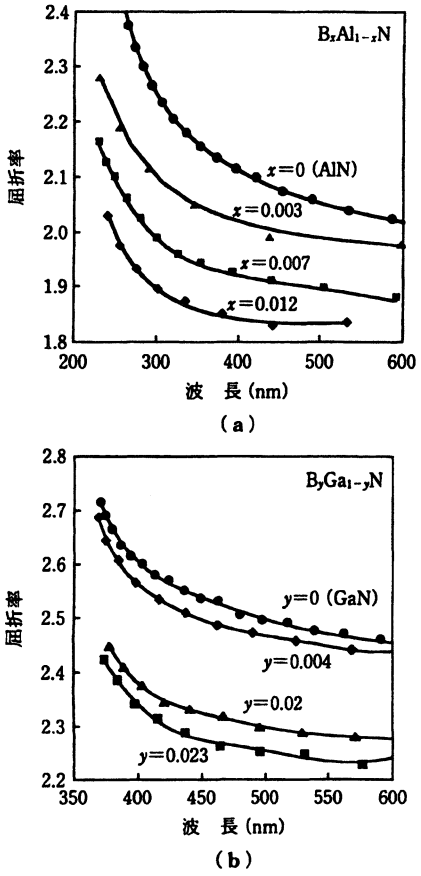

図5 (a) AlN と BAlN, および (b) GaN と BGaN の各波長での屈折率分散特性.

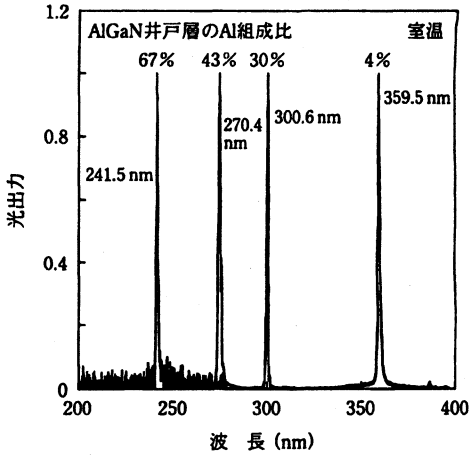

図6 室温における AlGaN 多重量子井戸型半導体レーザーの各発振波長スペクトル. 測定温度はすべて室温である.

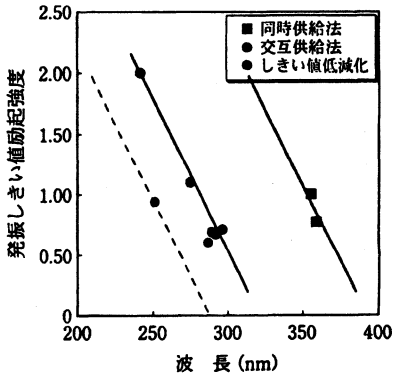

図7 発振しきい値励起強度のレーザー発振波長依存性. 図には, 同時供給法および交互供給法による結晶成長法が使用されている. 発振しきい値は, 発振波長が 359.5 nm の試料(同時供給法(■で記す)により成長した試料)のしきい値で規格化した. 交互供給法(●で記す)により製作した半導体レーザーの発振しきい値が, 図のように低下した.

の発振波長のスペクトル半値幅が最も狭いのは, 図7に示すように, この試料の発振しきい値が小さく, 励起強度が高いからである.

図7は, 光励起によって紫外から深紫外域の波長域でレーザー発振した試料の, 室温における発振しきい値励起強度のレーザー発振波長依存性を, 代表的なレーザー発振波長に対してまとめたものである. 同時供給法, 交互供給法いずれの場合も, 図に実線で示したように, 発振波長が短波長になるに従い, 発振しきい値励起強度は増加する傾向があるが, その物理的な合理的説明は今後の詳しい解析と分析とによって明らかになるであろう. 結果として発振波長を短くするに従って, 発振しきい値励起強度は高くなる.

現時点での主な理由は, 結晶品質に依存することが大きいと考えている. 例えば, ここで, 図7で最も長波長である 359.5 nm の試料 (図中で■で記している) は, 通常の同時供給法によって成長した. これに対し, 300 nm 以下の発振波長の試料 (図中で●で示した) は, 交互供給法によって成長した. 同時供給法と交互供給法の成長法による発振しきい値の差を, これらの実線の値で比較すると, 交互供給法で成長した場合, 規格化発振しきい値励起強度は, 約 1/8 に減少している. なお, 発振しきい値は, 359.5 nm で発振する半導体レーザーの発振しきい値で規格化した値で表記した. さらに, 短波長域で発振する試料では, 結晶成長条件をより調整することで, さらなる低しきい値化も可能であろう. 今後, AlGaN 結晶の高品質化に対する改善を期待する.

図8は, レーザー発振前・後の室温における発光スペクトルの変化を示している. 励起強度を増加するに従って, 自然放出光のピーク波長より長波長側でレーザー発振した. そのときの自然放出光 (λ=239.87 nm) と誘導放出光 (λ=241.55 nm) との波長差は約 1.68 nm であった. 一般的には, 室温では, 自然放出光のピーク波長にきわめて近いところか, 若干長波長側の波長で発振する傾向が強い.

一方, 241.55 nm の最も短波長でレーザー発振した半導体レーザーの発振波長の温度特性も求めた. 特徴的なところは, 約 170 K 以下の低温領域では, 発振波長は, 約 0.009 nm/K の温度係数で変化するのに対し, それ以上の温度領域では, 0.026 nm/K と温度係数が大きい. その主な理由は, 今後の検討を必要とするが, 発光プロセスが変化して

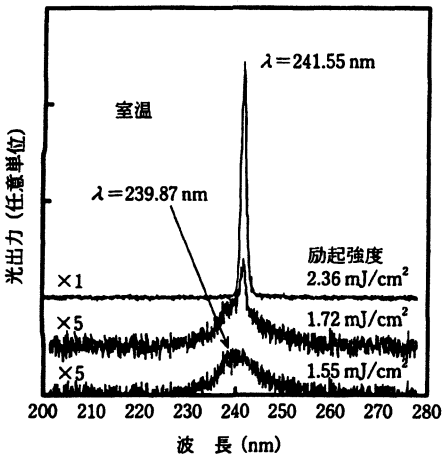

図8 励起強度を変化させた場合の発光スペクトルの変化．自然放出光の発光ピーク波長はλ=239.87 nmであるのに対し，レーザー発振波長は241.55 nm．

いると考えるほうが妥当であろう．なお，上の温度係数をエネルギーに変換した場合には，−0.19 meV/K，−0.55 meV/Kとなり，紫外および深紫外で発振する半導体レーザーの発振波長は，温度に対して比較的安定であるといえる．これは，ワイドバンドギャップ半導体の利点である．

6. むすび

ここでは光励起ではあるが，最近実現した，AlGaN多重量子井戸型深紫外半導体レーザーのレーザー発振についてまとめた．これまでに達成した最短波長は，室温で241.55 nmであった．このように，深紫外域といった未開発の波長域で半導体レーザーのレーザー発振が実現できた理由として，以下の2点があげられる．

（1）(AlN/GaN) 多重緩衝層構造 (MBLS) の導入
（2）交互供給法 (ASFE法) による高品質AlGaNのエピタキシャル層の実現

である．これらの技術の導入によってAlGaN結晶が高品質となり，その結果，世界で最短波長のレーザー発振が実現した．

この研究成果は，AlGaN結晶あるいは格子整合系BAlGaNなどのワイドバンドギャップ半導体結晶を利用し，深紫外域で動作する半導体レーザーを実現できる可能性を示し，今後の電流注入型深紫外半導体レーザーへの研究の発展の出発点になることを希望している．特に，ワイドバンドギャップ半導体の伝導性制御は今後に残された大きな研究課題である．ここでの研究を出発点に，この研究を進める研究機関，研究者が増えることを期待する．

文 献

1) Y. Bilenko, A. Lunev, X. Hu, J. Deng, T. M. Katona, J. Zhang, R. Gaska, M. S. Shur, W. Sun, V. Adivarahan, M. Shatalov and A. Khan: Jpn. J. Appl. Phys. **44**, L98 (2005).
2) M. Kneissl, D. W. Treat, M. Teepe, N. Miyashita and N. M. Johnson: Appl. Phys. Lett. **82**, 4441 (2003).
3) K. Iida, H. Kasugai, S. Mishima, Y. Miyake, A. Honshio, T. Kawashima, A. Miyazaki, M. Iwaya, S. Kamiyama, H. Amano and I. Akasaki: Jpn. J. Appl. Phys. **43**, L499 (2004).
4) T. J. Schmidt, Y. H. Cho and J. J. Song: Appl. Phys. Lett. **74**, 245 (1999).
5) T. Takano, Y. Ohtaki, Y. Narita and H. Kawanishi: Jpn. J. Appl. Phys. **43**, L1258 (2004).
6) M. Hiroki and N. Kobayashi: Jpn. J. Appl. Phys. **42**, L2305 (2003).
7) T. Takano, Y. Narita, A. Horiuchi and H. Kawanishi: Appl. Phys. Lett. **84**, 3567 (2004).
8) Y. Ishihara, J. Yamamoto, M. Kurimoto, T. Takano, T. Honda and H. Kawanishi: Jpn. J. Appl. Phys. **38**, L1296 (1999).
9) M. Kurimoto, T. Nakada, Y. Ishihara, M. Shibata, T. Honda and H. Kawanishi: Jpn. J. Appl. Phys. **38**, L551 (1999).
10) H. Kawanishi, Y. Ishihara, M. Kurimoto, T. Takano and T. Honda: *Abstr. 2nd Japan-Korea Joint Workshop Short-Wavelength Semiconductor Optoelectronic Device and Materials, Chiba, 1999*, p. 92.
11) H. Kawanishi, Y. Ishihara, M. Horie, T. Takano and J. Yamamoto: *Abstr. 3rd Japanese-German Workshop Recent Progress in Advanced Materials, Devices, Processing and Characterization, Berlin, 2000*, p. 31.
12) Y. Kuga, T. Shirai, M. Haruyama, H. Kawanishi and Y. Suematsu: Jpn. J. Appl. Phys. **34**, 4085 (1995).
13) H. Kawanishi and H. Ikeda: Jpn. J. Appl. Phys. **30**, 27 (1991).
14) S. Watanabe, T. Takano, K. Jinen, J. Yamamoto and H. Kawanishi: Phys. Status Solidi c **0**, 2691 (2003).
15) 川西英雄，末松安晴，白井俊雄，久我裕一郎：光反射構造およびその製法ならびに光デバイス，特願平7-90907 (1995).

(2005年7月20日 受理)

川西 英雄
1973年工学院大学大学院工学研究科電気工学専攻修士課程修了．同年，東京工業大学電子物理工学科助手．80年より工学院大学．講師，助教授を経て，91年電子工学科教授．工学博士．専門は光エレクトロニクス．75年よりGaAs系，InP系分布反射型半導体レーザーの研究を経て，97年より深紫外半導体レーザーの研究に従事．

高野 隆好
1999年工学院大学工学部電子工学科卒，01年同大大学院工学研究科電気・電子工学専攻修士課程修了，04年同大大学院博士後期課程修了．同年，松下電工(株)先行・融合技術研究所入所．工学博士．窒化物半導体を用いた照明器具の開発に従事．

瀬沼 正憲
2004年工学院大学工学部電子工学科卒．現在，同大大学院工学研究科電気・電子工学専攻修士課程に在籍．紫外域半導体レーザーの短波長化の研究に従事．

貫井 猛晶
2004年工学院大学工学部電子工学科卒．現在，同大大学院工学研究科電気・電子工学専攻修士課程に在籍．紫外域半導体レーザーの発振特性の研究に従事．

TM-mode lasing and anisotropic polarization properties of AlGaN multiple quantum well lasers in deep-ultraviolet spectral region

Hideo Kawanishi, Masanori Senuma, and Takeaki Nukui

Department of Electronic Engineering,
Kohgakuin University,
Nakano-machi 2665-1, Hachioji-shi, Tokyo 152-0015, JAPAN.

Abstract.

We investigated rolls of crystal-field split-off valence band (CH VB) in the deep-UV laser by measuring a transverse-magnetic-field (TM)-mode polarization of lasing and spontaneous surface and edge emissions above and below the lasing threshold from the AlGaN multiple-quantum-well (MQW) laser at 240.8 nm and the anisotropic optical properties of c-plane $Al_xGa_{1-x}N$ multiple quantum wells and m-plane $Al_xGa_{1-x}N$ single layer. These results indicate that CH VB plays an important role in (E//c) polarization and anisotropic emissions from $Al_xGa_{1-x}N$ with $x \geqq 0.5$.

Keywords: AlGaN MQW, deep-UV laser, TE-mode and TM-modes, anisotropic polarization, crystal-field sprit-off valence band

1. Introduction

Wurtzite-type BN, AlN, GaN, and related semiconductors are attractive materials for the production of laser diodes and light-emitting diodes with emission in the spectral range from ultraviolet (UV) to deep UV. The band structures and optical characteristics of GaN and AlN have been theoretically analyzed.[1-3] Unique optical properties of AlGaN have been pointed out experimentally in a few studies.[4, 5] The room temperature lasing of an AlGaN MQW laser was demonstrated in the spectral region from about 240 nm to 355 nm under optical pumping.[6, 7] In addition, we have achieved lasing at the shortest recorded wavelength of 228.9 nm at a lower temperature than 170 K.[8] To produce such lasers, high-quality AlGaN MQW structures, and cladding and guide layers were grown on 6H and 4H-SiC substrates using an epitaxial growth technique called alternate source-feeding epitaxy (ASFE).[7]

In this study, anisotropic polarizations of UV and deep-UV lasing and spontaneous surface and edge emissions from c-plane AlGaN MQW and m-plane AlGaN single layer grown on a SiC substrate were experimentally investigated in the spectral region from about 240 nm to 360 nm.

2. Experiments and Discussions

The sample structure was the same as that of AlGaN MQW lasers lasing in the 240 nm ~355 nm spectral region.[6, 8] A detailed description of the growth conditions and layer structure of the AlGaN MQW laser can be found in Refs.6 and 8.

Figure 1 is our experimental results on room temperature lasing of AlGaN MQW laser grown on c-plane SiC substrate in the ultraviolet (UV) and deep-UV spectral region under optical pumping. The shortest lasing wavelength was around 240nm at room temperature.

We have carefully investigated the optical polarization behavior of the spontaneous surface and edge emissions from

the UV and deep-UV AlGaN MQW. Figure 2 summarizes our experimental results on spontaneous edge emission from

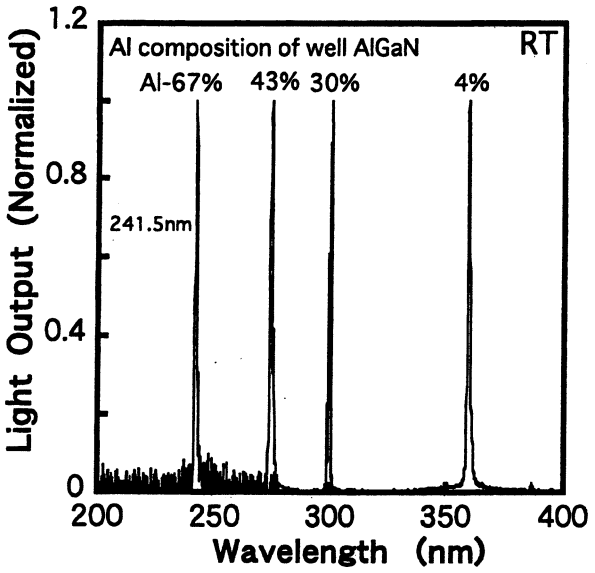

Fig. 1. Room temperature lasing spectrum of AlGaN MQW lasers

c-plane AlGaN MQW laser. As a result, symmetric and isotropic TE-mode (E//c) and TM-mode (E⊥c) emissions were observed for both the surface and edge emissions at 355.1 nm from the c-plane $Al_xGa_{1-x}N$ MQW (x=0.04) below the lasing threshold.[9, 10] However, only TM-mode emission was observed for the spontaneous edge emission at 240.8 nm from the c-plane $Al_xGa_{1-x}N$ MQW structure (x=0.66). This fact indicates that the spontaneous surface and edge emissions from the c-plane $Al_xGa_{1-x}N$ MQW structure (x=0.66) were polarized anisotropically.

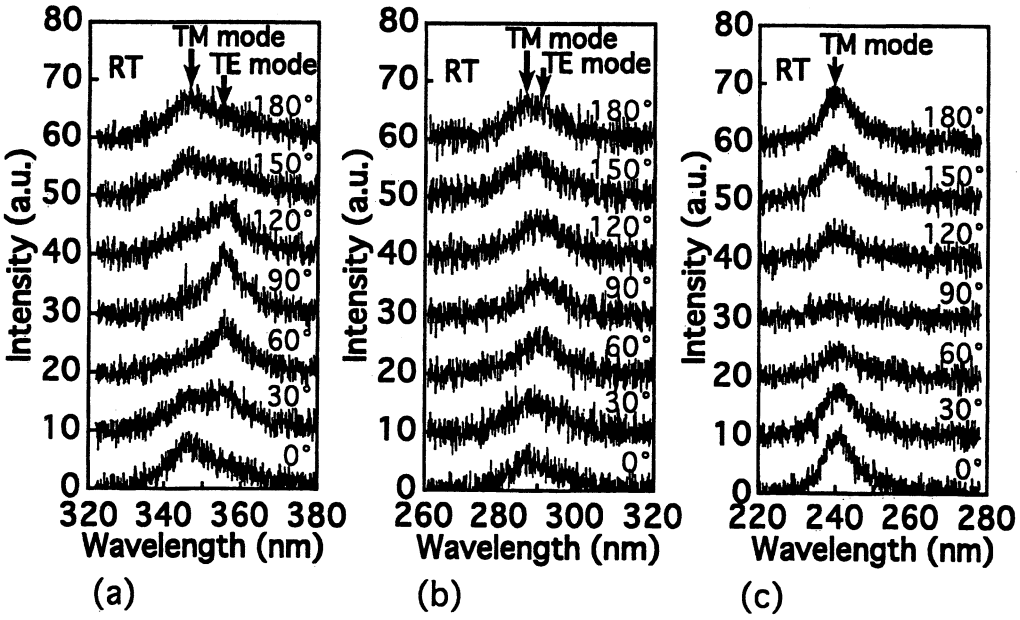

Fig.2. Polarization behaviors of spontaneous edge emission of AlGaN MQW lasers below threshold at room temperature. a TE- and TM-mode emissions, b TM- and weak TE-mode emissions, and c mostly TM-mode emission for AlGaN MQW lasers at 355.1, 289.8, and 240.8 nm, respectively.

In addition, we have examined the optical characteristics of the m-plane $Al_xGa_{1-x}N$ (x=0 to 0.76) single epitaxial layers (1.5 μm thick) grown on the (1-100) m-plane 6H-SiC substrate to clarify the mechanism of the anisotropic optical properties. Figure 3 summarizes our experimental results on spontaneous surface emission intensity from the m-plane GaN and AlGaN single layers. As we expected, strong surface emission was obtained from the m-plane $Al_xGa_{1-x}N$ (x=0 to 0.76) epitaxial single layers in the spectral region from 240 nm to 365 nm, but surface emission from the m-plane AlGaN decreased for wavelengths shorter than 240 nm, which is probably due to the poor crystalline quality of our m-plane AlGaN single layer compared with the c-plane AlGaN MQW.

On the other hand, The lasing light from the c-plane AlGaN MQW, which was detected through the cleaved m-plane facet, was optically polarized into the TM mode (E//c) for the c-plane laser operating at 240.77 nm, but into the TE mode (E⊥c) for the c-plane laser operating at 355.12 nm as shown in Fig. 4 (a) and (b).

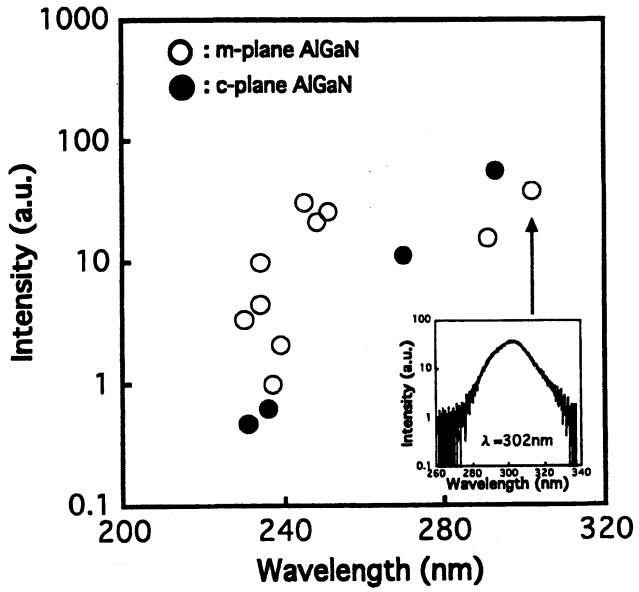

Fig.3. Surface emission intensity through *m* plane, plotted as open circles as function of emission wavelength from *m*-plane AlGaN single epitaxial layers grown on 1–100 *m*-plane 6*H*-SiC substrate

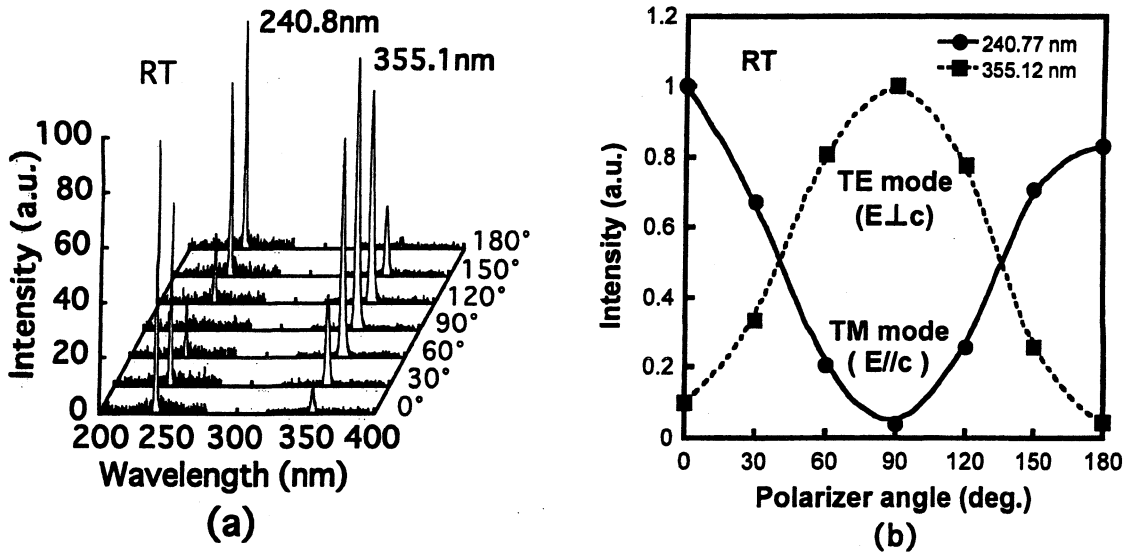

Fig. 4 (a) Polarization behaviors of lasing light of AlGaN MQW lasers operating at 240.8 and 355.1 nm. The polarizer angles of 0° and 180° indicate TM-mode polarization $E \; c$ axis , whereas that of 90° indicates TE-mode polarization $E \, c$ axis .

(b) Optical polarization characteristics of the lasing light from AlGaN MQW laser operating at 355.12 nm dotted line and at 240.77 nm solid line .

We also examined the energy difference between the TE- and TM-mode from the surface emission both from the c- and m-plane AlGaN with different Al composition. Figure 4 summarizes our experimental result on the energy difference and spontaneous emission intensity difference. Our experimental results on the optical properties, and energy difference between light-hole (LH) or heavy-hole (HH) valence band (VB) and crystal-field split-off hole (CH) VB suggest that the CH VB becomes the nearest VB to conduction band rather than the HH and LH VBs, then E//c polarization and anisotropic characteristics of emission are detected, because the CH band is active only to the polarized emission of E//c. Therefore, the dipole moment is formed only in parallel to the c-axis. This characteristic of the CH band is the origin of the weak surface emission from the c-plane AlGaN MQWs in the spectral region from 228 nm to 290 nm. We conclude that the energy difference between HH or LH VB and CH VB was zero at $x \approx 0.73$-0.78 for c- and m-plane $Al_xGa_{1-x}N$ as shown in Fig. 5. These results suggest a shorter carrier lifetime (larger optical gain) in the CH VB than in the HH and/or LH VBs.

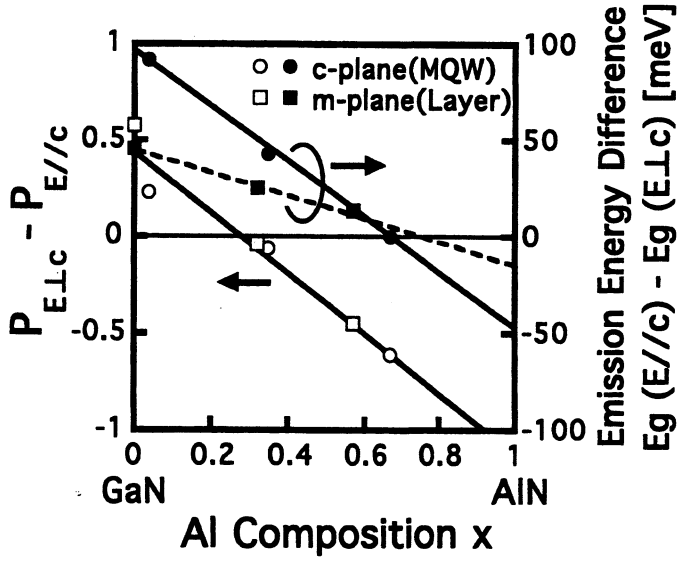

Fig. 5. Normalized polarization difference $P_E \, c$-$P_E \, c$ and emission energy difference $E_g \, E \, C$ -$E_g \, E \, C$ as functions of Al composition x for c-plane $Al_xGa_{1-x}N$ MQWs and

m-plane $Al_xGa_{1-x}N$ single layers. All data were taken at room temperature.

3. Summary

We investigated polarization properties of deep-UV lasing and spontaneous surface and edge emissions from c-plane and m-plane AlGaN MQW structures and single layers. The c-plane AlGaN MQW, which was detected through the cleaved m-plane facet, was optically polarized into the TM- mode (E//c) for the c-plane laser operating at 240.77 nm, but into the TE-mode (E⊥c) for the c-plane laser operating at 355.12 nm. The optical properties, and energy difference between LH or HH and CH suggest that the CH becomes the nearest VB to conduction band rather than the HH and LH, then E//c polarization and anisotropic characteristics of emission are detected. The energy difference between HH or LH and CH was zero at $x \approx 0.73$-0.78 for c- and m-plane $Al_xGa_{1-x}N$. These results suggest a shorter carrier lifetime (larger optical gain) in the CH VB than in the HH and/or LH VBs.

References

[1] R. Dingle, D. D. Sell, S. E. Stokowski, and M. Ilegems, Phys. Rev. (B), **4**, 1211 (1971).

[2] M. Suzuki, T. Uenoyama, and A. Yanase, Phys. Rev. **B 52**, 8132 (1995).

[3] J. Li, K. B. Nam, M. L. Nakarmi, J. Y. Lin, et. al, Appl. Phys. Lett. **83**, 5163 (2003).

[4] K. B. Num, J. Li, M. L. Nakarmi, J. Y. Lin, and H. X. Jiang, Appl. Phys. Lett. **84**, 5264 (2004).

[5] J. Shakya, K. Knabe, K. H. Kim, et. al, Appl. Phys. Lett. **86**, 091107 (2005).

[6] T. Takano, Y. Narita, A. Horiuchi, and H. Kawanishi, Appl. Phys. Lett. **84**, 3567 (2004).

[7] T. Takano, Y. Ohtaki, Y. Narita, and H. Kawanishi, Jpn. J. Appl. Phys. **43**, L1258 (2004).

[8] H. Kawanishi, M. Senuma, T. Nukui, et.al, 6th International Conf. on Nitride Semiconductors, Bremen, Germany, Tu-PD2-1, 2005.

[9] H. Kawanishi, M. Senuma, and T. Nukui, Appl. Phys. Lett. **89**, 041126(2006).

[10] H. Kawanishi, M. Senuma, M. Yamamoto, E. Niikura, and T. Nukui, Appl. Phys. Lett. **89**, 081121(2006).

Investigation on Conductivity at the GaN/AlN/SiC Substrate Interface for Vertical Nitride Power FETs

Y. Wakamiya, F. Hasegawa and H. Kawanishi

Department of Electronic Engineering, Kogakuin University, NAKANO-cho, HACHIOHJI, Tokyo, 192-0015 JAPAN

Received zzz, revised zzz, accepted zzz
Published online zzz

PACS 73.40.Kp, 81.15.Kk, 81.15.Gh

Power FETs are the next promising application of AlGaN/GaN hetero-structures. In order to reduce the device size and thermal conductivity, power nitride FETs should be a vertical structure on a conductive SiC or Si substrate. An AlN or/and AlN/GaN multi-buffer layer is inevitable to grow GaN on a SiC or Si substrate by MOVPE, therefore, current flow at the GaN/AlN/SiC interface is one of the important issues to be investigated. 17 to 350 nm AlN layers were grown on 8° off n⁻-epitaxial 4H-SiC substrates and on a GaN/AlGaN/AlN/SiC structure by alternate-source-feeding MOVPE. Ni/AlN/n⁻-epi-4H-SiC sample showed Schottky characteristics except 350nm thick AlN sample, indicating that the AlN was not working as an insulator. On the other hand, Ni/AlN/GaN/n⁻-epi-4H-SiC sample turned out MIS characteristics for the same AlN thickness. This difference can be explained by the heterovalent atomic structure at the interface between AlN(III-V) and SiC(IV-IV).

1 Introduction Power FETs are the next promising application of AlGaN/GaN hetero-structures after commercialization of blue LEDs and violet LDs. In order to reduce the device size and thermal conductivity, power nitride FETs are also required to have vertical current flow on a conductive SiC or Si substrate [1] as in the case of Si IGBTs. An AlN or/and AlN/GaN multi-buffer layer is inevitable to grow GaN on a SiC or Si substrate by MOVPE. On the other hand, AlN/SiC hetero-structure has been thought as a candidate of SiC MIS FET [2,3], though it has not been successful. The AlN/SiC hetero-structure is electrically hetero-valent i.e. III-V/IV-IV atomic interface structure. Electrical properties of hetero-valent structure have been investigated on a ZnSe/GaAs hetero-structure theoretically [4] and experimentally [5]. However, it has not been studied well on the GaN/SiC or AlN/SiC.

The purpose of this work is to investigate the conductivity at the GaN/AlN/SiC substrate interface, taking into account the hetero-valent property of AlN/SiC, for future vertical power FETs.

2 Experimental Growth of GaN, AlN and AlGaN on SiC substrate was performed by a LP-MOVPE. Details of the growth procedure are described in our previous reports [6]. 17 to 350 nm thick, non-doped AlN layers were grown directly on just Si face n⁺-4H-SiC or 8° off n⁻-epitaxial 4H-SiC substrates by alternate-source-feeding epitaxy (ASFE); 2 sec tri-methyl-aluminum (TMA) supply and 2 sec NH_3 supply without a sweep-out interval [7].

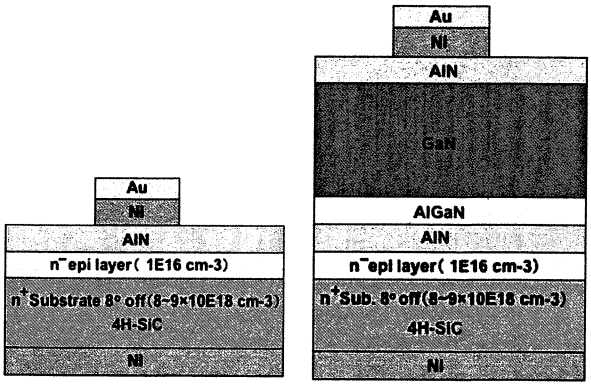

Figure 1 Measure sample structures.

An AlN/GaN/$Al_{0.1}Ga_{0.9}N$/AlN/SiC structure was also prepared for comparison of the AlN/SiC and AlN/GaN hetero-interfaces, because SiC and GaN have a similar bandgap but are consist of different atomic groups. The final sample structures are shown in Fig.1.
Au/Ni(100/100nm) Schottky contacts were deposited by an E-gun vacuum evaporator with a diffusion pump ($1x10^{-6}$ Torr) through a metal mask and the back Ni(100nm) contact was sputtered.

3 Results and discussion Ni/AlN/just n^+-SiC sample showed Ohmic current voltage (I-V) characteristics without any insulating MIS characteristics. Ni/AlN/n^--epi-4H-SiC sample showed Schottky characteristics except 350nm thick AlN sample, as shown by a curve tracer I-V (a) and logarithmic scale forward I-V (b) characteristics in Fig.2. The reverse leakage current is less than 10uA with the reverse breakdown voltage of more than 50V (Fig. 2(a)) and the ideality factors are less than 2.0 (Fig. 2(b)), indicating that the samples are reasonable Schottky diodes, though the series resistance increases with increase of the AlN thickness. Since the AlN should be high resistive, the current is considered to flow with a space charge limited current in the AlN layer as far as the AlN is thin enough.

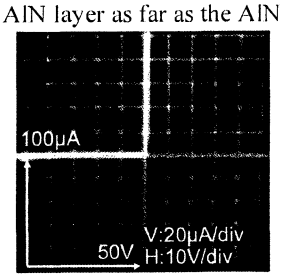

(a)

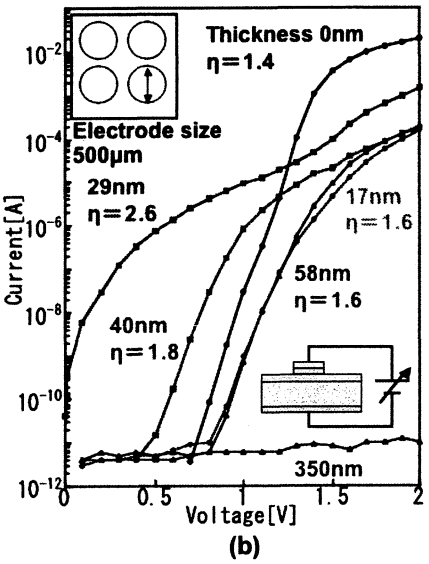

(b)

Figure 2 I-V characteristics of Ni/AlN/n^--epitaxial 4H-SiC. (a) Linear curve tracer I-V on the 17nm thick AlN sample. (b) Logarithmic scale, forward I-V for samples with different AlN thickness.

Since non-doped AlN should be insulator and the conduction band offset between AlN and SiC is about 1.3eV [8], we expected MIS characteristics as far as the AlN thickness is more than 10nm. However, the forward current flew as if there is no barrier between AlN and SiC. Since the ideality factors in Fig.2 are more than unity, the current should not be tunneling current due to piezoelectric field.

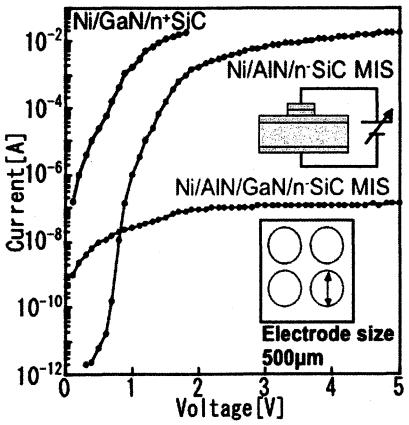

(a)

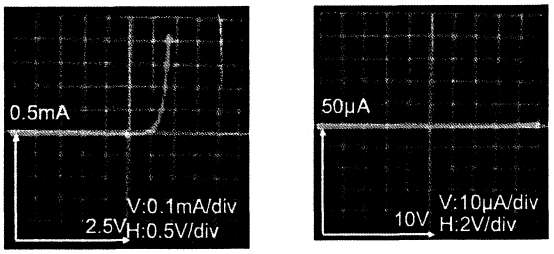

(b) (c)

Figure 3 Comparison of I-V characteristics of the samples with different structures; Ni/GaN/AlGaN/n^+-SiC, Ni/AlN/n^--epi-SiC and Ni/AlN/GaN/AlGaN/AlN/n^--epitaxial 4H-SiC. (a) Logarithmic scale, forward I-V. (b) Linear curve tracer I-V for the Ni/GaN/AlGaN/n^+-SiC sample. (c) Linear curve tracer I-V for the Ni/AlN/GaN/AlGaN/AlN/n^--epitaxial 4H-SiC sample.

In order to see effect of conduction band offset, we made Ni/AlN/GaN/AlGaN/AlN/n^--epi-4H-SiC sample in the same way with only difference of insertion of GaN layer between AlN and SiC. Since the band gap of GaN and the band offset of GaN to AlN are similar to those of SiC, similar results should be obtained if there is any problem in the AlN layer for the forward current flow. A Ni/GaN/$Al_{0.1}Ga_{0.9}N$/n^+-SiC sample was also made to see resistivity of the GaN layer. The results are shown in Fig.3. Ni/GaN/AlGaN/n^+-SiC and Ni/AlN/n^--epi-SiC samples showed Schottky characteristics as shown in Fig.3 (a) ---logarithmic scale I-V--- and in Fig. 3(b) ---linear curve tracer I-V---, but no forward and reverse currents flew for the Ni/AlN/GaN/AlGaN/AlN/n^--epi-4H-SiC sample as shown in Fig.3 (a) and in Fig. 3(b) ---linear curve tracer I-

V---. Difference is that there is AlN/GaN hetero barrier for the Ni/AlN/GaN/AlGaN/AlN/n⁻-epi-4H-SiC sample instead of direct AlN/SiC hetero barrier. It should be noted that AlN and GaN are the same III-V compound with different bandgap whereas SiC is IV-IV compound with similar bandgap difference.

The results can be explained by heterovalent atomic structure at the interface between AlN(III-V) and SiC(IV-IV). Since the SiC substrate is Si face and AlN grown on it should be Al polarity. there should be Si-N bonds at the AlN and SiC interface as shown in Fig.4(a). Number of electrons around the Si-N bond is 9 whereas those of Al-N and Si-C bond are 8. Because of smaller bandgap of SiC than that of AlN, extra electrons at the interface drop to the SiC side of the interface and make negative space charge at the SiC surface. The N atom at the interface loses electron and are positively charged. Thus dipoles are made at the AlN and SiC interface, and the energy band diagram at the interface is modified as shown in Fig.4(b). Due to the strong electric field resulting from the space charge and the dipole, the hetero junction barrier between AlN and SiC becomes very narrow. Therefore, electron can flow very easily from SiC side to AlN side without a blocking barrier. This must be the reason why the forward current can flow easily for the Ni/AlN/n⁻-epi-SiC samples.

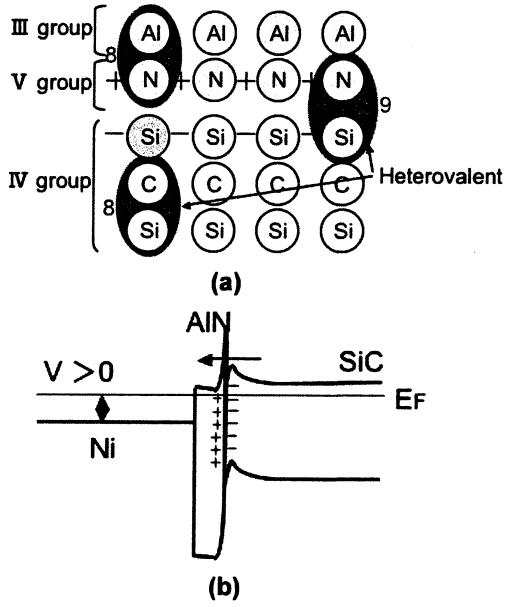

Figure 4 Schematic model of the heterovalent AlN/SiC hetero interface; (a) atomic and charge distribution, (b) energy band diagram.

4 Conclusion Vertical current flow at the GaN/AlN/SiC interface was investigated for future power nitride FETs. 17 to 350 nm AlN layers were grown on 8° off n⁻-epitaxial 4H-SiC substrates by MOVPE. Ni/AlN/n⁻-epi-4H-SiC sample showed Schottky characteristics. Ni/AlN/GaN/AlGaN/AlN/n⁻-epi-4H-SiC sample showed MIS characteristics for the same AlN thickness. This difference can be explained by the heterovalent atomic structure at the interface between AlN(III-V) and SiC(IV-IV).

Acknowledgements The authors express their thanks to professor Emeritus Y. Suematsu and professor Emeritus K. Iga of Tokyo Institute of Technology for their encouragement regarding our work. This work is partly supported by JSPS and MEXT, Grant-in-Aid for Scientific Research [Grant-in-Aid for Scientific Research (S) No. 17106005 and Grant-in-Aid for Scientific Research on Priority Areas No. 18069009].

References

[1] I. Ben-Yaacov, Y. K. Seck, U. K. Mishra, and S. P. DenBaars: J. Appl. Phys., 95(2004)2073.
[2] M. O. Aboelfotoh, R. S. Kern, S. Tanaka, R. F. Davis, and C. I. Harris: Appl. Phys. Lett., 69(1996)2873.
[3] C. -M. Zetterling, M. Ostling, N. Nordell, O. Schon, and M. Deschler: Appl. Phys. Lett., 70(1997)3549.
[4] T. Nakayama: J. Phys. Soc. Jpn., 61 (1992) 2458.
[5] R. Nicolini et al., Phys. Rev. lett., 72 (1994) 294.
[6] Y. Ishihara, J. Yamamoto, M. Kurimoto, T. Takano, T. Honda, and H. Kawanishi: Jpn. J. Appl. Phys. 38 (1999) L1296.
[7] M.Kurimoto, M.Shibata, J.Yamamoto, M.Tsubamoto, T.Honda, and H.Kawanishi: J. Cryst. Growth. 189-190 (1998) 189.
[8] J. Choi, R. Puthenkovilakam, and J. P. Chang: Appl. Phys. Lett., 86(2005)192101.

8.07f/W(Jul162004) + model | CRYS : 4079 | Prod.Type:FTP pp.1–4(col.fig.:2–5) | ED:Bhagyavati PAGN:anu SCAN:

Available online at www.sciencedirect.com

ScienceDirect

Journal of Crystal Growth ▮ (▮▮▮▮) ▮▮▮–▮▮▮

JOURNAL OF CRYSTAL GROWTH

www.elsevier.com/locate/jcrysgro

Improvement of crystal quality of AlN and AlGaN epitaxial layers by controlling the strain with the (AlN/GaN) multi-buffer layer

E. Niikura*, K. Murakawa, F. Hasegawa, H. Kawanishi

Department of Electronic Engineering, Kogakuin University, Nakanno-machi 2665-1, Hachioji-shi, Tokyo 192-0015, Japan

Abstract

AlN and AlGaN epitaxial layers with Al composition of 0.6–0.8 were grown by low-pressure metal organic vapor phase epitaxy on a (0 0 0 1) 6H–SiC substrate using the (AlN/GaN) multi-buffer layer structure (MBLS). Strain of the grown layer could be controlled by structure of the inserted (AlN/GaN) MBLS. It was found that the crystal quality of the grown layer could be improved with increase of the tensile strain in *a*-axis (compressive strain in *c*-axis): full-width at half-maximum (FWHM) of X-ray rocking curves (XRC) of both (0 0 0 2) plane (ω scan) and (1 0 $\bar{1}$ 2) plane (φ scan) were decreased from 1530 arcsec to 79 arcsec and 3962 arcsec to 853 arcsec for the AlN template, respectively. FWHM of the φ scan XRC was several times larger than that of the ω scan, though the former was roughly proportional to the latter.

Keywords: A1. AlN; A1. Crystal quality; A1. FWHM of XRC; A2. AlGaN; A3. (AlN/GaN) multi-buffer layer; A3. LP-MOVPE; B2. Strain control

1. Background and purpose

Control of crystal quality of AlN and AlGaN is very important for development of ultraviolet (UV) and deep-UV light-emitting diodes (LEDs) and laser diodes (LDs). These are generally grown on a lattice-mismatched substrate such as sapphire or SiC. The lattice mismatch is one of the origins of the crystal defects in the epitaxial layer. Misfit dislocations, the main defects due to the lattice mismatch, are reported to be controlled and decreased by various kinds of buffer layer structures and crystal growth techniques [1–3]. However, how the misfit (or sometimes called threading) dislocations can be reduced by the buffer layer is not necessarily made clear yet.

The purpose of this work is to find how the strain introduced by the (AlN/GaN) multi-buffer layer structure (MBLS) improves the crystal quality, probably by reducing the threading dislocation.

2. Experimental procedure

AlN and AlGaN epitaxial layers with Al composition of 0.6–0.8 were grown by low-pressure metal organic vapor phase epitaxy (LP-MOVPE) on a (0 0 0 1) 6H–SiC substrate using the (AlN/GaN) MBLS as shown in the inset of Fig. 1. The AlN and the (AlN/GaN) MBLS were grown by the alternate-source-feeding (ASF) technique [4]. Trimethyl-gallium (TMGa), trimethyl-aluminum (TMAl) and ammonia (NH_3) were used as source materials for gallium, aluminum and nitrogen, respectively. The source materials were introduced into the reactor through the flow channel with a hydrogen carrier gas. Residual strain of AlN template was changed by changing the structure of (AlN/GaN) MBLS [1–3]. Basic structure of MBLS is super-lattice structure (SLS) as shown in Fig. 2. Details of the growth method are described in our previous papers [5]. The grown layers were characterized by X-ray diffraction (XRD) in 2θ–ω scans for both *a*- and *c*-planes to see the strain in the grown layer, ω-scan of (0 0 0 2) plain to see the tilting (probably related to screw and mixed dislocations) and φ scan of (1 0 $\bar{1}$ 2) plain of AlN layers to see the twisting (probably related to edge dislocation). Gay et al.

*Corresponding author.
E-mail address: cm06027@ns.kogakuin.ac.jp (E. Niikura).

0022-0248/$ - see front matter © 2006 Published by Elsevier B.V.
doi:10.1016/j.jcrysgro.2006.10.152

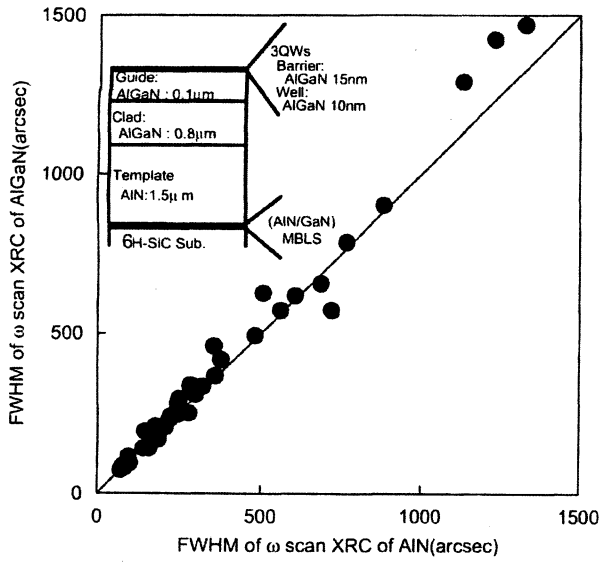

Fig. 1. Relation between (0 0 0 2) ω scan FWHM (tilt) of AlGaN and that of the AlN template underneath.

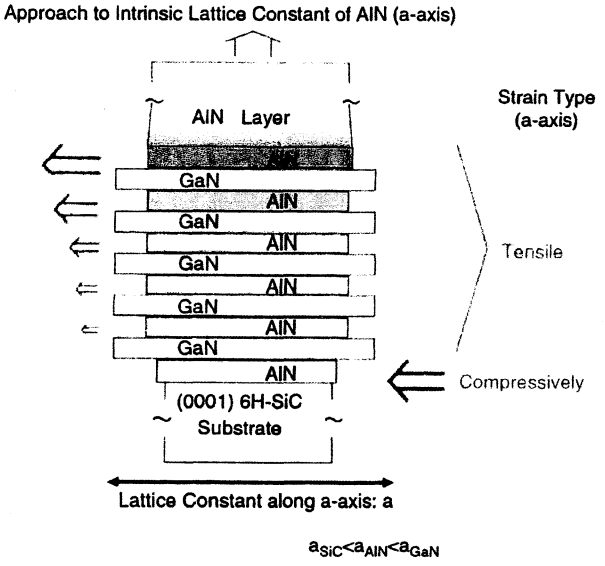

Fig. 2. Model of strain control of the AlN template by introduction of the (AlN/GaN) multi-buffer layer.

[6] have reported that the dislocation density can be estimated from FWHM of X-ray rocking curve (XRC) as follows; $D = F^2/(9b^2)$, where D is the dislocation density, F the FWHM in radian and b the Burger's vector. Usui et al. [7] demonstrated that this relation is valid for high quality halide VPE GaN. Therefore, crystal quality of the grown layers was evaluated by FWHM of both ω- and φ-scan XRC.

3. Results and discussion

The FWHM of the ω-scan XRC for the AlGaN-clad layer was proportional to that of the AlN template underneath as shown in Fig. 1. Therefore, evaluation of AlN is reasonable for evaluation of the whole layers. Fig. 3 shows an example of difference of the a- and c-axis lattice constants, i.e. difference of the strain, for the layers with different MBLS. Referring to the diffraction angle of the SiC substrate, one can see that quite a big difference of the strain is introduced between both the AlN layers: Diffraction peak of a-plane ($2\theta = 118.7°$, $a = 3.102$ Å) is much smaller, of c-plane ($2\theta = 36.11°$, $c = 4.971$ Å) is much larger, for one sample than those for the other, whose diffraction angles are almost the same as the reported ones ($2\theta = 117.8°$, $a_o = 3.116$ Å, $2\theta = 36.03°$, $c_o = 4.981$ Å) for so called relaxed AlN. Note that the a-axis is expanded and the c-axis is compressed. Relative residual strain of the grown film was estimated from difference between the measured lattice constant and that of the relaxed (free standing) AlN as $(c-c_o)/c_o$. Minus means that AlN layer is compressed in c-axis (tensile strained in a-axis). Since thermal expansion coefficients of a-axis are nearly the same for AlN and 6H–SiC (4.2×10^{-6}/K), this strain situation is the same even at the growth temperature. In other words, the AlN layer is tensile strained in a-axis during the growth.

FWHM of both (0 0 0 2) ω-scan and (1 0 $\bar{1}$ 2) φ-scan XRC are plotted against the residual strain expressed as $(c-c_o)/c_o$ in Fig. 4. The results indicate that the more the AlN layer is tensile strained in a-axis, the less dislocation is introduced. This tendency is the same for both FWHM of the ω scan (tilt) and φ scan (twist), meaning that both edge and screw dislocations are reduced with increase of the tensile strain in a-axis. Recently Amano et al. reported that dislocations in AlN on sapphire decreases with increase of the thickness, and that this is due to built-in tensile strain in AlN layer [8]. The same phenomenon should occur in our case: The (AlN/GaN) MBLS is introduced between AlN and the SiC substrate and growing AlN layer is tensile strained in a-axis during the growth in our case, therefore, the dislocations introduced at the MBLS/SiC interface are bent by the strain in the growing AlN, and resultantly a number of threading dislocations are reduced.

The FWHM of the φ scan (twist) is roughly proportional but not linearly to that of the ω scan (tilt), and the former is several times larger than the latter as shown in Fig. 5. This result agrees well with the generally spoken fact that density of edge dislocations is several times larger than that of screw dislocations [9]. It should be noted that FWHM of the φ scan (twist) decreases rapidly for the region of FWHM of the ω scan (tilt) less than 200 arcsec. In other words, FWHM of the φ scan (twist) scatters a lot for similar FWHM of the ω scan (tilt) less than 200 arcsec. Therefore, measurement of FWHM of the φ scan (twist) is necessary to evaluate crystal quality of the grown layer, especially to evaluate high quality AlGaN layers.

Please cite this article as: E. Niikura, et al., Improvement of crystal quality of AlN and AlGaN epitaxial layers by controlling the strain with the (AlN/GaN) multi-buffer layer, Journal of Crystal Growth (2006), doi:10.1016/j.jcrysgro.2006.10.152

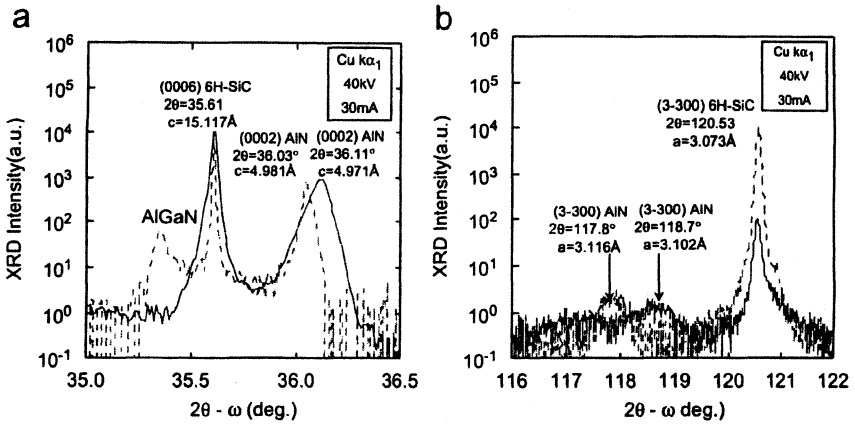

Fig. 3. Examples of 2θ–ω scan XRD spectra of the samples with different residual strains. (a) (0 0 0 2) diffraction and (b) (3-300)diffraction.

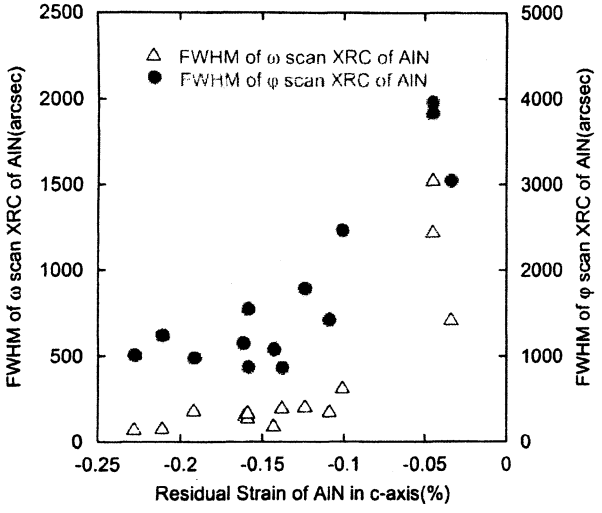

Fig. 4. Dependence of FWHM of the $(10\bar{1}2)$ φ scan and that of the (0 0 0 2) ω scan on the residual strain for the AlN template. The FWHM decreases with increase of the strain.

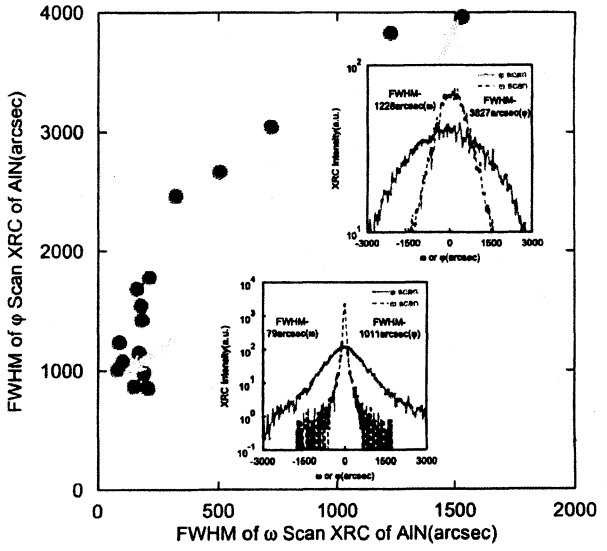

Fig. 5. Relationship between FWHM of the $(10\bar{1}2)$ φ scan and that of the (0 0 0 2) ω scan for the AlN template.

4. Conclusion

Strain of the AlN template and AlGaN active region could be controlled by the structure of the (AlN/GaN) multi-buffer layer. It was found that XRC FWHM of both (0 0 0 2) plane (tilt) and $(10\bar{1}2)$ plane (twist) could be improved with increase of the tensile strain in a-axis; from 1530 arcsec to 79 arcsec for the ω scan (tilt) and 3962 arcsec to 853 arcsec for the φ scan (twist) of the AlN template, respectively.

FWHM of the φ scan (twist) was several times larger than that of the ω scan (tilt), especially for small FWHM region of the ω scan (tilt), where it is nearly one order. Therefore, evaluation of crystal quality by XRD should be performed by φ scan (twist) rather than by ω scan (tilt).

Reference

[1] M. Kurimoto, T. Nakada, Y. Ishihara, M. Shibata, T. Takano, J. Yamamoto, T. Honda, H. Kawanishi, Phys. Status Solidi A 176 (1999) 665.

[2] M. Kurimoto, T. Nakada, Y. Ishihara, T. Takano, M. Shibata, T. Honda, H. Kawanishi, Jpn. J. Appl. Phys. 38 (1999) L551.

[3] Y. Ishihara, J. Yamamoto, M. Kurimoto, T. Takano, T. Honda, H. Kawanishi, Jpn. J. Appl. Phys. 38 (1999) L1296.

Please cite this article as: E. Niikura, et al., Improvement of crystal quality of AlN and AlGaN epitaxial layers by controlling the strain with the (AlN/GaN) multi-buffer layer, Journal of Crystal Growth (2006), doi:10.1016/j.jcrysgro.2006.10.152

[4] M. Kurimoto, M. Shibata, J. Yamamoto, M. Tsubamoto, T. Honda, H. Kawanishi, J. Crystal Growth 189/190 (1998) 189.
[5] T. Takano, Y. Narita, A. Horiutchi, H. Kawanishi, Appl. Phys. Lett. 84 (2004) 3567.
[6] P. Gay, P.B. Hirsch, A. Kelly, Acta Metall. 1 (1953) 315.
[7] A. Usui. H. Sunakawa, K. Kobayashi, H. Watanabe, M. Mizuta, Mater. Res. Soc. Symp. Proc. 639 (2001) G5.6.1.
[8] H. Amano, Presented at the First International Symposium on Growth of III Nitrides, Linkoping, Sweden, June 4–7, 2006, private communication.
[9] T. Miyajima, T. Hino, S. Tomiya, H. Nakajima, T. Araki, Y. Nanishi, A. Satake, Y. Masumoto, K. Akimoto, T. kobayashi, M. Ikeda, Phys. Status Solidi B 228 (2001) 395.

Please cite this article as: E. Niikura, et al., Improvement of crystal quality of AlN and AlGaN epitaxial layers by controlling the strain with the (AlN/GaN) multi-buffer layer, Journal of Crystal Growth (2006), doi:10.1016/j.jcrysgro.2006.10.152

発表論文

Ⅳ　デバイスへの応用

Ⅳ－③　液晶分子に対して双安定な配向特性をもつ基板表面の形成と
　　そのLCDへの応用

研究分担者　齊藤　進、　高橋　泰樹

IDW'07 pp.1697-1700

Bi-Stable Anchoring Properties for Nematic LCs Induced by Unidirectional Rubbing

Kazunori Shimoyama, Taiju Takahashi and Susumu Saito
Kogakuin University, 2665-1 Nakano-chyo Hachioji, Tokyo 192-0015, Japan, Email: cm06021@ns.kogakuin.ac.jp

Abstract: In this paper, a novel method is proposed to adapt in-plane bi-stable anchoring properties on the substrate. A mixed solution of PVCi and PI in same weight was used as an alignment material. It has been confirmed that two types of domains coexist in the sample cell, and molecules of liquid crystal align with the angle of ±45degree with respect to the rubbing direction. When a voltage was applied using an interdigital electrode, the homogeneous state of alignment changed to the twisted alignment. The twisted state memorized for a longer time than 50 h after the transition. Furthermore, an experimental expression for the surface free energy density function was determined for the in-plane bistable anchoring substrate.

Key Words: polyimide, PVCi, bi-stable, rubbing, mixed alignment material

1 Introduction

The orientational bistability in nematic liquid crystals (LCs) has attracted attention due to a potential to enhance multiplexability of a passive matrix liquid crystal display (LCD). In recent years, some kinds of bi-stable liquid crystal displays have been proposed. The bi-stable LCDs are classified into two types according to whether the bi-stability is based on the bi-stable anchoring properties of alignment layer or only on the bi-stability of configurations of molecular orientation [1,2]. Some techniques have been proposed to adapt the in-plane bi-stable anchoring properties to the alignment layer. B. Jerome et al have demonstrated an in-plane bi-stability using approximately 20 nm thick SiO films obliquely evaporated in a narrow range of incidence angles between 60° and 72°[3,4]. G. P. Bryan-Brown et al proposed the zenithal bi-stable device (ZBD)[5] in which a grating surface treated with a homeotropic surfactant was found to support two stable pretilt configurations when the groove depth to pitch is optimum[6]. J. H. Kim et al have demonstrated a robust in-plane bistability of liquid crystal alignment based on tailored submicrometer sized surface domains in a frustrated alignment. They used the atomic force microscope (AFM) to prepare an orientational checkerboard pattern on polyamide layer , consisting of square unit domain on which the alignment is locally constrained to be planar yet orthogonal between the neighboring domains[7,8]. T. N. Oo et al have proposed a micro-patterned liquid crystal device in which the patterns were formed by stripes of alternating planar and homeotropic anchoring[9,10]. They showed that the micro-patterned surface provides the bi-stable anchoring.

In this letter, a novel method is proposed to adapt an in-plane bi-stabile anchoring properties using the conventional unidirectional rubbing treatment conducted on a nano-sized domains which are constructed by the phase separation of a mixed solution of the poly vinyl cinnamate (PVCi) and the polyamide (PI). It has been known that the PVCi and PI make LC molecule align perpendicular and parallel, respectively, to the rubbing direction.

2 LC alignment using mixture of PVCi and PI solutions

2.1 Methods of Experiments

A mixed solution of PVCi and PI in same weight was used as an alignment material. The alignment material was coated on the substrate surface by a spin coater and was baked at 250□ for 60/min. , the surface of substrate was rubbed by a rubbing roller. By assembling a pair of substrates in such a way those rubbing directions become unti-parallel, sample cell with 6μm-thickness was fablicated. As a liuid crystal material, a single nematic compound, 5CB was used.

2.2Observation of LC alignment

The pictures of the sample cell which were taken under the conditions of the cross Nicol are shown in Figure 1. InFigure 1 (a), the transmission axis of polarizer was set to the rubbing direction. In Figure 1 (b), it was set at an angle of 45 degree.with respect to the rubbing direction

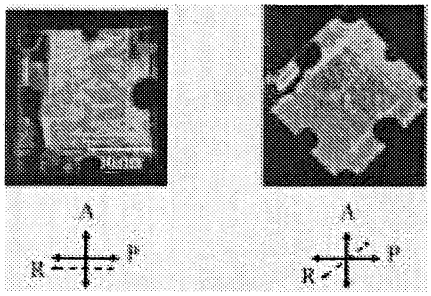

(a) (b)

Figure 1: Photographs of the cell under the cross Nicol condition

In Figure 1, the arrow indicated by R represents rubbing direction, and the arrows indicated by P and A represent the transmission axes of polarizer and analyzer, respectively.

In a usual homogeneous cell, we can observe the optical extinction region when the transmission axis of polarizer was set parallel or cross to the rubbing direction. In our sample cell, however the optical extinction regions were observed when the transmission axis of polarizer was set at an angle of 45 degree and -45 degree with respect to the rubbing direction.

In Figure 2, the images of the sample cell observed by using a polarizing optical micro-scope under the cross Nicol condition.

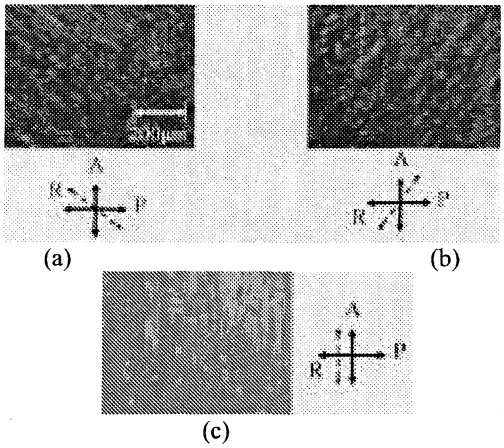

(a) (b)

(c)

Figure 2: Images of the sample cell observed by using polarizing optical micro-scope under the cross Nicol.

The transmission axis of polarizer was set: at an angle of (a)+45 degree, (b)-45 degree with respect to the rubbing direction, and (c) cross to the rubbing direction.
From these results, we can confirm that in our sample cell the alignment direction of LC does not consider with the rubbing direction. To determine the direction of LC alignment, we used the optical compensation method. In Figure 3, pictures of the sample cell which was optically compensated by a compensation plate. In these figures, the notation C represents the slow axis of the optical compensation plate. Due to the compensation of retardation, we can judge the alignment direction of LC molecules by the rubbing treatment. If the slow axis of the optical compensation plate is crossed to the alignment direction of LC molecules, we can observe the optical extinction.

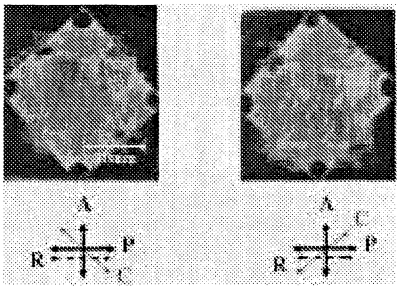

(a) (b)

Figure 3: Pictures of sample cell optically compensated by a compensation plate.

The slow axis of the compensation plate was set: at angle of (a) +45degree (b) -45 degree with respect to the rubbing direction.

Because when an optical compensate plate set on at an angle of ±45 degree with respect to the rubbing direction, extinction regions were observed, we can conclude that in our sample cell, two directions of LC alignment with the angle of ±45 degree with respect to the rubbing direction were caused.

2.3Switching of alignment directions by applying a In-Plane electric field

We attempted to switch electrically of alignment using an in-plane field. For that purpose, in-plane electrode with the inter-electrode distance of 35□m and the width of 25□m were constructed on one of the substrates.

On the other substrate, no electrode substrate was constructed. In Fig.4, a conceptual figure of switching of LC alignment using in-plane electrode is depicted.

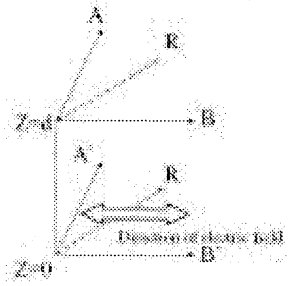

Figure 4: Image of switching using In-Plane electrode

In this figure, d represents the cell gap, the arrow indicated by R the rubbing direction, the arrows indicated by A, B, A' and B' the LC alignment directions on the substrate surfaces.

In the initial equilibrium state, two types of domain appear in the cell. In each domains, LC molecules align in either way A' to A or B' to B along the Z axis. When a voltage higher than the critical value is applied, the switching of LC alignment from a homogeneous state, A'A, to a twisted state, B'A, can be expected. It is thought that the twisted state B'A does not show optical extinction for any position of the turning table of the polarization optical micro-scope.

Furthermore, it is thought that the twisted angle of the twisted state B'A is equal to the angle of between the two degenerated directions in the cell. The pictures of the sample cell being in the initial equilibrium state of alignment are shown in Fig. 6.

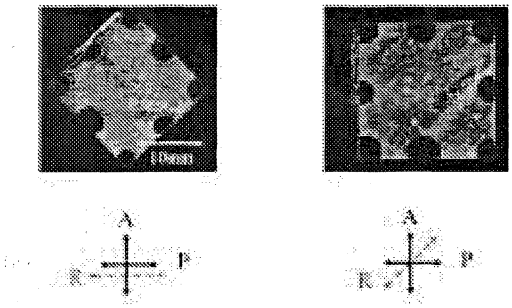

(a) (b)

Figure 5: The initial equilibrium state of alignment after injection of liquid crystal

The transmission axis of polarizer was set : at an angle of (a)parallel to the rubbing direction (b)45 degree with respect to the rubbing direction.

Optical extinction was observed when transmission axes of polarizer and analyzer were set at the angle of ±45 degree with respect to the rubbing direction. To determine the alignment direction, we used an optical compensation plate. In Fig. 6, the pictures of sample cell optically compensated are shown.

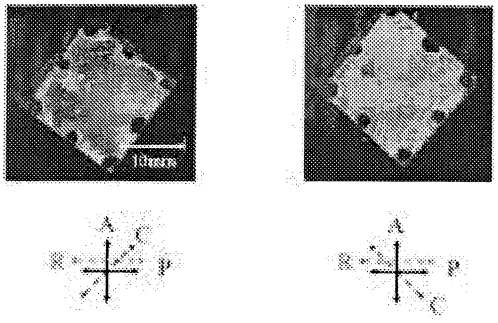

(a) (b)

Figure 6: Compensated result of retardation of sample cell using an optical compensation plate

The slow axis of the compensate plate was set : at the angle of (a)+45 degree (b)-45 degree with respect to the rubbing direction.

From these results, it can be known that almost molecules of liquid crystal near the surface aligned homogeneously and parallel direction to the in-plane electrode. In figure 8, when the ac voltage of 100 V was applied to the cell, the configuration of molecular alignment changed to the twisted state. This was confirmed from the fact that no extinction occurred for any rotation of the cell in the cross Nicole.

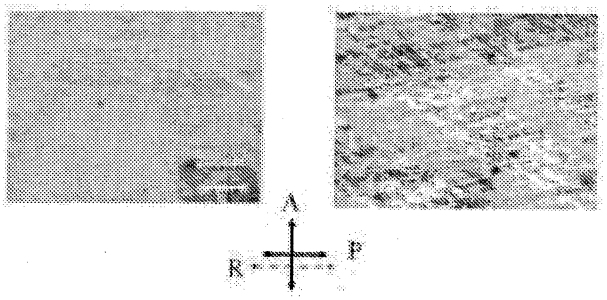

(a) (b)

Figure 7: Observed result of transition of LC alignment
(a)Before voltage application, (b) after voltage application

The twisted state was memorized for a longer time than 50 h after the transition. The twisted angle of the twisted state was about 70 degree. These facts mean that the energy barrier height between bi-stable alignments is sufficiently high to memorize the twisted state and, however, that the azimuth anchoring energy of bi-stable alignments obtained by using the mixed material are relatively weak.

3. Energy barrier between bi-stable states

3.1 Following expression

It is very important to know the height of energy barrier between bi-stable states from the viewpoint of the application. For this purpose, let's consider the cell in which one of the substrates (the substrate B) has the bi-stable anchoring properties and the other one (the substrate A) is mono-stable anchoring properties. The rubbing directions of those substrates are assembled so as to become anti-parallel. The z-axis is taken so as to be normal to the substrate surface. The substrates A and B exist at Z=0 and Z=d, respectively. We assume the strong anchoring for the substrate A. The following expression previously proposed by Yoneya et al[8] is used for the surface free energy density Fs on the substrate B with a bi-stable anchoring property.

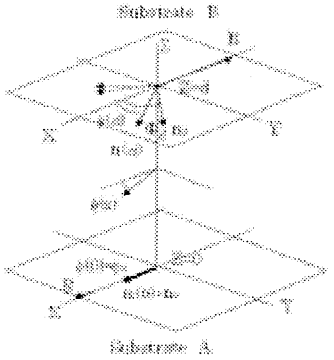

Figure 8: Definition chart for following expression

$$Fs = \frac{1}{2}A_2\left\{\sin^2\phi(d) + a_r\cos^2\phi(d)\right\} + \frac{1}{4}A_4\left\{\sin^4\phi(d) + a_r\cos^4\phi(d)\right\}, \quad (1)$$

where □d is the azimuth angle of the director at the surface measured from the rubbing direction, A_2 and A_4 are constants with the dimension of J/m^2. When the azimuth angles of the directions of bi-stable anchoring states are $\pm\Phi_d$ with respect to the rubbing direction, a_r is given by

$$a_r = \frac{1 + a_{42}\sin^2\Phi_d}{1 + a_{42}\cos^2\Phi_d}. \quad (2)$$

where

$$a_{42} = \frac{A_4}{A_2}. \quad (3)$$

Applying the mixed variation theory to the liquid crystal continuum theory, the following relation must be satisfied at the surface of substrate B when the pretilt angle on the substrate B is zero.

$$K_{22}\left(\frac{\partial\phi(z)}{\partial z}\right)_{z=d} + \frac{\partial F_s}{\partial\phi(d)} = 0, \quad (4)$$

where □(z) is the azimuth angle of director vector at Z=z, K_{22} is the twist elastic constant.
Assuming the following relation

$$\phi(z) = \left(\frac{\phi(d)}{d}\right)z, \quad (5)$$

one can obtain the following equation for A_2

$$A_2 = -\frac{2\phi(d)K_{22}}{d\sin 2\phi(d)\left[(1-a_r) + a_{42}(\sin^2\phi(d) - a_r\cos^2\phi(d)\right]} \quad (6)$$

Measuring □(d), □d and d, and assuming an appropriate value for a_{42}, one can obtain the value of A_2 using eq.(6). Thus, one can calculate Fs as a function of □(d). We should notice that although the value of $F_s(\phi(d))$ depends on the value of a_{42}, the value of $F_s(\phi(d)) - F_s(\Phi_d)$ is independent of a_{42}. Thus,

we can determine the height of energy barrier independently of a_{42}.

3.2 Experiments to estimate the height of energy barrier

To measure the bi-stable anchoring direction $\pm\Box_d$ with respect of the rubbing direction, we prepared an HAN (hybrid aligned nematic) cell in which one of the substrates has the bi-stable anchoring properties and the other one is treated so as to obtain the vertical alignment. The angle $\pm\Box_d$ were obtained from the optical quenching directions measured for those cells under the cross Nicole condition by using a polarizing optical microscope.

Using the substrate with the bi-stable anchoring properties and the substrate with the mono-stable parallel alignment, a sample cell as shown in Fig.8 was prepared to measure □(d). As the substrate B, we used the same one used in the HAN cell. The value □(d) was measured by using a polarizing optical microscope. Coinciding the transmission axis of polarizer with the rubbing direction of the substrate A, and rotating the transmission axis of analyzer so as to obtain the maximum transmittance, we obtained the angle □(d).

The experimental results are shown in table 1 together with the calculated results for A_2

Table 1: Expressional value and calculated result

d [mm]	$\Box_d$ [deg.]	(d) [deg.]	A_2 [J/m^2]
9.0	36	27	9.1×10^{-6}

The height of energy barrier, E_B., is defined as

$E_b = F_s(0) - F_s(\Phi_d)$.

By substituting values of (d), $\Box_d$, d and A_2 into eq.(1), we can obtain the anchoring function as shown in Fig. 9. From this result, the height of energy barrier is estimated as 1.1×10^{-7} [J/m^2].

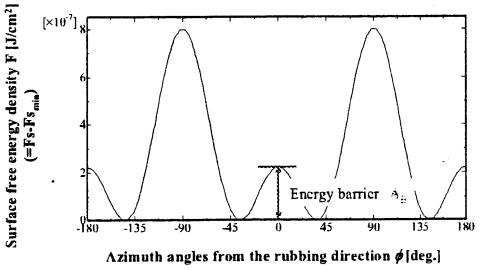

Figure 9: The calculated result of anchoring function

4 Conclusions

In this paper, a novel method has been proposed to adapt bi-stable anchoring properties on the substrate using rubbing treatment. A mixed solution of PVCi and PI in same weight was used as an alignment material. As the result, we successed to adapt the bi-stable anchoring characteristics on substrate surfaces. In this sample cell, molecules of liquid crystal aligned homogeneously at an angle of ±45 degree with respect to the rubbing direction. When applied voltage using In-Plane electrode, the homogeneous alignment was changed to the twisted alignment. The twisted state memorized for a longer time than 50 h.

We could obtain an expression of surface free energy density for the case when the substrate surface has bi-stable anchoring properties. From the result, energy barrier between bi-stable anchoring properties could be estimated as the order of 10^{-7}[J/m^2] .

5 References

(1) I. Dozov, M. Nobili, and G. Durand: Appl. Phys. Lett. 70 (1997) 1179.
(2) Ph. Martinot-Lagarde, I.Dozov, E.Polossant, M.Giocondo, I.Lelldis, G.Durand, J.Angele, B.Pecout and A.Boissler, SID'97 Digest, (1997) pp.41-44
(3) B. Jerome, P. Pieranski and M. Box: Europhys. Lett., 5 (1988) 693.
(4) R. Barberi, M. Boix, and G. Durand: 1989, Appl. Phys. Lett., 55, 2506
(5) G. P. Bryan-Brown, C. V. Brown, J. C. Johns, E. L. Wood, I. C. Sage, P. Brett and J. Rudin: SID '97 Digest (1997) 37.
(6) D. W. Berreman: Phys. Rev. Lett., 28 (1972) 1683.
(7) J. H. Kim, M. Yoneya, J. Yamamoto and H. Yokoyama: Appl. Phys. Lett.,78, (2001) 3055.
(8) J. H. Kim, M. Yoneya and H. Yokoyama: Nature 420 (2002) 159.
(9) T. N. Oo, R. Bansho, N. Tanaka, M. Kimura and T. Akahane: Jpn. J. Appl. Phys. 45 (2006) 4176
(10) T. N. Oo, M. Kimura and T Akahane: IDW '06 Digest (2006) 99.
(11) J.A.Catellano: Mol. Cryst. Liiq. Cryst., 94 (1983) 33.
(12) M. Nishikawa, T. Miyamoto, S. Kawamura, Y. Tsuda and N. Bessho: Proc. Of the 12th Int. Display Research Conf. (1982) 819.
(13) F. Sze-Yan yeung, F-C. Xie, H.-S. Kwok, J. Wan, O. Tsui, and P.Sheng: SID '05 Digest (2005) 1080.
(14) R. S. Filas and J. S. Patel: Appl. Phys. Lett. 50 (1987) 1426.
(15) Y. Iimura, S. Kobayashi, and K. Katoh: IEICE Trans. Elecron,. Vol. E79-C, No.8 August (1996) 1040.
(16) M. Yoneya, J. H. Kim and H. Yokoyama: Appl. Phys. Lett., 80 (2002) 374.

ラビング処理による双安定アンカリング界面の形成

Formation of Bi-Stable Anchoring Surface for Nematic LCs by Unidirectional Rubbing

下山　和則 ・ 高橋　泰樹 ・ 齊藤　進

Kazunori SHIMOYAMA ・ Taiju TAKAHASHI ・ Susumu SAITO

abstract

A novel method is proposed to adapt bi-stable anchoring properties on the substrate. A mixed solution of PVCi and PI in same weight was used as an alignment material. Unidirectional rubbing was conducted. As an LC material, a single nematic compound, 5CB was used. At the initial state, LC molecules are aligned in directions parallel or perpendicular to the rubbing direction without twist (the U state). The transition between the U and T states with the twist angle of about 90 deg. were observed by applying ac voltage of 100V, 10Hz. Both states of T and U were memorized for a long time.

1. はじめに

現在双安定な配向層表面を有する双安定型 LCD 方式として,基板界面に溝を形成するZBD(Zenithal Bistable Display)[1]や SiO_2 を基板に真空斜方蒸着する Surface Controlled Nematic Bistabilty[2],AFM 探針を用いて微小領域に配向処理をするナノラビング [3]等が報告されている.しかしいずれの方式も作製条件が非常にシビアであり,ディスプレイの大面積化が困難で工業的に不向きである.

本研究ではラビング方向にLC分子を配向させるポリイミド(PI)と,未架橋時にラビング方向に直交する方向に配向させるポリビニルシンナメート(PVCi) [4]に注目した.それらを混合し形成された膜に対して一般的な LC 分子配向方法であるラビング処理によって双方向のアンカリング特性を発現させることを試みた.

2. 実験方法

PI と PVCi を 2 : 1 の割合で溶媒に溶かしたものを配向材とし,スピンコート法によって基板に塗布し,250℃で60min. 焼成することで成膜した.成膜後は基板にラビング配向処理を施し,ラビング方向がアンチパラレルになるように貼り合わせした.尚,ギャップ材は 6μm のものを使用し,液晶はネマティック液晶である 5CB を用い,セルに等方相注入し除冷後に配向の様子の観測を行なった.

3. 観測結果

セルの観測結果を図 1 に示す.図中の P は偏光子の偏光方向を A は検光子の偏光方向を示

し,R はラビング方向を示している.

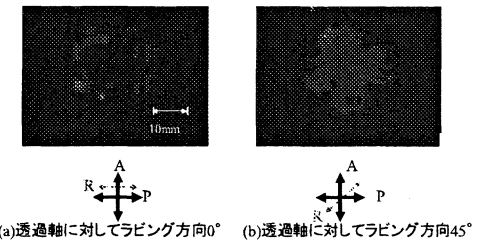

(a)透過軸に対してラビング方向0° (b)透過軸に対してラビング方向45°

図1 混合配向膜における液晶配向

図 1 に示すような偏光板の配置で消光位となった.また光学補償板を用いてリタデーションの補償条件を探ることで初期の配向方向はラビング方向であることが確認できた.偏光顕微鏡下での観測結果を図 2 に示す.

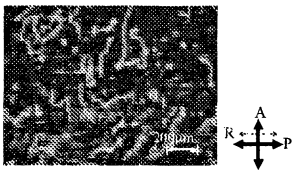

図2 混合配向膜における液晶配向の偏光顕微鏡下での観測

図 2 の観測結果から Nell Wall らしき配向欠陥が多数観測された.このことから PI と PVCi を混合するし,ラビングすることで生じるそれぞれの方向からの配向規制力の影響を受けて方位角アンカリングエネルギーが低下し,このような配向欠陥が観測されたと思われる.

このセルに 110V,10Hz の正弦波電圧を印加して瞬間的にオン／オフを切り替えた結果を図 3 に示す.

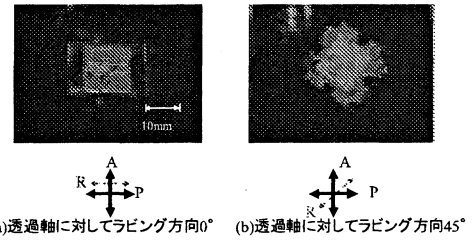

(a)透過軸に対してラビング方向0° (b)透過軸に対してラビング方向45°

図3 電圧印加による遷移後の配向

電圧を瞬間的に印加することで配向が遷移したことが確認できた.

セルを図中(a)の偏光板の配置で配向の観測したところ電極部が消光位ではなくなり,またセルを 360deg. 回転させても消光位にならなかったことから,電圧を印加することによってツイスト配向に遷移したことがわかった.この遷移後の配向は 2 週間以上のメモリー性を有していた.詳細については当日発表することとする。

参考文献

1). G.P.Bryan-Brown, C.V.Brown, J.C.Jones, et al : SID 97 Digest , 37 (1997).

2). R.Barberi , M.Boix and G.Durand : Appl.Phys.Lett.,60(9) , 1085 (1992).

3). J.H.Kim, M. Yoneya, J. Yamamoto, and H. Yokoyama: Appl. Phys. Lett., 78, 3055 (2001).

4). 中村浩之, 篠崎貴史, 飯村靖文, 小林駿介: 電気情報通信学会信学技報, EID96-37, p29(1996).

IDW'07 pp.1605-1608

A Novel Method to Calculate Electro-Optical Properties of Polymer Stabilized Nematic LC Cell

Y. Asakawa, T. Takahashi and S. Saito

Kogakuin Univ., 2665-1 Nakano, Hachioji, Tokyo 192-0015, Japan

ABSTRACT

In this report, a novel simple method is proposed to calculate theoretically the molecular alignment in an LC cell taking account of the variation of the polymer stabilization coefficient along the cell thickness direction. Due to the method, theoretical treatments become possible for the generation of pre-tilt angle by polymer stabilization under the voltage application condition and the static electro-optical properties of polymer stabilized nematic LC cell.

1. INTRODUCTION

It can be said that the traditional liquid crystal alignment technology was mainly based on the contribution of alignment layer on the substrate. Recently, it has problem with scarce alignment control of the liquid crystal molecule. The polymer stabilized method has been known as a technology that improves the scarce alignment control of liquid crystal molecule. The polymer stabilization technology make possible to control the molecular alignment based on the effect from the three dimensional bulk in addition to the two dimensional surface. The polymer stabilized bend alignment cell [1, 2] is representative which uses the contribution of polymer stabilization to liquid crystal bulk. In recent research, the improvement of characteristics of MVA-LCD [3] and control of pre-tilt angle [4] were proposed. It can be said that they used the contribution of polymer stabilization to surface. Although many experimental results concerning polymer stabilized alignment (PSA) technology have been reported, a theoretical investigation of PSA technology has hardly ever been reported. In this report, we experimentally and theoretically examined the contribution of polymer stabilization to liquid crystal alignment.

2. Theoretical Consideration

In our previous paper [5, 6], we introduced an additional term F_{stab} [7], polymer stabilization term, as shown in eq. (1), which represents the contribution of polymer stabilization to the free energy density F of liquid crystal bulk, to calculate theoretically the static behaviors of polymer stabilized LC cells.

$$F_{stab} = \frac{1}{2} A_{stab} \left[1 - (\mathbf{n}_{stab} \bullet \mathbf{n})^2 \right], \quad (1)$$

where A_{stab} is the polymer stabilization coefficient. It can be thought that $\mathbf{n}_{stab}$ is an interaction field. The profile of the interaction field $\mathbf{n}_{stab}$ coincides with the profile of director field when UV light is irradiated and it is memorized as the conformation of polymer network formed by UV light irradiation. The interaction between the polymer network and the director corresponds to the bulk anchoring of liquid crystal at the surface of polymer network memorizing the interaction field $\mathbf{n}_{stab}$. The polymer stabilization coefficient A_{stab} is regarded as the strength of interaction between the interaction field and the director field, and depends on the density of the polymer chain generated by a photo-polymerization reaction induced by UV light irradiation and on the manner of interaction between the polymer chain and liquid crystal molecules.

We calculated director profiles in homogeneous alignment taking account of F_{stab} as the contribution of polymer stabilization. The parameters of nematic liquid crystal ZLI-2293 were used in this calculation.

Dependence of director profiles on A_{stab} was shown in Figure 1. The dotted line in Figure 1 shows the director profiles of $\mathbf{n}_{stab}$ calculated for V_{stab}=20V, and solid line shows the director profiles resulting from the polymer stabilization for some values of A_{stab} when no voltage is applied. The director profiles resulting from the polymer stabilization was influenced by $\mathbf{n}_{stab}$ more strongly with increase of A_{stab} because of F_{stab} represents the contribution of polymer stabilization to liquid crystal bulk.

To take account of the contribution of polymer stabilization to surface, we introduced the spatial variation of the polymer stabilization coefficient, A_{stab}, along the direction of cell thickness as shown in eq. (2),

$$A_{stab} = A_{stab0} \cos^{2a}\left(\frac{\pi}{d} z\right), \quad (2)$$

where "a" is the accumulation coefficient, and d is cell thickness.

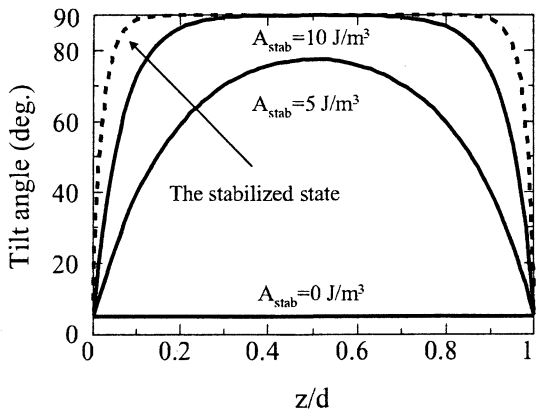

Fig. 1 Dependence of director profiles on polymer stabilization coefficient A_{stab}

Dependence of director profiles on A_{stab} taking account of contribution of polymer stabilization to surface was shown in Figure 2. The dotted line in Figure 2 shows the director profiles of n_{stab} calculated for V_{stab}=20V, and solid line shows the director profiles resulting from the polymer stabilization for some values of A_{stab0} and a=1750 when no voltage is applied. The director profiles resulting from the polymer stabilization was influenced strongly by n_{stab} in the vicinity of surface. The director of bulk was based on the contribution of polymer stabilization to surface.

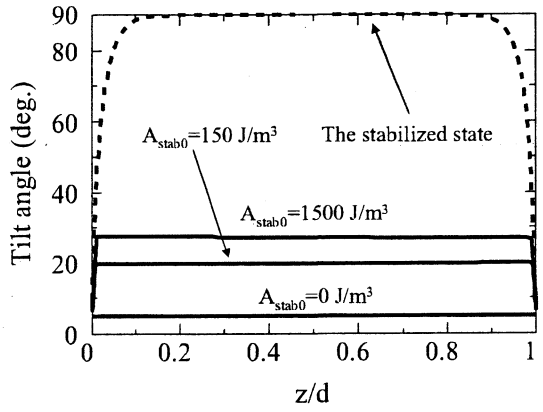

Fig. 2 Dependence of director profiles on polymer stabilization coefficient A_{stab} taking account of the contribution of polymer stabilization to surface

The applied voltage for polymer stabilization V_{stab} dependence of pre-tilt angle was shown in Figure 3 when A_{stab0}=150 and a=1750. As can be seen in the Figure 3, the pre-tilt angle is increased with increasing the V_{stab}.

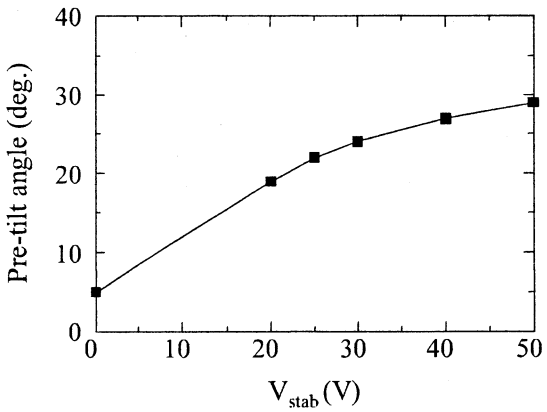

Fig. 3 Calculated results for the dependence of pre-tilt angle on V_{stab}

3. PSA Technology

We experimentally examined the contribution of polymer stabilization to liquid crystal bulk and surface. In this experiments, polymer stabilization has been performed by using two methods of UV light irradiation as shown by [A] and [B] in Figure 4. A light-emitting diode (LED) which radiates UV light including spectrums of the ultraviolet region centered by the wavelength of 365 nm (Nichia Chemical) was used as UV light source. In the method [A], the UV light was continuously irradiated. In the method [B], the UV-LED was turned on only around times at which the applied triangular wave voltage takes the maximum and the minimum.

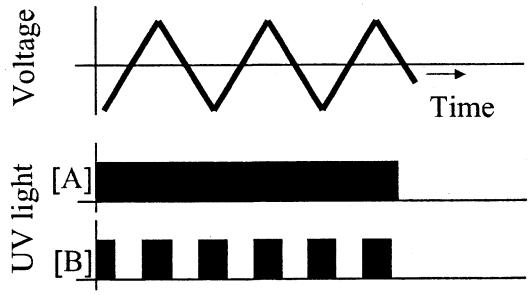

Fig. 4 Two methds of UV light irradiation and applied voltage waveform for polymer stabilization

Sample cells were fabricated by using about 23μm-gap homogeneous cells with tilted alignment produced by the polyimide PI-A (Nissan Chemical Industry, Ltd.) on the both plate. The NLC materials by using experiment is the liquid crystal mixtures ZLI-2293 and a reactive mesogen RMM34 which is a mixture of diacrylate and monoacrylate and a small amount (1-5 wt %) of photo-initiator, all

were supplied by Merck Ltd. The reactive mesogen RMM34 was added to the nematic liquid crystal mixture ZLI-2293 at concentrations of 1.5wt%.

In our previous research [8], we clarified that reactive mesogen or photo initiator was moved between top and bottom electrode of substrate by changing polarity of applied voltage. The UV light was irradiated when it was scattered in the whole of the liquid crystal cell in the case of [A], when reactive mesogen or photo initiator was gathered in the vicinity of the substrate in the case of [B]. Thus, the contribution of polymer stabilization to bulk in the case of [A], to surface was formed in the case of [B]. The bend alignment was stabilized in the case of [A]. The pre-tilt angle was controlled in the case of [B].

Figure 3 shows the V_{stab} dependence of pre-tilt angle. As can be seen in Figure 3, the pre-tilt angle is increased with increasing the V_{stab}.

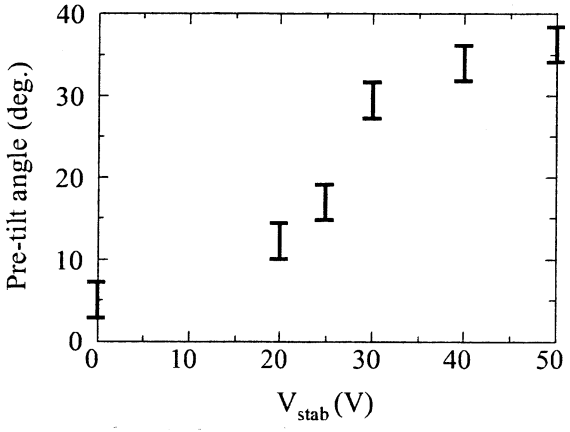

Fig. 5 Dependence of pre-tilt angle in experiments

4. Conclusions

We introduced polymer stabilization term, which represents the contribution of polymer stabilization to the free energy density F of liquid crystal bulk, to calculate theoretically the static behaviors of polymer stabilized LC cells. In this report, we introduced a weight function to polymer stabilized term to apply the contribution of polymer stabilization to surface. Due to the method, theoretical treatments become possible for the generation of pre-tilt angle by polymer stabilization under the voltage application condition and the static electro-optical properties of polymer stabilized nematic LC cell.

5. ACKNOWLEDGMENT

We express our most sincere thanks to Dr. Nakanowatari of Merk Co., Ltd. for his kind support in supplying UV curable liquid crystalline monomers, and to Mr. Takatuka and Mr. Sato for his cooperation in these experiments.

6. REFERENCES

[1] T. Konno, T. Miyashita and T. Uchida, "OCB-Cell Using Polymer Stabilized Bend Alignment," ASIA DISPLAY '95, pp. 581-583 (1995).

[2] S. H. Kim and L. C. Chien, "Electro-Optical Characteristics and Morphology of a Bend Nematic Liquid Crystal Device Having Templated Polymer Fibrils," Jpn. J. Appl. Phys, pp. 7643-7647, Vol. 43, No. 11A (2004).

[3] K. Hanaoka, Y. Nakanishi, Y. Inoue, S. Tanuma and Y. Koike, "A New MVA-LCD by Polymer Sustained Alignment Technology," SID 04 DIGEST, pp. 1200-1203 (2004).

[4] K. Maruyama, T. Houryu and Y. Iimura, "Application of Polymer-Stabilized Technique for VA STN-LCDs," SID 06 DIGEST, pp. 765-768 (2006).

[5] Y. Asakawa, K. Yokota, M. Nanaumi, N. Takatuka, T. Takahashi and S. Saito, "Stabilization of Bend Alignment Using Optical Polymerization of UV Curable Liquid Crystalline Monomers," Jpn. J. Appl. Phys, pp. 5878-5884, Vol. 45, No. 7 (2006).

[6] M. Kamio, M. Nanaumi, T. Takahashi and S. Saito, "Transient Behaviors of Polymer Stabilized Twisted Nematic Liquid Crystal Cells," IDW'04 Proc. of the 11th IDW (2004).

[7] T. Takahashi, T. Umeda, H. Furue and S. Kobayashi, "Modeling and Computer Simulation of the Electrooptic Response of Polymer-Stabilized Ferroelectric Liquid Crystal Cells," Jpn. J. Appl. Phys, pp.5991-5995, Vol. 38, No. 10 (1999).

[8] T. Nakanishi, T. Takahashi and S. Saito, "Influences of UV curable Liquid Crystaline Monomers Doped in LC and Those Optical Polymerization on VHR Characteristics of Nematic Liquid Crystal Cells," RESEACH REPORTS OF KOGAKUIN UNIVERSITY, pp.57-60, Vol.94, (2003) [in Japanese].

Reprinted from
Japanese Journal of Applied Physics
Vol. 45, No. 7, 2006, pp. 5878–5884

Stabilization of Bend Alignment Using Optical Polymerization of UV Curable Liquid Crystalline Monomers

Youichi ASAKAWA, Kouji YOKOTA, Makoto NANAUMI, Naoki TAKATUKA, Taiju TAKAHASHI and Susumu SAITO

Department of Electric Engineering and Electronics, Graduate School of Engineering, Kogakuin University, 2665-1 Nakano-cho, Hachioji, Tokyo 192-0015, Japan

Japanese Journal of Applied Physics
Vol. 45, No. 7, 2006, pp. 5878–5884

Stabilization of Bend Alignment Using Optical Polymerization of UV Curable Liquid Crystalline Monomers

Youichi ASAKAWA*, Kouji YOKOTA, Makoto NANAUMI, Naoki TAKATUKA, Taiju TAKAHASHI and Susumu SAITO

Department of Electric Engineering and Electronics, Graduate School of Engineering, Kogakuin University, 2665-1 Nakano-cho, Hachioji, Tokyo 192-0015, Japan

(Received January 20, 2006; accepted April 5, 2006; published online July 7, 2006)

Director profiles and electrooptical properties in polymer-stabilized π cells used in optically compensated bend (OCB) liquid crystal displays (LCDs) are theoretically investigated by introducing an additional term which expresses the effect of polymer stabilization on the free energy density. The conditions required to stabilize the bend alignment definitively have been theoretically clarified and experimentally confirmed. As a result, the bend alignment is successfully stabilized even if the twist state is more stable than the bend state before the application of polymer-stabilization treatment.
[DOI: 10.1143/JJAP.45.5878]

KEYWORDS: nematic liquid crystal, bend alignment, OCB-LCD, polymer stabilization, UV curable liquid crystalline monomers

1. Introduction

The optically compensated bend (OCB) nematic liquid crystal display (LCD) has attracted much attention due to its superior characteristics such as a fast response time and a wide viewing angle.[1,2] In the OCB-type LCD, the π cell is used with an optical compensation film. The π cell is constructed using a pair of substrates which are rubbed in parallel directions. The OCB-type LCD has one serious drawback in that it needs the initialing operation in which molecular alignment is made to undergo transition from splay to bend alignment by applying a high voltage at start-up, and always needs an operating voltage higher than its critical voltage to maintain the bend alignment.

To mitigate this problem, the following methods have been proposed. The first method is to complete the transition from splay alignment to bend alignment quickly by applying a high voltage[3] and by forming transition nuclei on the substrate surfaces.[4,5] However, this method does not effectively solve the problem, because the initial voltage application is still needed. The other method, which aims to make the initial voltage application unnecessary, involves polymer stabilization of the bend alignment by the formation of a polymer network[6,7] or an aligned polymer wall[8] using the optical polymerization of UV curable liquid crystalline monomers or reactive mesogen molecules dissolved within the liquid crystal host. This method is an effective means of solving the problem of the OCB-type LCD.

Uchida *et al.* first attempted this method to stabilize the bend alignment in the π cell.[6] However, it has been recognized that they could only stabilize the twist state but not the bend state. Recently, Kim and Chen successfully stabilized the bend state by experimentally optimizing the concentration of reactive mesogen and the irradiation energy of UV light and by observing in detail the morphology of the polymer network by scanning electron microscopy.[7]

Although many experimental results concerning polymer stabilization for nematic liquid crystal cells have been reported, a theoretical investigation has not been reported except in theoretical considerations made by Kossyrev *et al.*[9] concerning the Freedericksz transition. Takahashi *et al.* reported a theoretical simulation for polymer-stabilized ferroelectric liquid crystals.[10] In their report, they introduced the additional term for free energy density to express the effect of polymer stabilization.

In this report, the conditions required to stabilize the bend alignment definitively are investigated theoretically by applying the method proposed by Takahashi *et al.* to the case of nematic liquid crystals, after which, the theoretically simulated results are compared with the experimental results.

2. Theoretical Framework

2.1 Material equations

Based on the liquid crystal continuum theory by Frank and Oseen, elastic free energy density F_{elas} and dielectric free energy density F_{diel} are given by

$$F_{\mathrm{elas}} = \frac{1}{2}K_{11}(\mathrm{div}\,\mathbf{n})^2 + \frac{1}{2}K_{22}(\mathbf{n}\cdot\mathrm{rot}\,\mathbf{n})^2 + \frac{1}{2}K_{33}(\mathbf{n}\times\mathrm{rot}\,\mathbf{n})^2, \quad (1)$$

$$F_{\mathrm{diel}} = \frac{1}{2}\varepsilon_0[\varepsilon]\mathbf{E}\cdot\mathbf{E}, \quad (2)$$

where $\mathbf{n}$ is the director vector, $\mathbf{E}$ is the electric field vector, $[\varepsilon]$ is the relative dielectric tensor, ε_0 is the vacuum dielectric constant, and K_{11}, K_{22}, and K_{33} are elastic constants for splay, twist, and bend deformations, respectively.

An additional term F_{stab} shown in eq. (3) which represents the contribution of polymer stabilization to the free energy density F of liquid crystal bulk is introduced in addition to the sum of F_{elas} and F_{diel}

$$F_{\mathrm{stab}} = \frac{1}{2}A_{\mathrm{stab}}[1-(\mathbf{n}_{\mathrm{stab}}\cdot\mathbf{n})^2], \quad (3)$$

where A_{stab} is the polymer stabilization coefficient, and $\mathbf{n}_{\mathrm{stab}}$ represents the director profile when the polymer stabilization is carried out. The expression is similar to that first introduced by Takahashi *et al.* for a polymer-stabilized ferroelectric liquid crystal cell. It is thought that the polymer stabilization coefficient A_{stab} depends on the density of the polymer chain generated by a photopolymerization reaction induced by UV light irradiation and on the manner of

*E-mail address: cd05001@ns.kogakuin.ac.jp

interaction between the polymer chain and liquid crystal molecules.

The total free energy density is given by

$$F = F_{\text{elas}} + F_{\text{stab}} + F_{\text{dile}}. \tag{4}$$

In this analysis, one-dimensional approximation is assumed. That is, it is assumed that the director profile varies only along the normal direction, defined as the z axis, of the substrate surfaces.

Equations (1) to (3) can be rewritten as follows with respect to this model,

$$\begin{aligned} F_{\text{elas}} = {} & \frac{1}{2}K_{11}(\partial_z n_x) + \frac{1}{2}\{K_{33} + (K_{22} - K_{33})n_y^2\}(\partial_z n_x)^2 \\ & + \frac{1}{2}\{K_{33} + (K_{22} - K_{33})n_x^2\}(\partial_z n_y)^2 \\ & - (K_{22} - K_{33})n_x n_y(\partial_z n_x)(\partial_z n_y), \end{aligned} \tag{5}$$

$$F_{\text{stab}} = \frac{1}{2}A_{\text{stab}}[1 - (n_{\text{stab}x}n_x + n_{\text{stab}y}n_y + n_{\text{stab}z}n_z)^2], \tag{6}$$

$$F_{\text{diel}} = \frac{1}{2}D_x^2\varepsilon_0^{-1}(\varepsilon_n + \Delta\varepsilon n_z^2)^{-1}. \tag{7}$$

We assume the Rapini-Papoular potential as follows for the surface energy density.

$$\begin{aligned} F^s(l) &= \frac{1}{2}C_{\theta l}\sin^2(\theta(l) - \theta_l) + \frac{1}{2}C_{\phi l}\sin^2(\Delta\phi(l)) \\ &= \frac{1}{2}C_{\theta l}[1 - (\mathbf{n}_l \cdot \mathbf{n}'(l))^2] \\ &\quad + \frac{1}{2}C_{\phi l}[1 - (\mathbf{n}_{l0} \cdot \mathbf{n}'(l)_0)^2], \end{aligned} \tag{8}$$

where $l = 0$ for the interface at $z = 0$, $l = d$ for the interface at $z = d$, and $\mathbf{n}_l$ and $\mathbf{n}(l)$ represent the unit vector parallel to the easy axis and the director vector at the interface, respectively. The coefficients $C_{\theta l}$ and $C_{\phi l}$ are the polar anchoring energy and the azimuthal anchoring energy, respectively; $\mathbf{n}'(l)$ is the unit vector obtained by rotating $\mathbf{n}(l)$ to the plane which includes $\mathbf{n}_l$ and is perpendicular to the x–y plane with respect to the z axis. Furthermore, $\mathbf{n}_{l0}$ and $\mathbf{n}(l)_0$ are the unit vectors with projections of $\mathbf{n}_l$ and $\mathbf{n}(l)$ onto the substrate surfaces, respectively.

Rewriting eq. (8) with respect to the present model, one obtains the following equations:

$$\begin{aligned} F^s(l) = {} & \frac{1}{2}C_{\theta l}\Bigg[1 - \Big\{\sqrt{n_x(l)^2 + n_y(l)^2} \\ & \times (n_{lx}\cos\phi_l + n_{ly}\sin\phi_l) + n_{lz}n_z(l)\Big\}^2\Bigg] \\ & + \frac{1}{2}C_{\phi l}\Bigg[1 - \frac{1}{(n_{lx}^2 + n_{ly}^2)(n_x(l)^2 + n_y(l)^2)} \\ & \times \{n_{lx}n_x(l) + n_{ly}n_y(l)\}^2\Bigg]. \end{aligned} \tag{9}$$

2.2 *Differential equations to be solved to obtain director profiles*

The momentum balance equations for the LC bulk and the interfaces at $z = 0$ and d are to be solved. When the momentum balance equations are solved with respect to the tilt angle θ and azimuthal angle ϕ, the points at which ϕ takes the value of $\pi/2$ and either θ or ϕ varies discontinuously become singularity points. To avoid such singularity, a particular technique must be used.[11] We solved the momentum balance equations with respect to three components n_x, n_y, and n_z of $\mathbf{n}$, because we could get true solutions even at the singularity points without special procedures. It is easy to obtain the solutions with respect to θ and ϕ from n_x, n_y, and n_z. In this study, the rotational viscous torque and the surface anchoring effect are taken into account, but for simplicity, the flow effect and the surface dissipation are ignored. As a result, the following simultaneous nonlinear equations are obtained. For the LC bulk

$$\frac{\partial F}{\partial n_x} - \partial_z\frac{\partial F}{\partial(\partial_z n_x)} + \lambda_{\text{L}}n_x + \gamma_1\frac{\partial n_x}{\partial t} = 0, \tag{10}$$

$$\frac{\partial F}{\partial n_y} - \partial_z\frac{\partial F}{\partial(\partial_z n_y)} + \lambda_{\text{L}}n_y + \gamma_1\frac{\partial n_y}{\partial t} = 0, \tag{11}$$

$$n_x^2 + n_y^2 + n_z^2 = 1, \tag{12}$$

where γ_1 is the rotational viscous coefficient, and γ_{L} is a Lagrange multiplier.

For the surfaces at $z = 0$

$$\frac{\partial F^s(0)}{\partial n_x(0)} - \left.\frac{\partial F}{\partial(\partial_z n_x)}\right|_{z=0} = 0, \tag{13}$$

$$\frac{\partial F^s(0)}{\partial n_y(0)} - \left.\frac{\partial F}{\partial(\partial_z n_y)}\right|_{z=0} = 0, \tag{14}$$

$$n_x(0)^2 + n_y(0)^2 + n_z(0)^2 = 1. \tag{15}$$

For the surface at $z = d$

$$\frac{\partial F^s(d)}{\partial n_x(d)} + \left.\frac{\partial F}{\partial(\partial_z n_x)}\right|_{z=d} = 0, \tag{16}$$

$$\frac{\partial F^s(d)}{\partial n_y(d)} + \left.\frac{\partial F}{\partial(\partial_z n_y)}\right|_{z=d} = 0, \tag{17}$$

$$n_x(d)^2 + n_y(d)^2 + n_z(d)^2 = 1. \tag{18}$$

Detailed expressions of each term in eqs. (10), (11), (13), (14), (16), and (17) for this model are shown in the Appendix.

2.3 *Method of numerical calculation*

To solve the nonlinear simultaneous differential equations consisting of eqs. (10)–(18), we divided the interval $[0, d]$ into 100 subintervals and rewrote the equations in terms of differences. The simultaneous equations for the resultant 303 elements were numerically solved by Newton's method.

Considering that

$$\sum_i n_i\frac{\partial n_i}{\partial t} = \frac{1}{2}\frac{\partial\sum_i n_i n_i}{\partial t} = 0, \tag{19}$$

the Lagrange multiplier is determined by

$$\lambda_{\text{L}} = -\sum_i n_i\left[\frac{\partial F}{\partial n_i} - \partial_z\frac{\partial F}{\partial(\partial_z n_i)}\right]. \tag{20}$$

The notation $\sum_i$ means the sum with respect to x, y, and z.

To investigate the changes in the director profile with the increase or decrease in applied voltage, the applied voltage V was linearly varied with time. A sufficiently slow rate of variation for example 0.5 V/min, was assumed to obtain a solution as near as possible to the steady state.

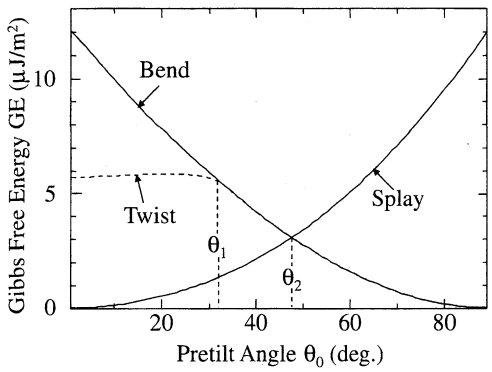

Fig. 1. Gibbs free energy for splay, bend, and twist states of alignment under condition of no voltage application.

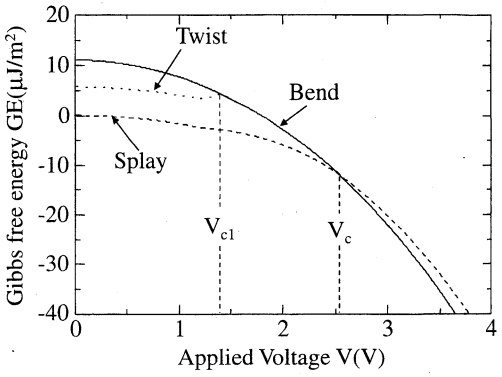

Fig. 2. Relationship between applied voltage and Gibbs free energy for splay, bend, and twist states of alignment.

3. Theoretical Considerations

3.1 Gibbs free energy for splay, bend, and twist alignment before polymer stabilization

3.1.1 Calculation of Gibbs energy

The Gibbs energy GE is calculated from

$$GE = \int_0^d (F_{\text{elas}} - F_{\text{diel}})\, dz. \tag{21}$$

Explicit expressions for F_{elas} and F_{diel} are given by eqs. (5) and (7), respectively. When no voltage is applied, it is assumed that $F_{\text{diel}} = 0$.

3.1.2 When no voltage is applied

In Fig. 1, the Gibbs free energy calculated as a function of pretilt angle θ_0, is plotted for the case of no voltage application. In these calculations, it was assumed that $F_{\text{diel}} = 0$ and $F_{\text{stab}} = 0$, that is, $V = 0$ and $A_{\text{stab}} = 0$. The parameters of the liquid crystal used in the calculation are listed for nematic liquid crystal ZLI-2293 in Table I. For the cell gap, $d = 6\,\mu\text{m}$ was assumed.

When the pretilt angle is lower than θ_2, as is shown in the figure, the splay alignment is the stable state since it has the lowest Gibbs free energy among the splay, bend, and twist states. Conversely, when the pretilt angle is higher than θ_2, the bend state is the stable state since it has the lowest Gibbs free energy of the three states.

When the pretilt angle is lower than θ_1, the twist alignment has a lower Gibbs free energy than the bend alignment. However, when the pretilt angle is higher than θ_1, the bend alignment and the twist alignment degenerate. The angle θ_1 depends strongly on the twist elastic constant K_{22}. For common nematic liquid crystals which are commercially available, the angle θ_1 is in the range of 25 to 35°. The pretilt angle obtained by the rubbing method using the polyimide alignment material is lower than θ_1, which is in the upper range. Thus, the twist alignment is in a lower metastable state than that of the bend alignment.

Table I. Parameters used in our calculations.

$K_{11} = 12.5 \times 10^{-12}$ N	$n_e = 1.63$
$K_{22} = 7.3 \times 10^{-12}$ N	$n_o = 1.50$
$K_{33} = 17.9 \times 10^{-12}$ N	$\gamma_1 = 149$ mPa s
$\varepsilon_p = 14.1$	$d = 6.0\,\mu$m
$\varepsilon_n = 4.1$	$\lambda = 550$ nm

3.1.3 When voltage is applied

Figure 2 shows the calculated results for the relationships between the applied voltage and the Gibbs free energy for the splay, twist and bend states of alignment. In these calculations, it was assumed that $F_{\text{stab}} = 0$, that is, $A_{\text{stab}} = 0$. Moreover, it was assumed that pretilt angle is 5°. The parameters of the liquid crystal used in the calculation are listed for nematic liquid crystal ZLI-2293 in Table I.

When no voltage is applied, the splay state has the lowest Gibbs free energy. Thus, the splay state is realized as the initial equilibrium state. When the applied voltage V is increased to over the voltage V_C, the configuration of molecular alignment changes to the bend state or the twist state from the splay state, since the Gibbs energy of the splay state become higher than the energies of the bend and twist states. If the applied voltage is decreased from a voltage higher than V_C, the configuration of molecular alignment takes the states of bend or twist within the range $V_C > V > V_{C1}$, and it takes the twist state in the range $V < V_{C1}$. The twist state finally relaxes to the splay state.

3.2 Simulation for director profile after polymer stabilization

3.2.1 Procedure of the calculation

The procedure for this simulation was conducted as follows. It was assumed that the initial configuration of the molecules was in the 180° twist state. Presuming that the voltage was increased from 0 V to V_{stab} at a constant rate, the director profiles were calculated for each time interval under the condition $A_{\text{stab}} = 0$. The voltage V_{stab} is selected to be in a range in which the center tilt angle is $\pi/2$. When the center tilt angle becomes $\pi/2$ the twist state transforms to the bend state. The director profile at $V = V_{\text{stab}}$ was memorized as the profile of $\mathbf{n}_{\text{stab}}$. Then assuming the appropriate value for A_{stab}, the applied voltage was decreased to 0 V at a constant rate. In this process, the director profile was also calculated for each time interval.

3.2.2 Simulated results and discussion

The parameters of the liquid crystal used in these calculations are listed for nematic liquid crystal ZLI-2293 in Table I, and the pretilt angle is assumed to be 5°.

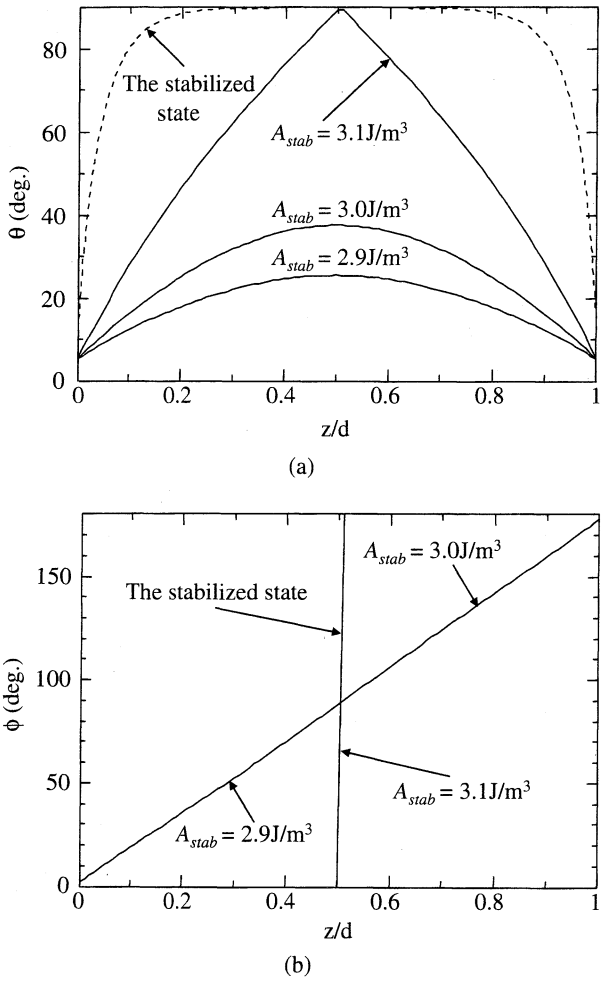

Fig. 3. Dependence of director profiles on polymer stabilization coefficient, A_{stab}, resulting from polymer stabilization treatment in bend alignment under application of $V_{stab} = 10$ V: (a) tilt angle and (b) azimuth angle.

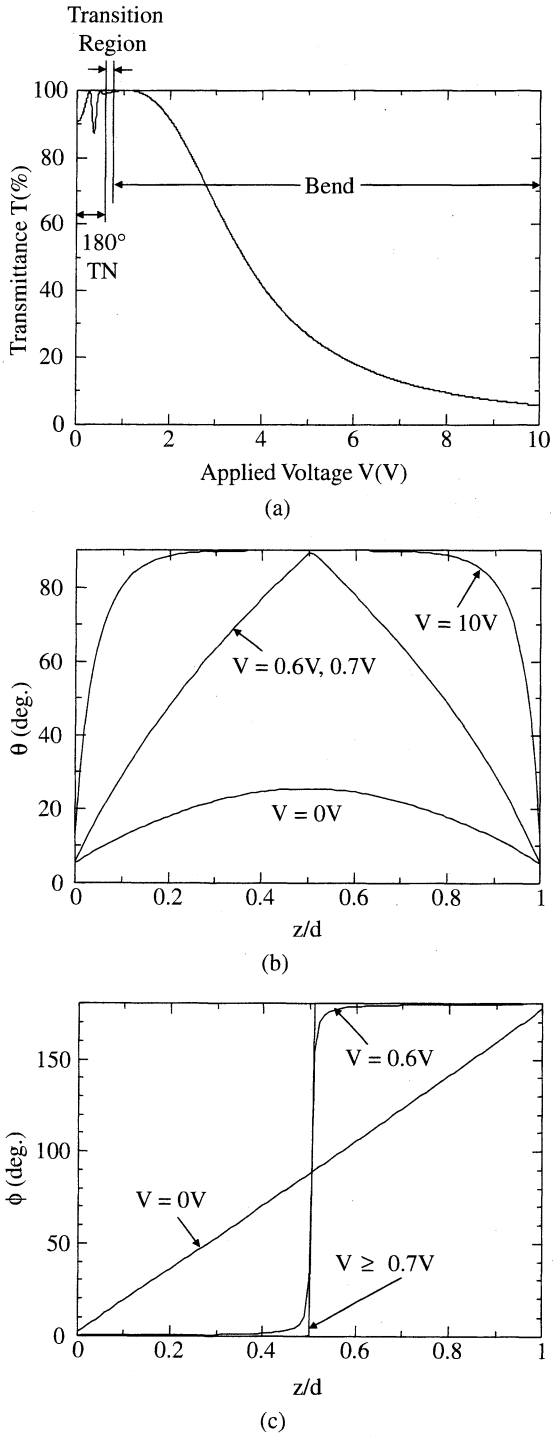

Fig. 4. *V–T* curves and director profiles at each voltage when A_{stab} is 2.9 J/m^3: (a) *V–T* curves, (b) tilt angle, and (c) azimuth angle.

The dotted line in Fig. 3 shows the director profiles of $\mathbf{n}_{stab}$ calculated for $V_{stab} = 10.0$ V, and the solid line shows the director profiles resulting from the polymer stabilization for some values of A_{stab} when no voltage is applied. Figures 3(a) and 3(b) show the profiles of the tilt angle and the azimuth angle, respectively. The tilt angle profile corresponding to the $\mathbf{n}_{stab}$ takes $\pi/2$ at $z = d/2$, and the azimuth angle profile of $\mathbf{n}_{stab}$ varies discontinuously at $z = d/2$ from 0 to π. This means that the polymer-stabilizing treatment was applied to the bend alignment. The director profiles resulting from the polymer stabilization for A_{stab} larger than the critical value $A_{stabc} = 3.1$ J/m^3 are apparently in the bend alignment, since in this case, the tilt angle is $\pi/2$ at $z = d/2$, and the azimuth angle changes discontinuously from 0 to π at $z = d/2$. When A_{stab} is smaller than A_{stabc}, however, the director profile resulting from the polymer stabilization is in the twist state, because the center tilt angle is lower than $\pi/2$ and the azimuth angle changes continuously from 0 to 180° along the z direction.

In Fig. 4(a), the V vs T relation is calculated for the change of director profiles, which are shown in Figs. 4(b) and 4(c). In these calculations, it was assumed that polymer stabilization was carried out under conditions where $V_{stab} = 10$ V and $A_{stab} = 2.9$ J/m^3. As can be seen, when $V = 0$ V, the director profile is in the twist alignment. When the applied voltage is increased from 0 V, the director profile transforms to the bend state above $V = 0.7$ V, because the center tilt angle becomes $\pi/2$ and the azimuth angle changes discontinuously at $z = d/2$. When the director profile is in the twist state below $V = 0.7$ V, the transmittance varies characteristically in the voltage range as shown in Fig. 4(a). However, when A_{stab} is larger than 3.1 J/m^3, the director profile adopts the bend alignment over all the voltage range and the transmittance varies with the increase in applied voltage as shown in Fig. 5(a). It should

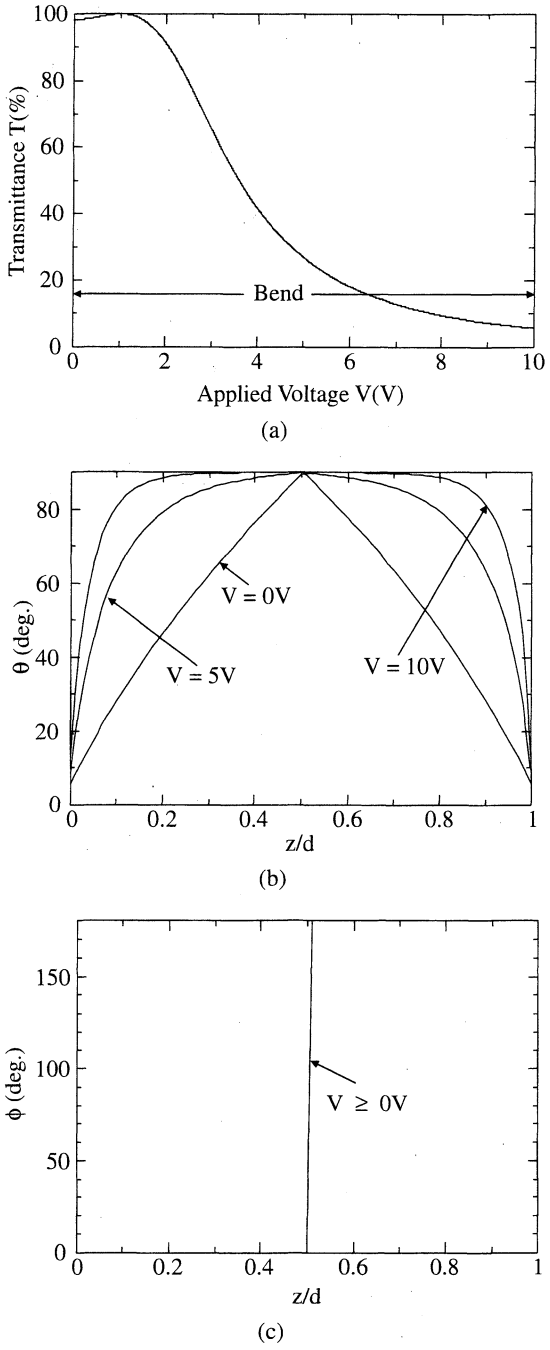

Fig. 5. *V–T* curves and director profiles at each voltage when A_{stab} is 3.1 J/m^3: (a) *V–T* curves, (b) tilt angle, and (c) azimuth angle.

be noted that A_{stab} must be larger than the critical value A_{stabc} to confidently obtain the bend alignment at $V = 0$ by polymer-stabilization treatment. The manner of variation of transmittance in the low voltage range can be used to judge whether the bend alignment is the result of the polymer stabilization.

4. Experimental Procedure

4.1 Sample preparation and experiments

Sample cells were made using the liquid crystal mixture ZLI-2293, and a reactive mesogen RMM34 which is a mixture of diacrylate and monoacrylate and a small amount (5–10 wt %) of photoinitiator, all supplied by Merck Ltd. The reactive mesogen RMM34 was added to the nematic

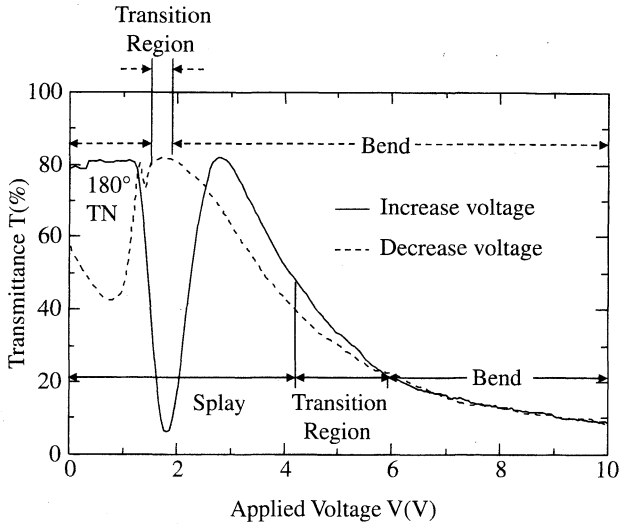

Fig. 6. Experimental results for relationship between transmittance and applied voltage before polymer stabilization.

liquid crystal mixture ZLI-2293 at concentrations in the range of 1 to 5 wt %. The final mixture was filled into 6-μm-gap liquid crystal cells with tilted alignment produced by the parallel rubbing of polyimide coating SE-610 (Nissan Chemical Industry) on both plates. Polymerization was induced by exposure to an ultra violet light source of approximately 0.6 mW/cm^2, centered around 365 nm (black-light) for an appropriate time. A 100 kHz sine wave voltage of 15 V was applied during exposure. The exposure time was determined so as to obtain appropriate irradiation energy density, E_{UV}, defined as the product of the irradiation power and the exposure time.

The relationship between the transmittance and the applied voltage, was measured for each sample cell. A sine wave voltage at a frequency of 1 kHz was applied. The changing rate of applied voltage was 3 V/min. Monochromatic light of wavelength 550 nm was used as the light source. The sample cell was set in a crossed Nicols. The transmission axis of polarizer was set at an angle of 45° with respect to the rubbing direction of the sample cell.

4.2 Experimental results and discussion

The *V–T* curves measured before UV light irradiation are shown in Fig. 6. In this figure, the solid line indicates the *V–T* curve with the increase of applied voltage. It can be seen that at the initial state of molecular alignment the configuration is in the splay alignment and the initial state is transformed to the bend state in the voltage range of 4.3 to 5.8 V. The dotted line in this figure indicates the *V–T* curve as the applied voltage decreases. Here it is observed that the bend state transforms into the twist state in the voltage range of 2.0 to 1.7 V. The twist state then naturally relaxes to the splay state.

Figure 7 shows the *V–T* curves measured for cells after being treated with the polymer-stabilizing method at the bend alignment. Figure 7(a) represents the case with the concentration of reactive mesogen $M_m = 2$ wt % and UV irradiation energy of $E_{UV} = 300$ mJ/cm^2, and Fig. 7(b) represents the case with $M_m = 3$ wt % and $E_{UV} = 400$ mJ/cm^2. In Fig. 7, the states of the alignment expected for each

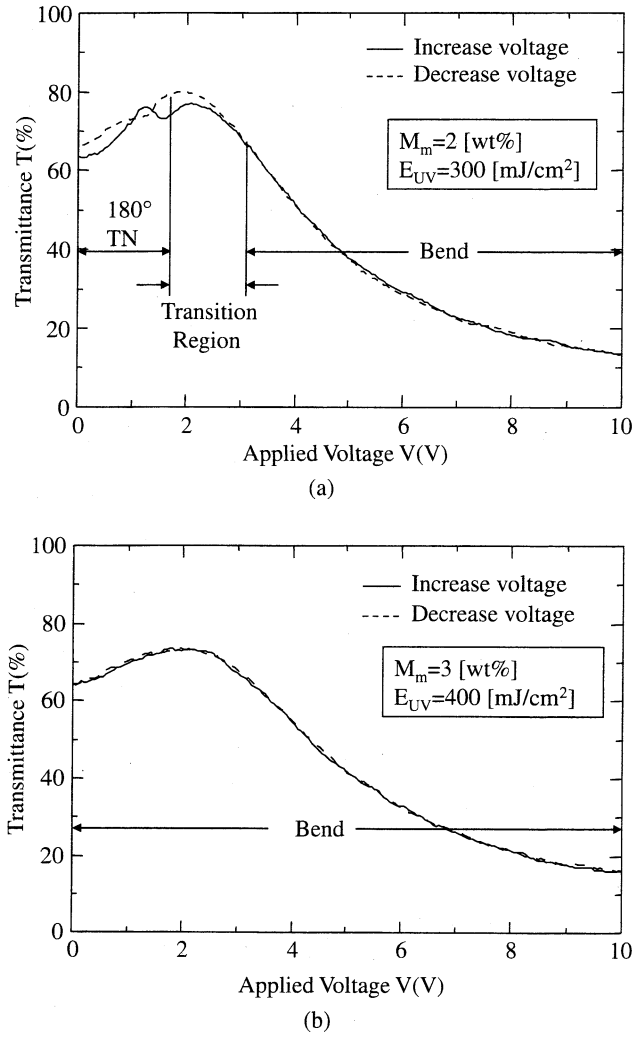

Fig. 7. Experimental result for the relation of transmittance vs applied voltage after polymer stabilization: (a) concentration of reactive mesogen $M_m = 2$ wt % and the UV irradiation energy $E_{UV} = 300\,mJ/cm^2$, and (b) concentration of reactive mesogen $M_m = 3$ wt % and the UV irradiation energy $E_{UV} = 400\,mJ/cm^2$.

voltage range are described. It can be seen that in the case of Fig. 7(a), the twist alignment resulted from the polymer stabilization when no voltage was applied, while in the case of Fig. 7(b), the bend alignment was definitively stabilized.

As mentioned, it is plausible to think that the value of A_{stab} depends on the density of polymer chains generated by photopolymerization reactions induced by UV light irradiation and on the manner of interaction between the polymer chain and liquid crystal molecules. It thought that the density of the polymer chain depends on the concentration of the reactive mesogen M_m when the UV irradiation energy E_{UV} is higher than the critical value. The UV irradiation energy E_{UV} irradiated on our sample cell exceeded the critical value. Thus, it is natural to think that the value of A_{stab} in the case of Fig. 7(b) is larger than that in the case of Fig. 7(a). This supports the theoretical prediction that the value of A_{stab} must be larger than the critical value A_{stabc} to definitively stabilize the bend state by polymer stabilization treatment.

5. Conclusions

Because of the introduction of an additional term which allows the explanation of the effect of polymer stabilization, it has become possible to investigate theoretically which director profile results from polymer-stabilization treatment in the nematic liquid crystal cell. As has been described in this study, the value of A_{stab} must be larger than the critical value A_{stabc} to definitively stabilize the bend alignment in the π cell. This was confirmed both theoretically and experimentally. The theoretical analysis and experimental considerations concerning the polymer-stabilization coefficient A_{stab} are left for study in the near future.

Acknowledgements

We express our most sincere thanks to Dr. Nakanowatari of Merck Co., Ltd. for his kind support in supplying UV curable liquid crystalline monomers, and to Mr. Niikura for his cooperation in these experiments.

This work was supported by a Grant-in-Aid for Scientific Research on High Technology from the Ministry of Education, Culture, Sports, Science and Technology.

Appendix

In eqs. (10)–(20),

$$\frac{\partial F}{\partial n_x} - \partial_z\left(\frac{\partial F}{\partial(\partial_z n_x)}\right) = -\{K_{33} + (K_{22} - K_{33})n_y^2\}(\partial_z^2 n_x) + (K_{22} - K_{33})n_x n_y(\partial_z^2 n_y) - K_{33}n_x(\partial_z n_x)^2 + (2K_{22} - K_{33})n_x(\partial_z n_y)^2 - 2K_{22}n_y(\partial_z n_x)(\partial_z n_y) - 2K_{33}n_z(\partial_z n_y)(\partial_z n_z) - A_{stab}(n_{stabx}n_x + n_{staby}n_y + n_{stabz}n_z)n_{stabx}, \quad (A\cdot1)$$

$$\frac{\partial F}{\partial n_y} - \partial_z\left(\frac{\partial F}{\partial(\partial_z n_y)}\right) = (K_{22} - K_{33})n_x n_y(\partial_z^2 n_x) - \{K_{33} + (K_{22} - K_{33})n_x^2\}(\partial_z^2 n_y) - (K_{33} - 2K_{22})n_y(\partial_z n_x)^2 - K_{33}n_z(\partial_z n_y)(\partial_z n_z) - 2K_{22}n_x(\partial_z n_x)(\partial_z n_y) - A_{stab}(n_{stabx}n_x + n_{staby}n_y + n_{stabz}n_z)n_{staby}, \quad (A\cdot2)$$

$$\frac{\partial F}{\partial n_z} - \partial_z\left(\frac{\partial F}{\partial(\partial_z n_z)}\right) = -K_{11}(\partial_z^2 n_z) + K_{33}n_z\{(\partial_z n_x)^2 + (\partial_z n_y)^2\} - A_{stab}(n_{stabx}n_x + n_{staby}n_y + n_{stabz}n_z)n_{stabz} - \frac{(\varepsilon_p - \varepsilon_n)n_z D_z^2}{\varepsilon_0\{\varepsilon_n + (\varepsilon_p - \varepsilon_n)n_z^2\}^2}. \quad (A\cdot3)$$

Since the effective dielectric constant with respect to the z direction is $\varepsilon_0\{\varepsilon_n + (\varepsilon_p - \varepsilon_n)n_z^2\}$, D_z is related to the voltage V across the electrodes as follows

$$D_z = \frac{V}{\displaystyle\int_0^d \frac{1}{\varepsilon_0\{\varepsilon_n + (\varepsilon_p - \varepsilon_n)n_z^2\}}\,dz}, \quad (A\cdot4)$$

In eqs. (13), (14), (16), and (17),

$$\frac{\partial F^s(l)}{\partial n_x(l)} = -C_{\theta l}\left\{(n_{lx}\cos\phi_l + n_{ly}\sin\phi_l)\sqrt{n_x(l)^2 + n_y(l)^2} + n_{lz}n_z(l)\right\} \times \{(n_{lx}\cos\phi_l + n_{ly}\sin\phi_l)n_x(l)(n_x(l)^2 + n_y(l)^2)^{-1/2} - n_{lz}n_x(l)/n_z(l)\} - C_{\phi l}\frac{n_y(l)\{n_{lx}n_x(l) + n_{ly}n_y(l)\}\{n_{lx}n_y(l) - n_{ly}n_x(l)\}}{(n_{lx}^2 + n_{ly}^2)\{n_x(l)^2 + n_y(l)^2\}^2}, \tag{A·5}$$

$$\frac{\partial F^s(l)}{\partial n_y(l)} = -C_{\theta l}\left\{(n_{lx}\cos\phi_l + n_{ly}\sin\phi_l)\sqrt{n_x(l)^2 + n_y(l)^2} + n_{lz}n_z(l)\right\} \times \{(n_{lx}\cos\phi_l + n_{ly}\sin\phi_l)n_y(l)(n_x(l)^2 + n_y(l)^2)^{-1/2} - n_{lz}n_y(l)/n_z(l)\} - C_{\phi l}\frac{n_x(l)\{n_{lx}n_x(l) + n_{ly}n_y(l)\}\{n_{ly}n_x(l) - n_{lx}n_y(l)\}}{(n_{lx}^2 + n_{ly}^2)\{n_x(l)^2 + n_y(l)^2\}^2}, \tag{A·6}$$

$$\left.\frac{\partial F}{\partial(\partial_z n_x)}\right|_{z=l} = \{K_{33} + (K_{22} - K_{33})n_y(l)^2\}(\partial_z n_x)|_{z=l} - (K_{22} - K_{33})n_x(l)n_y(l)(\partial_z n_y)|_{z=l}, \tag{A·7}$$

$$\left.\frac{\partial F}{\partial(\partial_z n_y)}\right|_{z=l} = \{K_{33} + (K_{22} - K_{33})n_x(l)^2\}(\partial_z n_y)|_{z=l} - (K_{22} - K_{33})n_x(l)n_y(l)(\partial_z n_x)|_{z=l}. \tag{A·8}$$

1) T. Miyashita, Y. Yamaguchi and T. Uchida: Jpn. J. Appl. Phys. **34** (1995) 177.
2) P. L. Bos and J. A. Rahman: SID Int. Symp. Dig. Tech. Pap., 1993, p. 273.
3) K. Sueoka, H. Nakamura and Y. Taira: Proc. AM-LCD & IDW, 1996, p. 133.
4) H. Mori, E. C. Gartland, Jr., J. R. Kelly and P. J. Bos: Proc. IDW, 1998, p. 77.
5) N. Nagae, T. Miyashita, T. Uchida, Y. Yamada and Y. Ishii: SID Int. Symp. Dig. Tech. Pap., 2000, p. 26.
6) T. Konno, T. Miyashita and T. Uchida: Asia Display '95, 1995, p. 581.
7) S. H. Kim and L. C. Chien: Jpn. J. Appl. Phys. **43** (2004) 7643.
8) H. Kikuchi, H. Yamamoto, H. Sato, M. Kawakita, K. Takizawa and H. Fujikake: Jpn. J. Appl. Phys. **44** (2005) 981.
9) P. A. Kossyrev, J. Qi, N. V. Priezjev, R. A. Pelcovits and G. P. Crawford: SID Int. Symp. Dig. Tech. Pap., 2002, p. 506.
10) T. Takahashi, T. Umeda, H. Furue and S. Kobayashi: Jpn. J. Appl. Phys. **38** (1999) 5991.
11) D. W. Berreman: J. Appl. Phys. **46** (1975) 3746.

Mol. Cryst. Liq. Cryst., Vol. 476, pp. 43/[289]–59/[305], 2007

ISSN: 1542-1406 print/1563-5287 online
DOI: 10.1080/15421400701733868

Taylor & Francis
Taylor & Francis Group

Optimization of Polymer Stabilization Condition of Bend Alignment in Pi-cell

Youichi Asakawa
Naoki Takatuka
Taiju Takahashi
Susumu Saito
Department of Electronic Engineering, Kogakuin University, Nakano-cho Hachioji-shi, Tokyo, Japan

Director profiles and electrooptical properties in polymer-stabilized π cells used in optically compensated bend (OCB) liquid crystal displays (LCDs) are theoretically investigated by introducing an additional term which expresses the effect of polymer stabilization on the free energy density. The conditions required to stabilize the bend alignment definitively have been theoretically clarified and experimentally confirmed. As a result, the bend alignment is successfully stabilized even if the twist state is more stable than the bend state before the application of polymer-stabilization treatment.

Keywords: bend alignment; nematic liquid crystal; OCB-LCD; polymer stabilization; UV curable liquid crystalline monomers

1. INTRODUCTION

The optically compensated bend (OCB) nematic liquid crystal display (LCD) has attracted much attention due to its superior characteristics such as a fast response time and a wide viewing angle [1,2]. In the OCB-type LCD, the π cell is used with an optical compensation film. The π cell is constructed using a pair of substrates which are rubbed in parallel directions. The OCB-type LCD has one serious drawback

We express our most sincere thanks to Dr. Nakanowatari of Merck Co., Ltd. for his kind support in supplying UV curable liquid crystalline monomers, and to Mr. Niikura for his cooperation in these experiments.

This work was supported by MEXT. HAITEKU(2005).

Address correspondence to Susumu Saito, Department of Electronic Engineering, Kogakuin University, 2665-1 Nakano-cho Hachioji-shi, Tokyo 192-0015, Japan. E-mail: cd05001@ns.kogakuin.ac.jp

in that it needs the initialing operation in which molecular alignment is made to undergo transition from splay to bend alignment by applying a high voltage at start-up, and always needs an operating voltage higher than its critical voltage to maintain the bend alignment.

To mitigate this problem, the following methods have been proposed. The first method is to complete the transition from splay alignment to bend alignment quickly by applying a high voltage [3] and by forming transition nuclei on the substrate surfaces [4,5]. However, this method does not effectively solve the problem, because the initial voltage application is still needed. The other method, which aims to make the initial voltage application unnecessary, involves polymer stabilization of the bend alignment by the formation of a polymer network [6,7] or an aligned polymer wall [8] using the optical polymerization of UV curable liquid crystalline monomers or reactive mesogen molecules dissolved within the liquid crystal host. This method is an effective means of solving the problem of the OCB-type LCD.

Uchida et al. first attempted this method to stabilize the bend alignment in the π cell [6]. However, it has been recognized that they could only stabilize the twist state but not the bend state. Recently, Kim and Chen successfully stabilized the bend state by experimentally optimizing the concentration of reactive mesogen and the irradiation energy of UV light and by observing in detail the morphology of the polymer network by scanning electron microscopy [7].

Although many experimental results concerning polymer stabilization for nematic liquid crystal cells have been reported, a theoretical investigation has not been reported except in theoretical considerations made by Kossyrev et al. [9] concerning the Freedericksz transition.

Takahashi et al. reported a theoretical simulation for polymer-stabilized ferroelectric liquid crystals [10]. In their report, they introduced the additional term for free energy density to express the effect of polymer stabilization.

In this report, the conditions required to stabilize the bend alignment definitively are investigated theoretically by applying the method proposed by Takahashi et al. to the case of nematic liquid crystals, after which, the theoretically simulated results are compared with the experimental results.

2. THEORETICAL FRAMEWORK

2.1. Material Equations

Based on the liquid crystal continuum theory by Frank and Oseen, elastic free energy density F_{elas} and dielectric free energy density F_{diel}

are given by

$$F_{elas} = \frac{1}{2}K_{11}(div\mathbf{n})^2 + \frac{1}{2}K_{22}(\mathbf{n} \cdot rot\mathbf{n})^2 + \frac{1}{2}K_{33}(\mathbf{n} \times rot\mathbf{n})^2, \quad (1)$$

$$F_{diel} = \frac{1}{2}\varepsilon_0 \varepsilon E \bullet E, \quad (2)$$

where $\mathbf{n}$ is the director vector, $\boldsymbol{E}$ is the electric field vector, ε is the relative dielectric tensor, ε_0 is the vacuum dielectric constant, and K_{11}, K_{22}, and K_{33} are elastic constants for splay, twist, and bend deformations, respectively.

An additional term F_{stab} shown in Eq. (3) which represents the contribution of polymer stabilization to the free energy density F of liquid crystal bulk is introduced in addition to the sum of F_{elas} and F_{diel}

$$F_{stab} = \frac{1}{2}A_{stab}[1 - (\mathbf{n}_{stab} \bullet \mathbf{n})^2], \quad (3)$$

where A_{stab} is the polymer stabilization coefficient, and $\mathbf{n}_{stab}$ represents the director profile when the polymer stabilization is carried out. The expression is similar to that first introduced by Takahashi et al. for a polymer-stabilized ferroelectric liquid crystal cell. It is thought that the polymer stabilization coefficient A_{stab} depends on the density of the polymer chain generated by a photopolymerization reaction induced by UV light irradiation and on the manner of interaction between the polymer chain and liquid crystal molecules.

The total free energy density is given by

$$F = F_{elas} + F_{stab} + F_{diel}. \quad (4)$$

In this analysis, one-dimensional approximation is assumed. That is, it is assumed that the director profile varies only along the normal direction, defined as the z axis, of the substrate surfaces.

Equations (1) to (3) can be rewritten as follows with respect to this model,

$$\begin{aligned} F_{elas} = {} & \frac{1}{2}K_{11}(\partial_z n_Z)^2 + \frac{1}{2}\{K_{33} + (K_{22} - K_{33})n_y^2\}(\partial_z n_x)^2 \\ & + \frac{1}{2}\{K_{33} + (K_{22} - K_{33})n_x^2\}(\partial_z n_y)^2 \\ & - (K_{22} - K_{33})n_x n_y(\partial_z n_x)(\partial_z n_y), \end{aligned} \quad (5)$$

$$F_{stab} = \frac{1}{2}A_{stab}[1 + (n_{stabx}\, n_x + n_{staby}\, n_y + n_{stabz}\, n_z)^2], \quad (6)$$

$$F_{diel} = \frac{1}{2} D_z^2 \, \varepsilon_0^{-1} (\varepsilon_n + \Delta\varepsilon n_z^2)^{-1}. \tag{7}$$

We assume the Rapini-Papoular potential as follows for the surface energy density.

$$\begin{aligned} F^S(l) &= \frac{1}{2} C_{0l} \sin^2(\theta(l) - \theta_l) + \frac{1}{2} C_{\phi l} \sin^2(\Delta\varphi(l)) \\ &= \frac{1}{2} C_{0l} [1 - (\mathbf{n}_l \bullet \mathbf{n}'(l))^2] + \frac{1}{2} C_{\phi l} [1 - (\mathbf{n}_{l_0} \bullet \mathbf{n}(l)_0)^2], \end{aligned} \tag{8}$$

where $l = 0$ for the interface at z = 0, l = d for the interface at z = d, and $\mathbf{n}_l$ and $\mathbf{n}(l)$ represent the unit vector parallel to the easy axis and the director vector at the interface, respectively. The coefficients C_{0l} and $C_{\phi l}$ are the polar anchoring energy and the azimuthal anchoring energy, respectively; $\mathbf{n}'(l)$ is the unit vector obtained by rotating $\mathbf{n}(l)$ to the plane which includes $\mathbf{n}_l$ and is perpendicular to the x-y planewith respect to the z axis. Furthermore, $\mathbf{n}_{l0}$ and $\mathbf{n}(l)_0$ are the unit vectors with projections of $\mathbf{n}_l$ and $\mathbf{n}(l)$ onto the substrate surfaces, respectively.

Rewriting Eq. (8) with respect to the present model, one obtains the following equations:

$$\begin{aligned} F^S(l) = \frac{1}{2} C_{0l} \left[1 - \left\{ \sqrt{n_x(l)^2 + n_y(l)^2} (n_{lx} \cos\phi_l + n_{ly} \sin\phi_l) + n_{lz} n_z(l) \right\}^2 \right] \\ + \frac{1}{2} C_{\phi l} \left[1 - \frac{1}{(n_{lx}^2 + n_{l_y}^2)(n_x(l)^2 + n_y(l)^2)} \{ n_{lx} n_x(l) + n_{ly} n_y(l) \}^2 \right]. \end{aligned} \tag{9}$$

2.2. Differential Equations to be Solved to Obtain Director Profiles

The momentum balance equations for the LC bulk and the interfaces at z = 0 and d are to be solved. When the momentum balance equations are solved with respect to the tilt angle θ and azimuthal angle ϕ, the points at which ϕ takes the value of $\pi/2$ and either θ or ϕ varies discontinuously become singularity points. To avoid such singularity, a particular technique must be used [11]. We solved the momentum balance equations with respect to three components n_x, n_y, and n_z of $\mathbf{n}$, because we could get true solutions even at the singularity points without special procedures. It is easy to obtain the solutions with respect to θ and ϕ from n_x, n_y, and n_z. In this study, the rotational viscous torque and the surface anchoring effect are taken into account, but for simplicity, the flow effect and the surface dissipation are

ignored. As a result, the following simultaneous nonlinear equations are obtained. For the LC bulk

$$\frac{\partial F}{\partial n_x} - \partial_z \frac{\partial F}{\partial(\partial_z n_x)} + \lambda_L n_x + \gamma_1 \frac{\partial n_x}{\partial t} = 0 \tag{10}$$

$$\frac{\partial F}{\partial n_y} - \partial_z \frac{\partial F}{\partial(\partial_z n_y)} + \lambda_L n_y + \gamma_1 \frac{\partial n_y}{\partial t} = 0 \tag{11}$$

$$n_x^2 + n_y^2 + n_z^2 = 1 \tag{12}$$

where γ_1 is the rotational viscous coefficient and λ_L a Lagrange multiplier.

For the surfaces at z = 0

$$\frac{\partial F^s(0)}{\partial n_x(0)} - \frac{\partial F}{\partial(\partial_z n_x)}\Big|_{z=0} = 0 \tag{13}$$

$$\frac{\partial F^s(0)}{\partial n_y(0)} - \frac{\partial F}{\partial(\partial_z n_y)}\Big|_{z=0} = 0 \tag{14}$$

$$n_x(0)^2 + n_y(0)^2 + n_z(0)^2 = 1 \tag{15}$$

For the surface at z = d

$$\frac{\partial F^s(d)}{\partial n_x(d)} + \frac{\partial F}{\partial(\partial_z n_x)}\Big|_{z=d} = 0 \tag{16}$$

$$\frac{\partial F^s(d)}{\partial n_y(d)} + \frac{\partial F}{\partial(\partial_z n_y)}\Big|_{z=d} = 0 \tag{17}$$

$$n_x(d)^2 + n_y(d)^2 + n_z(d)^2 = 1 \tag{18}$$

Detailed expressions of each terms in the eqs. (10), (11), (13), (14), (16) and (17) for this model are shown in the Appendix.

2.3. Method of Numerical Calculation

To solve the nonlinear simultaneous differential equations consisting of Eqs. (10)–(18), we divided the interval [0, d] into 100 subintervals and rewrote the equations in terms of differences. The simultaneous equations for the resultant 303 elements were numerically solved by Newton's method.

Considering that

$$\sum_i n_i \frac{\partial n_i}{\partial t} = \frac{1}{2} \frac{\partial \sum_i n_i n_i}{\partial t} = 0 \tag{19}$$

the Lagrange multiplier is determined by

$$\lambda_L = -\sum_i n_i \left[\frac{\partial F}{\partial n_i} - \partial_z \frac{\partial F}{\partial (\partial_z n_i)} \right]. \tag{20}$$

The notation $\sum_i$ means the sum with respect to x, y and z.

To investigate the changes in the director profile with the increase or decrease in applied voltage, the applied voltage V was linearly varied with time. A sufficiently slow rate of variation for example 0.5 V/min, was assumed to obtain a solution as near as possible to the steady state.

3. THEORETICAL CONSIDERATION

3.1. Gibbs Free Energy for the Splay, Bend, and Twist Alignments Before Polymer Stabilization

3.1.1. Calculation of the Gibbs Energy

The Gibbs energy GE are calculated from

$$GE = \int_0^d (F_{elas} - F_{diel}) dz. \tag{21}$$

Explicit expressions for F_{elas} and F_{diel} are given by Eq. (5) and Eq. (7), respectively. When no voltage is applied, it is assumed that $F_{diel} = 0$.

3.1.2. When No Voltage is Applied

In Figure 1 the Gibbs free energy calculated as a function of pretilt angle θ_0 is plotted for the case of no voltage application. In these calculations, it was assumed that $F_{diel} = 0$ and $F_{stab} = 0$, that is, V = 0 and $A_{stab} = 0$. The parameters of the liquid crystal used in the calculation are listed for nematic liquid crystal ZLI-2293 in Table 1. For the cell gap, d = 6 μm was assumed.

When the pretilt angle is lower than θ_2, as is shown in the figure, the splay alignment is the stable state since it has the lowest Gibbs free energy among the splay, bend, and twist states. Conversely, when the pretilt angle is higher than θ_2, the bend state is the stable state since it has the lowest Gibbs free energy of the three states.

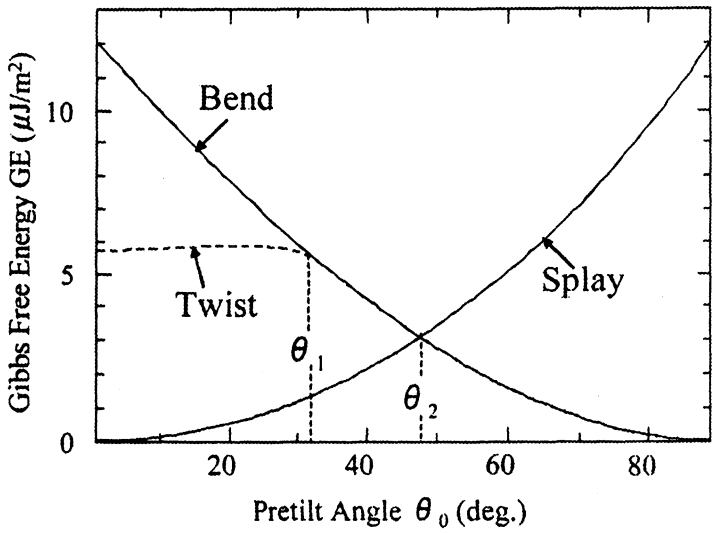

FIGURE 1 Gibbs free energy for splay, bend and twist states of alignment under the condition of no voltage application.

When the pretilt angle is lower than θ_1, the twist alignment has a lower Gibbs free energy than the bend alignment. However, when the pretilt angle is higher than θ_1, the bend alignment and the twist alignment degenerate as shown in Figure 2. The angle θ_1 depends strongly on the twist elastic constant K_{22}. For common nematic liquid crystals which are commercially available, the angle θ_1 is in the range of 25 to 35°. The pretilt angle obtained by the rubbing method using the polyimide alignment material is lower than θ_1, which is in the upper range. Thus, the twist alignment is in a lower metastable state than that of the bend alignment.

3.1.3. When Voltage is Applied

Figure 3 shows the calculated results for the relationships between the applied voltage and the Gibbs free energy for the splay, twist and bend states of alignment. In these calculations, it was assumed that $F_{stab} = 0$, that is, $A_{stab} = 0$. Moreover, it was assumed that pretilt angle is 5°. The parameters of the liquid crystal used in the calculation are listed for nematic liquid crystal ZLI-2293 in Table 1.

TABLE 1 Parameter Used in Our Calculations

$K_{11} = 12.5 \times 10^{-12}$ N	$n_e = 1.63$
$K_{22} = 7.3 \times 10^{-12}$N	$n_o = 1.50$
$K_{33} = 17.9 \times 10^{-12}$N	$\gamma_1 = 149$ mPas
$\varepsilon_p = 14.1$	d = 6.0 μm
$\varepsilon_n = 4.1$	$\lambda = 550$ nm

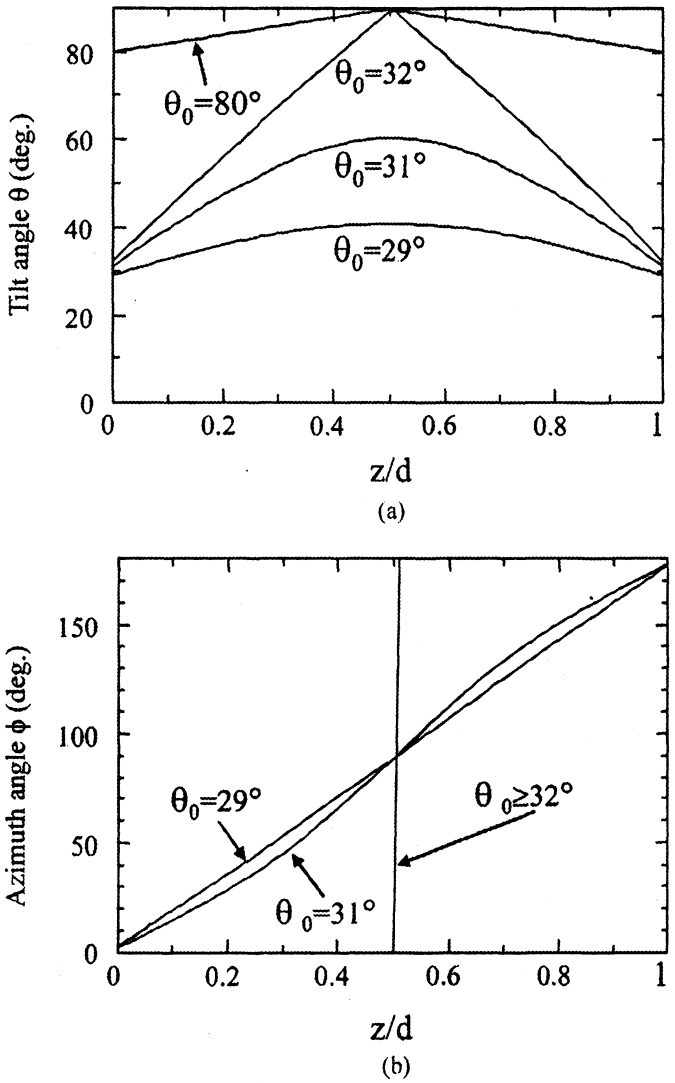

FIGURE 2 Dependence of director profiles on pretilt angle, θ_0, in 180° twist alignment: (a) tilt angle and (b) azimuth angle.

When no voltage is applied, the splay state has the lowest Gibbs free energy. Thus, the splay state is realized as the initial equilibrium state. When the applied voltage V is increased to over the voltage V_C, the configuration of molecular alignment changes to the bend state or the twist state from the splay state, since the Gibbs energy of the splay state become higher than the energies of the bend and twist states. If the applied voltage is decreased from a voltage higher than V_C, the configuration of molecular alignment takes the states of bend or twist within the range $V_C > V > V_{C1}$, and it takes the twist

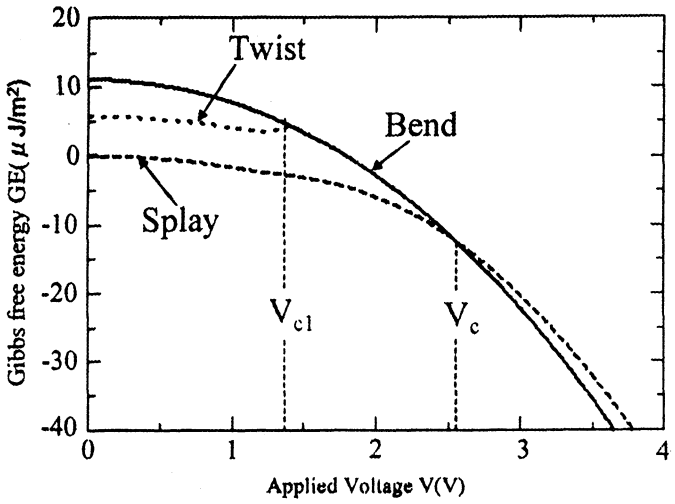

FIGURE 3 Relationship between applied voltage and Gibbs free energy for splay, bend and twist states of alignment.

state in the range $V < V_{C1}$. The twist state finally relaxes to the splay state.

3.2. Simulation for Director Profile After Polymer Stabilization

3.2.1. Procedure of the Calculation

The procedure for this simulation was conducted as follows. It was assumed that the initial configuration of the molecules was in the 180° twist state. Presuming that the voltage was increased from 0 V to V_{stab} at a constant rate, the director profiles were calculated for each time interval under the condition $A_{stab} = 0$. The voltage V_{stab} is selected to be in a range in which the center tilt angle is $\pi/2$. When the center tilt angle becomes $\pi/2$ the twist state transforms to the bend state. The director profile at $V = V_{stab}$ was memorized as the profile of $\mathbf{n}_{stab}$. Then assuming the appropriate value for A_{stab}, the applied voltage was decreased to 0 V at a constant rate. In this process, the director profile was also calculated for each time interval.

3.2.2. Simulated Results and Discussion

The parameters of the liquid crystal used in these calculations are listed for nematic liquid crystal ZLI-2293 in Table 1, and the pretilt angle is assumed to be 5°.

The dotted line in Figure 4 shows the director profiles of $\mathbf{n}_{stab}$ calculated for $V_{stab} = 10.0$ V, and the solid line shows the director profiles resulting from the polymer stabilization for some values of A_{stab} when

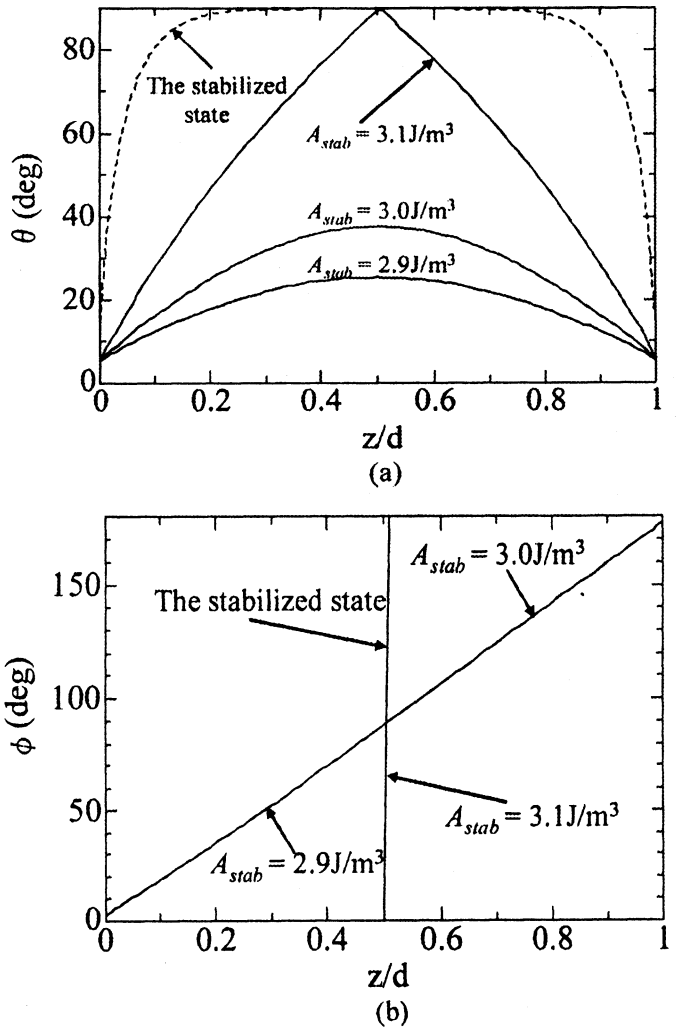

FIGURE 4 Dependence of director profiles on polymer stabilization coefficient, A_{stab}, resulting from polymer stabilization treatment in bend alignment under application of $V_{stab} = 10\,V$. (a) tilt angle and (b) azimuth angle.

no voltage is applied. Figures 4(a) and 4(b) show the profiles of the tilt angle and the azimuth angle, respectively. The tilt angle profile corresponding to the $\mathbf{n}_{stab}$ takes $\pi/2$ at $z = d/2$, and the azimuth angle profile of $\mathbf{n}_{stab}$ varies discontinuously at $z = d/2$ from 0 to π. This means that the polymer-stabilizing treatment was applied to the bend alignment. The director profiles resulting from the polymer stabilization for A_{stab} larger than the critical value $A_{stabc} = 3.1\,J/m^3$ are apparently in the bend alignment, since in this case, the tilt angle is $\pi/2$ at $z = d/2$, and the azimuth angle changes discontinuously from 0 to π at $= d/2$. When A_{stab} is smaller than A_{stabc}, however, the director profile

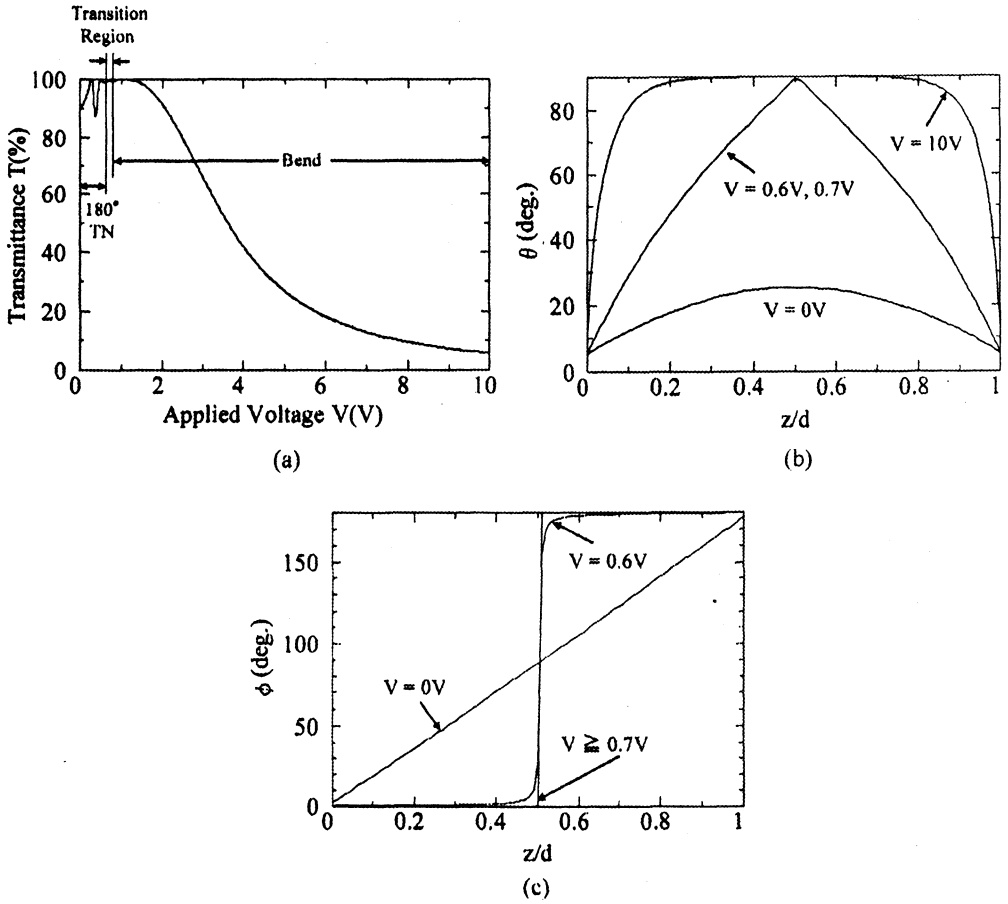

FIGURE 5 V-T curves and director profiles at each voltage when A_{stab} is $2.9\,J/m^3$: (a) V-T curve, (b) tilt angle, (c) azimuth angle.

resulting from the polymer stabilization is in the twist state, because the center tilt angle is lower than $\pi/2$ and the azimuth angle changes continuously from zero to 180° along the z direction.

In Figure 5(a), the V vs T relation is calculated for the change of director profiles, which are shown in Figures 5(b) and 5(c). In these calculations, it was assumed that polymer stabilization was carried out under conditions where $V_{stab} = 10\,V$ and $A_{stab} = 2.9\,J/m^3$. As can be seen, when $V = 0\,V$, the director profile is in the twist alignment. When the applied voltage is increased from 0 V, the director profile transforms to the bend state above $V = 0.7\,V$, because the center tilt angle becomes $\pi/2$ and the azimuth angle changes discontinuously at $z = d/2$. When the director profile is in the twist state below $V = 0.7\,V$, the transmittance varies characteristically in the voltage range as shown in Figure 5(a). However, when A_{stab} is larger than

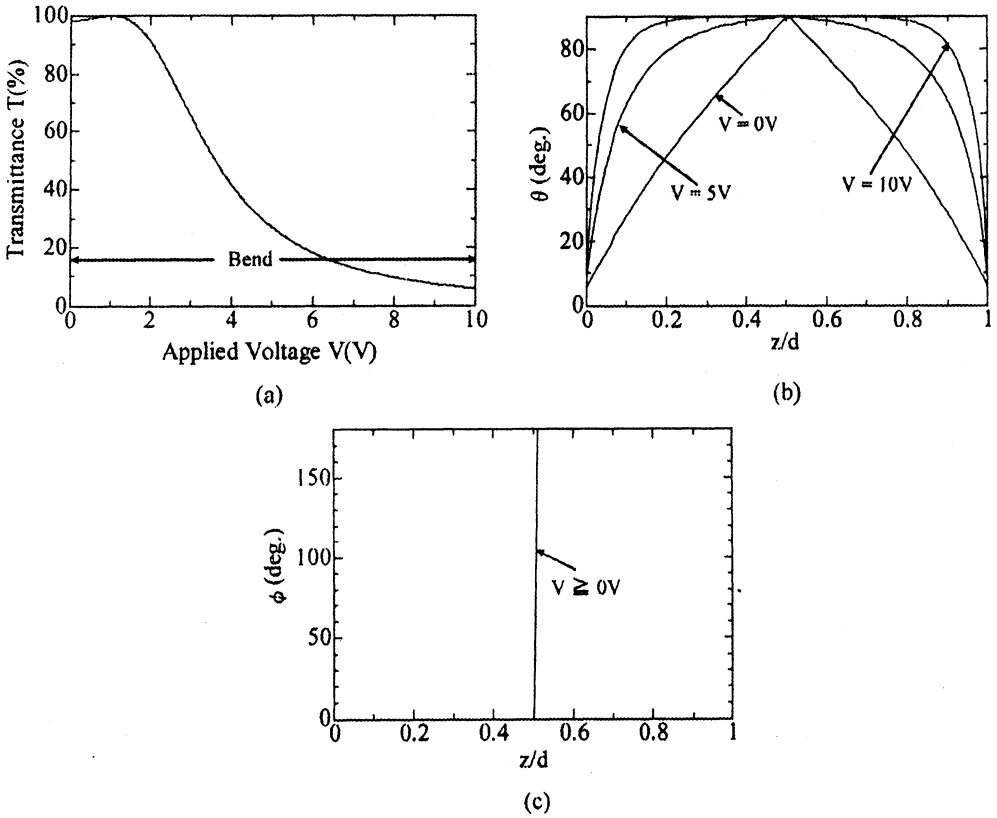

FIGURE 6 V-T curves and director profiles at each voltage when A_{stab} is $3.1\,J/m^3$: (a) V-T curves, (b) tilt angle, (c) azimuth angle.

$3.1\,J/m^3$, the director profile adopts the bend alignment over all the voltage range and the transmittance varies with the increase in applied voltage as shown in Figure 6(a). It should be noted that A_{stab} must be larger than the critical value A_{stabc} to confidently obtain the bend alignment at V = 0 by polymer-stabilization treatment.

The manner of variation of transmittance in the low voltage range can be used to judge whether the bend alignment is the result of the polymer stabilization.

4. EXPERIMENTAL PROCEDURE

4.1. Sample Preparation and Experiments

Sample cells were made using the liquid crystal mixture ZLI-2293, and a reactive mesogen RMM34 which is a mixture of diacrylate and monoacrylate and a small amount (5–10 wt%) of photoinitiator, all supplied by Merck Ltd. The reactive mesogen RMM34 was added to

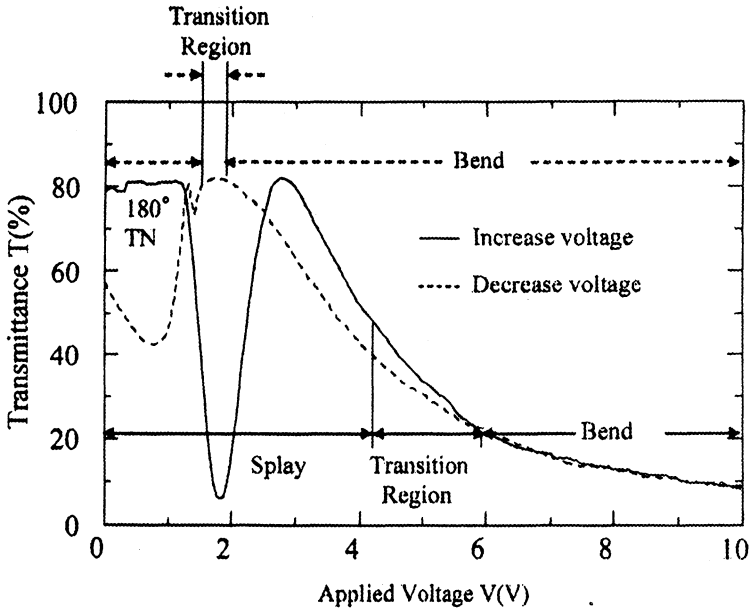

FIGURE 7 Experimental results for relationship between transmittance and applied voltage before polymer stabilization.

the nematic liquid crystal mixture ZLI-2293 at concentrations in the range of 1 to 5 wt%. The final mixture was filled into 6-μm-gap liquid crystal cells with tilted alignment produced by the parallel rubbing of polyimide coating SE-610 (Nissan Chemical Industry.) on both plates. Polymerization was induced by exposure to an ultra violet light source of approximately 0.6 mW/cm^2, centered around 365 nm (black-light) for an appropriate time. A 100 kHz sine wave voltage of 15 V was applied during exposure. The exposure time was determined so as to obtain appropriate irradiation energy density, E_{UV}, defined as the product of the irradiation power and the exposure time.

The relationship between the transmittance and the applied voltage, was measured for each sample cell. A sine wave voltage at a frequency of 1 kHz was applied. The changing rate of applied voltage was 3 V/min. Monochromatic light of wavelength 550 nm was used as the light source. The sample cell was set in a crossed Nicols. The transmission axis of polarizer was set at an angle of 45° with respect to the rubbing direction of the sample cell.

4.2. Experimental Results and Discussion

The V-T curves measured before UV light irradiation are shown in Figure 7. In this figure, the solid line indicates the V-T curve with the increase of applied voltage. It can be seen that at the initial state

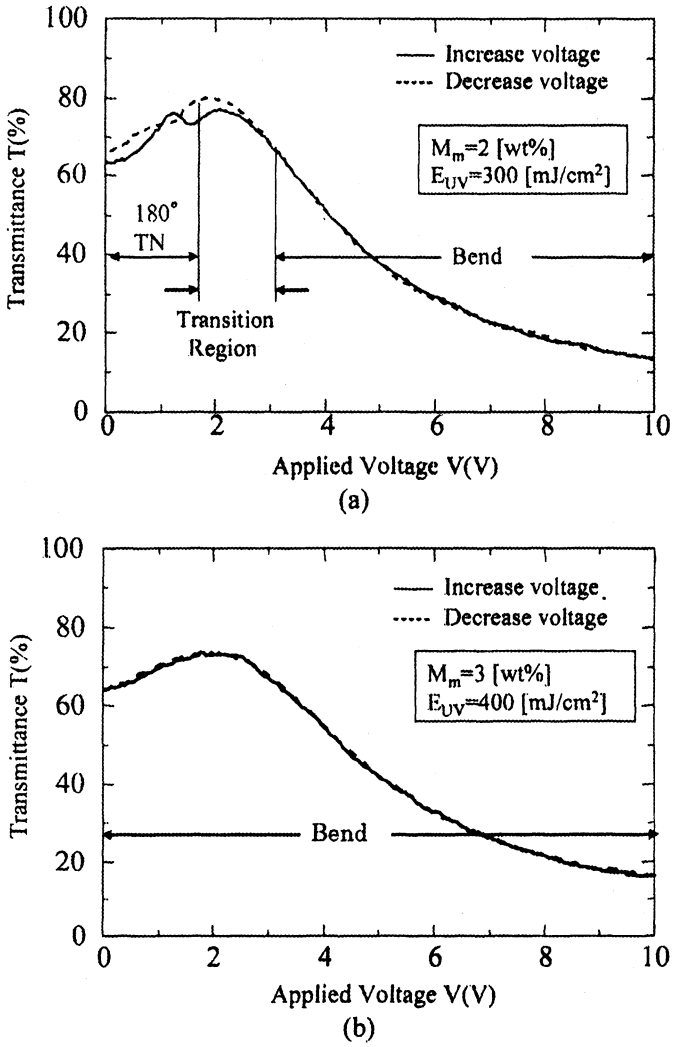

FIGURE 8 Experimental result for the relation of transmittance vs. applied voltage after polymer stabilization: (a) concentration of reactive mesogen $M_m = 2\,wt\%$ and the UV irradiation energy $E_{UV} = 300\,mJ/cm^2$, and (b) concentration of reactive mesogen $M_m = 3\,wt\%$ and the UV irradiation energy $E_{UV} = 400\,mJ/cm^2$.

of molecular alignment the configuration is in the splay alignment and the initial state is transformed to the bend state in the voltage range of 4.3 to 5.8 V. The dotted line in this figure indicates the V-T curve as the applied voltage decreases. Here it is observed that the bend state transforms into the twist state in the voltage range of 2.0 to 1.7 V. The twist state then naturally relaxes to the splay state.

Figure 8 shows the V-T curves measured for cells after being treated with the polymer-stabilizing method at the bend alignment.

Figure 8(a) represents the case with the concentration of reactive mesogen $M_m = 2\,wt\%$ and UV irradiation energy of $E_{UV} = 300\,mJ/cm^2$, and Figure 8(b) represents the case with $M_m = 3\,wt\%$ and $E_{UV} = 400\,mJ/cm^2$. In Figure 8, the states of the alignment expected for each voltage range are described. It can be seen that in the case of Figure 8(a), the twist alignment resulted from the polymer stabilization when no voltage was applied, while in the case of Figure 8(b), the bend alignment was definitively stabilized.

As mentioned, it is plausible to think that the value of A_{stab} depends on the density of polymer chains generated by photopolymerization reactions induced by UV light irradiation and on the manner of interaction between the polymer chain and liquid crystal molecules. It thought that the density of the polymer chain depends on the concentration of the reactive mesogen M_m when the UV irradiation energy E_{UV} is higher than the critical value. The UV irradiation energy E_{UV} irradiated on our sample cell exceeded the critical value. Thus, it is natural to think that the value of A_{stab} in the case of Figure 8(b) is larger than that in the case of Figure 8(a). This supports the theoretical prediction that the value of A_{stab} must be larger than the critical value A_{stabc} to definitively stabilize the bend state by polymer stabilization treatment.

5. CONCLUSIONS

Because of the introduction of an additional term which allows the explanation of the effect of polymer stabilization, it has become possible to investigate theoretically which director profile results from polymer-stabilization treatment in the nematic liquid crystal cell. As has been described in this study, the value of A_{stab} must be larger than the critical value A_{stabc} to definitively stabilize the bend alignment in the π cell. This was confirmed both theoretically and experimentally. The theoretical analysis and experimental considerations concerning the polymer-stabilization coefficient A_{stab} are left for study in the near future.

APPENDIX

In Eqs. (10), (11) and (20),

$$\begin{aligned}\frac{\partial F}{\partial n_x}-\partial_z\left(\frac{\partial F}{\partial(\partial_z n_x)}\right)=&-\{K_{33}+(K_{22}-K_{33})n_y^2\}(\partial_z^2 n_x)+(K_{22}-K_{33})n_x n_y(\partial_z^2 n_y)\\&-K_{33}n_x(\partial_z n_x)^2+(2K_{22}-K_{33})n_x(\partial_z n_y)^2\\&-K_{22}n_y(\partial_z n_x)(\partial_z n_y)-2K_{33}n_z(\partial_z n_y)(\partial_z n_z)\\&+A_{stab}(n_{stabx}n_x+n_{staby}n_y+n_{stabz}n_z)n_{stabx},\end{aligned}\tag{A-1}$$

$$\frac{\partial F}{\partial n_y}-\partial_z\left(\frac{\partial F}{\partial(\partial_z n_y)}\right)=(K_{22}-K_{33})n_x n_y(\partial_z^2 n_x)-\{K_{33}+(K_{22}-K_{33})n_x^2\}(\partial_z^2 n_y)$$
$$-(K_{33}-2K_{22})n_y(\partial_z n_x)^2-K_{33}n_z(\partial_z n_y)(\partial_z n_z)$$
$$-2K_{22}n_x(\partial_z n_x)(\partial_z n_y)-A_{stab}(n_{stabx}n_x+n_{stab}n_y$$
$$+n_{stabz}n_z)n_{staby}, \tag{A-2}$$

$$\frac{\partial F}{\partial n_z}-\partial_z\left(\frac{\partial F}{\partial(\partial_z n_z)}\right)=-K_{11}(\partial_z^2 n_z)+K_{33}n_z\{(\partial_z n_x)^2+(\partial_z n_y)^2\}$$
$$-A_{stab}(n_{stabx}n_x+n_{stab}n_y+n_{stabz}n_z)n_{stabz},$$
$$-\frac{(\varepsilon_p-\varepsilon_n)n_z D_z^2}{\varepsilon_0\{\varepsilon_n+(\varepsilon_p-\varepsilon_n)n_z^2\}^2}. \tag{A-3}$$

Since the effective dielectric constant with respect to the z direction is $\varepsilon_0\{\varepsilon_n+(\varepsilon_p-\varepsilon_n)n_z^2\}$, D_z is related to the voltage V across the electrodes as follows

$$D_z=\frac{V}{\int_0^d \frac{1}{\varepsilon_0\{\varepsilon_n+(\varepsilon_p-\varepsilon_n)n_z^2\}}dz}, \tag{A-4}$$

In the Eqs. (13), (14), (16) and (17),

$$\frac{\partial F^S(l)}{\partial n_x(l)}=-C_{0l}\left\{(n_{lx}\cos\phi_l+n_{ly}\sin\phi_l)\sqrt{n_x(l)^2+n_y(l)^2+n_{lz}n_z(l)}\right\}$$
$$\times\left\{(n_{lx}\cos\phi_l+n_{ly}\sin\phi_l)n_x(l)(n_x(l)^2+n_y(l)^2)^{-\frac{1}{2}}-n_{lz}n_x(l)/n_z(l)\right\}$$
$$-C_{\phi l}\frac{n_y(l)\{n_{lx}n_x(l)+n_{ly}n_y(l)\}\{n_{lx}n_y(l)-n_{ly}n_x(l)\}}{(n_{lx}^2+n_{ly}^2)\{n_x(l)^2+n_y(l)^2\}^2}, \tag{A-5}$$

$$\frac{\partial F^S(l)}{\partial n_y(l)}=-C_{0l}\left\{(n_{lx}\cos\phi_l+n_{ly}\sin\phi_l)\sqrt{n_x(l)^2+n_y(l)^2}+n_{lz}n_z(l)\right\}$$
$$\times\left\{(n_{lx}\cos\phi_l+n_{ly}\sin\phi_l)n_y(l)(n_x(l)^2+n_y(l)^2)^{-\frac{1}{2}}-n_{lz}n_y(l)/n_z(l)\right\}$$
$$-C_{\phi l}\frac{n_x(l)\{n_{lx}n_x(l)+n_{ly}n_y(l)\}\{n_{ly}n_x(l)-n_{lx}n_y(l)\}}{(n_{lx}^2+n_{ly}^2)\{n_x(l)^2+n_y(l)^2\}^2}, \tag{A-6}$$

$$\frac{\partial F}{\partial(\partial_z n_x)}\Big|Z=l=\{K_{33}+(K_{22}-K_{33})n_y(l)^2\}(\partial_z n_x)\Big|_{z=l}$$
$$-(K_{22}-K_{33})n_x(l)n_y(l)(\partial n_y)\Big|_{z=l}, \tag{A-7}$$

$$\frac{\partial F}{\partial(\partial_z n_y)}\Big|Z = l = \{K_{33} + (K_{22} - K_{33})n_x(l)^2\}(\partial_z n_y)\Big|_{z=l} - (K_{22} - K_{33})n_x(l)n_y(l)(\partial n_x)\Big|_{z=l}. \quad \text{(A-8)}$$

REFERENCES

[1] Miyashita, T., Yamaguchi, Y., & Uchida, T. (1995). *Jpn. J. Appl. Phys.*, *34*, 177.
[2] Bos, P. L. & Rahman, J. A. 1993 SID Int. Symp. Dig. Tech. Papers, 1993, p. 273.
[3] Sueoka, K., Nakamura, H., & Taira, Y. Proc. AM-LCD & IDW, 1996, p. 133.
[4] Mori, H., Gartland, E. C. Jr., Kelly, J. R., & Bos, P. J. Proc. IDW, 1998, p. 77.
[5] Nagae, N., Miyashita, T., Uchida, T., Yamada, Y., & Ishii, Y. 2000 SID Int. Symp. Dig. Tech. Papers, 2000, p. 26.
[6] Konno, T., Miyashita, T., & Uchida, T. (1995). *ASIA DISPLAY '95*, 581.
[7] Kim, S. H. & Chien, L. C. (2004). *Jpn. J. Appl. Phys.*, *43*, 7643.
[8] Kikuchi, H., Yamamoto, H., Sato, H., Kawakita, M., Takizawa, K., & Fujikake, H. (2005). *Jpn. J. Appl. Phys.*, *44*, 981.
[9] Kossyrev, P. A., Qi, J., Priezjev, N. V., Pelcovits, R. A., & Crawford, G.-P. 2002 SID Int. Symp. Dig. Tech. Papers, 2002, p. 506.
[10] Takahashi, T., Umeda, T., Furue, H., & Kobayashi, S. (1999). *Jpn. J. Appl. Phys.*, *38*, 5991.
[11] Berreman, D. W. (1975). *J. Appl. Phys.*, *46*, 3740.

Reprinted from
Japanese Journal of Applied Physics
Vol. 46, No. 12, 2007, pp. 7774–7781

Transient Response Characteristics of Polymer Stabilized Bend Alignment State of Nematic Liquid Crystal in Pi-Cell

Youichi ASAKAWA, Taiju TAKAHASHI, and Susumu SAITO

Department of Electronic Engineering, Kogakuin University, 2665-1 Nakano-cho, Hachioji, Tokyo 192-0015, Japan

Japanese Journal of Applied Physics
Vol. 46, No. 12, 2007, pp. 7774–7781

Transient Response Characteristics of Polymer Stabilized Bend Alignment State of Nematic Liquid Crystal in Pi-Cell

Youichi ASAKAWA, Taiju TAKAHASHI, and Susumu SAITO

Department of Electronic Engineering, Kogakuin University, 2665-1 Nakano-cho, Hachioji, Tokyo 192-0015, Japan

(Received June 6, 2007; revised September 14, 2007; accepted September 21, 2007; published online December 6, 2007)

It is shown that the transient response characteristics of the polymer stabilized bend (PSB) cell are deteriorated by the polymer stabilization treatment. The increase in rotational viscosity γ_1 due to polymer stabilization is experimentally confirmed by the transient displacement current method proposed previously by Imai *et al.* [Jpn. J. Appl. Phys. **33** (1994) L119] It is shown that the deterioration of the transient characteristics of the PSB cell is caused by the increase in rotational viscosity and the decrease in flow velocity due to the changes in Leslie viscosities resulting from the polymer stabilization treatment.
[DOI: 10.1143/JJAP.46.7774]

KEYWORDS: nematic liquid crystal, UV-curable liquid crystalline monomer, polymer stabilization, OCB-LCD, polymer-stabilized bend cells, transient response characteristics, rotational viscosity, Leslie viscosities, flow effect

1. Introduction

The optically compensated bend (OCB) nematic liquid crystal display (LCD) has attracted considerable attention due to its superior characteristics such as a fast response time and a wide viewing angle.[1] In the OCB-type LCD, the pi-cell[2] is used with an optical compensation film. The pi-cell is constructed using a pair of substrates rubbed in parallel directions. When the pretilt angle is lower than the critical angle, the pi-cell takes the splay configuration as the stable state.[2] Thus, the OCB-type LCD needs the initial transition operation from the splay alignment to the bend alignment by applying high voltage at start-up, and always needs an operating voltage higher than its critical voltage to maintain the bend alignment. This is one serious drawback of the OCB-type LCD.

To mitigate this problem, some methods have been proposed. One of the methods is to adapt a pretilt angle above a certain critical pretilt angle,[3] making the bend configuration become stable without the need to apply voltage. However, it has been known that this method results in an increase in response time.[4] As an alternative approach, the polymer stabilization method has been proposed, in which the bend alignment is stabilized by forming a polymer network[5,6] or an aligned polymer wall[7] using the optical polymerization of UV-curable crystalline monomers, i.e., reactive mesogen molecules dissolved within the LC host. Using the polymer stabilization method, the LC can be stabilized in the bend state and remains in this state without the electric field because of the bulk anchoring of the LC at the surface of the bend polymer network formed by polymerization.[6] This method is an effective means to solve essentially the problem that the OCB mode has.

So far, it has been reported that the polymer stabilization treatment is effective not only in stabilizing a certain conformation of molecular alignments in a LC cell, but also in lowering the threshold voltage,[8] to improve the transient response characteristics[8,9] of a twisted nematic (TN) cell and to adapt a high pretilt angle.[8]

In our previous paper, we reported that the effect of polymer stabilization on the static characteristics of polymer stabilized bend (PSB) cell can be well explained in terms of the polymer stabilization coefficient A_{stab},[10] which is introduced in the additional term to the free energy density.[11] However, in our recent experiments, we knew that the transient response characteristics cannt be explained only in terms of the effect of A_{stab}. Concretely speaking, although we obtained experimental results in which both the rise and decay times in the transient responses of the bend cell are deteriorated by the polymer stabilization treatment, the theoretically calculated results that are based on the elastic hydrodynamics theory in which the polymer stabilization term was taken into account are inconsistent with those of experimental results. In this paper, the origins of such discrepancy between the experimental results and theoretically calculated results are clarified.

2. Experiments

2.1 Sample preparation

A no polymer stabilized bend (NPSB) cell and a PSB cell were fabricated using about 6-μm-gap pi cells with tilted alignment produced by the parallel rubbing of polyimide PI-A (Nissan Chemical Industry) on both plates. The nematic LC (NLC) material, ZLI-2293, was used in the NPSB cell. For the PSB cell, a mixture of ZLI-2293 and a reactive mesogen RMM34 including a small amount (1–5 wt %) of photoinitiator were used. All of these materials were supplied by Merck. The reactive mesogen RMM34 was added to the NLC mixture ZLI-2293 at a concentration of 3 wt % in the PSB cell. By using the reactive mesogen, LC molecules of the bulk are easily stabilized because the reactive mesogen aligns with the LC molecules and a polymer network is formed along with the alignment of the LC molecules when UV light is irradiated. The PSB cell was obtained using the polymer stabilization method after transition from the splay alignment to the bend alignment by applying high voltage. Polymerization was induced by exposure to an UV light source of approximately 2.0 mW/cm^2 power density, centered around $\lambda = 365$ nm (black light) for an irradiation energy density of $E_{UV} = 10$ J/cm^2. A square wave voltage of 10 V with a frequency of 100 kHz was applied during exposure to definitively stabilize the bend alignment. The exposure time was 5000 s so as to obtain $E_{UV} = 10$ J/cm^2, which is defined as the product of the irradiation power and the exposure time.

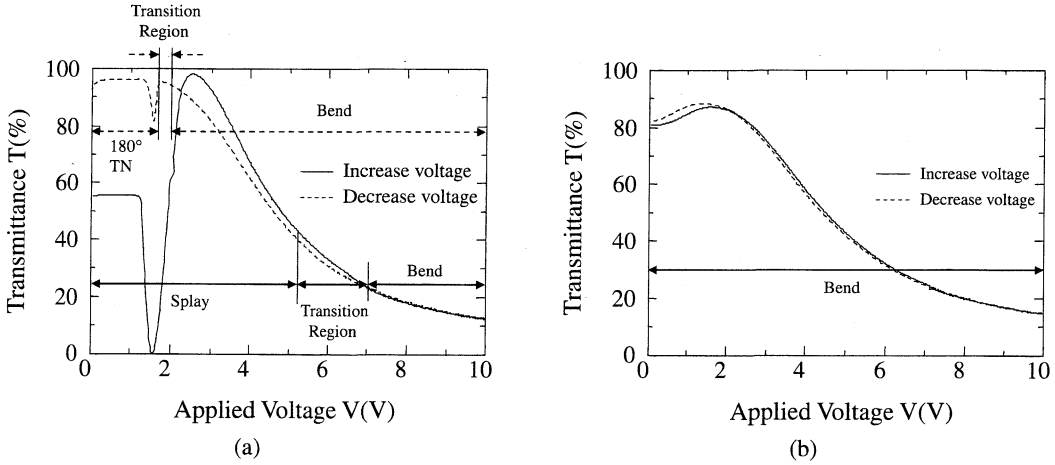

Fig. 1. Experimental results for the relationship between transmittance and applied voltage: (a) the NPSB cell is a pi-cell without polymerization and (b) the PSB cell is polymer-stabilized bend alignment cell.

2.2 *Experimental results*

2.2.1 *Voltage-dependent transmittance of polymer-stabilized bend cell*

The relationships between the transmittance and the applied voltage, V–T curves, were measured for each sample cell. A square wave voltage with a frequency of 1 kHz was applied. The change rate of applied voltage was 3 V/min. Monochromatic light with a wavelength 632.8 nm was used as the light source. The sample cell was set in a crossed Nicols arrangement. The transmission axis was set at an angle of 45° with respect to the rubbing direction of the sample cell.

The V–T curves are shown in Fig. 1. Figure 1(a) represents the case of the NPSB cell where the concentration of reactive mesogen is $M_m = 0$ wt % and the UV irradiation energy is $E_{UV} = 0\,J/cm^2$, and Fig. 1(b) represents the case of the PSB cell where $M_m = 3$ wt % and $E_{UV} = 10\,J/cm^2$.

In Fig. 1(a), the solid line indicats the V–T curve with an increase in applied voltage. It can be seen that at the initial state of molecular alignment, the configuration is in the splay alignment and the initial state is transformed to the bend state in that voltage range of 5.2 to 7.0 V. The dotted line in this figure indicates the V–T curve with the decrease in applied voltage. Here it is observed that the bend state transforms into the twist state in the voltage range of 2.0 to 1.7 V. The twist state then naturally relaxes to the splay state.

Figure 1(b) shows the V–T curves measured for the PSB cell after being treated using the polymer stabilizing method at the bend alignment. It can be seen that in the case of Fig. 1(b), the bend alignment was surely stabilized.

In Fig. 1, the states of alignment expected in each voltage range have been described for the comparison of V–T curves obtained by experiments and by calculations based on the LC continuum theory.

2.2.2 *Transient response characteristics of polymer-stabilized bend cell*

The transient response characteristics were measured for each sample cell. The monochromatic light of 632.8 nm wavelength was used as the light source. The sample cell was set in a crossed Nicols arrangement. The transmission axis of the polarizer was set at an angle of 45° with respect to the rubbing direction of the sample cell. A pulse wave-voltage with a frequency of 20 kHz was used as the applied voltage. The rise time τ_{rise} was defined as the time during which the retardation δ changes by 90% from the initial value when the applied voltage is increased from the bias voltage (= 3 V). The decay time τ_{decay} is defined as the corresponding time when the voltage is switched from an applied voltage to the bias voltage. The bend alignment is always maintained in each sample cell during the measurement.

Figure 2(a) shows the rise transient response characteristics of the NPSB cell and PSB cell when the voltage is switched from 3 to 4 V. Figure 2(b) shows the decay transient characteristics of those cells when the voltage is switched from 4 to 3 V. We obtained 2.3 ms as the rise time and 2.59 ms as the decay time for the NPSB cell, and 3.48 ms as the rise time and 5 ms as the decay time for the PSB cell.

The applied voltage dependence of transient response times is shown in Fig. 3. In this figure, the solid line and dotted line indicate the applied voltage dependences of the response times of the NPSB cell and the PSB cell, respectively. It should be noted that both rise and decay times are increased by polymer stabilization. Similar results were obtained for the cell with a different monomer concentration.

3. Theoretical Considerations

In our previous paper,[9,11] we introduced an additional term F_{stab} as shown in eq. (1), which represents the contribution of polymer stabilization to the free energy density F of the liquid crystal bulk, to calculate theoretically the behaviors of polymer-stabilized LC cells.

$$F_{stab} = \frac{1}{2} A_{stab}[1 - (\boldsymbol{n}_{stab} \cdot \boldsymbol{n})^2], \quad (1)$$

A_{stab} is the polymer stabilization coefficient. It can be thought that $\boldsymbol{n}_{stab}$ is an interaction field. The profile of the interaction field $\boldsymbol{n}_{stab}$ coincides with the profile of the director field when UV light is irradiated and it is memorized as the conformation of the polymer network formed by UV light irradiation. The interaction between the polymer

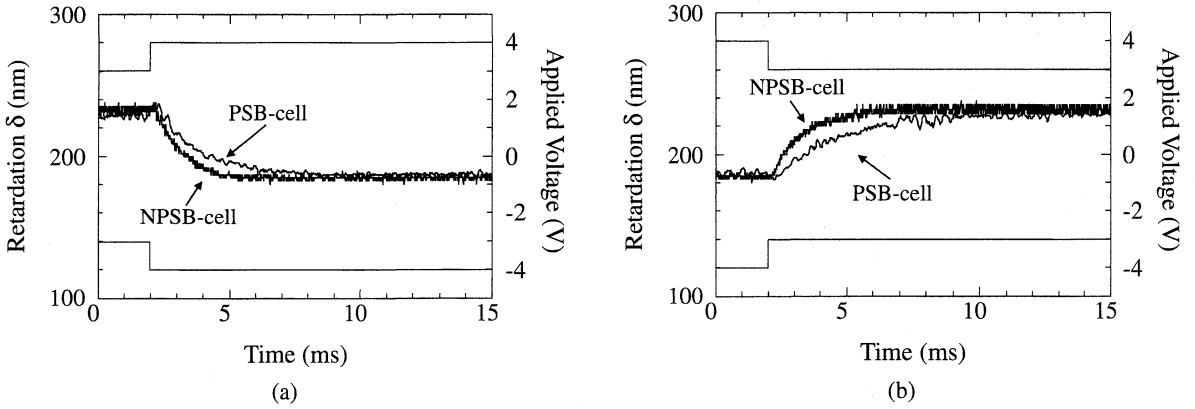

Fig. 2. Experimental results on transient response characteristics of NPSB cell (bend alignment cell without polymerization) and PSB cell (polymer stabilized bend cell): Retardation δ changes (a) when applied voltage is switched from 3 to 4 V and (b) when switched from 4 to 3 V.

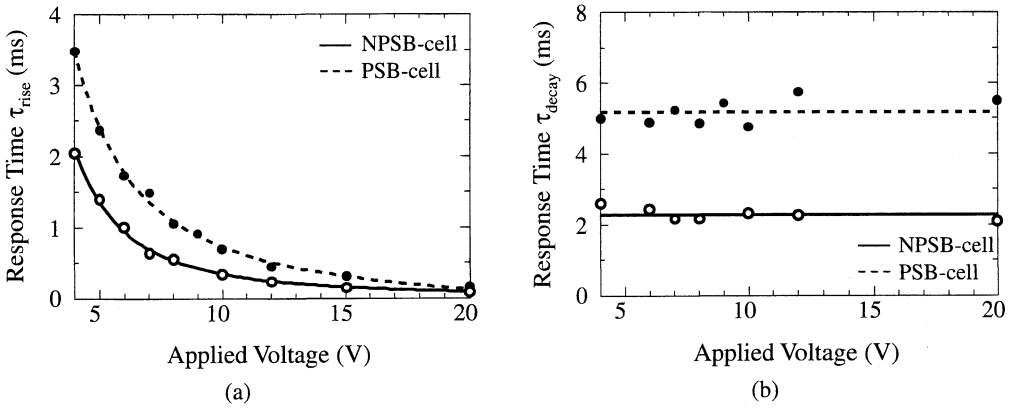

Fig. 3. Experimental results on the applied voltage dependence of transient response time for NPSB cell (bend alignment cell without polymerization) and PSB cell (polymer-stabilized bend cell): (a) response time τ_{rise} when the voltage is switched from 3 V to some voltages higher than 3 V and (b) response time τ_{decay} when the voltage is switched from some voltages higher than 3 to 3 V.

network and the director corresponds to the bulk anchoring of the LC at the surface of the polymer network memorizing the interaction field $\boldsymbol{n}_{stab}$. The polymer stabilization coefficient A_{stab} is regarded as the strength of interaction between the interaction field and the director field, and depends on the density of the polymer chain generated by a photo polymerization reaction induced by UV light irradiation and on the manner of interaction between the polymer chain and LC molecules.

Due to the introduction of the polymer stabilization term F_{stab} as is shown in eq. (1), we could theoretically treat the phenomenon of the polymer stabilization of the bend alignment in a pi-cell.

Now, we describe the outline of the calculated results regarding the effect of polymer stabilization treatment on the electro-optical properties of a pi-cell.

3.1 Calculated results for voltage dependent transmittance

The parameters of the LC used in these calculations are listed in Table I for NLC ZLI-2293. The values of parameters except Leslie viscosities α_i: $i = 1$–6 were obtained from our experiments.

Calculated results for voltage dependent transmittance are shown in Fig. 4. IN the calculation, we assumed a sufficiently slow and linear change in applied voltage. In Fig. 4(a), it was assumed that polymer stabilization was carried out under the conditions of $V_{stab} = 10$ V and $A_{stab} = 4.0\,\mathrm{J/m^3}$. As can be seen, when $V = 0$ V, the director profile is in the twist alignment. When applied voltage is increased from 0 V, the director profile transforms to the bend state above $V = 1.2$ V. However, when A_{stab} is larger than 6.0 $\mathrm{J/m^3}$, the director profile adopts the bend alignment over the entire voltage range and the transmittance varies as shown in Fig. 4(b), with the increase in applied voltage. It should be noted that A_{stab} must be larger than the critical value A_{stabc} to confidently obtain the bend alignment at $V = 0$ by polymer stabilization treatment. Comparing the calculated results shown in Fig. 4 with the experimental results shown in Fig. 1, it can be found that the static characteristics of the polymer stabilized bend cell can be well explained as the effect of the polymer stabilization coefficient A_{stab}.

Table I. Cell and LC material parameters used in the calculation, taking account of only F_{stab} as the effects of polymer stabilization.

Cell thickness (μm)	6	α_1 (mPa·s)	0
Pretilt angle (deg)	5	α_2 (mPa·s)	−167.6
K_{11} (pN)	12.5	α_3 (mPa·s)	23.4
K_{22} (pN)	5	α_4 (mPa·s)	109.6
K_{33} (pN)	23	α_5 (mPa·s)	32.8
ε_p	12.5	α_6 (mPa·s)	−111.4
ε_n	3.8		

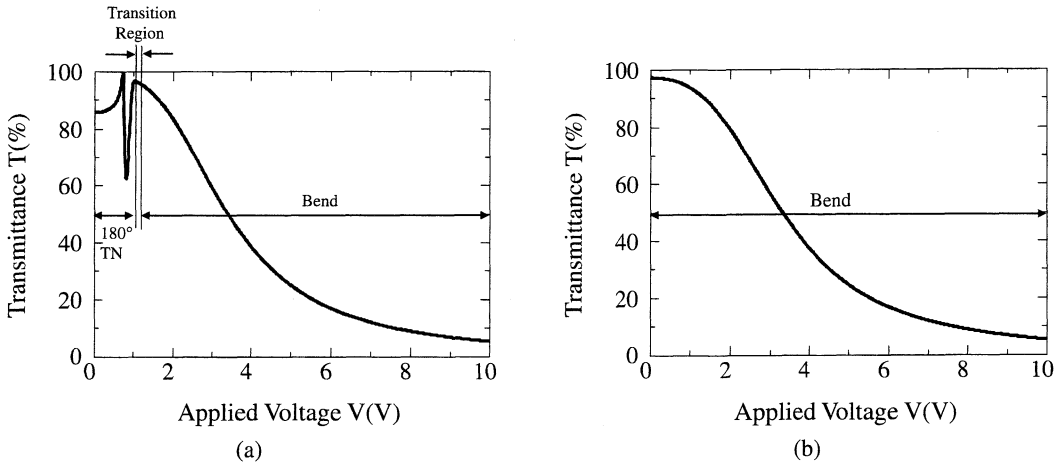

Fig. 4. Voltage dependence of transmittance calculated taking account of the polymer stabilization term F_{stab}: (a) Twist alignment is stabilized under the conditions of $V_{stab} = 10\,V$ and $A_{stab} = 4.0\,J/m^3$ and (b) the PSB cell is obtained under the conditions of $V_{stab} = 10\,V$ and $A_{stab} = 6.0\,J/m^3$.

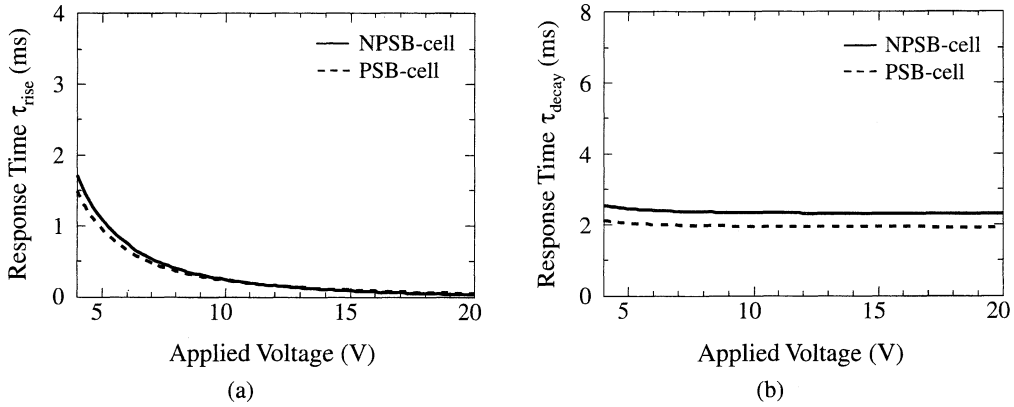

Fig. 5. Calculated results on the applied voltage dependence of transient response time for NPSB cell and PSB cell. For the case of the PSB cell, calculations were carried out under the conditions of $V_{stab} = 10\,V$ and $A_{stab} = 6.0\,J/m^3$: (a) response time τ_{rise} when the voltage is switched from 3 V to some voltages higher than 3 V and (b) response time τ_{decay} when the voltage is switched from some voltages higher than 3 to 3 V.

3.2 *Calculated results for transient response characteristics*

Figure 5 shows transient response characteristics calculated under the assumption that the effect of polymer stabilization on the transient response characteristics can be described by only the polymer stabilization term introduced as an additional term to a free energy density of LC. The parameters of the LC used in the calculation are listed for the NLC ZLI-2293 in Table I. The values of Leslie viscosities $\{\alpha_i: i = 2, 3, 5, 6\}$ were obtained using the MVS method proposed by Funatsu *et al.*[12] Then, it was assumed that $\alpha_1 = 0\,mPa{\cdot}s$ and α_4 were assumed to be equal to that for MBBA[13] since there are no dependable values for ZLI-2293.

In Fig. 5, the solid line corresponds to the NPSB cell and the dotted line corresponds to the PSB cell in the experiments. The equations used in the calculation are shown in Appendix A. For the case of the PSB cell, these calculations were carried out under the conditions of $V_{stab} = 10\,V$ and $A_{stab} = 6.0\,J/m^3$ with F_{stab} as the effect of polymer stabilization using $M_m = 3\,wt\,\%$ and $E_{UV} = 10\,J/cm^2$ in the experiment. On the other hand, in the case of the NSB cell, calculations were carried out under the condition of $A_{stab} = 0\,J/m^3$.

As can be seen from Fig. 5, the PSB cell is faster than the NPSB cell in transient response characteristics. This tendency disagrees with the tendency revealed in our experimental results shown in Fig. 3. This means that the effect of polymer stabilization on the transient response cannot be explained by only the polymer stabilization term.

We thought that the decrease in the transient response speed of the PSB cell must be caused by changes in viscosities and in the flow velocity pattern induced by polymerization. In the following section, this is described in detail.

4. Dependence of Rotational Viscosity γ_1 on Monomer Concentration

4.1 *Transient displacement current method taking account of polymer stabilization*

For the measurement of the rotational viscosity of NLC, we used the transient displacement current method proposed by Imai *et al.*[14] At first, we must confirm whether the transient displacement current method can be applicable for the case when the polymer stabilization term is introduced.

Now we consider a NLC cell having a homogeneous alignment with the pretilt angle θ_0 at both boundaries. The dielectric anisotropy of the NLC used in the cell is assumed to be positive. It is assumed that the polymer stabilization treatment is carried out under no voltage application. Since the coupling between orientation and flow can be neglected for such cells in the case when a steplike voltage is applied, the dynamic motion of the director is expressed by the torque balance equation as presented in Appendix B. Since it is known that the director distribution of the bulk region is uniform in a dynamic motion, the torque balance equation in the bulk region can be approximated as follows;

$$\gamma_1 \frac{\partial \theta}{\partial z} = \frac{1}{2}\varepsilon_0 \Delta\varepsilon E_b^2 \sqrt{\left(1 - \frac{A_{stab}}{\varepsilon_0 \Delta\varepsilon E_b^2}\cos 2\theta_0\right)^2 + \left(\frac{A_{stab}}{\varepsilon_0 \Delta\varepsilon E_b}\sin 2\theta_0\right)^2}\,\sin(2\theta + \theta'), \tag{2}$$

where θ_0 is the pretilt angle, E_b is the electric field in the bulk region, A_{stab} is the polymer stabilization coefficient, γ_1 is the rotational viscosity, and θ' is given by eq. (B·4).

The NLC has such a high resistivity that the conduction current is negligible in comparison with the displacement current. The displacement current is given by

$$I(t) = SE_b \frac{\partial \varepsilon(\theta(t))}{\partial t} = SE_b \sin 2\theta(t) \frac{\partial \theta(t)}{\partial t}, \tag{3}$$

where S is the effective area of the electrode.

From eqs. (2) and (3), the current peak, I_P, appears at $\theta = (\pi/4) - (\theta'/2)$ and is given by

$$I_p = \frac{S(\varepsilon_0 \Delta\varepsilon)^2}{2\gamma_1} \sin 2\left(\frac{\pi}{4} + \frac{\theta'}{2}\right) E_b^3 \sqrt{\left(1 - \frac{A_{stab}}{\varepsilon_0 \Delta\varepsilon E_b^2}\cos 2\theta_0\right)^2 + \left(\frac{A_{stab}}{\varepsilon_0 \Delta\varepsilon E_b^2}\sin 2\theta_0\right)^2}. \tag{4}$$

The relationship between E_b and V is assumed as

$$E_b = \frac{V}{\left(1 + \frac{\beta}{V}\right)d}, \tag{5}$$

where β is a positive constant and d is the cell thickness.

When $1/V$ approaches zero, E_b approaches infinity. Thus, when $1/V$ approaches zero, the value of $V/(I_p^{1/3}d)$ approaches the right side of eq. (6).

$$\left(\frac{1}{I_p}\right)^{1/3}\left(\frac{V}{d}\right) = \left(\frac{2\gamma_1}{S(\varepsilon_0 \Delta\varepsilon)^2}\right)^{1/3} \tag{6}$$

As has been proposed by Imai *et al.* we can obtain the value of rotational viscosity γ_1 using eq. (6) if the value of $V/(I_p^{1/3}d)$ at $1/V = 0$ can be accurately determined. The method has an advantage that the value of γ_1 can be determined independently of elastic constants.

Calculated plots of $V/(I_p^{1/3}d)$ versus $1/V$ as a parameter of A_{stab} are shown in Fig. 6. The values of parameters used in the calculation are listed in Table II. It should be noted that the relationship of $V/(I_p^{1/3}d)$ versus $1/V$ becomes nonlinear with the increase in A_{stab}. In real experiments, it becomes difficult to separate accurately the peak value of displacement current because of the increase in charging current in the high voltage range and the decrease in S/N ratio for the displacement current in the low voltage range. Thus, we can obtain an accurate value of I_p only in the limited range of applied voltage V from about 15 to 25 V. This means that to obtain the intersection with the vertical axis of the $V/(I_p^{1/3}d)$ versus $1/V$ relation, it is necessary to extrapolate the curve in the range of $0.040 \leq 1/V \leq 0.067$ to $1/V = 0$. For the reason mentioned above, the values of the right side of eq. (5) obtained by extrapolation tend to become lower than the valid value as can be seen from the dotted line in Fig. 6 for $A_{stab} = 10\,J/m^3$. The value of γ_1 obtained from this figure is 295 mPa·s for $A_{stab} = 10\,J/m^3$. The value is smaller by only 1.36% than 299 mPa·s for $A_{stab} = 0\,J/m^3$. This means that A_{stab} is smaller than $10\,J/m^3$, the value of γ_1 can be estimated with sufficient accuracy by using the transient displacement current method.

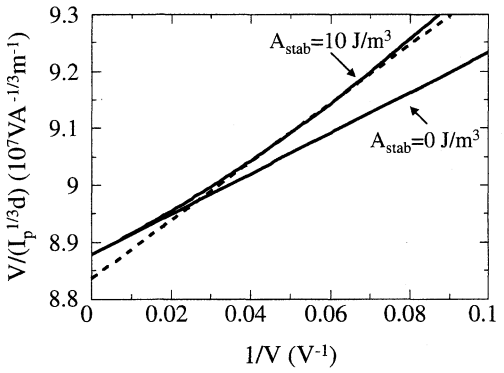

Fig. 6. Calculated results for the relationship between $V/(I_p^{1/3}d)$ and $1/V$ as a parameter of A_{stab}. The dotted line is extrapolated from solid line at $A_{stab} = 10\,J/m^3$ in the range of $0.040 \leq 1/V \leq 0.067$.

Table II. Values of parameters used in calculation for determining the relationship between $V/(I_p^{1/3}d)$ and $1/V$ as a parameter of A_{stab}.

S (mm^2)	144
d (μm)	5.9
θ_0 (deg)	0
β	0.4
ε_p	12.5
ε_n	3.8
γ_1 (mPa·s)	299

4.2 *Experimental results and discussion*

Sample cells were made using the LC mixture ZLI-2293, and a reactive mesogen RMM34, which is a mixture of diacrylate and monoacrylate and a small amount (1–5 wt %) of photoinitiator, all supplied by Merck. The reactive mesogen RMM34 was added to the NLC mixture ZLI-

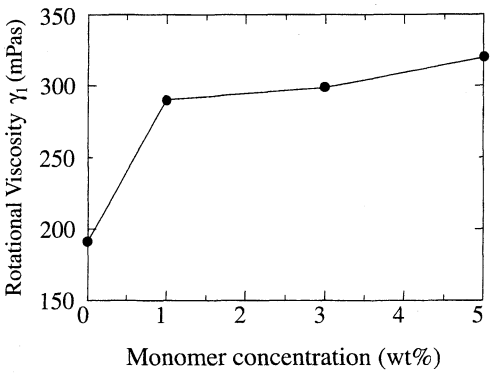

Fig. 7. Experimental results for the dependence of rotational viscosity γ_1 on the monomer concentration.

2293 in the range of 1 to 5 wt %. The final mixture was filled into about-6-μm-gap LC cells with tilted alignment produced by the antiparallel rubbing of polyimide coating PI-A (Nissan Chemical Industry) on both plates. Polymerization was induced by exposure to an ultraviolet light source of approximately 2.0 mW/cm^2 power density, centered around $\lambda = 365$ nm (black light) for an irradiation energy density of $E_{UV} = 10$ J/cm^2 with no applied voltage.

The dependence of rotational viscosity on monomer concentration is shown in Fig. 7. The rotational viscosity increased with monomer concentration.

Taking into account the increase in rotational viscosity caused by polymerization, numerical calculations for the transient response times were carried out. The applied voltage dependences of rise and decay times are shown in Figs. 8(a) and 8(b). For the case of the PSB cell, these calculations were carried out under the conditions of $V_{stab} = 10$ V and $A_{stab} = 6.0$ J/m^3 with F_{stab}. On the other hand, in the case of the NSB-cell, calculations were carried out under the condition of $A_{stab} = 0$ J/m^3. The parameters of the LC used in the calculation for the NPSB cell are listed in Table I. The parameter for the PSB cell are listed in Table III. The rotational viscosities used in the calculations are $\gamma_1 = 191$ mPa·s in the NPSB cell, and $\gamma_1 = 299$ mPa·s in the PSB cell, as obtained from Fig. 7. Since the rotational viscosity γ_1 is related with the Leslie viscosities α_2 and α_3 as $\gamma_1 = \alpha_3 - \alpha_2$, the values of α_2, α_3, α_5, and α_6 in Table III were determined by fitting the calculated results to the experimental results for the transient response characteristics of the PSB cell under the condition of constant γ_1 and the Parodi relation as $\alpha_2 + \alpha_3 = \alpha_6 - \alpha_5$.

In Fig. 7, we confirmed experimentally that the rotational viscosity γ_1 of LC increases by about 50% due to the polymer stabilization treatment at a monomer concentration of 3 wt %. As can be seen from Fig. 3, the rate of deterioration of transient response times exceeds about 100%. Thus, the deterioration of transient response cannot be explained in terms of only the increase in γ_1. From our calculated results shown in Fig. 8, it was clarified that the changes in Leslie viscosities including α_2, α_3, α_5, and α_6 caused by polymer stabilization result in changes in the flow velocity pattern and corresponding changes in the flow pattern, in addition to the increase in γ_1, deteriorates the transient response characteristics of the PSB cell. Calculated results for flow patterns in a NPSB cell and a PSB cell are shown in Fig. 9. Figure 9(a) represents flow patterns at turn-on when the applied voltage is switched from 3 to 4 V. Figure 9(b) represents those at turn-off when switching from 4 to 3 V.

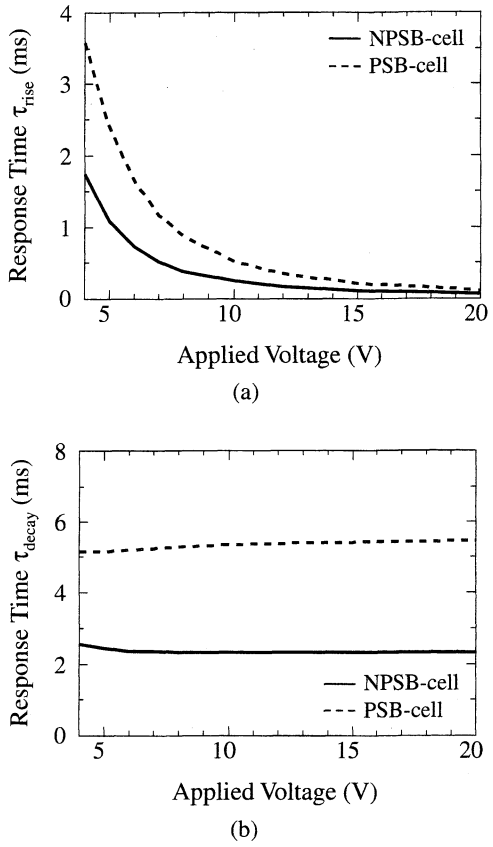

Fig. 8. Calculated results for the applied voltage dependence of transient response characteristics for NPSB cell and PSB cell which taking account of the increase in rotational viscosity caused by polymerization: (a) response time τ_{rise} when the voltage is switched from 3 V to some voltages higher than 3 V and (b) response time τ_{decay} when the voltage is switched from some voltages higher than 3 to 3 V.

Table III. Cell and LC material parameters used in calculations, taking account of F_{stab} as the effect of polymer stabilization in addition to the variation in Leslie viscosities with the increase in rotational viscosity caused by polymerization.

Cell thickness (μm)	6	α_1 (mPa·s)	0
Pretilt angle (deg)	5	α_2 (mPa·s)	−187.6
K_{11} (pN)	12.5	α_3 (mPa·s)	111.4
K_{22} (pN)	5	α_4 (mPa·s)	109.6
K_{33} (pN)	23	α_5 (mPa·s)	32.8
ε_p	12.5	α_6 (mPa·s)	−43.4
ε_n	3.8		

It has been well known that the high-response speed characteristics of the NPSB cell appear owing to the flow effect. Therefore, it can be thought that the decrease in flow effect caused by polymerization results in the deterioration of transient response characteristics in the PSB cell.

5. Conclusions

The effects of polymerization on the transient response characteristics of the bend configuration of molecular orientation in a pi-cell were investigated both experimentally and theoretically. It was shown experimentally that the transient response characteristics of the PSB cell are deteriorated by polymer stabilization. The deterioration of transient response

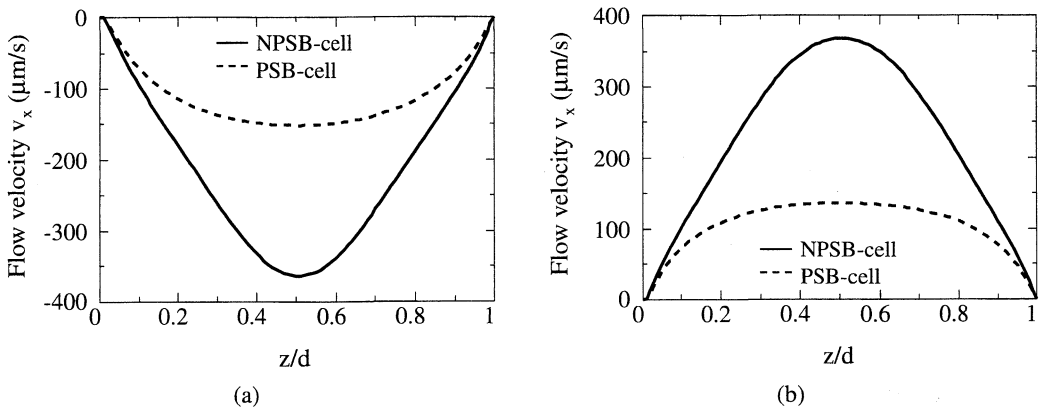

Fig. 9. Calculated results for the flow patterns of the NPSB cell and the PSB cell. These calculations were carried out taking account of the increase in rotational viscosity caused by polymerization. For the case of the PSB cell, calculations were carried out under the conditions of $V_{stab} = 10\,V$ and $A_{stab} = 6.0\,J/m^3$: (a) flow patterns that appeared in the x direction when the voltage was switched from 3 to 4 V, and (b) when the voltage was switched from 3 to 4 V.

cannot be explained in terms of only the effect of the polymer stabilization term introduced in the expression for free energy density as an additional term. It was clarified that the changes in Leslie viscosities including α_2, α_3, α_5, and α_6 caused by polymer stabilization result in changes in the flow velocity pattern and corresponding changes in the flow pattern, in addition to an increase in γ_1, deteriorates the transient response characteristics of the PSB cell.

Acknowledgements

We would like to express our most sincere thanks to Dr. Nakanowatari of Merck for his kind support in supplying UV-curable liquid crystalline monomers.

This work was supported by a Grant-in-Aid for Scientific Research on High Technology from the Ministry of Education, Culture, Sports, Science and Technology.

Appendix A: Equations Used in the Calculation

We solved the momentum equations that describe flow with respect to five components n_x, n_y, n_z, v_x, and v_z. For the LC bulk

$$\frac{\partial}{\partial z}\frac{\partial F}{\partial n_{x,z}} - \frac{\partial F}{\partial n_x} - \gamma_1\left(\frac{\partial n_x}{\partial t} - \frac{1}{2}\frac{\partial v_x}{\partial z}n_z\right) - \gamma_2\frac{1}{2}\frac{\partial v_x}{\partial z}n_z + \lambda_L n_x = 0, \tag{A·1}$$

$$\frac{\partial}{\partial z}\frac{\partial F}{\partial n_{y,z}} - \frac{\partial F}{\partial n_y} - \gamma_1\left(\frac{\partial n_y}{\partial t} - \frac{1}{2}\frac{\partial v_y}{\partial z}n_z\right) - \gamma_2\frac{1}{2}\frac{\partial v_y}{\partial z}n_z + \lambda_L n_y = 0, \tag{A·2}$$

$$n_x^2 + n_y^2 + n_z^2 = 1. \tag{A·3}$$

The stress equations are

$$\sigma_{zx} = \alpha_2\dot{n}_x n_z + \alpha_3\dot{n}_z n_x + \left(\alpha_1 n_x n_y n_z^2 + \frac{1}{2}\alpha_3 n_x n_y + \frac{1}{2}\alpha_6 n_x n_y\right)\frac{\partial v_y}{\partial z} + \frac{1}{2}(2\alpha_1 n_x^2 n_z^2 - \alpha_2 n_z^2 + \alpha_3 n_x^2 + \alpha_4 + \alpha_5 n_z^2 + \alpha_6 n_x^2)\frac{\partial v_x}{\partial z}, \tag{A·4}$$

$$\sigma_{zy} = \alpha_2\dot{n}_y n_z + \alpha_3\dot{n}_z n_y + \left(\alpha_1 n_x n_y n_z^2 + \frac{1}{2}\alpha_3 n_x n_y + \frac{1}{2}\alpha_6 n_x n_y\right)\frac{\partial v_x}{\partial z} + \frac{1}{2}(2\alpha_1 n_y^2 n_z^2 - \alpha_2 n_z^2 + \alpha_3 n_y^2 + \alpha_4 + \alpha_5 n_z^2 + \alpha_6 n_y^2)\frac{\partial v_y}{\partial z}, \tag{A·5}$$

where γ_1 is the rotational viscous coefficient, γ_2 is the twist coefficient on the velocity gradient, λ_L is a Lagrange multiplier, and α_i represents the Leslie viscosities.

The flow effect is ignored on the surfaces. For the surfaces at $z = 0$,

$$\frac{\partial F^s(0)}{\partial n_x(0)} - \left.\frac{\partial F}{\partial(\partial_z n_x)}\right|_{z=0} + \frac{\partial D^s(0)}{\partial \dot{n}_x(0)} = 0, \tag{A·6}$$

$$\frac{\partial F^s(0)}{\partial n_y(0)} - \left.\frac{\partial F}{\partial(\partial_z n_y)}\right|_{z=0} + \frac{\partial D^s(0)}{\partial \dot{n}_y(0)} = 0, \tag{A·7}$$

$$n_x(0)^2 + n_y(0)^2 + n_z(0)^2 = 1. \tag{A·8}$$

For the surface at $z = d$

$$\frac{\partial F^s(d)}{\partial n_x(d)} - \left.\frac{\partial F}{\partial(\partial_z n_x)}\right|_{z=d} + \frac{\partial D^s(d)}{\partial \dot{n}_x(d)} = 0, \tag{A·9}$$

$$\frac{\partial F^s(d)}{\partial n_y(d)} - \left.\frac{\partial F}{\partial(\partial_z n_y)}\right|_{z=d} + \frac{\partial D^s(d)}{\partial \dot{n}_y(d)} = 0, \tag{A·10}$$

$$n_x(d)^2 + n_y(d)^2 + n_z(d)^2 = 1, \tag{A·11}$$

where $D^S(0)$ and $D^S(d)$ are the surface dissipation functions at $z = 0$ and $z = d$, respectively.

The Lagrange multiplier is determined using

$$\lambda_{\mathrm{L}} = -\sum_i n_i \left[\frac{\partial F}{\partial n_i} - \partial_z \frac{\partial F}{\partial(\partial_z n_i)} - \frac{\partial D}{\partial \dot{n}_i} \right]. \quad \text{(A·12)}$$

The notation $\sum_i$ means the sum with respect to x, y, and z.

The surface dissipation function is determined by

$$D^{\mathrm{S}}(l) = \frac{1}{2}\alpha_p^{\mathrm{S}}(n_l \cdot n(l))^2 \dot{n}(l)^2 + \frac{1}{2}\alpha_n^{\mathrm{S}}(n_l \cdot \dot{n}(l))^2 + \frac{1}{2}\alpha_{\mathrm{mix}}^{\mathrm{S}}(n_l \cdot \dot{n}(l))^2 (n_l \cdot n(l))^2, \quad \text{(A·13)}$$

where α_p^{S} is the parallel viscosity, α_n^{S} the perpendicular viscosity, $\alpha_{\mathrm{mix}}^{\mathrm{S}}$ is the mixed viscosity, and n_l is the preferred surface orientation.

Appendix B: Influence of Polymer Stabilization on the Transient Displacement Current

We consider the one-dimensional distortion of the director along the z-axis, which is defined as the direction normal to the substrate surface. In our geometry, the distorted angle, θ, measured from a plane parallel to the substrate surface, is a function of z and hence the director is expressed as $\boldsymbol{n} = (\cos\theta, 0, \sin\theta)$.

The free energy density, f, is given by

$$f = \frac{1}{2}K_{11}(1 + k\sin^2\theta)\left(\frac{\partial\theta}{\partial z}\right)^2 + \frac{1}{2}A_{\mathrm{stab}}\sin^2(\theta - \theta_0), \quad \text{(B·1)}$$

where the first and second terms are the contribution from the elastic free energy and the polymer stabilization energy density described in §3, respectively. K_{11} is the splay elastic constant and $k = (K_{33} - K_{11})/K_{11}$, where K_{33} is the bend elastic constant. A_{stab} is the polymer stabilized coefficient and θ_0 is the pretilt angle on the substrate surfaces. We assumed that polymer stabilization treatment was carried out under the condition of no voltage application. When the coupling between orientation and flow can be neglected, the dynamic motion of the director is expressed by the torque balance equation

$$\gamma_1 \frac{\partial\theta}{\partial t} = K_{11}(1 + k\sin^2\theta)\left(\frac{\partial^2\theta}{\partial z^2}\right) + \frac{1}{2}K_{11}k\sin 2\theta\left(\frac{\partial\theta}{\partial z}\right)^2 - \frac{1}{2}A_{\mathrm{stab}}\sin 2(\theta - \theta_0) + \frac{1}{2}\varepsilon_0\Delta\varepsilon E_z^2\sin 2\theta, \quad \text{(B·2)}$$

where ε_0 is the vacuum dielectric constant and $\Delta\varepsilon = \varepsilon_p - \varepsilon_n$, where ε_p and ε_n are the relative dielectric constants parallel and perpendicular to the director, respectively. E_z is the z component of the electric field.

In a transient response of the director to a step voltage application, the director distribution is assumed to be uniform in the bulk region except in the vicinity of the boundary layer. That is, it is assumed that $\partial\theta/\partial z = 0$ and $\partial^2\theta/\partial z^2 = 0$ in the bulk region. Then one obtains

$$\gamma_1 \frac{\partial\theta}{\partial t} = \frac{1}{2}\varepsilon_0\Delta\varepsilon E_{\mathrm{b}}^2 \sqrt{\left(1 - \frac{A_{\mathrm{stab}}}{\varepsilon_0\Delta\varepsilon E_{\mathrm{b}}^2}\cos 2\theta_0\right)^2 + \left(\frac{A_{\mathrm{stab}}}{\varepsilon_0\Delta\varepsilon E_{\mathrm{b}}^2}\sin 2\theta_0\right)^2}\,\sin(2\theta + \theta'), \quad \text{(B·3)}$$

where

$$\theta' = \tan^{-1}\left(\frac{A_{\mathrm{stab}}\sin 2\theta_0}{\varepsilon_0\Delta\varepsilon E_{\mathrm{b}}^2 - A_{\mathrm{stab}}\cos 2\theta_0}\right), \quad \text{(B·4)}$$

$$\theta = \tan^{-1}\left[\tan\left(\theta_0 + \frac{\theta'}{2}\right)\exp\left(\frac{\varepsilon_0\Delta\varepsilon E_{\mathrm{b}}^2\sqrt{\left(1 - \frac{A_{\mathrm{stab}}}{\varepsilon_0\Delta\varepsilon E_{\mathrm{b}}^2}\cos 2\theta_0\right)^2 + \left(\frac{A_{\mathrm{stab}}}{\varepsilon_0\Delta\varepsilon E_{\mathrm{b}}^2}\sin 2\theta_0\right)^2}}{\gamma_1}t\right)\right] - \frac{\theta'}{2}. \quad \text{(B·5)}$$

1) T. Miyashita, Y. Yamaguchi, and T. Uchida: Jpn. J. Appl. Phys. **34** (1995) 177.
2) S. Saito, Y. Shirakura, and M. Kamihara: Trans. IEICE Electron. **E63-C** (1980) 32.
3) M. Xu, D.-K. Yang, J. Bos, X. Jin, F. W. Harris, and S. Z. D. Cheng: SID Int. Symp. Dig. Tech. Pap. **29** (1998) 139.
4) X.-D. Mi, M. Xu, D.-K. Yang, and P. J. Bos: SID Int. Symp. Dig. Tech. Pap. **30** (1999) 24.
5) T. Konno, T. Miyashita, and T. Uchida: Asia Display '95, 1995, p. 581.
6) S. H. Kim and L. C. Chien: Jpn. J. Appl. Phys. **43** (2004) 7643.
7) H. Kikuchi, H. Yamamoto, H. Sato, M. Kawakita, K. Takizawa, and H. Fujikake: Jpn. J. Appl. Phys. **44** (2005) 981.
8) P. J. Bos and J. A. Rahman: SID Int. Symp. Dig. Tech. Pap., 1993, p. 273.
9) M. Kamio, M. Nanaumi, T. Takahashi, and S. Saito: Proc. 11th Int. Display Workshop, 2004, p. 219.
10) T. Takahashi, T. Umeda, H. Furue, and S. Kobayashi: Jpn. J. Appl. Phys. **38** (1999) 5991.
11) Y. Asakawa, K. Yokota, M. Nanaumi, N. Takatuka, T. Takahashi, and S. Saito: Jpn. J. Appl. Phys. **45** (2006) 5878.
12) Y. Funatsu, T. Miyashita, T. Ishinabe, and T. Uchida: Proc. 10th Int. Display Workshop, 2003, p. 69.
13) I. C. Khoo and S. T. Wu: *Optics and Nonlinear Optics of Liquid Crystals* (World Scientific, Singapore, 1993) p. 183.
14) M. Imai, H. Naito, M. Okuda, and A. Sugimura: Jpn. J. Appl. Phys. **33** (1994) L119.